AIT Series

Trends in earth observation

Volume 2

Planet Care from Space

Edited by Dessena M.A., Melis M.T and Rossi P.

Planet Care from Space

Edited by

Maria Antonietta Dessena, Maria Teresa Melis and Patrizia Rossi

AIT Series: Trends in earth observation

Volume 2 - Published in September 2021
Edited by Maria Antonietta Dessena, Maria Teresa Melis and Patrizia Rossi
Published on behalf of the Associazione Italiana di Telerilevamento (AIT)
Via Lucca 50
50142 Firenze, Italy

ISSN 2612-7148
ISBN 978-88-944687-0-0
DOI: 10.978.88944687/00

All contributions published in the Volume "Planet Care from Space" were subject to blind peer review from independent reviewers.

Publication Ethics and Publication Malpractice Statement
Editors, Reviewers and Authors agreed with Publication Ethics and Publication Malpractice Statement

Preface

The 10th International Conference "Planet Care from Space", set as a virtual event in Cagliari, Sardinia, is the natural continuation of the AIT mission to achieve a wider diffusion of Remote Sensing technologies, techniques, and culture, after the Palermo and Firenze events in 2016 and 2018 respectively.
We are therefore proud, after the 2020 halt due to Covid-19, to introduce a new Volume of the Series of "Trends in Earth Observation", focused on Geo-Envi-Hazards and Climate Change investigations, but including the complete range of EO state-of-the-art and its applications.

AIT is continuing to collaborate with the Copernicus world, ASITA, EARSeL, EARSC, ISPRS, Universities and private and public Agencies to provide its partners with the widest dynamic, scientific and operational information, always with a synoptic and integrated point of view.

During the last decades, EO has gone through various cultural steps.
When our association was born (between 1986 and the early '90s) the questions we received, the most were about what we could actually do with RS. A long, often completely theoretical list, was the most common answer. Then, EO was gradually seen as the solution for any territorial problem, namely through EO algorithms or classifications that were suitable for the needs of the user. Furthermore, our technology has recently been considered an important component of several Artificial Intelligence procedures, especially analytic processes through big data treatments.

Nowadays, the social situation created by the pandemic and the increasingly dire and visible effects of climate changes are generating a new political and social awareness, (such as the various worldwide national plans of recovery and resilience, like the one of the EU) which is bringing forth to us, scientists, operators, administrators, and simple citizens the awareness of the real priorities of protecting and safeguard the health of the planet and the continuation of the life of the human species.

So, dear colleagues, this is the core of our mission: to offer powerful tools to anyone who senses the need to protect and safeguard the biosphere and the human lives, indicating sustainable exploitations through synoptic, georeferenced and accessible "consolidated applications".
Our duty will be to collect, show, map, measure and calculate any dangerous or "hidden situations" that are unsustainable in any natural, semi-natural and human areas and activities.

The diffusion of this volume to others than our usual community, such as politicians, managers and decision-makers could help to speed-up the achievements of this new Earth Observation service position.
Special thanks to the Conference organization: Maria Teresa Melis and Maria Antonietta Dessena who spent their effort with passion and successful, the entire AIT Board and all the friends who have contributed to this result.

AIT President
Livio Rossi

Contents

Introduction

Planet Care from Space

Dessena M.A., Melis M.T., Rossi P.

This papers' collection represents the 2nd volume of the series "Trends in Earth Observation", born on the occasion of the IX AIT International Conference promoted by the Italian Association of Remote Sensing, that took place in 2018 in Florence.
In this volume several international experiences, coming from researcher groups and companies are collected. The theme is strategic and intentionally provocative: what is the Earth health state, how is the world moving in the analysis of critical issues, how much is the cost of the climate crisis, and which economic damage does it cause? Extreme events such as droughts, fires, heat waves and storms can cause long-term economic damage, due to their impact on health, savings and labour productivity. In particular, limiting the growth of the global average temperature on the surface of the oceans and land to a maximum of 2 degrees Celsius, compared to pre-industrial levels, by the end of the century, "would allow the whole world to save 54 trillion dollars".
Soon, Incheon-Songdo, South Korea, will be the location of "negotiations related to the drafting by the IPCC (Intergovernmental Group on Climate Change) of its Special Report 15 (SR15). An intermediate - but crucial – report, in view of the realization of the 6th report, which is expected to be published in 2022".
Measures connected to a deep knowledge and monitoring of Earth phenomena, due to climate changes, are expected to be use by all countries. Remote Sensing data, and the promoted dedicated services by the spatial agencies play a crucial role in this topic.
In this Volume, 45 papers are divided into 7 main topics. They are grouped by different themes of analysis of the state of "Health of the Earth", both in the continental and marine context, using different sensors and dedicated tools. Modern remote sensing data acquisition systems are illustrated both in the public and in the private sector, and by those who manage the space through missions and the development of cutting-edge vectors.
The first chapter "Forest fires: new tools for an old threat" focuses attention on a sadly current topic: fires, their identification, delimitation and monitoring in different European countries.
The second chapter "Geohazards, Earth and Planetary geological mapping" analyzes various problems of geological, geomorphological and hydrogeological risk in mining, volcanic, marine areas; moreover, a methodological geological planet study is proposed.
The third chapter "Marine Remote Sensing and Coastal Hazard" concerns numerous applications in the marine environment ,as demonstrated by contributions focused on coastal erosion, in terms of human impact and monitoring systems for coastal risk recognition.
The fourth chapter "Monitoring Forest health" is focused on monitoring health state of forests, using different strategy analysis, even outside Europe.
The fifth chapter "New Remote Sensing tools in precision farming" shows different applications of use of the Sentinel2 satellite to estimate the growth state of some crops and the variables that allow their recognition.
The sixth chapter "Urban Health from Space: actual and past scenarios" shows varied experiences ranging, from the recognition of prehistoric and historical structures, to urban dynamics linked to the presence of greenery.
Finally, the seventh chapter "Recent advancement in Remote Sensing Technologies" ranges through multisensor approaches, from satellite to aircraft and UAVs, showing new application tools for Earth observation.
The editors thank all those who collaborated and shared the enthusiasm of the authors of the papers and of all the participants in the X International Conference AIT, who wanted to participate in this "online" experience born of an important international emergency, but which did not stop the scholars, and all experts of remote sensing who care about the health of the Earth in all its manifestations.

Forest fires: new tools for an old threat

DETECTION AND CHARACTERIZATION OF FOREST FIRE USING SENTINEL-1 CROSS-RATIO TIME SERIES DECOMPOSITION APPROACH. PRELIMINARY RESULTS ABOUT THE SUSA FIRE OF AUTUMN 2017

S. De Petris *, F. Sarvia , E. Borgogno-Mondino

DISAFA, Departemnt of Agriculture,Forest and Food Sciences of Torino University, L.go Braccini 2, Grugliasco 10095, Italy
(samuele.depetris, filippo.sarvia, enrico.borgogno)@unito.it

KEY WORDS: Forest Fire, Sentinel-1, SAR, Time Series Decomposition, Fire Severity, Fire Detection

ABSTRACT:

Forest Fire detection and monitoring is a key concept for addressing post-fire management decisions. Many approaches based on multitemporal analysis of optical-retrieved vegetation index time series were successfully applied to describe forest disturbances like forest fires; conversely, only few works make use of multitemporal Synthetic Aperture Radar (SAR) data. The European Sentinel-1 mission can provide SAR data with high temporal resolution making possible to improve vegetation monitoring. In this work, a multitemporal approach was used, based on Sentinel-1 cross-ratio polarimetric index time series directly calculated on Google Earth Engine platform, to detect forest burned areas and characterize their ecological response in the period 2015-2019. Some statistical-based approaches were applied on very small, but reliable, areas producing promising results that are expected to better focus future researches in forest fire severity characterization.

1. INTRODUCTION

The assessment of forest fire effects is a key concept for addressing post-fire management decisions (e.g. reforestation, salvage logging or natural development). Fire changes landscape and causes an economical value loss related to damaged trees. A precise knowledge about fire-induced damages, in particular those affecting the canopy, is particularly important in mountain areas where forests often provide protection against other natural hazards (i.e. rainfall erosion, landslides, snow avalanches, rockfalls). Many approaches based on multitemporal analysis of optical-retrieved vegetation index time series were successfully applied to describe forest disturbances like forest fires (De Petris et al., 2020); conversely, only few works make use of multitemporal Synthetic Aperture Radar (SAR) data. The European Sentinel-1 (S1) mission can provide SAR data with high temporal resolution making possible to improve vegetation monitoring (De Petris et al., 2021). In this work, a multitemporal approach was used, based on time series data directly processed in Google Earth Engine platform (GEE) to map the cross ratio polarimetric index; forest burned areas detection and characterization of their ecological response were at the basis of this work. The approach relies on some statistical-based concerns applied, for the period 2015-2019, on very small, but reliable, areas. Results were promising and are expected to better focus future research activities.

2. METRIALS AND METHODS

2.1 Study area

The area of interest (AOI) is located on Susa Valley (Italian Western Alps) that was interested by a great wildfire at the end of October 2017. To explore fire effects over forest canopy two sample areas affected by forest fire were selected (Fig 1): one (hereinafter called HS), sizing 3.17 ha, was characterized by high severity; the other (hereinafter called LS), sizing 2.73 ha, was characterized by a very low severity. The areas borders were obtained as a polygon vector layer by photointerpretation of a true-colour orthomosaic having a geometric resolution of 0.1 m derived by an aerial photogrammetric survey performed few days after the fire stop and deeply discussed in (De Petris et al., 2020). Both forest areas are characterized by dominance of scot pine stands having the same tree density.

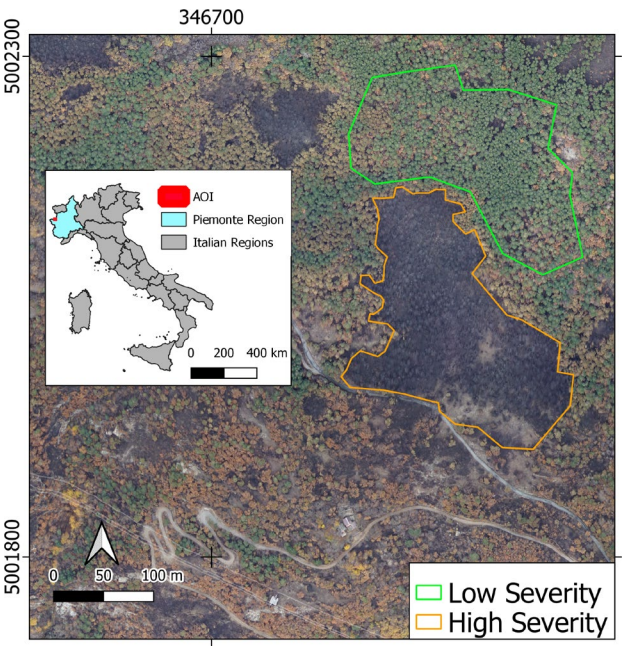

Figure 1. AOI location; high and low severity areas. Reference frame is WGS84 UTM32N.

* Corresponding author

2.2 Available data

Several authors have highlighted that the complexity of SAR data pre-processing is one of the main reasons for its slow uptake by a wider user community, especially while exploratory analysis have to be performed to assess the feasibility of a given experimental method (Vollrath et al., 2020). From this point of view, the Google Earth Engine (GEE) web-based platform allows an immediate access to image collections making users able to directly focus on the expected information (Gorelick et al., 2017). For this work, Copernicus Sentinel 1 (S1) ground range detected (GRD) IW (Interferometric Wide swath) image collection was used. S1 GRD products consist of focused, detected, multi-looked SAR data geocoded using range-doppler terrain correction based on the 30 m gridded SRTM (Shuttle Radar Topography Mission) DEM (Digital Elevation Model). The S1 GRD product has an approximately squared pixel sizing about 10 m, projected into an appropriate reference system (WGS84 UTM32N for this work). Both VV and VH polarizations (provided already calibrated in σ^0 [dB] values) were used from 218 ascending S1 images (relative orbit number = 161) covering the period 1st November 2015 - 30th November 2019.

2.3 Data Processing

In order to reduce speckle, VV and VH images were monthly averaged at-pixel level (about 5 images per month) generating a time series of 49 images. This type of despeckle was adopted to avoid ordinary local smoothing algorithms that could possibly compromise detection of small disturbed patches (Mermoz and Le Toan, 2016). Then the Cross-ratio index (CR) was calculated in GEE as the ratio between σ^0_{VH} (backscattered power in H polarization) and σ^0_{VV} (backscattered power in V polarization) (Mandal et al., 2020; Vreugdenhil et al., 2018). CR values tend to 0 for highly depolarizing vegetation (high density canopy) and decreases while canopy density reduces. CR can be used to coarsely separate volume and surface scattering mechanisms. Minchella et al. (2009) proved that, over burnt areas, volume backscattering significantly decreases being replaced by surface backscattering. For this work, a time series of 49 CR mapped were used. Local pixel values were averaged within the two available polygons (high and low severity burnt areas) to generate the correspondent two CR temporal profiles (monthly time step), that were downloaded as *.csv* file that entered a processing step entirely achieved by *R vs. 3.6.3* (R Team, 2013). The non-parametric *Pettitt's test* (Pettitt, 1979) was performed to detect a significant single change-point along the two analysed time series, assuming that it could possibly related to the fire. Moreover, CR time series was decomposed applying the STL (Seasonal Trend Decomposition with LOESS) algorithm to separate the temporal signal into its three main components, namely: trend, seasonal and residual (Eckert et al., 2015; Forkel et al., 2013). In particular, the trend component was obtained using *LOESS* (locally estimated scatterplot smoothing) with time span= 0.2 and a 2nd order polynomial. The non-parametric *Mann-Kendall* trend test (McLeod 2005) was run to assess the significance of the two trends. In addition, CR time series was detrended and the resulting series analysed using the Fast Fourier Transform (FFT). The stronger harmonic was used to model the seasonal oscillation. The *Chi-squared* goodness-of-fit test was performed to test the likelihood of the modelled seasonal variation. The modelled seasonal component was further subtracted to the de-trended CR time series to obtain the residual component (noise). The *Shapiro-Wilk* test (Shapiro and Wilk, 1965) was used to assess the normality of residuals; the one-sample *t-test* (Ross and Willson 2017) was used to test the zero-mean condition of residuals (white noise) to ensure that all biases were somehow modelled in the previous steps (Kuo, 2018). The trend component was finally modelled by a 1st order polynomial, calibrated by Ordinary Least Squares, to facilitate the comparison of the two trends (high and low severity burnt areas). Significance of slope difference was tested by the *Warton-test* (Warton and Weber, 2002).

3. RESULTS AND DISCUSSIONS

Since vegetation volume is an important player in SAR signal depolarization, CR is expected to be a good predictor of canopy volume changes, included those from fires. To test this hypothesis, two CR time series from the available reference areas (HS and LS) were assessed. The non-parametric *Pettitt's test* was performed to detect a significant single breakpoint in each time series, possibly related to fire effects. A significant breakpoint located at October 2017 was found for HS ($U = 884$, $p < 0.001$); the same test failed for LS (October 2015, $U = 410$, $p > 0.05$). CR time series decomposition was performed applying *LOESS* and FFT algorithms in order to split the contribution of the three main signal components: trend, seasonal and residual (Fig 2).

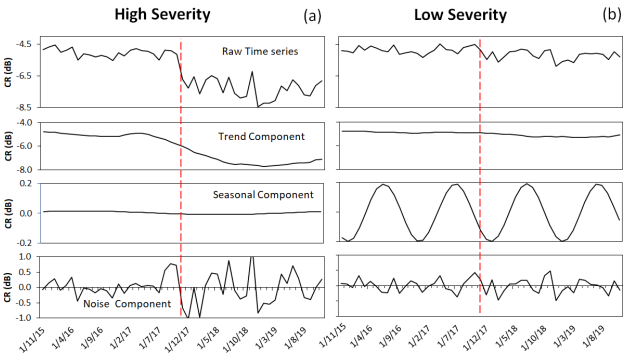

Figure 2. CR time series decomposition for high (a) and low (b) severity burnt areas.

Trend component was used to compare the degree of fire severity. The *Mann-Kendall* test showed that HS showed a significant decreasing trend ($S = -868$, $p < 0.001$), thus proving that tree crowns were drastically altered after the fire; differently, LS showed no significant trend ($S = -162$, $p = 0.3$) proving that fire did not significantly changed forest canopy. The FFT-based analysis of the de-trended CR time series showed that a significant seasonal component was present for LS as demonstrated by the Chi-squared goodness-of-fit test ($\chi^2 = 2.409$, $p < 0.001$), suggesting the presence of 4 phenological seasons (Fig 2b); conversely, HS did not show any significant seasonal component ($\chi^2 = 10.842$, $p = 0.999$). This can be interpreted admitting that high fire severity can completely alter the phenological behavior of the previous forest canopy, hindering the detection of the seasonal component. Nevertheless, both HS and LS showed significant trends as supported by *Mann-Kendall* test and noise component analysis. In particular, the *Shapiro-Wilk* test and one sample *t-test* proved that residuals of HS and LS CR time series were comparable to a white noise (Tab. 1) excluding the presence of eventual, not modelled, biases.

	High Severity	Low Severity
Shapiro-Wilk		
W	0.9722	0.9851
p-value	0.1863	0.6730
One sample *t-test*		
t	-0.0667	0.1264
p-value	0.9470	0.8998

Table 1. Statistical hypothesis tests performed on CR noise component.

To summarize these deductions into more operative tools a numerical index was introduced based on the computation of the 1st order polynomial regression of the CR signal trend component, making possible an immediate and easy comparison of the modelled dynamics. The slope value of regression was used for this purpose. It was found that the slope value for HS (*slope* = -0.047, p <0.001) was negative, statistically significant and smaller than the one computed for LS (*slope* = 0.0023, p = 0.2). The *Warton-test* was applied to compare these values proving that they were significantly different (F = 125.29, p < 0.001). Summarizing, all these results suggest that SAR cross-ratio time series appear to be able to detect the moment when medium-high severity fire occurs. Moreover, time series decomposition can support the definition of a new index (trend slope value) for forest disturbance detection and mid-terms severity assessment.

4. CONCLUSIONS

In this work, an approach for detecting and characterizing forest fire severity based on time series decomposition of CR using S1 data was proposed. Using the *Pettitt's test*, significant breakpoints related to the fire event were correctly detected. Moreover, trend, seasonal and noise components were extracted and some statistical tests performed to support the deductions derived by these preliminary results. Finally, the slope value of the linear regression describing the trend component of the CR temporal profile was used to summarize fire severity into a more operative parameter. Due to the very small size of the analysed areas, results could not certainly be generalized for the whole burnt area. Nevertheless, future experiences will be expected to apply such an approach at-pixel-level aiming at mapping fire boundaries and quantify fire severity.

REFERENCES

De Petris, S., Momo, E.J., Borgogno-Mondino, E., 2020. Supporting Assessment of Forest Burned Areas by Aerial Photogrammetry: The Susa Valley (NW Italy) Fires of Autumn 2017. Lecture Notes in Computer Science (including subseries Lecture Notes in Artificial Intelligence and Lecture Notes in Bioinformatics) 12252 LNCS, 829–844. https://doi.org/10.1007/978-3-030-58811-3_59

De Petris, S., Sarvia, F., Gullino, M., Tarantino, E., Borgogno-Mondino, E., 2021. Sentinel-1 Polarimetry to Map Apple Orchard Damage after a Storm. Remote Sensing 13, 1030. https://doi.org/10.3390/rs13051030

Eckert, S., Hüsler, F., Liniger, H., Hodel, E., 2015. Trend analysis of MODIS NDVI time series for detecting land degradation and regeneration in Mongolia. Journal of Arid Environments 113, 16–28.

Forkel, M., Carvalhais, N., Verbesselt, J., Mahecha, M.D., Neigh, C.S., Reichstein, M., 2013. Trend change detection in NDVI time series: Effects of inter-annual variability and methodology. Remote Sensing 5, 2113–2144.

Gorelick, N., Hancher, M., Dixon, M., Ilyushchenko, S., Thau, D., Moore, R., 2017. Google Earth Engine: Planetary-scale geospatial analysis for everyone. Remote Sensing of Environment, Big Remotely Sensed Data: tools, applications and experiences 202, 18–27. https://doi.org/10.1016/j.rse.2017.06.031

Kuo, H.-H., 2018. White noise distribution theory. CRC press.

Mandal, D., Kumar, V., Ratha, D., Dey, S., Bhattacharya, A., Lopez-Sanchez, J.M., McNairn, H., Rao, Y.S., 2020. Dual polarimetric radar vegetation index for crop growth monitoring using sentinel-1 SAR data. Remote Sensing of Environment 247, 111954.

Mermoz, S., Le Toan, T., 2016. Forest disturbances and regrowth assessment using ALOS PALSAR data from 2007 to 2010 in Vietnam, Cambodia and Lao PDR. Remote Sensing 8, 217.

Minchella, A., Del Frate, F., Capogna, F., Anselmi, S., Manes, F., 2009. Use of multitemporal SAR data for monitoring vegetation recovery of Mediterranean burned areas. Remote Sensing of Environment 113, 588–597.

Pettitt, A.N., 1979. A non-parametric approach to the change-point problem. Journal of the Royal Statistical Society: Series C (Applied Statistics) 28, 126–135.

Shapiro, S.S., Wilk, M.B., 1965. An analysis of variance test for normality (complete samples). Biometrika 52, 591–611.

Team, R.C., 2013. R: A language and environment for statistical computing.

Vollrath, A., Mullissa, A., Reiche, J., 2020. Angular-based radiometric slope correction for Sentinel-1 on google earth engine. Remote Sensing 12, 1867.

Vreugdenhil, M., Wagner, W., Bauer-Marschallinger, B., Pfeil, I., Teubner, I., Rüdiger, C., Strauss, P., 2018. Sensitivity of Sentinel-1 backscatter to vegetation dynamics: An Austrian case study. Remote Sensing 10, 1396.

Warton, D.I., Weber, N.C., 2002. Common slope tests for bivariate errors-in-variables models. Biometrical Journal: Journal of Mathematical Methods in Biosciences 44, 161–174.

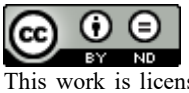

FOREST FIRE RISK ASSESSMENT IN THE GREEK ISLANDS OF CEPHALONIA AND ITHACA USING MULTICRITERIAL ANALYSIS OF SPATIAL DATA AND REMOTELY SENSED PRODUCTS

E. Panagiotidou [1], S. Kolios [1, 2, *]

[1] Open University of Cyprus, Faculty of Pure and Applied Sciences, 2220, Latsia, Nicosia, Cyprus - panagiotidouelena9@gmail.com
[2] National and Kapodistrian University of Athens, Department of Aerospace Science and Technology, 34400, Euboea, Greece – skolios@aerospace.uoa.gr

KEY WORDS: Ionian Islands, forest fire hazard, mapping, multicriterial analysis, remote sensing, Sentinel 2

ABSTRACT:

The study is an effort to map analytically fire hazard zones and assess the fire risk within Cephalonia and Ithaca islands (in western Greece), utilizing modern and reliable Sentinel 2 satellite multispectral imagery as well as several other related geospatial datasets. According to the extracted zonal statistics in relation to the natural factors, the "moderate" to "high" hazard of fire exists in areas with a predominant vegetation structure of sparse shrubs and trees, slopes ranging between 10-30% and aspect of land surfaces of mainly north to east or northwest orientation. Regarding anthropogenic factors, it appears that the zones of "moderate" to "very high" hazard are located at a distance of more than six hundred meters from the roads and more than three kilometres from the settlements. The final map of the potential fire risk areas, is a reliable informational background for updated strategical plans of forest fires in the Cephalonia and Ithaca islands, indicating areas, locations and routes for planning actions or establishment of appropriate infrastructure, aiming at early warning and decrease of the forest fires across the whole study area**.**

1. INTRODUCTION

The frequency of occurrence of forest fires is increasing globally with significant impacts on the natural environmental and human lives. The forest fires have several adverse ecological impacts (Zhang et al. 2016),causing massive losses of lives and properties (Russell-Smith et al. 2007; Bowman et al. 2009). Satellite data can help detect forest fires in different land use (e.g. Justice et al. 2006) while GIS (Geographical Information System) and remote sensing techniques have been used widely to assess and predict fire frequency (e.g. Giglio et al. 2006; Abedi Gheshlaghi et al. 2020). The fire regimes are intended to increase due to the changing climate, with several studies reporting an increasing number of fires, burnt regimes, and intensity of future fires events (e.g. Hurteau et al., 2014; Rocca et al. 2014; Riley et al. 2016).

The accurate detection of the spatial patterns of areas with high potential in fires occurrence is essential in disaster risk management, however, this aspect is often neglected (e.g. Middendorp et al. 2013). The detection of fire risk zones is a key-point for protection and risk management (Jaiswal et al. 2002; Erten et al. 2004). Fire-risk maps are widely developed in many countries using many different data and methods. The modern multispectral remote sensing data coming from satellites like Landsat 8 and Sentinel 2 can support accurate and up-to-date fire risk zones, operating as an early warning component. The study aims to develop an analytic map of forest fire risk in the island complex of the Ionian Sea (Greek islands of Cephalonia and Ithaca) using multicriterial analysis (e.g. Odu, 2019) of different remote sensing products and other spatial data to contribute as a guide for an optimal fire risk assessment. The novelty of this study concerns the combined use of different high-resolution data in order to create an updated fire risk map in areas with important biodiversity and increasing tourism activity (study doamin). Moreover, such detailed analysis focused exclusively in the study area has never done before. Similar studies concern greater areas and were used datasets of a coarser resolution than the data used in this study.

2. DATA AND METHODS

For the scope of the study, many different datasets were used, and their relative parameters of interest were extracted (Table 1).

Parameter	Dataset
Slope Aspect	SRTM Digital Elevation Model (DEM)
Coastline	GeoData (official data from the Greek Ministry of Environment)
Urban fabric Forested areas Reforested areas	Forest map (official data from the Greek Ministry of Environment)
Road network	GeoData (official data from the Greek Ministry of Environment)
Land use/land cover Satellite data	Multispectral Sentinel 2 and CORINE 2018

Table 1. Data and parameters were used in the study.

More specifically, the slope and aspect were extracted from the Shuttle Radar Topography Mission (SRTM) Digital Elevation

* Corresponding author

Model (DEM) with spatial resolution of 30 m. The coastline and the road network of the study area are open data retrieved from the official platform of the Greek Ministry of Environment. The urban fabric as well as the forested/reforested areas were extracted from the official forest maps of the Greek Ministry of Environment. Finally, the land use/land cover data (year: 2018) from CORINE service (https://land.copernicus.eu/) were used as training data to classify a recent multispectral image scene of Sentinel 2 (acquisition date: 17/08/2019) and to create an updated thematic map of the vegetation types over the whole study area. The bands 4-8 as well as the bands 11 and 12 of the Sentinel 2 were used for the supervised classification of the selected image scene to conclude to the optimal detection of vegetation – forest fuel types. Figure 1 illustrates the schematic flowchart of the procedures were followed to calculate the forest fire risk assessment map of the study area. At this point it is noted that in the classification process, the supervised approach using the "maximum likelihood" classifier was chosen because of its efficient accuracy (e.g. Kolios and Stylios, 2013). Then, a multicriterial analysis was conducted to conclude to the different levels of fire risk (five different fire risk levels were defined). The Simple Additive Weighting (SAW) technique was applied during the multicriterial analysis through the combined use of QGIS and ArcGIS software packages. More specifically, for each different dataset was used in the study (Table 1), five fire risk levels ("very low", "low", "medium", "high" and "vey high") were linked with them at pixel basis. The link was done through the reclassification process and according to their role and their physical relation with the fire risk. Then, a unique weight coefficient (0-100%) was linked with every used parameter according to its importance in the forest fire risk (Table 2). As mentioned before, the forest maps of the Greek Ministry of Environment, the CORINE dataset and the satellite image scene were used during the data pre-processing in order to construct a detailed and representative vegetation - fuel type data layer. This dataset was used as a final parameter in the multicriterial analysis (Table 2).

Final parameter	Weight coefficient (%)
Vegetation - fuel type	40
Slope	20
Aspect	20
Urban fabric	10
Road network	10

Table 2. Final parameters were used in the multicriterial analysis along with their weight coefficients (based on their importance in the fire risk).

The final (normalized) weight coefficient for every parameter was calculated according to the principles of the SAW technique and the reclassified data multiplied with the relative final weight coefficient. The sum of all the datasets in pixel basis define the final forest risk levels (fire hazard zones).
A characteristic example for this methodological step can be seen in Figure 2. The final map of the fire risk assessment was based on the approach of the multicriterial analysis by blending all the data used in this study through fire risk labeling and weighting their importance and their role to the fire risk assessment as previously mentioned.
The blue colored lines in Figure 1, refer to the datasets used for the Sentinel 2 image scene classification and the final detection of the different vegetation types over the whole study area. The black colored lines are referred to the data used to construct the final forest fire risk assessment map through the multicriterial analysis.

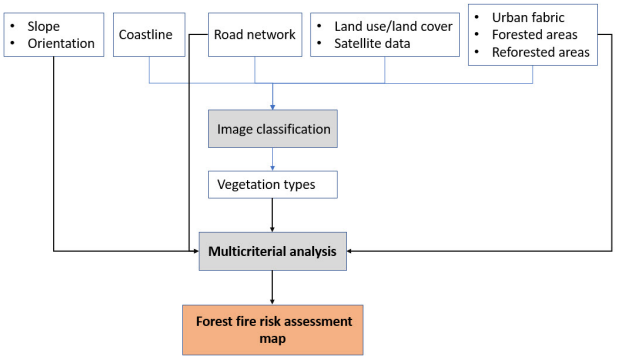

Figure 1. Schematic flowchart of the procedures was followed to calculate the forest fire risk assessment of the study area.

Following thoroughly the analyses were described before, an analytic map of the recent vegetation types of the study area, was constructed. At this point it must be noted that the acquisition date of the Sentinel 2 image scene was on 17/08/2019. Finally, using all the selected parameters as well as the secondary parameters that were calculated (forest fuel-vegetation types), the result of the multicriterial analysis was led to the creation of the final forest fire risk assessment thematic map.

3. RESULTS

In Figure 2, it can be seen analytically, all the detected vegetation types and the relative fire risk level linked with each one of them. Similar maps and relations were created for all the used data and then all these relations, blended through the multicriterial analysis to construct the final map of the forest fire risk assessment for the domain of the study. The data blending, practically means that different fire risk levels were defined for different classes of values in each of the datasets were used, considering sets of criteria based on distance of the road network, the vegetation types, urban fabric locations as well as topographic features. All these criteria helped to assign different forest fire risk levels for each dataset and then (using a weighting approach because of the different contribution of each parameter in the forest fire), the result of the multicriterial analysis led to the final map (Figure 3).
In Figure 3, it can be clearly seen that the most exposed areas to a high/very high fire risk, are concentrated in the main mountain ridge of Cephalonia island as well as in the north and south parts of Ithaca island. There are also dispersed areas of high levels of fire risk all over the examined islandic complex but are very small. Nevertheless, the largest fire risk class is the "moderate" and covers almost the 50% of the total examined study domain (Table 3). Moreover, the class is present in the whole study domain which is an additional factor of an increased forest fire hazard (Figure 3). This finding is very interesting and important because practically highlights that these two islands are a in potential fire risk danger. Considering the facts that the restoration of vegetation and the reforestation processes are more complicated and difficult in comparison with areas of the mainland as well as the increasing tourism activity in summer season, these areas seem to be vulnerable in fires and their natural ecosystems are in danger.

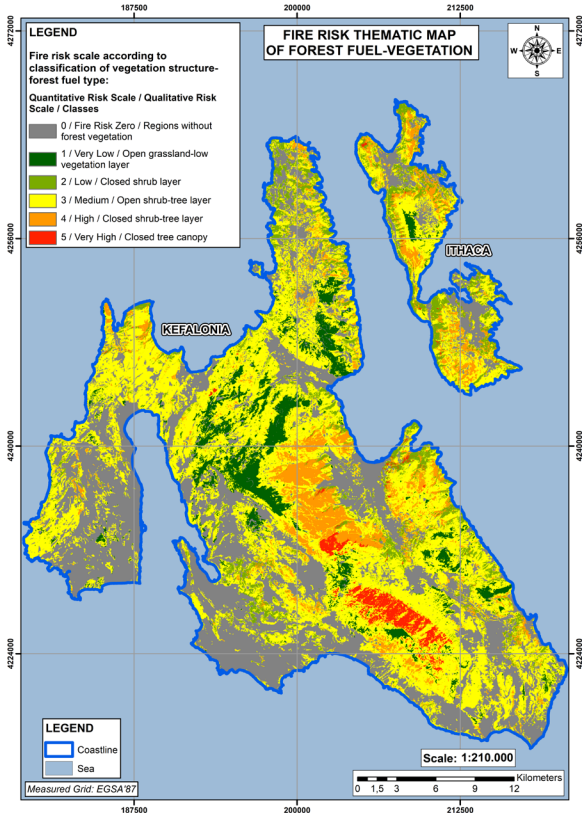

Figure 2. Forest fuel-vegetation type for the study area.

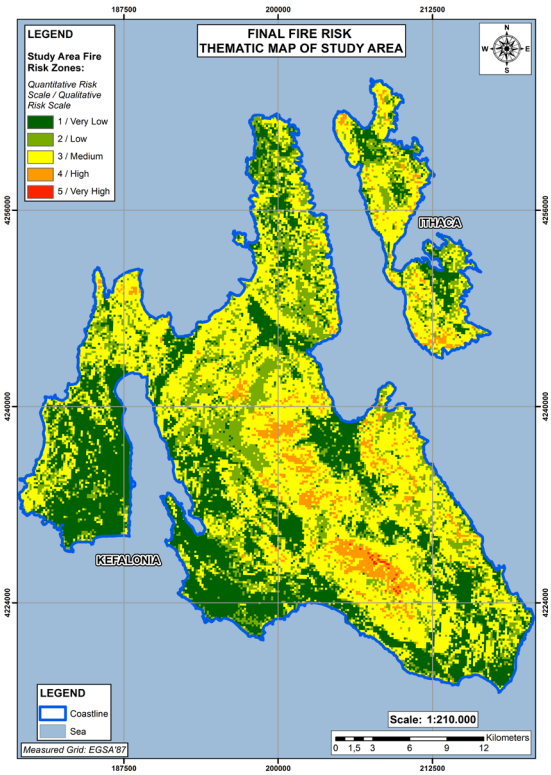

Figure 3. final map of the forest fire risk assessment for the study area.

Fire risk label	Fire risk label (description)	Area (ha)	Percentage (%)
1	Very low	17.412,23	19,9
2	Low	22.341,19	25,5
3	Medium	41.442,32	47,3
4	High	6.173,84	7,0
5	Very high	68,85	0,07

Table 3. The areal extent of the different fire risk levels over the study domain.

4. CONCLUSIONS

The study is an effort to develop an analytic map of forest fire risk assessment to operate as a guide for integrated planning to decrease forest fire risk in the study area (islandic complex of Cephalonia and Ithaca, Greece) and prevent a potential destruction of the natural ecosystems along with their unique flora and fauna. This study is an attempt to combine multispectral satellite image data from the Sentinel 2, the latest CORINE dataset and detailed forest maps of a high spatial resolution. The data blending of such accurate datasets through a multicriterial analysis was finally led to the creation of a detailed forest fire risk assessment map, useful for the planning against the forest fire hazard.

The main finding of this study is that 47,3 % of the whole study domain has a “medium” level of fire risk while 7 % was identified as “high” (Table 3). These percentages, highlight the significant forest fire risk in the study area and in parallel the necessity to organize local communities and authorities and supply them with all the necessary facilities and equipment to contribute to the decrease of this potential risk. Another important conclusion of the study is that regarding the examined anthropogenic factors, it appears that the zones of "moderate" to "very high" hazard are located at a distance of more than six hundred meters from roads and more than three kilometres from settlements. Moreover, according to the extracted zonal statistics in relation to the natural factors, the "moderate" to "high" hazard of fire exists in areas with a predominant vegetation structure of sparse shrubs and trees, slopes ranging between 10-30% and aspect of land surfaces of mainly north to east or northwest orientation.

A future step of this study is to evaluate the spatial accuracy of the final product (forest fire risk assessment thematic map) using an extensive list of previous forest fires over the whole study domain. Moreover, another future step is to extend this study in other islands of the Ionian Sea where the climate change and the continuously increasing tourism activity cause extensive and abrupt changes in the natural ecosystems and enhance their vulnerability.

REFERENCES

Abedi Gheshlaghi H, Feizizadeh B, Blaschke T. 2020. GIS-based forest fire risk mapping using the analytical network process and fuzzy logic. J Environ Plann Manage. 63(3):481–419.

Bowman DMJS, Balch JK, Artaxo P, Bond WJ, Carlson JM, Cochrane MA, D'Antonio CM, DeFries RS, Doyle JC, Harrison SP, et al. 2009. Fire in the earth system. Science. 324(5926):481–484.

Erten E, Kurgun V, Musaoglu N. 2004. Forest fire risk zone mapping from satellite imagery and GIS: a case study. Proceedings of 20th Congress of ISPRS, Istanbul, Turkey.

Giglio L, van der Werf GR, Randerson JT, Collatz GJ, Kasibhatla P. 2006. Global estimation of burned area using MODIS active fire observations. Atmos Chem Phys. 6(4):957–974.

Hurteau, M.D.; Bradford, J.B.; Fulé, P.Z.; Taylor, A.H.; Martin, K.L. Climate change, fire management, and ecological services in the southwestern US. For. Ecol. Manag. 2014, 327, 280–289.

Jaiswal RK, Mukherjee S, Raju KD, Saxena R. 2002. Forest fire risk zone mapping from satellite imagery and GIS. International Journal of Applied Earth Observation and Geoinformation 4, on the Aegean Archipelago. Environ Sci Policy. 4(1):1–421.

Justice C, Giglio L, Boschetti L, Roy D, Csiszar I, Morisette J, Kaufman Y. 2006. MODIS Fire products algorithm theoretical background document, Version 2.3 ed.

Kolios S, Stylios, 2013. Identification of land cover/land use changes in the greater area of the Preveza peninsula in Greece using Landsat satellite data. Appl. Geography, 40, 150-160

Middendorp RS, Vlam M, Rebel KT, Baker PJ, Bunyavejchewin S, Zuidema PA. 2013. Disturbance history of a seasonal tropical forest in western thailand: a spatial dendroecological analysis. Biotropica. 45(5):578–586.

Odu G. 2019. Weighting methods for multi-criteria decision making technique. J Appl Sci Environ Manag 23(8):1449, DOI: 10.4314/jasem.v23i8.7

Rocca, M.E.; Brown, P.M.; MacDonald, L.H.; Carrico, C.M. Climate change impacts on fire regimes and key ecosystem services in Rocky Mountain forests. For. Ecol. Manag. 2014, 327, 290–305.

Riley, K.L.; Loehman, R.A. Mid-21st-century climate changes increase predicted fire occurrence and fire season length, Northern Rocky Mountains, United States. Ecosphere 2016, 7, e01543

Russell-Smith J, Yates CP, Whitehead PJ, Smith R, Craig R, Allan GE, Thackway R, Frakes I, Cridland S, Meyer MCP, et al. 2007. Bushfires ‘down under’: patterns and implications of contemporary Australian landscape burning. Int J Wildland Fire. 16(4):361–377.

Zhang Y, Lim S, Sharples J. 2016. Modelling spatial patterns of wildfire occurrence in South-Eastern Australia.Geomatics. Natural Hazards and Risk. 7:1–16.

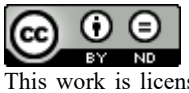

SEMI-AUTOMATIC APPROACH OF BURNT AREA EXTRACTION BASED ON DIFFERENT INDICES

E. Ilardi[1]*, S. Morreale[1], S. Bassetti[1], E. Arco[2], P. Boccardo[2]

[1] ITHACA (Information Technology for Humanitarian Assistance, Cooperation and Action), Via Pier Carlo Boggio 61, 10138 Torino (TO)

[2] Politecnico di Torino –DIST (Dipartimento Interateneo di Scienze, Progetto e Politiche del Territorio) -Viale Matteotti 39, 10125 Torino (TO)

KEY WORDS: Fires, Remote Sensing, Vegetation indices, Sentinel-2, Semi-automatic Extraction, Emergency Management

ABSTRACT:

The following study is focused on the analysis of burnt areas extracted by the use of an automatic tool. The burnt areas are obtained by applying different vegetation and burnt areas indices available in the literature (NDVI, NDB, SAVI, BAIM and BAIS2), calculated as combinations of two or more bands of the satellite images to synthesize the information carried by multispectral sensors and frequently used for the mapping fires. The research aims to find strong and alternative methods to combine with survey field activities. Traditional methods can often be subject to sampling errors or even to the non-perimeter of the event where the area is inaccessible. Satellite images allow to perform these activities simply and automatically, reducing costs and significantly increasing the accuracy and completeness of the data. Some areas analysed in the Copernicus Rapid Mapping and Risk and Recovery Mapping service were taken as case studies. A validation test has been made on all the selected indices, to evaluate the limits and potential of the different approaches and provide a burnt area closer to reality. Not having ground surveys data, the reference information for validation is given by the photointerpretation by experts in the sector.

1. INTRODUCTION

Wildfires are among the most destructive disasters, with an enormous impact in populated regions, where population is forced to move or killed, houses and infrastructures are damaged or destroyed, but also in isolated ones, where natural vegetation and animals are affected. In recent years wildfires are growing, partly due to the effect of global warming, with the increase of extremely high temperature and drought (Kerr, 2007), partly due to illegal wildfires, linked to land management policy that favours agriculture and pastures.

Remote sensing multispectral imagery has proved to be a valuable tool in fire's monitoring. In particular, the variation in content of chlorophyll in vegetation can be derived from the analysis of the spectral firm of a particular vegetated area, which highlights areas that have little content or have been deprived of it, as in the case of vegetated areas devastated by a fire. These indices, known as vegetation indices, are mainly used to evaluate the state of the vegetation, a topic widely explored in remote sensing research applications, but are also used to detect, delineate, and quantify burnt areas. In addition, the use of remote sensing products allows the monitoring of large and remote places, contributing to planning actions of Civil Protection, Forestry Corps and other actors involved in the emergency management.

The Copernicus Emergency Management Service (EMS) is an on-demand service of European community devoted to providing relevant and updated geospatial information to give a timeline response to various types of disaster using remote sensing imagery[1]. The EMS is divided into two components: Rapid Mapping, that provides geospatial information within hours or days in the immediate aftermath of a disaster, and Risk & Recovery Mapping, which supports prevention, preparedness, risk reduction and recovery phases activities. A focal point of these services is the timeliness in product delivery: the use of fast and reliable automatic and semi-automatic extraction tools of imagery, which are then manually refined thanks to the team's expertise, are one of the keys to reduce delivery time. In this study, a two-step QGIS plugin has been developed in order to calculate five different vegetation indices and then automatically extract burnt areas over imagery, depending on a threshold value decided by an expert operator by means of visual interpretation. Through the tool the authors aim to automate the comparison the five indices result and evaluate which one better extract a burnt area. Thanks to a validation activity, performed on ten EMS wildfire activations, the accuracy of the burnt areas extracted with the plugin is compared with the same areas manually digitized by photointerpretation. Results of validation are discussed to estimate the different performances of vegetation indices in the burnt area identification. In addition, the validation results are used to demonstrate the timesaving of plugin processing with respect to a manual photointerpretation extraction: the effectiveness of the plugin makes it a good candidate to be used for wildfire extraction in the Copernicus Rapid Mapping and Risk and Recovery Workflow. Finally, the strengths and the critical points of the used images and the implemented plugin are discussed, to identify the main problems encountered during the processing and the possible future developments.

2. METHODOLOGY

2.1 Vegetation indices and plugin processing

The first aim of the authors was to develop a tool to extract burnt areas from a satellite image in a more automated way, by relying on the calculation of a vegetation index.

Following previous burnt land studies, five spectral indices based on the Red, Near Infrared (NIR) and Short-Wavelength Infrared (SWIR) spectral domains, have been chosen: the Normalized Difference Vegetation Index (NDVI), the Soil Adjusted

* Corresponding author

[1] https://emergency.copernicus.eu/

Vegetation Index (SAVI), the Normalized Burn Ratio (NBR), The Burnt Area Index for MODIS (BAIM) and the Burnt Area Index for Sentinel-2 (BAIS2).
The NDVI is an indicator of the greenness of the biomes, which has been extensively used also in burnt land discrimination (Fernandez et al. 1997). Thanks to its simple formulation it is widely used for ecosystem monitoring. The SAVI was developed with the aim to correct the NDVI when the vegetative cover is low (< 40%): it applies a "soil brightness correction factor" to the NDVI, in order to minimize the soil reflectance effect, which can influence the NDVI value up to 20% (Richardson et al. 1992). The other three indices are specifically designed to delineate burnt areas. In particular, the NBR index is very similar to the NDVI, but combines the use of both NIR and SWIR wavelengths, because the difference between the spectral responses of healthy vegetation and burnt areas reach their peak in the NIR and the SWIR regions of the spectrum (Keeley, J. E. 2009). The BAIM (Martín et al., 2006) is designed to analyse large regions using the MODIS sensor, and focus on the maximisation of the spectral distance between coal and other land covers, which can be potentially confused with burnt areas. The BAIS2 is a newly developed index specifically designed to take advantage of the S2 MSI spectral characteristics which have been demonstrated to be suitable for post-fire burnt area detection at 20 m spatial resolution (Filipponi F, 2018).

Figure 1 shows the workflow of the procedure defined to extract burnt areas, implemented through the development of two QGIS plugins.

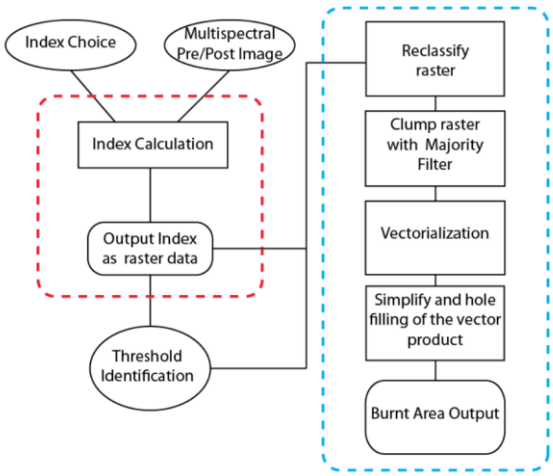

Figure 1. Workflow for burnt area extraction.

In the first plugin, "Burnt Index Tool", whose workflow is shown in the red box in Figure 1, the operator can choose between the five different vegetation indices previously described. In addition, in order to reduce the processing time, he can add a region of interest, drawn as a rough polygon around the burnt area (used to clip the image) and/or choose a cell resample value. Usually, for emergency mapping purposes, a 20 meters resolution is considered enough to obtain a homogeneous result, even if it may affect the precision of the burnt area delineation. In general, the resampling value choice is left to the expertise of the operator. However, if the post event image shows a well-defined and homogeneous burnt area limit, setting the resampling value equal to the input image resolution allows precise delineation results. The output of the first plugin is a raster representing the index selected. This raster must be manually analysed by the operator, which has to visually identify the burnt/unburnt threshold pixel value needed as input parameter for the second plugin. Sometimes it is a good practice to stretch the image properly, in order to raise the contrast of the burnt and the unburnt areas.
The processing steps of the second plugin "Extraction of Burnt Area" are shown in the blue box of Figure 1. Using the threshold value identified previously by the operator, the second plugin classifies the input index raster into a Boolean raster, which is divided into burnt or unburnt values (0 or 1). Next, after a clumping with a majority filter, the tool generates a rough burnt area polygon. A final edge smooth and hole filling are applied to the polygon, and the burnt area is saved as shapefile.
In order to avoid false positives led by clouds, smoke and shadows, the plugin allows to add a delineation of these elements through a shapefile, that will be used as erase features over the burnt area extracted. Using the SWIR post image band as additional input, it is also possible to extract the active flames using a threshold value identified on this band. For the purposes of this work this last product was not considered.

2.2 Validation

In order to properly test and validate the plugins, a validation procedure was applied to the ten forest fires in analysis, selected from the EMS Rapid Mapping and Risk and Recovery Activations list and shown in Figure 2.
The selected wildfires span from August 2019 to April 2021, have different sizes (the Areas of Interest range from 1,300 ha to 254,000 ha around), and are located in different countries of the world, in particular seven in Europe, two in Australia and one in South America.

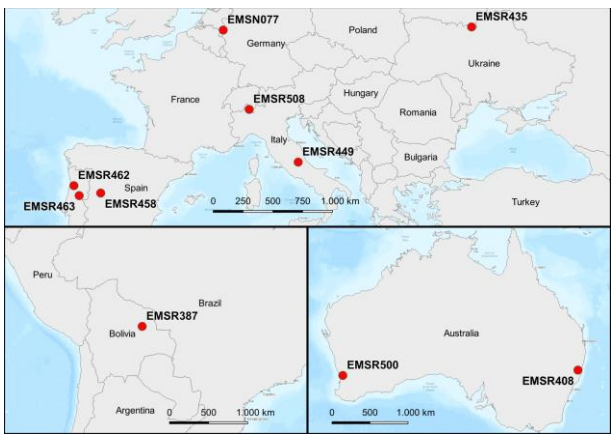

Figure 2. Pilot cases with the relative activation name.

To obtain more consistent results in the validation process, Sentinel-2 (S2) images have been used for all the analysed wildfires, thanks to their great spatial (10 meters) and temporal (potential five-day) resolution, and their open and easy access (Malenovský et al. 2012). In addition, they are particularly suitable for chlorophyll analysis (and burnt area detection), as the Multispectral Instrument (MSI) has 13 bands, with the visible RGB and the NIR bands available at a 10 meters spatial resolution, and four red-edge bands available at 20 m spatial resolution (De Simone et al. 2020).
Twenty S2 images were downloaded for analysis, two S2 for each area acquired a few days or weeks before and after the fire, to reduce the vegetation differences caused by the different seasons. All the images are downloaded as level 2A (atmospherically, radiometrically and geometrically corrected) and cloud free.
The validation applied in this study is a thematic validation with a binary classification i.e., burnt or unburnt area. The methodology is based on a publication of the JRC "International

workshop Validation of geo-information products for crisis management" (Corbane et al. 2009). In the specific case it was not possible to validate the plugin result with ground truth data, therefore representative and independent reference data were used, considered intrinsically more accurate than the product to be evaluated, i.e., the digitization of the burnt area carried out on S2 images by expert digitizers (Broglia et al. 2010).
As a first step of the validation, the burnt areas for each single index were extracted so that the accuracy of all 5 indices could be analysed. Subsequently, five indicators necessary to calculate the thematic accuracy for each individual index were calculated, as shown in Figure 3.

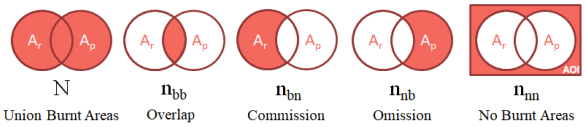

Figure 3. Description of the 5 indicators. A_r is the reference data's burnt area and A_p is the plugin's burnt area and AOI is the Area of Interest (Readapted from Broglia, 2010).

In order to accurately and completely validate the plugin results, the indicators described above were used to calculate three final factors of the thematic validation: the overall thematic accuracy, the omissions (i.e., the burnt areas that the plugin has not recognized as such) and commissions (i.e., the unburnt areas that the plugin has classified as burnt). The calculations performed are shown in Table 1.

THEMATIC VALIDATION			
Burnt Area		Plugin	
		Burnt (ha)	Not Burnt (ha)
Reference data	Burnt (ha)	n_{bb}	n_{bn}
	Not Burnt (ha)	n_{nb}	n_{nn}
OVERALL THEMATIC ACCURACY %		$\frac{n_{bb}}{n_{nb}+n_{bb}+n_{bn}}100$	
COMMISSION %		$\frac{n_{bn}}{n_{nb}+n_{bb}+n_{bn}}100$	
OMISSION %		$\frac{n_{nb}}{n_{nb}+n_{bb}+n_{bn}}100$	

Table 1. Scheme of the calculations performed in the validation (Readapted from Broglia, 2010).

3. RESULTS

This chapter presents the analysis and the validation results. The authors focused on two main aspects: the identification of the index that best suited this kind of automation and the analysis of the characteristics of each studied area, to highlight the natural elements that may affect the final result.
The chart in Figure 5 shows the overall thematic accuracy for each individual index and the respective errors of omission and commission.
NBR is the index with the highest precision (about 83%). It was an expected result, indeed NBR is the most widely used and studied index in literature and which, thanks to the use of the SWIR band, has characteristics that are well suited to the extraction of burnt areas. Despite this, the SAVI is in second place with an accuracy of about 77%; it is certainly an unexpected result. BAIM and NDVI indices have similar thematic accuracy values. Finally, the BAIS2 index, which should instead be specific to S2, and therefore higher accuracy values were expected, is the least performing.

For all the indices there is a higher percentage of omissions compared to commissions; this certainly depends on the threshold value established by the operator and on the presence of clouds or areas without vegetation that affect the resulting index calculation.

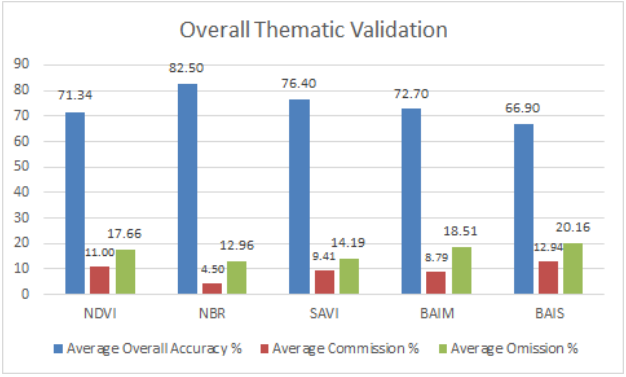

Figure 5. Average thematic accuracy, omissions, and commissions for each index.

Figure 6 shows a detail of the extraction of the burnt area for EMSR500 activation in which is shown how the various indices behave compared to the reference data.

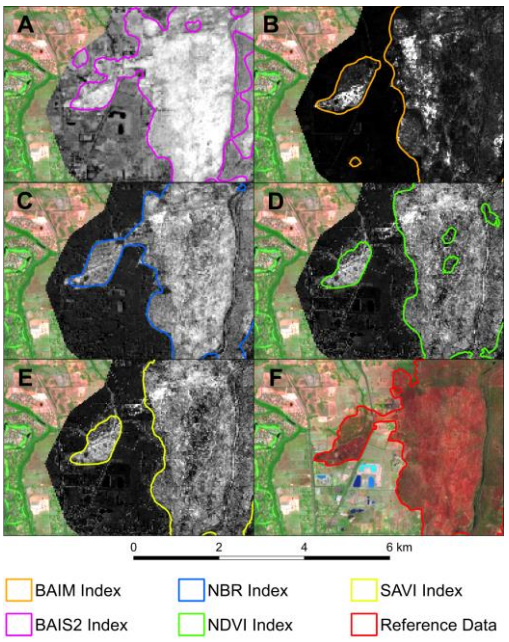

Figure 6. From Figure A to Figure E are shown the five raster indices on the EMSR500 and the respective five extracted burnt areas. Figure F shows the reference data used for validation.

Finally, in Figure 7, the overall thematic accuracy for each activation is reported. These results are important to investigate the reasons for low or high accuracy highlighting the tool's limits, which will then be described with greater precision and completeness in the last chapter.
The EMSR463 activation is the case study with high thematic accuracy for all indices. The reason is that the perimeter of the fire is very clear, most of the area was probably covered by a canopy fire, in fact the vegetation is visibly compromised, and the plugin does not create holes inside of the polygon of the burnt area. On the contrary, in the EMSR435 activation, the area was probably crossed by a crawling fire that causes patches in which the index does not perceive a change in the vegetative state of the

plants, as the canopy has remained intact. The EMSR387 activation has quite high accuracy values, despite the presence of many clouds, which usually, together with the relative shadows, create problems in the extracted area, since there the index shows values similar to the burnt area. This demonstrates the usefulness of the plugin's feature which allows to delete the clouds areas in the image, using a previously digitized cloud shapefile.
The activation in which lower accuracy values were found is the EMSR449. Following an accurate analysis, it was noted that the fire is difficult to identify even for an expert, because it was very jagged and arose in an area with already little if not non-existent vegetation. The lack of vegetation, before and after the fire, prevents the index from classifying that area as burnt.

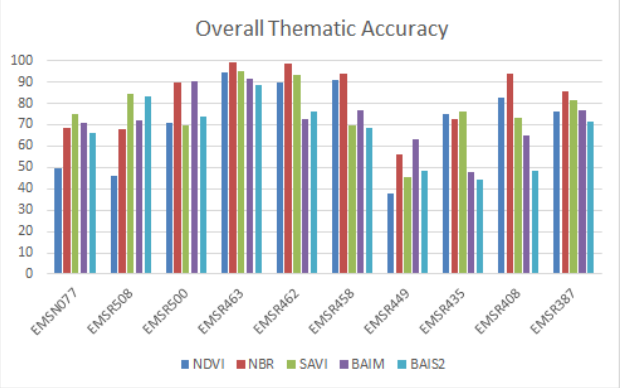

Figure 7. Overall thematic accuracy for each activation.

4. CONCLUSIONS

Wildfires manual delineation can be a time-consuming procedure that can require from several minutes to several hours of interpretation of pre and post event images and digitalization, especially in Rapid Mapping service where timeliness is a crucial part of the service. In this paper, the authors provided a procedure based on a bundle of two QGIS Plugins that can considerably reduce the operative time of wildfire delineation methods.
The validation process has demonstrated the appropriateness of the plugin to extract a burnt area with a good thematic accuracy and in a short time and the NBR index results the most appropriate to delineate burnt area in the context of the Rapid Mapping. The tool contributes to saving time respect to a manual delineation in case of large wildfires, whereas is not recommended for small burnt areas. The use of QGIS for the implementation guarantees a user-friendly interface and ease of sharing.
Between limits of the proposed approach, the automated extraction has generally an inaccurate result in case of crawling fires, where the canopy not burned may cover the burned area on the ground, and in case of not uniform land cover or large presence of non-vegetated area. In addition, the plugin still relies on the strong expertise of the operator. The initial choice of the resample value must be guided by evaluation of the scale of analysis and the type of wildfire, to not get a rough output polygon, and the identification of the appropriate threshold in the second step of the plugin, is conditioned by the operator and may results in a loose delineation.
As further development, in order to reduce the contribute of the operator in the approach, the authors propose to automate the choice of the threshold value on range list, depending on the type of image used as input, index chosen, type of wildfire and characteristic land cover of the area. This may be achieved through a machine learning approach on a larger amount of wildfire cases, based on a classification of wildfire types, land cover and scale of analysis.

REFERENCES

Broglia, B., Corbane, C., Carrion, D., Lemoine, G., and Pesaresi, M., 2010. Validation Protocol for Emergency Response Geo-information Products. JRC Scientific and Technical reports.

Corbane C., Broglia M., Carrion D., Lemoine G., and Pesaresi M., 2009. International workshop on Validation of geo-information products for crisis management. Valgeo.

De Simone W., Di Musciano M., Di Cecco V., Ferella G., and Frattaroli AR., 2020. The potentiality of Sentinel-2 to assess the effect of fire events on Mediterranean mountain vegetation, In: *Plant Sociology* 57(1): 11-22.

Fernández, A., Illera, P., Casanova, J.L., 1997. Automatic mapping of surfaces affected by forest fires in Spain using AVHRR NDVI composite image data, In: *Remote Sensing of Environment*, Vol. 60, Issue 2, pp. 153-162, ISSN0034-4257, https://doi.org/10.1016/S0034-4257(96)00178-2.

Filipponi, F., 2018, BAIS2: Burned Area Index for Sentinel-2, In: *Proceedings*, Vol.2(7), 364. https://doi.org/10.3390/ecrs-2-05177

Keeley, J. E., 2009. Fire intensity, fire severity and burn severity: A brief review and suggested usage. In: *International Journal of Wildland Fire*, 18(1), 116–126.

Kerr, R.A., 2007. Global Warming is Changing the World. In: *Science*, Vol. 316(5822), pp. 188-190. https://10.1126/science.316.5822.188

Malenovský Z., Rott H., Cihlar J. Schaepman M.E., García-Santos G., Fernandes R., Berger M., 2012. Sentinels for science: Potential of Sentinel-1, -2, and-3 missions for scientific observations of ocean, cryosphere, and land. In: *Remote Sensing of Environment* 120: 91–101.

Martin, M.P., Gómez, I., and Chuvieco, E., 2006. Burnt Area Index (BAIM) for burned area discrimination at regional scale using MODIS data. In: *Forest Ecology and Management*, Vol. 234, pp. 193-197 https://doi.org/10.1016/j.foreco.2006.08.248.

Richardson, A.J., and J.H., Everitt, 1992. Using spectral vegetation indices to estimate rangeland productivity. In: *Geocarto International* 7(1):63-69.

Sampling scheme and reference fire perimeters from Sentinel-2 data for validation of burned area products in Africa

M. Sali [1,*], L. Busetto [1], M. Boschetti [1], M. Franquesa[2], E. Chuvieco[2], D. Stroppiana [1]

[1] Consiglio Nazionale delle Ricerche – Istituto per il Rilevamento Elettromagnetico dell'Ambiente (CNR-IREA), Via Bassini 15, 20133 Milano, Italy - (sali.m, boschetti.m, stroppiana.d)@irea.cnr.it

[2] University of Alcala, Department of Geology, Geography and the Environment, Colegios 2 – 28801 Alcalá de Henares, Spain – (magin.franquesa, emilio.chuvieco)@uah.es

KEY WORDS: Validation, Burned Area, Sentinel-2, stratification random sampling, accuracy metrics

ABSTRACT:

This work describes an approach for building a dataset of fire reference perimeters over sub-Saharan Africa (latitude range 25°N-35°S) from Sentinel-2 (S2) time series based on a sampling scheme designed on the characteristics of the S2 tiling system. A stratified random sampling scheme is adopted to select 50 validation sites distributed over the African continent and across Olson biomes (Olson et al. 2001) and fire intensity strata. S2 time series are extracted over each validation site after a preliminary analysis of data availability; S2 consecutive pairs are classified with a Random Forest (RF) algorithm for building a dataset of fire reference perimeters.

1. INTRODUCTION

Validation is a key step in the production of Burned Area (BA) products to assess the accuracy of geo-spatial information derived from processing medium to coarse spatial resolution Earth Observation (EO) datasets. Validation provides a quantitative assessment of the thematic accuracy, which is relevant for both scientists and end-users (Congalton and Green 1999). With increasing availability of regional and global burned area products delivered at different scales, agreement on protocols and data to be used as reference has to be achieved; although a largely shared protocol for validation has not been defined, there are some widely accepted good practises that should be followed. Moreover, for large-area (global and/or continental) EO-based BA products, validation is even more challenging because of the great variety of ecosystem and climatic conditions that could affect mapping accuracy (Chuvieco et al., 2008).

The need for the definition of standard approaches and protocols for validation of EO products led to the creation of international working groups such as the Committee on Earth Observation Satellites' Land Product Validation Subgroup (CEOS-LPVS) (http://lpvs.gsfc.nasa.gov/, accessed June 2021). CEOS-LPVS defines validation as: "The process of assessing, by independent means, the quality of the data products derived from the system outputs" (European Space Agency, 2007; Morisette et al. 2006).

Among the continental and global BA products (Chuvieco et al., 2019; Franquesa et al., 2020) the most recent ones are the ESA FireCCI BA products (Lizundia-Loiola et al., 2020) and the NASA MODIS MCD64A1 (Giglio et al., 2018).

In this work we propose a methodology for building a fire reference perimeter dataset suitable for validating continental BA maps from the Small Fire Database (SFD) (FireCCISFD20) of the FireCCI project (https://climate.esa.int/en/projects/fire/, last access June 2021); the FireCCISFD20 is the new and improved version of the FireCCISFD11 (Roteta et al., 2019) and it will be soon delivered for the year 2019 for Sub-Saharan Africa.

2. VALIDATION PROTOCOL

Sampling is the temporal and spatial selection of validation sites/units for the estimation of accuracy metrics. Sampling is critical in any validation and several approaches have been proposed and implemented in the literature for validating large area BA maps (Boschetti et al., 2016; Padilla et al., 2015; Padilla et al., 2014; Roy et al., 2008). Although some widely accepted guidelines can be outlined.

Major steps in validation of BA products are:

1. identification of validation units
2. spatio-temporal sampling
3. generation of the fire reference perimeters
4. estimation of the accuracy metrics

For burned area assessment globally or regionally, the use of *in-situ* reference field data (i.e. ground truth) is not feasible or very expensive in time and effort. Therefore, remote sensing validation projects rely on reference fire perimeters derived from satellite images of higher spatial resolution. At present, the major data sources used for this purpose are certainly the Landsat and Sentinel missions; among them, Landsat is the only mission that can provide historical long-term archives for validation of multi-annual BA products.

Since burned area spectral signal in some ecosystems tends to disappear quickly, with shortest durations in savanna ecosystems (Trigg and Flasse, 2000), reference data should be simultaneous to the product to be validated. A widely used approach is to extract fire reference perimeters between two acquisitions of the source satellite mission (either Landsat or Sentinel) so that comparison of burned areas from independent reference data and the global/continental product can be carried out for the period between two dates (Boschetti et al., 2016).

Independence is a crucial requirement of validation, since it assures unbiased estimation of accuracy metrics; independence implies that reference datasets should not be used during the calibration or "tuning" of BA algorithms. It is, however, considered acceptable that EO data (i.e. satellite imagery) used for deriving BA products (to be validated) is also used for deriving the reference datasets as long as processing is

* Corresponding author

separated and independent. Moreover, the independent reference data must be derived with minimum error, by visual interpretation or by application of semi-automatic supervised algorithms followed by visual checking (Roy et al., 2005; Boschetti et al., 2006; Roy and Boschetti, 2009; Giglio et al., 2009; Padilla et al., 2014, 2015).
Since the comparison of reference and BA products considers two dimensions, space and time, a validation unit can be defined as a spatio-temporal sampling of the source image data archive used to extract fire reference perimeters.
Spatially, the area to be validated (global and/or continental) is divided into non-overlapping regions to assure equally distributed sampling probability between units. Temporally, a unit is assumed to be composed of two or more consecutive cloud free image data scenes that should satisfy a given set of requirements (explained in the next section).
The validation units selected are distributed among the major biomes over the globe (for global products) or the continent (for continental products) (Olson et al., 2001) and over region with high and low fire activity.
Once validation units are sampled, fire reference perimeters are generated for comparison with the BA products. Accuracy metrics are then estimated through cross-tabulation, by accounting for the spatio-temporal coincidences and disagreements on estimates of location and timing of burns between a reference map and the target map (Padilla et al. 2017; Padilla et al. 2014; Padilla et al. 2015). In this framework accuracy is measured in terms of global agreement of the common overlapping area of reference and classified products.

3. VALIDATION SCHEME FOR CONTINENTAL AFRICA BA PRODUCT

The protocol described in the previous section was adapted for the validation of the FireCCI Small Fire Database (SFD) (FireCCISFD20) covering the year 2019. This product, first release on October 2018, comprises maps of Burned Area for Sub-Saharan Africa; BA maps are obtained combining spectral information from Sentinel-2 at 20 m resolution and thermal information from the MODIS active fire products (https://geogra.uah.es/fire_cci/fireccisfd11.php, last access June 2021). The algorithm of the first release (FireCCISFD11) is fully described in Roteta et al., (2019); a new and improved version of the product will soon be available within the FireCCI project.
Fire reference perimeters for validation are extracted from Sentinel-2 (S2) data over the validation units and validation workflow is described in the following sections.

3.1 Definition of the sampling units

Sampling unit is the spatio-temporal sampling of the image source archive, that in this case is S2. The spatial dimension of the validation unit is defined by the area, i.e. the portion of the surface, where reference and BA product are compared; the temporal dimension is defined by the dates of S2 images.
According to the FireCCI project requirements, the validation area of each unit must cover approximately 100 km by 100 km hence it overlaps the extent for S2 tiles, that were selected as validation units. However, in order to provide a robust statistical sampling and avoid overlapping between units that could determine an area with higher probability of been selected, two major issues were first addressed and solved.
First, S2 tiles crossing different orbits are discarded (Figure 1a). This is done because in overlapping tiles only a portion of the total 100 km x 100 km area is observed on a given date; since fires are a dynamic phenomenon, reference perimeters should be extracted from images acquired on the same date. Hence, only S2 tiles fully covered by a single orbit (i.e. the surface observed on the same date) are retained (Figure 1b).

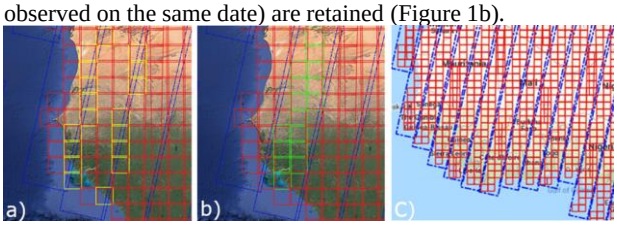

Figure 1. a) example S2 tiles covering different orbits (yellow); b) example S2 tiles covering the same orbit (green); c) all S2 tiles suitable for sampling (after first filtering) in the example area centred in Senegal.

The second issue is generated by S2 tiles overlapping due to adjacent zones of the UTM coordinate projection system (yellow polygons in Figure 2a). In these conditions, keeping both overlapping tiles would increase sampling probability of the common land area; hence, only one S2 tile is randomly selected and retained (Figure 2b).
Once the two previous filtering conditions are applied to the S2 tiling grid system, the population of tiles suitable for sampling is identified.

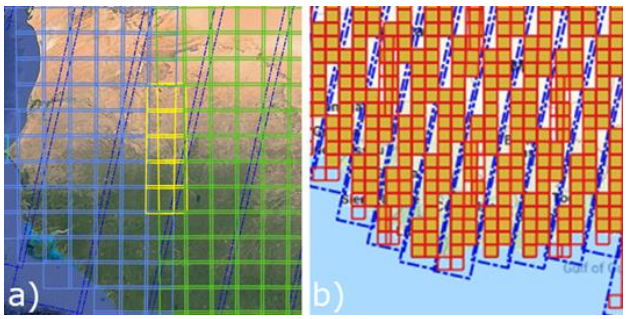

Figure 2. a) example S2 tiles suitable (green/blue) and not suitable (yellow) as validation areas for sampling due to overlap of adjacent UTM zones; b) S2 tiles suitable (orange) for sampling using a random selection in the example area centred in Senegal.

For each of the selected tiles, i) the total annual burned area from the FireCCI51 BA product and ii) the major Olson biome (Olson et al., 2001) are computed to create the strata for random stratified sampling.

Temporal sampling is carried out by selecting S2 time series over the tiles suitable for sampling and satisfying conditions on:
1. Cloud cover percentage on each scene
2. Time step between consecutive images
3. Length of the time series

3.2 Sampling cardinality

The total number of validation units to be sampled is distributed among strata based on (1).

$$n_h \propto N_h \sqrt{\overline{BA}_h} \quad (1)$$

where n_h: number of units to be sampled for each stratum h, BA_h is the average total annual burned area for stratum h and N_h is the total amount of units available for sampling for each stratum h. For smaller strata a minimum of $n_h = 2$ is assigned. As explained above, strata are given by the high/low fire intensity

partition of each biome (Padilla et al. 2014; 2015) estimated from annual global FireCCI51 BA product (Chuvieco et al., 2018; Lizundia-Loiola et al., 2020).
A total of 50 S2 tiles were sampled and the distribution is shown in Figure 3.

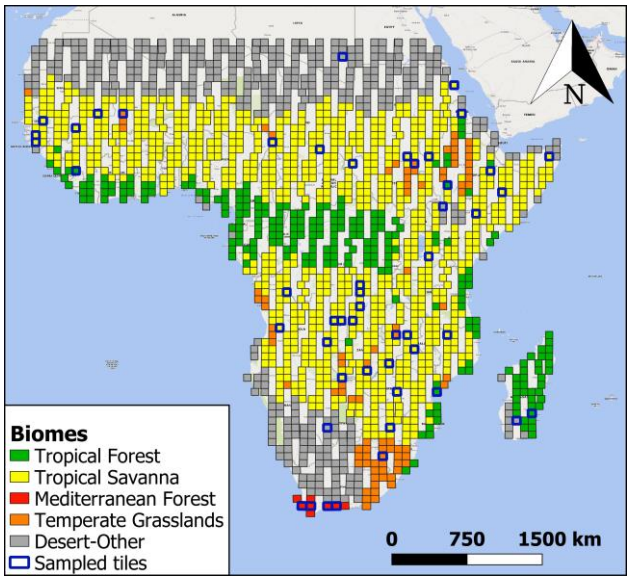

Figure 3. The S2 tiles selected for validation.

4. FIRE REFERENCE PERIMETERS

For each S2 tile, fire reference perimeters are generated by classifying pairs of consecutive S2 images (also called "short units"); all short units over the same validation unit are combined to derive fire perimeters over the "long validation unit" (from the first to the last date of the time series) (Figure 4).

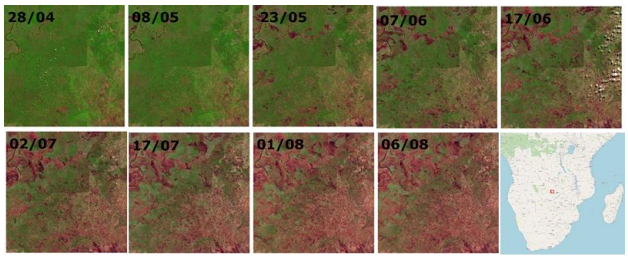

Figure 4. Short (t_n-t_{n-1}) and long (t_1-t_n: 28/04/2019 to 06/08/2019) sampling units for an example tile in Africa.

The validation area of 100 km x 100 km (S2 tile) is classified in Google Earth Engine (GEE, https://earthengine.google.com/, last access June 2021) with a supervised classification Random Forest (RF) algorithm (Breiman, 2001) applied to S2 "short units to map areas burned between the two dates (t_1, t_2). Input to the RF classifier are spectral indices NBR, NBR2 and NDVI and their temporal differences (t_1, t_2) and training polygons for burned/unburned areas selected by photointerpretation of RGB false colour composites in GEE.
The flowchart of the classification processing is depicted in Figure 5 from the selection of the S2 time series, for each validation unit, to the final fire reference perimeters.
BA reference files are delivered as ESRI© shapefiles and contain, besides the burned and unburned categories, unobserved areas or not valid pixels (i.e. regions where the surface conditions could not be observed and assigned to neither of the two burned and unburned categories).

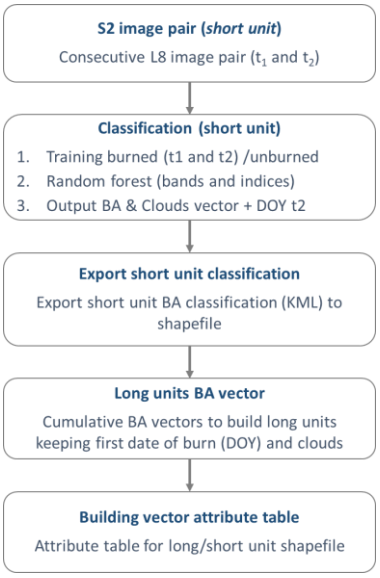

Figure 5. Flowchart of the classification processing

Figure 6 shows an example fire reference perimeter product over S2 tile 36LTP, in Zambia. Over the long unit, fire perimeters can be represented as burned/unburned (red/green) polygons, as shown in the left panel of the figure. Since the dates of the short units are retained in the attribute table of the shapefile, fire polygons can also be depicted with the date when each polygon was first observed as burned (panel on the right). Clouds masked out in any of the short units are depicted as black regions. Since the cloud cover area is cumulated over the long unit, we decided to keep max cloud cover percentage over the short units below 10%; this condition allows us to create reference fire perimeter datasets with least contamination from cloud coverage.

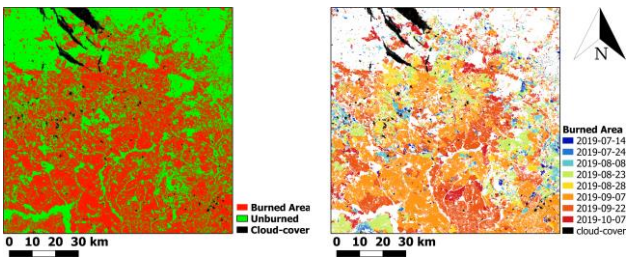

Figure 6. Reference perimeters of S2 tile 36LTP in Zambia. On the left panel the burned-unburned representation, on the right panel the date of detection (post-date) of the burned area.

5. ACCURACY METRICS

Reference and BA product are overlaid and intersected to extract the confusion matrices (Congalton and Green 1999; Latifovic and Olthof 2004); each cell of the confusion matrix expresses the proportion of area of agreement or disagreement for all pixels of the validation area (i.e. S2 tile). Confusion matrices are summed up over all of the validation units to compute the following accuracy metrics: Commission error, Omission error, Dice coefficient, Relative Bias.

6. CONCLUSIONS

This work presents an approach for building a dataset of fire reference perimeters for validation of continental/global BA products. In particular, the scheme was designed to generate reference perimeters for the validation of the FireCCI Small

Fire Database (SFD) (FireCCISFD20) BA product covering the year 2019. The major steps of the validation scheme are described: definition of the validation units, sampling, stratification, generation of reference burned polygons and estimation of the accuracy metrics.

ACKNOWLEDGEMENTS

This study has been funded by the Fire_cci project (contract no 4000115006/15/I-NB), which is part of the European Space Agency's Climate Change Initiative Programme.

REFERENCES

Boschetti, L., Stehman, S.V., and Roy, D.P., 2016. A stratified random sampling design in space and time for regional to global scale burned area product validation, Remote Sensing of Environment, 186, 465-478, https://doi.org/10.1016/j.rse.2016.09.016.

Breiman, L. (2001). Random Forests. Machine Learning, 45, 5-32.

Chuvieco, E., Lizundia-Loiola, J., Pettinari, M. L., Ramo, R., Padilla, M., Tansey, K., Mouillot, F., Laurent, P., Storm, T., Heil, A., and Plummer, S., 2018. Generation and analysis of a new global burned area product based on MODIS 250 m reflectance bands and thermal anomalies, Earth Syst. Sci. Data, 10, 2015-2031, https://doi.org/10.5194/essd-10-2015-2018.

Chuvieco, E., Mouillot, F., Van der Werf, G.R., San Miguel, J., Tanase, M., Koutsias, N., García, M., Yebra, M., Padilla, M., Gitas, I., Heil, A., Hawbaker, T.J., and Giglio, L., 2019. Historical background and current developments for mapping burned area from satellite Earth observation,", Remote Sens. Environ., 225, pp. 45-64, https://doi.org/10.1016/j.rse.2019.02.013.

Congalton, R.G., and Green, K., 1999. Assessing the Accuracy of Remotely Sensed Data: Principles and Applications. Boca Raton: Lewis Publishers.

Franquesa, M., Vanderhoof, M.K., Stavrakoudis, D., Gitas, I., Roteta, E., Padilla, M., and Chuvieco, E., 2020. Development of a standard database of reference sites for validating global burned area products, Earth Syst. Sci. Data, 12, pp. 3229–3246, https://doi.org/10.5194/essd-12-3229-2020.

Giglio, L., Boschetti, L., Roy, D.P., Humber, M.L., and Justice, C.O., 2018. The Collection 6 MODIS burned area mapping algorithm and product, Remote Sens. Environ., 217, pp. 72-85.

Latifovic, R., Olthof, I. (2004). Accuracy assessment using sub-pixel fractional error matrices of global land cover products derived from satellite data. Remote Sensing of Environment, 90, 153-165.

Lizundia-Loiola, J., Otón, G., Ramo, R., and Chuvieco, E., 2020. A spatio-temporal active-fire clustering approach for global burned area mapping at 250 m from MODIS data, Remote Sens. Environ., 236, pp. 111493, https://doi.org/10.1016/j.rse.2019.111493.

Morisette, J.T., Baret, F., and Liang, S., 2006. Special issue on global land product validation. IEEE Trans. Geosci. Remote Sens. 44, 1695–1697.

Olson, D.M., Dinerstein, E., Wikramanayake, E.D., Burgess, N.D., Powell, G.V.N., Underwood, E.C., D'Amico, J.A., Itoua, I., Strand, H.E., Morrison, J.C., Loucks, C.J., Allnutt, T.F., Ricketts, T.H., Kura, Y., Lamoreux, J.F., Wettengel, W.W., Hedao, P., & Kassem, K.R. (2001). Terrestrial Ecoregions of the World: A New Map of Life on Earth. BioScience, 51, 933-938.

Padilla, M., Stehman, S.V., and Chuvieco, E., 2014. Validation of the 2008 MODIS-MCD45 global burned area product using stratified random sampling, Remote Sensing of Environment, 144, 187-196, ISSN 0034-4257, https://doi.org/10.1016/j.rse.2014.01.008.

Padilla, M., Stehman, S.V., Ramo, R., Corti, D., Hantson, S., Oliva, P., Alonso, I., Bradley, A., Tansey, K., Mota, B., Pereira, J.M., and Chuvieco, E., 2015. Comparing the Accuracies of Remote Sensing Global Burned Area Products using Stratified Random Sampling and Estimation. Remote Sensing of Environment, 160, 114-121.

Roteta, E., Bastarrika, A., Padilla, M., Storm, T., Chuvieco, E., 2019. Development of a Sentinel-2 burned area algorithm: Generation of a small fire database for sub-Saharan Africa, Remote Sensing of Environment, 222, 1-17, https://doi.org/10.1016/j.rse.2018.12.011.

Roy, D.P., Boschetti, L., Justice, C.O., and Ju, J., 2008. The collection 5 MODIS burned area product - Global evaluation by comparison with the MODIS active fire product. Remote Sensing of Environment, 112, 3690-3707.

Roy, D.P., and Boschetti, L., 2009. Southern Africa validation of the MODIS, L3JRC, and GlobCarbon burned-area products. IEEE Trans. Geosci. Remote Sens. 47, 1032–1044.

Roy, D.P., Frost, P.G.H., Justice, C.O., Landmann, T., Le Roux, J.L., Gumbo, K., Makungwa, S., Dunham, K., Du Toit, R., Mhwandagara, K., Zacarias, A., Tacheba, B., Dube, O.P., Pereira, J.M.C., Mushove, P., Morisette, J.T., Vannan, S.K.S., Davies, D., 2005. The Southern Africa Fire Network (SAFNet) regional burned-area product validation protocol. Int. J. Remote Sens. 26, 4265–4292.

Geohazards, Earth and Planetary geological mapping

GEOLOGICAL MINING SURVEY THROUGH THE ANALYSIS OF ASTER AND LANDSAT 8 IMAGES IN THE SOUTHER SECTOR OF ECUADOR

Danny Bladimir Medina Aldas[1], Andy Joel Penafiel Lara[1], Eduardo Diaz Arias[1], David Ricardo Altamirano Moran [1], Maurizio Mulas[1],[2]*

[1] Escuela Superior Politécnica del Litoral, ESPOL, Facultad de Ingeniería en Ciencias de la Tierra, Campus Gustavo Galindo Km 30.5 Vía Perimetral, P.O. Box 09-01-5863, Guayaquil, Ecuador - (dbmedina, anjopena, edudia, darialta, mmulas)@espol.edu.ec

[2] Instituto Panamericano de Geografía e Historia (IPGH) secion Ecuador

KEY WORDS: ASTER, LANSAT8, Targets, Hydrothermal alteration, Spectral Signature

ABSTRACT:

The identification of hydrothermal minerals through the use of multispectral satellite images provides essential information in the first phases of mining prospection. The main goal of this research is to recognize by means analyses of satellite images of the studied zone that could be suitable for the mining activity. Lansat-8 and ASTER multispectral imagines were carried out by different spectral mapping techniques to extract the data. The RGB technique was used to mapping the altered minerals analysing band ratios and spectral indices to highlight areas of abundance of iron oxides, clay minerals and carbonates. The principal component analysis helped in the discrimination of mineral alterations as advanced argillic, intermediate argillic and propylitic alteration. On the other side, the spectral analysis method (SAM) and the lineal spectral unit (LSU) classification method helps defining mineralogical associations and new exploration targets. This methodology allows to recognize an advanced argillic alteration, intermediate argillic alteration, and oxides as hematite and jarosite zones. Carbonates are present in variable concentrations all over the studied area. The results were integrated with the cartographic and metallogenetic information and it was verified by mean the application of reflectance spectrometry. There is an agreement in the results of the application of the multispectral techniques PCA, SAM, LSU in the data set of the Lansat-8 and ASTER sensors for the mapping of alteration minerals. In conclusion this study permitted to optimize the first prospective phases to localize potential target for future mining activity.

1. INTRODUCTION

The interpretation of Aster and Landsat 8 multispectral images applied in mining survey help to remotely identify different lithological units, minerals, structural lineaments, and geomorphological units (Sheikhrahimi et al. 2019). They have been used successfully in the regional mapping of mineral resources in arid and semi-arid zones in the initial stage of exploration. (Parsa et al. 2016). However, over terrains with a dense vegetation coverage, it represents a challenge for remote sensing studies. The main features of the different minerals are quite similar with vegetation (Salisbury et al. 1994, Harris et al. 1998, Pour and Hashim 2017). The 4/2, 6/7, 7/5 band ratios of Landsat 8 have been used to identify iron oxides / hydroxides, hydroxyl-containing carbonates and clay minerals in the mapping of hydrothermal alterations in different metallogenetic provinces (Safari et al. 2018, Pour and Hashim 2015). The main hydrothermal alteration minerals can be differentiated with respect to epithermal minerals during gold exploration using ASTER multispectral imaging. The 3 bands of the VNIR subsystem are used to detect iron oxide and hydroxide minerals. The zones of argillic, phyllic and propylitic alterations can be recognized in the SWIR bands (1.6 to 2.43µm). The zones with alunite and kaolinite minerals can be detected due to the strong absorption of Al-OH in the band 5 to 2.17 µm. The minerals that form the sericitic alteration are detected by the absorption of Al-OH in the band 6 to 2.20 µm. To identify calcite chlorite, epidote is used absorption in band 8 at 2.35 µm (Boloki, and Poormirzaee 2010, Moore et al. 2008). The TIR thermal bands are used to identify quartz, carbonate and silica Ghasemi et al. 2018). In this study, PCA has been used in principal component analysis to identify the spectral characteristics of specific mineral. In addition, two spectral matching methods have been implemented: the spectral angle mapping (SAM) and the linear spectral unmixing technique (LSU) in the bands 4, 5, 6, 7, 8, 9 ASTER image to delimit the alterations. as advanced argillic, phyllic-silico, silicification and propylitic (Van der Meer et al. 2012, Hosseinjani and Tangestani 2011, Pour and Hashim 2017). The development of capabilities of ENVI multispectral image processing software has improved the precision to mapping mineral resource (Zeinelabdein and El Nadi 2014).

The government promotes the mining sector as a productive alternative for the economic and social reactivation of Ecuador (Vela, 2018). On the other hand, in Ecuador, there is a problem during the field-work due to social conflicts against mining activities and there are problems related with the COVID-19 pandemic crisis that can affect the normal development of prospecting activities.

The goal of this research is, primarily, the identification of hydrothermal alteration zones applying band combination techniques, band relation, spectral indices, PCA (Principal Component Analysis), supervised classification methods SAM (Spectral Angle Mapper), LSU (Linear Spectral Unmixing). Subsequently, these data would be used to integrate the information with local geology, metallogenetic strips and field work for the generation of mineral potential maps.

.

2. MATERIAL AND METHODS

The geological data was obtained from the Geological Map of the Western Cordillera of Ecuador between 3 ° - 4 ° S Scale 1: 200,000 (Pratt, 1997), and from the geological sheets scale 1: 100.00 of Cuenca, Girón, Gualaquiza, Saraguro and Sigsig. The geological maps were digitalized, and georeferenced using the WGS 84 Datum, UTM 17 S with ArcGIS software.

2.1 Remote sensing and images

The LANSAT 8 and ASTER satellite images were performed through the official USGS (United States Geological Survey) website (https://earthexplorer.usgs.gov/). A Landsat-8 scene of July 13, 2015 was acquired with two ASTER scenes of October 16, 2016 that cover the study area. The acquisition of this information could be done through access to the official site

* Corresponding author

https://earthexplorer.usgs.gov/ of the US Geological Survey (USGS), which provides free satellite images. The scenes captured from ASTER show a cloudiness less than a 10%, while the scenes from Landsat 8 show more than 20% of cloudiness.

2.2 Pre-processing of Remote Sensing Data

The processing of the images of the ASTER and OLI sensors was carried out in the ENVI 5.6 software. The pre-processing process included the radiometric calibration through the Radiometric Calibration module (Chander et al. 2009). In addition, the atmospheric calibration to reduce absorption and all scattering disturbances was made using the Fast Line-of-sight Atmospheric Analysis of Spectral Hypercubes (FLAASH) module. Subsequently, the masking process was carried out because the scenes (satellite images) displayed several elements like vegetation, clouds, and water using combination techniques and band quotient.

2.3 Processing of Remote Sensing Data

The normalized vegetation index present in the ENVI 5.6 tools was applied. Combining the information of the VNIR and SWIR sub-systems in the red, green and blue channels (RGB), false color images were determined multiple features of the studied area. To extract the information on the spectral properties of the different minerals and lithological units in the Landsat 8 and ASTER images, different methodologies are evaluated to be integrated using GIS tools to generate mineral footprint maps (Table 1).

Table 1 Summary of Spectral Band Ratios

Mineral sector	Quotients	Satélite	References
Iron oxid	2/1	Aster	(Bhadra et al. 2013)
Al-Si-(OH) minerals	5/6		(Pour and Hashim 2012).
Mg-Si-(OH) minerals	8/9		
Muscovite	7/6		
Silicate and limestone	14/12 13/14		
Alunite	4/5		Mahdevar et al. 2015
Calcite	4/7		
Kaolinite	4/6		
Phillic zone (yellow-reddish) - Clay zone (green) - Propilitic (azul)	7/6, 5/6, 9/8		(Pour and Hashim 2012).
Clay mineras and limestone	6/7	Landsat8	(Zoheir et al., 2012)
Iron silicate	6/5		
Iron oxid	4/2		
Kaolinite and montmorillonite	7/5		

Clay minerals have absorption properties of 2.1 to 2.4 µm and reflectance properties of 1.55 to 1.75 µm (Ourhzif et al., 2019). Alunite shows absorption ranges in approximate wave magnitudes of 1.50 and 2.2 µm. These ranges correspond to the SWIR subsystem of the ASTER sensor respectively in bands 4 and 7, therefore, it would be expected to identify them easier by means their range of absorption. The RGB combination 4/5, 4/6. 4/7 shows areas with white pixels that indicate the response of band 5, band 6 (AL-OH) and band 7 (Fe-OH). The propylitic alteration appears in dark green color while the phyllic alteration appears as yellow color (Mahdevar et al. 2015). The RGB combination (band7 + band9) / band8 clearly show the pixels with abundance of CaCO3 and MgOH, such as carbonate, chlorite and epidote because these minerals show a high absorption in band 8. Last, the combination RGB = (Band 4 + Band 6) / Band 5 is used to recognize kaolinite, alunite, and pyrophyllite minerals.

These combinations of different bands show the reflectance of the terrain surface at different wavelengths an allow to identify the relative abundance of alteration minerals (San et al. 2004). Ninomiya (2005) proposes lithological indices for the identification of areas with occurrence of different types of alteration such as KLI, ALI, CLI (Ninomiya, 2003), OHIa, OHIb, PI, QI, CI and SiO2 content Index (Ninomiya, 2005).

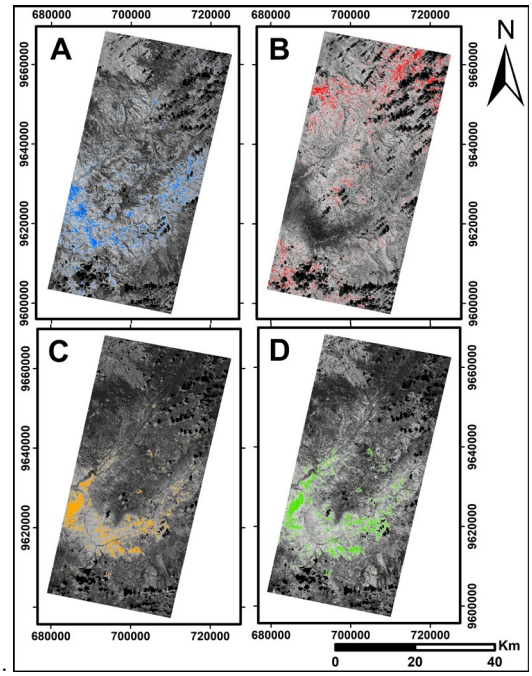

Figure 1. Areal distribution of the main mineralogical association: a) Iron oxid / hydroxid; b) hidroxil; c) clasy minerals; d) Iron minerals

3. RESULTS

Band relations with reflection features were applied to map the alteration minerals and identify the hydrothermal alteration in the volcanic deposits. Lansat 8 OLI 4/2 band ratio was assigned to reveal iron oxides/hydroxide (Figure 1a). The map result shows high concentrations of these minerals in the southern and south-western sector where outcrops andesitic lavas and scattered dacitic tuffs. Figure 1b shows areas of altered rocks containing hydroxyl by means the product of the 6/7 band ratio, with high concentrations in the ignimbrites breccias, conglomerates, and andesitic lavas in the northern sector. The distribution of clay minerals such as kaolinite and montmorillonite are highlighted by the 7/5 band ratio (Figure 1c), principally in the south-western part of the study area. Finally, the product of the 6/5 ratio (Figure 1d) shows iron minerals concentrated mainly in the south of the scene.

We applied the Principal Component Analysis (PCA) in Landsat-8 bands 2, 5, 6, 7 to map the hydroxyl-containing minerals. PCA4 eigenvector loading was selected due to high absorption values in band 5 (-0.55) and strong reflectance in band 7 (0.78). The spatial distribution of hydroxyl minerals was shown in a wide area to the south of the studied area and a lower concentration in the northeast sector. Bands 2,4,5,6 were used to identify iron oxides/hydroxides. Due to the moderate contribution of band 6 (0.43) and a strong negative charge in

band 5 (-0.75), the PCA2 was selected. The uploading of eigenvalues in the bands (VNIR + SWIR) of the Aster sensor was selected following the absorption and reflection features of the hydrothermal alteration minerals. The graphical representation of advanced argillic alteration was selected PCA3 due to the high absorption in band 4 (0.50) and the reflection in-band (-0.48). According to the uploading of the eigenvectors for the argillic-philic alteration, the PCA4 was selected with a negative absorption value in band 5 (-0.71) and a high reflectance value in band 6 (0.70). The distribution of the propylitic alteration in the PCA4 image has been identified by the negative absorption value of band 5 (-0.63) and the high reflection of band 6 (0.76). The map of mineral abundance, the product of applying the supervised classification method of the SAM spectral angle in the bands of the SWIR subsystem, was selected to represent the areas of advanced argillic alteration, argillic-philic, and oxides. The reference spectra were selected from the ENVI 5.3 *usgs_min* spectral library. Before applying these methodologies, the spectral signatures were resampled by intersecting the reference spectrum with the SWIR bands of ASTER and generating a new curve with the wavelengths corrected to the multispectral image.

The similarity degree between the reference spectrum and the image pixels shows alunite in varying concentrations to the north-east and southern part of the studied area. There is a low concentration of argillic-phyllic alteration in the center and south of the area due to the absorption of the kaolinite in band 5. Hematite appears only in the northeast sector. The linear spectral sample classification technique was applied to generate a map of the abundance of hydrothermal alteration minerals. The final members were selected from the ENVI 5.3 spectral library adjusted to the pixels of the SWIR subsystem bands. The results show the spatial distribution of alunite in isolated areas in the northeast, center of the studied area, and dickite in the northeast. The high concentration of montmorillonite indicates zones of argillic-phyllic alteration at the southwest. The oxides are present in different concentrations along the studied area. The results of the application of the SAM spectral mapping technique show three different mineralogical associations. The areas are rich in clays, and montmorillonite and kaolinite predominate in high and low concentrations towards the south and north, respectively, of the studied area. The silica-rich clays, specifical opal, are present principally in the southern zone in the Nabón canton while the propyl alteration occurs near the Nabón canton. Figure 2 shows the result of the LSU spectral classification technique using the spectral information of the measurement equipment. Four mineralogical assemblages were established. The first is clays rich in sulfates (red tones), representing alunite, dickite, and quartz in variable concentrations. The yellow pixels represent kaolinite and montmorillonite. The spatial distribution of the intermediate argillic alteration is evidenced in high concentrations to the northeast and southwest. Silica-rich clays are shown in light blue tones and represent opal. The opal concentration is variable and is distributed in the northeast-southwest fringes of the area of interest. The propylitic alteration is characterized by the presence of chlorite that was mapped in small areas as green pixels in small concentrations to the south-western.

4. DISCUSSION AND CONCLUSION

Multispectral information from the Landsat 8 and Aster remote sensors was used to map hydrothermal alteration zones related to epithermal gold mineralization in the Occidental Mountain range in the southern Ecuador. The vegetation is covering a large area of the sector, but a considerable percentage of exposed rock are noticed in the south-southwestern part.

The areas with abundant clays and oxides were identified by the processing techniques: band ratios, spectral indices, and PCA. For the spatial distribution of iron oxides/hydroxides, the 4/2 of Landsat 8 and 2/1 of ASTER have been applied. In Landsat 8, the zones containing oxides are mainly mapped to the south of the zone. It resembles the results of ASTER; however, the spatial distribution of the mineral in Landsat 8 covers a higher concentration of oxides in the study area. The PCA2 image of the Landsat 8 bands (2,4,5,6) represents the spatial distribution of iron oxide/hydroxide near the mineralization zones with a better correspondence due to the suppression of the noise components of the bands. The sector with a high concentration of quartz, carbonate, and silica were mapped by ASTER TIR bands using the indices (QI), (CI), (SiO2) (Ninomiya et al. (2005). Using the PCA 4 image of Lansat 8 (bands 2,5,6,7), zones containing hydroxyl were mapped in the exposed rock at the limits of the Nabón and Oña cantons. Generally, areas rich with carbonates and hydroxyl harbor are present gold mineralization (Bolouki et al. 2020). The PCA3, PCA4 images generated by principal component analysis in the bands (1,4,6,7), (1,3,5,6), (1,3,5,8) of ASTER, respectively, detect areas of advanced argillic, argillic-philic, and propylitic alteration. Then, SAM and LSU supervised classification methods were used in the bands of the ASTER SWIR subsystem to identify the assemblages of hydrothermal alteration minerals.

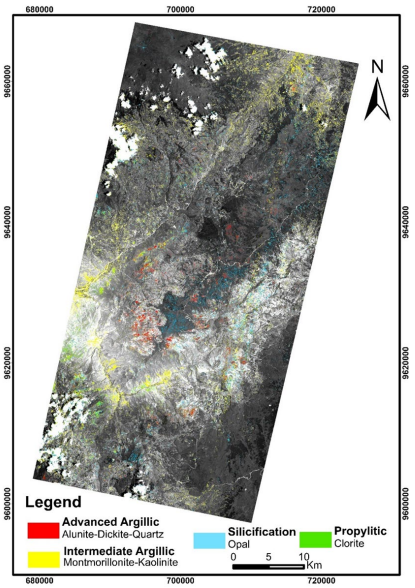

Figure 2 Distribution of the main alteration associations.

Finally, the propylitic alteration is far away from areas that host advanced argillic alterations. intermediate and silicification. The evaluation using the spectra has been taken by the reflectance spectrometry equipment for the SAM and LSU classification showing a strong coincidence in the mapping of the concentration of the intermediate argillic alteration and silicification. However, the direct comparison shows the superior capacity of the LSU classification to map hydrothermal alteration minerals. In conclusion, this research demonstrates using the data of the OLI multispectral sensors of Landsat 8 and ASTER to generate a potential map of hydrothermal alteration minerals indicating prospective zones of epithermal gold mineralization in the southern sector of Ecuador.

The groups of altered minerals located to the north-east, south-east, and south-west of the study area are stand out as prospective zones. The high prospecting potential targets are

located in the Nabón and Oña cantons. The prospective zones are related to the epithermal gold deposits belonging to the Azuay district in the Oligocene-Miocene gold-copper metallogenetic belt. The local geology corresponds to the volcanic deposits of the Saraguro group that host the mineralization and structural control of the regional faults with north dip, northeast southwest.

ACKNOWLEDGEMENTS (OPTIONAL)

This project was founded by ESPOL proyect “FICT-02-2019” (Caracterización paleomagnetica y geoquimica de ignimbritas del sector Cuenca - Pasaje (Sur Ecuador).

REFERENCES

Boloki, M., & Poormirzaee, M. (2010). Using ASTER image processing for hydrothermal alteration and key alteration minerals mapping in Siyahrud. Iran International Journal of Geology, 2, 38–43.

Chander, G.; Markham, B.; Helder, D. Summary of current radiometric calibration coecients for Landsat MSS, TM, ETM+, and EO-1 ALI sensors. Remote Sens. Environ. 2009, 113, 893–903.

Ghasemi, K., Pradhan, B., & Jena, R. (2018). Spatial identification of key alteration minerals using ASTER and Landsat 8 data in a heavily vegetated tropical area. Journal of the Indian Society of Remote Sensing, 46(7), 1061-1073.

Hosseinjani, M. and Tangestani, M.H., 2011. Mapping alteration minerals using sub-pixel unmixing of ASTER data in the Sarduiyeh area, SE Kerman, Iran. International Journal of Digital Earth, 4 (6), 487–504. doi:10.1080/17538947.2010.550937.

Harris, J. R., Rencz, A. N., Ballantyne, B., & Sheridon, C. (1998). Mapping altered rocks using LANDSAT TM and lithogeochemical data: Sulphurets-Brucejack Lake district, British Columbia,Canada. Photogrammetric Engineering and Remote Sensing, 64(4), 309–322.

Ninomiya, Y., 2003. A stabilized vegetation index and several mineralogic indices defined for ASTER VNIR and SWIR data. In Geoscience and remote sensing symposium, 2003. IGARSS’03. Proceedings. 2003 IEEE international (Vol. 3), Toulouse, France, 1552–1554.

Ninomiya, Y., Fu, B., and Cudahy, T.J., 2005. Detecting lithology with advanced spaceborne thermal emission and reflectance radiometer (ASTER) multispectral thermal infrared radiance-at-sensor data. Remote Sensing of Environment, 99, 127–139. doi: 10.1016/j.rse.2005.06.009

Mahdevar, M. R., Ketabi, P., Saadatkhah, N., Rahnamarad, J., & Mohammadi, S. S. (2015). Application of ASTER SWIR data on detection of alteration zone in the Sheikhabad area, eastern Iran. Arabian Journal of Geosciences, 8(8), 5909-5919.

Moore, F., Rastmanesh, F., Asadi, H., & Modabberi, S. (2008). Mapping mineralogical alteration using principal-component analysis and matched filter processing in the Takab area, northwest Iran, from ASTER data. International Journal of Remote Sensing, 29(10), 2851–2867.

Ourhzif, Z., Algouti, A., & Hadach, F. (2019). LITHOLOGICAL MAPPING USING LANDSAT 8 OLI AND ASTER MULTISPECTRAL DATA IN IMINI-OUNILLA DISTRICT SOUTH HIGH ATLAS OF MARRAKECH. International Archives of the Photogrammetry, Remote Sensing & Spatial Information Sciences.

Parsa, M.; Maghsoudi, A.; Yousefi, M.; Sadeghi, M. Recognition of significant multi-element geochemical signatures of porphyry Cu deposits in Noghdouz area, NW Iran. J. Geochem. Explor. 2016, 165, 111–124.

Pohl, C., & van Genderen, J. (2014). Remote sensing image fusion: an update in the context of Digital Earth. International Journal of Digital Earth, 7(2), 158-172.

Pour, A.B. and Hashim, M., 2012. Identifying areas of high economic-potential copper mineralization using ASTER data in the Urumieh–dokhtar Volcanic Belt, Iran. Advances in Space Research, 49 (4), 753–769. doi:10.1016/j.asr.2011.11.028

Pour, A. B., & Hashim, M. (2015). Hydrothermal alteration mapping from Landsat-8 data, Sar Cheshmeh copper mining district, south-eastern Islamic Republic of Iran. Journal of TaibahUniversity for Science, 9(2), 155–166.

Pour, B.A., Hashim, M., 2017. Application of Landsat-8 and ALOS-2 data for structural and landslide hazard mapping in Kelantan, Malaysia. Nat. Hazards Earth Syst. Sci., 17,1285–1303.

Pratt, E; Figueroa, J & Flores, B. (1997). Informe N° 1, Proyecto de Desarrollo Minero Control Ambiental, Programa de Información Cartográfica y Geológica: Mapa escala 1: 200.000. Geology of the Cordillera Occidental of Ecuador between 3° S and 4° S. CODIGEM -BGS, Quito – Ecuador 58 pp.

Roy, D.P., et al., 2014. Landsat-8: science and product vision for terrestrial global change research. Remote Sensing of Environment, 145, 154–172. doi:10.1016/j.rse.2014.02.001

Safari, M., Maghsoudi, A., & Pour, A. B. (2018). Application of Landsat-8 and ASTER satellite remote sensing data for porphyry copper exploration: a case study from Shahr-e-Babak, Kerman, south of Iran. Geocarto International, 33(11), 1186-1201.

Salisbury, J. W., Wald, A., & D’Aria, D. M. (1994). Thermal-infrared remote sensing and Kirchhoff’s law: 1. Laboratory measurements.Journal of Geophysical Research: Solid Earth, 99, 11897–11911. https://doi.org/10.1029/93JB03600.

San, B.T., et al. 2004. Comparison of band ratioing and spectral indices methods for detecting alunite and kaolinite minerals using ASTER data in Biga region, Turkey. In Proceedings ISPRS, Istanbul, Turkey.

Sheikhrahimi, A., Pour, A. B., Pradhan, B., & Zoheir, B. (2019). Mapping hydrothermal alteration zones and lineaments associated with orogenic gold mineralization using ASTER data: A case study from the Sanandaj-Sirjan Zone, Iran. Advances in Space Research, 63(10), 3315-3332.

Thalmann, H.E. 1946. Micropalaeontology of Upper Cretaceous and Paleocene in Western Ecuador. Bulletin
of the American Association of Petroleum Geologists, 30, 337-347

Van der Meer, F.D., et al. 2012. Multi-and hyperspectral geologic remote sensing: A review. International Journal of Applied Earth Observation and Geoinformation, 14 (1), 112–128. doi:10.1016/j.jag.2011.08.002

Vela-Almeida, D. (2018). Territorial partitions, the production of mining territory and the building of a post-neoliberal and plurinational state in Ecuador. Political Geography, 62, 126-136.

Zeinelabdein, K.A.E. and El Nadi, A.H.H., 2014. the use of landsat 8 oli image for the delineation of gossanic ridges in the red sea hills of NE Sudan. American Journal of Earth Sciences, 1 (3),62–67.

A TOOL FOR DIGITAL RESOURCES ANALYSIS METHODOLOGY TO PLANNING GEOLOGICAL SURVEY ACTIVITIES

M. Villalta *, A. Viña , E. Larreta , M. Mulas

Escuela Superior Politécnica del Litoral ESPOL, Facultad de Ingenieria en Ciencias de la Tierra FICT, Campus Gustavo Galindo km 30.5 vía Perimetral, P.O. Box 09-05-5683, Guayaquil, Ecuador - micdevil@espol.edu.ec, agvina@espol.edu.ec; elarreta@espol.edu.ec; mmulas@espol.edu.ec

KEY WORDS: TPI, DEM, ArcGIS, South America, geological alignments, geological formation

ABSTRACT:

The development of new remote sensing and GIS techniques has improved planning analyses prior to field activities for geological mapping and analysis of impervian areas. This study details a proposal of methodology for the first remote geological and structural characterization of a study area, focused in the southern sector of Ecuador. This research establishes an analysis of geological lineaments and the first recognition of lithological units by means of the analysis of digital elevation models (DEM) with a resolution of 12.5 meters and their derived models. The geological lineaments were obtained from a Topographic Position Index (TPI) model using the PCI Geomatica software and afterwards were analysed in ArcGIS. Later, the delimitation of the geological units was carried out through the discretization of the topographic changes, taking in account the analysis of the texture and roughness patterns of the TPI model by means the software ArcGIS. Finally, the validation process was carried out comparing the lithological units recognized with the existing cartography, showing a 89% of correspondence. In South America and especially in Ecuador there are many problems due to social movements against mining activity. This methodology will help to better plan the prospective activity optimizing the resources and optimizing the prospective activity in the field.

1. INTRODUCTION

Geomatics has facilitated obtaining geological and structural information from large or hard-to-reach areas through satellite imagery analysis, with Geographic Information Systems (GIS) and database management (Lu et al., 1999; Guoan, 2014). The radar images analysis and DEMs are particularly useful to identify linear features (guidelines that may indicate the existence of geological structures), and allow to obtain information on large-scale structures, tectonic characteristics of a region and the estimation of different lithological units (Singhroy et al., 1999; Jaboyedoff et al., 2009).

The lineaments are defined as mappable linear surface and generally it is considered as a surficial expression of discontinuities of geological structures (Minar et al., 2009). Structural lineaments can be identified directly by the presence of rupture characteristic figures, displacement of outcrops or can be inferred from the presence of morphological elements (slope changes, fault scarps, presence of valleys and depressions) (Marchionni., 2014). If lineament detection is based on the morphometric properties of the land surface, lineaments are automatically extracted either directly from a digital elevation model (DEM) or from different derived models (Hillshade, TPI, second derivative) (Abdullah et al., 2010; Mallast et al., 2011; Vaz, 2011). Automatic extraction depends on the efficiency of the algorithms, as well as the content of the information in the image (Al-Dossary et al., 2007).

The topographic variability of an area is shown by the roughness analysis (changes in patterns and textures roughness) and from the processing of survey data by a DEM (Sánchez, 1998). Roughness contrast occurs in areas where the slope changes sharply. These areas of contrasted roughness reflect differences in lithology that can generate differential erosion processes. Therefore, these changes in landform can be considered as a feature to identify and delimit geological changes (Dirik, 2005). In this paper is proposed a methodology that allows a priori characterization of the local geology. Through the analysis of DEM and satellite images, an automatic extraction of lineaments is carried out to obtain structural lineaments and the geological units are delimited from a topographic discretization of the study area from a TPI model. This allows to obtain a first draft of the geological map of the sector under study for the planning of field activities, allowing to optimize time and resources for the field activity.

2. METHODOLOGY

The study area (Figure 1) is located in the inter-Andean region of the southern sector of Ecuador in the province of Azuay. The site covers an area of 2348 km^2 and corresponds to a complex mosaic of geological units and topographical features. The sector is characterized by an Oligo-Miocene sedimentary succession interbedded with volcanic units (Pratt et al., 1997). The geomorphology of the sector is characterized by relatively steep slopes (average slope = 18.87°). The higher areas rise steeply from the central zone to the north and northwest of the study site.

2.1 Data

The base model used is DEM ALOS PALSAR with 12.5 m spatial resolution obtained from NASA's Alaska Satellite Facilities open access platform, from which Hillshade, Log 10 and TPI models were generated.

The TPI model was generated using the following equation:

$$TPI = \frac{DEM_{Mean} - DEM_{Min}}{DEM_{Max} - DEM_{Min}} \quad (1)$$

where DEM_{Mean} = mean values raster.
DEM_{Min} = minimum values raster.
DEM_{Max} = maximum values raster.

Each of these values was obtained using the ArcGIS focal statistics tool from the base DEM model.

* Corresponding author

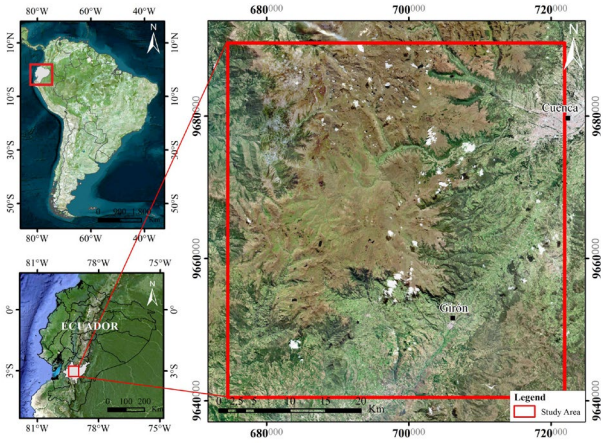

Figure 1 Study area. Coordinate system is UTM WGS84 17S

Then, the automatic extraction of lineaments was carried out from the TPI model using the LINE module of PCI Geomatics (2020). The LINE module extracts lineaments from an image and converts these linear features into vector form using six parameters: RADI (Radius of filter - pixels), GTHR (Threshold for edge gradient), LTHR (Threshold for curve length), FTHR (Threshold for line fitting error), ATHR (Threshold for angular difference) and DTHR (Threshold for linking distance).

The length and number of extracted lineaments depend on the input parameters being assigned (PCI Geomatic, 2020; El-Sawy et al., 2016). The parameters used in this study (Table 1) were established after the analysis of the values proposed by the LINE module and by several authors (Hashim, 2013; Prasad et al., 2013; Abdullah et al., 2010). The tests show that the parameters that had the greatest weight in our case were GTHR, that influenced the number and length of the lines, FTHR, that influenced the spatial precision (higher values of this parameter gave longer lines and lower values gave shorter lines) and DTHR, that influenced the separation between the lines.

Parameters	Suggested values	Parameters	Suggested values
RADI	20	FTHR	10
GTHR	150	ATHR	30
LTHR	30	DTHR	35

Table 1 Suggested parameters values.

2.2 Analysis of the lineaments

The process of automatic extraction of lineaments from the study area (Figure 2a) shows a high density of lines. Given the spatial resolution of the base model, the extension of the study area and the working scale (1:50000), the lineaments that had lengths less than 1500 meters were filter out (Figure 2b). Later, they were analyzed by creating a lineament density map with ArcGIS 10.7.1 software, to calculate the frequency of lineaments per unit area (Greenbaum, 1985). This process consists of adding the available lineament lengths in a defined grid size. In this case, for practical reasons, the grid size was defined as 1 km (Hashim et al., 2013). From an engineering point of view, areas of high lineament density are less suitable for dam construction, as they have a high risk related with geohazards, such as slope failure. (Lim et al., 2001). The interpretation and classification of the automatic lineaments based on visual criteria characteristic of photogeology (García et al., 2008) such as changes in the shape of the relief, very deep and linear ravines, changes in drainage patterns, morphology of the riverbeds, alignments and very linear behavior of the mountain tops, terrain ruptures. Following the identification of the main lineaments, the attention is focused on the lithological variations through the analysis of the TPI model.

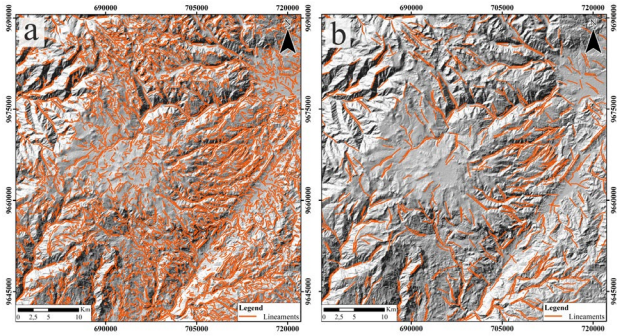

Figure 2 a) Lineaments obtained by automated extraction. b) Lineaments after filtering.

2.3 Lithology identification

The lithology identification is carried out by differentiation and delimitation of areas with roughness contrast in the TPI model. The identification of roughness patterns was performed using the Topographic Position Index (TPI), where the identified patterns were drawn on an image of the TPI digitally. A fist discretization, made at macroscale, permit to identify sector with similar behavior.

After that, the zoning was carried out at mayor detail **(**Figure 3) Once the pattern changes were delimited, areas with similar roughness characteristics (called units) were generated and named. For a better delimitation of the patterns and definition of the units, the drainages, the lagoon behavior, the geoforms and the tectonic structures of the area were taken into consideration (García et al., 2008).

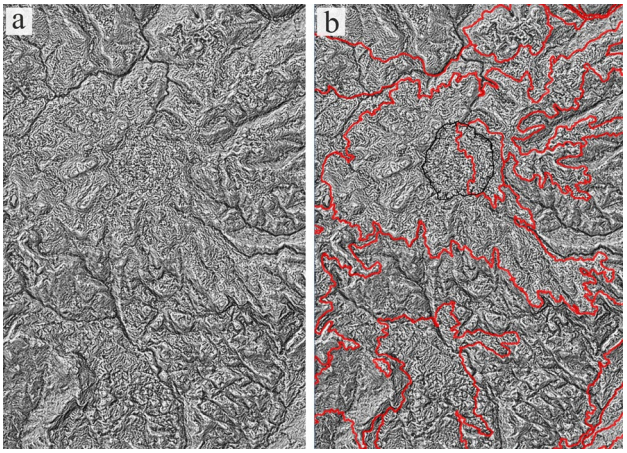

Figure 3 Identifying patterns from the roughness of the TPI. In **a)** the TPI model is shown and in **b)** the identified patterns that delimit different roughness textures in their respective locations are observed.

Finally, the validation process was carried out by means of an area comparison of the scheme of units previously obtained with the geological cartography of the Geological Map of Cuenca (53 CT NV F4) and Girón (54 CT NVI Ba) scale 1:100000, to know the percentage of similarity. The percentage of similarity is calculated comparing the units obtained in this work with the formations of the base cartography. This process was carried out with 10 sections of our scheme and their corresponding sections in the base cartography.

$$\% \, per \, unit = \frac{A_{unit}}{A_{Formation}} \cdot 100 \quad (2)$$

$$\% \, similitud = \frac{\sum_{i=1}^{n} \% \, per \, unit_i}{n} \cdot 100 \quad (3)$$

where A_{unit} = area of the unit obtained in this study.
$F_{ormación}$ = area of the geologic formation.
n = number of percentages to use

3. RESULTS AND DISCUSSION

A total of 4881 lines were obtained by means the automated extraction according to the parameters entered adapting to the variations and linearities of the AOI. The result shows that the maximum length of linear structures is 6947.7 m and the majority of the lineaments are minor than 900 m. The figure 4a shows that in an area of 14 km^2 (red), sited in the central-east and southwest sectors of the studied area, are present an high number of lineaments. The north central section shows a density of moderate to high, this area corresponds to the Cajas National Park. A total of 110 faults were recognized (Figure 4b), with a preferential NW - SE orientation for the longest fault and NE - SW orientation for the shortest ones.

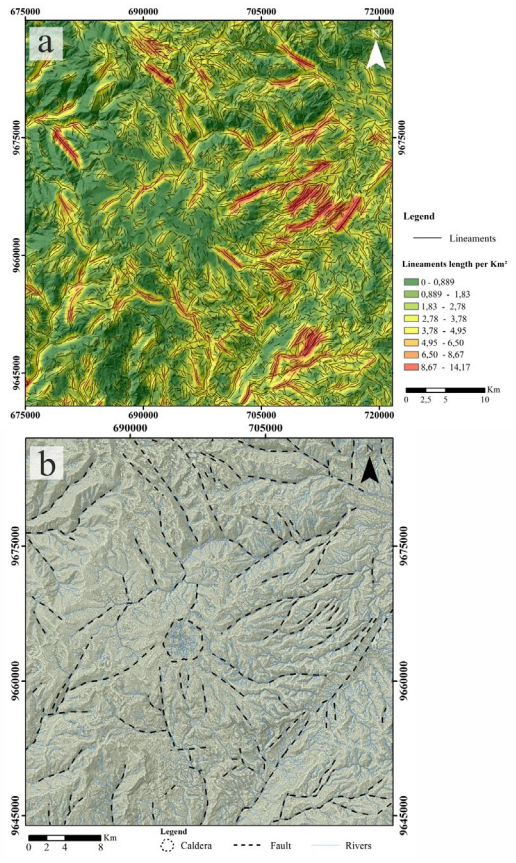

Figure 4 a) Lineaments density map of the automatically extracted lineaments; b) structures of the zone of study

3.1 Delimitation of the caldera

From the DEM analysis and its derivatives (Hillshade and TPI), a radial drainage was recognized in the sector (Figure 5a). Through topographic profiles (Figure 5c) in this same sector was evidenced a depression interpreted as a caldera (Figure 5b). This caldera has a circular shape, with a diameter between 4.5 to 5 km. According to the features highlighted with the profiles (Figure 54c), the caldera shows greater erosion in the northern and northwestern flank.

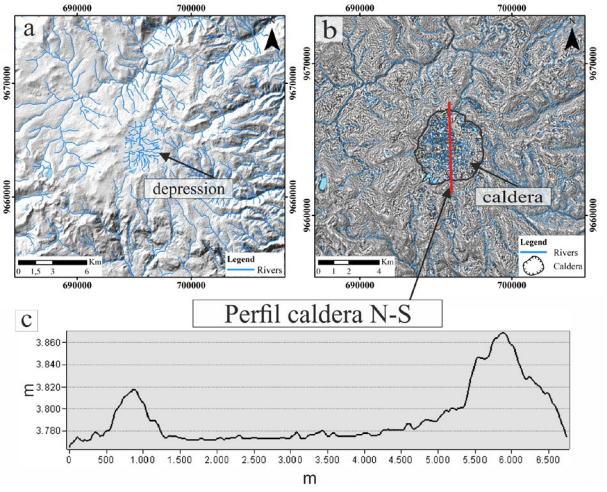

Figure 5 a) Radial drainage, and relief of the caldera area, b) Delimited caldera and c) Caldera profile

3.2 Geological units

The process to recognizing the main patterns and the changes in roughness textures clearly show the roughness contrasts (Figure 3). These changes are interpreted as signs of lithological changes, therefore the units delimited with this process are considered as geological units. The central and eastern areas of the studied area present a great textural contrast, thus allowing better identification of the changes and consequently defining the units. The drainage change served as support for a better delimitation.

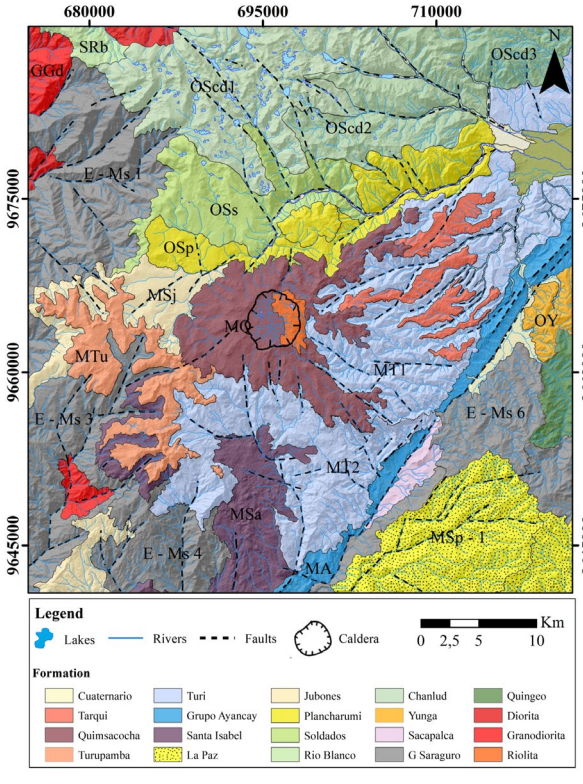

Figure 6 Final geological map

Thirty-seven units were differentiated. Then a comparison was made with the official geological cartography, showing great similarities in the central and E zones of the study area. The level of detail reached will depend on the resolution of the base information. The geological units delimited with this methodology may be different from the existing ones (existing cartography). New formations can be proposed, or the same formation can be subdivided into different units. The comparison of areas between the current cartography and the result obtained by following our methodology gives a similarity percentage of 87%.

Comparisons are made to establish the equivalence between the units and the formations of the base cartography in order to be able to assign to the units the name of the formation with greater similarity and correspondence (Figure 6). To assign the names the following considerations were taken: a) The unit receives the name of the formation with the greatest similarity and geographical correspondence; b) If a unit covers two or more formations on the reference map, it takes the name of the formation with the largest area; c) If there are different units and when countering with the reference base map these correspond to a single formation, the name of that formation is assigned, but a numerical and color distinction is made.

4. CONCLUSIONS

The methodology proposed in this work allows to obtaining previous data and thus optimizing resources for a successive field phase. The comparison between the generated map and the current geological map of the Cuenca and Girón chart, determined an 87% agreement. This methodology can be applied to generate the base map used in the planning of field trips studies and investigations allowing to optimize time and costs.

ACKNOWLEDGEMENTS

This project was founded by ESPOL proyect “FICT-02-2019” (Caracterización paleomagnetica y geoquimica de ignimbritas del sector Cuenca - Pasaje (Sur Ecuador) directed by M.M. We are grateful to the anonymous referee for the detailed reviews that helped us improve the manuscript.

REFERENCES

Abdullah, A., Akhir, J. M., and Abdullah, I. (2010). Automatic mapping of lineaments using shaded relief images derived from digital elevation model (DEMs) in the Maran–Sungi Lembing area, Malaysia. Electronic Journal of Geotechnical Engineering, 15(6), 949-958.

Al-Dossary, S., and Marfurt, K. J. (2007). Lineament-preserving filtering. Geophysics, 72(1), P1-P8.

Dirik, K. (2005). Advanced photogeology–lecture notes. Geological Engineering Dept., Hacettepe University.

El-Sawy, K., Ibrahim, A. M., El-Bastawesy, M. A., & El-Saud, W. A. (2016). Automated, manual lineaments extraction and geospatial analysis for Cairo-Suez district (Northeastern Cairo-Egypt), using remote sensing and GIS. International Journal of Innovative Science, Engineering & Technology, 3(5), 491-500.

Guoan, T. (2014). Progress of DEM and digital terrain analysis in China. Acta Geographica Sinica, 69(9), 1305-1325.

García, A., Zamorano, J. J., López-Miguel, C., Galván-García, A., Carlos-Valerio, V., Ortega, R., and Macías, J. L. (2008). El arreglo morfoestructural de la Sierra de Las Cruces, México central. Revista mexicana de ciencias geológicas, 25(1), 158-178.

Greenbaum, D., (1985) Review of remote sensing applications to groundwater exploration in basement and regolith, Brit GeolSurv Rep OD, Vol. 85/8, 36p.

Hashim, M., Ahmad, S., Johari, M. A. M., and Pour, A. B. (2013). Automatic lineament extraction in a heavily vegetated region using Landsat Enhanced Thematic Mapper (ETM+) imagery. Advances in Space Research, 51(5), 874-890.

Jaboyedoff, M., Couture, R., and Locat, P. (2009). Structural analysis of Turtle Mountain (Alberta) using digital elevation model: toward a progressive failure. Geomorphology, 103(1), 5-16.

Lim, C.S., Ibrahim, K., Tjia, H.D. (2001) Radiometric and Geometric information content of TiungSat-l MSEIS data, in: TiungSAT-1: From Inception to Inauguration, pp. 169–184.

Lu, P. F., and An, P. (1999). A metric for spatial data layers in favorability mapping for geological events. IEEE transactions on geoscience and remote sensing, 37(3), 1194-1198.

Mallast, U., Gloaguen, R., Geyer, S., Rödiger, T., and Siebert, C. (2011). Derivation of groundwater flow-paths based on semi-automatic extraction of lineaments from remote sensing data. Hydrology and Earth System Sciences, 15(8), 2665-2678.

Marchionni, D. S., and Cavayas, F. (2014). La teledetección por radar como fuente de información litológica y estructural. Geoacta, 39.

Paladines, A., Guzman, J., (1980) Geological Map of Cuenca (53 CT NV F4) 1:100000. IIGE Quito.

PALSAR_Radiometric_Terrain_Corrected_high_res; Includes Material © JAXA/METI 2007. Accessed through ASF DAAC 04 Julio 2020. DOI: 10.5067/Z97HFCNKR6VA

PCI Geomatis (2020). Line: Lineament extraction. Recuperado el 10 de marzo del 2021 website:https://www.pcigeomatics.com/geomatica-help/references/pciFunction_r/python/P_line.html

Pratt, E, Figueroa, J., Flores, B. (1997). Informe N° 1, Proyecto de Desarrollo Minero y Control Ambiental, Programa de Información Cartográfica y Geológica: Mapa escala 1: 200.000. Geology of the Cordillera Occidental of Ecuador between 3° S and 4° S. CODIGEM -BGS, Quito – Ecuador 58 pp.

Randel, R. P., (1974) Geological Map of Cuenca Giron (54 CT NVI Ba) 1:100000. IIGE Quito.

Sánchez Serrano, F., Tejero López, R., & Bergamín de la Viña,J. F. (1998). Análisis de la variabilidad del relieve a partir de modelos digitales del terreno. Revista de la Sociedad Geológica de España, 11(1-2), 139-149.

Singhroy, V., and Saint-Jean, R. (1999). Effects of relief on the selection of RADARSAT-1 incidence angle for geological applications. Canadian Journal of Remote Sensing, 25(3), 211-217.

Vaz, D. A. (2011). Analysis of a Thaumasia Planum rift through automatic mapping and strain characterization of normal faults. Planetary and Space Science, 59(11-12), 1210-1221. DOI:10.1016/j.pss.2010.07.008

MULTI-SOURCE AND MULTI-SCALE MONITORING SYSTEM OF DEEP-SEATED GRAVITATIONAL SLOPE DEFORMATION IN EAST-CENTRAL SARDINIA.

Valentino Demurtas*, Paolo Emanuele Orru', Giacomo Deiana

Department of Chemical and Geological Sciences, University of Cagliari, Italy.

KEY WORDS: DSGSDs, UAV, Monitoring, InSAR, GNSS, Geomorphology, Early-warning system

ABSTRACT:

Deep-seated gravitational slope deformations (DSGSDs) are slow-moving rock-mass movements that encompass entire valley flanks or hillslopes. An acceleration of slope movements leading to a potential catastrophic failure poses a threat to communities and monitoring of these slopes is important for early-warning and risk reduction. Therefore, we studied in detail DSGSDs and landslides in the inhabited areas of Pardu Valley in eastern-central Sardinia using integrated remote-sensing techniques, field mapping, and monitoring systems.
Space-borne Interferometric Synthetic Aperture Radar (InSAR) data using Sentinel-1 satellites identified downslope movement of up to 10 mm per year on Bruncu Pranedda DSGSD (Ulassai). To analyse the DSGSDs at local scale we used high-resolution digital elevation models acquired UAV (Uncrewed Aerial Vehicle), supported by structural and geomorphological field mapping surveys. This allowed to create a geological 3D models of the slope deformations.
To better understand the kinematics and temporal evolution of deformation of the unstable slopes, a monitoring system, consisting of GNSS antenna, tiltmeter, and extensometer, has been installed along the DSGSDs near urban areas. A distribution of GNSS measurement points in the unstable area and adjacent stable areas has since 2021 provided periodic measurements of the deformation. With continuous acquisition, extensometers and tiltmeters have been recording changes in large block inclinations and movements over prominent fractures since 2021. Historical InSAR displacement rate and monitoring data support our model of rock slope deformation indicating large scale-toppling. Our 24/7 monitoring system could become an essential component of an early-warning system.

1. INTRODUCTION

Central East Sardinia is characterized by steep plateau and adjacent deep valleys (Maxia et al., 1973; Marini & Ulzega, 1977). This context is particularly susceptible to geohazards, mainly DSGSDs, rockfalls, rock avalanches and giant toppling. This setting represents high geological risk inserted in an urban context.
In particular, the municipality of Ulassai is located under the walls edges of a carbonate plateau affected by all these different gravitational processes. In this urban context there is a need to map, characterize and monitor these processes and design an early-warning system.
Using innovative technologies such as UAV surveys, integrated by geological, geomorphological and structural field surveys, allowed an accurate mapping of the related surface evidences and gravitational processes. To characterize the landslides at different spatial and time scale, a temporal series of InSAR data was analysed. The aim of this study is to integrate field and remote sensing data to deep understand the DSGSD process in these areas and secondary landslides and design an GNSS and geotechnical monitoring system.

2. STUDY AREA

The east-central Sardinia (Italy) is characterised by a Jurassic dolomitic Plateau (Tacchi) overlying a Metamorphic Palaeozoic basement, mainly composed by metasandstone, quartzites and phyllites. Towards the coast, the basement is composed by Permo-Carboniferous granitic rocks. The main faults (NW-SE direction) are associated to the lower Miocene rotation of the Corsican-Sardinian block. These faults have been reactivated during the opening stage of the Tyrrhenian Sea. Erosion has mainly acted on the Oligo-Miocene strike-slip faults with an increase in the erosive rate during the Plio-Pleistocenic extensional tectonics, that in this sector of Sardinia was manifested with an Uplift (Carmignani et al., 2016). In the internal area the rivers have cut deeply valleys whit high slope energy (up to about 700 m). The mean geomorphological units are Rio Pardu valley and the carbonate plateau called "Tacco di Ulassai". These slopes are often characterised by landslides and DSGSDs with Sackung and Lateral spread features (Cruden & Varnes, 1996; Zichinsky, 1966).
.

3. METHODOLOGY AND RESULTS

The proposed methodology is based on a phase of reconstruction of the detailed geological and geomorphological context (Figure 1). A mapping and characterization of the gravitational processes affecting the urban area was performed also with the support of UAV surveys. Based on these preliminary data, a multiscale and multisource monitoring of the processes was started.

3.1 Geomorphological and UAV analysis

DSGSD 3D models have been extracted from a series of digital photos acquired from UAV. The study areas are often not accessible due to their steep slope, therefore require surveys remote sensing systems to complete the field investigations. UAV digital photogrammetric surveys have been used to create a high-resolution topography (Figure 2). The model has been corrected and georeferenced by Ground Control Points acquired by GNSS.

* Corresponding author

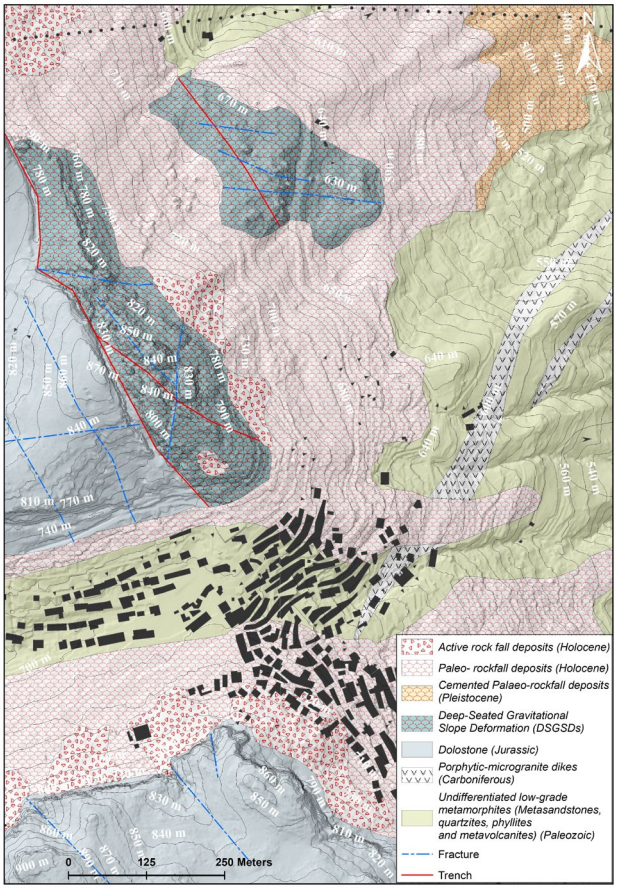

1 - Geological map of Ulassai.

GCP have been fixed on the ground and they are visible in the photograms to permit the co-registration using the software Photoscan.

Field surveys were carried out with the following objectives:

- Analyse the geological and structural setting of the area around the inhabited centre of Ulassai;
- Detailed geomorphological survey in particular of the carbonate walls;
- Identification of both quiescent and active gravitational processes;
- Detailed analysis of Deep-seated gravitational slope deformations.

The surveys made possible to map the gravitational processes affecting the inhabited centre of Ulassai (Figure 3). In particular were identified:

- Widespread processes of rock fall in the walls projecting the inhabited centre;
- Marginal sectors of the plateau affected by the toppling of dolomitic giant prismatic block;
- The north side of Ulassai slope (Bruncu Pranedda) affected by DSGSD.

The Bruncu Pranedda DSGSD shows two sectors with different settings located in the top and middle slopes.

In the top slope to the east of the largest extensional trenches called Pranedda Canyon, the rock mass show high fracturing strata attitude of the Dorgali Formation is toward the east, with a dip up to 40°. Field data and 3D elaboration allow to hypothesize shear basal surface in the marls and clay located between the dolomitic plateau and the metamorphic basement. This setting indicates a deformation kinematics type lateral spread (Cruden & Varnes, 1996).

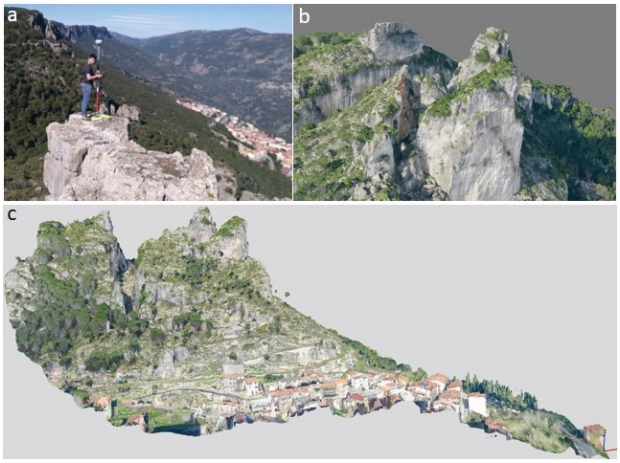

2 – a) GNSS ground control points acquisition; b) UAV 3D model detail of top slope of Bruncu Pranedda DSGSD; c) UAV 3D model of "Bruncu Pranedda DSGSD".

In the middle slope, the DSGSD shows a more evolved stage, represented by dolomitic formation sinking into the metamorphic basement. In this case the basal shear surface involves the top of the metamorphytes with high fracturing and chemical alteration. The kinematic deformation of this area is Sackung type (Zichinsky, 1966).

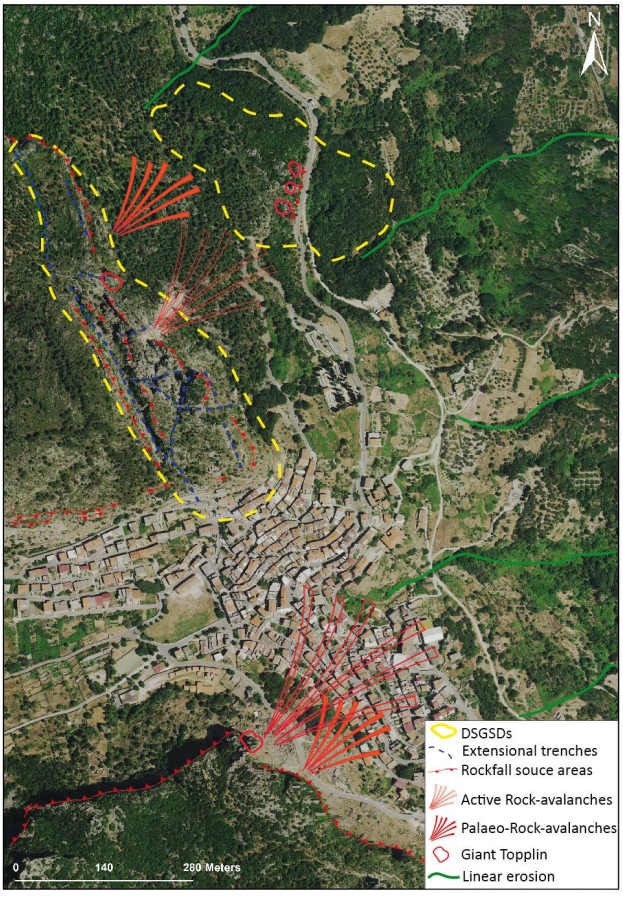

3 – Orthophoto 2016 showing main gravitational affecting Ulassai urban area.

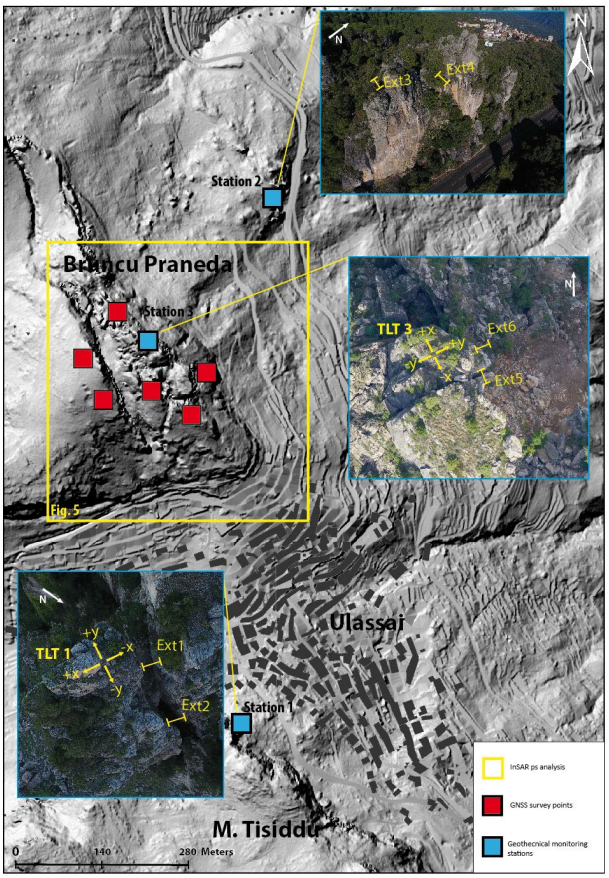

4 – Location of different monitoring stations

3.2 InSar

Space-borne Interferometric Synthetic Aperture Radar (InSAR) data have been used to analyse the slope deformation (Ferretti, 2014). Using Sentinel-1 satellite, taking into account the LOS (Line of Sight) velocities, we identified downslope movement of up to 1 cm/y in the ascending geometry in Bruncu Pranedda mountain. The data on the period 2014–2020 indicate up to 0.2 km2 large slope area identified as DSGSDs to be active. (Figure 5). We used only high PS (Permanent scatters) coherence (0.6 – 1) located in the rocky outcrops. Low coherence points are located on rockfall deposits and in vegetate areas.
PS analyses show stable surface on the urban area and in the west slope of the main extensional trench of Pranedda Canyon. While, in accordance with the geomorphological evidence, downstream the main trench, the speeds of the PS show LOS displacement up to 1 mm / y. The main component of the movement is vertical. No movements were detected in the DSGSD downstream of Bruncu Pranedda due to low PS coherence due to dense vegetation.

3.3 GNSS monitoring

On the basis of geomorphological and InSAR data, a network of topographic nails was built to measure the movements with geodetic techniques (Gili J. A. et al., 2000). GNSS surveys points was installed in Bruncu Pranedda in 2020, and measurements have been realised with intervals of 3 months. The aim is to measure the movements of coherent blocks of rock mass separated from the trenches in order to understand the differential movements. Topographic survey points with brass support have been created to mount the GNSS antenna

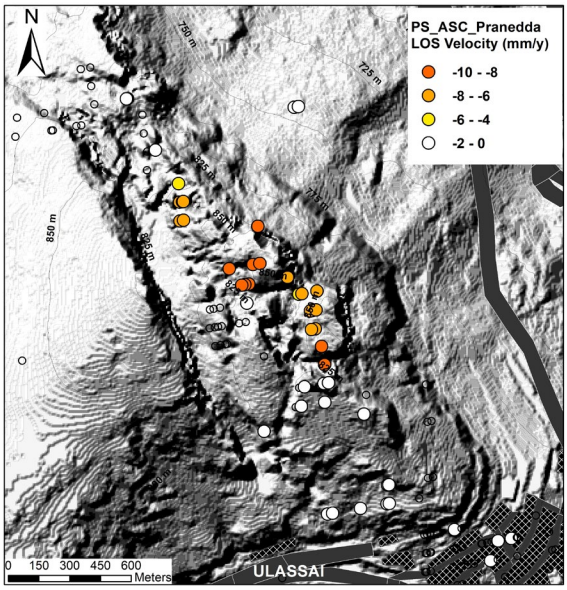

5 - Results of PS InSAR interferometry of Bruncu Pranedda DSGSD.

and reduce the positioning error to fractions of mm. The acquisitions are performed with Trimble R8 GNSS in static mode with an acquisition of 1 hour and 30 min.

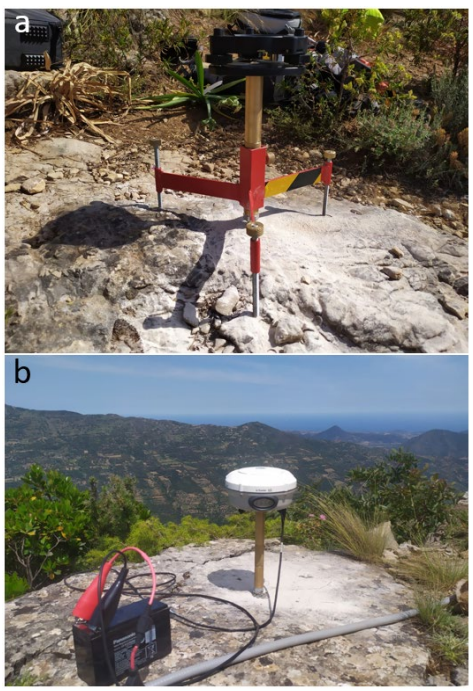

6 – a) System for the vertical positioning of topographic nails.
b) GNSS data acquisition phase in static mode.

3.4 Geotechnical monitoring

A geotechnical monitoring network in extension fractures was designed in 3 sites to validate InSAR and GNSS displacement data. 6 extensimeters and 2 tiltmeters were installed to continuously monitor deformations (Figure 7). The monitoring system is powered by batteries recharged from a photovoltaic panel. The data with continuous acquisition are managed by Campbell scientific CR1000X control unit with Sierra Wireless

RV50X remote data transmission system. The sensors installed are Extensimeters GEFRAN GSF1800 and Tiltmeters MEMS Earth System.
The data are managed through the HMS-WED online platform created by Hortus srl.

7 – Geothecnical station trumentations a) Data logger station 1 on Tisiddu Mountain; b) Extensimeter Ext 1; c) Tiltmeter Tlt1.

The data loggers, central acquisition components, are configured as follows:

- Sensor sampling interval: 30 s;
- Data storage interval: 10 min;
- Automatic data transmission to HMS-WEB platform: 5 min;

The analysis of the preliminary data acquired since January 2021 show low velocity deformation. In particular the extensimeter E1, E4 and E5 show no movement; E2 and E6 show a closing movement up to 1,3 mm; while E3 registered a total closing movement of 5 mm. The tiltmeters show a tilting of about 0,5° to southeast in the sector 1 and a tilting of 1 ° to North East in the sector 3.

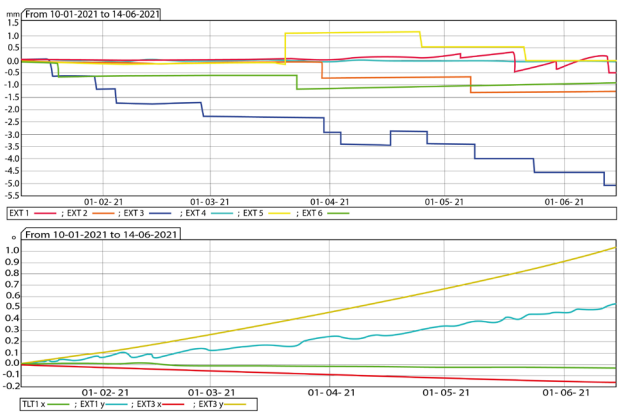

8 - Extensimeters and tiltmeters movements. Ubication of sensors and displacement direction in Figure 4.

3.5 early-warning system

The early warning system will be based on the measurements of the geotechnical instrumentation, in particular by continuously monitoring the opening or closing of fractures with extensimeters and the inclination of large blocks with tiltmeters. The alert thresholds are based on the observed displacement rates from the InSAR series which correspond to about 10 mm/y. The defined thresholds are 2.5 mm/h and 5 mm/day for extensimeters and 0.3 °/h and 0.5 °/day for tiltmeters. These thresholds will be calibrated through the movements recorded by the sensors over the course of a year. The alert measures proposed are based on information actions such as visual and audible alarms by siren and evacuation of the areas affected by mega-toppling processes.

4. DISCUSSION AND CONCLUSIONS

Analysis of the geological and geomorphological setting of plateau edge in Ulassai using UAV photogrammetry and high resolution field surveys allowed to identify different gravitational geological hazard. Landslides with different kinematic and magnitude has been identified: DSGSDs with sackung and lateral spread kinematic, giant toppling and widespread rockfalls. Different techniques aiming to understand the temporal evolution of DSGSD and giant toppling and future dynamics have been applied in three areas in Ulassai.
InSAR data indicate in the lateral spread of Bruncu Pranedda a large slope side affected by a deformation about 1 cm/y downslope in the last 6 years. In this area we stared a geodetic monitoring system to validate and calibrate satellite data and to understand the differential movement under deformation slope. To analyse the deformation at fracture scale three geotechnical monitoring stations were installed with continuous acquisition in order to project an early-warning system. In conclusion, based on high resolution geomorphological model of the gravitational process affecting Ulassai, we build multi-source and multi-scale monitoring system.

Table 1- Multi-source and multi-scale monitoring system synthesis.

Technique	Spatial scale	Temporal scale
InSAR	Slope scale	Years
Geodetic	Rockmass	Months
Geotechnic	Fractures	Day/hour

REFERENCES

Carmignani, L., Oggiano, G., Funedda, A., Conti, P., & Pasci, S., 2016. The geological map of Sardinia (Italy) at 1:250,000 scale. *Journal of Maps*, 12(5), 826–835.

Cruden, D. M., Varnes, D.J., 1996. Landslide Types and Processes, Transportation Research Board, U.S. *National Academy of Sciences*, 247, 36-75.

Ferretti, A., 2014. Satellite InSAR Data Reservoir Monitoring from Space, *EAGE Publications bv*.

Marini, A,. & Ulzega, A., 1977. Osservazioni geomorfologiche sul tacco di Ulassai - *Rendiconti Seminario Facoltà Scienze Università di Cagliari*, 47 (1- 2), 192-208.

Maxia, C., Ulzega, A., & Marini, C., 1973. Studio idrogeologico dei dissesti nel bacino del rio Pardu (Sardegna centro-orientale) *Pubblicazione dell'Istituto di Geologia, Paleontologia e Geografia Fisica*, 121(12), 9.

Gili, J. A., Corominas, J., Rius, J., 2000. Using Global Positioning System techniques in landslide monitoring, *Engineering Geology* ,55, 167-192,

ZischinskY, U., 1969. Über Sackungen. *Rock Mechanics*, 1 (1), 30-52.

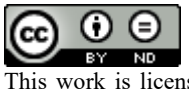

MORPHOLOGICAL AND COMPOSITIONAL INVESTIGATION OF KRIEGER CRATER (MOON)

C. Collu [1*], S. Podda [1], M.T. Melis [1,]

[1] Dept. of Chemical and Geological Sciences, University of Cagliari, Monserrato, Italy

KEY WORDS: Planetary geology, Moon, Spectroscopy, Krieger crater, Surface

ABSTRACT:

Krieger crater is an impact lunar crater located in the Oceanus Procellarum, on the western near-side of the Moon. It is partly overlaid by Van Biesbroeck impact crater on the southern rim; a sinuous rille, Rima Krieger, originates from the western rim. Krieger is surrounded by wrinkle ridges, linear structural features, and different mare materials. In order to investigate the geomorphological setting, we used remote sensing datasets from Lunar Reconnaissance Orbiter and Kaguya for photogeological and topographic analysis through high-resolution imagery and DEM, and Moon Mineralogy Mapper hyperspectral data for surface compositional investigation. Krieger is characterized by a polygonal-shaped rim, an asymmetrical ejecta blanket, oriented north-south (indicating a potential oblique impact) and a complex floor configuration, with morphologic features, like hummocks, large mounds, a possible central peak, and unclear concentric fractures. Both Krieger and Van Biesbroeck walls exhibit melt coating features, fresh exposed materials, melt veneers, and mass wasting morphologies. Hyperspectral analysis determined several surface mineral compositions, differing especially in olivine and glass content. Important compositional differences were observed in the Krieger floor, where mare-like basalts have been detected, suggesting an internal post-impact volcanism which resulted in the breaching of the western rim and subsequent lava flow outside the crater, originating Rima Krieger. We found also the contamination of highland material in the southern ejecta, potentially derived from the Aristarchus crater impact. Thus, this complex geological setting suggests that post-impact modification processes, including volcanism, tectonic movements and later impacts, played a key role in shaping up the present Krieger crater.

1. INTRODUCTION

Impact craters are the most common surface features on many solid planets, including Earth's Moon. Based on the diameter size, craters can be classified in simple craters (< 15 km) and complex craters (>20 km). Krieger is an Imbrian complex crater, that has a diameter of ~ 25 km. It is located in the Oceanus Procellarum, on the western near-side of the Moon, in the Aristarchus-Harbinger Region (Figure. 1), known as the most geologically complex region of the Moon (Zisk, et al., 1977). In this work, remote sensing data from Lunar Reconnaissance Orbiter (LRO), Kaguya and Chandrayaan-1 missions have been used to investigate the surface morphology and composition of Krieger crater, in order to better understanding the geological processes that affected the present appearance of the crater.

2. DATA AND PROCESSING

Narrow Angle Cameras (NAC) high resolution images from LRO mission, the Digital Elevation Model (SLDEM2015), and Moon Mineralogy Mapper (M3) reflectance data (Chandrayaan-1 mission) were used in this work. All data were downloaded from the Planetary Data System (PDS) Geosciences Node Lunar Orbiter Data Explorer.

High resolution images from NAC are 8-bit panchromatic imagery, with a spatial resolution of ~0.5 m/pixel. In this work we used 40 calibrated NAC images from CDRNAC data products, with sun incidence angles range from 0° to 80°, in order to observe surface reflectance variations and/or recognize morphological features enhanced by shadows.

SLDEM2015 consists of a co-registered data from geodetically-accurate topographic heights of the Lunar Orbiter Laser Altimeter (LOLA) onboard the Lunar Reconnaissance Orbiter

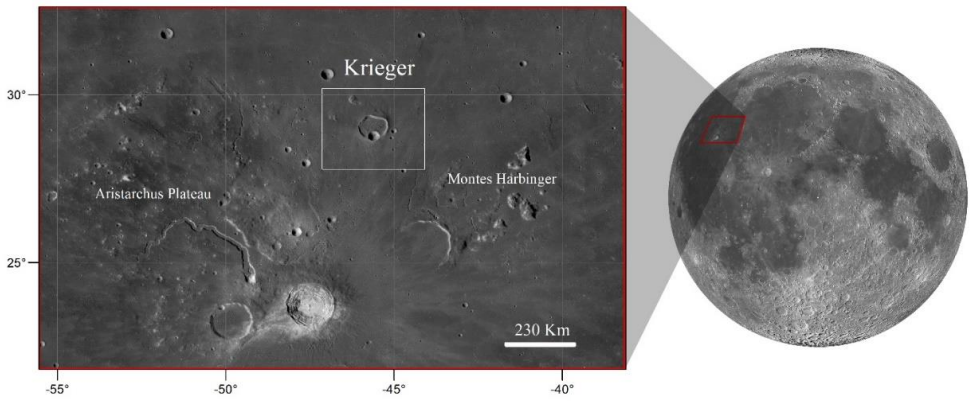

Figure 1. A portion of LRO Wide Angle Camera (WAC) mosaic showing the study area. Krieger crater (enclosed in the white rectangle) is located in the Aristarchus-Harbinger Region, in the Oceanus Procellarum, centered at ~ (29.0°N, 45.6°W).

* Corresponding author

and, 43,200 stereo-derived DEMs (each) from the SELENE Terrain Camera (TC) (~1010 pixels total) (Barker, et al, 2016). This DEM has a spatial resolution of 512 pixels per degree (~60 m at the equator) and a vertical accuracy of ~3 to 4 m. For this study we used two mosaicked tiles: "SLDEM2015_512_00N_30N_270_315" and "SLDEM2015_512_00N_30N_270_315".

We used global mode photometrically calibrated reflectance data (REFIMG) of Moon Mineralogy Mapper (M3), in particular the "M3G20090209T033051_V01_RFL" imagery. M3 reflectance data covers the wavelength range from 430 nm to 3000 nm with a spatial resolution of ~ 140 m/pixel, and the spectral resolution of 20-40 nm. The reflectance image has been processed in IDL-ENVI software, performing first a spatial and spectral resize, in order to exclude areas of no interest. Moreover, data with wavelength beyond 2600 nm, affected by thermal emission component, that makes difficult the analysis of adsorption features (Clark, 1979), have been ignored. Then, noise reduction was carried out using Maximum Noise Fraction (MNF) method.

3. METHODS

Geomorphological investigation of Krieger crater region has been mainly performed through photogeological observations from NAC high resolution images, that include albedo variations, surface texture analysis and identification of distinctive geologic features; the SLDEM2015 has been used for landscape analysis, through topographic sections and 3D visualizations, especially for define crater rims morphology.

Surface compositional analysis has been carried out on M^3 reflectance data, in order to define spatial distribution of distinct compositional units in the study area. A preliminary investigation was performed by calculating three spectral parameters used in several studies (Pieters, 1978; Staid, et al., 2011), and combining them in an RGB colour composite map: the 1 and 2 μm band depths (assigned in red and green channel respectively) and the reflectance at 1,58 μm (blue channel).

Then, we used RGB composite map as a guide for identify regions of compositional interest and collect characteristic spectra, in order to build a spectral library that describes the Krieger region. Further spectra were collected through ENVI Pixel Purity Index (PPI) algorithm. Thus, in order to identify spatial distribution of the reference spectra of the library, we used ENVI Spectral Angle Mapper (SAM) algorithm, assigning a different maximum angle to each spectrum, with values between 0,02 and 0,1 radians, based on the presence of residual noise, that could affect the classification. In addition, we investigated individually all the library spectra, analysing continuum slopes, band minimum position, band depth, band width and symmetry of spectral adsorptions, related to mineral composition (Singer, 1981; Cloutis, et al., 1986; Horgan, et al., 2014). However, in order to enhance spectral absorption features before this analysis, continuum of the spectra was removed (McCord, et al., 1981; Horgan, et al., 2014). We considered a linear continuum broken in two segments with three tie points at 730, 1209 or 1578 and 2616 nm for pyroxene-dominant compositions, whereas for olivine-rich compositions

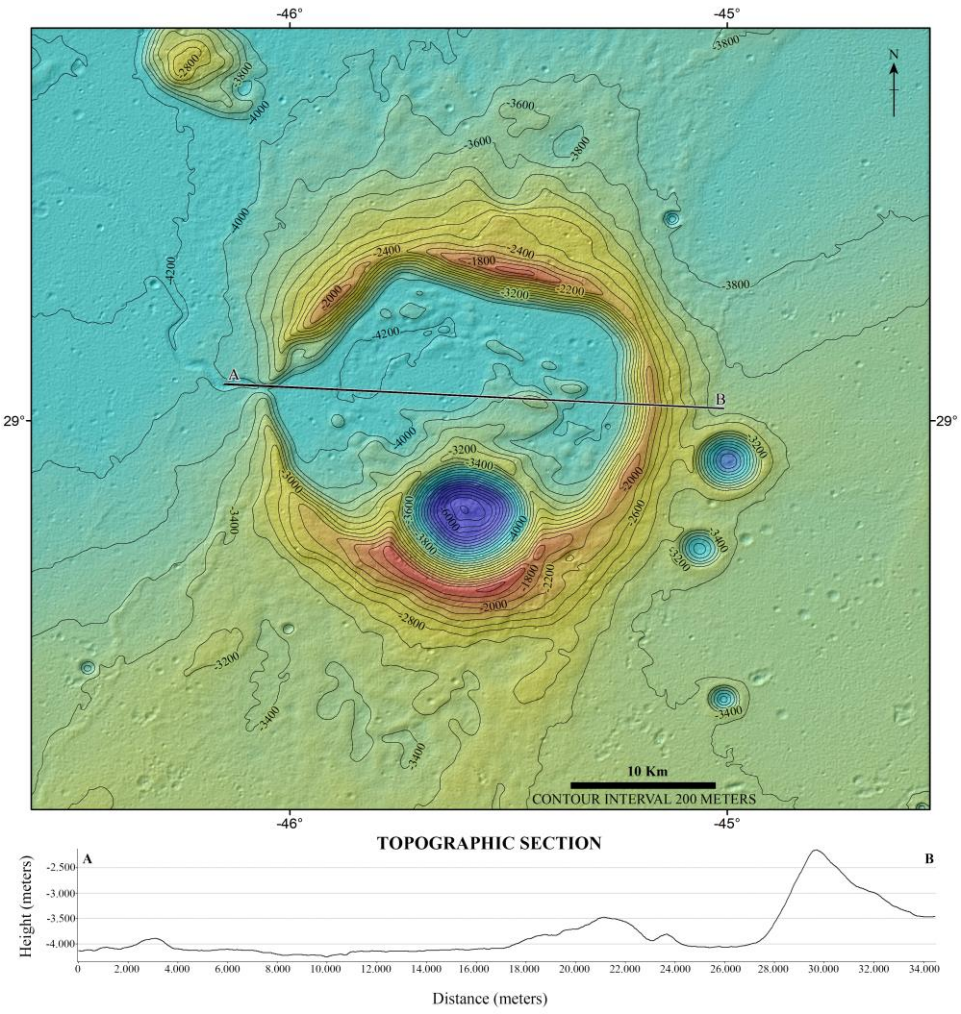

Figure 2. Topographic map and topographic section extracted from SLDEM2015; contour interval: 200 meters.

we adjusted tie points at 700, 1778 and 2616 nm, because olivines exhibit a broad 1 µm band adsorption, centred at longer wavelengths (Sunshine & Pieters, 1998; Horgan, et al., 2014). Continuum removal was achieved by dividing the continuum into the actual spectrum.

4. RESULTS

The Krieger crater shows a polygonal-shaped rim, with the southern part partly overlaid by a smaller Eratosthenian simple crater, Van Biesbroeck, and an asymmetric ejecta blanket, characterized by a north-south orientation. A rille, Rima Krieger, extends from the breached western rim out of the crater, at first with deep and angular meanders, suggesting the presence of different substratum material and/or a control by underlying structures (Podda, et al., 2020). To the southeast of Krieger two small Eratosthenian craters are located, Rocco and Ruth. Furthermore, Krieger is surrounded by several wrinkle ridges trending north-northeast to south-southwest.

NAC images show in the crater a significant albedo variation between northern and southern areas, probably related to different surface compositions. Moreover, further observations through NAC imagines revealed a complex floor configuration, with the presence of unclear concentric linear features, hummocks, large mounds (isolated or in clusters) and a possible central peak, characterized by a rougher surface texture and a higher crater density compared with the other reliefs. Crater walls of both Krieger and Van Biesbroeck exhibit melt coating features and frequent scarps in the upper part, whereas several mass wasting morphologies like boulder rolling features and block deposits occur in the lower areas. Between these wall units, a more coherent material is exposed, covered by dark thin melt veneers and coarse depositional materials “debris flows”, often with boulder-rich termination deposits.

Topography analysis through SLDEM2015 shows that in the Krieger crater region heights range between -6321 and -1328 meters, with general slope trending towards north-west. Morphology of Krieger was investigated through topographic sections, revealing an average rim-to-rim diameter of ~ 25,2 km, average depth of ~ 557,7 meters (below the pre-existing surface) and average rim height of ~ 1409,6 meters (above pre-existing surface); western breached wall shows a rim height almost 2 km lower (Figure 2). A marked asymmetry in rim height was found also between Van Biesbroeck’s northern and southern rim, that is almost 1,7 km higher; this asymmetry can be due to the irregular pre-impact topography, represented by the rim of Krieger. Moreover, in the north-western wall of Krieger a sudden slope decrease has been detected, and interpreted as a distinctive landslide deposit. On Krieger floor the large mounds and reliefs range from 1 to 4 km in diameter, heights between 30 m and 400 m, with slopes ranging from 20° to 40°. Outside the Krieger crater, ejecta blanket morphology is asymmetrical, with the northern deposits clearly thicker than southern ones. This difference could be related to variations in the pre-existing topography or post-impact modification triggered by nearby wrinkle ridges.

Preliminary spectral analysis through RGB colour composite map (Figure 3b) allowed the identification of fundamental characteristics of surface composition. The yellow hues in the southern areas and northern Krieger ejecta show both 1 and 2 µm strong adsorptions, indicating a pyroxene-dominant composition (Cloutis, et al., 1991; Staid, et al., 2011; Horgan, et al., 2014). On the contrary, blue/cyan hues in the southern ejecta of Krieger are characterized by high albedo and weak 1 µm adsorption, suggesting a less mafic compositions, typical of highlands. Red hues located in northern areas suggest strong adsorption band near 1 µm and relatively weak 2 µm absorption, typical of olivine-dominant compositions (Staid, et al., 2011; Sunshine & Pieters, 1998). In addition, 17 characteristic spectra of the Krieger crater region were collected and investigated (Figure 3d). All spectra show the typical reddening, due to fine Fe^0 particle sizes and space weathering (Pieters, 1978; Horgan, et al., 2014). Spectral signatures from B1 to VE2 (from top to bottom in figure 3d) clearly represent soils (regolith), since they have much weaker adsorption features than the other signatures, that characterize fresh rock materials on crater walls. Moreover, most of the signatures present the 1 µm band minimum at 0,98 or 1,09 and the 2 µm

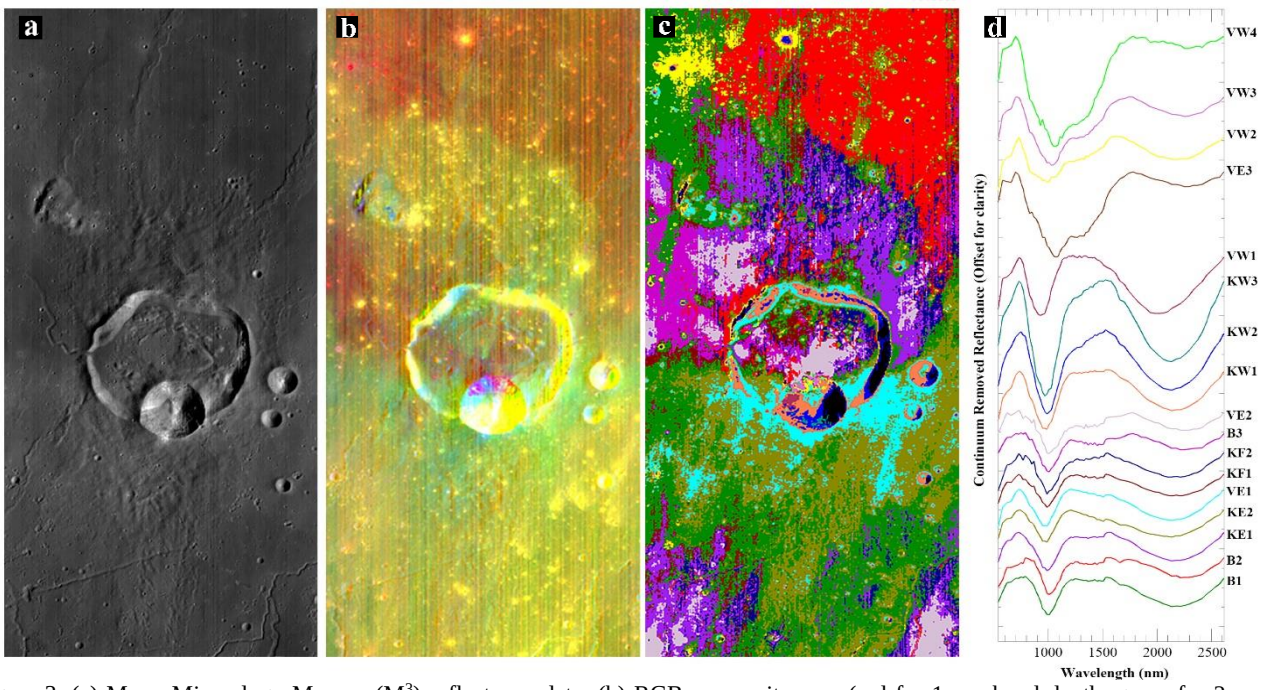

Figure 3. (a) Moon Mineralogy Mapper (M^3) reflectance data; (b) RGB composite map (red for 1 µm band depth, green for 2 µm band depth, blue for reflectance at 1.58 mm); SAM classification (c) and relative continuum removed spectral signatures (d) of the Krieger crater region.

band minimum at 2,14 or 2,22 µm, consistent with a Clinopyroxene (CPX)-rich composition, likely mixed with Orthopyroxene (OPX). However, the position of band minimum at longer wavelengths could also be due to a higher content in glass (Tomkins & Pieters, 2010). On the contrary, VW1 has band adsorptions centred at 0,93 and 2,02 µm, suggesting an OPX-dominant composition. The analysis of 1 µm band configuration (width and symmetry) allows to discriminate olivine rich-compositions. VW4 has an almost pure olivine signature, characterized by a broad and asymmetric band adsorption centred near 1,06 µm, and a very weak 2 µm band. VW2, VW3, and VE2 have stronger 2 µm band adsorption and broad asymmetric 1 µm band adsorption, both centred at longer wavelength compered to pyroxene-dominant compositions, suggesting an olivine-pyroxene mixture mineralogy, with possible glass content. Olivine presence was identified also in crater walls covered by melt veneers (KW2 and KW3), even though in less abundance compared to VW2, VW3, and VE2, and in soils (B2, KE1, KF2, B3 and VE2), that show the highest values of 1µm band asymmetry of soil signatures. On the contrary, soils lacking of olivine are represented by B1, KF1, KE2 and VE1 signatures, that show pyroxene-dominant composition, with possible contamination by highland components, including feldspar and Mg-Spinels, particularly for KE2 and VE1 (Cheek & Pieters, 2014).

5. CONCLUSIONS

Geomorphologic and spectral analysis of Krieger crater revealed several landforms and surface mineralogic compositions. The shape of rims and ejecta blanket suggest that Krieger likely formed as a result of an oblique impact on a mare basalt poor in olivine. The complex floor configuration and the presence of mare-like materials rich in olivine (B3) suggest intense post-impact modification processes, typical of floor fractured craters (Schultz, 1976), including floor uplift and volcanism triggered by the intrusion of a magma chamber beneath the crater. These processes are probably responsible of the development of concentric fractures, hummocks and mounds. Volcanic eruptions partly inundated the Krieger floor, leading to the breach of western rim and subsequent emplacement of basalts outside the crater. Then, the impact that generated Van Biesbroeck excavated Krieger floor and exposed deep materials rich in olivine, detected in the northern walls and ejecta of Van Biesbroeck. Later, southern materials of the Krieger region have been contaminated with highland components derived from Aristarchus ejecta. Thus, post-impact modification processes, including tectonic movements, volcanism and later impacts, played a key role in shaping up the present Krieger crater.

REFERENCES

Barker M.K., Mazarico E., Neumann G.A., Zuber M.T., Haruyama J., Smith D.E. (2016). A new lunar digital elevation model from the Lunar Orbiter Laser Altimeter and SELENE Terrain Camera. *Icarus*, vol. 273,2016. Pages 346-355. ISSN 0019-1035. Doi:10.1016/j.icarus.2015.07.039

Cheek, L. C., & Pieters, C. M. (2014). Reflectance spectroscopy of plagioclase-dominated mineral mixtures: Implications for characterizing lunar anorthosites remotely. *American Mineralogist*, vol. 99, doi:10.2138/am-2014-4785

Clark, R. N. (1979). Planetary reflectance measurements in the region of planetary thermal emission. *Icarus*, vol. 40, no. 1, Art. no. 1, doi:10.1016/0019-1035(79)90056-3

Cloutis, E. A., & Gaffey, M. J. (1991). Pyroxene spectroscopy revisited: Spectral-compositional correlations and relationship to geothermometry. *Journal of Geophysical Research*, vol. 96, no. E5, Art. no. E5. doi:10.1029/91je02512

Cloutis, E. A., Gaffey, M. J., Jackowski, T. L., & Reed, K. L. (1986). Calibrations of phase abundance, composition, and particle size distribution for olivine-orthopyroxene mixtures from reflectance spectra. *Journal of Geophysical Research*, vol. 91, no. B11, Art. no. B11. doi:10.1029/jb091ib11p11641

Horgan, B. H., Cloutis, E. A., Mann, P., & Bell, J. F. (2014). Near-infrared spectra of ferrous mineral mixtures and methods for their identification in planetary surface spectra. *Icarus*, vol. 234, 132–154. doi:10.1016/j.icarus.2014.02.031

McCord, T. B., Clark, R. N., Hawke, B. R., McFadden, L. A., Owensby, P. D., Pieters, C. M., & Adams, J. B. (1981). Moon: Near-infrared spectral reflectance, A first good look. *Journal of Geophysical Research: Solid Earth*, vol. 86, no. B11, Art. no. B11. doi:10.1029/jb086ib11p10883

Pieters, C. M. (1978). Mare basalt types on the front side of the Moon: a summary of spectral reflectance data. *Proc. Lunar Planet. Sci. Conf. 9th*, 2825–2849.

Podda, S., Melis, M. T., Collu, C., Demurtas, V., Perseu, F. O., Brunetti, M. T., & Scaioni, M. (2020). New Morphometric Data of Lunar Sinuous Rilles. *IEEE Journal of Selected Topics in Applied Earth Observations and Remote Sensing*, vol. 13, 3304–3316. doi:10.1109/jstars.2020.3003080

Schultz, P. H. (1976). Floor-fractured lunar craters. *The moon*, vol. 15, no. 3, Art. no. 3. doi:10.1007/BF00562240

Singer, R. B. (1981). Near-infrared spectral reflectance of mineral mixtures: Systematic combinations of pyroxenes, olivine, and iron oxides. *Journal of Geophysical Research: Solid Earth*, doi:10.1029/jb086ib09p07967

Staid, M. I., Pieters, C. M., Besse, S., Boardman, J., Dhingra, D., Green, R., Taylor, L. A. (2011). The mineralogy of late stage lunar volcanism as observed by the Moon Mineralogy Mapper on Chandrayaan-1. *Journal of Geophysical Research: Planets*, doi:10.1029/2010JE003735.

Sunshine, J. M., & Pieters, C. M. (1998). Determining the composition of olivine from reflectance spectroscopy. *Journal of Geophysical Research: Planets*, doi:10.1029/98je01217

Tomkins, S., & Pieters, C. M. (2010). Spectral characteristics of lunar impact melts and inferred mineralogy. *Meteoritics & Planetary Science*, doi:10.1111/j.1945-5100.2010.01074.x

Zisk, S. H., Hodges, C. A., Moore, H. J., Shorthill, R. W., Thompson, T. W., Whitaker, E. A., & Wilhelms, D. E. (1977). The Aristarchus-Harbinger region of the moon: Surface geology and history from recent remote-sensing observations. *The moon*, vol. 17, no. 1, Art. no. 1. doi:10.1007/BF00566853

DYNAMICS OF STROMBOLIAN EXPLOSIONS: THE FEBRUARY 2020 ETNA SEQUENCE

M. Palmas [1], L. Pioli [1], S. Scollo [2], B. Behncke [2], E. De Beni [2], M. Cantarero [2]

[1] Dipartimento di Scienze Chimiche e Geologiche, Università degli Studi di Cagliari, Cittadella Universitaria, Blocco A - 09042 Monserrato (Italy) – (m.palmas20@studenti.unica.it, laura.pioli@unica.it)
[2] Istituto Nazionale di Geofisica e Vulcanologia, Osservatorio Etneo - Sezione di Catania, Piazza Roma, 2, 95125 Catania, Italy – (simona.scollo, boris.behncke, emanuela.debeni, massimo.cantarero)@ingv.it

KEY WORDS: Etna, Strombolian activity, survival analysis, volcanic hazard, statistical analysis, image analysis

ABSTRACT:

Mt. Etna, in Italy, is one of the most active basaltic volcanoes on the Earth and is characterized by a wide range of explosive styles. Strombolian activity is very frequent and a powerful spectacle attracting thousands of tourists every year, approaching the volcano summit with sparse safety measures. At this moment, despite the extensive monitoring of this volcano, little is known on their exact dynamics, precluding precise quantification of the hazard associated with it. For this reason, we have analysed video recordings of an explosion sequence occurred in February 2020 recorded from the Voragine and Bocca Nuova craters rims in parallel with UAV surveys. We analysed videos to obtain the frequency of explosions, particle exit speeds and study eruption dynamics. Survival analysis of the repose time between explosions revealed that they are distributed according to log logistic distributions, in analogy with known sequences at other open vent volcanoes. We found differences among low intensity and high intensity explosions. Low intensity events are characterized by instantaneous pulses of magma associated with the burst of a gas slug. High intensity events are composed by multiple pulses, where volcanic particles can reach speeds of up to 150 m/s, separated by gas streaming and followed by a stationary phase, where particles are emitted at constant velocity, and a declining phase emitting a few small particles with speeds lower than 10 m/s. Finally, we emphasize how remote sensing monitoring of small-scale explosions is a very effective tool providing data for their quantification and modelling.

1. INTRODUCTION

Basaltic volcanic manifestations are characterized by a large style range, including lava flows, outgassing explosive events of variable intensity, from lava fountaining to ash plumes. (Edwards et al., 2018). Their eruptive style depends to various parameters like magma viscosity and volatile content, rise and feeding rates (Taddeucci et al., 2015).
In particular, the explosion frequency in Strombolian dynamics is related to the rising dynamics of gas slugs, whose rapid expansion leads to the fragmentation and release of magma, and, in some cases, small quantities of lithic stones present inside the conduct (Balckburn et al., 1976). Exit speeds can exceed 150 m/s and ejecta can reach distances up hundreds of m up to a few km from the vent. Strombolian activity is also a nature spectacle attracting tourists and local people who climb volcanoes up to a short distances from the active vents (Scollo et al., 2013). For this reason, the study of Etna's Strombolian eruptions is relevant not only for understanding the dynamics of these events but also for the hazard quantification. Unfortunately, despite Etna is one of the most studied and monitored volcano in the world, Strombolian activity is often overlooked, because of its limited impact with respect to lava fountain events, reaching up to Subplinian scale (Branca and Del Carlo, 2005). Monitoring Strombolian eruptions, whose product are hard to sample because they typically occur at open vent volcanoes is ideally made by collecting ground remote sensing data.
This study aims to provide useful data to quantify and model the Strombolian activity of this volcano through the measurement and analysis of spatial and temporal parameters, also by comparing it with other volcanic systems with similar characteristics. In this paper, we discuss on the Strombolian dynamics events that occurred at Etna on February 2020. This study is based on quantitative analysis of high resolution videos, that were recorded on the 25th February 2020 on the edges of Voragine and Bocca Nuova Craters.

2. MATERIALS AND METHODS

The data collection was possible by the acquisition of four videos, documenting the activity of 25th February 2020. These videos were acquired with a frequency of 25 fps (frames per second) and a resolution of 1080x1920 pixels. Images were acquired with a Nikon Coolpix P1000 camera equipped with a 4.3-539 mm optical zoom. Sensor size is 6.16x4.62 mm.
The films were then splitted into individual frames, studied with image analysis techniques using the software Fiji (Schindelin et al, 2012).

Video	Date (local hour)	Duration	Recording distance from cone	number of explosions
		[min:s]	[m]	
8039	25/02/2020, 12:39	1:57	136	34
8081	25/02/2020, 13:58	3:41	136	41
8073	25/02/2020, 13:22	4:53	403	76
8079	25/02/2020, 13:29	3:58	403	71

Table 1. Videos analysed and their characteristics

2.2 Image calibration

The images were calibrated for the distance conversion from pixels to meters.

* Corresponding author

Definition of the FOV (Field of View) area was in fact obtained using known distances (i.e. the crater rim diameter), measured by UAV surveys. Sometimes, image sequences from single videos have required multiple calibrations if the optical zoom of the camera was activated. Moreover, to reduce the measure uncertainty, pixel calibration was repeated and averaged over a sequence of fixed optics images. Image resolution was calculated as the inverse of the average scale factor calculated based on Fiji analysis of the calibration images:

$$m = \frac{D}{d} \tag{1}$$

where m = resolution, px/m
D = known distance, m
d = known distance, px

2.1. Time series analysis

Time series data were obtained by calculating the time between consecutive images obtained by converting the videos based on recording speed (fps). Time between images (in seconds) was calculated as:

$$t = \frac{nf}{fps} \tag{2}$$

where nf= number of frames between two images in the series

Duration of explosions was calculated based on the number of frames comprised between the one showing the first particle exiting the vent and the one showing the last particle exiting the vent).
The repose time between two contiguous explosions was calculated as the difference between the starting times of two consecutive explosions:

$$trt = ti_2 - ti_1 \tag{3}$$

where trt = repose time
ti_1= starting time of the first explosion
ti_2 = starting time of the next explosion

Finally, the interval between two contiguous explosions, defined as the difference between the second explosion starting time and the first explosion ending time, was calculated:

$$i = ti_2 - tf_1 \tag{4}$$

where i = repose time
ti_2 = second explosion starting time
tf_1= first explosion ending time

2.3. Distances and particle exit speeds

For each explosion, we calculated the vertical exit speed of the emitted particles, based on two algorithms.
When the particles remained within the FOV along their entire trajectory, conservation of energy was applied:

$$U_0 + U_1 = K_0 + K_1 \tag{5}$$

where U_0 = initial potential energy
U_1 = final potential energy
K_0 = initial kinetic energy
K_1 = final kinetic energy

Neglecting friction (which is not relevant considering the uncertainty of the measures) we obtain:

$$v = \sqrt{2gh} \tag{6}$$

where v = particle speed
g = gravitational acceleration
h = maximum particle height above the crater rim

When the particle trajectory exceeded the FOV, speed where calculated measuring the distance covered in a time of 3 consecutive frames:

$$v = (h_2 - h_1)\frac{25}{2} \tag{7}$$

where v = particle speed
h_2 = particle height in the third consecutive frame
h_1 = particle height in the initial frame

2.2. Particle tracking

The four largest explosions, characterized by the longest duration, and the largest number of particles emitted, were studied in detail. Time evolution of the eruption parameters (i.e. particle speed and size) was quantified with temporal resolution of tenths of seconds.

3. RESULTS

The videos recorded a sequence of 34 to 76 explosions, occurring from up to two vents within the Voragine crater (table 1). Explosions lasted from 0.04 to 8 s, with average values around 1 s in all recorded videos. Repose times between explosions ranged between 0.76 to 13.24 s with average values around 4 s. Time intervals ranged between 0.04 to 11.28 s (table 2).
Survival analysis of the repose times revealed that they are best reproduced by log logistic distributions, even if a Gaussian distribution could reproduce data satisfactorily; other known distribution such as the exponential one, instead do not fit satisfactorily the empirical probability curves (Table 3).

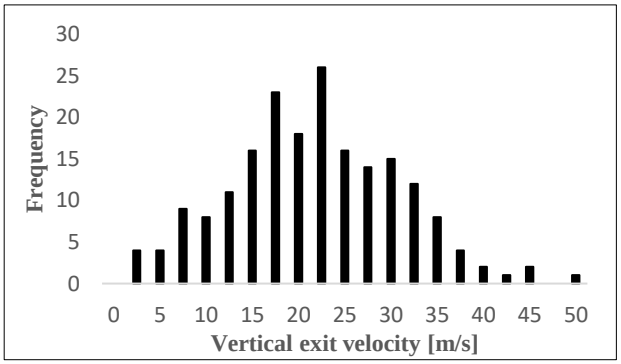

Figure 1. Analysis of speed frequencies.

Particle vertical exit speed were measured for the fastest particles in each of the 222 explosions studied. Speeds range from varies from 1.3 to 47.7 m/s, with average value of about 20 m/s. Speeds distribute accordingly to an almost symmetrical trend, with two modes close to the median values. Maximum exit speed was measured in the 4 major explosions (fig. 1, table 4).

Repose times (s)				
Video	Average	Median	Minimum	Maximum
8039	3.49	3.08	0.76	10.96
8081	5.403	4.96	1.4	13.24
8073	3.85	3.40	1.16	10.32
8079	3.34	3.02	1.08	7.28
Explosion durations (s)				
Video	Average	Median	Minimum	Maximum
8039	1.21	1.16	0.04	6.12
8081	1.58	1.2	0.04	6.96
8073	2.26	1.8	0.2	8
8079	1.77	1.64	0.04	5.2
Time interval between contiguous events (s)				
Video	Average	Median	Minimum	Maximum
8039	2.27	2.12	0.12	5.64
8081	3.82	3.52	1.2	11.28
8073	1.59	1.44	0.08	7.52
8079	1.57	1.16	0.04	5.6

Table 2. Basic statistical parameters

Repose times								
Video	Log logistic			Gaussian			Exponential	
	μ	σ	LL	μ	σ	LL	μ	LL
8039	4.3	0.3	171	87.1	51.3	176	230.2	180
8081	4.8	0.3	208	133.1	62.4	210	466.6	223
8073	4.4	0.3	383	96.2	46.6	393	123.2	417
8079	4.3	0.3	354	83.4	41.1	359	99.3	379

Table 3. Fitting results of repose times between explosions
LL= negative log likelihood

Vertical maximum speed				
Video	Medium value	Median	Minimum	Maximum
8039	21.12	21.14	8.46	37.76
8081	24.23	23.59	13.43	36.09
8073	18.14	15.24	1.30	47.75
8079	20.88	20.66	2.48	33.66

Table 4 Statistical speed analysis

2.4. Dynamics of the four major explosions

Major explosions lasted from 2.04 to 2.56 seconds. They were divided into three to four phases, with distinct dynamics. Firstly, an intense outgassing that the explosion onset (fig. a, e). First particles, ash and lapilli-sized, exited from the vent during the onset.
In a few tenths of seconds, the number of particles emitted suddenly increase, forming a thicker eruptive column (second pulse). In three explosions, a third pulse follow the second one; it is the most intense (in terms of number of emitted particles) and it is characterised emission of larger particles (bombs to lapilli sized) accompanied by limited gas emission (fig. b, c, d, f).

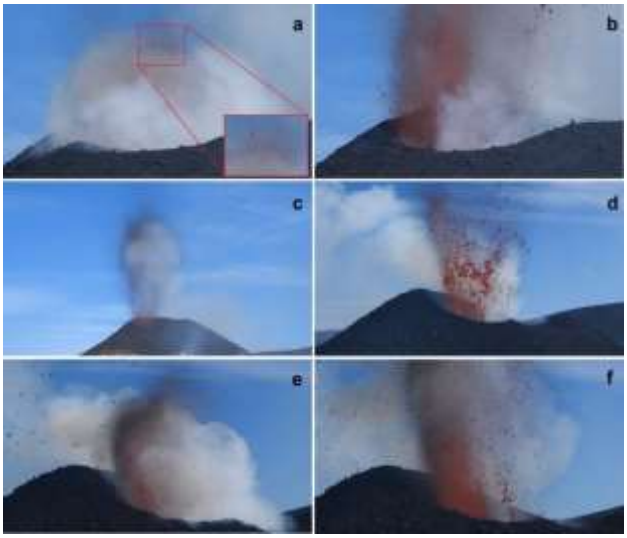

Figure 2. Dynamics of major explosions as pictured in the recorded frames: outgassing during first and second (in the frame) pulses, characterized respectively by a large and a smaller eruptive column thickness (a); Bombs and lapilli erupted during sustained phase (b, c d and f); first pulse with ash emission and outgassing (e).

Particle tracking within consecutive frames of major explosions showed a typical decrease in energy from onset to subsequent pulses (Alatorre-Ibargüengoitia et al., 2011) followed by a stationary phase (second to third pulse) lasting less than 1 s.

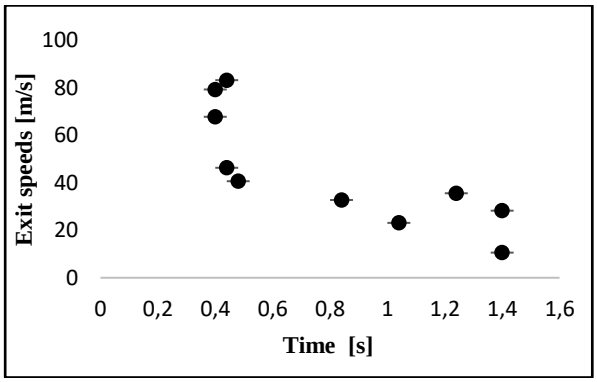

Figure 3. Evolution of speeds during a major explosion. Error on speed estimation is smaller than the symbol used.

3. CONCLUSIONS

This study estimated fundamental parameters of the Strombolian dynamics at Etna volcano. Strombolian activity consists of regular (i.e. time between explosion follow log logistic distributions) series of explosions with very similar dynamics. Short median repose times suggest low viscosity of the emitted (Dominguez et al., 2016), associated with limited gas emission, (corresponding to low particles exist speeds, (Alatorre - Ibargüengoitia et al., 2011). Therefore, explosions are marked by heights and speeds much lower than typical Strombolian regime (Taddeucci et al., 2012). Data presented here, although representing the first assessment of Strombolian dynamics at Etna, are only preliminary. We underline the importance of ground remote sensing systems of explosive eruptions as the main method for collecting low intensity eruption parameters which could not be estimated by the study of tephra collection or using satellite techniques.
This data could be compared with other volcanic systems to have a deeper and more general understanding of Strombolian activity.
Strombolian dynamics is very similar to other type volcanoes such as Stromboli and Yasur (Taddeucci et al., 2012; Gaudin et al., 2014). Explosions are fed by the rise of pressurized gas slugs rupturing the free magma surface into fragments of variable size (ash to bombs), with dynamics similar to the sudden release of a mass of pressurized gas within a shock tube (Alatorre - Ibargüengoitia et al., 2011). In major explosions, multiple pulses suggest the rise of a series of slugs.
.

4. ACKNOWLEDGEMENTS

This work has been realised as part of the first author's degree thesis. L.P. was supported by FNS grant n 200021_162439.

5. REFERENCES

Alatorre-Ibargüengoitia, M. A., Scheu, B., Dingwell, D. B., 2011. Influence of the Fragmentation Process on the Dynamics of Vulcanian Eruptions: An Experimental Approach. *Earth and Planetary Science Letters*, 302(1–2), pp. 51-59, https://doi.org/10.1016/j.epsl.2010.11.045

Blackburn, E. A., Wilson, L., Sparks J., 1976. Mechanisms and Dynamics of Strombolian Activity. *Journal of the Geological Society*, 132(4), pp. 429-440, https://doi.org/10.1144/gsjgs.132.4.0429

Branca, S., Del Carlo, P., 2005. Types of Eruptions of Etna Volcano AD 1670–2003: Implications for Short-Term Eruptive Behaviour. *Bulletin of Volcanology*, 67(8), pp. 732-42, https://doi.org/10.1007/s00445-005-0412-z

Dominguez, L., Pioli L., Bonadonna C., Connon, C. B., Andronico, D., Harris, A. J. L., Ripepe, M., 2016. Quantifying Unsteadiness and Dynamics of Pulsatory Volcanic Activity. *Earth and Planetary Science Letters*, 444, pp. 160-68, https://doi.org/10.1016/j.epsl.2016.03.048

Edwards, M. J., Pioli, L., Andronico D., Scollo, S., Ferrari, F., Cristaldi, A., 2018. Shallow Factors Controlling the Explosivity of Basaltic Magmas: The 17–25 May 2016 Eruption of Etna Volcano (Italy). *Journal of Volcanology and Geothermal Research*, 357, pp. 425-36, https://doi.org/10.1016/j.jvolgeores.2018.05.015

Gaudin, D., Taddeucci, J., Scarlato P., Morini, M., Freda, C., Gaeta M., Palladino, D.M., 2014. Pyroclast Tracking Velocimetry Illuminates Bomb Ejection and Explosion Dynamics at Stromboli (Italy) and Yasur (Vanuatu) Volcanoes. *Journal of Geophysical Research: Solid Earth*, 119(7), pp. 5384-97, https://doi.org/10.1002/2014JB011096

Schindelin, J., Arganda-Carreras, I., Frise, E., Kaynig, V., Longair, M., Pietzsch, T., Preibisch, S., Rueden, C., Saalfeld, S., Schmid, B., Tinevez, J., White, D. J., Hartenstein, V., Eliceiri, K., Tomancak, P., Cardona, A., 2012. Fiji: An Open-Source Platform for Biological-Image Analysis. *Nature Methods*, 9(7), pp. 676-82, https://doi.org/10.1038/nmeth.2019

Scollo, S., Coltelli, M., Bonadonna, C., Del Carlo, P., 2013. Tephra Hazard Assessment at Mt. Etna (Italy). *Natural Hazards and Earth System Sciences*, 13(12), pp. 3221-33, https://doi.org/10.5194/nhess-13-3221-2013

Taddeucci, J., Scarlato P., Capponi, A., Del Bello, E., Cimarelli, C., Palladino, D.M., Kueppers, U., 2012. High-Speed Imaging of Strombolian Explosions: The Ejection Velocity of Pyroclasts. *Geophysical Research Letters*, 39(2), pp. 1-6, https://doi.org/10.1029/2011GL050404

Taddeucci, J., Edmonds, M., Houghton, B., James, M. R., Vergniolle, S., 2015. "Hawaiian and Strombolian eruptions." In: *Encyclopedia of volcanoes,* ed. H. Sigurdsson. Academic Press, pp. 485-503, https://doi.org/10.1016/B978-0-12-385938-9.00027-4

OBJECTIVE GEOLOGICAL AND GEOMORPHOLOGICAL MAPPING OF MARTIAN SEDIMENTARY DEPOSITS: AN EXAMPLE FROM THE SOUTHEASTERN MARGIN OF HOLDEN CRATER

I. Di Pietro [1], M. Pondrelli [2], A. Frigeri [3], L. Marinangeli [1], A.C. Tangari [1] , M. Pantaloni [4], E. Luzzi [5], R. Pozzobon [6], A. Nass [7], M. Massironi[6], A.P. Rossi [5]

[1] Laboratorio di Telerilevamento e Planetologia, DISPUTer, Università G. d'Annunzio, Chieti, Italy – (ilaria.dipietro, lucia.marinangeli, a.tangari)@unich.it
[2] IRSPS, Università G. d'Annunzio, Pescara, Italy - monica.pondrelli@unich.it
[3] Istituto di Astrofisica e Planetologia Spaziali, Istituto Nazionale di Astrofisica, Roma, Italy - alessandro.frigeri@inaf.it
[4] Servizio Geologico d'Italia, ISPRA, Rome, Italy - marco.pantaloni@isprambiente.it
[5] Department of Physics and Earth Sciences, Jacobs University Bremen, Bremen, Germany – (e.luzzi, an.rossi)@jacobs-university.de
[6] Department of Geosciences, University of Padova, Padova, Italy – (riccardo.pozzobon, matteo.massironi)@unipd.it
[7] DLR, Institute of Planetary Research, Berlin, Germany - Andrea.Nass@dlr.de

KEY WORDS: geological mapping, mars, sedimentary environments, geomorphology, fluvial deposits, lacustrine deposits

ABSTRACT: Sedimentary environments and associated deposits and morphologies are among the most important geologic records present on Mars' surface, due to their implication with past climatic conditions and their variations through geological times. Fortunately, the constant improvement of available datasets favors ever more detailed analysis and to edit topical maps with an approach somewhat akin to the relatively 'objective' geological mapping approach on Earth. In particular, the planetary mapping process is more significant in small areas (e.g., basins) where data coverage is extremely dense and has high-resolution. In these conditions, deposits are distinguished based on their objectively defined characteristics apart from the genetic interpretation provided by the morphology. A clear distinction between descriptive (objective) and interpretative (subjective) units is specifically useful when geomorphological interpretation is particularly controversial. Unlike on Earth, sedimentary systems are well-preserved down to the deep stratigraphic succession, making stratigraphy a pivotal concept that needs to be included within map information and a prerequisite to a well constrained interpretation of the Martian geological environments. Within the Europlanet H2024-GMAP (Geologic MApping of Planetary bodies) infrastructure, we have attempted to apply all these different but complementary concepts and information in a single cartographic product of southeastern Holden crater. For such an aim we have borrowed, where possible, the Earth symbols designed for the Geological Map of Italy (ISPRA, 2009; 2018) aiming to make the 'language' of geological maps of Mars and Earth as uniform as possible.

1. INTRODUCTION

1.1 Science rationale

Sedimentary deposits and associated morphologies are among the most interesting geological records present on Mars surface, because of their implication in the understanding of climatic conditions and variability through Mars' geological history. In the last couple of decades, the increase of the quantity, quality, and type of available Martian datasets let ever more detailed studies of these deposits and their related environments. The integration of available datasets with different scale and scientific content (visible, altimetry, mineralogy, etc.) in a Geographical Information Systems (GIS) provides an impressive suite of tools to develop meaningful planetary geological maps for specific areas. The method we propose aims to reproduce somehow the relatively 'objective' geological mapping method well-known on Earth and ensures the mapping product more significant in correspondence of small areas (e.g., basins – local scale) where data coverage is extremely dense and at high-resolution. Although, a 'true' geological map should be based on the lithological characteristics of the mapped units; this method may represent an adequate planetary alternative. This approach lets to independently distinguish the objective characteristics of the deposits (i.e., tone, texture, absence/presence of sedimentary structures, compositional hints, etc.) from the genetic (subjective) interpretation provided by the whole characteristics of the units and the context. In particular, a clear distinction between description and interpretation of the units is specifically suitable when the geomorphological interpretation is not totally clear.

On Mars, sedimentary (and not only) systems preserve their morphological mutual stacking pattern down to the deep stratigraphic record, making the recognition of stratigraphic relations a prerequisite to a well constrained interpretation. In light of this, it is important to include the stratigraphy within map information. Fortunately, the advantage of being relatively objective makes this method potentially more useful for geological context and lateral stratigraphic correlation analyses.

In the framework of the EPN2024-GMAP (Geologic MApping of Planetary bodies) infrastructure, we present an attempt to gather all these complementary information in one cartographic product, taking advantage of GIS-based tools. Moreover, we aim at testing, where possible, the Earth born symbols designed for the Geological Map of Italy (ISPRA, 2009; 2018) in order to make the 'language' of geological maps more universal than before. The GMAP project represents an opportunity to share our experience and to collect current practices in planetary and terrestrial geological and geomorphological mapping, identifying what key elements are still lacking and need to be discussed and/or developed in planetary science. Therefore, this work aims to pursuit scientific goals related to the geological evolution of the southeastern Holden crater, while improving and trying to standardize the methodology of planetary geological mapping.

* Corresponding author

1.2 Study area

Holden crater is 154km in diameter within the Margaritifer Sinus quadrangle (MC-19) region. The crater is set close to the transition from the Noachian to the Hesperian epoch (Grant et al., 2008; Pondrelli et al., 2005; Scott and Tanaka, 1986).
Since the crater interrupts the Uzboi-Ladon-Morava meso-scale outflow system that dominates the ancient drainage system in southwest Margaritifer Terra, Holden is a suitable area for looking for water-related morphologies on Mars.
In order to pursuit our goals, we focused specifically on a series of putative fluvio-lacustrine morphologies along the south-eastern inner rim of Holden crater (coordinates 26.9°S-33.5°W) (Fig. 1).

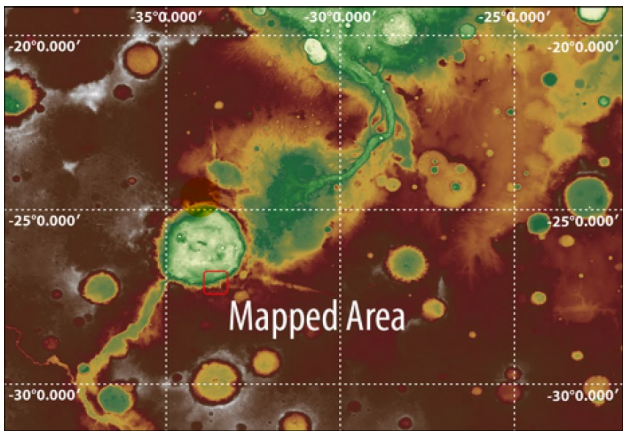

Figure 1. Location map of the study area.

Holden crater is well known because of its hydrological activity history, although the details of such evolution (i.e., water level fluctuations, timing, intensity, etc.) remain still unknown (Pondrelli et al., 2005; Grant et al., 2008; 2011). The selected area shows the presence of superposed fan-shaped features reflecting a complex basin evolution (Fig. 2).

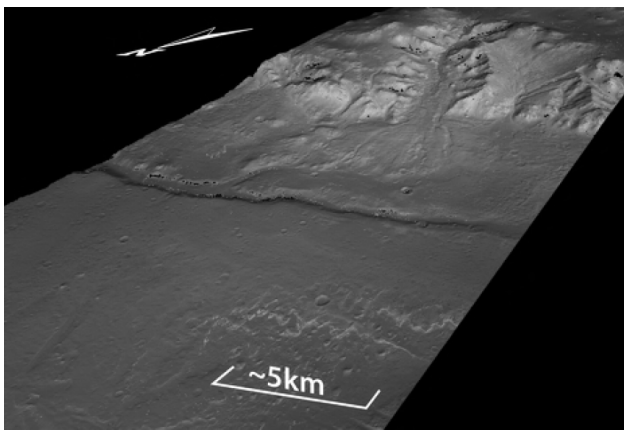

Figure 2. CTX-based perspective view of the study area.

2. DATA AND METHODS

Visible imagery at different scale was used to investigate the study area. The Context (CTX) camera (6 m pixel–1) (Malin et al., 2007) and the High Resolution Imaging Science Experiment (HiRISE) camera (25 cm pixel–1) (McEwen et al., 2007), both on board the NASA Mars Reconnaissance Orbiter (MRO), provided detailed images which were useful to reconstruct the stratigraphic relationships.

At places, the availability of stereo-pair images also allowed Digital Terrain Models (DTMs) generation using the NASA Ames Stereo Pipeline (ASP)(Sucharski et al., 2020; Sides et al., 2017; Anderson et al., 2004; Gaddis et al., 1997) and the USGS Integrated Software for Imagers and Spectrometers (ISIS) (Beyer et al., 2018; Shean et al., 2016; Broxton & Edwards, 2008) to radiometrically correct and project the images. Derived CTX and HiRISE DTMs have a minimum gridding of 6 and 1 m pixel–1, respectively. However, extensive topographic reconstructions were possible using the High Resolution Stereo Camera (HRSC) on board of ESA Mars Express (MEX) (Neukum et al., 2004). Digital elevation models (DEMs) constructed from HRSC stereo images have a spatial resolution of ~50–150 m pixel–1.

In addition, compositional constraints can be provided by the spectral data coming from Observatoire pour la Minéralogie, l'Eau, les Glaces, et l'Activité (OMEGA) (Bibring et al., 2004) on board MEX and from Compact Reconnaissance Imaging Spectrometer for Mars (CRISM) on board the NASA Mars Reconnaissance Orbiter (MRO) (Murchie et al., 2007).

3. MAPPING APPROACH

We propose to use a hierarchical path of thought to identify the units (i.e., mapping). This approach uses a combination of some criteria, scrolling through several levels of knowledge with different hierarchy as shown in Fig. 3.
First, scale and illumination conditions (incidence angle and azimuth) are required as a priori information before to start the mapping. The scale gives the idea of the entity of the geological process, and it is tied to the resolution of the images (or data) we intend to use. The knowledge of the scale prevents any morphological convergence issues that might exist between different orders of scales since very similar morphologies may result from different geological processes. Whilst, the knowledge of illumination conditions avoids being tricked by the concavity/convexity appearance, and, hence, relief inversion misinterpretations.

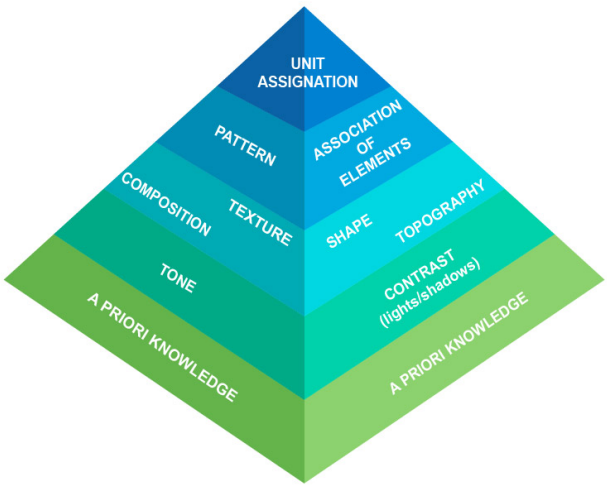

Figure 3. Unit recognition and assignation process.

Second, to fulfil our goals and to reflect the objectivity of the proposed method, we identified the units using the following

combination of criteria, defined both at the CTX and, when possible, at the HiRISE scale, including:

- their main topographic and geological characteristics;
- their surface properties (e.g., rough or smooth textures, albedo, etc.);
- their orbital facies (e.g., bedforms, layering, etc.).

The geological map has three different layers:

- a polygon shapefile representing the units which are described using as objective as possible characteristics (listed above);
- a linear shapefile defining the nature of the stratigraphic boundaries (e.g., disconformity, nonconformity, etc.);
- a linear shapefile marking tectonic features and interpretative geomorphological structures.

Although geology is born as an interpretative science and it is never really unconstrained from interpretation, this approach allows to simultaneously, but separately, focus: on the description, the stratigraphic relations (emphasizing the missing time) including different hierarchy, and on the genetic interpretation. The genetic interpretation, in turn, is constrained by the reconstruction of the vertical and lateral relationships among the units that allows to interpret the formation process of a specific landform in the framework of a context of associated landforms (i.e., landscape).

4. PRELIMINARY RESULTS

Preliminary results are shown in Fig. 4.

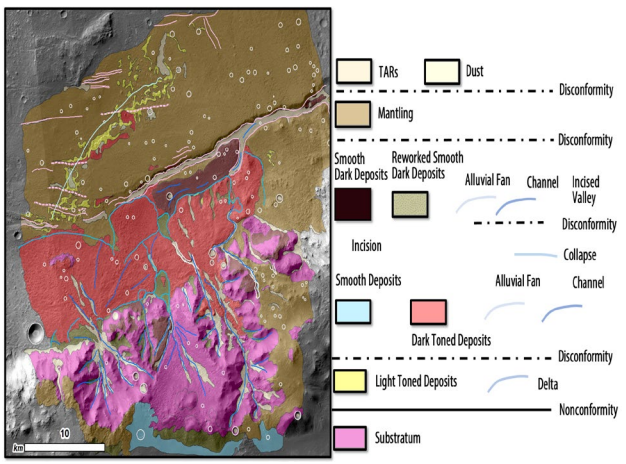

Figure 4. Geological map of the studied area.

We defined a 'morpho-stratotype' in correspondence of each single unit taking into account and being aware of the differences with the formal definition of 'stratotype' on Earth. However, we wanted to introduce a concept that addresses the 'objective' description of the units considering the available dataset that might favour the reproducibility of observations in different areas/settings on Mars.

As an example (Fig. 5), the Light Toned Deposits (LTD) were described as light toned, moderately rough, layered and associated with flat or very low dipping terrains at CTX scale. Whereas they show a bed sets thickness of few meters, and they are disrupted in a post- depositional meter-scale polygonal pattern at the HiRISE scale. The Light Toned Deposits unit onlaps the older 'Substratum' and is covered in disconformity by the dark-toned layered deposits or by the mantling unit. The stratigraphic reconstructions allowed to identify a succession of depositional events separated by unconformities which are expressed by space-space and space-time reconstructions.

The genetic interpretations associated to such schemes allowed to reconstruct the geological history of the studied area which can be outlined in four main stages as follows.
An impact event, correspondent to the emplacement of Holden crater predates a 'water-related' phase, including a sustained phase of fluvio-lacustrine activities followed by discontinuous ephemeral alluvial episodes.
The youngest part of the stratigraphic succession is represented by an aeolian phase composed of several generations of mega ripples and dunes, some of which are still active.

Figure 5. Morpho-stratotype of the LTD unit at HiRISE scale (ESP_011542_1530).

5. CONCLUSIONS

This first attempt showed how an 'objective' approach is feasible even in planetary science, as long as the available data have a good coverage and high spatial resolution for the selected area.
Holden crater lend itself to be deeply investigated in this sense due to the high-resolution and extremely dense data coverage.

The next step will include the hyperspectral data in the unit definitions taking into account that some Martian surface properties, such as angle of incidence, grain size and mineralogical heterogeneity, can influence the spectral resolution of hyperspectral data (Mustard and Pieters 1989; Hapke, 1993). These conditions impact the quality, shape and response of the spectral dataset and may produce difficulty in the interpretation of the mineralogy. Nevertheless, the problem of different resolution among the visible imagery and the spectral data will be addressed in order to organize a consistent legend.

Then, we will identify a possible set of graphical symbols describing the surface features, locating potential limits in current GIS symbology implementation. This work is the first step in developing a 'language' as uniform as possible between Earth and Planetary geological-geomorphological maps.

ACKNOWLEDGEMENTS

This work has been performed within the GMAP activity of the Europlanet 2024 RI, and it has received funding from the European Union's Horizon 2020 research and innovation programme under Grant Agreement No. 871149. Data were obtained from the PDS Geoscience Node and processed using ISIS and the NASA AMES tools.

REFERENCES

Anderson, J.A., Sides, S.C., Soltesz, D.L., Sucharski, T.L. and Becker, K.J., 2004. March. Modernization of the integrated software for imagers and spectrometers. In Lunar and Planetary Science Conference (p. 2039).

Beyer, R. A., Alexandrov, O., and McMichael, S., 2018. The Ames Stereo Pipeline: NASA's open source software for deriving and processing terrain data. Earth and Space Science, 5(9), 537-548.

Bibring JP, Soufflot A, Berthé M, Langevin Y, Gondet B, Drossart P, Bouyé M, Combes M, Puget P, Semery A, and Bellucci G., 2004. OMEGA, Observatoire pour la Minéralogie, l'Eau, les Glaces et l'Activité. InMars Express: the scientific payload 2004 Aug (Vol. 1240, pp. 37-49).

Broxton, M. J. and L. J. Edwards, 2008. The Ames Stereo Pipeline: Automated 3D Surface Reconstruction from Orbital Imagery. Lunar and Planetary Science Conference 39, abstract #2419.

Gaddis, L., Anderson, J., Becker, K., Becker, T., Cook, D., Edwards, K., Eliason, E., Hare, T., Kieffer, H., Lee, E.M. and Mathews, J., 1997.. An overview of the integrated software for imaging spectrometers (ISIS). In Lunar and Planetary Science Conference (Vol. 28, p. 387).

Grant, J.A., Irwin III, R.P., Wilson, S.A., Buczkowski, D. and Siebach, K., 2011. A lake in Uzboi Vallis and implications for Late Noachian–Early Hesperian climate on Mars. Icarus, 212(1), pp.110-122.

Grant, J.A., Irwin III, R.P., Grotzinger, J.P., Milliken, R.E., Tornabene, L.L., McEwen, A.S., Weitz, C.M., Squyres, S.W., Glotch, T.D. and Thomson, B.J., 2008. HiRISE imaging of impact megabreccia and sub-meter aqueous strata in Holden Crater, Mars. Geology, 36(3), pp.195-198.

Hapke, B., 1993. Theory of reflectance and emittance spectroscopy. Cambridge Univ. Press Cambridge.

ISPRA, Carta Geomorfologica d'Italia, 2018. Guida alla rappresentazione cartografica. Modifiche e integrazioni al Quaderno 4/1994, pp 95.

ISPRA, Carta Geologica d'Italia, 2009. Guida alla rappresentazione cartografica. Modifiche e integrazioni ai Quaderni 2/1996 e 6/1997, pp 166.

Malin, M. C., J. F. Bell, B. A. Cantor, M. A. Caplinger, W. M. Calvin, T. R. Clancy, K. S. Edgett, L. Edwards, R. M. Haberle, and P. B. James, 2007. Context camera investigation on board the Mars Reconnaissance Orbiter, Journal of Geophysical Research: Planets (1991–2012), 112(E5).

McEwen, A.S., Banks, M.E., Baugh, N., Becker, K., Boyd, A., Bergstrom, J.W., Beyer, R.A., Bortolini, E., Bridges, N.T., Byrne, S. and Castalia, B., 2010. The high resolution imaging science experiment (HiRISE) during MRO's primary science phase (PSP). Icarus, 205(1), pp.2-37.

Murchie, S., Roach, L., Seelos, F., Milliken, R., Mustard, J., Arvidson, R., Wiseman, S., Lichtenberg, K., Andrews-Hanna, J., Bishop, J. and Bibring, J.P., 2009. Evidence for the origin of layered deposits in Candor Chasma, Mars, from mineral composition and hydrologic modeling. Journal of Geophysical Research: Planets, 114(E2).

Mustard, J.F. and Pieters, C.M., 1989. Photometric phase functions of common geologic minerals and applications to quantitative analysis of mineral mixture reflectance spectra. Journal of Geophysical Research: Solid Earth, 94(B10), pp.13619-13634.

Neukum, G. and Jaumann, R., 2004. HRSC: The high resolution stereo camera of Mars Express. In Mars Express: The Scientific Payload (Vol. 1240, pp. 17-35).

Pondrelli, M., Baliva, A., Di Lorenzo, S., Marinangeli, L., & Rossi, A. P., 2005. Complex evolution of paleolacustrine systems on Mars: An example from the Holden crater. Journal of Geophysical Research: Planets, 110(E4).

Scott, D.H. and Tanaka, K.L., 1986. Geologic map of the western equatorial region of Mars.

Sides, S.C., Becker, T.L., Becker, K.J., Edmundson, K.L., Backer, J.W., Wilson, T.J., Weller, L.A., Humphrey, I.R., Berry, K.L., Shepherd, M.R. and Hahn, M.A., 2017. The USGS Integrated Software for Imagers and Spectrometers (ISIS 3) instrument support, new capabilities, and releases. In Lunar and Planetary Science Conference (No. 1964, p. 2739).

Shean, D. E., O. Alexandrov, Z. Moratto, B. E. Smith, I. R. Joughin, C. C. Porter, Morin, P. J., 2016. An automated, open-source pipeline for mass production of digital elevation models (DEMs) from very high-resolution commercial stereo satellite imagery. ISPRS Journal of Photogrammetry and Remote Sensing. 116.

Sucharski, T., Mapel J., Backer J.C.W., Lee K. K., Agoins K., et alii, 2020. USGS-Astrogeology/ISIS3: ISIS 4.2.0 Public Release (Version 4.2.0). Zenodo. http://doi.org/10.5281/zenodo.3962369

SOIL AND WATER SALINIZATION OF AN OASIS ECOSYSTEM IN THE ZIBAN REGION (TOLGA), ALGERIA

S. Belghemmaz [1], M. Fenni [1], G.M. Afrasinei [2]*, Y. Louadj [3]

[1] Laboratory of Valorisation of Biological and Natural Resources, Faculty of Life and Natural Sciences, Ferhat Abbas University, Sétif-1, 19000 Algeria - sbelghemmaz@yahoo.fr
[2] School of Surveying and Construction Management, College of Engineering and Built Environment, Technological Univ. Dublin, Bolton Street, Dublin, Ireland - gabrielamihaela.afrasinei@tudublin.ie, https://orcid.org/0000-0002-0387-5932
[3] Department of agronomic sciences, Faculty of Life and Natural Sciences, Ferhat Abbas University, Sétif-1, 19000 Algeria - pedologist899@gmail.com

KEY WORDS: drylands, salinization, oasis ecosystem, remote sensing, decision tree classifier, soil/water sampling, statistical analysis

ABSTRACT:

In the Ziban arid and semi-arid region of Algeria, oasis agro-ecosystems are developing at a fast pace, implying a higher demand for water supply. This has led to the secondary salinization of soil, waterlogging problem and even alkalinisation of soil. The aim of this study is to assess soil salinization and water salinity in three different oases in the Tolga region. These oases differ in terms of age, morphology, and surface state of soil. Remote sensing, analytical and statistical analyses were employed to assess the functional drainage network and degradation state of the three oases. The hydro-pedological characterisation of water and soil samples (pH, EC, calcium carbonate content) was performed through laboratory analysis. Remote sensing data and techniques were employed for the extraction of saline surfaces and land cover features. The results show that the oasis no. 3, which is located in a depression, is the most affected by salinization. Coupled with ancillary data, this outcome can be linked to morphology and the lack of an efficient drainage system. Concerning the oases 1 and 2, there is a low to no risk of salinization and waterlogging, possibly due to an efficient drainage and a favourable geomorphological setting. The two latter oases have satisfactory conditions for an efficient drainage and salt leaching. Despite the strong constraints of this Saharan context, our preliminary results suggest that the sustainable management of oasis ecosystems is achievable, providing valuable reference of the impact of climate change and human activities.

1. INTRODUCTION

1.1 Introduction

In the Saharan Region, oasis agro-ecosystems represent the best management practice of lands characterized high geo-biophysical constraints. An oasis does not only consist of a food-production system but it is also a living ecosystem ecosystem (Mihi, Tarai, and Chenchouni 2017; Liu et al. 2017; Sedra 2015). According to PGDEO (2014, Projet de Gestion Durable des Ecosystèmes Oasiens en Tunisie. Plan de développement participatif de l'oasis de Chebika, Gouvernorat de Tozeur, Tunisie, 56 p.), an oasis is also a cultural and socio-economic heritage, being a patrimony that must be preserved. Algerian Saharan Oases are mostly located in endorheic depressions. Their hydrological functioning must be well balanced. Nowadays, they can suffer from excess water and waterlogging (Idder et al. 2014). Excessive anthropisation, demanding management of agricultural practices, and extreme climatic conditions can lead to the transformation of the oases into a non-productive area. Sand encroachment and the salinization of soil and water are the two major threats to the oasis of Algerian Sahara (Mihi, Tarai, and Chenchouni 2017; G. M. Afrasinei et al. 2017; G M Afrasinei et al. 2018). These threats are confirmed by other studies regarding the use of saline water of a Saharan oasis and also in the south of Tunisia (Trabelsi et al. 2012; Macdonald and Davies 2000; Ghiglieri et al. 2013). In Algeria, (Boumaraf 2013; Idder et al. 2014; Daniel Dubost 1986) focused their interest on some Saharan areas where the natural resources (water, soil, flora, and fauna) have been exposed constantly to excessive anthropisation and harsh climatic conditions.

The oases of Tolga are located in an area known as the Occidental Zeb in the western part of Biskra Region (Northeast of Algeria). Past research shows that some oases are prone to palm disease (Fusariose) while others lack water for irrigation or have waterlogging and salinization problems (Mihi, Tarai, and Chenchouni 2017). Salt accumulation in the soil of the oasis can originate from saline irrigation waters (secondary salinization), high evapotranspiration, seepage, and poor drainage network (Daoud and Halitim 1994; Yahiaoui et al. 2015; G. I. Metternicht and Zinck 2003; G. Metternicht and Zinck 2008). Considering these major threats for land and soil degradation, several studies had addressed these questions in an oasis agro-ecosystem but the issue needs more insight. Therefore, the aim of our research is to assess the state of the soil and water salinisation problem in three different oases in the Tolga area.

2. STUDY AREA

The Tolga area is located West of Biskra and it is well known for being the most important oasis of Ziban in Biskra (Fig. 1, North-East of Algeria, at the limit the Sahara desert) in terms of date production and exportation of the high-quality variety 'Deglet-Nour'. The Biskra region has an arid climate (annual *mean rainfall less than 20 mm)* (Pouget 1980; Gabriela M

* Corresponding author

Afrasinei et al. 2017). The soils of these oases would have resulted from the combined action of colluvium and aeolian transport. They have a predominantly sandy texture.

3. METHOD AND DATASET

The preliminary prospection work of the palm groves of the Tolga region had led us to take into account several criteria for the establishment of methodology. Among the criteria, we considered the morphological setting and their position in the landscape, the age of palm trees, the irrigation and drainage system, vegetation cover and soil distribution. The chosen study oases are located between Bordj Ben Azzouz (BBA) and Lioua region (Fig. 1). The prospection work has led us to notice that the major threat to the oasis agro-ecosystem is soil and water salinization. This phenomenon is widespread across the date palm groves of Tolga region, and affects these oases at different levels.

For the assessment of the current state of salinization of these oases ecosystems, we relied on spectral analysis and land cover classification, and a characterization of several parameters of the soil and water samples. Salt features and main land cover classes were extracted using a customised decision tree, as presented in section "Remote sensing approach". The sampling was done in April 2016 in 3 different oases (Fig. 1).

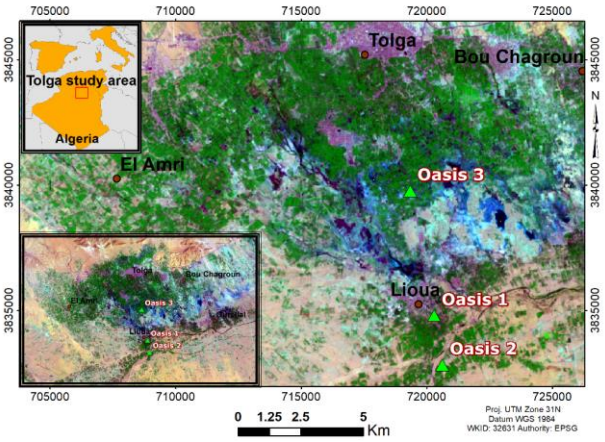

Figure 1 Geographic location of sampling profiles in the three oases. False color composite 752 of Landsat 8 scene of April 19, 2016. Saline and hydrosaline areas small sabkha and daia areas) are visible in cyan and blue – dark blue hues.

The coordinates of the sampling locations are given as follows: 34° 37' 53" N and 5° 24' 12" E for Oasis 1, 34° 36' 49" N and 5° 24' 23" E for Oasis 2, and 34° 40' 35" N and 5° 23' 39" E for Oasis 3.

In each oasis, we performed a soil profile with a manual auger according to three different soil depths (0-20 cm, 20-50 cm and > 50 cm). At each oasis, we took three water samples, which have different sources as follows: groundwater (oasis 1), drainage water (oasis 2) and discharge drainage water (oasis 3).

Soil and water samples were analysed according to the methods recommended by (Mathieu and Pieltain 2003). Concerning soil samples, pH and EC are measured on a 1:5 water extract (1:5) using the potentiometric method. Total calcium carbonate content (%) was also measured using a volumetric method (calcimetry). For the water samples, we analysed the pH and EC using the potentiometric method. Each parameter was measured with 3 repetitions.

3.1 Remote sensing approach

Decision tree (DT) tools have frequently been found to yield higher classification accuracies than parametric classifiers, being able to cope with non-normal distributions and intra-class variation. DTs can perform automatic feature selection and complexity reduction, lacking assumptions concerning the frequency distributions of data in each class, being flexible, and able to handle non-linear relationships between features and classes (Rogan, Franklin, and Roberts 2002; Otukei and Blaschke 2010; Ruiz, Guasselli, and Caten 2017; G. M. Afrasinei 2016; G M Afrasinei et al. 2018).

Landsat satellite imagery of 19 April 2016, was obtained by courtesy of USGS. Satellite image preprocessing, processing and a supervised classification using a manual customized decision tree approach (G. M. Afrasinei et al. 2017; Gabriela M Afrasinei et al. 2017) was performed.

The Landsat image of April 19, 2016, path 194, row 36 was a L1TP product of processing level (Precision terrain). It was systematically, radiometrically, geometrically, and topographically corrected by the provider using ground control points, being a product of the highest quality (NASA 2016; Roy et al. 2014). The 16-bit native radiometric resolution of the OLI bands provide further detail of information and high quality. In this work, for the extraction of land cover and soil salinity features, only the multispectral bands of the OLI instrument were employed, and the Cirrus and Panchromatic not considered. Using the metadata file, the image was pre-processed to surface reflectance and Dark Object Subtraction was performed as atmospheric correction procedure (using the software ENVI ITT Vis Exelis).

3.2 Statistical analysis

We performed a one-way ANOVA analysis using the soil profiles (taken at three different depths in the three oases as a factor. Subsequently, we made a one-way ANOVA using the source of provenance of the waters (drainage waters, groundwater, and drainage discharge water) as a factor. Whenever there is an effect of the factor, we make a comparison of means using Tukey's HSD (Honestly Significant Difference). All tests were carried out at 5% level of significance.

4. RESULTS AND DISCUSSION

4.1 Decision Tree classifier

Following reference (Gabriela M Afrasinei et al. 2017; G M Afrasinei et al. 2018), eleven spectral indices were applied and thresholds were calculated using mean and standard deviation values of each index image. These indices were particularly designed to cope with spectral confusion problems given by the extraction of highly reflective desert features and arid areas land cover features.

The twelve classes extracted are presented in Fig. 2 and their description follows the one proposed by (Gabriela M Afrasinei et al. 2017).

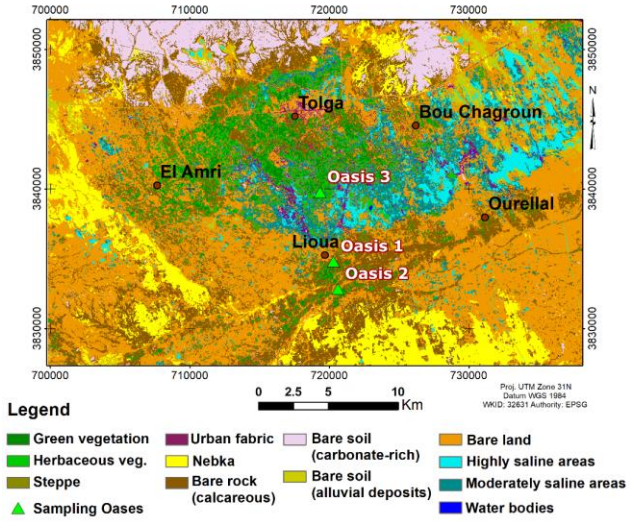

Figure 2 Decision Tree classification of the 19th of April, 2016 Landsat image, Biskra area, Algeria

4.2 Soil and water characterisation

The obtained analytical results of the three oases are summarised in the Table 1. In general, we noticed that the soil pH is alkaline. Furthermore, according to standard interpretation of soil salinity, we can say that all soil samples are saline (Mathieu and Pieltain 2003). We can see that the total carbonate content of all the samples is moderate to low. These results are in agreement with the interpretation given by (Baize 2006). Concerning the water samples, we can observe that the pH is alkaline. Concerning salinity, according the standard of the interpretation of suitability of the water for irrigation (Ayers and Westcot 1994), all these waters are not suitable (Class 5). However, there is a pattern emerging where the salinity increases from the sample taking from the drainage ditch (Oasis 2) to the drainage discharge area near Oasis 3.

Nature and origin of samples	Soil parameters				Water parameters	
	Soil Depths (cm)	pH ($_{water}$)	EC (dS/m) at 25 °C	$CaCO_3$ (%)	pH	EC (dS/m) at 25°c
Oasis 1 (Soil and Underground water)	0-20	8,18	1.951	4.57	7.48	4.16
	20-50	8.12	2.235	14.15		
	>50	7.96	2.795	4.63		
Oasis 2 (Soil and Drainage water ditches)	0-20	7.94	2.032	0.007	8.11	9.46
	20-50	7.80	2.105	2		
	>50	8.11	2.02	9.01		
Oasis 3 (Soil and drainage waters discharge area)	0-20	8.48	8.304	9.40	8.94	67.16
	20-50	8.26	8.760	15.80		
	> 50	8.48	10.988	16.1		

Table 1 Measured Soil and Water Parameters

4.3 Comparison of soil Characteristics of the three Oases

The ANOVA analysis using the soil profiles as a factor shows a significant difference for pH and EC soil characteristics between the three oases; however, there is no significant difference for CaCO3 between the three oases. The result of the comparison of soil pH (1:5) and EC (1:5) between the three soil profiles sampled at three oases is presented in Table 2.

The result of comparison of soil pH at three soil depths using the Tukey $HSD_{0.05}$ between oasis 1 and 2 and between 1 and 3, shows no statistical significant difference. However, there is a statistical significant difference for soil pH between oasis 2 and oasis 3.

Soil parameters	Soil depths (cm)	Oasis 1	Oasis 2	Oasis 3
pH (1:5)	0-20	8.18	7.94	8.48
	20-50	8.12	7.8	8.26
	>50	7.96	8.11	8.48
	Mean	8.08	7.95	8.40
	H	**0.33**		
	$SD_{0.05}$			
EC (1:5) (dS/m) at 25°c	0-20	1.95	2.03	8.3
	20-50	2.23	2.1	8.76
	> 50	7.96	2.02	10.98
	Mean	2.32	2.05	9.34
	HSD $_{0.05}$	**2.15**		

Table 2 Comparison of soil pH and EC in the three oases

With respect to the EC parameters, the Tukey's test comparison reveals that there is no statistical difference between oasis 1 and 2. However, there is a statistical significant difference between oasis 1 and 3 and 2 and 3.

Water parameters		Drainage water	Groundwater	Discharge drainage water
pH	R1*	8,89	8,05	7,36
	R2	8,95	8,12	7,5
	R3	9	8,16	7,59
	Mean	8.94	8.11	7.48
	HSD $_{0.05}$	**0.20**		
EC	R1	10.89	2.7	69.4
	R2	6.91	5.12	68.3
	R3	10.6	5.13	63.8
	Mean	9.46	4.31	67.16
	HSD $_{0.05}$	**5.69**		

**R1, R2 and R3 are Repetitions 1, 2 and 3.*

Table 3 Results of the comparison between water samples according to their sources

4.4 Comparison of alkalinity and salinity of waters

The comparison of the mean of the EC and pH parameters of the waters of the three sources is presented in Table 3. For water alkalinity, there is a statistical significant difference of the three water sources at 5 % level of significance. Regarding the water salinity, there is a statistical significant difference between the drainage water and groundwater, on the one hand, and the discharge drainage water at 5 % level of significance, on the other hand.

4.5 Assessment of Degradation State in the three oases

This aspect is discussed according to the hydro-pedological characteristics and of the drainage network functioning.
The results of $CaCO_3$ content in the soils of the three oases show no significant difference. This result is in accordance with the results of (Mostephaoui, Bensaid, and Saker 2013). In fact, these authors found that the main pedological characteristic of these soils is given by the presence of gypsum accumulation and encrusting. Therefore, in our discussion of the state of degradation of these three oases, we will focus on pH, EC, and the visual presence of gypsum accumulation.

4.5.1 Oasis 1

Soil pH values showed that the alkalinity gradient increases from top to bottom of soil profile. The same pattern emerges for soil salinity (descending type of salinization). Concerning groundwater, despite its unsuitable chemical quality in terms of salinity, the farmers can still use it because the texture of the soil (mainly sandy, presenting a high drainage rate). Added to this, it seems that the drainage network is functioning well in this oasis.

4.5.2 Oasis 2

The main pedological feature in this oasis is the presence of gypsum encrusting called 'Deb Deb' at more than 2 meters of soil depth (Fig. 3). The pH and EC are not very high and are almost constant through the soil profile. This seems to be in agreement with results reported by (Mostephaoui, Bensaid, and Saker 2013; Sedrati 2011; Hiouani and Bensaid 2009), and justifies the pedological specificity of these soils consisting of the presence of gypsum accumulation. In fact, the only constraint in this oasis is the presence of gypsum encrusting which requires specific management for the plantation of new date palm trees (Belghemmaz et al. 2018).

4.5.3 Oasis 3

In this Oasis (Fig. 4), the soil salinity is high with a descending saline profile (maximum of salinity at depth). From the morphological perspective, we noticed the presence of saline efflorescence at certain points, in accordance with the work of (Aubert 1963) undergone in an oasis in South of Biskra.
We think that the salinization phenomenon in the oasis compromises severely the growth of date palm tree. As such, (Dubost 1991) found that date palm trees could suffer from the presence of water table at a depth of less than 120 meters. This suggests that the drainage network must function well, but the prospection work in this oasis has revealed that drainage network is poor.
The Oasis 3 is located nearby a drainage water discharge, where taken. We found that the water salinity is six times more saline than the drainage water ditches (Oasis 2). This water also has a very high alkaline pH. The water presents low quality, and the risk of soil degradation in this oasis can increase. In their study conducted in Tunisia in a modern oasis, (Askri and Bouhlila 2010) found that the EC of the water drainage between 11.8 and 18.7 dS/m can induce, in addition to soil salinization, an alkalinization of soil near a drainage discharge area.
As regards the frequent saline efflorescence, which appear on the surface of the soil in this oasis, this may prove that the both leaching and drainage are failing. The same issue was observed in Tunisia by (Hatira et al. 2007) and was explained by the fact that due to the lack of leaching, salts do not reach the drainage channels to be evacuated to the outlet. The presence of salt efflorescence is also consistent with the spectral analysis and the DT classification, since Oasis 3 overlaps the 'highly saline areas' class, having a big extent in the surrounding area (Fig 2, a radius of minimum 5 km). However, it diminishes towards South and, eventually, it does not appear (or at least it is not superficially detectable by the sensor) nearby the locations of Oasis 1 (in a radius of 1 km) and Oasis 2 (in a radius of 2.5 km).
Finally, a fact that has particularly marked the oasis agriculture in region of Tolga and caught our attention is the deployment of plasticulture observed in the field. Reference (Kebibeche 2013) has also described this trend. This has systematically led to a change in the land/soil use and water, and inevitably affected the oasis environment (Belghemmaz et al. 2018). In this context, we noticed several date palm-grove oases that were abandoned by the farmers, and others, which apparently had no restriction in their functioning. This situation of oasis environment (aridity and saline conditions), management and means (technical, human, and financial) that the farmers use can be a determinant factor for the evolution of these agro-ecosystems in a sustainable manner.

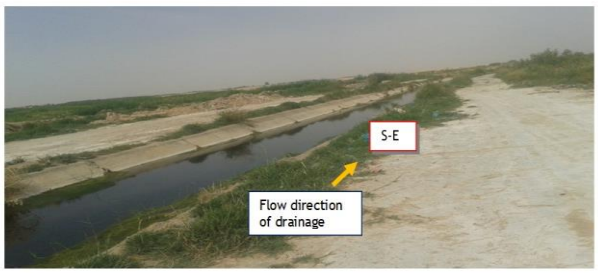

Figure 3 Good functioning of drainage ditches (oasis 2). There is no risk of degradation of the palm groves.

Figure 4 Drainage ditches infested by vegetation (oasis 3). It shows the problem of waterlogging because of poor or defective drainage. Here, the salinity is excessive and the alkalinity is high.

5. CONCLUSION AND RECOMMENDATION

The land cover comparison of water and soil salinity of three different oases located in the arid and semi-arid Ziban region of Biskra (Northeast of Algeria) helped us emphasize the role of drainage network in the sustainability of these oasis agro-ecosystems. The employed methods consisting of remote sensing techniques, field and laboratory analysis of water and soil samples (pH, EC, calcium carbonate content) allowed us to obtain valid results on salinization degree and state of degradation of soils. We can state that in the Ziban region, where the Algerian state is helping the farmers to invest in the date palms, the supply of water into the oasis will increase. Consequently, this would accentuate the degradation of the

oasis environment by salinization and probably also by alkalinisation. This would further compromise the oasis ecosystem well-functioning. Therefore, water accumulation and salinization processes may still affect new areas. Hence, the rational use of water for irrigation and the maintenance of an efficient and functional drainage network are the main recommendations in order to avoid further salinization and degradation of these oasis ecosystems. It is in this way that we can maintain the sustainability of the oases and preserve their productive potential.

In order to better assess the risk of salinization and its repercussions on the sustainability of the oasis ecosystem in this region, we plan to continue our study, using the same approach and focus on other oasis sites.

REFERENCES

Afrasinei, G. M. 2016. "Study of Land Degradation and Desertification Dynamics in North Africa Areas Using Remote Sensing Techniques." University of Cagliari. doi:10.13140/RG.2.1.2412.6327.

Afrasinei, G. M., M.T. Melis, C. Buttau, C. Arras, A. Zerrim, M. Guied, M. Ouessar, et al. 2017. "Classification Methods for Detecting and Evaluating Changes in Desertification-Related Features in Arid and Semi-Arid Environments." *Euro-Mediterranean Journal for Environmental Integration—Springer* 21. doi:DOI 10.1007/s41207-017-0021-1.

Afrasinei, Gabriela M, Maria T Melis, Cristina Buttau, John M Bradd, Claudio Arras, and Giorgio Ghiglieri. 2017. "Assessment of Remote Sensing-Based Classification Methods for Change Detection of Salt-Affected Areas (Biskra Area, Algeria)." *Journal of Applied Remote Sensing* 11 (1): 16025. doi:10.1117/1.JRS.11.016025.

Afrasinei, G M, Maria Teresa Melis, Claudio Arras, Marco Pistis, Cristina Buttau, and Giorgio Ghiglieri. 2018. "Spatiotemporal and Spectral Analysis of Sand Encroachment Dynamics in Southern Tunisia." *European Journal of Remote Sensing* 51 (1): 352–74. doi:10.1080/22797254.2018.1439343.

Askri, B, and R Bouhlila. 2010. "Évolution de La Salinité Dans Une Oasis Moderne de La Tunisie." *Etude et Gestion Des Sols* 17 (3–4): 197–212.

Aubert, Georges. 1963. "Observations Sur Les Caractéristiques, La Dénomination et La Classification Des Sols Salés Ou Salsodique." In *XII Congres de l'Association Internationale de Science Du Sol*, XX:73–78. New Delhi: Cah. ORSTOM. http://horizon.documentation.ird.fr/exl-doc/pleins_textes/cahiers/PTP/3481.PDF.

Ayers, R.S., and D.W. Westcot. 1994. *Water Quality for Agriculture*. 29 Rev. 1. Rome: Food and Agriculture Organization of the United Nations, FAO.

Baize, Denis. 2006. *Guide Des Analyses En Pédologie*. Edited by INRA. 2ème éditi.

Belghemmaz Salah, Fenni Mohamed, Gabriela Mihaela Afrasinei, Louadj Yacine and Degui Nouara. 2018. "Assesment of Land Degradation Related To Groundwater Irrigation of Osis Environments. Case Study: The Zibans (Biskra), Algeria. in Recent Advances in Environmental Science from the Euro-Mediterranean and Surrounding Regions. Technology & Innovation, https://doi.org/10.1007/978-3-319-70548-4_378

Boumaraf, Belkacem. 2013. "Caracteristiques et Fonctionnement Des Sols Dans La Vallee d'Oued Righ, Sahara Nord Oriental, Algerie." University of Reims.

Daoud, Y, and A Halitim. 1994. "Irrigation et Salinisation Au Sahara Algérien." Sécheresse 5 (3): 151 –160.

Dubost, D. 1991. Ecologie, Aménagement et Développement Agricole Des Oasis Algériennes. Atelier Nat. de Reprod. des Thèses de l'Univ. de Lille 3. https://books.google.it/books?id=P6EbvgAACAAJ.

Dubost, Daniel. 1986. "Nouvelles Perspectives Agricoles Du Sahara Algérien." Revue de l'Occident Musulman et de La Méditerranée 41–42: 339–56. doi:10.3406/remmm.1986.2466.

Ghiglieri, Giorgio, Gabriela Afrasinei, Claudio Arras, Mohamedou Oulb Baba Sy, Manuela Barbieri, Oumelkheir Belkheiri, Mongi Ben Zaied, et al. 2013. "WADIS-MAR - Water Harvesting and Agricultural Techniques in Dry Lands: An Integrated and Sustainable Model in Maghreb Regions." In *Water, Environment and Agriculture:challenges for Sustainable Development*, edited by N. Lamaddalena, M. Todorovic, and L. S. Pereira, 55–56.

Hatira, A., L. Baccar, M. Grira, and T. Gallali. 2007. "Analyse de Sensibilité Du Système Oasien et Mesures de Sauvegarde de L'oasis de Métouia (Tunisie)." *Revue Des Sciences de l'Eau* 20 (1): 59–69. doi:10.7202/014907ar.

Hiouani, F, and R Bensaid. 2009. "Effect of Salinity on the Retention of Water by Gypseous Soils in Ain Benoui Region (Biskra)." *Courrier Du Savoir* – 9: 85–89.

Idder, Tahar, Abdelhak Idder, Abdourahamane Tankari Dan-Badjo, Amina Benzida, Soumia Merabet, Hamza Negais, and Aïcha Serraye. 2014. "Les Oasis Du Sahara Algérien, Entre Excédents Hydriques et Salinité." *Revue Des Sciences de l'Eau* 27 (2): 155–64. doi:10.7202/1025565ar.

Kebibeche, Djawad. 2013. "Dynamique de La Plasticulture Dans La Commune d'El Ghrous, Wilaya de Biskra."

Liu, Chang-an, Kadambot H M Siddique, Shuai Hua, and Xin Rao. 2017. "The Trade-O Ff in the Establishment of Arti Fi Cial Plantations by Evaluating Soil Properties at the Margins of Oases." *Catena* 157 (May). Elsevier: 363–71. doi:10.1016/j.catena.2017.05.031.

Macdonald, A M, and J Davies. 2000. "A Brief Review of Groundwater for Rural Water Supply in Sub-Saharan." *British Geological Survey Technical Report WC/00/33*, 13. http://www.rural-water-supply.net/en/resources/details/130.

Mathieu, C., and F. Pieltain. 2003. *Analyse Chimique Des Sols Méthodes Choisies*. Tec et Doc. Paris.

Metternicht, G I, and J A Zinck. 2003. "Remote Sensing of Soil Salinity: Potentials and Constraints." *Remote Sensing of Environment* 85 (1): 1–20. doi:http://dx.doi.org/10.1016/S0034-4257(02)00188-8.

Metternicht, Graciela, and J Alfred Zinck. 2008. "Spectral Behavior of Salt Types." In *Remote Sensing of Soil Salinization*. CRC Press. doi:doi:10.1201/9781420065039.ch210.1201/978142006

5039.ch2.

Mihi, Ali, Nacer Tarai, and Haroun Chenchouni. 2017. “Can Palm Date Plantations and Oasification Be Used as a Proxy to Fi Ght Sustainably against Desertification and Sand Encroachment in Hot Drylands ?” *Ecological Indicators* in press. doi:10.1016/j.ecolind.2017.11.027.

Mostephaoui, Tewfik, Rabah Bensaid, and Mohamed Lakhdar Saker. 2013. “Localization and Delimitation of the Arid Soils by Remote Sensing and in-Situ Measurements in an Arid Area: Case of Oued Djedi Watershed, Biskra, Algeria.” *World Applied Sciences Journal* 24 (3): 370–82. doi:10.5829/idosi.wasj.2013.24.03.972.

NASA. 2016. “Landsat 7 Science Data Users Handbook.”

Otukei, J R, and T Blaschke. 2010. “Land Cover Change Assessment Using Decision Trees, Support Vector Machines and Maximum Likelihood Classification Algorithms.” *International Journal of Applied Earth Observation and Geoinformation* 12, Supple (0): S27–31. doi:http://dx.doi.org/10.1016/j.jag.2009.11.002.

Pouget, Marcel. 1980. *Les Relations Sol-Végétation Dans Les Steppes Sud-Algéroises. Travaux et Documents de l’ORSTOM*. Paris.

Rogan, John, Janet Franklin, and Dar A Roberts. 2002. “A Comparison of Methods for Monitoring Multitemporal Vegetation Change Using Thematic Mapper Imagery.” *Remote Sensing of Environment* 80 (1): 143–56. doi:http://dx.doi.org/10.1016/S0034-4257(01)00296-6.

Roy, D P, M A Wulder, T R Loveland, Woodcock C.E, R G Allen, M C Anderson, D Helder, et al. 2014. “Landsat-8: Science and Product Vision for Terrestrial Global Change Research.” *Remote Sensing of Environment* 145 (0): 154–72. doi:http://dx.doi.org/10.1016/j.rse.2014.02.001.

Ruiz, L F C, L A Guasselli, and A T Caten. 2017. “Object Based Analysis and Decision Tree for the Classification of Submetrical Spatial Resolution Images Captured by UAV [Árvore de Decisão E Análise Baseada Em Objetos Na Classificação de Imagens Com Resolução Espacial Submétrica Adquiridas Por Vant].” *Boletim de Ciencias Geodesicas* 23 (2): 252–67. doi:10.1590/S1982-21702017000200016.

Sedra, Moulay Hassan. 2015. “Date Palm Status and Perspective in Morocco.” In *Date Palm Genetic Resources and Utilization*, 257–323. Dordrecht: Springer Netherlands. doi:10.1007/978-94-017-9694-1_8.

Sedrati, Nassima. 2011. “Origines et Caractéristiques Physico-Chimiques Des Eaux de La Wilaya de Biskra-Sud-Est-Algérien-.” http://biblio.univ-annaba.dz/wp-content/uploads/2014/05/these-SEDRATI.pdf.

Simonneau, P, and G Aubert. 1963. “L’utilisation Des Eaux Salées Au Sahara.” *Annales Agronomiques* 14 (5): 859–72. http://www.documentation.ird.fr/hor/fdi:11033.

Trabelsi, Rim, Kamel Abid, Kamel Zouari, and Houcine Yahyaoui. 2012. “Groundwater Salinization Processes in Shallow Coastal Aquifer of Djeffara Plain of Medenine, Southeastern Tunisia.” *Environmental Earth Sciences* 66 (2): 641–53. doi:10.1007/s12665-011-1273-8.

Yahiaoui, Ibrahim, Abdelkader Douaoui, Qiang Zhang, and Ahmed Ziane. 2015. “Soil Salinity Prediction in the Lower Cheliff Plain (Algeria) Based on Remote Sensing and Topographic Feature Analysis.” *Journal of Arid Land* 7 (6): 794–805. doi:10.1007/s40333-015-0053-9.

Marine Remote Sensing and Coastal Hazard

ANALYSIS OF THE EROSIVE PROCESSES TRIGGERED BY THE CONSTRUCTION OF PORTS USING REMOTE SENSING. CASE STUDY: CALABRIA (ITALY)

G. Foti [1], G. Barbaro [1], G.C. Barillà [1]*, P. Mancuso [2], P. Puntorieri [1], R. Piria [1]

[1] Mediterranea University of Reggio Calabria, DICEAM Department, località Feo di Vito, 89122 Reggio Calabria Italy - giandomenico.foti@unirc.it; giuseppe.barbaro@unirc.it; chiara.barilla@unirc.it; pierfabrizio.puntorieri@unirc.it; prirti95e62i537j@studenti.unirc.it

[2] Public Works Department of Calabria Region, località Germaneto, 88100 Catanzaro Italy – pierluigi.mancuso@regione.calabria.it

KEY WORDS: Port, coastal erosion, erosive processes, shoreline changes, remote sensing, QGIS.

ABSTRACT:

In recent decades, the Italian territory has been subject to intense anthropization processes, which have also affected coastal areas and riverbeds. Along with this process, there has also been an increase in road and sea traffic which has encouraged the construction of new ports and the expansion of most of the existing ones. These structures, however, can interfere with coastal dynamics by altering the natural conditions of the coasts, even at considerable distances from them. This problem is of fundamental importance in areas with considerable coastal development such as Calabria characterized by over 700 km of coasts. The paper analyzes the state of the Calabrian port network, focusing specifically on the type of ports presents, and any effects induced on the adjacent coasts. The analysis is performed on QGIS software by comparing the shorelines of different years. The cartographic data of the Open Data sections of the Italian and Calabrian Geoportals and the historic satellite imagery of Google Earth were used as input data. In addition, three significant case studies are described, relating to the ports of Badolato, Saline Joniche and Amantea in which both significant erosive processes in the coasts below the port and problems of silting up the port entrance were observed with a significant limitation of operations. Finally, the methodology described in this paper is of interest in the field of coastal area planning and management as it leads to the rapid analysis of cartographic data from different sources using free software.

1. INTRODUCTION

Ports allow the exchange of people and goods and, historically, have make easy the development of adjacent populations and territories: the first ports built in the Mediterranean Sea date back to the third millennium BC (Bosworth, 1915).

On the other hand, the construction of a port can significantly alters coastal dynamics, triggering and propagating erosive phenomena. Indeed, the equilibrium of the coastal areas is influenced by natural and anthropogenic factors (Komar, 2000) and the alteration of the equilibrium conditions affects the shoreline position triggering erosive processes (Komar, 2000; Boak and Turner, 2005; Foti and Sicilia, 2011; van Rijn, 2011; Addo, 2013; Barbaro, 2016; Barbaro et al., 2017; Williams et al., 2017; Mavromatidi et al., 2018; Tomasicchio et al., 2020).

The construction of a port is one of the anthropogenic factors that cause erosive processes, together with the construction of coastal structures (D'Alessandro et al., 2011; Barbaro, 2013; Sarma, 2015; Prumm and Iglesias, 2016; Miduri et al., 2017), the construction of dams and weirs, the sediment withdrawal, and the subsidence (Walling, 2006; Andreadaki et al., 2014; Zema et al., 2014; Fortugno et al., 2017; Versaci et al., 2018; Valderrama-Landeros and Flores-de-Santiago, 2019; Foti et al., 2020; Nguyen and Takewaka, 2020).

In addition to anthropogenic pressure, various natural factors can also alter coastal dynamics. The main natural factors are the wave climate (Gunaydin and Kabdasli, 2003; Barbaro et al., 2013; Bacino et al., 2013; Wang et al., 2020) and the sedimentary balance between longshore and river transport (Barbaro et al., 2012; Barbaro et al., 2014; Barbaro et al., 2019a; Foti et al., 2019; Marchesiello et al., 2019).

Other effects of anthropogenic pressure in coastal areas concern the increase in the vulnerability of these areas to the action of floods and sea storms (Fiori et al., 2014; Scionti et al., 2018; Barbaro et al., 2020; Barbaro et al., 2021; Mori et al., 2021), whose effects are amplified in the case of concurrent events (Barbaro et al., 2019b; Canale et al., 2020; Canale et al., 2021).

The paper analyzes the state of the Calabrian port network, focusing specifically on the type of ports presents, and any effects induced on the adjacent coasts. The analysis is performed on QGIS software by comparing the shorelines of different years.

2. SITE DESCRIPTION

Calabria is a region in southern Italy, located at the tip of the typical Italian "boot" in the center of the Mediterranean Sea (Fig. 1). From the morphological point of view, Calabria is characterized by hills and mountains, with a percentage of less than 10% of flat lands. Its narrow and elongated shape means that it has over 750 km of coastline, with an alternating mainly sandy and pebbly beaches, and high coasts. Calabria is enclosed by two seas, the Tyrrhenian and the Ionian, by the Straits of Messina and by the Gulf of Taranto, each of them with different climatic characteristics and with different fetch extensions. These differences lead to a remarkable variability of weather and sea conditions between the different coastal areas which influences the coastal dynamics.

* Corresponding author

Figure 1. The Calabrian region (shown with red dotted line).

3. CALABRIAN PORT NETWORK

3.1 Classification

Information on the Calabrian port network was found on the websites www.pagineazzurre.com and www.tuttobarche.it and on the websites of each port.
In Calabria there are 40 ports (Fig. 2) which can be classified according to typology and location.
With regard to the typology, they are divided into:
12 marinas;
8 equipped beaches;
7 tourist and fishing;
4 tourist piers;
3 commercial, industrial and tourist;
2 commercial, tourist and passenger;
1 industrial;
1 commercial and fishing;
1 commercial, tourist and fishing;
1 commercial pier.

Regarding the location, they are divided into:
21 on the Ionian coast;
3 in the Strait of Messina;
16 on the Tyrrhenian coast.

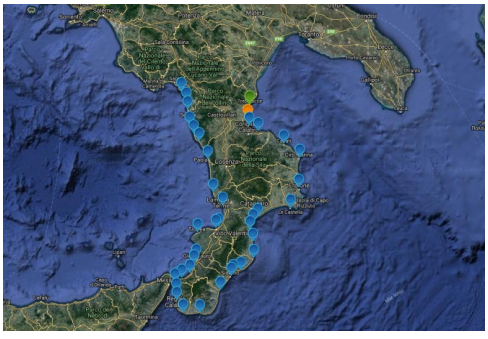

Figure 2. Calabrian port network (blue dot, source: www.pagineazzurre.com).

3.2 Analysis of the impacts on the shoreline

The analysis of the effects induced by ports on adjacent coasts was carried out through the comparison of various cartography data, which consists of: historical shorelines of 1954, 1998, 2000 and 2008 taken from the Open Data section of the Calabrian Geoportal; orthophotos of 1989, 1996, 2006 and 2012 taken from the Open Data section of the Italian Geoportal; and satellite imagery from 2015 to today provided by Google Earth.
The comparison between the different shorelines was carried out on QGIS. Preliminarily, it was necessary to manually digitize the missing shorelines, using QGIS for each orthophotos and using the spatial analysis tools of Google Earth Pro for each satellite imagery. Due to the varying oceanographic conditions among the different cartographies, the reference line chosen was the wet/dry line. It has been shown that the wet/dry line closely approximates the High-Water Line (HWL, Moore, 2000). Also, in Calabria, the tidal excursion is of the order of tens of centimeters (Sannino et al., 2015) so the effects on the variation of the shoreline position are negligible. The digitalization of the shoreline was carried out on a scale of 1:1000 on QGIS and on a higher scale on Google Earth Pro. Therefore, the shoreline position has precision of the order of the meter and the shoreline changes have been approximated to the meter. This accuracy agrees with the aims of the paper, which concern the evaluate of the effects induced by ports on adjacent coasts in terms of erosion and advancement, and not their precise quantification.
The analysis carried out highlighted that the construction of ports outside the shoreline has triggered erosive processes, except in the ports built near headlands. The amount of the erosive processes is extremely variable, with a maximum of over 200 m behind the ports of Amantea, Badolato and Saline Joniche. The variability of these processes depends on the characteristics of the wave climate (mainly direction and intensity), on the direction and amount of the longshore transport, and on the coastal morphology. For example, the construction of the port of Palmi has shaped the coast like a bay and slight erosions have been observed behind it. Instead, the most relevant erosive processes were observed behind the ports of Badolato, Saline and Amantea, which were built in straight coastal stretches without headlands and structures.
In detail, Badolato is located on the Ionian coast of Calabria. The most intense wave climate comes from South-East, along directions characterized by fetches of the order of a thousand kilometers and is generated by Scirocco winds. Another intense wave climate comes from North-East and is generated by Grecale winds. The highest significant wave heights are of the order of 6.5 m. The marina of Badolato was built in 2005 not far from the mouth of the Gallipari river. After the construction there was an accumulation of solid material South of the port which in 2009 caused the silting up and the obstruction of the port mouth and dredging operation was necessary in 2011. This intervention did not solve the problem because after a few years the mouth is partially obstructed. Also, the presence of the port has triggered considerable erosion in the coast North of the port.
Saline Joniche is located on the Ionian coast of Calabria near the Strait of Messina. The most intense wave climate comes from South-East, along directions characterized by fetches of the order of a thousand kilometers and is generated by Scirocco winds. Another frequent, but not very intense, wave climate comes from North-West and is generated by the characteristic winds of the Strait of Messina. The highest significant wave heights are less than 6.5 m. The port of Saline Joniche was built in the 1970s to serve the industrial area of Liquichimica Biosynthesis, an industrial settlement that has never been active. After the construction there was an accumulation of solid material East of the port which caused the obstruction of the port mouth, and which triggered considerable erosion processes West of the port. In 2003, a storm caused the collapse of a 100 m section of the breakwater, which was never restored. Occasionally, dredging interventions have been carried out who never solved the problem. The port has practically never been operational as the industrial site has never been active and no redevelopment interventions have ever been carried out.
Amantea is located on the Tyrrhenian coast of Calabria. The most intense wave climate comes from North-West, along directions characterized by fetches of the order of hundreds of kilometers and is generated by Mistral winds. Among the locations examined it is the one characterized by the most intense wave climate, in fact the highest significant wave heights are of the order of 9.5 m. The port of Amantea was built

in the early 2000s and after the construction there was an accumulation of solid material South of the port which caused the obstruction of the port mouth and triggered considerable erosion processes North of the port. In 2004 the mouth was completely obstructed but the dredging carried out the following year restored its functionality. Recently, there was a new obstruction of the port mouth, making it necessary to carry out a new dredging operation.

Figure 3. Ports of Badolato (on the left) and Amantea (to the right). Legend: the red line is the 2000 shoreline and the background is the Google satellite image.

Figure 4. Port of Saline. Legend: the red line is the 1954 shoreline and the background is the Google satellite image.

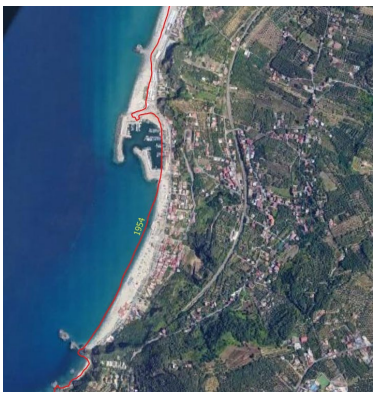

Figure 5. Port of Palmi. Legend: the red line is the 1954 shoreline and the background is the Google satellite image.

4. CONCLUSIONS

The paper analyzed the state of the Calabrian port network, focusing specifically on the type of ports presents, and any effects induced on the adjacent coasts.

The analysis carried out highlighted that the construction of ports outside the shoreline has triggered erosive processes, except in the ports built near headlands. The amount of the erosive processes is extremely variable, with a maximum of over 200 m behind the ports of Amantea, Badolato and Saline Joniche. The variability of these processes depends on the characteristics of the wave climate (mainly direction and intensity), on the direction and amount of the longshore transport, and on the coastal morphology.

The analysis described in this paper is useful for the planning and management phase of coastal areas. Indeed, the presence of ports of different types and locations allows us to analyze the advantages and the disadvantages of each configuration.

REFERENCES

Addo, K.A., 2013. Shoreline morphological changes and the human factor. Case study of Accra Ghana. *Journal of Coastal Conservation*, 17(1), pp. 85-91.

Andredaki, M., Georgoulas, A., Hrissanthou, V., Kotsovinos, N., 2014. Assessment of reservoir sedimentation effect on coastal erosion in the case of Nestos River, Greece. *International Journal of Sediment Research*, 29(1), pp. 34-48.

Bacino, G.L., Dragani, W.C., Codignotto, J.O., 2019. Changes in wave climate and its impact on the coastal erosion in Samborombón Bay, Río de la Plata estuary, Argentina. *Estuarine, Coastal and Shelf Science*, 219, pp. 71-80.

Barbaro, G. 2013. Saline Joniche: a predicted disaster. *Disaster Advances*, 6, pp. 1-3.

Barbaro, G., 2016. Master Plan of solutions to mitigate the risk of coastal erosion in Calabria (Italy), a case study. *Ocean & Coastal Management*, 132, pp. 24-35.

Barbaro, G., Bombino, G., Foti, G., Borrello, M.M., Puntorieri, P., 2019a. Shoreline evolution near river mouth: Case study of Petrace River (Calabria, Italy). *Regional Studies in Marine Science*, 29, article number 100619.

Barbaro, G., Fiamma, V., Barrile, V., Foti, G., Ielo, G., 2017. Analysis of the shoreline changes of Reggio Calabria (Italy). *International Journal of Civil Engineering and Technology*, 8(10), pp. 1777-1791.

Barbaro, G., Foti, G., Malara, G. 2013. Set-up due to random waves. *Transactions of the Royal Institution of Naval Architects Part A: International Journal of Maritime Engineering*, 155(PART A3).

Barbaro, G., Foti, G., Mandaglio, G., Mandaglio, M., Sicilia, C.L., 2012. Estimate of sediment transport capacity in the basin of the Fiumara Annunziata (RC). *Rendiconti Online Società Geologica Italiana*, 21(1), pp. 696-697.

Barbaro, G., Foti, G., Nucera, A., Barillà, G.C., Canale, C., Puntorieri, P., Minniti, F., 2020. Risk mapping of coastal flooding areas. Case studies: Scilla and Monasterace (Italy). *International Journal of Safety and Security Engineering*, 10(1), pp. 59-67.

Barbaro, G., Foti, G., Sicilia, C.L., Malara, G., 2014. A formula for the calculation of the longshore sediment transport including spectral effects. *Journal of Coastal Research*, 30, pp. 961-966.

Barbaro, G., Miguez, M.G., De Sousa, M.M., Da Cruz Franco, A.B.R., De Magalhaes, P.M.C., Foti, G., Valadao, M.R., Occhiuto, I., 2021. Innovations in best practices: Approaches to

managing urban areas and reducing flood risk in Reggio Calabria (Italy). *Sustainability*, 13(6), article number 3463.

Barbaro, G., Petrucci, O., Canale, C., Foti, G., Mancuso, P., Puntorieri P., 2019b. Contemporaneity of floods and storms. A case study of Metropolitan Area of Reggio Calabria in Southern Italy. In: *Prooceedings of New Metropolitan Perspectives (NMP)* (Reggio Calabria, Italy), Smart Innovation, Systems and Technologies, 101, pp. 614-620.

Boak, E.H., Turner, I.L., 2005. Shoreline definition and detection: a review. *Journal of Coastal Research*, 21(4), pp. 688-703.

Bosworth, G.F., 1915. *Ships, Shipping and Fishing: with Some Account of Our Seaports and Their Industries*. University Press, Cambridge.

Canale, C., Barbaro, G., Petrucci, O., Fiamma, V., Foti, G., Barillà, G.C., Puntorieri, P., Minniti, F., Bruzzaniti, L., 2020. Analysis of floods and storms: concurrent conditions. *Italian Journal of Engineering, Geology and Environ.*, 1, pp. 23-29.

Canale, C., Barbaro, G., Foti, G., Petrucci, O., Besio, G., Barillà G.C., 2021. Bruzzano river mouth damage due to meteorological events. *International Journal of River Basin Management*.

D'Alessandro, F., Tomasicchio, G.R., Frega, F., Carbone, M., 2011. Design and management aspects of a coastal protection system. A case history in the South of Italy. *Journal of Coastal Research*, 64, pp. 492-495.

Fiori, E., Comellas, A., Molini, L., Rebora, N., Siccardi, F., Gochis, D.J., Tanelli, S., Parodi, A., 2014. Analysis and hindcast simulations of an extreme rainfall event in the Mediterranean area: The Genoa 2011 case. *Atmospheric Research*, 138, pp. 13-29.

Fortugno, D., Boix-Fayos, C., Bombino, G., Denisi, P., Quinonero Rubio, J.M., Tamburino, V., Zema, D.A., 2017. Adjustments in channel morphology due to land-use changes and check dam installation in mountain torrents of Calabria (southern Italy). *Earth Surface Processes and Landforms*, 42(14), pp. 2469-2483.

Foti, G., Barbaro, G., Bombino, G., Fiamma, V., Puntorieri, P., Minniti, F., Pezzimenti C., 2019. Shoreline changes near river mouth: case study of Sant'Agata River (Reggio Calabria, Italy). *European Journal of Remote Sensing*, 52(sup.4), pp. 102-112.

Foti, G., Barbaro, G., Manti, A., Foti, P., La Torre, A., Geria, P.F., Puntorieri P., Tramontana, N., 2020. A methodology to evaluate the effects of river sediment withdrawal: The case study of the Amendolea River in southern Italy. *Aquatic Ecosystem Health & Management*, 23(4), pp. 465-473.

Foti, G., Sicilia, C.L., 2013. Analysis, evaluation and innovative methodologies to prevent coastal erosion. *WIT Transactions on Ecology and the Environment*, 169, pp. 219-230.

Günaydın, K., Kabdaşlı, M.S., 2003. Characteristics of coastal erosion geometry under regular and irregular waves. *Ocean Engineering*, 30(13), pp. 1579-1593.

Komar, P.D., 2000. Coastal erosion–underlying factors and human impacts. *Shore & Beach*, 68(1), pp. 3-16.

Marchesiello, P., Nguyen, N.M., Gratiot, N., Loisel, H., Anthony, E.J., Dinh, C.S., Nguyen, T., Almar, R., Kestenare, E., 2019. Erosion of the coastal Mekong delta: Assessing natural against man induced processes. *Continental Shelf Research*, 181, pp. 72-89.

Mavromatidi, A., Briche, E., Claeys, C., 2018. Mapping and analyzing socio-environmental vulnerability to coastal hazards induced by climate change: an application to coastal Mediterranean cities in France. *Cities*, 72, pp. 189-200.

Miduri, M., Foti G., Puntorieri P., 2017. Impact generated by Marina of Badolato (Italy) on adjacent coast. In: *Proceeding of 13th International Congress on Coastal and Marine Sciences, Engineering, Management and Conservation MEDCOAST* (Mellieha, Malta), 2, pp. 935-945.

Moore, L.J., 2000. Shoreline mapping techniques: *Journal of Coastal Research*, 16, pp. 111-124.

Mori, N., Takemi, T., Tachikawa, Y., Tatano, H., Shimura, T., Tanaka, T., Fujimi, T., Osakada, Y., Webb, A., Nakakita, E., 2021. Recent nationwide climate change impact assessments of natural hazards in Japan and East Asia. *Weather and Climate Extremes*, 32, article number 100309.

Nguyen, Q.H., Takewaka, S., 2020. Land subsidence and its effects on coastal erosion in the Nam Dinh Coast (Vietnam). *Continental Shelf Research*, 207, article number 104227.

Prumm, M., Iglesias, G., 2016. Impacts of port development on estuarine morphodynamics: Ribadeo (Spain). *Ocean & Coastal management*, 130, pp. 58-72.

Sannino, G., Carillo, A., Pisacane, G., Naranjo, C., 2015. On the relevance of tidal forcing in modeling the Mediterranean thermohailine circulation. *Progress in Oceanography*, 134, pp. 304-329.

Sarma, K.G.S., 2015. Siltation and Coastal Erosion at Shoreline Harbours. *Procedia Engineering*, 116, pp. 12-19.

Scionti, F., Miguez, M.G., Barbaro, G., De Sousa, M.M., Foti, G., Canale, C., 2018. Integrated methodology for urban flood risk mitigation in Cittanova, Italy. *Journal of Water Resources, Planning and Management*, 144(10), article number 05018013.

Tomasicchio, G.R., Francone, A., Simmonds, D.J., D'Alessandro, F., Frega, F., 2020. Prediction of shoreline evolution. Reliability of a general model for the mixed beach case. *Journal of Marine Science and Engineering*, 8(5), 361.

Valderrama-Landeros, L., Flores-de-Santiago, F., 2019. Assessing coastal erosion and accretion trends along two contrasting subtropical rivers based on remote sensing data. *Ocean & Coastal Management*, 169, pp. 58-67.

van Rijn, L.C., 2011. Coastal erosion and control. *Ocean & Coastal Management*, 54(12), pp. 867-887.

Versaci, R., Minniti, F., Foti, G., Canale, C., Barillà, G.C., 2018. River anthropization, case studies in Reggio Calabria (Italy). *WIT Transactions on Ecology and the Environment*, 217, pp. 903-912.

Walling, D.E., 2006. Human impact on land–ocean sediment transfer by the world's rivers. *Geomorphology*, 79(3-4), pp. 192-216.

Wang, J., You, Z.J., Liang, B., 2020. Laboratory investigation of coastal beach erosion processes under storm waves of slowly varying height. *Marine Geology*, 430, article number 106321.

Williams, A.T., Rangel-Buitrago, N., Pranzini, E., Anfuso, G., 2017. The management of coastal erosion. *Ocean & Coastal Management*, 156, pp. 4-20.

Zema, D.A., Bombino, G., Boix-Fayos, C., Tamburino, V., Zimbone, S.M., Fortugno, D., 2014. Evaluation and modeling of scouring and sedimentation around check dams in a Mediterranean torrent in Calabria, Italy. *Journal of Soil and Water Conservation*, 69(4), pp. 316-329.

MARINE REMOTE SENSING FOR A SUSTAINABLE DEVELOPMENT

Maurizio Migliaccio *, Ferdinando Nunziata, Andrea Buono

Università degli Studi di Napoli Parthenope – Dipartimento di Ingegneria – Centro Direzionale isola C4 – 80143 Napoli, Italy
(name.surname)@uniparthenope.it

KEY WORDS: Sea, remote sensing, microwave, sustainability

ABSTRACT: The five oceans and the several seas along with their coastal areas form an integrated and essential component of the earth's ecosystem and are critical to sustainable development. They cover more than two-thirds of the earth's surface and contain 97% of the planet's water. Over three billion people depend on marine and coastal resources for their livelihoods. Further, marine ecosystem is crucial for global food security and human health. It is an ecosystem that represents the primary regulator of the global climate and a huge reservoir of biodiversity. However, human economic activities are growing and growing along with its threatening. Sustainable development is the idea that human societies must live and meet their needs without compromising the ability of future generations to meet their own needs. But this general objective was contrasted in real life activities. In fact, in the late 60's Hardin underlined that if individuals act independently, rationally and focused on pursuing their individual interests, they would end up going against the common interests of their communities and exhaust the planet's natural resources. By this time many advancements have been made on the theoretical economics, on the policies and on the definition of target indicators. In this keynote special focus is made on satellite microwave remote sensing to observe the marine ecosystem to assist a sustainable development of the human activities. Particular emphasis is paid to the United Nations (UN) Sustainable Development Goals (SDG).

1. INTRODUCTION

Oceans are the largest water areas over the Earth. There are five oceans, separated by the continents, with the Atlantic, Pacific, and Indian ocean linked in the southern emisphere by the Southern ocean. The Arctic ocean is in the upper north emisphere. Each ocean is characterized by a range of different temperature and salinity that is one of drivers of the ocean conveyor belt. In very simple terms the combination of thermohaline currents (thermo = temperature; haline = salinity) in the deep ocean and wind-driven currents on the surface generates a motion that rules the climate (Rahmstorf, 2006).
Related to such a fundamental process there is also the interest to monitor the polynya, a name adapted from the Russian, that means an area of open water surrounded by sea ice.

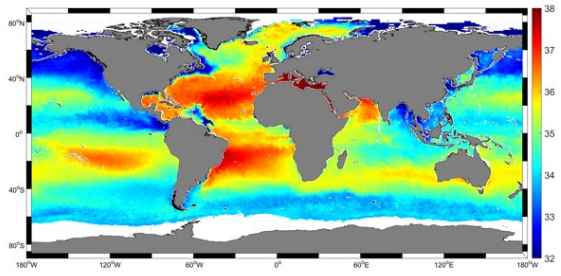

Fig.1: Sea salinity (ESA, 2019)

But oceans (and seas) are of paramount economical interest. The ocean economy is the sum of the economic activities of ocean-based industries, together with the assets, goods and services of marine ecosystems. They include a wide range of economic sectors, from the more conventional fisheries, aquaculture, maritime transport, tourism, but even emergent activities as renewable energy. It must be noted however that includes extractive industries, whose sustainability is prone to much debate. About 30% of global oil extraction takes place offshore. But even industrial fisheries are on the spot: according to the Food and Agriculture Organisation (FAO) of the UN, in 2017 seafood accounted for 7% of all protein consumed globally and for about 17% of total animal protein. The consumption and production of fish is expected to continue to increase.
In modern language it used the term "blue economy" where the impact of such economical activities on the environment should be also considered and possibly minimized.
As reported by official UN documents (WB & UN, 2017): "The "blue economy" concept seeks to promote economic growth, social inclusion, and the preservation or improvement of livelihoods while at the same time ensuring environmental sustainability of the oceans and coastal areas".
In economic terms the global contribution of the "ocean economy" is estimated to be about $3.6trn, 1 trillion is one million million, a year and worth more than 150 million jobs, according to the UN Development Programme.
The fundamental question is if such an economical and environmental goal is realistic: Is it possible to figure out a sustainable blue economy ?
The pillar to reply to such a question is represented by the paper on the subject of G.Hardin (Hardin, 1968). Hardin refers to an earlier study by the British economist William Forster Lloyd who used a hypothetical example of the effects of unregulated pasture on common land, thus the name commons in the Hardin paper. Of course, in the years the commons have been meant as any open-access and unregulated resource such as the oceans. Although the interested reader is referred to the paper of Hardin (Hardin, 1968) for all details it is worthwhile to point out some key elements.
The first point he underlines is that such a problem has no technical solution, i.e. a solution that only requires technical changes but not a change on the human values and or ideas of morality (Hardin, 1968). Another fundamental point underlined by Hardin is that a finite world can support only a finite population (Hardin, 1968). This apparent naïve concept leads to contrast the spirit of Adam Smith economy model (Smith, 1776). According to A. Smith an "invisible hand" makes that the single individual tends to assume decisions that will be the best decisions for the whole society.
Hardin contrast such an economic model and notes also that "the morality of an act is a function of the state of the system at the time is performed" (Hardin, 1968).

* Corresponding author

Abandoning commons to free riders will lead to ruin (Hardin, 1968). Accepting a limitation of our freedom is the only way to mitigate the tragedy of commons (Hardin, 1968).
In summary, it must be clearly stated that sustainability is not at all a technical problem but a problem that can tackled only by considering new values, values that are long-terms value instead of short-term values and that impact our moral vision.
Once that such values are shared the freedom limitation that is enforced can be monitored by satellite measurements. Within this framework this paper is to be meant.

2. MICROWAVE SATELLITE REMOTE SENSING

2.1 Passive sensor

The reference passive microwave sensor is the Microwave Radiometer. It is a sensor that measures the electromagnetic wave emitted by the sea surface at different frequencies and polarizations. The measurements are combined to generate added-valued of relevance for marine monitoring.
Just to mention few applications the hurricane monitoring must be considered. In fact, in the last 50 years, tropical cyclones have killed more than 779,000 people and caused $1.4 trillion in economic losses worldwide, according to the World Meteorological Organization (WMO). The 2020 Atlantic hurricane season had an unprecedented 30 named storms, marking the fifth year in a row with above-average hurricane activity.

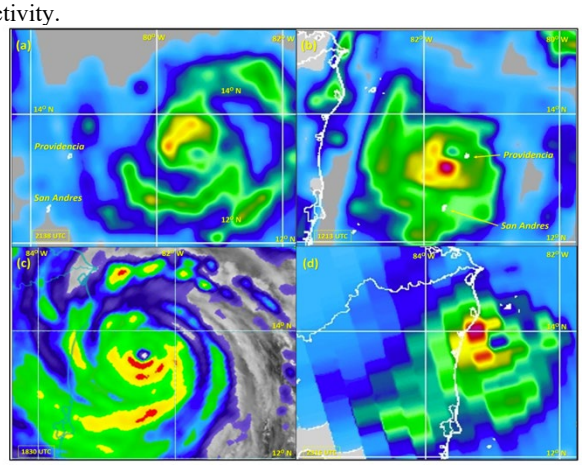

Fig.2: Passive microwave rain rate products of Hurricane Iota. Note the asymmetrical inner-core convection. (a) Nov, 15 2020 (b) Nov, 16 2020 (c) Nov, 16 2020 (d) Nov, 16 2020 (different hours) (Stewart, 2021).

The benefit of using large-scale sensor such as a microwave radiometer is evident by observing the acquired images and the added-value products. It is sensor that can provide a whole picture of an hurricane and therefore provide a set of key information to the institutions meant to mitigate casualties and damages. Operational services currently use such a type of measurements and added-value products.
At such a scale it is also possible to exploit the particular L-band sensitivity to sea surface salinity (SSS). Physical justification can be explained by the plot in Fig.3 (Kilic et al., 2021).
Although in real practice the idea that at L-band the emission is insensitive to sea surface wind speed (OWS) and sea surface temperature (SST) has been corrected, see for instance the NASA Aquarius mission design, it is true that the sea emission is mostly influenced by SSS at L-band (Kilic et al., 2021).

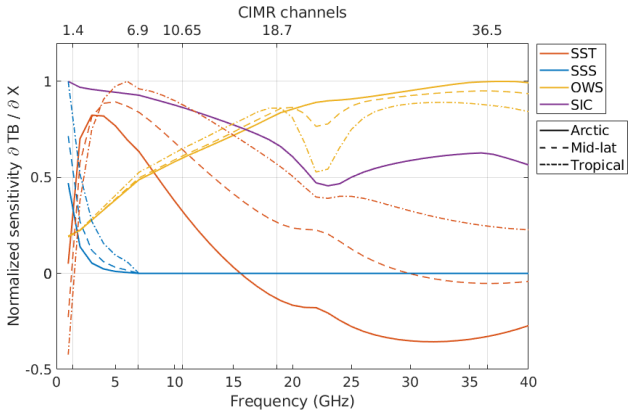

Fig.3: SSS vs frequency (Kilic et al, 2021)

Both applications can be framed under the UN SDG 13.

2.2 Active sensors

Active sensors are such that transmit and receive an electromagnetic pulse and according to the change into the structure of the scattered (received) electromagnetic field one can extract geophysical information.
Active sensors can be sorted into two main classes: large-scale and regional scale or small-scale. In the first class we have the scatterometer and the radar altimeter.
The scatterometer is a high radiometric resolution sensor that measures the backscattered electromagnetic field at variance of azimuthal direction. The special configuration of the radar scatterometer is such that by proper retrieval procedure it is possible to estimate the sea surface wind field, i.e. the wind speed and the wind direction. The scatterometer wind field estimate is at mesoscale.
Typical use of such scatterometer wind field is at the basis of meteorological forecast but sea surface wind field is also at the basis of offshore wind farms. In such a case, finer spatial resolutions are needed and use of Synthetic Aperture Radar (SAR) measurements is due. Typically, VV-polarization is used for sea surface wind estimation but for high wind regime HV-polarization is better tailored.
Innovative exploitation of the speckle, a geophysical “noise” occurring on the SAR image plane due to the coherent narrow-band nature of such sensor for wind speed estimation is under study (Migliaccio et al., 2019). This is just to say that although sea wind estimation appears to be and is for some aspects a mature and operational topic there are still new insights to be explored.
Mesoscale wind field estimation can be associated to radiometer measurements and therefore can be framed under the UN SDG 13 but fine scale wind estimation based on SAR measurements are logically associated to UN SDG 7 that is related to renewable energies. However, it must be underlined that offshore wind farms are not the only renewable energy sources although the most relevant for sure with respect to sea.
Another environment that if of great interest and that can be monitored by microwave satellite sensor is the one related to small islands and atolls in particular. For instance, the Maldives is a country made by 26 atolls covering an area of about 300 square kilometers but spread over 90,000 square kilometers ! the average sea level is 1.5 m above sea level, thus very critical in the event of tsunami o sea level rise. For such a country a tsunami alert system is very important as well as a system that monitor the coastline change due to persistent sea level rising.

With respect to tsunami monitoring use of radar altimeter is coupled with dedicated buoy system (Smith et al., 2005). The most advanced system is the US Tsunami Warning System.
Again, the radar altimeter is large-scale sensor so if one is interested to monitor with fine spatial resolution a smaller area the SAR is proper sensor.
Analysis of such islands requires to model the backscattering even on the land part, it is very interesting for example to monitor very highly vegetated islands and their coastlines (Sarti et al., 2017 & Ferrentino et al., 2017).
Coastline estimation by SAR measurements can be improved once polarimetric SAR measurements are at disposal. An interesting study was conducted taking benefit of the peculiar polarimetric SAR Cosmo-SkyMed mode known as Ping-Pong (Migliaccio et al., 2014). The two polarimetric channels that are measured are the VV and HH channels and in such a mode the two polarimetric acquisition are made at a time interval that is sensitive to sea changes. Since at low-to-moderate wind regimes the VV and HH returns are highly correlated it is possible to design a physically based filter that discriminate among different scattering scenarios (Migliaccio et al., 2014).
The studies related to small islands can be framed primarly under the UN SDG 14 but also under the UN SDG 13.
Polarimetric methodologies can be also exploited to monitor man-made structure at sea and oil spills. An ESA Sentinel-1 SAR image relevant to the Ever Given container ship blocking the Suez channel in March 2021 is shown in Fig.4.

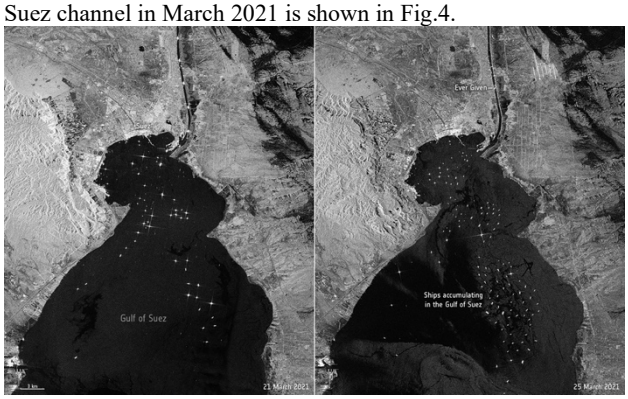

Fig.4: ESA Sentinel-1 SAR images acquired on March 2021. On the left it is shown the area on March, 21 2021 (before the accident) and on the right it is shown the area on March 25, 2021 (after the accident and when the Suez channels was blocked). ESA Courtesy.

Only apparently SAR ship detection is an easy task. In fact, it is challenging because of the limited revisit time of a single SAR satellite but also because not all ships have a strong backscattering return because of their material or their size.
On a similar but different ground one can consider the oil and gas platform SAR monitoring as well as the offshore farm turbines SAR monitoring.
In Fig.5 it is shown a SAR image of a large offshore wind farm off the coast of the United Kingdom in the North Sea (ESA, 2010). In particular, the Thanet Offshore Wind Farm is imaged in such a SAR image. The ENVISAT ASAR image was acquired Sept., 14 2010 few days before the operational start.
While apparently the case shown in Fig.5 seems identical to the one shown in Fig.4 this is untrue (Ferrentino et al, 2019). The polarimetric scattering analysis described and discussed in (Ferrentino et al, 2019) demonstrates that operating wind turbines have a polarimetric scattering that is peculiar.
With reference to the offshore wind farms monitoring it is also appropriate to show the plot of Fig.6 that demonstrates the growing and growing interest in such renewable source of energy.

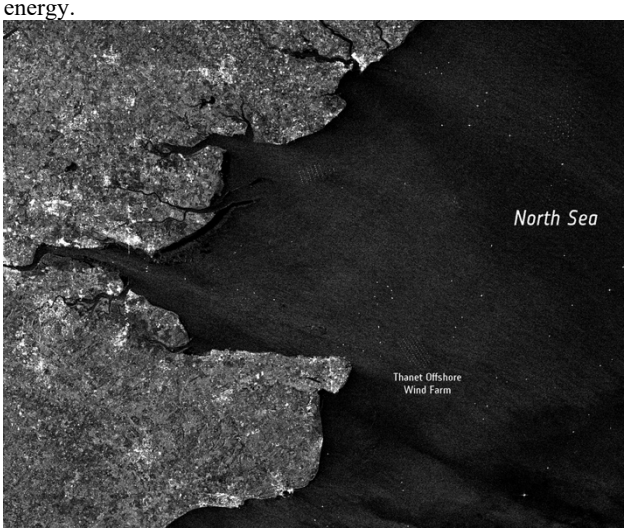

Fig.5: ESA ENVISAT ASAR image of an offshore wind farm (ESA, 2010). ESA Courtesy.

A finer analysis shows that China, Germany and UK are the countries more involved.

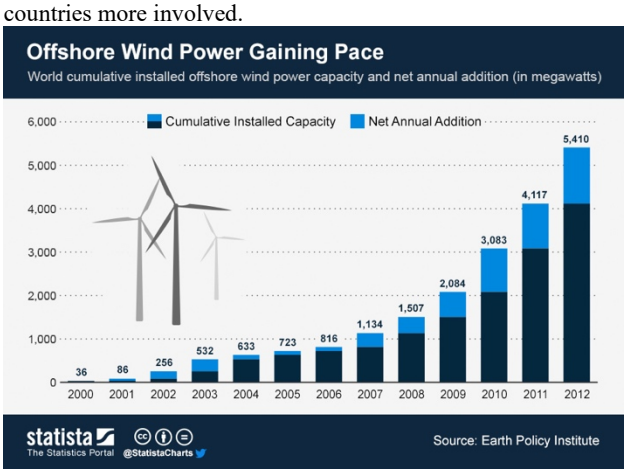

Fig.6: Relevant to the growing interest into offshore wind farms.

Another interesting class of man-made structures at sea is made by aquacultures. In fact, the FAO statistic tells that world aquaculture has been growing to more than 100 million of tonnes (from 0) in years ranging from 1960 to 2015. In this case China dominates the global aquaculture (1/3 of the total produced live weight). It was recently estimated that aquaculture provides 43% of all the fish consumed by humans today. This industry is not without controversies since the highly densely populated farms are the large use of chemicals and drugs to control viral, bacterial, fungal or other pathogens. In simple terms most of the aquaculture production is of some concern for human health.
Aquaculture can be observed by SAR and polarimetric SAR (Profeti, 2010 & Ballester-Berman, 2018).
Aquaculture falls into the general problem of fishing. In fact, industrial fishing generates overexploitation. If the amount of wild fish we catch exceeds the rate at which fish can reproduce and replenish, populations will decline over time. Such populations we would call ‘overexploited’. In Fig.7 it is shown that most of the decline in sustainable fish populations occurred through the 1970s and 1980s. Over the past few decades there has

been a marked slowdown of overexploitation. This is in part owed to the fact that increased demand has instead been met by aquaculture (fish farming) rather than wild catch.

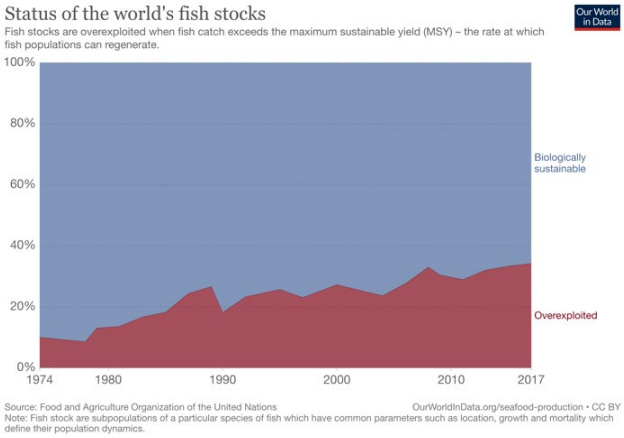

Fig.7: On the status of the world's fish stocks.

Independent observation of oil slick at sea is another relevant environmental issue. Oil at sea is very harmful to many fish species including corals. Three main classes of oil slicks can be considered, micro oil slick, macro oil slick and gigantic oil slick (Migliaccio et al., 2015). The first class is generally associated to deliberate and illegal oil discharge by ships, the second class is usually connected to oil-tank accidents and the third one can be connected to oil platform accident such as the BP accident in Gulf of Mexico in 2010 (Migliaccio et al., 2015). The most tailored satellite remote sensing sensor to observe oil slick at sea is the SAR but most of the operational procedures are tailored to the macro oil slicks. As a consequence, most of the open available statistics undervalue the overall oil spill pollution. The interested reader can find all details of new physically based procedures to observe oil slicks at sea in (Migliaccio et al., 2015) but hereafter a single polarimetric SAR image is shown in Fig.8.

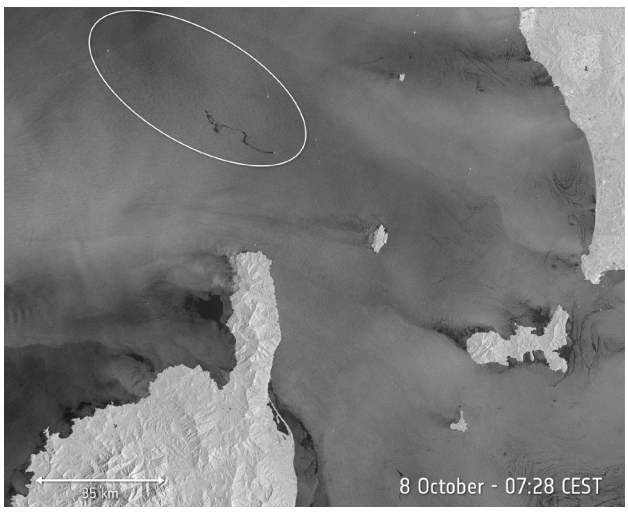

Fig.8: ESA Sentinel-1 SAR image of an oil slick in the Mediterranean Sea, north of Corsica. The spill was about 20 km to 35 km long. The image was acquired on oct., 2018. ESA Courtesy.

The benefit of using polarimetric Sar is that the peculiar sea low-to-moderate Bragg scattering does not apply to heavy damping oil spill and therefore the multi steps classical single polarimetric procedure that must be assisted by human personnel can be fully automated.

All referred monitoring activities fall into the UN SDGs and especially the SDG 14.

3. CONCLUSIONS

A critical discussion about the sea sustainability concept and practice has been reviewed to emphasize that it has no pure technical solution (Hardin, 1968). Once that a new scale of value has been agreed satellite microwave remote sensing can be exploited to enforce the necessary quality norms.

REFERENCES

ESA, 2010, website: http://www.esa.int/Applications/Observing_the_Earth/Earth_from_Space_Giant_wind_farm_opens

ESA, 2019, website: http://www.esa.int/Applications/Observing_the_Earth/Space_for_our_climate/Mapping_salty_waters

Ballester-Berman J.D., Sanchez-Jerez P., and Marino A., "Detection of aquaculture structures using Sentinel-1 data" in Proceeding of EUSAR 2018.

Ferrentino E., Nunziata F. and Migliaccio M., 2017, "Full-polarimetric SAR Measurements for Coastline Extraction and Coastal Area Classification", *International Journal of Remote Sensing*, 38(23), pp.7405-7421.

Ferrentino E., Nunziata F., Marino A., Migliaccio M. and Li X., 2019, "Detection of Wind Turbines in Intertidal Areas Using SAR Polarimetry", *IEEE Geoscience and Remote Sensing Letters*, 16(10), pp.1516-1520.

Hardin, G, 1968, "The Tragedy of Commons", *Science*, 162(12), pp.1243-1248.

Kilic L, Prigent C., Jimenez C., and Donlon C., 2021, "Technical note: A sensitivity analysis from 1 to 40 GHz for observing the Arctic Ocean with the Copernicus Imaging Microwave Radiometer", *Ocean Science,* 17, pp.455–461.

Migliaccio M., Huang L., and Buono A., 2019, "SAR Speckle Dependence on Ocean Surface Wind Field", *IEEE Transactions on Geoscience and Remote Sensing*, 57(8), pp.5447-5455.

Migliaccio M., Nunziata F., and Buono A., 2015, "SAR Polarimetry for Sea Oil Slick Observation," *International Journal of Remote Sensing*, 36(12), pp.3243-3273.

Migliaccio M., Mascolo L., Nunziata F., Sarti M., and Mazzarella G., 2014, "COSMO-SkyMed HH/VV PingPong Mode SAR Data to Discriminate among Sea, Urban and Vegetated Areas", *IEEE Journal of Selected Topics in Applied Earth Observations and Remote Sensing*, 7(7), pp.2880-2894.

Profeti G. and Travaglia C, 2010, "Monitoring Aquaculture Structures by SAR Imagery", *Geospatial World*, pp.1.

Rahmstorf, S., 2006, "Thermohaline Ocean Circulation" in: *Encyclopedia of Quaternary Sciences*, Edited by S. A. Elias. Elsevier, Amsterdam.

Sarti M., Migliaccio M., Nunziata, F. Mascolo L., and Brugnoli E., 2017, "On the Sensitivity of Polarimetric SAR Measurements

to Vegetation Cover: the Coiba National Park, Panama", *International Journal of Remote Sensing*, 38(23), pp.6755-6768.
Smith, A, 1776, *An Inquiry into the Nature and Causes of the Wealth of Nations*, Strahan and Cadell, London.

Smith, W.H.F., Scharroo R., Titov V.V., Arcas D., and Arbic A.K., 2005, "Satellite Altimeters Measure Tsunami", *Oceanography*, 18(2), pp.11-13.

Stewart, S.R., 2021: Hurricane Iota, National Hurricane Center – Tropical Cyclone Report.

World Bank and United Nations Department of Economic and Social Affairs, 2017. *The Potential of the Blue Economy: Increasing Long-term Benefits of the Sustainable Use of Marine Resources for Small Island Developing States and Coastal Least Developed Countries*, World Bank, Washington DC.

ANALYSIS OF THE VERTICAL MOVEMENT OF ACTIVE GNSS STATIONS AS A RESULT OF SEMIDIURNAL TIDES

Rose Pearson, Eugen Niculae,

Technological University Dublin, Bolton Street, Dublin 1, Ireland
rosepearson14@hotmail.com/ C17330076@mytudublin.ie ; eugen.niculae@TUDublin.ie

KEYWORDS: Precise Point Positioning, Vertical Land Motion, Semidiurnal Tides, Static GNSS, Time-series Analysis

ABSTRACT

Ireland is subject to the constant effects and influence of semidiurnal tides. Western coastal regions are exposed to tidal ranges up to and exceeding five metres, consequentially introducing varied water volumes with temporal intervals. In addition, the Earth is elastic in composition, resulting in morphing and warping at the hands of celestial and oceanic forces.

This study looked at Online Precise Point Positioning (PPP) service to accurately monitor the vertical movement of coastal lands. In addition, GNSS Static Post-processing was conducted to discern which method of the global navigation satellite system (GNSS) processing is best for detecting VLM (vertical land motion). The study took place throughout 2020, focusing on the tidal peaks and troughs of the 21st of each month. Six-hour time windows were created around tidal peaks and troughs using data from the Marine Institute. GNSS data files replicating these time windows were processed using both PPP and manual network adjustment methods. MATLAB Online analysis aided in concluding the study.

Results were inconclusive in determining which method of GNSS processing were best for identifying VLM. Based on the evidence provided by this study, the influence of semidiurnal tidal peaks and troughs cannot be deemed significant in magnitude to require mitigation. Western Irish coastal zones are therefore not subjected to large scale VLM. Similar studies of coastal zones that experience tidal ranges exceeding five metres would be recommended. An extended study period would also be recommended to better understand semidiurnal tidal influences in Ireland.

1. INTRODUCTION

This project looked at the Earth dynamics effects on heights of coastal active GNSS stations as a consequence of semidiurnal tides. The authors aimed to:

- Determine whether semidiurnal tides have an influence over coastal vertical positions.
- Determine the magnitude of the semidiurnal tidal influences.
- Determine whether trends are present in semidiurnal tidal influences with respect to tidal maximum and minimum levels or periods of the year.

2. METHODOLOGY AND DATA PROCESSING

2.1 Tide Gauge Location and Data Acquisition

Tidal predictions were utilised for this study due to the availability of the data. Tidal predictions are approximated values to the water level, derived "from harmonic analysis of data measured at the tide gauges around the Irish coast" (Marine Institute, 2020), which form the Irish National Tide Gauge Network. Tidal predictions are available for download from the Marine Institute website (http://www.marine.ie/Home/site-area/data-services/marine-forecasts/tidal-predictions link accessed 20 October 2020).

Fenit tide gauge was selected to provide coverage over the susceptible southwest of Ireland (Quine, 2015). In addition, Sligo tide gauge and Galway Port tide gauge were added to the study to facilitate site dispersion and full western coverage.

* Corresponding author

2.2 Active GNSS Station Location and Data Acquisition

Active GNSS stations, part of the Irish Network of Continuously Operating Reference Stations (CORS), were utilised to monitor the vertical displacement resulting from semidiurnal tidal due to such data's inherent accuracy and reputation. Brown and Ogundare (2020) similarly used permanent GNSS stations to analyse the effects of Post Glacial Rebound (PGR), further affirming this data acquisition method.

Ordinance Survey Ireland (OSI), Ireland's national mapping agency, is responsible for maintaining a network of real-time kinematic GNSS stations. This network consists of a number of CORS stations that actively receive multi constellational GNSS transmissions. CORS stations facilitate the "collection of high precision positional data" (Quine, 2015), which is freely available for download to the public (https://www.osi.ie/services/geodetic-services/active-gnss-data/ link accessed 5 October 2020). In addition, the whole 24-hour period of the 21st day was downloaded in RINEX (Receiver Independent Exchange Format) to ensure tidal data correlation.

To correspond with the tide gauges selected above, Sligo (SLGO), Galway (GLW1) and Tralee (TRL2) CORS stations were selected for study (Figure 1). In addition, Portlaoise (PRT2) was also selected under the assumption this midland location would be unaffected by tidal influences. Therefore, PRT2 would act as the control station for the network adjustment.

2.3 Tide Gauge - CORS Relationship

Tide gauges and CORS stations are not coincident in this study. The tide gauges are located directly on the coast, while active GNSS receivers are installed inland on prominent buildings in the vicinity.

No tidal delay coefficient was applied as distances between tide gauges, and GNSS stations were less than 15 kilometres (Table 1).

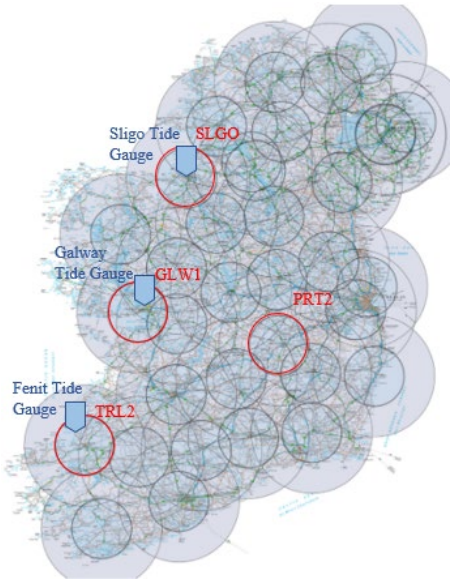

Figure 1. OSI CORS Network with stations and tide gauges (OSI, n.d. with author edits)

CORS Station	Tide Gauge	Distance (km)
Sligo (SLGO)	Sligo	8.70
Galway (GLW1)	Galway Port	1.55
Tralee (TRL2)	Fenit	13.12

Table 1. Straight-line distance between CORS stations and tide gauge

2.4 Selection of Study Day

For consistency of data collection, the 21st of each month was chosen. As tidal influence was the main concern, collecting data during a period of celestial prominence was imperative. Upon analysis of moon phases (https://www.timeanddate.com/moon/phases/@3230615?year=2020 link accessed 18 March 2021) for Sligo, Galway and Tralee – a substantial range of dates for the occurrence of New Moon and Full Moons were noted. Full moon occurrences fell within the range of the 1st to the 30th. The New moon had a shorter span of the 14th to the 24th day of the month. Thus, the 21st provided a tidal average.

2.5 Pre-Processing

Tidal data was segmented into six-hour windows, corresponding to 3 hours on either side of the tidal peak and trough on the 21st. If this occurrence took place within the first thirty minutes of the hour, the hour itself was taken. Any time after this was considered to be the following hour.

WinTEQC Editor desktop application provided the software solution behind time windowing GNSS data to create a single RINEX file containing six-hours of GNSS data for submission with the Canadian Spatial Reference System-Precise Point Positioning Service (CSRS-PPP).

This process was conducted for SLGO, GLW1 and TRL2 CORS stations for tidal peaks and troughs, ending with a total of 72 RINEX files.

2.6 PPP GNSS Processing and Post-Processing

CSRS-PPP online service was used for GNSS data. Users can immediately access the free, reliable services (Alkan et al., 2020) of the CSRS-PPP online service following email registration with Natural Resources Canada (NRCan). Compressed folders of results were returned via email within twenty-four hours of submittal. As GNSS data was obtained from a CORS station, 'Static' mode was selected for processing. Through selecting static, "one corrected averaged single point" (NRCan, 2020 B) was computed for each submitted RINEX file. The option of inserting an ocean tide loading file was withheld to prevent the effects of semidiurnal tides being dampened or cancelled out.

The International Terrestrial Reference Frame (ITRF) was selected as the data output spatial reference system. ITRF could be considered the "official scientific global spatial reference frame", according to Natural Resources Canada (2020 B). The version of ITRF utilised by CSRS-PPP has been "realised by the International GNSS Service (IGS) at the epoch for which the precise GNSS orbit ephemerides were computed" (NRCan, 2020 B). Through opting for ITRF, coordinates could be easily converted into the national spatial reference system of Ireland.

Single point averaged figures were sourced within the compressed files and stated in ITRF. ITRF ellipsoidal heights were transformed to ITM using the Grid InQuest II desktop application. The application provides seamless three-dimensional coordinate transformations between global and national coordinate systems across Great Britain and Ireland (OSI, 2018). Only vertical components were of interest to this study. ITRF input values were extracted from CSRS-PPP summary reports, compiled into Comma-Separated Value (.csv) file formats and transformed into Irish Transverse Mercator with an accuracy of 0.4m (95% data) (Grid InQuest II, n.d.).

2.7 Static GNSS Network Adjustment

A network adjustment within Trimble Business Centre (TBC) was carried out to compute adjusted GNSS elevations tied to a fixed static point. Processed vectors are run through a least-squares adjustment to estimate and proportionally distribute any random errors present within the data, thus minimising their effects, to deliver a single adjusted solution. The network adjustment was computed iteratively on an automatic basis. A fixed point (PRT2), constrained in both two dimensions and elevation, is used to shift all other coordinates around by assigning control quality.

Raw RINEX files (time windowed as in 2.5) for GLW1, SLGO and TRL2 were imported, in addition to twenty-four hours of data gathered from PRT2. GNSS high tide and low tide data were imported separately to prevent the merging of results and consequential loss of tidal relevance.

The International GNSS Service (IGS) produce a number of orbit combination solutions, namely; ultra-rapid, rapid and final (IGS, n.d). Final orbit products corresponding to the day in question were imported into processing software. By employing final orbit products, the precision level of final GNSS coordinates could be significantly improved to an accuracy of ~75 ps Root Mean Square and ~20 ps Standard Deviation (IGS, 2020). Héroux & Kouba (2001) accredit the accuracy of IGS final orbits to the

process by which they are captured, whereby IGS Analysis Centres (ACs) feed into the combined IGS product.
The GNSS network was adjusted using processed baselines from above. PRT2 was held to create a constrained network, allowing SLGO, GLW1 and TRL2 to shift relative to a fixed position. Network adjustment reports were reviewed. In some instances, scalars were applied to achieve the best fit. Adjusted grid coordinates were extracted from adjustment reports and compiled into an Excel spreadsheet. PPP processed results were added to facilitate direct monthly comparisons between the data. The Elevation value supplied by the OSI for Active Network Stations was appended to provide a standardised value

Average monthly GNSS elevations were obtained via PPP (2.6) and TBC network adjustments (2.7), as above. Excel charts provided the means for analysis. Deviations between PPP and TBC values were analysed.

2.8 MATLAB Online

Data analysis was carried out using MATLAB. MATLAB Online facilitates data investigation and analysis through an online platform, accessible through any web browser (Mathworks, n,d.).

A regression learner application was employed to identify models that best predict GNSS heights due to high and low tide occurrences over twelve months. The Regression Learner application enables users to "interactively train, validate, and tune regression models" (Mathworks, n.d. B). Thus, this application is ideal when the data type and subsequently the model type is unknown i.e., data does not clearly fit as linear, non-linear etc and machine learning is required.

The application cycles through all possible models and trains each model to the data points supplied within the working dataset. An analysis of the root mean square error (RMSE), the model that forms the best predictor is easily identified. This exhaustive method of regression model training ensures the best predictor of the dataset was identified.

Curve fitting was conducted to identify any seasonal trends within the data, analysing high and low tides separately.
Research efforts of Brown & Ogundare (2020), were considered during the curve fitting of GNSS data influenced by the effects of tidal maximums and minimums in Ireland. Brown & Ogundare (2020) determined the effects of PGR on GNSS station "behaved like a sine wave" (Brown & Ogundare, 2020). This pattern was attributed to seasonal variation, reflected by the wavelength approximating to the length of a year.

On account of this finding, a sine wave was trialled to ascertain whether GNSS data influenced by the tide would conform to a sine wave. It was assumed GNSS stations in proximity to the coast would respond similarly to the effects of PGR through presenting movement along the vertical axis. PGR incurs rates of uplift dependent on the mass of displaced glacier. Semidiurnal tides incur pressure maximums and minimums along coastal regions due to varied water volumes. Tidal influenced uplift could therefore be expected to be cyclically represented.

Fourier model was also applied. A Fourier series contains terms of cosine and sine; thus, the possibility of a better fit was likely. R-Squared (coefficient of determination) and RMSE were compared to identify the model of best fit. See Figure 2 for the best Fourier fit achieved across datasets.

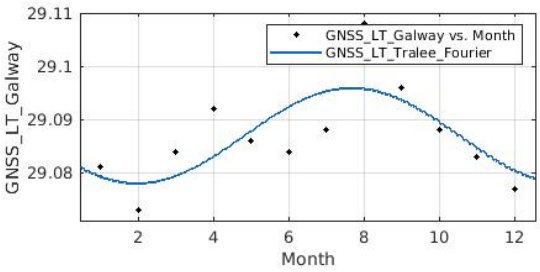

Figure 2. Galway GNSS Low Tide Fourier Plot

Autocorrelation Function (ACF) was applied using the '*autocorr(y)'* command. This plots the "sample autocorrelation function of the univariate, stochastic time series y with confidence bounds" (Mathworks, n.d C). 'y' corresponds to the GNSS elevation observed during high or low tide. The plots generated graphically represent the relationship between observations in a time series with observations taken at prior moments in time (Machine Learning Mastery, 2020).

Partial Autocorrelation Function (PACF) was conducted using the command' *parcorr(y)'*. PACF seeks to determine the correlation between an observation and its lag. This is at variance to the ACF, whereby a relationship between an observation and any other previously observed observation - both direct and indirect dependence is possible (Machine Learning Mastery, 2020).

The '*fitmethis'* command was used to create an interactive and numerical method of determining the best distribution fit to the GNSS elevation data. *Fitmethis* seeks out the "best-fitting distribution to data vector" and permits the selection of continuous or discrete distributions (Mathworks, n.d D). Results were analysed based on their Akaike Information Criterion (AIC). The AIC provides a method for model selection. When comparing the AIC values generated for models, Akaike's theory states that the most accurate model will have the lowest AIC (Mathworks, n.d E). Thus, the AIC determines the quality of models representing the data relative to each other. This makes the AIC an essential factor in optimal model selection.

3. CONCLUSIONS

No model exists to predict GNSS height to an acceptable standard through analysing the Regression Learner data. This has been proved through training all regression models available to the user in the MATLAB suite and analysing the results of the best predictor. The best models have been found to poorly represent GNSS elevations and cannot be used as a predictor for future values. The best level of fit achieved was in Galway at low tide with an R-Squared of 0.40. This indicates a fit of less than 50%, thus deeming it weak. Visual analysis of the Response, Observed versus Predicted, and Residual plots reinforced this. The use of the Regression Learner proved that GNSS elevations for a year might only be poorly predicted using regression models.

The sum of the sine model was trialled on the data to surmise how well it fitted to the GNSS tidal influenced data instead of PGR incurred motion. Relatively low R-Square and adjusted R-Square values manifested from the sine model on the research data. The Fourier model provided higher R-Square and adjusted R-Square values, indicating a better fit. Out of all curve fitting options available to the user in MATLAB Online, the Fourier

series best represented the plot of data points for each location and tidal period. It must be noted that a twelve-month period of data was all that was available for analysis. Therefore, determining a trend within the data was not possible. Curve fitting with a more extended period of time would assist in identifying the possibility of seasonality within the data.

The following table summarises the presence or absence of both autocorrelation and partial autocorrelation. Combinational lags of ACF do not influence successive month's GNSS elevation values. Partial autocorrelation has been noted in the majority of plots, except for Tralee at high tide. Specific individual lags, therefore, have an influence over successive months. Consistent peaks at position six across most graphs are of interest. Overall, it is difficult to confidently say the significance of the identified partial autocorrelation over GNSS monthly elevations as no consistency is evident within twelve-month periods.

Occurrence	Autocorrelation	Partial Autocorrelation
Galway High Tide	No	Yes
Sligo High Tide	No	Yes
Tralee High Tide	No	No
Galway Low Tide	No	Yes
Sligo Low Tide	No	Yes
Tralee Low Tide	No	Yes

Table 2. Summary of Autocorrelation and Partial Autocorrelation Plots

No significant conclusion can be drawn from the data values to confidently state whether PPP or TBC is the more reliable method of processing. PPP values tended to follow a higher rate of consistency in terms of deviation from the published value. Deviations of TBC from published values tended to fluctuate at a higher rate. With this said, TBC values agreed with published values very satisfactorily in Sligo. This fit is seemingly unknown as the distance between Sligo's tide gauge; and consequently, the coast; lies 8.7km from the active station. On a proximity basis, it would be expected that Galway would demonstrate the largest trends as distance here is only 1.55km.

The VLM hypothesis based on the relationship between coastal water volumes and varying pressures on the land remains unknown. Tabulated below is a summary of derivation behaviours. Derived values equalling to those published are classed as a disagreement to the hypothesis as a clear increase/decrease in elevation as a result of water volume cannot be identified.

Occurrence	PPP Hypothesis Status	TBC Hypothesis Status
Galway High Tide	Agree	Agree
Sligo High Tide	Disagree	Disagree
Tralee High Tide	Agree	Agree
Galway Low Tide	Disagree	Disagree
Sligo Low Tide	Agree	Disagree
Tralee Low Tide	Disagree	Disagree

Table 3. Vertical Land Motion Hypothesis

No conclusive evidence is present to determine which processing method provides the best results as deviations are evident between both datasets. Neither method drastically disagrees with published values. Consistency is the only factor which can be drawn in to make a conclusion.

As a result of running the *'fitmethis'* command, the optimal distribution type could be identified. The AIC value was enlisted to identify the best distribution type. In each case, this was the Uniform distribution model. A goodness of fit script aided in assessing the quality of this fit. Values of *'h'* and *'p'* enabled the assessment of the hypothesis status. Therefore, the null hypothesis (H_0) can be accepted meaning that the data is uniformly distributed for each location and tidal occurrence.

Similar to GNSS satellites, remote sensing technologies can be employed to monitor Earth movement, as well as the more commonly used physical analysis of the Earth surface. Remote sensing relies on the return signal of emitted and reflected radiation to discern characteristics of the Earth's surface (USGS, n.d.). This technology could be enlisted to identify periods of high and low tide at coastal areas. Spring and Neap tides could be identified through analysis of remotely sensed imagery, thus providing a visual validation of the strongest tidal occurrences.

Further to this, SqueeSAR and PSinSAR are additional remote sensing technologies which quantify ground displacement (OpenEI, 2013). Both are restricted by satellite footprint and period to revisit. Conditions allowing, such methods could be applied for detection of land movement due to semidiurnal tides.

With respect to predefined study aims:

- Semidiurnal tides have an influence over coastal vertical positions identified through deviation from the OSI published height value.
- A definitive magnitude of semidiurnal tidal influences could not be drawn due to disparities between PPP and network adjusted results.
- Trends adhering to a Fourier model best represent semidiurnal tidal influences with respect to tidal maximum and minimum levels along the west coast.

Conclusions drawn above could be substantially improved upon with a larger data range.

REFERENCES

Alkan, R. M., Erol, S., Ozulu, I. M., & Ilci, V. (2020). *Accuracy comparison of post-processed PPP and real-time absolute positioning techniques*. Geomatics, Natural Hazards and Risk, 11(1),178–190. https://doi.org/10.1080/19475705.2020.1714752 [accessed 16 December 2020].

Brown, W. & Ogundare, J. (2020) Time Series Analysis of Vertical Positions of High-Precision GNSS Stations in Eastern Canada: A Case Study. , p.15. [accessed 16 October 2020].

OSI. (2018). *Grid InQuest II: Coordinate Transformation Service for Great Britain and Ireland Version 1.01* [online]. Available from: https://www.osi.ie/services/geodetic-services/download-co-ordinate-converter/ [accessed 21 July 2021].

Héroux, P., & Kouba, J. (2001). *GPS precise point positioning using IGS orbit products*. Physics and Chemistry of the Earth, Part A: Solid Earth and Geodesy, 26(6–8), 573–578. https://doi.org/10.1016/S1464-1895(01)00103-X [accessed 3 March 2021].

IGS. (2020). *Products.* Available from: https://www.igs.org/products/#about [accessed 19 July 2021].

Machine Learning Mastery. (2020). *A Gentle Introduction to Autocorrelation and Partial Autocorrelation* [online]. Available from: https://machinelearningmastery.com/gentle-introduction-autocorrelation-partial-autocorrelation/ [accessed 2 March 2021].

Marine Institute. (2020). Tidal Predictions. Available from: http://www.marine.ie/Home/site-area/data-services/marine-forecasts/tidal-predictions [accessed 29 January 2021].

Mathworks. (n.d.). *What is MATLAB Online?* [online]. Available from: https://www.mathworks.com/help/matlab/matlab_env/what-is-matlab-online.html [accessed 18 February 2021].

Mathworks. (n.d. B). *Regression Learner App* [online]. Available from: https://www.mathworks.com/help/stats/regression-learner-app.html [accessed 17 February 2021].

Mathworks. (n.d. C). *autocorr* [online]. Available from: https://www.mathworks.com/help/econ/autocorr.html#d122e127414 [accessed 2 March 2021].

Mathworks. (n.d. D). *fitmethis* [online]. Available from: https://www.mathworks.com/matlabcentral/fileexchange/40167-fitmethis [accessed 16 March 2021].

Mathworks. (n.d. E). *aic* [online]. Available from: https://www.mathworks.com/help/ident/ref/idgrey.aic.html [accessed 19 March 2021].

My Trimble Protected. (2008). *User Guide Trimble Business Center: Version 2.00* [online]. Available from: https://mytrimbleprotected.com/knowledge/docushare/retrieve?handle=File-503698 [accessed 25 January 2021].

NRCan. (2019). *Height Reference System Modernization* [online]. Available from: https://www.nrcan.gc.ca/maps-tools-publications/maps/height-reference-system-modernization/9054 [accessed 4 February 2021].

NRCan. (2020 B). *Geodetic Tools and Applications* [online]. Available from: https://www.nrcan.gc.ca/maps-tools-publications/maps/tools-applications/10925#ppp [accessed 13 February 2021].

OpenEI. (2013). *Exploration Technique: SqueeSAR* [online]. Available from: https://openei.org/wiki/SqueeSAR [accessed 22 July 2021].

OSI. (n.d.). Active GNSS Network [image online]. Available from: https://www.osi.ie/wp-content/uploads/2016/05/Ireland_GPS_Radius_05-2016_A0_smaller_1.jpg [accessed 7 January 2021].

OSI. (2018). *Grid InQuest II: Coordinate Transformation Service for Great Britain and Ireland Version 1.01* [online]. Available from: https://www.osi.ie/services/geodetic-services/download-co-ordinate-converter/ [accessed 19 January 2021].

Quine, P. (2015) An Analysis of Ocean Tide Loading and Modelling Techniques for GNSS Precise Point Positioning in Britain & Ireland. , p.131. [accessed 25 October 2020].

USGS. (n.d.). *What is Remote Sensing and what is it used for?* [online]. Available from: https://www.usgs.gov/faqs/what-remote-sensing-and-what-it-used?qt-news_science_products=0#qt-news_science_products [accessed 22 July 2

COASTAL FLOODING: CASE STUDIES IN CALABRIA (ITALY)

G. Barbaro, G. Bombino, G. Foti, G.C. Barillà, G. Mauro*, P. Puntorieri, M. Mandalari

Mediterranea University of Reggio Calabria, DICEAM Department, località Feo di Vito, 89122 Reggio Calabria Italy
giuseppe.barbaro@unirc.it; giuseppe.bombino@unirc.it; giandomenico.foti@unirc.it; chiara.barilla@unirc.it;
giuseppe.mauro@unirc.it; pierfabrizio.puntorieri@unirc.it; mariamandalari.mm@gmail.com

KEY WORDS: Coastal flooding, sea storms, wave climate, shoreline changes, flood risk mapping, QGIS.

ABSTRACT:

Coastal flooding is a hazard to people who live near coasts. It is therefore necessary to increase knowledge of the causes of coastal flooding through scientific research. Furthermore, the correct assessment of flooding areas is very important for the management of coastal areas. Given this, the current European legislation (Directive 2007/60/EC) requires flood areas to be mapped, but to date in Italy each region is still adopting different procedures to reach the goal.
The paper describes two case studies of coastal flooding occurred in November 2019 in Saline Joniche and in December 2019 in Favazzina, two towns located in southern Ionian and Tyrrhenian Calabria, respectively. These storms have caused severe erosions, also damaging and flooding houses and roads close to the beach.
The methodology used is divided into three phases, one concerning the analysis of the wave climate and of the storms, one concerning the analysis of the shoreline changes and the last concerning the flood risk mapping. In detail, the data from the last 40 years present in the MeteOcean database are used to evaluate the wave climate and the storm characteristics (such as height, duration, return period etc.). The analysis of the shoreline changes is carried out on QGIS using open data from Calabrian and Italian Geoportal and from Google Earth. Finally, QGIS is also used to draw flood risk maps.

1. INTRODUCTION

Coastal flooding is a very topical issue, due to climate change (Lemee et al., 2020) and the significant increase in anthropogenic pressure observed in the second half of the last century (Barragan and De Andres, 2015).
Climate change is causing an increase in the frequency and intensity of various natural phenomena such as floods, sea storms, etc. (Fiori et al., 2014; Scionti et al., 2018; Mori et al., 2021), whose effects are amplified in the case of concurrent events (Barbaro et al., 2019b; Canale et al., 2020; Canale et al., 2021). These issues are particularly important in coastal areas which are often very populated. Anthropogenic pressure alters the natural balance conditions, increasing the effects of natural events and triggering erosive processes in coastal areas, that increase their vulnerability (Komar, 2000; Foti and Sicilia, 2011; van Rijn, 2011; Barbaro, 2016; Barbaro et al., 2017; Mavromatidi et al., 2018). Therefore, coastal floods are caused by both natural and anthropogenic factors whose knowledge is important for the analysis and mapping phases of flood risk areas (Bernatchez et al., 2011).
The main natural factors are the wave climate (Gunaydin and Kabdasli, 2003; Barbaro et al., 2013; Bacino et al., 2013) and the sedimentary balance between longshore and river transport (Barbaro et al., 2012; Barbaro et al., 2014; Barbaro et al., 2019a; Foti et al., 2019; Marchesiello et al., 2019). Regarding the anthropogenic pressure, it can concern both rivers and coasts. In the river area it is mainly the construction of dams and weirs, the sediment withdrawal, and the subsidence (Andreadaki et al., 2014; Zema et al., 2014; Versaci et al., 2018; Foti et al., 2020). In the coastal areas it is mainly the construction of port and coastal structures (Barbaro, 2013; Sarma, 2015; Miduri et al., 2017).
Regarding the mapping phase, the legislation currently in force in Europe is the Flood Directive 2007/60/EC, implemented in Italy by Decree No. 49/2010.
However, many Italian and European regions use coastal flood risk mapping methodologies that differ from the Decree and the Flood Directive (Perini et al., 2016; Di Risio et al., 2017; Ferreira Silva et al., 2017; De Angeli et al., 2018; Lemee et al., 2018; Barbaro et al., 2020). Some examples of this difference concern the return periods that delimit the hazard levels and the examined factors. In this issue, the use of a GIS is of great importance.
The paper describes two case studies of coastal flooding occurred in November 2019 in Saline Joniche and in December 2019 in Favazzina, two towns located in southern Ionian and Tyrrhenian Calabria, respectively. The methodology is divided into three phases, one concerning the analysis of the wave climate and of the storms, one concerning the analysis of the shoreline changes and the other concerning the flood risk mapping.

2. SITES DESCRIPTION

2.1 Saline Joniche

Saline Joniche is a coastal town with about 5,000 inhabitants, located in the southern part of the Calabria region (Figure 1). It is located on the Ionian coast near Reggio Calabria and is characterized by the presence of infrastructures (port and railway) that were built to serve an industrial area. Furthermore, there is a natural oasis consisting of two brackish lakes, last witnesses of an ancient salt pan in that area.
The examined area has a length of about 2 km and is bounded by the mouth of the Molaro river to the north and the first small lake to the south. The beach is made up of very coarse sand and has numerous breakwaters placed to protect houses and infrastructures (Figure 2).

* Corresponding author

On 12 November 2019, Saline Joniche was hit by a violent sea storm that flooded streets and houses, causing a lot of damages (Figure 3).

Figure 1. Location of Saline Joniche.

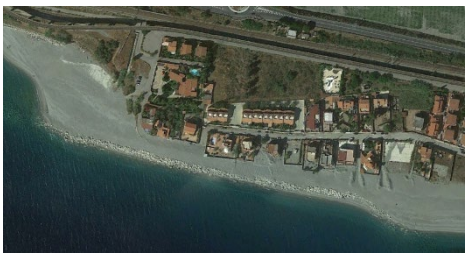
Figure 2. Saline Joniche: focus on the grazing cliffs.

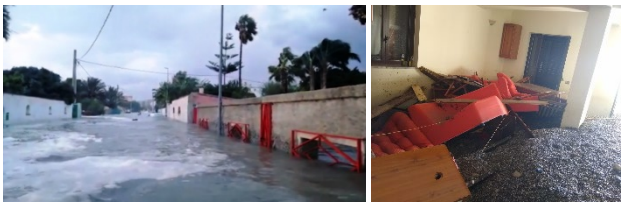
Figure 3. Saline Joniche: flooded streets and damaged houses due to the sea storm of 12 November 2019.

2.2 Favazzina

The town of Favazzina is located at about five kilometers from Scilla, a small town located on the Tyrrhenian coast in the southern part of the Calabria region (Figure 4). Favazzina is exposed to the III and IV quadrants of the Tyrrhenian Sea.
Its coast extends for about 1 km and is bordered to the south by a promontory and to the north by the mouth of the Favazzina river. The beach is composed by gravel mixed with pebbles and has numerous breakwaters and groins to protect it from the erosive action of the sea (Figure 5).
On 23 December 2019, the town of Favazzina was hit by a strong sea storm that damaged the houses and the coastal roads, destroying the beach, which is fundamental for summer tourism (Figure 6).

Figure 4. Location of Favazzina.


Figure 5. Favazzina: focus on the breakwater cliffs.


Figure 6. Favazzina: destroyed beach and damaged houses due to the sea storm of 23 December 2019.

3. METHODOLOGY

The methodological approach consisted in three phases:

1. analysis of the wave climate and of the sea storms;
2. analysis of the changes in the shoreline;
3. flood risk mapping.

For the first phase, the wave data from the last 40 years, reconstructed from the Climate Forecast System Reanalysis (CFSR) database and populating the database developed by the MeteOcean group of the University of Genoa, were used. Their statistical analysis allowed to estimate the characteristic parameters of the location, which in turn made possible to calculate the significant wave height of the fixed return period: among these, two parameters (u and w) describe a Weibull-type statistical distribution of the probability of exceeding a fixed significant wave height threshold (Boccotti, 2015), while the other two (a_{10} and b_{10}) are related to the equivalent triangular storm model (ETS) and represent the average values of the heights and of the bases of the ETS, referring to a sample of the N strongest real sea storms recorded, with N equal to 10 for the number of recorded years. Secondly, were analysed the storms and their characteristics (maximum significant wave height and duration). Finally, the run-up obtained with different models was evaluated starting from the maximum sea state recorded by the storm: in particular, the models of Stockdon et al. (2006), Mase (1989), Nielsen & Hanslow (1991,1993) and of the "Shoreline Management Guidelines" (2017) were used. The obtained values were later compared with the maximum values reached during the real event, obtained by analysing photographs and videos broadcast by the newspapers. This comparison allowed to identify a run-up calculation model valid for the study location, able to be used to estimate the run-up values related to different hazard levels and to draw the flood hazard maps.
Regards the second phase, the analysis of the shoreline changes was carried out using QGIS and open data from Calabrian and Italian Geoportal and from Google Earth. QGIS Processing tools were used to draw the transepts, orthogonal to the coast, and to assess the shoreline changes in terms of end point rate (EPR) and net shoreline movement (NSM) statistics. The assessment of the evolutionary trend of each study area is based on the estimation of a shoreline variation rate, calculated as a weighted mean rate, where the weight is given by the influence areas of each transept. Also, this analysis was conducted at different time scales: last 70 years, last 30 years, last 20 years, last 5 years and, finally, between the two most recent shorelines available.
The last phase concerned the flood risk mapping. After a careful and preliminary analysis of the legislations and of the

methodologies used at regional scale, it was chosen to use the return periods of 1, 20 and 100 years. The latter are the limit value for defining the hazard levels P3, P2 and P1. For each hazard level, or for each return period, the significant wave height limit value and the relative run-up value were assessed. In order to create the hazard maps, LiDAR derived DEM with 1m cell size m (freely available in the Italian National Geoportal) were compared with the run-up values reached by the sea storms of fixed return period. All the areas with elevations below these values for the three return periods were mapped, thus obtaining the hazard mapping.

4. RESULTS AND DISCUSSION

From data provided by the MeteOcean group, the location's characteristic parameters were calculated. For the location of Saline Joniche the following values were obtained: $u = 1.11$, $w = 0.64$ m, $a_{10} = 2.91$ m, $b_{10} = 70.10$ hours. While for the location of Favazzina the following values were obtained: $u = 0.89$, $w = 0.42$ m, $a_{10} = 2.76$ m, $b_{10} = 66.79$ hours. Figures 7 and 8 represent the examined sea storms of which both the maximum significant wave height and the duration have been calculated. Boccotti's criterion (2015) was used to identify a sea storm. The following values were obtained: a maximum significant wave height of 4.99 meters and a duration of 56 hours for Saline Joniche and a maximum significant wave height of 4.26 meters and a duration of 130 hours for Favazzina. Starting from the maximum sea state recorded by each storm, the relative run-up values was evaluated using several models. The back analysis model that obtained the most congruent results is that of Stockdon et al. (2006) which was later used to assess the run-up values for the three hazard levels. Also, its use is recommended in the Flood Directive 2007/60/EC.

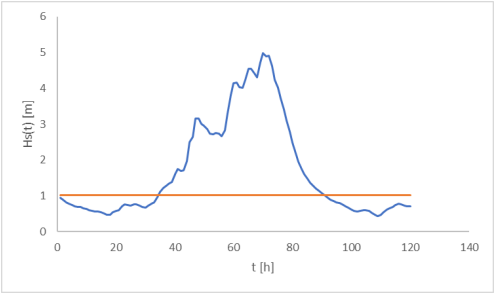

Figure 7. Sea storm occurred in Saline Joniche. The red line represents the critical significant wave height threshold used to identify a sea storm following Boccotti's criterion (2015).

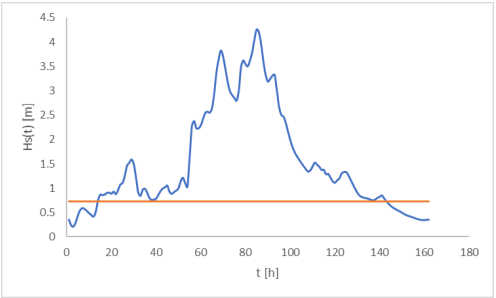

Figure 8. Sea storm occurred in Favazzina. The red line represents the critical significant wave height threshold used to identify a sea storm following Boccotti's criterion (2015).

Hazard level	R [years]	h (R) [m]	$R_{u,2\%}$ [m]
P_3	1	3.68	2.24
P_2	20	5.26	3.19
P_1	100	6.06	3.68

Table 1. Results obtained for the three hazard levels for the location of Saline Joniche, defined by the three values of return periods R.

Hazard level	R [years]	h (R) [m]	$R_{u,2\%}$ [m]
P_3	1	3.66	2.66
P_2	20	5.78	4.20
P_1	100	6.94	5.03

Table 2. Results obtained for the three hazard levels for the location of Favazzina, defined by the three values of return periods R.

The tables 1 and 2 shows the significant wave height and the run-up values for the three hazard levels, defined by the return periods of 1, 20 and 100 years. Therefore, the hazard maps have been plotted (Figs. 9 and 10).

Figure 9. Hazard map of Saline Joniche. Legend: red = P3, yellow = P2 and green = P1.

Figure 10. Hazard map of Favazzina. Legend: red = P3, yellow = P2 and green = P1.

The second phase of the methodology was applied only to the location of Favazzina, whose beach was destroyed by the sea storm. For this analysis, among the different available cartographic sources, the shorelines of 1954, 1989, 2000, 2017 and 2018 were considered and about 20 1km-long transepts have been traced. The following results were obtained in terms of shoreline variation rate: a value of 2.16 m/year for a most recent time interval, a value of 0.76 m/year for a short-term one, a value of -0.29 m/year for a middle-term one, a value of -0.59 m/year for a long-term one and a value of -0.13 m/year for a very long-term one.

The hazard maps of both locations were plotted as a function of the run-up values obtained for the three hazard levels.

5. CONCLUSIONS

The paper describes two case studies of coastal flooding that occurred in Calabria. The methodological approach used was based on the analysis of real past events that have damaged to structures and infrastructures located in the coastal areas and have destroyed the beach. The analysis carried out allowed to reconstruct the sea storms and to identify the run-up model that provide results consistent with the real ones. This procedure has consented to assess the coastal flooding hazard levels and to draw the related maps. Therefore, the methodology described in this paper is useful for the planning and management phases of coastal areas.

REFERENCES

Andreadaki, M., Georgoulas, A., Hrissanthou, V., Kotsovinos, N., 2014. Assessment of reservoir sedimentation effect on coastal erosion in the case of Nestos River, Greece. *International Journal of Sediment Research*, 29(1), pp. 34-48.

Bacino, G.L., Dragani, W.C., Codignotto, J.O., 2019. Changes in wave climate and its impact on the coastal erosion in Samborombón Bay, Río de la Plata estuary, Argentina. *Estuarine, Coastal and Shelf Science*, 219, pp. 71-80.

Barbaro, G. 2013. Saline Joniche: a predicted disaster. *Disaster Advances*, 6, pp. 1-3.

Barbaro, G., 2016. Master Plan of solutions to mitigate the risk of coastal erosion in Calabria (Italy), a case study. *Ocean & Coastal Management*, 132, pp. 24-35.

Barbaro, G., Bombino, G., Foti, G., Borrello, M.M., Puntorieri, P., 2019a. Shoreline evolution near river mouth: Case study of Petrace River (Calabria, Italy). *Regional Studies in Marine Science*, 29, article number 100619.

Barbaro, G., Fiamma, V., Barrile, V., Foti, G., Ielo, G., 2017. Analysis of the shoreline changes of Reggio Calabria (Italy). *International Journal of Civil Engineering and Technology*, 8(10), pp. 1777-1791.

Barbaro, G., Foti, G., Malara, G. 2013. Set-up due to random waves. *Transactions of the Royal Institution of Naval Architects Part A: International Journal of Maritime Engineering*, 155(PART A3).

Barbaro, G., Foti, G., Mandaglio, G., Mandaglio, M., Sicilia, C.L., 2012. Estimate of sediment transport capacity in the basin of the Fiumara Annunziata (RC). *Rendiconti Online Società Geologica Italiana*, 21(1), pp. 696-697.

Barbaro, G., Foti, G., Nucera, A., Barillà, G.C., Canale, C., Puntorieri, P., Minniti, F., 2020. Risk mapping of coastal flooding areas. Case studies: Scilla and Monasterace (Italy). *International Journal of Safety and Security Engineering*, 10(1), pp. 59-67.

Barbaro, G., Foti, G., Sicilia, C.L., Malara, G., 2014. A formula for the calculation of the longshore sediment transport including spectral effects. *Journal of Coastal Research*, 30, pp. 961-966.

Barbaro, G., Petrucci, O., Canale, C., Foti, G., Mancuso, P., Puntorieri P., 2019b. Contemporaneity of floods and storms. A case study of Metropolitan Area of Reggio Calabria in Southern Italy. In: *Prooceedings of New Metropolitan Perspectives (NMP)* (Reggio Calabria, Italy), Smart Innovation, Systems and Technologies, 101, pp. 614-620.

Barragán, J.M., de Andrés, M., 2015. Analysis and trends of the world's coastal cities and agglomerations. *Ocean & Coastal Management*, 114, pp. 11-20.

Bernatchez, P., Fraser, C., Lefaivre, D., Dugas, S., 2011. Integrating anthropogenic factors, geomorphological indicators and local knowledge in the analysis of coastal flooding and erosion hazards. *Ocean Coast. Manage.*, 54(8), pp. 621-632.

Boccotti, P., 2015. *Wave mechanics and wave loads on marine structures*. Elsevier BH, Oxford (UK).

Canale, C., Barbaro, G., Petrucci, O., Fiamma, V., Foti, G., Barillà, G.C., Puntorieri, P., Minniti, F., Bruzzaniti, L., 2020. Analysis of floods and storms: concurrent conditions. *Italian Journal of Engineering, Geology and Environ.*, 1, pp. 23-29.

Canale, C., Barbaro, G., Foti, G., Petrucci, O., Besio, G., Barillà G.C., 2021. Bruzzano river mouth damage due to meteorological events. *International Journal of River Basin Management*.

De Angeli, S., D'Andrea, M., Cazzola, G., Dolia, D., Duo, E., Rebora, N., 2018. Coastal Risk Assessment Framework: Comparison of modelled fluvial and marine inundation impacts, Bocca di Magra, Ligurian coast, Italy. *Coastal Engineering*, 134, pp. 229-240.

Di Risio, M., Bruschi, A., Lisi, I., Pesarino, V., Pasquali, D., 2017. Comparative analysis of coastal flooding vulnerability and hazard assessment at national scale. *Journal of Marine Science and Engineering*, 5(4), 51.

Ferreira Silva, S., Martinho, M., Capitao, R., Reis, T., Fortes, C.J., Ferreira, J.C., 2017. An index-based method for coastal-flood risk assessment in low-lying areas (Costa de Caparica, Portugal). *Ocean & Coastal Management*, 144, pp. 90-104.

Fiori, E., Comellas, A., Molini, L., Rebora, N., Siccardi, F., Gochis, D.J., Tanelli, S., Parodi, A., 2014. Analysis and hindcast simulations of an extreme rainfall event in the Mediterranean area: The Genoa 2011 case. *Atmospheric Research*, 138, pp. 13-29.

Foti, G., Barbaro, G., Bombino, G., Fiamma, V., Puntorieri, P., Minniti, F., Pezzimenti C., 2019. Shoreline changes near river mouth: case study of Sant'Agata River (Reggio Calabria, Italy). *European Journal of Remote Sensing*, 52(sup.4), pp. 102-112.

Foti, G., Barbaro, G., Manti, A., Foti, P., La Torre, A., Geria, P.F., Puntorieri P., Tramontana, N., 2020. A methodology to evaluate the effects of river sediment withdrawal: The case study of the Amendolea River in southern Italy. *Aquatic Ecosystem Health & Management*, 23(4), pp. 465-473.

Foti, G., Sicilia, C.L., 2013. Analysis, evaluation and innovative methodologies to prevent coastal erosion. *WIT Transactions on Ecology and the Environment*, 169, pp. 219-230.

Günaydın, K., Kabdaşlı, M.S., 2003. Characteristics of coastal erosion geometry under regular and irregular waves. *Ocean Engineering*, 30(13), pp. 1579-1593.

Komar, P.D., 2000. Coastal erosion–underlying factors and human impacts. *Shore & Beach*, 68(1), pp. 3-16.

Lemee, C., Fleury-Bahi, G., Krien, N., Dededalle, A., Mercier, D., Coquet, M., Rommel, D., Navarro, O., 2018. Factorial structure of the coastal flooding risk perception and validation of a French coastal flooding risk evaluation scale (CFRES) for non-experts. *Ocean & Coastal Management*, 155, pp. 68-75.

Lemee, C., Navarro, O., Restrepo-Ochoa, D., Mercier, D., Fleury-Bahi, G., 2020. Protective behaviors regarding coastal flooding risk in a context of climate change. *Advances in Climate Change Research*, 11(4), pp. 310-316.

Mangor, K., Drønen, N. K., Kærgaard, K. H., & Kristensen, S. E., 2017. *Shoreline management guidelines*.

Marchesiello, P., Nguyen, N.M., Gratiot, N., Loisel, H., Anthony, E.J., Dinh, C.S., Nguyen, T., Almar, R., Kestenare, E., 2019. Erosion of the coastal Mekong delta: Assessing natural against man induced processes. *Continental Shelf Research*, 181, pp. 72-89.

Mase, H., 1989. Random wave runup height on gentle slope. *Journal of Waterway, Port, Coastal and Ocean Engineering*, 115(5), pp. 649-661.

Mavromatidi, A., Briche, E., Claeys, C., 2018. Mapping and analyzing socio-environmental vulnerability to coastal hazards

induced by climate change: an application to coastal Mediterranean cities in France. *Cities*, 72, pp. 189-200.
Miduri, M., Foti G., Puntorieri P., 2017. Impact generated by Marina of Badolato (Italy) on adjacent coast. In: *Proceeding of 13th International Congress on Coastal and Marine Sciences, Engineering, Management and Conservation MEDCOAST* (Mellieha, Malta), 2, pp. 935-945.
Mori, N., Takemi, T., Tachikawa, Y., Tatano, H., Shimura, T., Tanaka, T., Fujimi, T., Osakada, Y., Webb, A., Nakakita, E., 2021. Recent nationwide climate change impact assessments of natural hazards in Japan and East Asia. *Weather and Climate Extremes*, 32, article number 100309.
Nielsen, P. Hanslow, D.J., 1991. Wave runup distributions on natural beaches. *Journal of Coastal Research*, 7(4), pp. 1139-1152.
Hanslow, D. J., Nielsen, P., 1993. Wave setup on beaches and in river entrances. *Coastal Engineering 1992*, pp. 240-252.
Perini, L., Calabrese, L., Salerno, G., Ciavola, P., Armaroli, C., 2016. Evaluation of coastal vulnerability to flooding: comparison of two different methodologies adopted by the Emilia-Romagna region (Italy). *Natural Hazards and Earth System Sciences*, 16(1), pp. 181-194.
Sarma, K.G.S., 2015. Siltation and Coastal Erosion at Shoreline Harbours. *Procedia Engineering*, 116, pp. 12-19.
Scionti, F., Miguez, M.G., Barbaro, G., De Sousa, M.M., Foti, G., Canale, C., 2018. Integrated methodology for urban flood risk mitigation in Cittanova, Italy. *Journal of Water Resources, Planning and Management*, 144(10), article number 05018013.
Stockdon, H.F., Holman, R.A., Howd, P.A., Sallenger, A.H.J., 2006. Empirical parameterization of setup, swash, and runup. *Coastal Engineering*, 53(7), pp. 573–588.
van Rijn, L.C., 2011. Coastal erosion and control. *Ocean & Coastal Management*, 54(12), pp. 867-887.
Versaci, R., Minniti, F., Foti, G., Canale, C., Barillà, G.C., 2018. River anthropization, case studies in Reggio Calabria (Italy). *WIT Transactions on Ecology and the Environment*, 217, pp. 903-912.
Zema, D.A., Bombino, G., Boix-Fayos, C., Tamburino, V., Zimbone, S.M., Fortugno, D., 2014. Evaluation and modeling of scouring and sedimentation around check dams in a Mediterranean torrent in Calabria, Italy. *Journal of Soil and Water Conservation*, 69(4), pp. 316-329.

ANALYSIS OF THE CORRELATION BETWEEN COASTAL EROSION AND ANTHROPOGENIC PROCESSES USING REMOTE SENSING. CASE STUDY: CALABRIA (ITALY)

G. Foti [1], G. Barbaro [1], G.C. Barillà [1]*, P. Mancuso [2], P. Puntorieri [1], M. Mandalari[1]

[1] Mediterranea University of Reggio Calabria, DICEAM Department, località Feo di Vito, 89122 Reggio Calabria Italy - giandomenico.foti@unirc.it; giuseppe.barbaro@unirc.it; chiara.barilla@unirc.it; pierfabrizio.puntorieri@unirc.it; mariamandalari.mm@gmail.com

[2] Public Works Department of Calabria Region, località Germaneto, 88100 Catanzaro Italy – pierluigi.mancuso@regione.calabria.it

KEY WORDS: Coastal erosion, anthropogenic processes, man-made areas, shoreline changes, remote sensing, QGIS.

ABSTRACT:

The issue of coastal erosion currently affects most of the world's coastal territories. This erosion causes the alteration of coastal dynamic both due to the action of natural factors and to the increase in anthropogenic pressure which characterized the second half of the last century. Indeed, many coastal areas have been built up, reducing the natural beach and totally or partially destroying many dune systems, altering the coastal equilibrium conditions, and triggering erosion processes. This issue is particularly important in areas such as Calabria, characterized by over 750 km of coastline, many of which are subject to considerable anthropogenic pressures which have caused extensive erosion.

The paper analyzes the correlations between eroded areas and anthropogenic pressure in Calabria. The analysis is divided into the following phases: identification of the man-made areas in the last 60 years; analysis of variation of the presence of dune systems in these areas; identification of eroded areas and comparison between eroded and man-made areas to identify possible correlations between them. The analysis is performed on QGIS software. The cartographic data of the Open Data sections of the Italian and Calabrian Geoportals and the historic satellite imagery of Google Earth were used as input data. Finally, the methodology described in this paper is of interest in the field of coastal area planning and management as it leads to the rapid analysis of cartographic data from different sources using free software.

1. INTRODUCTION

Anthropogenic pressure is a current problem, which affects many territories (Dias et al., 2013) and which has accelerated since the second half of the last century (Barragan and De Andres, 2015). Currently, about 20% of the world population lives within 25 km of the coast (Rangel-Buitrago et al., 2018) and the number of coastal cities has quintupled in the last 70 years (Stronkhorst et al., 2018).

One of the main effects of the increase in anthropogenic pressure in coastal areas concerns the increase in the vulnerability of these areas to the action of floods and sea storms (Fiori et al., 2014; Scionti et al., 2018; Barbaro et al., 2020; Barbaro et al., 2021; Mori et al., 2021), whose effects are amplified in the case of concurrent events (Barbaro et al., 2019b; Canale et al., 2020; Canale et al., 2021). Also, anthropogenic pressure can alter the natural equilibrium conditions, increasing the effects of natural events and triggering erosive processes (Komar, 2000; Foti and Sicilia, 2011; van Rijn, 2011; Barbaro, 2016; Barbaro et al., 2017; Williams et al., 2017; Mavromatidi et al., 2018; Tomasicchio et al., 2020).

Anthropogenic pressure concern both rivers and coasts. In the river area it is mainly the construction of dams and weirs, the sediment withdrawal, and the subsidence (Walling, 2006; Andreadaki et al., 2014; Zema et al., 2014; Fortugno et al., 2017; Versaci et al., 2018; Valderrama-Landeros and Flores-de-Santiago, 2019; Foti et al., 2020; Nguyen and Takewaka, 2020). In the coastal areas it is mainly the construction of port and coastal structures (D'Alessandro et al., 2011; Barbaro, 2013; Sarma, 2015; Prumm and Iglesias, 2016; Miduri et al., 2017).

In addition to anthropogenic pressure, various natural factors can also alter the natural equilibrium conditions. The main natural factors are the wave climate (Gunaydin and Kabdasli, 2003; Barbaro et al., 2013; Bacino et al., 2013; Wang et al., 2020) and the sedimentary balance between longshore and river transport (Barbaro et al., 2012; Barbaro et al., 2014; Barbaro et al., 2019a; Foti et al., 2019; Marchesiello et al., 2019).

The paper analyzes the correlations between eroded areas and anthropogenic pressure in Calabria. The analysis is divided into the following phases: identification of the man-made areas in the last 60 years by analyzing recent satellite images and by comparison with the man-made areas of 1954; analysis of variation of the presence of dune systems in these areas; identification of eroded areas by comparing the shorelines of different years; comparison between eroded and man-made areas to identify possible correlations between them. The analysis is performed on QGIS software.

2. SITES DESCRIPTION

Calabria is a region of southern Italy, located exactly in the center of the Mediterranean Sea. It represents the tip of the typical Italian boot (Fig. 1). Morphologically, Calabria is characterized by hills and mountains, while the plains are less than 10% of the entire territory. Its narrow and elongated conformation means that it has about 750 km of coastline, with an alternation of beaches, mainly sandy and pebbly, and high coasts. Calabria is bathed by two seas, Tyrrhenian, and Ionian,

* Corresponding author

by the Strait of Messina and by the Gulf of Taranto, each of them with different climatic characteristics and with different fetches extensions. These differences lead to a remarkable variability of weather and sea conditions between the different coastal areas, that influence coastal dynamics. Furthermore, Calabrian rivers are characterized by torrential and irregular hydrological regime, with extensive dry periods and frequent sudden flood, generated by short and intense rainfall. Consequently, these characteristics can cause a high variation in solid transport and an alteration of the coastal dynamics and of the shoreline evolution near the river mouths.

Furthermore, the Calabria region is rich in dune systems, mostly present on the Ionian coast. Their presence is particularly important for the conservation of the coastal zone. Indeed, dune systems represent a "natural system" to dissipate the wave energy. Consequently, they can reduce the risk of erosion, as they constitute a reserve of sediment, and can counteract the risk of flooding of the hinterland. However, due to the recent anthropogenic pressure developed between the beginning of the last century and the early nineties, in Calabria, as well as throughout Italy, the surface area consisting of dune systems has reduced by 80% (EUCC, 1993). Unfortunately, it has often happened that these natural systems, instead of being preserved, have been entirely supplanted by tourist-accommodation facilities, villages and summer houses.

Figure 1. The Calabrian region (shown in red).

3. METHODOLOGY

The following methodology allows to analyze the correlations between eroded areas and anthropogenic pressure in Calabria. In particular, the study considered the reduction in the presence of dune systems due to the anthropization processes of the coastal areas that took place in the last 60 years.

For this purpose, the cartographic data of the Open Data sections of the Italian and Calabrian Geoportals and the historic satellite imagery of Google Earth were used as input data. In detail, the following were used:

- a shapefile of the inhabited centers of 1954;
- a shapefile of the dune systems detected in 1957;
- a shapefile of the historical shoreline of 1954;
- a shapefile of the dune systems detected in the second decade of the 2000s;
- recent satellite imageries provided by Google, which made it possible to detect the current consistency of the inhabited centers and the current coastline and thus compare it with those of the past.

The analysis is performed on QGIS software and can be divided into four phases:

1. Identification of coastal areas of recent anthropogenic development, through the comparison between the shapefile of 1954 and the current satellite imageries.
2. Analysis of the current presence of dune systems in these areas and comparison with the 1957 shapefile.
3. Analysis of the variation of the shoreline in these areas between 1954 and today, in order to identify eroded areas over the past 60 years.
4. Identification of possible correlations between eroded and man-made areas.

As regards the third phase, several QGIS Processing tools were used to draw the transepts and to calculate the increase or loss of beach surface from 1954 to today.

4. RESULTS AND DISCUSSION

This section describes the results obtained in some Calabrian locations applying the methodology above mentioned. In detail, three locations on the Tyrrhenian coast and three locations on the Ionian coast were chosen. The first three are Tortora, Diamante and Zambrone, the others are Ardore, Monasterace and Calopezzati.

The following figures show in green the shapefiles of to the dune systems detected in 1957, in red the shapefiles of the inhabited centres of 1954, in yellow the shapefiles of the beach and the coastal dunes detected in recent times and in yellow the shoreline of 1954.

In all the figures shown, it can be seen how the examined coast is set back compared to 1954. Except for Ardore (fig. 5), where there was already an inhabited center that is evidently much larger today, the other locations are characterized by large, developed towns recently (as not present in the 1954 survey) close to the coastal strip, taking the place of notable dune systems, now mostly non-existent.

Consequently, in these localities, it is evident that the anthropization process can be correlated to that of coastal erosion, due to the destruction of the systems that naturally protect the hinterland from marine intrusion, such as dune and vegetative systems.

Furthermore, it can be noted how the width of the beach has reduced over time due to anthropogenic pressure. Instead, in the back of the beach there are often promenades and infrastructures where once dune systems stood.

For this reason, for the purposes of the analysis described in this paper, it is also necessary to quantify the eroded surface in the last 60 years. However, it should be noted that coastal dynamics is an extraordinarily complex process, in which natural and anthropogenic factors come into play. Consequently, the correlation between eroded areas and anthropogenic pressure is plausible, but the anthropization process is certainly not the only factor that has had an impact, such to produce the calculated erosion rate.

Then, the results for the third phase are reported below. For the location of Tortora (fig.2), on the Tyrrhenian coast, the eroded surface from 1954 to today is equal to 112,262 m^2. For the location of Diamante, in the area between the two promontories shown in the fig.3, the eroded surface from 1954 to today is equal to 64,175 m^2. In the location of Zambrone (fig.4), in the area south of the promontory where dune systems once stood, there has been an erosion from 1954 to today of 81,790 m^2. On the Ionian coast, in the location of Ardore (fig.5) the eroded surface amounts to 74,375 m^2, despite the dune systems are still present in the more peripheral parts of the territory. In the location of Monasterace (fig.6) an area eroded in the last 60 years of 265,725 m^2 has been counted. In this area the protection strategies of the dunes are fundamental, because to the north of the inhabited center there is an important archaeological site on a dune (Barbaro et al., 2016). Finally, in the location of Calopezzati (fig.7), the eroded surface from 1954 to today amounts to 40,334 m^2.

Figure 2. Tortora, on the Tyrrhenian coast.

Figure 3. Diamante, on the Tyrrhenian coast.

Figure 4. Zambrone, on the Tyrrhenian coast.

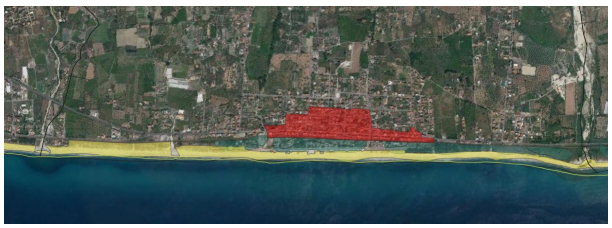

Figure 5. Ardore, on the Ionian coast.

Figure 6. Monasterace, on the Ionian coast.

Figure 7. Calopezzati, on the Ionian coast.

5. CONCLUSIONS

The paper described an analysis of the correlations between eroded areas and anthropogenic pressure in Calabria.
The analysis carried out highlighted that the processes of anthropization of coastal areas represent an important factor in the shoreline evolution, mainly due to the destruction of natural defense systems of the territory from coastal erosion and flooding, such as dune and vegetative systems. Consequently, the correlation is plausible, but certainly the results obtained in terms of eroded areas cannot strictly depend only from these processes, even if their influence can be substantial.
The analysis described in this paper has mainly focused on the influence that the anthropic processes developed in the last 60 years have had in the localities of Tortora, Diamante and Zambrone, located on the Tyrrhenian coast, and of Ardore, Monasterace and Calopezzati, located on the Ionian coast.
This analysis is useful for the planning and management phases of coastal areas. In particular, the paper makes it possible to identify the importance of adopting protection strategies for natural systems, where they still exist.

REFERENCES

Andredaki, M., Georgoulas, A., Hrissanthou, V., Kotsovinos, N., 2014. Assessment of reservoir sedimentation effect on coastal erosion in the case of Nestos River, Greece. *International Journal of Sediment Research*, 29(1), pp. 34-48.

Bacino, G.L., Dragani, W.C., Codignotto, J.O., 2019. Changes in wave climate and its impact on the coastal erosion in Samborombón Bay, Río de la Plata estuary, Argentina. *Estuarine, Coastal and Shelf Science*, 219, pp. 71-80.

Barbaro, G. 2013. Saline Joniche: a predicted disaster. *Disaster Advances*, 6, pp. 1-3.

Barbaro, G., 2016. Master Plan of solutions to mitigate the risk of coastal erosion in Calabria (Italy), a case study. *Ocean & Coastal Management*, 132, pp. 24-35.

Barbaro, G., Bombino, G., Foti, G., Borrello, M.M., Puntorieri, P., 2019a. Shoreline evolution near river mouth: Case study of Petrace River (Calabria, Italy). *Regional Studies in Marine Science*, 29, article number 100619.

Barbaro, G., Fiamma, V., Barrile, V., Foti, G., Ielo, G., 2017. Analysis of the shoreline changes of Reggio Calabria (Italy). *International Journal of Civil Engineering and Technology*, 8(10), pp. 1777-1791.

Barbaro, G., Foti, G., Malara, G. 2013. Set-up due to random waves. *Transactions of the Royal Institution of Naval Architects Part A: International Journal of Maritime Engineering*, 155(PART A3).

Barbaro, G., Foti, G., Mandaglio, G., Mandaglio, M., Sicilia, C.L., 2012. Estimate of sediment transport capacity in the basin of the Fiumara Annunziata (RC). *Rendiconti Online Società Geologica Italiana*, 21(1), pp. 696-697.

Barbaro, G., Foti, G., Nucera, A., Barillà, G.C., Canale, C., Puntorieri, P., Minniti, F., 2020. Risk mapping of coastal flooding areas. Case studies: Scilla and Monasterace (Italy). *International Journal of Safety and Security Engineering*, 10(1), pp. 59-67.

Barbaro, G., Foti, G., Sicilia, C.L., 2016. Erosive phenomena in the proximity of Kaulon archaeological park: origins and remedies. In: *Proceedings of the 2nd International Symposium New Metropolitan Perspectives (ISTH2020)* (Reggio Calabria, Italy), Procedia – Social and Behavioral Sciences, 223, pp. 714-719

Barbaro, G., Foti, G., Sicilia, C.L., Malara, G., 2014. A formula for the calculation of the longshore sediment transport including spectral effects. *Journal of Coastal Research*, 30, pp. 961-966.

Barbaro, G., Miguez, M.G., De Sousa, M.M., Da Cruz Franco, A.B.R., De Magalhaes, P.M.C., Foti, G., Valadao, M.R., Occhiuto, I., 2021. Innovations in best practices: Approaches to managing urban areas and reducing flood risk in Reggio Calabria (Italy). *Sustainability*, 13(6), article number 3463.

Barbaro, G., Petrucci, O., Canale, C., Foti, G., Mancuso, P., Puntorieri P., 2019b. Contemporaneity of floods and storms. A case study of Metropolitan Area of Reggio Calabria in Southern Italy. In: *Prooceedings of New Metropolitan Perspectives (NMP)* (Reggio Calabria, Italy), Smart Innovation, Systems and Technologies, 101, pp. 614-620.

Barragán, J.M., de Andrés, M., 2015. Analysis and trends of the world's coastal cities and agglomerations. *Ocean & Coastal Management*, 114, pp. 11-20.

Canale, C., Barbaro, G., Petrucci, O., Fiamma, V., Foti, G., Barillà, G.C., Puntorieri, P., Minniti, F., Bruzzaniti, L., 2020. Analysis of floods and storms: concurrent conditions. *Italian Journal of Engineering, Geology and Environ.*, 1, pp. 23-29.

Canale, C., Barbaro, G., Foti, G., Petrucci, O., Besio, G., Barillà G.C., 2021. Bruzzano river mouth damage due to meteorological events. *International Journal of River Basin Management*.

D'Alessandro, F., Tomasicchio, G.R., Frega, F., Carbone, M., 2011. Design and management aspects of a coastal protection system. A case history in the South of Italy. *Journal of Coastal Research*, 64, pp. 492-495.

Dias, J.A., Cearreta, A., Isla, F.I., Michaelovitch de Mahiques, M., 2013. Anthropogenic impacts on Iberoamerican coastal areas: Historical processes, present challenges, and consequences for coastal zone management. *Ocean & Coastal Management*, 77, pp. 80-88.

EUCC (European Union for Conservation of Coast), 1993. Changing Coastal Zone, Chances for Sustainable Development, to appear in Coastline Magazine.

Fiori, E., Comellas, A., Molini, L., Rebora, N., Siccardi, F., Gochis, D.J., Tanelli, S., Parodi, A., 2014. Analysis and hindcast simulations of an extreme rainfall event in the Mediterranean area: The Genoa 2011 case. *Atmospheric Research*, 138, pp. 13-29.

Fortugno, D., Boix-Fayos, C., Bombino, G., Denisi, P., Quinonero Rubio, J.M., Tamburino, V., Zema, D.A., 2017. Adjustments in channel morphology due to land-use changes and check dam installation in mountain torrents of Calabria (southern Italy). *Earth Surface Processes and Landforms*, 42(14), pp. 2469-2483.

Foti, G., Barbaro, G., Bombino, G., Fiamma, V., Puntorieri, P., Minniti, F., Pezzimenti C., 2019. Shoreline changes near river mouth: case study of Sant'Agata River (Reggio Calabria, Italy). *European Journal of Remote Sensing*, 52(sup.4), pp. 102-112.

Foti, G., Barbaro, G., Manti, A., Foti, P., La Torre, A., Geria, P.F., Puntorieri P., Tramontana, N., 2020. A methodology to evaluate the effects of river sediment withdrawal: The case study of the Amendolea River in southern Italy. *Aquatic Ecosystem Health & Management*, 23(4), pp. 465-473.

Foti, G., Sicilia, C.L., 2013. Analysis, evaluation and innovative methodologies to prevent coastal erosion. *WIT Transactions on Ecology and the Environment*, 169, pp. 219-230.

Günaydın, K., Kabdaşlı, M.S., 2003. Characteristics of coastal erosion geometry under regular and irregular waves. *Ocean Engineering*, 30(13), pp. 1579-1593.

Komar, P.D., 2000. Coastal erosion–underlying factors and human impacts. *Shore & Beach*, 68(1), pp. 3-16.

Marchesiello, P., Nguyen, N.M., Gratiot, N., Loisel, H., Anthony, E.J., Dinh, C.S., Nguyen, T., Almar, R., Kestenare, E., 2019. Erosion of the coastal Mekong delta: Assessing natural against man induced processes. *Continental Shelf Research*, 181, pp. 72-89.

Mavromatidi, A., Briche, E., Claeys, C., 2018. Mapping and analyzing socio-environmental vulnerability to coastal hazards induced by climate change: an application to coastal Mediterranean cities in France. *Cities*, 72, pp. 189-200.

Miduri, M., Foti G., Puntorieri P., 2017. Impact generated by Marina of Badolato (Italy) on adjacent coast. In: *Proceeding of 13th International Congress on Coastal and Marine Sciences, Engineering, Management and Conservation MEDCOAST* (Mellieha, Malta), 2, pp. 935-945.

Mori, N., Takemi, T., Tachikawa, Y., Tatano, H., Shimura, T., Tanaka, T., Fujimi, T., Osakada, Y., Webb, A., Nakakita, E., 2021. Recent nationwide climate change impact assessments of natural hazards in Japan and East Asia. *Weather and Climate Extremes*, 32, article number 100309.

Nguyen, Q.H., Takewaka, S., 2020. Land subsidence and its effects on coastal erosion in the Nam Dinh Coast (Vietnam). *Continental Shelf Research*, 207, article number 104227.

Prumm, M., Iglesias, G., 2016. Impacts of port development on estuarine morphodynamics: Ribadeo (Spain). *Ocean & Coastal management*, 130, pp. 58-72.

Rangel-Buitrago, N., Williams, A., Anfuso, G., 2018. Hard protection structures as a principal coastal erosion management strategy along the Caribbean coast of Colombia. A chronicle of pitfalls. *Ocean & Coastal Management*, 156, pp. 58-75.

Sarma, K.G.S., 2015. Siltation and Coastal Erosion at Shoreline Harbours. *Procedia Engineering*, 116, pp. 12-19.

Scionti, F., Miguez, M.G., Barbaro, G., De Sousa, M.M., Foti, G., Canale, C., 2018. Integrated methodology for urban flood risk mitigation in Cittanova, Italy. *Journal of Water Resources, Planning and Management*, 144(10), article number 05018013.

Stronkhorst, J., Levering, A., Hendriksen, G., Rangel-Buitrago, N., Appelquist, L.R., 2018. Regional coastal erosion assessment based on global open access data: a case study for Colombia. *Journal of Coastal Conservation*, pp. 1-12.

Tomasicchio, G.R., Francone, A., Simmonds, D.J., D'Alessandro, F., Frega, F., 2020. Prediction of shoreline evolution. Reliability of a general model for the mixed beach case. *Journal of Marine Science and Engineering*, 8(5), 361.

Valderrama-Landeros, L., Flores-de-Santiago, F., 2019. Assessing coastal erosion and accretion trends along two contrasting subtropical rivers based on remote sensing data. *Ocean & Coastal Management*, 169, pp. 58-67.

van Rijn, L.C., 2011. Coastal erosion and control. *Ocean & Coastal Management*, 54(12), pp. 867-887.

Versaci, R., Minniti, F., Foti, G., Canale, C., Barillà, G.C., 2018. River anthropization, case studies in Reggio Calabria (Italy). *WIT Transactions on Ecology and the Environment*, 217, pp. 903-912.

Walling, D.E., 2006. Human impact on land–ocean sediment transfer by the world's rivers. *Geomorphology*, 79(3-4), pp. 192-216.

Wang, J., You, Z.J., Liang, B., 2020. Laboratory investigation of coastal beach erosion processes under storm waves of slowly varying height. *Marine Geology*, 430, article number 106321.

Williams, A.T., Rangel-Buitrago, N., Pranzini, E., Anfuso, G., 2017. The management of coastal erosion. *Ocean & Coastal Management*, 156, pp. 4-20.

Zema, D.A., Bombino, G., Boix-Fayos, C., Tamburino, V., Zimbone, S.M., Fortugno, D., 2014. Evaluation and modeling of scouring and sedimentation around check dams in a Mediterranean torrent in Calabria, Italy. *Journal of Soil and Water Conservation*, 69(4), pp. 316-329.

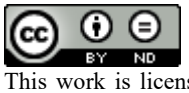

SEA STATE ANALYSIS USING GNSS-R IN FAR-FROM-SPECULAR ACQUISITION GEOMETRIES

G. Di Martino, A. Di Simone*, A. Iodice, D. Riccio, G. Ruello

Department of Electrical Engineering and Information Technology, University of Naples "Federico II", 80125 Naples, Italy
(gerardo.dimartino, alessio.disimone, iodice, daniele.riccio, ruello)@unina.it

KEY WORDS: GNSS-Reflectometry, two-scale model, bistatic radar, sea surface scattering, target detection, delay-Doppler map simulation

ABSTRACT:

Over oceans, Global Navigation Satellite System-Reflectometry (GNSS-R) is typically designed to collect the left-hand circularly-polarized (LHCP) component of the signal scattered off the sea surface. Accordingly, Geometrical Optics (GO) is safely adopted for modelling the sea surface return in retrieval algorithms and end-to-end GNSS-R simulators. However, the applicability of GNSS-R for maritime surveillance applications, e.g., ship detection, requires unconventional far-from-specular acquisition geometries and right-hand circular polarization channel, where GO may be no longer reliable for an accurate description of sea surface scattering. In this paper, we carry out a link budget analysis of the sea surface return in arbitrary acquisition geometries, also including backscattering, and circular polarization channel. Assuming the conventional GNSS-R processing chain, it is demonstrated that a reliable simulation of GNSS-R signals acquired by airborne receivers in far-from-specular acquisition geometries calls for scattering models more advanced than GO.

1. INTRODUCTION

The exploitation of Global Navigation Satellite System (GNSS) signals as opportunistic sources for remote sensing applications has been widely demonstrated in the last decades. So far, GNSS-reflectometry (GNSS-R) has been successfully applied over oceans for the retrieval of wind speed, sea surface altimetry, sea surface roughness; over land for the retrieval of biomass and soil moisture; over cryosphere for the monitoring of sea ice sheets and glaciers (Zavorotny, 2014).

As compared to other remote sensing technologies, such as synthetic aperture radar and optical/multi-spectral sensors, GNSS-R exhibits numerous advantages, including low cost, light weight and the free availability of a large (>100) number of GNSS transmitters which provide seamless and global coverage of the Earth' surface. Such key factors make GNSS-R an invaluable support to Earth observation activities and an intriguing technology for space-based maritime situational awareness, including global maritime surveillance (Soldi, 2021).

GNSS-R typically collects the left-hand circularly-polarized (LHCP) component of the GNSS signal scattered off the Earth' surface and operates in a forward-scattering configuration where the received signal comes from a region surrounding the specular reflection point, the so-called *glistening zone.* Over oceans, such a conventional GNSS-R provides best performance for sea state analysis, as sea surface reflects the GNSS signal mainly in the specular direction and, additionally, causes a significant depolarization of the impinging right-hand-circularly polarized (RHCP) GNSS signal, which is then mainly LHCP after reflection.

Unfortunately, conventional GNSS-R is poorly suited to maritime surveillance applications, e.g., ship detection, as it has been demonstrated in numerous works (Clarizia, 2015), (Di Simone, 2017a), (Di Simone, 2017b), (Di Simone, 2018a). Indeed, in a maritime scenario where an isolated large vessel is illuminated by a microwave source in far field, the main scattering contribution from the target is the double-bounce term arising from the interaction between the ship hull and the surrounding sea surface (Di Simone, 2020). Such a contribution propagates in a direction close to backscattering, depending on the target orientation. Additionally, the metallic hull of the ship reverses the polarization of the impinging EM wave. Accordingly, the double scattering term exhibits a non-negligible RHCP component, same as the transmitted waveform. As a result of such phenomena, a conventional GNSS-R receiver will collect only a negligible quote of the target echo. Conversely, GNSS-R receivers operating in back-scattering configuration and equipped with a RHCP receiving nadir antenna are suited to maritime surveillance applications, at least from airborne altitudes. Such unconventional GNSS-R have been recently investigated in both theoretical (Di Simone, 2018b) and simulation (Beltramonte, 2020) analyses, which have confirmed the feasibility of ship detection using DDMs acquired from unconventional airborne GNSS-R delay-Doppler maps, whereas ship detection using spaceborne GNSS-R remains a challenging task unless further modifications related to, e.g., signal processing, are introduced. Additionally, for a reliable simulation of spaceborne GNSS-R signals, GO proved to be accurate enough regardless of the acquisition geometry (Di Martino, 2021a). Indeed, at spaceborne altitudes, GO becomes inaccurate at SNR values well below 0 dB, i.e., where DDM is dominated by thermal noise. For such reasons, here we limit our analysis to airborne GNSS-R.

In sea surface analysis using conventional GNSS-R, Geometrical Optics (GO) is the typical microwave scattering model adopted to describe sea surface scattering thanks to its

* Corresponding author

mathematical treatability and reliability at and around the specular direction. However, when moving far from the specular reflection direction, GO becomes inaccurate and more advanced scattering models may be required for a proper link budget analysis and simulation of GNSS-R data in arbitrary acquisition geometries.
In this paper, we describe sea surface scattering via the bistatic anisotropic polarimetric two-scale model (BA-PTSM), which provides closed-form expressions of the covariance matrix of sea surface scattering in a wide range of bistatic geometries. BA-PTSM is then adopted to provide a more accurate link budget analysis of the sea surface return at L-band, where GNSSs operate. Other key factors influencing the received signal strength, such as the receiver processing scheme and the antenna beam are taken into account as well. The results of our analysis might be fruitfully exploited for a more accurate simulation of GNSS signals scattered off sea surface in arbitrary acquisition geometries, including backscattering.

The paper is organized as follows: Section 2 introduces the BA-PTSM adopted here for the evaluation of sea surface scattering at arbitrary viewing geometries; Section 3 describes the SNR analysis for the sea surface return; Section 4 presents numerical results of link budget for airborne GNSS-R receivers and considering GO and BA-PTSM as scattering models. Concluding remarks are highlighted in Section 5.

2. BISTATIC ANISOTROPIC POLARIMETRIC TWO-SCALE MODEL

BA-PTSM has been derived in (Di Martino, 2021b) within the framework of the two-scale model (TSM), first presented in (Valenzuela, 1968). TSM allows for the evaluation of the backscattering from a rough surface which is described as the superposition of two terms: a small-scale roughness and a large-scale roughness. The Small Perturbation Method (SPM) is adopted for evaluating EM scattering from the small-scale component, which is then described in terms of its power spectral density (PSD). Conversely, GO is used for the large-scale component, which is modeled as a collection of randomly tilted smooth facets. The former scattering contribution is responsible for the incoherent scattering at far-from-specular direction, whereas the latter dominates scattering in and around the specular direction. BA-PTSM generalizes the TSM under two respects: first, the surface isotropy assumption of TSM is removed in BA-PTSM, which, then, allows for evaluation of scattering from anistropic surfaces; second, BA-PTSM is not limited to backscattering and bistatic scattering geometries can be analyzed. Additionally, TSM allows for closed-form evaluation of co-polarized scattering coefficients only, while BA-PTSM as a polarimetric version of TSM provides analytical formulas for the whole covariance matrix, then allowing for a fast evaluation of both cross-polarization and de-polarization effects. This avoids computationally-demanding numerical evaluation of four-fold integrals. Finally, it is worth mentioning that the small-scale scattering contribution vanishes in and around the specular direction, where BA-PTSM reduces to GO; in all other scattering directions, BA-PTSM offers much higher reliability than GO. More specifically, BA-PTSM has been demonstrated to be as accurate as advanced numerical models, such as the second-order small-slope approximation (SSA2), and much more efficient (Di Martino, 2021b).

3. GNSS-R LINK BUDGET FOR SEA SURFACE

In order to provide a link budget for the received signal at the output of the GNSS-R receiver, here we focus our analysis to airborne GNSS-R and to the standard GNSS-R processing chain which consists of a coherent integration over a time interval T_c, whose output is the single-snapshot DDM, followed by an incoherent integration of subsequent DDMs over a time interval T_i, whose result is a multilook DDM with reduced noise. The strength of the sea surface return at the output of the standard GNSS-R processing scheme can be expressed as follows:

$$P_{r,sea} = P_t G_t G_r \frac{1}{(4\pi)^3}\left(\frac{\lambda cos\vartheta cos\vartheta_s}{h_t h_r}\right)^2 A_{sea}\sigma^0_{sea}(\vartheta,\vartheta_s,\varphi_s)\,, \quad (1)$$

where the sea surface scattering coefficient σ^0_{sea} is evaluated through the BA-PTSM and depends on the viewing angle ϑ, and the scattering angles ϑ_s and φ_s, which are defined according to coordinate system shown in Fig. 1. The reference system is defined so that the incident wavevector lies in the xz plane, being the z-axis normal to the mean plane of the sea surface.

The received signal strength in (1) is proportional to the area of the DDM resolution cell A_{sea}, that is here evaluated numerically given the configuration of iso-delay and iso-Doppler lines and the receiving antenna beam, that at airborne altitudes may limit the resolution cell area. In this study we assume a beamwidth of 30°, which is typical of GNSS-R receiving antennas. For an accurate evaluation of A_{sea}, we also account for the acquisition geometry – i.e., the viewing and scattering angles, the GNSS-R receiver altitude – and the delay and Doppler resolutions of the GNSS-R receiver.

The thermal noise power at the output of the coherent integration can be written as:

$$P_n = \frac{k_B(T_a + T_e)}{T_c}, \quad (2)$$

i.e., it is inversely proportional to the coherent integration time T_c.

Finally, the signal-to-noise ratio (SNR) at the output of the incoherent integration is evaluated as:

$$SNR = \sqrt{\frac{T_i}{T_c}}\frac{P_{r,sea}}{P_n}\,. \quad (3)$$

where the factor T_i/T_c is the number of incoherently integrated DDMs, i.e., the incoherent integration gain. In (2), k_B is the Boltzmann constant, while remaining symbols appearing in (1) are defined in Table 1.

Finally, it is worth mentioning that, in the considered reference frame, the backscattering direction is $\vartheta_s = \vartheta$ and $\varphi_s = 180°$, while the forward-scattering one, typical of conventional GNSS-R, corresponds to $\vartheta_s = \vartheta$ and $\varphi_s = 0°$.

4. NUMERICAL RESULTS

In this section, some results of the link budget analysis presented in Section 3 are provided. Numerical simulations have been set up according to values listed in Table 1. More specifically, in this work we assume GPS as the transmitting GNSS, while GOLD-RTR is adopted as the airborne GNSS-R receiver (Nogués-Correig, 2007). Additionally, we limit our analysis to GNSS-R equipped with RHCP channel, as it has been proved to be more suited to detect ship targets.

Symbol	Parameter	Value
P_t	Transmitted power	26.61 W
G_t	Transmitting antenna gain	13 dBi
G_r	Receiving antenna gain	15.05 dBi
λ	GNSS wavelength	0.19 m
ϑ	Viewing angle	10°, 20°, 30°
ϑ_s	Zenith scattering angle	Ranging in [0°,85°]
φ_s	Azimuth scattering angle	Ranging in [0°,180°]
h_t	Transmitter altitude	20200 km
h_r	Receiver altitude	10 km (airborne)
A_{sea}	Scattering area	Varying
σ^0_{sea}	Sea scattering coefficient	Evaluated via BA-PTSM
T_a	Receiving antenna noise temperature	99.4 K
T_e	Receiver noise temperature	161.23 K
B_W	Receiver bandwidth	24 MHz
T_i	Incoherent integration time	1 s
T_c	Coherent integration time	10 ms
τ_c	Chip length	977.52 ns

Table 1. List of symbols and corresponding definition and value

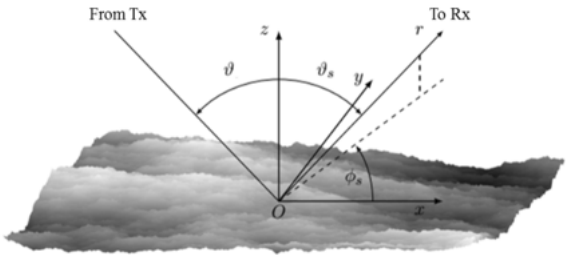

Figure 1. Reference system for incidence and scattering angles definition

Figure 2 (a, c, e) shows the SNR using BA-PTSM as a function of the zenith and azimuth scattering angles and for the viewing angles reported in Table 1. Wind blows along the positive *x*-axis and its speed is set to 15 m/s. As it would be expected, larger SNR values are measured close to the specular reflection direction, identified by a red cross in Figure 2. However, incoherent scattering and the spatial configuration of the resolution cells deviate the peak SNR from the specular direction. Additionally, SNR values larger than 0 dB are obtained not only around the specular reflection direction, but approximately in a cone whose axis gets closer to zenith with increasing viewing angle. In such regions, an accurate modeling of the sea surface return is required as well. It is also worth noting that for viewing angles ranging approximately from 10° to 20°, the backscattered signal is above noise level as well: a proper backscattering model is then required for such angles.

For a better assessment of the accuracy achievable with GO, Figure 2 (b, d, f) shows the ratio in dB between the SNR maps evaluated through BA-PTSM and GO. It is evident that BA-PTSM reduces to GO around the specular reflection direction where scattering from the large-scale roughness dominates. Additionally, for the scope of accurate GNSS-R signals simulation, GO is reliable in a rather limited region around the specular reflection, i.e., for ϑ_s close to ϑ and small values of φ_s. For out-of-plane scattering and backscattering GO is no longer reliable, thus justifying the adoption of more advanced scattering models, such as BA-PTSM, if target detection applications are of interest. More specifically, the SNR ratio map reveals that GO is unreliable in a range of large ϑ_s values whose width increases with increasing φ_s.

5. CONCLUSIONS

In this paper, we presented a link budget analysis for the GNSS-R return from sea surface at arbitrary acquisition geometries, focusing on airborne GNSS-R operating at far-from-specular directions, which proved to be more suited to maritime surveillance applications, e.g., ship detection. We relied on a recent bistatic two-scale scattering model, called BA-PTSM, that allows for fast and accurate evaluation of sea surface scattering in a wider range of bistatic geometries compared to GO. A numerical tool for the evaluation of the scattering sea cell taking into account the receiving antenna beam and the actual configuration of iso-delay and iso-Doppler lines has been implemented as well to estimate the received signal strength.
The link budget analysis has been carried out assuming standard processing chain and an actual airborne GNSS-R receiver, namely, GOLD-RTR.

Numerical results comparing BA-PTSM and GO show that GO is accurate enough for airborne GNSS-R signals simulation only in a limited region around the specular reflection direction, where larger SNR values are expected. However, for simulation of unconventional GNSS-R operating in far-from-specular acquisition geometries more accurate scattering models, such as BA-PTSM, are required. Notwithstanding, it is noteworthy that BA-PTSM reduces to GO in forward-scattering configurations. Accordingly, in the scope of simulation of airborne GNSS-R signals, BA-PTSM can be safely adopted as an efficient and accurate scattering model regardless of the viewing geometry.

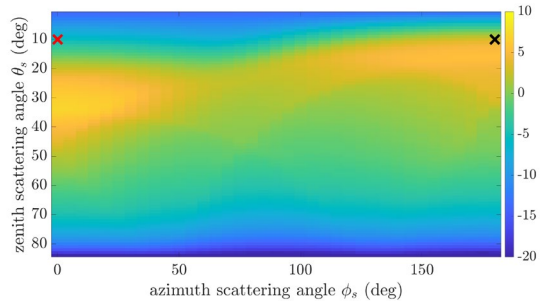

(a)

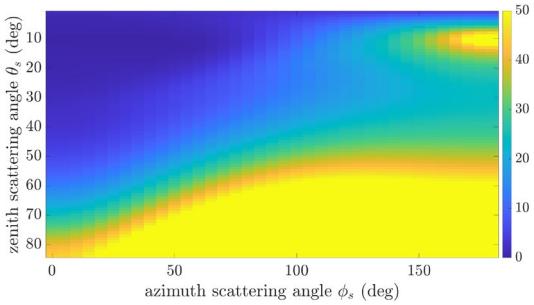

(b)

Figure 2. *cont.*

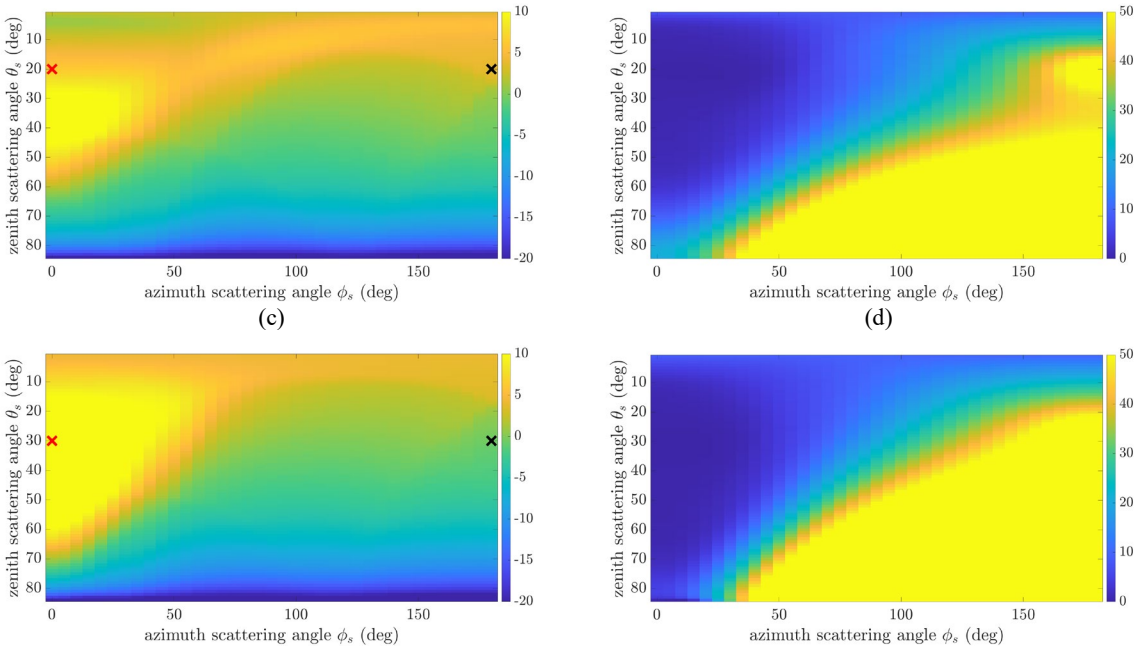

Figure 2. (a, c, e) SNR map in dB obtained using BA-PTSM and (b, d, f) SNR ratio in dB between BA-PTSM and GO, assuming (a)-(b) ϑ = 10°; (c)-(d) ϑ = 20°; (e)-(f) ϑ = 30°. The red and black crosses indicate the specular reflection direction and the backscattering direction, respectively. An airborne GNSS-R receiver working in RHCP has been considered; wind speed is 15 m/s and wind direction is the positive *x*-axis. Remaining simulation parameters are listed in Table 1.

REFERENCES

Beltramonte, T., *et al.*, 2020. Simulation-Based Feasibility Analysis of Ship Detection Using GNSS-R Delay-Doppler Maps. *IEEE J. Sel. Topics Appl. Earth Observ. Remote Sens.*, 13, pp. 1385-1399.

Clarizia, M.P., *et al.*, 2015. Target detection using GPS signals of opportunity. *2015 18th International Conference on Information Fusion*, Washington, DC, pp. 1429-1436.

Di Martino, G., Di Simone, A., Iodice, A., Riccio, D., Ruello, G., 2021a. Simulation of GNSS-R Signals in Arbitrary Viewing Geometry with a Closed-Form Bistatic Two-Scale Model. *2021 IEEE International Geoscience and Remote Sensing Symposium (IGARSS)*, Brussels, Belgium.

Di Martino, G., Di Simone, A., Iodice, A., Riccio, D., 2021b. Bistatic Scattering From Anisotropic Rough Surfaces via a Closed-Form Two-Scale Model. *IEEE Trans. Geosci. Remote Sens.*, 59(5), pp. 3656-3671.

Di Simone, A., *et al.*, 2017a. Sea target detection using spaceborne GNSS-R delay-Doppler maps: Theory and experimental proof of concept using TDS-1 data. *IEEE J. Sel. Topics Appl. Earth Observ. Remote Sens.*, 10(9), pp. 4237–4255.

Di Simone, A., Iodice, A., Riccio, D., Camps, A., Park, H., 2017b. GNSS-R: A useful tool for sea target detection in near real-time. *2017 IEEE 3rd International Forum on Research and Technologies for Society and Industry (RTSI)*, pp. 1–6.

Di Simone, A., Braca, P., Millefiori, L. M., Willett, P., 2018a. Ship detection using GNSS-reflectometry in backscattering configuration. *2018 IEEE Radar Conference (RadarConf18)*, Oklahoma City, OK, pp. 1589-1593.

Di Simone, A., *et al.*, 2018b. Spaceborne GNSS-reflectometry for ship-detection applications: Impact of acquisition geometry and polarization. *2018 IEEE International Geoscience and Remote Sensing Symposium (IGARSS)*, Valencia, Spain, pp. 1071-1074.

Di Simone, A., *et al.,* 2020. Analytical Models for the Electromagnetic Scattering from Isolated Targets in Bistatic Configuration: Geometrical Optics Solution. *IEEE Trans. Geosci. Remote Sens.*, 58(2), pp. 861-880.

Nogués-Correig, O., *et al.*, 2007. A GPS-reflections receiver that computes Doppler/delay maps in real time. *IEEE Trans. Geosci. Remote Sens.*, 45(1), pp. 156–174.

Soldi, G., *et al.*, 2021. Space-Based Global Maritime Surveillance. Part I: Satellite Technologies. *IEEE Aerospace and Electronic Systems Magazine*, in press, DOI: 10.1109/MAES.2021.3070862.

Valenzuela, G. R., 1968. Scattering of Electromagnetic Waves from a Tilted Slightly Rough Surface. *Radio Sci.*, 3, pp. 1057-1066.

Zavorotny, V. U., Gleason, S., Cardellach, E., Camps, A., 2014. Tutorial on remote sensing using GNSS bistatic radar of opportunity. *IEEE Geoscience and Remote Sensing Magazine*, 2(4), pp. 8-45.

EVALUATING THE POTENTIALITIES OF COPERNICUS VERY HIGH RESOLUTION (VHR) OPTICAL DATASETS FOR ASSESSING THE SHORELINE EROSION HAZARD IN MICROTIDAL ENVIRONMENTS

L. Cenci [1 *], V. Pampanoni [2], G. Laneve [2], C. Santella [1], V. Boccia [3]

[1] Serco Italia SpA, Frascati, Italy - (luca.cenci, carla.santella)@serco.com
[2] Sapienza University of Rome, Rome, Italy - (valerio.pampanoni, giovanni.laneve)@uniroma1.it
[3] European Space Agency, Frascati, Italy - valentina.boccia@esa.int

KEY WORDS: Copernicus, Earth Observation (EO), Shoreline Erosion, Coastal Hazard and Risk, Very High Resolution (VHR)

ABSTRACT:

In the past years, several studies have shown that Earth Observation (EO) data can be successfully used for analysing shoreline evolution trends and assessing coastal erosion hazard/risk. Within this framework, the exploitation of long-term archives of sensors data characterised by moderate spatial resolution (e.g., Landsat) has shown its potential; particularly in higher energy coastal environments (e.g., Oceanic areas) where the magnitude of long-term erosion/accretion processes (e.g., decadal) can be resolved by the abovementioned sensors. However, the spatial resolution of these data may prevent an accurate analysis in microtidal coastal environments (e.g., Mediterranean Sea), especially for analyses focused on a short-term period (e.g., few years). This is mainly due to the high level of uncertainty associated with the occurrence of erosion/accretion processes of lower magnitude detected by EO sensors retaining a moderate spatial resolution. Within this context, this work was conceived to evaluate the potentialities of the Copernicus Very High Resolution (VHR) optical datasets (spatial resolution: 2-4 m) for assessing the shoreline evolution trends in an exemplifying urbanised coastal area of the Mediterranean Sea (i.e., Lido di Ostia, Rome, Italy), over a short-term period (i.e., 4 years). To achieve this objective, an automatic technique of shoreline detection and extraction at subpixel level was tested. Results allowed to: i) detect a shoreline evolution trend coherent with the geomorphological characteristics of the study area; ii) smoothly identify/quantify fine-scale variations of accretion/erosion patterns along the coast. This is extremely important to map the areas most exposed to shoreline erosion hazard/risk.

1. INTRODUCTION

In the past years, several studies proved the potentialities of using Earth Observation (EO) data for studying shoreline evolution through time (Apostolopoulos and Nikolakopoulos, 2021). These analyses are fundamental for Integrated Coastal Management (ICM) purposes and objectives: e.g., assessing the shoreline erosion hazard and risk; defining the most appropriate risk adaptation and mitigation strategies; monitoring the impact/effectiveness of coastal protection methods (e.g., hard structures, soft techniques, etc.). In this context, the exploitation of long-term archives of EO data acquired by sensors retaining a moderate spatial resolution (e.g., Landsat) has shown its potential; particularly in higher energy coastal environments (e.g., Oceanic areas) where the magnitude of long-term erosion/accretion processes (e.g., decadal) can be resolved by the abovementioned instruments. However, the spatial resolution of these data may prevent an accurate analysis in microtidal coastal environments (e.g., Mediterranean Sea), especially for short-term analyses (e.g., covering a time period of few years). This is mainly due to the high level of uncertainty associated with the occurrence of erosion/accretion processes of lower magnitude detected by EO sensors retaining a moderate spatial resolution (Cenci et al., 2018).

Considering the well-known issues related to the definition of the "true" shoreline concept, and the consequent practical complexities derived from its identification and mapping, the shoreline evolution through time is usually inferred by observing the advancement/retreat of specific coastal features called shoreline proxies: e.g., the Instantaneous Water Line (IWL), the base/top of bluff/cliff, the Stable Dune Vegetation Line (StDVL), etc. (Boak and Turner, 2005). One of the possible ways to map and monitor shoreline proxies through time is via EO data. In this case, standardised methodologies that guarantee their coherence in space and time should be used (Cenci et al., 2013). This is a fundamental prerequisite for performing reliable multitemporal analyses. The choice of the most suitable proxy to use for a given study area mostly depends on different factors: e.g., the geomorphological characteristics of the coast (e.g., if the dunes and/or the vegetation are present); the methodological approach used for their definition and mapping; the data availability (e.g., in case of EO images, the characteristics of the sensor used for acquiring the data).

Considering that the quantification of shoreline evolution trends (i.e., annual rate or total net movement of advance/retreat) is as reliable as the measurement (σ_m) and positional (σ_p) errors accounted for when mapping the exact position of the proxy, the quantification of the main uncertainty factors associated to the proxy extraction is of paramount importance (Fletcher et al., 2003; Himmelstoss et al., 2018). σ_m is related to operator-based factors, such as data source/s characteristics and data processing (e.g., spatial resolution of the sensor and orthorectification accuracy, in case of EO-based analyses). σ_p is related to the factors influencing the definition of the real proxy position during a given year (e.g., tide and waves influence on the shoreline position etc.). These uncertainties are assumed to be random, not correlated and can be used to quantify an overall total uncertainty (σ_{tot}) (Fletcher et al., 2003).

Within this framework, this work was conceived to evaluate the potentialities of the Copernicus Very High Resolution (VHR) datasets (ESA, 2021) for assessing the shoreline evolution trends in an exemplifying coastal area of the Mediterranean Sea over a short-term period (i.e., 4 years). Considering that the EO

* Corresponding author

data used for the analysis have a spatial resolution (i.e., Ground Sampling Distance - GSD) of ca. 2 m, this work aims at evaluating their potential for performing such analysis in a microtidal environment where the occurrence of erosion/accretion processes of (relatively) low(er) magnitude (e.g., if compared against the ones occurring in Oceanic areas) may be accurately detected by taking advantage of VHR data. Indeed, the images used for the aforementioned analysis are characterised by a (relatively) low(er) σ_m, because this parameter is strongly influenced by the spatial resolution of the instrument used for acquiring the data. This is particularly important for performing the shoreline erosion hazard assessment in coastal zones characterised by a strong anthropic influence, as is usually the case in the Mediterranean area. Indeed, in such places, erosive processes may produce strong economic damages to the exposed assets (e.g., business activities, public and private properties, etc.). To this aim, the analysis presented in this paper was carried out in Lido di Ostia, which is the coastal district of the city of Rome (Italy). As such, the area is characterised by assets potentially exposed to the shoreline erosion hazard and risk. Analysis results were thus interpreted by taking into account the geomorphological characteristics of the coast and in an Integrated Coastal Management (ICM) framework.

2. STUDY AREA AND DATA SOURCE

The study area selected for performing the analysis described in this paper is the coastal area of the city of Rome (Italy): Lido di Ostia (Figure 1). This district is located on the Tyrrhenian Sea and it is ca. 25 km far from the Rome city centre. A detailed description of the study area can be found in Ferrante et al. (1992) and Tomasicchio (1996). Instead, the information most relevant for the presented analyses is summarised below. Lido di Ostia is characterised by a typical Mediterranean climate. The local tidal range is small (i.e., < 0.5 m), but deep-water waves may exceed a significant height of 5 m and a period of 10 s. The longshore current is directed southwards. The littoral (length: ca. 20 km) is composed by sandy beaches, that stretch along the southern delta cusp of the Tiber River. The shoreline continuity is interrupted by a touristic harbour (located in the northernmost part of the study area), and by an artificial channel (width: ca. 20 m) named Canale dei Pescatori (located in the central part of the study area). The geomorphological evolution of the coastal environment has been strongly influenced by the Tiber. From the ‘50s onwards, erosive processes affected the study area. These were mainly originated by the strong reduction of the sediment load transported by the river (due to upstream dams and extraction of building material from the riverbed), with a subsequent deficit in the coastal sand budget. Being Lido di Ostia the *de facto* coastal district of the Italian capital city (i.e., Rome), it is characterised by strong anthropic pressure. This translates into a high concentration of vulnerable assets and economic activities exposed to coastal risk induced by the shoreline erosion hazard. This is particularly true in the northern and in the central parts of the study area, where the coast is strongly urbanised and the dunal/vegetation system has been destroyed and replaced by anthropic buildings and features; thus, removing the natural protection of the beach from coastal risk. Instead, in the southern part of the study area, the natural environment of the coast (including the dunal/vegetation system) have been preserved. In this part, the presence of anthropic assets and economic activities can be considered negligible with respect to the northern and central part. Since the ‘70s, different defence structures and protective strategies were set up in the northern and central parts to reduce the impact of the shoreline erosion hazard on the exposed assets. Hard defence structures were mostly built in the northern part. Instead, soft defence structures and nourishment strategies were typically preferred in the central one. Within this context, it is important to highlight that the inlet of the Canale dei Pescatori acts as a groyne that affects the sediment transport capacity of the longshore current. This generated strong erosion problems in the coastal areas located to the South of the Canale dei Pescatori, that in turn caused economic damages to the beach clubs and even to the littoral road during storm periods.

The satellite data used for performing the analysis described in this paper are part of the Copernicus VHR 2015 and 2018 datasets. The Copernicus VHR datasets provide, every 3±1 years, a cloud-free coverage of Europe (EEA39 area) derived from optical sensors retaining a GSD ranging between 2 and 4 m. The data are acquired by selected Copernicus Contributing Missions (CCMs) during the vegetation season of the reference year of the dataset (e.g., 2015, 2018, etc.), ±1 year for ensuring the full coverage of the target area. All the CCMs have similar characteristics (e.g., in terms of geometric, radiometric and spectral resolutions) and provide multispectral data in the visible (blue, green and red spectral bands) and Near InfraRed (NIR) interval of the electromagnetic spectrum. These data are then processed to generate products geometrically and radiometrically consistent across the same (and other) VHR dataset(s). The latter are then distributed with two different: i) pixel sizes (i.e., 2 and 4 m, according to the different, native GSDs of the sensors used for acquiring the data); ii) processing levels (i.e., ortho-ready and orthorectified). The VHR dataset products are accompanied by comprehensive metadata that provide relevant information to the users, for instance: i) the parameters needed to calibrate the data to Top Of Atmosphere (TOA) radiance and reflectance (ρ); ii) the accuracy of the orthorectification process (expressed in terms of Root Mean Square Error - RMSE), for orthorectified products; etc. Further information about Copernicus VHR datasets can be found in ESA (2021). Concerning the work described in this paper, the images used for performing the analysis were acquired in July 2014 (VHR 2015 dataset) and June, July and August 2018 (VHR 2018 dataset). In the first case, only 1 image was sufficient for covering the whole study area. In the second case, 3 images were required. All the products used for the analysis were distributed with a pixel size of 2 m.

3. METHODOLOGY

Concerning the choice of the coastal feature to use as shoreline proxy, the one selected for the analysis was the IWL: i.e., the position of the beach–sea boundary at an instant in time (Boak and Turner, 2005). With respect to vegetation-based proxy (e.g., StDVL) this feature is characterised by a higher level of uncertainty because its σ_p is influenced by different factors, such as tide and waves effects (Cenci et al., 2018). However, considering the characteristics of the study area (i.e., absence of dunal/vegetation system in the northern and central parts), it was the only viable option.

The following analyses were performed on subset areas of the VHR dataset products. These subsets were obtained by: i) downloading the European Environment Agency (EEA) coastline dataset (from https://www.eea.europa.eu/) as a vector (polyline) layer; ii) clipping it on the extent of the study area; iii) creating a 1 km buffer layer (i.e., 500 m seaward and 500 m landward); iv) using the buffer layer to cut the subsets from all the images. Then, the subset images were calibrated to TOA ρ by using the required information provided in the product metadata. Subsequently, the Normalised Difference Water

Index (NDWI) was computed for every image by using the green and the NIR spectral bands (Bishop-Taylor et al., 2019). Since NDWI values range from -1.0 (land) to 1.0 (water), a threshold value must be defined to identify the beach–sea boundary. To account for possible differences in the radiometric response (i.e., TOA ρ values) of the coastal environment in different acquisition days (e.g., due to diverse atmospheric and weather-related conditions), the Otsu method was used for performing an automatic threshold selection for each product under analysis (Bishop-Taylor et al., 2019). Indeed, this method allowed to coherently extract the same feature (i.e., the IWL), in different images, by using different threshold values identified by exploiting a statistical approach. Consequently, a specific threshold value was computed for every single NDWI image by considering the statistical distribution of its land/water pixels present in the coastal area. To take into account the Otsu assumption of bimodality, the portion of the coastal areas to use for the threshold selection was defined by creating a buffer of 60 m (i.e., 30 m seaward and 30 m landward) from each side of the "first guess" coastline. The "first guess" coastline was extracted by segmenting the NDWI subset image via the K-means algorithm (with K=2). Then, the IWL was automatically extracted with subpixel precision as a vector (polyline) layer, from every NDWI image, by using the marching squares approach with linear interpolation algorithm (Bishop-Taylor et al., 2019). This method linearly interpolates between the NDWI values of neighbouring pixels to identify the exact location of the IWL according to a specified threshold value (i.e., the one that was previously estimated, for every image, via Otsu). Afterwards, the IWL vector layers were edited to remove local inaccuracies due to the extraction processes. Finally, the 3 IWL layers extracted from the VHR 2018 dataset images were merged to create a single IWL referred to 2018. Since the whole 2014 IWL was extracted from a single product, this step was not required for the 2014 case. The overall total uncertainty (σ_{tot}) associated with the 2014 and 2018 IWLs was estimated by following the approach used by Virdis et al. (2012) and Cenci et al. (2018). Consequently, the factors determining σ_m were: i) the spatial resolution error (σ_{sr}); ii) the orthorectification error (σ_o). The factors determining σ_p were: iii) the tidal fluctuation error (σ_t); iv) the wave fluctuation error (σ_w). σ_t and σ_w were taken into account for considering possible fluctuations in IWL positions depending on variations in tide and wave height levels. Although the IWLs were extracted by using a subpixel approach, σ_{sr} was approximated to the pixel size of the images (i.e., 2 m). σ_o was calculated as the mean of the RMSE values reported in the metadata of the products (i.e., 1.96 m). σ_t was estimated as the projection of the standard deviation of the mean tidal level (i.e., 0.09 m) on the beach slope. Tidal measurements were recorded by the Civitavecchia Harbour tide gauge station (located ca. 60 km North of the study area) in the 2011–2020 summertime (i.e., from June to August). Data were downloaded from https://www.mareografico.it/. σ_w was estimated as the projection of the standard deviation of the mean wave height (i.e., 0.38 m) on the beach slope. Wave height measurements were recorded by the Civitavecchia buoy in the 2002–2014 summertime. Data were downloaded from http://dati.isprambiente.it/. For both σ_t and σ_w, the beach slope was obtained by using the Copernicus Digital Elevation Model (COP-DEM) dataset (ESA, 2021; Cenci et al., 2021). More precisely, the EEA-10 (DGED) instance of the COP-DEM dataset was used (spatial resolution: ca. 12 m). The beach slope of the study area (ca. 3°) was estimated as the average slope value computed over the last 15 m before the COP-DEM shoreline (i.e., the boundary between land and sea represented on the COP-DEM). The values attributed to σ_t and σ_w correspond to 1.8 m and 7.26 m, respectively. Following Fletcher et al. (2003), the overall total uncertainty was calculated as the square root of the sum of the squares of all the above-mentioned uncertainty factors (i.e., σ_{sr}, σ_o, σ_t, σ_w). Therefore, $\pm\sigma_{tot}$ value is ±8 m.

The 2014 and 2018 IWLs vector layers were then used to analyse the shoreline net movements and evolution trends along equally spaced transects cast every 2 m perpendicularly to the shore. The elaboration was performed by means of the Digital Shoreline Analysis System (DSAS), a freely available application that works within the ESRI ArcGIS software (Himmelstoss et al., 2018). DSAS allowed us to compute the Net Shoreline Movement (NSM): i.e., the distance between the oldest (2014) and the youngest (2018) IWL for each transect (unit: m). If this distance is divided by the time elapsed between the two proxy positions (i.e., 4 years), the result is the End Point Rate (EPR): i.e., the rate of change associated with the shoreline movements (unit: m/y). In both cases, positive values are associated with transects where the shoreline advanced; negative values are associated with transects where the shoreline retreated. The latter can be linked with areas characterised by erosive processes.

4. RESULTS

The results of the analysis are shown in Figure 1, where the NSM and EPR values of each transect are displayed. A red-to-green colour scale was used to highlight trends of retreat or advancement, respectively. Additionally, a binary colour scale classification was used to identify 2 typologies of transects: "Type 1" are transects whose NSM ranges between $\pm\sigma_{tot}$ (displayed in black); "Type 2" are transects whose NSM is $< -\sigma_{tot}$ or $> +\sigma_{tot}$ (displayed in white).

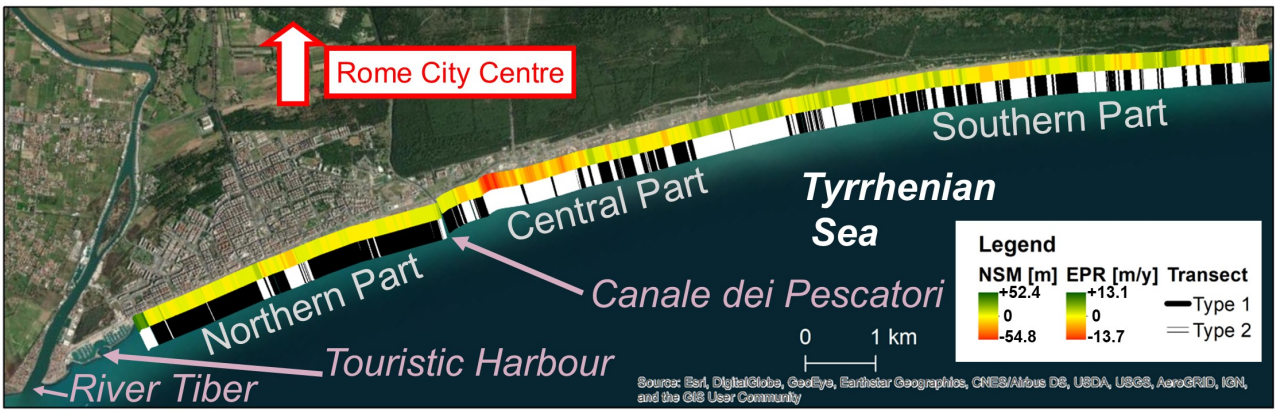

Figure 1 The figure shows the study area and the results of the analysis (i.e., NSM and EPR values associated to each transect).

5. DISCUSSION AND CONCLUSIONS

By observing Figure 1 it can be stated that, in the time period under investigation, the northern part of the study area was characterised by an advancement of the shoreline. This can be mostly explained by the stronger presence of hard defence structures. Nevertheless, the analysis still highlighted some small areas (i.e., cluster of neighbouring transects) characterised by erosive processes, and thus exposed to coastal erosion risk. The strongest shoreline advance was observed in the northernmost part of the study areas, nearby the touristic harbour. The greatest erosive processes, instead, were recorded in the central part of the study area, more precisely South of the Canale dei Pescatori. In the past decades this zone has been known to be affected by shoreline erosion hazard (Ferrante et al., 1992; Tomasicchio, 1996) and, considering the presence of the vulnerable assets, it can be still considered highly exposed to coastal risk. In the remaining part of the central area and in the southern one, an alternation of zones characterised by erosive and accretion processes can be observed, with a prevalence of the latter. Because of the lack of recent studies carried out to evaluate the shoreline evolution dynamics of the study area with analogous methodologies, a quantitative validation of the results was not possible. However, the analysis of NSM and EPR values derived from VHR data allowed us to detect a shoreline evolution trend coherent with the geomorphological characteristics of the study area and previous literature findings (Ferrante et al., 1992; Tomasicchio, 1996). Importantly, the joint exploitation of VHR data and the automatic subpixel approach used for extracting the shoreline proxy allowed us to smoothly identify fine-scale variations of accretion/erosion patterns along the coast. This is extremely important for ICM purposes and objectives. The presented analysis also showed a not negligible percentage of "Type 1" transects: ca. 55%. These transects can be associated with areas in which the differences between the 2014 and 2018 IWL positions can be largely influenced by σ_{tot} factors, rather than associated with proper shoreline evolution dynamics. However, the exploitation of Copernicus VHR datasets allowed us to lower the percentage of "Type 1" transects, by reducing σ_m contribution in σ_{tot}. Since the characteristic of the study area imposed the choice of the IWL as proxy, the (relatively) large(r) contribution of σ_p in σ_{tot} prevented a further reduction of the overall total uncertainty of the analysis, and thus of the percentage of "Type 1" transects.

To conclude, the results of the analysis presented in this paper showed the potential of the Copernicus VHR datasets for shoreline evolution analyses in microtidal environments carried out over a short period of time. Findings also highlighted one of the societal benefits that can be achieved via the Copernicus programme (e.g., to support ICM). Future studies are encouraged to further evaluate the potentialities of the Copernicus VHR datasets for performing analyses similar to the one presented in this paper, but carried out in coastal areas characterised by different environmental characteristics (e.g., mesotidal and macrotidal environments) to: i) confirm the findings of the presented research; ii) evaluate the VHR data potential for multi-proxy analyses, if possible (Cenci et al., 2018). Moreover, follow up activities are also suggested to test the performance of the automatic subpixel approach used for extracting the proxy when applied to EO data characterised by lower spatial resolution but higher temporal resolution (e.g., Sentinel 2 and Landsat data) in similar case studies. Importantly, for these future analyses, shoreline evolution trends obtained by exploiting Copernicus VHR datasets can be used as reference data to validate the results.

ACKNOWLEDGEMENTS

Activity carried out by the Copernicus Coordinated data Quality Control (CQC) service - run by Serco Italia SpA - and La Sapienza University of Rome within the ESA PRISM contract.

REFERENCES

Apostolopoulos, D., and Nikolakopoulos, K., 2021. A Review and Meta-Analysis of Remote Sensing Data, GIS Methods, Materials and Indices Used for Monitoring the Coastline Evolution over the Last Twenty Years. *European Journal of Remote Sensing*, 54(1), pp. 240–265. doi:10.1080/22797254.2021.1904293

Bishop-Taylor, R., et al., 2019. Sub-Pixel Waterline Extraction: Characterising Accuracy and Sensitivity to Indices and Spectra. *Remote Sensing*, 11(24), 2984. doi:10.3390/rs11242984

Boak, E.H., and Turner, I.L., 2005. Shoreline Definition and Detection: A Review. *Journal of Coastal Research*, 21(4), pp. 688–703. doi:10.2112/03-0071.1

Cenci, L., et al., 2018. Integrating Remote Sensing and GIS Techniques for Monitoring and Modeling Shoreline Evolution to Support Coastal Risk Management. *GIScience and Remote Sensing*, 55(3), pp. 355–375. https://doi.org/10.1080/15481603.2017.1376370

Cenci, L., et al., 2013. Geomatics for Integrated Coastal Zone Management: Multitemporal Shoreline Analysis and Future Regional Perspective for the Portuguese Central Region. *Journal of Coastal Research*, 65, pp. 1349–1354. https://doi.org/10.2112/SI65-228.1

Cenci, L., et al., 2021. Describing the Quality Assessment Workflow Designed for DEM Products Distributed via the Copernicus Programme. Case Study: The Absolute Vertical Accuracy of the Copernicus DEM Dataset in Spain. *In: Proceedings of the 2021 IEEE International Geoscience and Remote Sensing Symposium (IGARSS), Brussels, Belgium, 2021*, pp. 6143-6146.

ESA, 2021. Copernicus Space Component Data Access Portfolio: Data Warehouse 2014 - 2022. https://copernicusdata.esa.int/web/cscda/home

Ferrante, A., et al., 1992. Modelling and Monitoring of a Perched Beach at Lido Di Ostia (Rome). *Coastal Engineering 1992*, pp., 3305–3318. doi:10.1061/9780872629332.251

Fletcher, C., et al., 2003. Mapping Shoreline Change Using Digital Orthophotogrammetry on Maui, Hawaii. *Journal of Coastal Research*, 38, pp. 106–124. https://www.jstor.org/stable/25736602

Himmelstoss, E.A., et al., 2018. Digital Shoreline Analysis System (DSAS) Version 5.0. *U.S. Geological Survey Open-File Report 2018–1179*, doi:https://doi.org/10.3133/ ofr20181179

Tomasicchio, U., 1996. Submerged Breakwaters for the Defence of the Shoreline at Ostia Field Experiences, Comparison. *Coastal Engineering 1996*, pp. 2404-2417. doi:10.1061/9780784402429.186

Virdis, S.G.P., et al., 2012. A Geomatics Approach to Multitemporal Shoreline Analysis in Western Mediterranean: The Case of Platamona-Maritza Beach (Northwest Sardinia, Italy). *Journal of Coastal Research*, 28(3), pp. 624–640. doi:10.2112/JCOASTRES-D-11-00078.1

WATER COLOR DATA ANALYSIS SYSTEM FOR COASTAL ZONE MONITORING

F. Filipponi [1]*, C. Ippoliti [2], S. Tora [2], C. Giansante [2], E. Scamosci [3], M. Petrini [3], N. Di Deo [3], A. Conte [2]

[1] ISPRA – Istituto Superiore per la Protezione e la Ricerca Ambientale, Via Vitaliano Brancati 48, 00144 Roma, Italy - federico.filipponi@isprambiente.it

[2] IZSAM – Istituto Zooprofilattico Sperimentale dell'Abruzzo e del Molise "G. Caporale", Campo Boario, 64100 Teramo, Italy – (c.ippoliti, s.tora, c.giansante, a.conte)@izs.it

[3] ARTA Abruzzo – Viale Guglielmo Marconi 178, 65127 Pescara, Germany – (e.scamosci, m.petrini, n.dideo)@ artaabruzzo.it

KEY WORDS: Ocean Color, Water quality, calibration, coastal waters, Sentinel-2 MSI, operational monitoring, Chlorophyll-a, turbidity

ABSTRACT:

Satellite Earth Observation plays a fundamental role within the context of integrated monitoring of coastal and marine waters, providing quantitative estimates of oceanographic and bio-geophysical parameters. Water quality parameters estimated from satellite optical multispectral imaging allow to identify spatial variability of bio-geophysical variables, like near-surface concentrations of Chlorophyll-a (Chl-a) and Total Suspended Matter (TSM), which is higher in coastal areas due to riverine freshwater input, sediment resuspension processes, human activities, thermal conditions and fine scale circulation patterns.
This research study presents a data analysis system that integrates processing chains to regionally calibrate retrieval algorithms for the estimation of seawater bio-geophysical parameters from various optical multispectral satellite data, and to analyze satellite time series in order to extract meaningful information and maps. A test case for central Adriatic coastal zone has been realized in order to demonstrate the operational capability for monitoring water quality, and depending on this, the nutrient availability and the sanitary status of the farmed species in aquaculture sites. In situ data, acquired within a monitoring sampling plan that ARTA Abruzzo carried out along the central Adriatic coast, have been used to calibrate retrieval algorithms, exploited to produce time series maps of Chl-a and turbidity. Results show performances of calibrated algorithms and the data system suitability to contribute to the production of monitoring maps and indicators, informing domain specific decision making and supporting services for integrated coastal zone management.

1. INTRODUCTION

Satellite Earth Observation plays a fundamental role within the context of integrated monitoring of coastal and marine waters, providing quantitative estimates of oceanographic and bio-geophysical parameters. Satellite multispectral and hyperspectral optical sensors can be used to retrieve inherent optical properties (IOPs) of waters, representing information that depend only on the dissolved and suspended substances in water. Bio-optical models, used to quantitatively estimate water characteristics from satellite radiometry, usually group the huge variety of water constituents into three classes, namely coloured dissolved organic matter, phytoplankton, and non-algal particles, on the base of their contributions to the absorption an the backscattering of the water body (Giardino et al., 2019).
Water quality parameters are typically estimated from moderate resolution imaging acquired by optical multispectral satellite sensors, daily sensing the Earth surface, equipped with spectral bands to sense the specific absorption of chlorophyll-a, the absorption of coloured dissolved organic matter and the specific absorption and backscattering of non-algal particles. Spatial variability of bio-geophysical variables, like near-surface concentrations of Chlorophyll-a (Chl-a), Total Suspended Matter (TSM) and turbidity, is higher in coastal waters due to riverine freshwater input, sediment resuspension processes (Filipponi et al., 2015a), human activities, thermal conditions and fine scale circulation patterns (Filipponi et al., 2015b). Concentration of Chl-a, the photosynthetic pigment of phytoplankton species, is a common proxy of the trophic status in the water bodies. The dynamics of phytoplankton biomass, and particularly harmful blooms or the bloom effects caused by river discharge (Garcia et al., 2016), are major stressors impacting the aquatic food web and habitats, biogeochemical cycles, and aquaculture. Turbidity is specifically listed as a mandatory parameter to be measured for water quality monitoring by EU member states in the Marine Strategy Framework Directive. Suspended particulate matter is the parameter of main interest in sediment transport studies, while turbidity should be preferred as an effective indicator of water quality and, being an optical property, is more tightly related to the backscattering coefficient and thus to reflectance than is the estimated suspended particulate matter (Dogliotti et al., 2015). In order to comprehensively monitor coastal zones from space, medium spatial resolution data should be complemented with satellite high spatial resolution optical multispectral data, despite their reduced revisit time. Generally speaking, considering the high spatial variability in coastal areas, local calibration of retrieval algorithm with in situ data is required to accurately estimate concentrations of near-surface parameters. Proper atmospheric correction procedure plays a key role in the accurate estimation of IOPs, especially for very turbid waters. It is typically assured by medium resolution optical multispectral sensors onboard satellites, like Moderate Resolution Imaging Spectroradiometer (MODIS), Visible Infrared Imaging Radiometer Suite (VIIRS), MEdium Resolution Imaging Spectrometer (MERIS) and Ocean and Land Colour Instrument (OLCI), with specific spectral bands configuration designed to generate ocean color products. Sentinel-2 and Landsat-8 satellites, equipped with MultiSpectral Instrument (MSI) and Operational Land Imager (OLI) optical sensors respectively, whose spectral bands perform a more accurate atmospheric correction than spectral bands configuration on previous high resolution optical sensors, open up new opportunities and use

* Corresponding author

scenarios for the monitoring water color from space, thanks to high spatial resolution and a short revisit time.
On the one hand, the Sentinel-2 MSI 5 days revisit time with 10 m spatial resolution of VNIR bands allows fine scale mapping and the extension of water color observation to medium rivers and other small water bodies, on the other hand, Landsat-8 is significantly less affected by sun-glint effects, has the advantage of higher SNR in its 30 m bands, resulting in a less noisy signal for low reflectances characterizing liquid water (Filipponi, 2018).
Among the software tools to process high resolution multispectral data the ACOLITE algorithm, initially developed to perform atmospheric correction over water from Landsat-8 OLI optical multispectral data, and to estimate water constituents from water-leaving reflectances, has been extended for the use of Sentinel-2 MSI data and other optical multispectral sensors (Vanhellemont et al., 2019). Recently, SWIR bands have been used to extend the existing turbid water atmospheric correction of the ACOLITE algorithm to extremely turbid waters. Atmospheric correction based on SWIR bands has been demonstrated to retrieve more accurate water-leaving reflectances over extremely turbid waters, and to improve the algorithm for detecting black suspended sediments from dredging and dumping operations (Vanhellemont et al., 2015). ACOLITE algorithm allow to perform sun-glint correction over water surface, that typically affects Sentinel-2 MSI acquisitions at mid-latitude, especially nearby summer solstice period. The C2RCC algorithm, developed to estimate water quality parameters from optical multispectral data acquired by many different satellite sensors, relies on a large database (derived from in-situ measurements) of radiative transfer simulations inverted by neural networks. C2RCC has been validated for different sensors, with good results for optically complex waters (i.e. Case2 coastal waters), and additional neural nets have been trained for extreme IOP ranges (Brockmann et al., 2016). It has been designed to be easily adapted to local site conditions, by suppling a set of calibrated coefficients to be used for the estimation of water quality parameters from IOPs.
Earth Observation emerged as an essential tool for monitoring water quality and maritime spatial planning (Zanuttigh et al., 2015), in example for monitoring nutrient availability in coastal waters and the sanitary status of the farmed species in aquaculture sites. Earth Observation operational products, locally calibrated for coastal waters, may represent spatially explicit information that complement in situ monitoring plans.
This research study presents the Water Color Data Analysis System (WC-DAS), a tool for operational generation of maps and indicators useful in the monitoring of water quality. The tool is available at repository https://github.com/ffilipponi/WCDAS. Operational capability for monitoring water quality is demonstrated with locally calibrated C2RCC algorithm, using in situ data acquired within a monitoring sampling plan carried out along the central Adriatic coast.

2. DATA ANALYSIS SYSTEM

2.1 Data Analysis System

A Water Color Data Analysis System (WC-DAS) has been developed in order to provide end users with an operational tool to promote the operational generation of maps and indicators useful in the monitoring of water quality.
The WC-DAS facilitates data processing of satellite optical multispectral data acquired by Sentinel-3 OLCI, Sentinel-2 MSI and Landsat-8 OLI sensors. Users can optionally provide a set of calibrated parameters to process a list of input satellite data.
The algorithms Case 2 Regional CoastColour (C2RCC) (Brockmann et al., 2016) and Atmospheric Correction for OLI 'lite' (ACOLITE) (Vanhellemont et al., 2016) are implemented: they perform atmospheric correction to derive water-leaving reflectances from Top-Of-Atmospere reflectances, that are later used for water quality parameters estimation. Both algorithms present strengths and weaknesses, users may select which algorithm to use, depending on specific needs and site conditions. WC-DAS allows to select the neural net set to be used by C2RCC algorithm, and to optionally keep intermediate products like water-leaving reflectances and IOPs (i.e. absorption of pigments or backscattering of solid particulates).
Regional calibration of coefficients, desirable by retrieval algorithms for an accurate estimation of seawater bio-geophysical parameters considering local conditions, can be performed in order to generate a set of coefficients that can be later supplied for operationally deriving calibrated water quality maps. This research study specifically uses WC-DAS to locally calibrate coefficients for the estimation of Chl-a and turbidity maps using C2RCC.

2.2 Study area and datasets

Study area is located in central Adriatic Sea, it corresponds to the coastal area of the Abruzzo region of Italy (Figure 1). It is a characterized by sedimentary processes, like river plume dispersion and sediment resuspension from seafloor, coastal eutrophication during summer period and longshore dominant current.

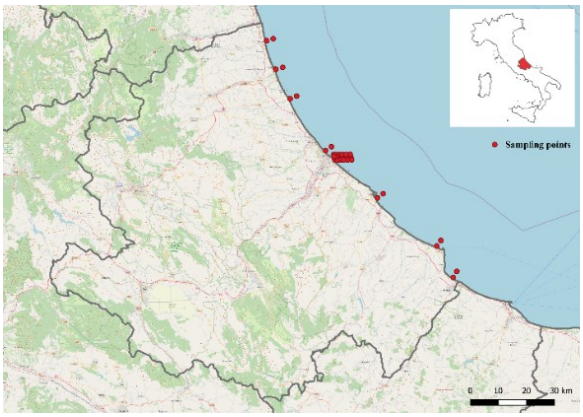

Figure 1. Map of the study area. Red dots represent location of in situ sampling sites.

In situ data used to calibrate coefficients for the estimation of Chl-a concentration and turbidity were collected by Agenzia Regionale per la Tutela dell'Ambiente (ARTA) Abruzzo during the period 2018-2020 at 34 different geographic location in the study area (Figure 1). A total of 238 near surface water measurements were acquired using multiparameter water probes during coastal water quality monitoring activities and ad-hoc sampling campaigns.
A set of 16 Sentinel-2 MSI L1C satellite data, acquired synchronously with in situ measurements and corresponding to tiles T33TVG and T33TVH, have been collected from Copernicus Sentinel Hub and used for the analysis.

2.3 Algorithm coefficients calibration

Calibration of coefficients for Chl-a estimation has been done for deriving Chl-a in C2RCC, using pigments absorption IOP estimated from water-leaving reflectances, according to formula:

$$Chl = fac * (A_{pig}{}^{exp}) \text{ [mg * m}^{-3}\text{]} \quad (1)$$

where fac = factor coefficient
A_{pig} = phytoplankton pigments absorption (m^{-1})
exp = exponent coefficient

The turbidity retrieval algorithm selected for this study makes use of both red (λ = 665nm) and near infrared (λ = 865nm) bands, the latter demonstrated to have higher pure water absorption (Kou et al., 1993) and avoid saturation at lower wavelengths in sediment-dominated waters with moderate to high turbidity in coastal and estuarine waters. The estimates from the two bands are retrieved separately and later blended using a linear weight for ρ_w(665 nm) range between 0.05 and 0.07 (Dogliotti et al., 2015). Turbidity is estimated according to formula (Nechad et al., 2010):

$$Turbidity = \frac{A_T^{\lambda}\rho_W(\lambda)}{(1-\rho_W(\lambda)/C^{\lambda})}\ [FNU] \quad (2)$$

where A_T = wavelength-dependent coefficient
λ= wavelength
ρ_w= wavelength-dependent water-leaving reflectance
C^{λ} = wavelength-dependent coefficient

The two calibration parameters A_T and C^{λ} have very different importance: any errors in calibration of C^{λ} have no impact in the linear regime where the algorithm will mainly be used (Nechad et al. 2010). For this reason, C^{λ} calibrated using standard IOPs data has been used and only A_T coefficient has been calibrated with in situ data.
Turbidity estimates have been demonstrated to have an overall agreement with TSM estimates, even using different retrieval algorithms (Giardino et al., 2017). For this reason, coefficients required for TSM estimation in C2RCC has been calibrated using in situ turbidity values. Turbidity is therefore calculated using particulate and white particles backscatter IOPs, estimated from water-leaving reflectances in C2RCC after performing pixel removal using Quality Flags, according to the following TSM formula:

$$Turbidity = fac * ((B_{part} + B_{wit})^{exp})\ [FNU] \quad (3)$$

where fac = factor coefficient
B_{part} = particulate backscatter (m^{-1})
B_{wit} = white particles backscatter (m^{-1})
exp = exponent coefficient

3. RESULTS

Results from algorithms coefficients calibrations are reported in Table 1. Statistics of fitting are given in the scatter plots in Figures 2-4 as number of samples (n), coefficient of determination (R^2), Root Means Square Error (RMSE) and Mean Absolute Error (MAE).

Parameter	Coefficient	Value
Chl-a	fact	8.6674
Chl-a	exp	0.8233
Turbidity	fact	0.9656
Turbidity	exp	0.6129
Turbidity (B3)	A_T (ρw665)	34.7427
Turbidity (B8A)	A_T (ρw865)	3855.183

Table 1. Calibrated coefficients.

Figure 2 shows the distribution of Chl-a in situ and estimated concentrations using locally calibrated algorithm. Despite calibrated coefficients improved estimates, as compared to standard coefficients, Chl-a estimates still reveal a scattered distribution. This is consistent with results described on a similar case study (Ippoliti et al., 2020) on the same coastal area. It might be related to high turbid waters in the study area due to sediment resuspension and longshore transport, that frames coastal waters as Case2 water where IOPs estimation results in higher uncertainties.

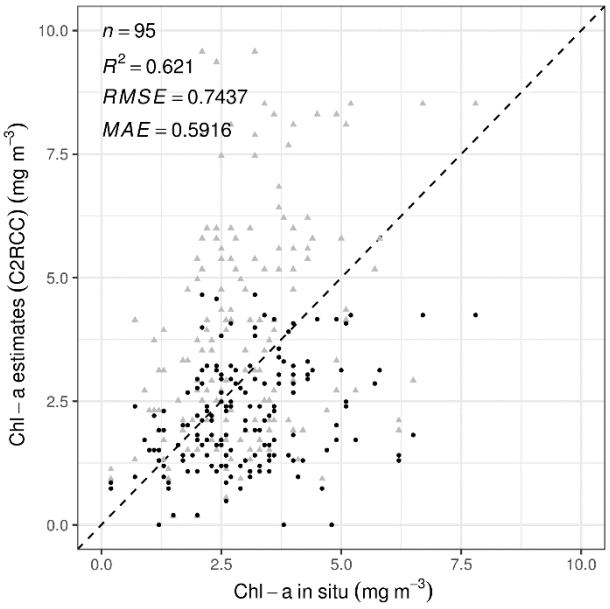

Figure 2. Scatter plot of in situ Chl-a concentrations and Chl-a estimates from Sentinel-2 data using formula (1). Black dots show estimates from calibrated coefficients, grey triangles show estimates using standard coefficients.

Turbidity estimated using two spectral bands calibrated algorithm resulted in more accurate values compared to the use of standard coefficients. The use of particulate and white particles backscatter to estimate turbidity, e.g the TSM formulation available in C2RCC with calibrated coefficients, resulted in an underestimation at higher turbidity values.

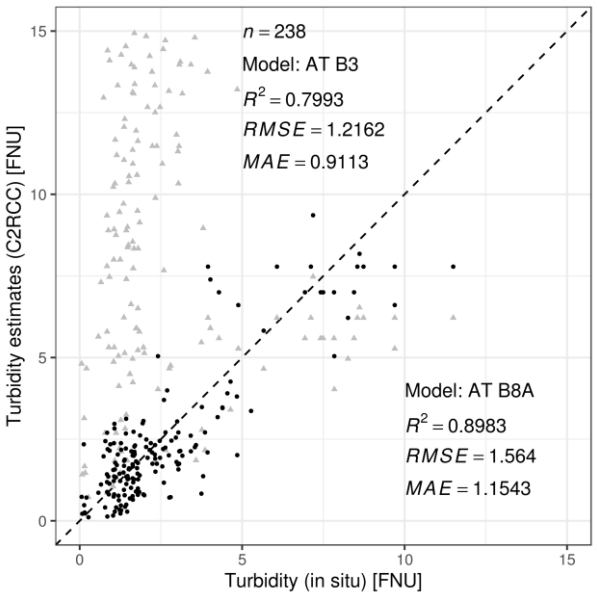

Figure 3. Scatter plot of in situ turbidity concentrations and turbidity estimates from Sentinel-2 data using formula (2). Black dots show estimates from calibrated coefficients, grey triangles show estimates using standard coefficients.

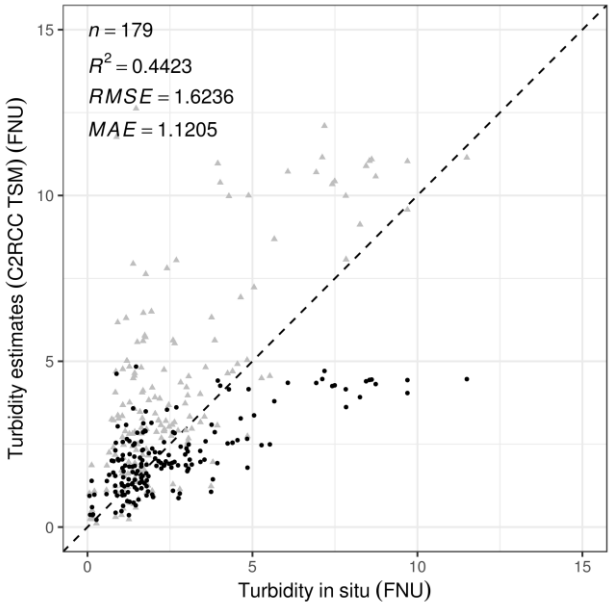

Figure 4. Scatter plot of in situ turbidity concentrations and turbidity estimates from Sentinel-2 data using formula (3). Black dots show estimates from calibrated coefficients, grey triangles show estimates using standard coefficients.

4. CONCLUSIONS

Results demonstrate how calibrated algorithms for the retrieval of water quality parameters in coastal waters allow the generation of more accurate estimates, required for the development of operational and effective monitoring tools. Among future developments of the WC-DAS it is planned the support of additional optical multispectral satellite data. Operational generation of Earth Observation products informs domain specific decision making and supports services for integrated coastal zone management, like water quality monitoring, maritime spatial planning (e.g. aquaculture sites location), environmental assessment and health surveillance.

ACKNOWLEDGEMENTS

This work contains modified Copernicus Sentinel data (2021). The authors are grateful to the many individuals working on the development of free and open-source software for supporting the sharing of knowledge.

REFERENCES

Brockmann, C., Doerffer, R., Peters, M., Kerstin, S., Embacher, S., Ruescas, A., 2016. Evolution of the C2RCC neural network for Sentinel 2 and 3 for the retrieval of ocean colour products in normal and extreme optically complex waters. In *Proc. Living Planet Symposium (ed. Ouwehand, L.), ESA-SP*, Vol. 740.

Dogliotti, A. I., Ruddick, K. G., Nechad, B., Doxaran, D., Knaeps, E., 2015. A single algorithm to retrieve turbidity from remotely-sensed data in all coastal and estuarine waters. *Remote Sensing of Environment*, 156, pp. 157–168.

Filipponi, F., Taramelli, A., Zucca, F., Valentini, E., El Serafy, G.Y., 2015a. Ten years sediment dynamics in northern Adriatic Sea investigated through optical Remote Sensing observations. In *International Geoscience and Remote Sensing Symposium (IGARSS)* (IEEE International), pp. 2265–2268.

Filipponi, F., Zucca, F., Taramelli, A., Valentini, E., 2015b. Total Suspended Matter (TSM) and maximum signal depth (Z90_max) for monitoring the evolution of sediment resuspension processes in shallow coastal environments. In *Proceedings of "Sentinel-3 for Science Workshop", ESA SP,* Vol. 734.

Filipponi, F., 2018. River Color Monitoring Using Optical Satellite Data. *Proceedings*, 2(10), 569.

Garcia, L.E., Rodriguez, D.J., Wijen, M., Pakulski, I., 2016. Earth Observation for Water Resources Management: Current Use and Future Opportunities for the Water Sector. World Bank Group: Washington, DC, USA.

Giardino, C., Bresciani, M., Braga, F., Cazzaniga, I., De Keukelaere, L., Knaeps, E., Brando, V. E., 2017. Bio-optical modeling of total suspended solids. In: *Bio-optical modeling and remote sensing of inland waters* (pp. 129-156). Elsevier.

Giardino, C., Brando, V. E., Gege, P., Pinnel, N., Hochberg, E., Knaeps, E., Reusen, I., Doerffer, R., Bresciani, M., Braga, F., Foerster, S., Champollion, N., Dekker, A., 2019. Imaging spectrometry of inland and coastal waters: state of the art, achievements and perspectives. *Surveys in Geophysics*, 40(3), pp. 401–429.

Ippoliti, C., Tora, S., Giansante, C., Salini, R., Filipponi, F., Scamosci, E., Petrini, M., Di Deo, N., Conte, A., 2020. Sentinel-2 e campionamenti in situ per il monitoraggio delle acque marine dell'Abruzzo: primi risultati. In *Proceedings of the Eighth International Symposium: Monitoring of Mediterranean Coastal Areas, Problems and Measurement Techniques*, pp. 557-568.

Kou, L., Labrie, D., Chylek, P., 1993. Refractive indices of water and ice in the 0.65–2.5 μm spectral range. *Applied Optics*, 32, 3531–3540.

Nechad, B., Ruddick, K. G., Park, Y., 2010. Calibration and validation of a generic multisensor algorithm for mapping of total suspended matter in turbid waters. *Remote Sensing of the Environment*, 114, 854–866.

Vanhellemont, Q., Ruddik, K., 2015. Advantages of high quality SWIR bands for ocean colour processing: Examples from Landsat-8. *Remote Sensing of Environment*, 161, 89–106.

Vanhellemont, Q., Ruddick, K., 2016. ACOLITE for Sentinel-2: Aquatic applications of MSI imagery. In *Proc. Living Planet Symposium (ed. Ouwehand, L.), ESA-SP*, Vol. 740.

Vanhellemont, Q., 2019. Adaptation of the dark spectrum fitting atmospheric correction for aquatic applications of the Landsat and Sentinel-2 archives. *Remote Sensing of Environment* 225, pp. 175–192.

Zanuttigh, B., Angelelli, E., Bellotti, G., Romano, A., Krontira, Y., Troianos, D., Suffredini, R., Franceschi, G., Cantù, M., Airoldi, L., Zagonari, F., Taramelli, A., Filipponi, F., Jimenez, C., Evriviadou, M., Broszeit, S., 2015. Boosting Blue Growth in a Mild Sea: Analysis of the Synergies Produced by a Multi-Purpose Offshore Installation in the Northern Adriatic, Italy. *Sustainability*, 7(6), pp. 6804-6853.

A SELF-ORGANIZING-MAP BASED METHOD FOR FINDING PLASTIC PATCHES ON THE SEA

C. Calledda, A. Montisci*, M.C. Porcu, A. Rashid[1]

University of Cagliari, Cagliari, Italy - car.call86@gmail.com, (augusto.montisci, mcporcu)@unica.it, a.rashid@studenti.unica.it

KEY WORDS: Ocean Garbage Patches, Multispectral Satellite Images, Remote Sensing, Environment Monitoring, Self Organizing Maps, Machine Learning

ABSTRACT:

The presence of waste in the oceans, in particular those made of plastic, now represents an emergency on a planetary scale due to the implications on the ecosystem and directly on human health. The plastic dispersed in the environment is collected by sea currents and tends to accumulate, giving rise to formations as large as continents. At the same time, plastic waste tends to break up, giving rise to the phenomenon of micro-plastics. Due to the sea currents, the problem that originates locally necessarily produces global effects, for which nations are urgently called upon to implement coordinated solutions. A first fundamental step to take is to identify effective methods to identify the sources from which this waste is dispersed. This article presents a method of analysis of multispectral satellite images, based on artificial neural networks, which allow to identify the presence of different percentages of plastics in sea water.

1. INTRODUCTION

For several years, the alarm has been raised for the accumulation of plastic waste in the marine environment, with serious consequences on human health and the entire ecosystem (Ostle et al. 2019, Maximenko et al. 2019). From various studies it emerges that the accumulation of plastic waste is a problem that affects all the marine environments of the planet, as it is noted that the most relevant formations, in particular the Great Pacific Garbage Patch, is constantly expanding (Lebreton et al. 2018). The problem of plastics in the oceans has important effects on the environment and on human health, because of toxic substances and microplastics, which enter the food chain (Rochman et al. 2015). Most plastics originate in coastal areas, where they arrive transported by rivers and bathers, while sea currents are responsible for their transport to the open sea (Willis et al. 2017).

The determination of the distribution of plastics in the oceans is challenging, because except for some particularly critical areas, the debris is very dispersed, and are by their nature subject to transport by currents, wind, heat exchange processes (Zhang 2017). Most of the studies that aim to determine the distribution of plastic debris use in-situ methods, which, although they guarantee high efficiency, require huge economic resources even to explore limited regions. For this reason, remote sensing methods based on satellite images have been proposed (Ge et al 2016, Acuna-Ruz et al. 2018, Arii et al. 2014), which however entail difficulties deriving from the large amount of data to be managed and from the fact that , however high the resolution of the images, they do not allow to identify single objects.

In this article, considering the importance of coastal zone monitoring and the advantages that can derive from the use of satellite images, a method of analysis of multispectral satellite images is presented to identify the characteristics features of plastic debris patches from a multispectral high-resolution satellite images. The aim of the study is to preliminary evaluate the suitability of an analysis, based on unsupervised learning, of one-shot satellite images. The analysis is performed by resorting to a Self Organizing Map (SOM) neural network, by means of which the pixels of the explored area are clustered in the multi-dimensional space which dimensions corresponds to the wavelength of the spectrum. The suitability of the approach is validated by comparing the shape of the clusters with results retrieved from the literature. In particular, the coastal area of Honduras, which has been analysed in (Kikaki et al. 2020), is here considered.

The paper is organized as follows. In section 2 the materials and methods are briefly described. In section 3 the results of the analysis are reported. In section 4 the results are discussed, and some conclusions end the paper.

2. MATERIALS AND METHODS

2.1 Satellite data

The images used are those of Sentinel-2, available free of charge from the Copernicus Hub website (https://scihub.copernicus.eu/). For each shot, reflectance images are available evaluated on 13 different wavelengths, among which there are 7 with the maximum spatial resolution of 10 m. Only these 7 images were used for the present analysis. In general, nothing prevents from using the other images as well, oversampling them in order to obtain all images with the same size. The images correspond to a single acquisition made in June 2021. In the image there is a significant presence of clouds, mostly concentrated on the mainland, so they do not compromise the analysis. From a first inspection, none of the 7 high-resolution images selected show patches in any way attributable to the transport of some material by sea currents. Since the resolution of these images is 10 m, more than the shape of the debris, we can think of tracing the presence of plastic materials present in an area 10m x 10m corresponding to one pixel of the image. In fact, we know that plastic has a very different reflection spectrum of sunlight both from that of water and from that of plant species, which in the visible spectrum could constitute patches that can easily be confused with those of plastic debris (Kikaki et al. 2020). Even more, very often near the coast the patches that can be viewed by satellite are made up partly of plants and partly of plastic debris. Therefore, the multispectral analysis should potentially provide an investigation tool capable of establishing for each pixel the

* Corresponding author

percentage of plastic material contained in the corresponding area.

2.2 Self Organizing Maps (SOM)

The SOM (Kohonen 1982) is a type of Artificial Neural Network (ANN) which makes use of unsupervised learning. The characteristic of this Machine Learning (ML) paradigm is that during the learning phase no correspondence between the patterns and the desired outputs is indicated to the network, but it is the same network that labels the input data on the basis of their distribution in the input space. This type of learning makes it possible to identify properties of a distribution that would otherwise be very complicated to determine, especially when the space in which the distribution is defined has a very large size. Among the properties that one has an interest in determining, there is certainly the possibility of identifying clusters of points. Surveys based on satellite images represent a clear example of a context in which clustering is of particular interest, both because of the size of the data that make up a single instance, and because in general the number of instances is very high (Montisci et al. 2020). In the present work, the instances of the training set are the pixels of the image under examination, each of which is a pattern of 7 components, corresponding to the reflectance in the wavelengths considered. The purpose of the training is to establish pixel clusters, or sub-sets of pixels that can be considered homogeneous and distinguishable from each other. Since clustering is carried out on the basis of reflectances, training carried out in a specific geographical area could represent a valid knowledge base for any other region of the world. Alternatively, through a cluster labelling process using in-situ sample analysis, it is possible to monitor the input of waste over time starting from a specific stretch of the coast. In the specific case, the labelling of the clusters is carried out on the basis of a qualitative analysis of the distribution of pixels belonging to the same cluster and the comparison with literature data relating to the same geographical area (Kikaki et al. 2020).
A very important hyper-parameter in the definition of a SOM is the number of clusters, that is, of outputs of the neural network, which must be defined a priori. Since the number of clusters is generally not known a priori, usually a trial and error procedure is adopted, bearing in mind that if the number of outputs were less than the number of clusters in the distribution, the result will be that different clusters will be aggregated by the network, while if the number of outputs is higher, some outputs will not be populated (dead units), i.e. no instance will be associated with them. The presence of dead units does not represent a disadvantage for the analysis, while the aggregation of distinct clusters into a single sub-set represents a limitation of the information that can be drawn from the distribution, for which it is generally preferred to size the output layer of the neural network in such a way that there is a significant number of dead units or with a very small number of outliers. Furthermore, since the solution depends on an initial randomization of the parameters of the neural network, it is a good practice to carry out several trainings, to check whether clusters tend to be obtained with the same composition.

2.3 Training of SOM

The training set is obtained from the set of pixels of a single image with 7 channels, corresponding to as many wavelengths. The selected image has dimensions 10980x10980 in pixels, for which a total of 120 560 400 patterns are available. To limit the computational complexity, the training set consists of a sub-set of 120 560 patterns, obtained by taking a pattern from the matrix with a regular pitch of 1000, in order to evenly distribute the training pixels on the image. The step was chosen so that it is not a submultiple of the two dimensions of the image, so that the sampled pixels do not all fall on the same column. To verify that the set of points is representative of the entire population, the distribution of the incidence of the different clusters in the training set was compared with that of the entire set, and it was verified that the two distributions were similar. The training continued until it was found that the number of examples among all clusters had settled. Assuming a margin on the number of epochs, training at 200 epochs was interrupted.
Through a series of test training, it was possible to define a number of output neurons equal to 100, arranged on a 10x10 grid. The SOM training algorithm adopts the winner-takes-all criterion, whereby each example is attributed to one and only one cluster. It follows that for each input to the network a 10x10 matrix is calculated at the output of which only one element is equal to 1, while all the other elements are equal to 0.
Once the network learned the training set, a recall is carried out on the entire set, i.e. on all 120 560 400 pixels of the image. The network output assigns each pixel to the cluster whose output turns on, so it is possible to view the distribution of each of the 100 clusters on the image, in order to check which ones can be associated with an agglomeration of plastic debris.

3. RESULTS

Some of the most significant images obtained with the previously described method are analysed below. The maps of the pixels aggregated to the same cluster are compared with one of the images provided by the satellite, from which it is possible to distinguish the mainland from the sea, the presence of clouds, the profile of the coast, and numerous other details. In fact, it is possible to discard a priori many of the clusters as from a quick examination it can be deduced with certainty that they do not represent a cluster of plastic materials, for example because the points are placed on the mainland, or they correspond to cloud formations present in the original image. To choose from the remaining images which indicate the presence of plastic debris in the sea, reference should be made to other information, such as in situ examinations or literature data.

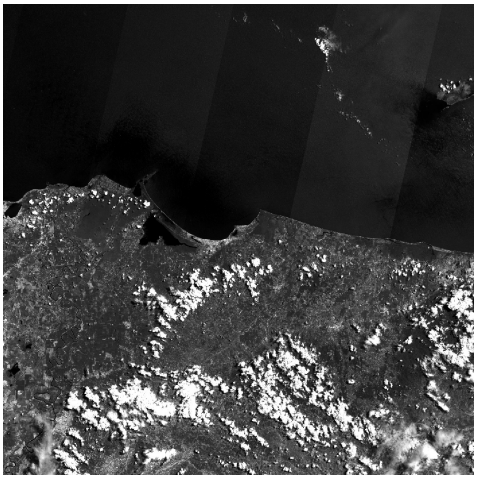

Figure 1 – Reference image (Bay of Tela - Honduras).

Fig. 1 shows one of the 7 monochrome images of the area under examination. The Bay of Tela, in Honduras, is recognized in the centre of the area. Cloud formations can be recognized at the mainland, while some small clouds are present at the top right. Some less obvious details are highlighted by some of the

clusters. As indicated above, the network generates as many maps as the outputs. Here we will report only the most significant ones.
Fig. 2 shows the example of cluster no. 1. From a comparison with Fig, 1 it is clearly seen that the cluster is not significant for our purpose, as the pixels of the cluster all fall in correspondence with the mainland.
Fig. 3, on the other hand, is more interesting. The distribution of the pixels belonging to the cluster are compatible with the flow of debris, with the tendency to leave the central part free, as if an obstacle were present. It can easily be verified that in that point there are rocks at low depth, which can give rise to turbulent currents even on the surface. To complete the verification, and therefore to label the cluster as representative of a plastic patch, an in situ investigation is necessary.

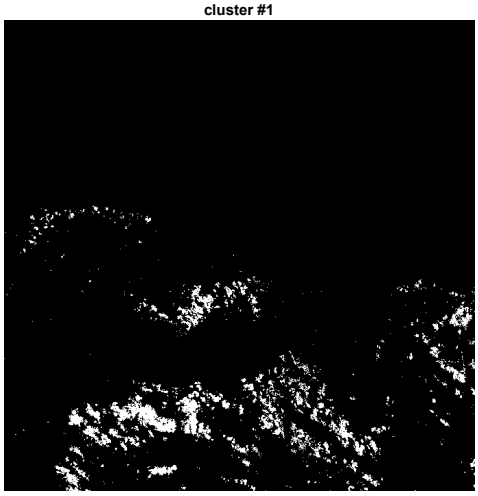

Figure 2 – Cluster no. 1 map. Tall the pixels are on the mainland.

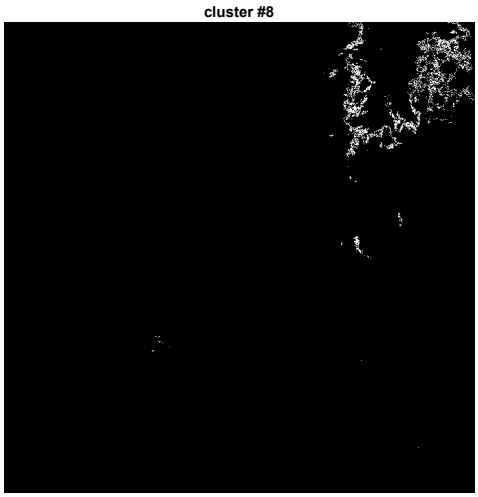

Figure 3 – Cluster no. 8 map. Potentially, pixels could represent a patch of plastic debris.

In Fig. 4 there is a patch similar to the previous one but distributed more uniformly inside it. The fact that clusters of points insist on the same area is consistent with the fact that the reflectance degree of a pixel depends on the amount of plastic present in the corresponding area, of dimensions 10m x 10m, and that presumably the density of plastic debris at the area inside is never evenly distributed within the patch.

In Fig. 5 the map of cluster no. 27 is shown. The cluster is not significant because it aggregates pixels on land and in the sea. The common element of the two areas is the presence of clouds, and in fact clouds can be recognized in correspondence with the area identified in the sea.

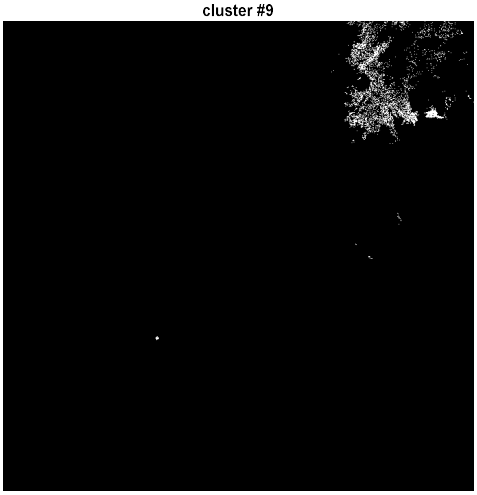

Figure 4 – Cluster no. 8-like formation.

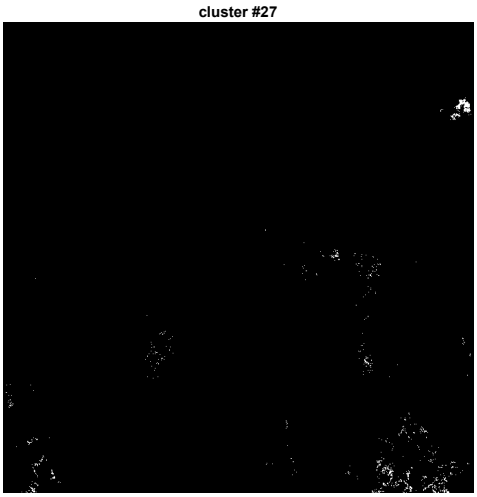

Figure 5- Cluster no. 27 map. It includes both sea and land pixels, therefore it does not correspond to plastic debris.

A particularly interesting cluster is shown in Fig. 6, because it is compatible with the distribution of plastic debris identified for the same area in (Kikaki et al. 2020). The pixels are arranged as if they originated from a precise point on the coast, which can easily be verified corresponds to the mouth of the Lean river.
The cluster no. 70 deployment shown in Fig. 7 is particularly important. One can clearly observe the course of the Ulua river on the left of the image, and in a less defined way other nearby rivers, such as Chamelecon and Tinto. As seen above, rivers are among the main vehicles of plastic debris towards the sea, and here it is observed that the reflectance spectrum of the river is similar to that of a large number of pixels in the sea, distributed in shapes compatible with transport of materials by sea currents. Furthermore, the maximum concentration of pixels of the cluster occurs at the mouth of the river, compatibly with the behaviour of the plastic waste and with the results of the study in (Kikaki et al. 2020).

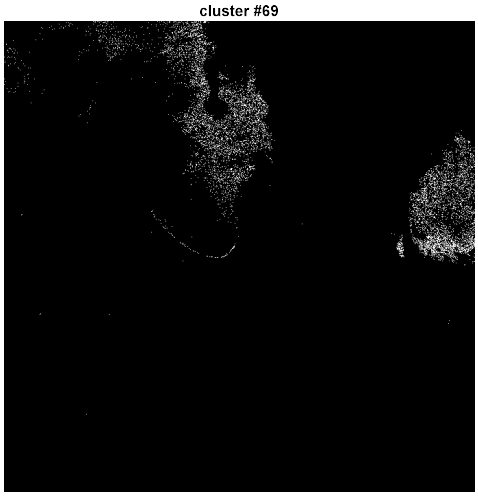

Figure 6 – Cluster no. 69 map. Patches compatible with the transport of materials with the current appear.

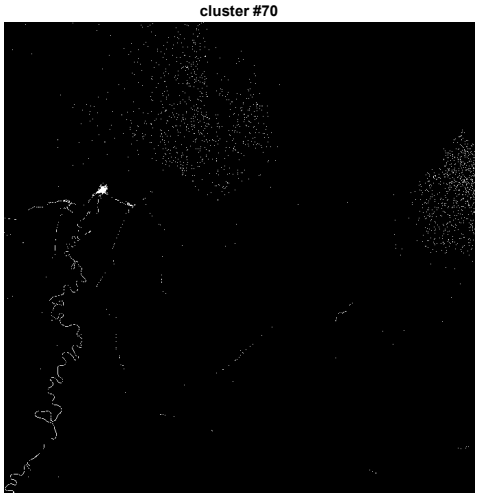

Figure 7 – Cluster no. 70 map. The course of the Ulua river is evident on the left.

4. CONCLUSION

This work represents a preliminary study on the possibility of using the unsupervised learning paradigm to identify Ocean Plastic Debris Patches from multispectral satellite images. The pixels of the image are associated with a pattern consisting of the reflectance spectrum detected by the satellite. Since the reflection spectrum of plastic is different from any other formation found in the sea, it can be used as a feature for identifying patches in the oceans. The purpose of unsupervised learning is to cluster the pixels of satellite images, in order to define homogeneous groups, among which to subsequently identify those associated with the presence of plastics. In principle, once a significant number of clusters have been typed, it is possible to extend the results of the analysis to other geographical areas.

ACKNOWLEDGEMENTS

This research has been funded by the project ARGOSAT, funded by Fondazione di Sardegna (Italy)

REFERENCES

Ostle, C.; et al. 2019. The rise in ocean plastics evidenced from a 60-year time series. *Nature Communications*, 10, pp. 1–6.

Maximenko N., et al. 2019. Toward the integrated marine debris observing system. *Frontiers in Marine Science*, 6, art. 447.

Lebreton, L. et al. 2018. Evidence that the Great Pacific Garbage Patch is rapidly accumulating plastic. *Scientific Reports*, 8, pp. 1–15.

Rochman, C.M., et al. 2015. Anthropogenic debris in seafood: Plastic debris and fibers from textiles in fish and bivalves sold for human consumption. *Scientific Reports*, 5, art. 14340.

Willis K., 2017. Differentiating littering, urban runoff and marine transport as sources of marine debris in coastal and estuarine environments. *Scientific Reports,* 7, art. 44479

Zhang, H. 2017. Transport of microplastics in coastal areas. *Estuarine, Coastal and Shelf Science*, 199, pp. 74–86.

Ge Z. et al. 2016. Semi-automatic recognition of marine debris on beaches. *Scientific Reports,* 6, 1–9.

Acuna-Ruz T. et al. 2018. Anthropogenic marine debris over beaches: Spectral characterization for remote sensing applications. *Remote Sensing of Environment*, 217, 309–322.

Arii, M. et al. 2014. Applicability of Sar to marine debris surveillance after the great east Japan earthquake. *IEEE Journal of Selected Topics in Applied Earth Observations and Remote Sensing*, 7, pp. 1729–1744

Kikaki A. et al. 2020. Remotely Sensing the Source and Transport of Marine Plastic Debris in Bay Islands of Honduras (Caribbean Sea), *Remote Sensing*, 12, art. 1727

Kohonen, T, 1982 Self-organized formation of topologically correct feature maps. *Biological cybernetics*, 43(1), pp. 59-69.

Montisci, A., Porcu, M.C. 2020. Self-organizing-Map Analysis of InSAR Time Series for the Early Warning of Structural Safety in Urban Areas. *Lecture Notes in Computer Science*, 12255, pp. 864-876

Monitoring Forest health

A SPATIAL APPROACH FOR MULTI-TEMPORAL ESTIMATION OF FOREST GROWING STOCK VOLUME AND ABOVEGROUND CARBON POOL. A CASE STUDY IN TUSCANY (ITALY).

Elia Vangi[1,2]*, Giovanni D'Amico[1], Saverio Francini[1,2,3], Costanza Borghi[1], Francesca Giannetti[1], Davide Travaglini[1], Guido Pellis[4], Marina Vitullo[4], Gherardo Chirici[1]

[1]Dipartimento di Scienze e Tecnologie Agrarie, Alimentari, Ambientali e Forestali, Università degli Studi di Firenze
[2]Dipartimento di Bioscienze e Territorio, Università degli Studi del Molise
[3]Dipartimento per la Innovazione nei sistemi Biologici, Agroalimentari e Forestali, Università degli Studi della Tuscia
[4]Istituto Superiore per la Protezione e la Ricerca Ambientale

KEYWORDS: National Forest Inventory, carbon stock, forest modeling, spatial estimation, Italy.

ABSTRACT: Within the United Nations Framework Convention on Climate Change (UNFCCC) and the Paris Agreement's Enhanced Transparency Framework, national greenhouse gas inventories are the key requirement to report GHG emissions by sources and removals by sinks, being the central element of transparency and understanding of the impact of climate mitigation. In this framework, quantitative information about forests plays a pivotal role in national and international monitoring programs and reporting activities. National forest inventories (NFI), complemented by wall-to-wall maps of forest variables, are usually the primary source of such information. NFIs are not designed as monitoring tools, since they are updated only every 5 or 10 years, but models can be used to produce annual carbon stock changes and fluxes. Following the approach of the FOR-EST model we present here a spatial approach to update growing stock volume (GSV) changes for years between national forest inventories, taking Tuscany (Italy) as a case study. The GSV update is mainly driven by the GSV current increment, predicted with forest types-specific growth models derived from yield tables. The spatial-explicit estimation of GSV is based on an initial GSV map, forest types, and forest disturbances maps. The spatial approach has provided comparable results with the original FOR-EST model, reaching a relative root mean square error (RMSE%) of 8.3% against the data reported by Italy under the UNFCCC. We also validated the results of our approach against an independent dataset of 342 circular plots distributed over the study area, measured between 2006 and 2019, reaching a mean RMSE% of 42 % and an R^2 of 0.55 across the years.

1. INTRODUCTION

Updated information about forests are essential in national and international forest inventories, monitoring programs, and reporting activities (FAO, 2015). Under the United Nations Framework Convention on Climate Change (UNFCCC) and under the incoming Enhanced Transparent Framework (ETF) under the Paris Agreement, each Party must report periodically an inventory of its annual anthropogenic greenhouse gases (GHGs) emissions by sources and removals by sinks .

According to the Intergovernamental Panel on Climate Change (IPCC) Guidelines (IPCC, 2006), forestry-related emissions and removals have to be assessed for five carbon pools (i.e. above-ground and below-ground biomass, deadwood and litter, soil), usally acting as carbon sink or source. National Forest Inventories (NFI) are usually the key data source in the estimation process. While NFIs are usually updated every 5-10 years, UNFCCC guidances force the Parties to provide annual forestry-related carbon stock change or flux estimates. To accomplish this goal, there is the need to estimate carbon stock changes in the years between consecutive NFIs, with a methodology based on annually measured forest parameters, rather than a simple interpolation between years (Federici et al., 2008). For such purposes, Federici et al. (2008) developed a methodology to update carbon stock changes in the five UNFCCC carbon pools in Italy, called the FOR-EST model. The FOR-EST is based on NFI GSV data and species-specific growth curves derived from yield tables, used to estimate the annual current increment. The model can estimate the annual GSV at the regional level by adding to the previous year GSV the current increment and subtracting the losses due to natural mortality, harvesting, and forest fires. Finally, the GSV is converted to AGB and then to carbon stock by species-specific parameters.

Nowadays, the NFI ground surveys can be used with remotely sensed data to produce continuous spatial predictions of forest variables (the so-called wall-to-wall maps) (Kangas et al., 2018, Vangi et al., 2021). Wall-to-wall data can be integrated into decision support systems and used to produce small area estimations by aggregating pixel-level predictions. From a retrospective point of view, remote sensing data can provide valuable baseline information for understanding forest dynamics and carbon fluxes changes (Matasci et al., 2018). In this context the Landsat time-series data has valuable potential for studying vegetation trends with an annual/seasonal frequency, thanks to its 30 m spatial resolution, a revisiting time of 16 days, a spectral range between visible and short wave infra-red, and more than 35 years of earth observation missions.

This study aims to estimate annual GSV and above-ground carbon pool for all the years after the last Italian NFI (2005) until 2019 at 23x23 meter spatial resolution in the Tuscany region in central Italy. The approach proposed adapted the FOR-EST workflow carrying out the annual estimation on a spatial basis

2. MATERIALS

2.1 Study area

The study was carried out in the administrative region of Tuscany, in central Italy, which covers 22,992 km^2 (Fig. 1). According to the 2nd NFI (INFC, 2007), Tuscany is the most wooded region in Italy, with forests and other wooded lands covering 1,086,000 ha, about 47% of the region. Forests are dominated by deciduous oaks (*Quercus pubescens* W., *Q. cerris* L.), with 414,000 ha, followed by chestnut (*Castanea sativa* Mill.) (177,000 ha) and European beech (*Fagus sylvatica* L.) (76,000 ha).

* Corresponding author

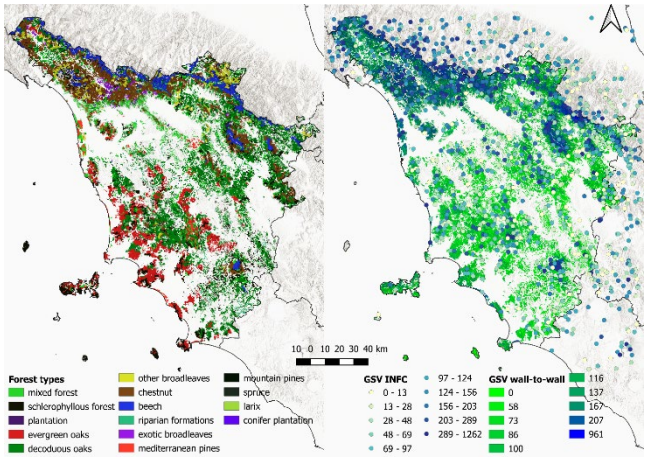

Figure. 1 - Study area. Forest types from CLC 2006 (left); GSV map with NFI field plots used to build it (right).

2.2 2005 GSV map

For the assessment of GSV in the years following the last NFI, we used as initial GSV data the GSV map produced by Chirici et al. (2020) for Tuscany. This map consists of GSV predictions created with the random forests model with Landsat and other predictors at 23m x 23m resolution for all forest pixels. Such pixel size mimics the area of the field plots measured in the field in the NFI program. The pixel-level predictions ranged between 0 and 690 m^3ha^{-1} with a standard deviation of 68.5 m^3ha^{-1}. A more detailed description of the method used to produce the GSV map for 2005 is provided by Chirici et al. (2020).

2.3 CLC IV level

Information and distribution of forest types were derived from the IV level of the Corine Land Cover (CLC) map for the reference years 2006, 2012, and 2018. CLC uses a minimum mapping unit (MMU) of 25 hectares (EEA, 2007). The IV level used in this study were produced by the *Istituto Superiore per la Protezione e la Ricerca Ambientale* (ISPRA). To derive the CLC forest types maps, we first rasterized the vector product to the 23m × 23m spatial resolution of the 2005 GSV map. Then we masked out the non-forest categories by assigning them to the "non-forest" class, retaining the categories 2.2.4 and 3.x, for a total of 18 forest types.

2.4 Yield tables

The collection of national yield tables was used to model the current increment of forests, being the only source that provides both GSV and current volume increment at the regional level (Federici et al., 2008). Yield tables reported the GSV and current increment as a function of forest age for 27 species within 13 genera. The 27 species were linked to CLC forest types with specific harmonization bridges developed for this study, to maintain the characteristics of the data based on different definitions, enabling their comparability at a higher hierarchical level

3. METHODS

3.1 Forest disturbances map

For the multitemporal spatial estimation of GSV, data on the spatial distribution of forest disturbances in the period 2005-2019 were needed. These data were produced with the three indices three dimensions (3I3D) algorithm, developed by Francini et al. (2021). 3I3D is an unsupervised algorithm that requires no input parameters or calibration to predict the probability of forest change by analyzings the trend over three consecutive years of three photosynthetic activity indices (3I) used as the axes of a three-dimensional space (3D). Following this procedure, we used the Best Available Pixel (BAP) procedure (Griffiths et al 2013; White et al., 2014) producing a cloud-free composites for every year to predict all forest disturbances (MMU = 500 m^2) that occurred in the study area over the study period. Using these maps, we calculated for each disturbed pixel the "age" as the number of years since the last disturb using 2019 as the reference year.

3.2 Overwiew of the model

GSV and carbon stock were predicted at the pixel level, using GSV and forest age as unique drivers. The GSV prediction relies on growth models derived from yield tables based on the initial GSV, the forest types distribution and forest disturbances. The spatial prediction of GSV for years not covered by the NFI was accomplished differently for undisturbed forest areas (i.e., those not subject to logging, fire, or other disturbances) and disturbed ones due to the lack of spatial information on the residual GSV after disturbing events. In the former areas, for each year and each CLC forest type, the GSV (referred to GSV_n) was computed from the previous year GSV (GSV_{n-1}) by adding the current increment calculated with the first derivative of the Richards function (Federici et al. 2008). In the latter areas, the GSV_n was calculated as a function of the numbers of years since the last disturbance (forest age), based on the relationships between age and GSV for each CLC forest type, derived from yield tables. The methodologies are described in detail below.

3.3 Models for undisturbed areas: the Richards growth function

Following the original idea of Federici et al. (2008), we used an age-indepentent relation to model the current increment. Types-specific growth models were constructed using data from national yield tables, and the bridges developed *ad hoc*. The first derivative of the Richards function was used to calculate the current increment as a function of GSV. This function is bounded and monotonic with four parameters and is defined by the following equation:

$$y = a \cdot \left[1 - e^{(\beta - kt)}\right]^{-\frac{1}{v}} \quad (1)$$

With the following constraints for the parameters: a, k > 0; $-1 \leq \beta \leq \infty$; $v \neq 0$. In the models building, the GSV represents the independent variable x, while the dependent variable y is the correspondent current increment.

3.4 Models for disturbed areas: polynomial regression

While the age could not be appropriate for estimating the productivity in natural stands, in most disturbed forest stands the regrown trees are in the same age class, forming an even-aged stand, at least for the first years after a disturbing event. This is the case of clearcuts, the most common forest disturbances in the study area. In such a situation, forest age can be used to predict growth at stand level.
To construct types-specific models between age and GSV, a second-order polynomial regression model was chosen.

3.5 GSV and carbon stock estimation

In undisturbed areas, we followed the approach developed by Federici et al. (2008). Starting from the initial GSV (GSV_{n-1}) map produced by Chirici et al. (2020), the current increment per hectare ($m^3\ ha^{-1}\ y^{-1}$) was computed with the Richards function (described in § 3.1) for every CLC forest type, thus obtaining the current increment map for the year *n-1*. For each year, the GSV_n ($m^3 ha^{-1}$) was computed from the previous GSV_{n-1} map adding the current increment map for the year *n-1* and subtracting losses due to natural mortality. The average mortality rate used for the calculation was 0.116%, for evergreen types, 0.117% for deciduous types, and 0.1165% for mixed types, under the GPG for LULUCF (Good Practice Guidance for Land Use, Land-Use Change, and Forestry) (IPCC, 2003).
In disturbed areas, identified by the 3I3D algorithm for each year and each CLC type, the GSV was computed by applying the type-specific growth models described in § 3.2, derived from the yield tables. The age of the disturbed forest for year *n* was used as the independent variable to predict the GSV_n in each disturbed pixel, resulting in a GSV map of forest disturbances for each year between 2005 and 2019.
The final GSV map for year *n* was obtained by overlaying the GSV_n map of the disturbed forest with the GSV_n map of the undisturbed one.
GSV maps were converted to AGB maps to obtain the forest carbon stock map for each year between 2005 and 2019 ($t\ ha^{-1}$), following the approach presented in Federici et al. (2008).
Carbon stock maps were derived by applying the default carbon fraction factor of 0.50 to AGB maps, following the methodology reported in the IPCC guidelines for GHGs inventory (IPCC, 2006). The pixel-level predictions of volume and stored carbon were aggregated at regional level for each year.

3.6 Validation data

To validate the annual GSV estimation results, we used independent field data from 342 circular plots from an independent dataset created for research activities, distributed over the study area and measured between 2006 and 2019. The plots were representative of all forest types in the study area. The mean GSV in the validation dataset is 263 $m^3\ ha^{-1}$, with a standard deviation of 154 $m^3\ ha^{-1}$. The maps' accuracies were evaluated in terms of R^2, bias and relative root mean square error (RMSE%).

4. RESULTS

The total and average values of volume and carbon stock for each year, aggregated at the regional level, are reported in Table 1.
The aggregated results were compared with the output of the FOR-EST model for the same period (2005-2019). We obtained an RMSE% of 8% and 3% and an R^2 of 0.96 and 0.99, respectively for GSV and carbon stock. Based on the spatial approach, the increase in GSV over 2005-2019 was 49 million m^3 moving from an average of 50.5 $m^3\ ha^{-1}$ to 71.8 $m^3\ ha^{-1}$. Carbon stock increased by 574 million t in the same period, moving from 56.9 $t\ ha^{-1}$ to 79.3 $t\ ha^{-1}$. The forest types that mainly contributed were deciduous oaks and chestnut forests, followed by mixed forests and sclerophyll forests.

5. DISCUSSION

The comparison of total carbon stock obtained by the aggregation of pixel level predictions and FOR-EST model is reported in figure 2.

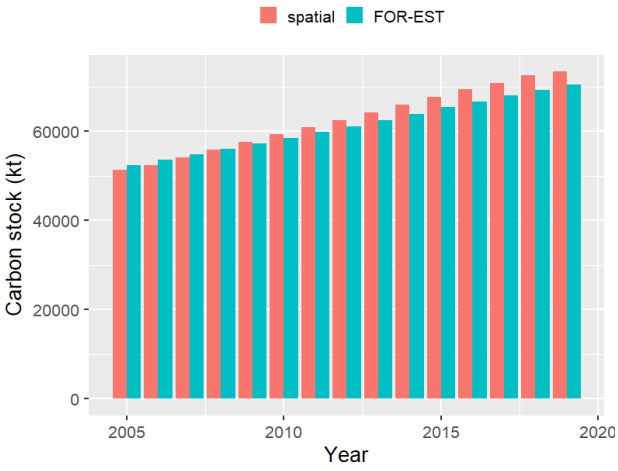

Figure 2 – comparison of the total carbon stock from the spatial approach and FOR-EST model.

Although our approach leads to a progressive overestimation of the total GSV over the years, probably due to the underestimation of current increments combined with the larger forest area of CLC maps than used in the FOR-EST model, these results are very much consistent with the original estimates produced by FOR-EST for the Tuscany region and included by Italy in the official Italian Greenhouse Gas Inventory 1990-2019 (ISPRA, 2021).

Table 1 – Total and mean GSV and carbon stock at regional level over the period 2006-2019

Year	Total GSV (m^3)	Mean GSV (m^3/ha)	Total carbon stock (t)	Mean carbon stock (t/ha)
2006	149105791	133.0	52382916	56.9
2007	155082179	138.3	54078735	58.8
2008	160892582	143.5	55849730	60.8
2009	166806469	148.7	57570615	62.9
2010	172755928	154.1	59315614	64.8
2011	178385510	159.1	60845914	66.7
2012	184028522	164.1	62519046	68.6
2013	189586992	169.1	64187677	70.3
2014	194778958	173.7	65915830	72.1
2015	200192558	178.5	67633748	73.9
2016	205563897	183.3	69381644	75.7
2017	210858665	188.0	70859048	77.6
2018	216270899	192.9	72545155	79.3
2019	221268502	197.3	73380336	79.3

The accuracy assessment against the independent validation set is reported in Figure 3. When we compared our GSV results with the independent dataset we found an R^2 of 0.55, in line with other studies (Immitzer et al., 2016; Chirici et al., 2020) considering that we were not able to use Airborne Laser Scanning (ALS) data, that the Italian forests are very complex and that a high resolution forest map was not available. Furthermore, other limitations of this approach can be listed: the use of outdated yield tables, which probably lead to an underestimation of types-specific current increment, as reported by Federici et al. (2008); the underestimation of forest disturbances, especially in high forests of Apennine areas, where silvicultural treatments are based on continuous canopy cover approaches which are not always visible from satellite images.

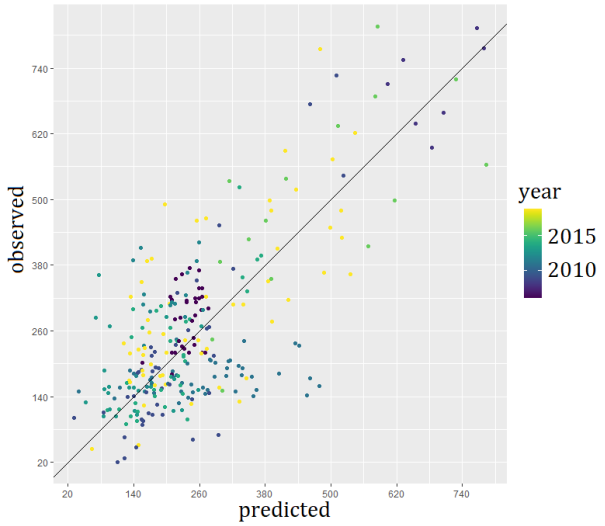

Figure 3 - Predicted against observed GSV for the validation set.

6. CONCLUSION

The proposed approach has provided the first multitemporal spatial estimations of GSV and carbon stock in the study area and it could be applied at a national scale, using the 2005 GSV map produced by Vangi et al. (2021) and integrating the regional databases of forest disturbances (natural or anthropogenic) and yield tables, if available. The approach uses GSV as a unique driver for deriving the above-ground biomass and carbon stock change in areas never disturbed by harvest, fire, or other forest disturbances, representing 93,3% of the total forest land in the investigation period. In disturbed areas it was possible to derive the age of the forest, thanks to the 3I3D algorithm, to apply age-dependent relationships available in yield tables.

The 23m × 23m resolution GSV and carbon stock maps produced in the study can support the requirements of national and regional forest bodies and produce small area estimation, augmenting the spatial resolution of traditional NFI design-based estimates (Chirici et al., 2020).

The availability of the new NFI data (INFC 2015) will provide new important information for the calibration and validation of this approach. The availability of an official high-resolution national forest map and wall-to-wall multitemporal ALS data is also essential to improve the quality of GSV and carbon stock spatial estimations.

7. REFERENCES

Chirici G., Giannetti F., McRoberts R.E., Travaglini D., Pecchi, M., Maselli F., Chiesi M., Corona P., 2020a. Wall-to-wall spatial prediction of growing stock volume based on Italian National Forest Inventory plots and remotely sensed data. Int. J. Appl. Earth Obs. Geoinf. 84, 101959. https://doi.org/10.1016/J.JAG.2019.101959.

D'Amico G., Vangi E., Francini S., Giannetti F., Nicolaci A., Travaglini D., Massai L., Giambastiani Y., Terranova C., Chirici G. (2021). Are we ready for a National Forest Information System? State of the art of forest maps and airborne laser scanning data availability in Italy. iForest 14: 144-154. - doi: 10.3832/ifor3648-014

FAO; UNCCD. Sustainable Financing for Forest and Landscape Restoration: The Role of Public Policy Makers; FAO: Rome, Italy, 2015; p.12.

Federici S, Vitullo M, Tulipano S, De Lauretis R, Seufert G, 2008. An approach to estimate carbon stocks change in forest carbon pools under the UNFCCC: the Italian case. iForest 1: 86-95 [online: 2008-05-19] URL: http://www.sisef.it/iforest/

Francini S., Ronald E. McRoberts, Francesca Giannetti, Marco Marchetti, Giuseppe Scarascia Mugnozza & Gherardo Chirici (2021) The Three Indices Three Dimensions (3I3D) algorithm: a new method for forest disturbance mapping and area estimation based on optical remotely sensed imagery, International Journal of Remote Sensing, 42:12, 4693-4711, DOI: 10.1080/01431161.2021.1899334

Garcia O, 1993. Stand growth models: Theory and practice. In: Advancement in Forest Inventory and Forest Management Sciences. Proceedings of the IUFRO Seoul Conference. Forestry Research Institute of the Republic of Korea, pp. 22-45.

Griffiths, P., van der Linden, S., Kuemmerle, T., and Hostert, P. 2013. A pixel-based Landsat compositing algorithm for large area land cover mapping. Journal of Selected Topics in Applied Earth Observations and Remote Sensing, Vol. 6(No. 5): pp. 2088–2101.

Kangas A., Astrup R., Breidenbach J., Fridman, J., Gobakken T., Korhonen K.T., Maltamo M., Nilsson M., Nord-Larsen T., Næsset E.,et al. 2018. Remote sensing and forest inventories in Nordic countries–roadmap for the future. Scand. J. For. Res. 2018, 33,397–412.

Immitzer M., Stepper C., Böck S., Straub C., Atzberger C., 2016. Forest Ecology and Management Use of WorldView-2 stereo imagery and National Forest Inventory data for wall-to-wall mapping of growing stock. For. Ecol. Manage. 359, 232‑246. https://doi.org/10.1016/j.foreco.2015.10.018.

INFC. Le stime di superficie 2005-seconda parte. In Inventario Nazionale delle Foreste e dei Serbatoi Forestali di Carbonio; Tabacchi,A.G., De Natale, F., Di Cosmo, L., Floris, A., Gagliano, C., Gasparini, P., Salvadori, I., Scrinzi, G., Tosi, V., Eds.; MiPAF–Corpo Forestale dello Stato-Ispettorato Generale, CRA-ISAFA: Trento, Italy, 2007

IPCC (2006). IPCC Guidelines for greenhouse gases inventory. A primer, Prepared by the National Greenhouse Gas Inventories Programme, Eggleston H.S., Miwa K., Srivastava N. and Tanabe K. (eds). Published: IGES, Japan.

ISAFA (2004). RiselvItalia Project. [online] URL: http://www.ricercaforestale.it/riselvitalia/index.htm. Kennedy, R. E., Yang, Z., Gorelick, N., Braaten, J., Cavalcante, L., Cohen, W. B., & Healey, S. (2018). Implementation of the LandTrendr algorithm on google earth engine. Remote Sensing, 10(5), 691.

ISPRA, 2021. National Inventory Report 2021 - Italian Greenhouse Gas Inventory 1990-2019. ISPRA Rapporti341/2021

Matasci G., Hermosilla T., Wulder M.A., White J.C., Coops N.C., Hobart G.W., Zald H.S.J., 2018. Large-area mapping of Canadian boreal forest cover, height, biomass, and other structural attributes using Landsat composites and lidar plots. Remote Sens. Environ. 209, 90‑106. https://doi.org/10.1016/j.rse.2017.12.020.

Vangi E., D'Amico G., Francini S., Giannetti F., Lasserre B.; Marchetti M., McRoberts R.E., Chirici G. The Effect of Forest Mask Quality in the Wall-to-Wall Estimation of Growing Stock Volume. Remote Sens. 2021, 13, 1038. https://doi.org/10.3390/rs13051038

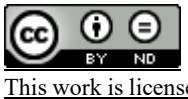

AMAZON FOREST MONITORING USING FULLY CONVOLUTIONAL NEURAL NETWORKS

A. Pugliese [1], V. Yordanov [1,2], B. Delipetrev [3], M. Brovelli [1,*]

[1] Department of Civil and Environmental Engineering (DICA), Politecnico di Milano, Piazza Leonardo da Vinci 32, 20133 Milano, Italy; angellyde.pugliese@mail.polimi.it; (maria.brovelli, vasil.yordanov)@polimi.it
[2] Vasil Levski National Military University, Veliko Tarnovo, Bulgaria
[3] European Commission, Joint Research Centre (JRC), 21027 Ispra, Italy; Blagoj.DELIPETREV@ec.europa.eu
*correspondence: maria.brovelli@polimi.it

KEY WORDS: Land cover, machine learning, Amazon rainforest, earth observation, U-Net.

ABSTRACT:

The aim of this experiment is to classify forest and non-forest areas in the Amazon rainforest in a specific area of interest using documented Fully Convolutional Neural Networks (FCNN) like U-Net, utilizing Google Colab with Keras and TensorFlow as processing tools, and Google Earth Engine (GEE) as a satellite imagery data source and classified training data source.
Several classifications were performed, each one during the period may-august in different years in an approximately 5-year interval, ergo, different satellite missions were considered to cover a long monitoring period, e.g., 20 years. The satellite missions that were used to classify forest land cover are Landsat 5, Landsat 8, and Sentinel 2.
FCNN was trained by patches of 3.87 x 3.87 km² and 1.29 x 1.29 km² for Landsat and Sentinel, respectively, equivalent to 128x128 pixel containing 4 bands: Red, Green, Blue, Near Infrared and a fifth additional band that is the Random Forest (RF) classification which contains the binary labels. This RF classification is performed using the GEE classifier and is taken as the ground truth, therefore, one assumes that RF classification errors can be inherited to the FCNN classification, although, in some cases, it may learn to discard some patterns. The validation of this classification is performed using randomly generated validation points that were manually classified through Collect Earth and high-resolution images, depicting the high goodness of the computed product. The experiment overall produced around 96% accuracy in RF classification and 97% with FCNN.

1. INTRODUCTION

Land cover classification is a very important task as it allows us to monitor the forest change in time. This task was performed using open satellite imagery from Landsat and Sentinel missions, and the classification was a binary one: forest and non-forest. The experiment was performed utilizing Google Colaboratory (Colab), Google Earth Engine (GEE) and Google Cloud Storage, TensorFlow with Keras, QGIS, and the AcaTaMa plugin.

Several classifications were performed, each one during the period may-august in different years in an approximately 5-year interval, ergo, different satellite missions were considered to cover a longer monitoring period. The satellite missions that were used to classify forest land cover are Landsat 5, Landsat 8, and Sentinel 2.

In the following section, the tools used and the process to generate the FCNN models will be described. Then, the results of the classifications, their metrics, and the forest change will be specified for each satellite mission.

2. METHODOLOGY

2.1 Area of interest

The classifications that will be presented are located in an area of interest (AOI) in the Brazilian Amazon in the state of Pará.

According to the Brazilian National Institute for Space Research the state is the most affected by deforestation processes (TerraBrasilis, 2021) and in specific the regions around São Félix do Xingu became an active hotspots for deforestation activities in the last two decades. The main driving forces for those processes are mainly human induced activities related to cattle ranching, construction of infrastructures and land occupations (Jusys, 2016). The AOI has 48657 km².

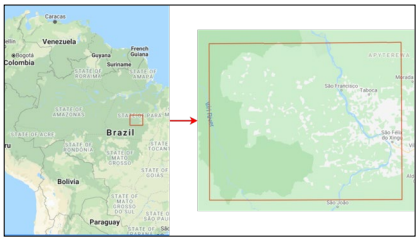

Figure 1. Area of interest

2.2 Processing

The pixel classification of forest and non-forest was done by making the predictions, a set of probabilities per pixel, using a previously trained U-Net model. The classification task can be divided into three: preprocessing, training, and prediction.

The model needs data to train, which is provided as a set of training patches that are produced in the following way: first, we need an already classified raster which will be produced using the Random Forest classifier in GEE (Brovelli et al., 2020) which is taken as the ground truth. Later, this raster was used to randomly generate training and testing sampling points in the AOI which were exported to GEE. Then, we use these sampling points to generate the training and testing patches (Aybar, 2019), which are the description of the neighborhood of each sampling point and are a composite image from may to

* Corresponding author

august of the RGB bands, the near-infrared band (NIR), and an additional band containing the RF classification. Figure 2 shows two views of the training samples of the Landsat 8 mission. On the left the RGB rendering, and on the right the RF classified band.

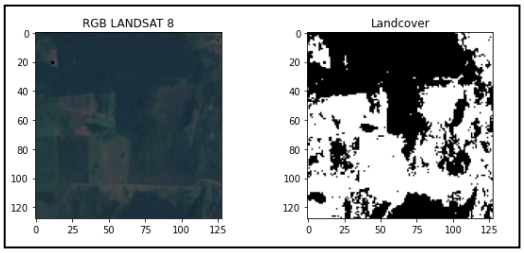

Figure 2. Train patch example

In this first experiment, the kernel size used to construct the patches was 64 pixels to exploit the U-Net architecture, therefore, the patch size is 129x129 pixels, which corresponds to 3.87 x 3.87 km² or 1.29 x 1.29 km² for Landsat and Sentinel respectively. It is calculated using the spatial resolution of each satellite, which is 30m for Landsat and 10m for Sentinel.

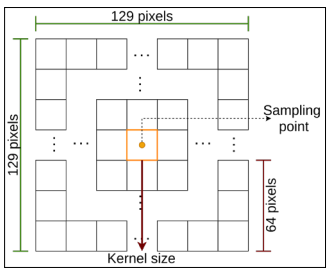

Figure 3. Kernel size and point neighborhood

These generated training and testing patches were used to train a U-Net model (Ronneberger et al., 2015) composed of 4 encoder layers, 4 decoder layers, and one output layer. The loss functions that were used here are the Dice loss function (Milletari, 2016) to measure the overlap between two samples, and the binary cross-entropy function to compare predictions with the testing patches during the training phase. Regarding the optimizer, the chosen one was the Adaptive Momentum (Adam) optimizer (Kingma et al., 2015) due to its excellent performance (Yaqub et al., 2020). A different model was trained for each satellite mission, using their corresponding imagery to generate the training and testing patches as each mission works with different sensors. The training process was done for around 100 epochs for each satellite model.

The predictions were performed using the trained models, one per satellite mission, giving as input a composite image in a specific AOI and time period from the corresponding satellite mission. The prediction output is a set of probabilities of a pixel to be forest, and the final image is constructed by classifying the pixels with probability greater than 50% as forest, and non-forest otherwise.

3. RESULTS

The classification process was performed in the year 2019 using Sentinel 2 and Landsat 8, in the year 2015 using only Landsat 8 and in the years 2010, 2005, and 2000 using Landsat 5. This allows us to cover a 19 year monitoring period and to output the forest gain and loss every 5 years.

The validation of the classification is done using the same high-resolution imagery used to validate the RF classification (Brovelli et al., 2020). For most of the classifications, the accuracy indices that will be considered are user's accuracy, producer's accuracy, overall accuracy, and the Cohen's kappa coefficient (Tung and LeDrew, 1988). The accuracy indices are subject to the availability of validation data in the corresponding year.

3.1 Landsat 8

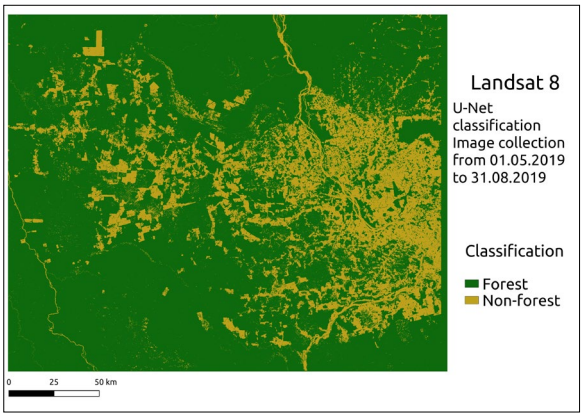

Figure 4. Landsat 8, 2019 classification

Landsat 8 2019	Forest	Non-forest	User accuracy
Forest	553	21	0.96
Non-forest	25	503	0.95
Producer accuracy	0.96	0.96	
Overall accuracy			0.96
Kappa			0.92

Table 1. Landsat 8, 2019 classification indices

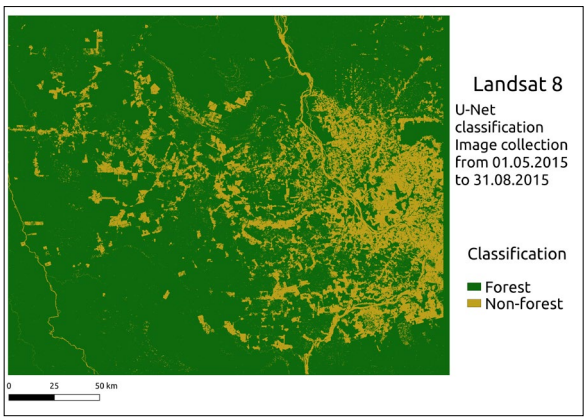

Figure 5. Landsat 8, 2015 classification

Landsat 8 2015	Forest	Non-forest	User accuracy
Forest	570	5	0.99
Non-forest	8	507	0.98
Producer accuracy	0.99	0.99	
Overall accuracy			0.99
Kappa			0.98

Table 2. Landsat 8, 2015 classification indices

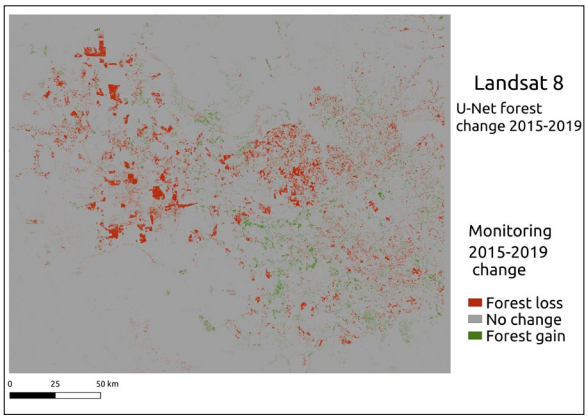

Figure 6. Landsat 8, forest change 2015-2019

3.2 Sentinel 2

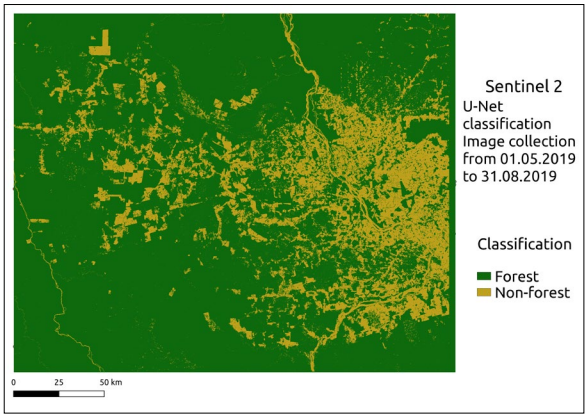

Figure 7. Sentinel 2, 2019 classification

Sentinel 2 2019	Forest	Non-forest	User accuracy
Forest	587	1	1
Non-forest	11	512	0.98
Producer accuracy	0.98	1	
Overall accuracy			0.99
Kappa			0.98

Table 4. Sentinel 2, 2019 classification

3.3 Landsat 5

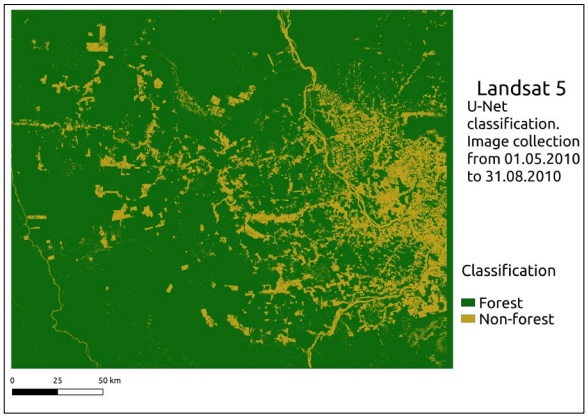

Figure 8. Landsat 5, 2010 classification

Landsat 5 2010	Forest	Non-forest	User accuracy
Forest	578	5	0.99
Non-forest	35	489	0.93
Producer accuracy	0.94	0.99	
Overall accuracy			0.96
Kappa			0.93

Table 5. Landsat 5, 2010 classification

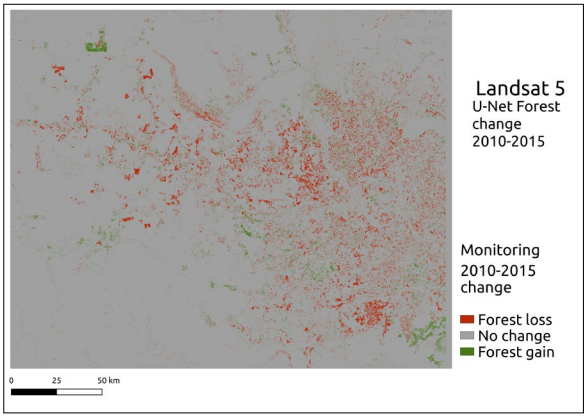

Figure 9. Landsat 8 and Landsat 5, forest change 2010-2015

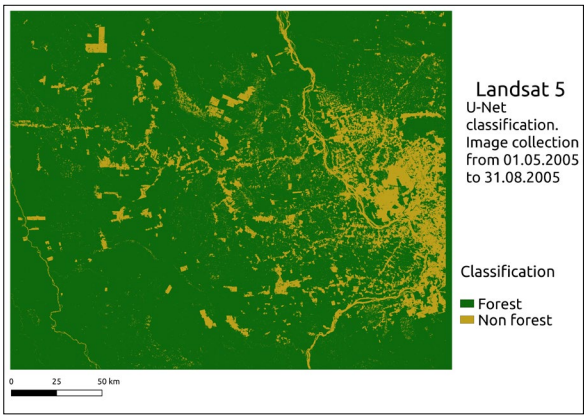

Figure 10. Landsat 5, 2005 classification

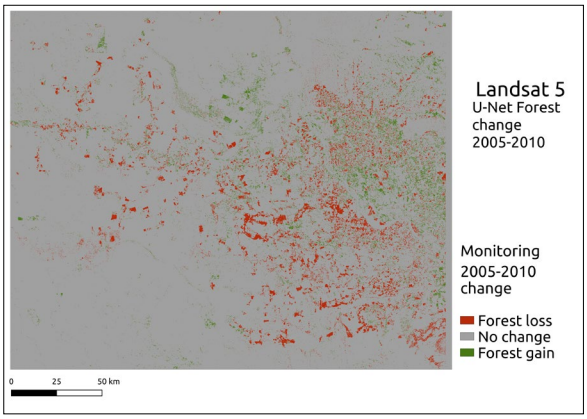

Figure 11. Landsat 5, 2005-2010 forest change

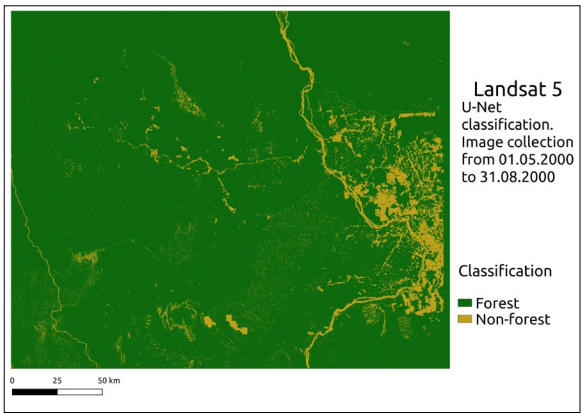

Figure 12. Landsat 5, 2000 classification

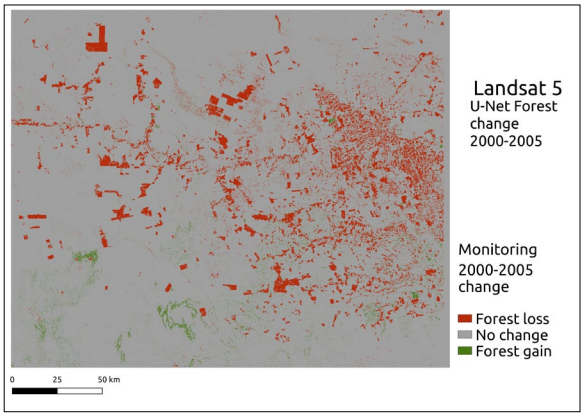

Figure 13. Landsat 5, 2000-2005 forest change

Forest change	Loss (km²)	Gain (km²)
2000-2005	4052	623
2005-2010	2101	1407
2010-2015	2139	825
2015-2019	2101	839

Table 6. Forest change resume

Landsat 8 classifications of 2019 and 2015 output overall accuracies of 0.96 and 0.99 respectively. The results of the 2019 classification can be compared to the Sentinel 2 classification of the same year that outputs an overall accuracy of 0.99 which can be due to the higher spatial resolution. Landsat 5 classifications were performed in 2010, 2005, and 2000. The overall accuracy of the 2010 year was 0.96. For the other two years, there was no high-resolution imagery to validate the results.

The forest change was computed in 4 intervals using the Landsat 8 and Landsat 5 classifications, this is shown in table 6 where the forest loss started with an approximately 4000 km² loss and increased constantly with half the amount during the next monitoring intervals.

The overall accuracy of the whole experiment, computed as the average of each available overall accuracy, was 0.97.

CONCLUSIONS

U-Net FCNN is an excellent approach to binary classification of open satellite imagery. In general, Landsat classifications had a good overall accuracy but Sentinel 2 outperformed them due to, most probably, its higher spatial resolution. Regarding the comparison between RF and U-Net classification, the latter performed slightly better in most of the cases considering that the second was defined to be the ground truth. The average overall accuracy of the U-Net classification was 0.97, while the RF one (Brovelli et al., 2020) was 0.96.

U-Net classification is a good option for ad-hoc classifications where the user wants to personalize parameters, e.g., the number of classes to be classified, the kernel size to get a pixel neighborhood, the availability of good quality training, and validation data. In this first experiment, the kernel size chosen was 64 pixels, in future experiments, smaller kernel sizes, e.g., 32, 16 and 8, will be considered and its accuracies will be compared.

These classifications allowed us to compute the forest change in a 20-year monitoring period with a 5-year frequency. This frequency can be increased to 1 year to have more accurate results.

REFERENCES

Aybar, C., 2019. Integrating Earth Engine with Tensorflow II – U-net. https://csaybar.github.io/blog/2019/06/21/eetf2/

Brovelli, M.A., Sun, Y., Yordanov, V., 2020. Monitoring forest change in the amazon using multi-temporal remote sensing data and machine learning classification on Google Earth Engine. ISPRS International Journal of Geo-Information, 9(10). https://doi.org/10.3390/ijgi9100580

Jusys, T., 2016. Fundamental causes and spatial heterogeneity of deforestation in Legal Amazon. Applied Geography, 75, pp.188-199.

Kingma, D. P., Ba, J. L., 2015. Adam: A method for stochastic optimization. 3rd International Conference on Learning Representations, ICLR 2015 - Conference Track Proceedings. https://arxiv.org/abs/1412.6980v9

Milletari, F., Navab, N., Ahmadi, S.-A., 2016. V-Net: Fully Convolutional Neural Networks for Volumetric Medical Image Segmentation. Proceedings - 2016 4th International Conference on 3D Vision, 3DV 2016, 565–571. http://arxiv.org/abs/1606.04797

Ronneberger, O., Fischer, P., Brox, T., 2015. U-Net: Convolutional Networks for Biomedical Image Segmentation. http://lmb.informatik.uni-freiburg.de/

TerraBrasilis. Available online: http://terrabrasilis.dpi.inpe.br/app/dashboard/deforestation/biomes/legal_amazon/rates (accessed on 09 June 2021).

Tung, F., LeDrew, E., 1988. The Determination of Optimal Threshold Levels for Change Detection Using Various Accuracy Indices. PHOTOGRAMMETRIC ENGINEERING AND REMOTE SENSING, Vol. 54, No. 10, October 1988, pp. 1449-1454.

Yaqub, M., Jinchao, F., Zia, M. S., Arshid, K., Jia, K., Rehman, Z. U., Mehmood, A., 2020. State-of-the-art CNN optimizer for brain tumor segmentation in magnetic resonance images. Brain Sciences, 10(7), 1–19. https://doi.org/10.3390/brainsci10070427

ASSESSING THEMATIC LAND COVER CHANGE OF WORLD'S LARGEST MANGROVE FOREST (SUNDARBANS) USING REMOTELY SENSED DATA

Akbar Hossain Kanan[1]*, Francesco Pirotti[1,2], Mauro Masiero[1]

[1] Department of Land, Environment, Agriculture and Forestry, University of Padova, Italy kanan.sust@gmail.com, francesco.pirotti@unipd.it, mauro.masiero@unipd.it

[2] CIRGEO Interdepartmental Research Center of Geomatics, University of Padova, Italy

KEY WORDS: Sundarbans mangrove, Landsat, Thematic maps, Anthropogenic disturbances, environmental factors

ABSTRACT:

Mangroves forests are distributed in the intertidal region between sea and land in the tropical and subtropical latitudes. The World Heritage Site "Sundarbans" is the largest contiguous mangrove forest of the world. It covers 3% of the global mangroves forest area and is a hotspot for biodiversity conservation, and provides a wide range of ecosystem services for 7.5 million of people. Accurate monitoring of land cover change is key for determining impact on Sundarbans functions. In this study, maximum likelihood classification was performed on Landsat images spanning 45 years with cloud-free images in 1975, 1990, 2005 and 2020 and extracting dense forest, moderate dense forest, sparse forest, barren land and water. After that, change detection was carried out. For accuracy assessment, 100 Ground Control Points (GCPs) were collected and verified with Google Earth historical images. Partial results show dense forest decreasing by 1.3% from 1975 to 2020 mostly converted to moderate and sparse forest. The alteration rate was lowest from 1990 to 2005. The thematic changes from moderate dense to sparse forest increased gradually from 1975 to 2020. Moderate dense to dense forest classes is reported (56741 ha) with significantly higher rate between 1990 to 2005 than others two periods. The annual increment rate of water pixels was 0.58% from 1975 to 2020.

1. INTRODUCTION

Mangroves forests are found in the tropical and sub-tropical areas of the world, and create forest in the intertidal region between sea and land (FAO, 2010). Sundarbans is the largest contiguous mangrove forest of the world. Globally it covers 3% of total mangroves forest (Chanda et al., 2016). Total area of Sundarbans mangroves is 10,000 km^2, where 62% (6,200 km^2) are placed in Bangladesh and rest 38% (3800 km^2) are in India (Ghosh et al., 2015). Sundarbans was a single entity until the partition of India in 1947. Now, this forest is managed separately by Bangladesh and India, but from ecological and socioeconomic perspectives the region is a single unit (Ortolano, et al., 2016).

Sundarbans mangrove forest is a hotspot for biodiversity conservation, and important provider of wide range of ecosystem services (Payo et al., 2016). This ecosystem services includes provisioning (e.g. timber, food, fuel, thatching materials, fibre, fish, crab, honey, wax and so on), regulating (e.g. carbon storage, protection from cyclone, storm and flood), cultural (e.g. recreation and tourism) and supporting services (e.g: habitat for plants and animals, soil formation, nutrient cycling etc.) (Millennium Ecosystem Assessment, 2005). About 3.5 million Bangladeshi and 4 million Indian people directly or indirectly dependent on these ecosystem services (Ortolano et al., 2016; Roy et al., 2013; Giri et al., 2007). Sundarbans provides habitat for wild fauna and flora which is important to maintain coastal biodiversity and ecological integrity (Barbier, 2007). This comprises hosting numerous threatened and endangered species, such as the Royal Bengal tiger, estuarine crocodile, Indian python, and some species of river dolphins (Ortolano et al., 2016). Recognizing the significance and uniqueness of Sundarbans ecosystem, the Sundarbans National Park (SNP) in India and the Sundarbans Reserve Forest (SRF) in Bangladesh have been declared World Heritage Sites by the United Nations Educational, Scientific and Cultural Organization (UNESCO) in 1987 and 1997 respectively. SRF has also been included as a Ramsar site in 1992 (Quader et al., 2017; Rahman et al., 2015; Ghosh et al., 2015).

However, Sundarbans mangrove in Bangladesh and India are decreasing at an alarming rate due to natural and anthropogenic causes. These causes include over exploitation of wood and Non Timber Forest Products (NTFPs), expansion of agricultural (shrimp farming and paddy cultivation) and industrial activities (power plant, ship yard, oil spills from boats and ships, polder construction and so on) sea level rise, salinity, siltation, damage due to cyclones and storm surges (Islam, 2010). Sea level rise is considered the greatest climate change related threat to Sundarbans mangrove regions. Uddin et al., (2013) studied that, about 84% of present dry lands of Sundarbans will be lost due to 88 cm sea level rise in 2100. As a result, the most bio-diverse areas in Sundarbans will be reduced from 60% to 30% in the year 2100 (Uddin et al., 2013). Neogi et al., (2017) also studied that, cyclonic storms are increased by 26% from 1881 to 2001 towards the Sundarbans coastal area. Das and Datta (2016) reported that anthropogenic activities are one of the major causes for ecological degradation of Sundarbans. Giri et al. (2007) reported that Sundarbans mangrove forest area decreased by 1.2% from 1970 to 2000. But, the thematic change detection of Sundarbans is still unknown. In this study we explored thematic land cover change of Sundarbans.

2. METHODOLOGY

2.1 Study site

The Sundarbans are formed on the estuary created by the Ganges, Brahmaputra and Meghna rivers in the Bay of Bengal. Geographically they are located within 21°32′ to 22°40′N and 88°05′ to 89°51′E (Fig 1). About 30% of the Sundarbans is covered by water and shaped by rivers, canals and tidal flows (Nishat et al., 2019). The forest is inundated twice a day by the tide (Barlow et al., 2011), and characterized by a tropical climate with dry and monsoon seasons. During the monsoon,

* Corresponding author

tropical cyclones and smaller tidal events regularly hit the Sundarbans, causing severe flooding and wind damage (Ghosh et al., 2015). We considered the whole Sundarbans Mangrove Forest (including Bangladesh and Indian part) as a study area.

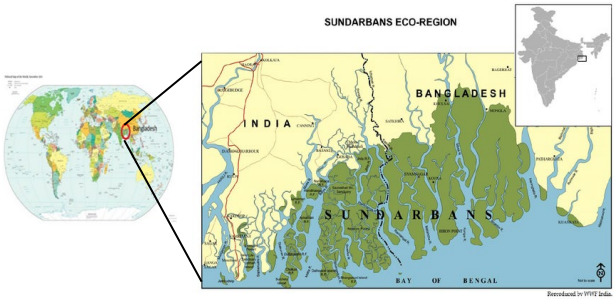

Figure 1. Sundarbans (study area)

2.2 Image collection and pre-processing

We collected Landsat images from the United State Geological Survey (USGS) for the years of 1975, 1990, 2005 and 2020. All the images were acquired between January to February- is the best time to find cloud free images from Landsat for the Sundarbans. Atmospheric and radiometric correction of collected images were completed using Fast Line-of-sight Atmospheric Analysis of Hypercubes (FLAASH) in ENVI 5.3. The FLAASH model includes a method (equation 1 & 2) for minimizing the inconsistency of radiometric and atmospheric (i.e: water vapour, haze, smoke, fog, dust) effect in images (Matthew et al., 2020; Kaufman et al., 1997).

$$L = \left(\frac{A\rho}{1-\rho_e S}\right) + \left(\frac{A\rho_e}{1-\rho_e S}\right) + La \qquad (1)$$

Where, L is the spectral radiance at sensor pixel, ρ is the pixel surface reflectance, ρ_e is an average surface reflectance for the pixel and a surrounding region, S is the spherical albedo of the atmosphere, La is the radiance back scattered by the atmosphere, A and B are coefficients that depend on atmospheric and geometric conditions but not on the surface.

The values of A, B, S and La are strongly dependent on the water vapour column amount. The equation (1) is solved for the pixel surface reflectance in all of the sensor channels. The solution method involves computing a spatially averaged radiance image Le, from which the spatially averaged reflectance ρ_e is estimated using the approximate equation (2):

$$L_e \approx \left[\frac{(A+B)\rho_e}{1-\rho_e S} + L_a\right] \qquad (2)$$

Modified pseudo-invariant features (PIF) method was applied as part of the relative radiometric correction of the scenes of Landsat sensor. The PIF method aims of reducing the inconsistency between different scenes of the same mosaic of images (Quader et al., 2017).

2.3 Image classification, accuracy assessment and mapping

Supervised maximum likelihood classification was performed on the study area at four time periods over 45 years (1975, 1990, 2005 and 2020). The classification assigned the following five classes: dense / moderate / sparse forest, barren land and water.

For accuracy assessment of classified images, we verified 100 Ground Control Points (GCPs) with Google Earth historical images for the study year 1975, 1990, 2005 and 2020. Classification accuracy for the four classified images were computed by kappa coefficients and error matrix (Stehman, 1996). The calculation of kappa coefficients (K) and root mean square error (RMSE) are described in the equations (3) and (4).

$$K = \frac{\left[n\sum_{i=1}^{r} x_{ij} - \sum_{i=1}^{r}(x_i x_j)\right]}{\left[n^2 - \sum_{i=1}^{r}(x_i x_j)\right]} \qquad (3)$$

Where, n is the total of sample, x_{ij} is the total corrected sample, x_i is the column total and x_i is the raw total.

$$RMSE = \sqrt{\frac{\sum_{i=1}^{n}(y_i - x_i)^2}{n}} \qquad (4)$$

Where, y_i is the actual value, x_i is the observed value and , n is the total number of observations.

After the accuracy assessment, the final map were produced for four different study years, and estimated thematic changes of different LULC from 1975 to 1990, 1990 to 2005, 2005 to 2020 and 1975 to 2020.

3. RESULTS AND DISCUSSION

Our finding showed that the annual decreasing rate of dense forest were 1.3% from 1975 to 2020. Most of the dense forests were converted to moderate and sparse forest from 1975 to 2020, however, the annual alternation rate was less from 1990 to 2005 (Fig 2). Giri et al. (2007) stated that Sundarbans mangrove forest area declined by 1.2% from 1970 to 2000. Our study revealed that, degradation was more in east, west and north side than southern part of the Sundarbans. This might be due to less accessibility of forest dependent people. Rahman et al. (2018) reported that, Sundarbans mangrove forest is quickly disappearing and reducing biodiversity at an alarming rate due to encroachment of forest areas and illegal poaching of wildlife.

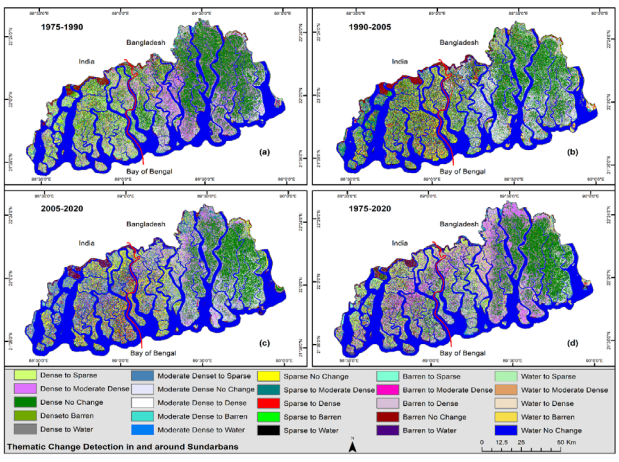

Figure 2. Thematic land cover change of Sundarbans from 1975 to 2020

The thematic changes from moderate dense to sparse forest was increased gradually from 1975 to 2020. But, moderate dense to

dense forest was increased (56741 ha) significantly more from 1990 to 2005 than others two periods (1975 to 1990, 2005 to 2020) (Fig 3). The north-eastern part of Sundarbans constitutes dense forest with Sundri trees (*Heritiera fomes*). However, salinity increase has affected the regular succession patterns and is the primary reason for top dying of Sundri trees in the Sundarbans. About 32% Bangladesh Sundarbans was covered by only Sundri trees in 1959 that reduced to 21% in 1983. The most of the Sundri stand was converted by Sundri-Gewa composition, because, Sundri mostly prefer fresh water zone rather than saline zone (Ahmed et al., 2011). For this reasons most of the dense and moderate dense forest turned into sparse forest.

The significant amount of barren, sparse, dense and moderate dense forests areas turned into water bodies from 1975 to 2020, where, very little areas gained from water (Fig 3). The annual increment rate of water bodies were 0.58% from 1975 to 2020. The gradual increment indicates sea level rise of this area. Nishat et al. (2019) reported that the sea level rise adjacent to the Sundarbans is +3.90±0.46 mm/year. Rahman et al. (2013) reported that, 40-60% mangrove area will be decreased if sea level rise up to 1 m.

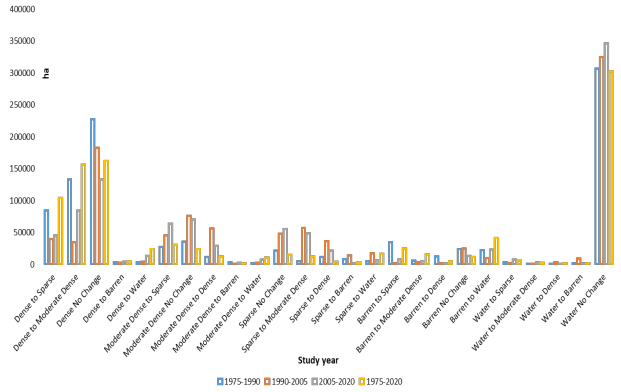

Figure 3. Trend of thematic land cover change of Sundarbans over time

4. CONCLUSIONS

We concluded that the density of the Sundarbans mangrove forest decreasing significantly, where, dense forest turned into moderate dense and then into sparse forest. The zones accessible to human activities are significantly more affected by land cover changes. Therefore, needs strategic planning to control human disturbances along with environmental aspects (e.g., sea level and salinity rise, erosion control).

REFERENCES

Ahmed, A., Aziz, A., Khan, A.N.A., Islam, M.N., Iqubal, K.F., Nazma, Islam, M.S. 2011. Tree diversity as affected by salinity in the Sundarban Mangrove Forests, Bangladesh. Bangladesh Journal of Botany, 40(2), pp. 197-202.

Barbier, E.B., 2007. Valuing ecosystem services as productive inputs. Economic Policy, 22, pp. 177–229. https://doi.org/10.1111/j.1468-0327.2007.00174.x.

Barlow, A.C.D., Smith, J.L.D., Ahmad, I.U., Hossain, A.N.M., Rahman, M., Howlader, A., 2011. Female tiger Panthera tigris home range size in the Bangladesh Sundarbans: The value of this mangrove ecosystem for the species-conservation. Oryx 45(1), pp. 125–128. https://doi.org/10.1017/S0030605310001456.

Chanda, A., Mukhopadhyay, A., Ghosh, T., Akhand, A., Mondal, P., Ghosh, S., Hazra, S., 2016. Blue Carbon Stock of the Bangladesh Sundarban Mangroves: What could Be the Scenario after a Century? Wetlands, 36(6), pp. 1033–1045. https://doi.org/10.1007/s13157-016-0819-7.

Das, G.K., Datta, S., 2016. Man-Made Environmental Degradation at Sunderbans. Reason-A Technical Journal, 13(0), pp. 89. https://doi.org/10.21843/reas/2014/89-106/108127.

FAO, 2010. Global forest resources assessment 2010: main report. Food and Agriculture Organization of the United Nations. Forestry Paper. https://doi.org/ISBN 978-92-5-106654-6.

Ghosh, A., Schmidt, S., Fickert, T., Nüsser, M., 2015. The Indian Sundarban Mangrove Forests: History, Utilization, Conservation Strategies and Local Perception. Diversity, pp. 149–169. https://doi.org/10.3390/d7020149.

Giri, Chandra, Pengra, B., Zhu, Z., Singh, A., & Tieszen, L.L., 2007. Monitoring mangrove forest dynamics of the Sundarbans in Bangladesh and India using multi-temporal satellite data from 1973 to 2000. Estuarine, Coastal and Shelf Science 73, pp. 91-100. https://doi.org/10.1016/j.ecss.2006.12.019.

Islam, D.K.M.N., 2010. Integrated Protected Area Co-Management (IPAC) - A Study of the Principal Marketed Value Chains Derived from the Sundarbans Reserved Forest. USAID, Bangladesh.

Kaufman, Y.J., Wald, A.E., Remer, L.A., Gao, B.C., Li, R.R., Flynn, L., 1997. The MODIS 2.1-□m Channel-Correlation with Visible Reflectance for Use in Remote Sensing of Aerosol. IEEE Transactions on Geoscience and Remote Sensing, 35, pp. 1286-1298.

Matthew, M.W., Adler-Golden, S.M., Berk, A., Richtsmeier, S.C., Levine, R.Y., Bernstein, L.S., Acharya, P.K., Anderson, G.P., Felde, G.W., Hoke, M.P., Ratkowski, A., Burke, H.H., Kaiser, R.D., Miller, D.P., 2000. Status of Atmospheric Correction Using a MODTRAN4-based Algorithm. SPIE Proceedings, Algorithms for Multispectral, Hyperspectral, and Ultraspectral Imagery, 4049, pp. 199-207.

Millennium Ecosystem Assessment. 2005. Ecosystems and Human Well-Being: Current State and Trends. Island Press, Washington DC.

Neogi, S.B., Dey, M., Kabir, S.L., Masum, S.J.H., Kopprio, G., Yamasaki, S., Lara, R., 2017. Sundarban mangroves: diversity, ecosystem services and climate change impacts. Asian Journal of Medical and Biological Research, 2(4), pp. 488–507. https://doi.org/10.3329/ajmbr.v2i4.30988.

Nishat, B., Rahman, A.J.M.Z., Mahmud, S., 2019. Landscape Narrative of the Sundarban : Towards Collaborative Management by Bangladesh and India, 1–207. Retrieved from http://documents.worldbank.org/curated/en/539771546853079693.

Ortolano, L., Sánchez-Triana, E., Paul, T., Ferdausi, S.A., 2016. Managing the Sundarbans region: Opportunities for mutual gain by India and Bangladesh. International Journal of Environment and Sustainable Development, 15(1), 16–31. https://doi.org/10.1504/IJESD.2016.07333.

Payo, A., Mukhopadhyay, A., Hazra, S., Ghosh, T., Ghosh, S., Brown, S., Lázár, A.N., 2016. Projected changes in area of the Sundarban mangrove forest in Bangladesh due to SLR by 2100. Climatic Change, 139, pp. 279–291https://doi.org/10.1007/s10584-016-1769-z.

Quader, M.A, Agrawal, S., Kervyn, M.,2017. Multi-decadal land cover evolution in the Sundarban , the largest mangrove forest in the world. Ocean and Coastal Management, 139, pp. 113–124. https://doi.org/10.1016/j.ocecoaman.2017.02.008.

Rahman, M., Asaduzzaman, M., 2013. Ecology of Sundarban, Bangladesh. Journal of Science Foundation, 8(1–2), 35–47. https://doi.org/10.3329/jsf.v8i1-2.14618.

Rahman, M.M., Jiang, Y., Irvine, K., 2018. Assessing wetland services for improved development decision-making: a case study of mangroves in coastal Bangladesh. Wetlands Ecology and Management, 26(4), pp. 563–580. https://doi.org/10.1007/s11273-018-9592-0.

Rahman, M.M., Khan, M.N.I., Hoque, A.F., Ahmed, I., 2015. Carbon stock in the Sundarban mangrove forest: spatial variations in vegetation types and salinity zones. Wetlands Ecology and Management, 23, pp. 269–283. https://doi.org/10.1007/s11273-014-9379-x.

Roy, A.K.D., Alam, K., Gow, J., 2013. Community perceptions of state forest ownership and management: A case study of the Sundarbans Mangrove Forest in Bangladesh. Journal of Environmental Management, 117, pp. 141-149. https://doi.org/10.1016/j.jenvman.2012.12.004.

Stehman, S.V., 1996. Estimating the kappa coefficient and its variance under stratified random sampling. PE&RS. ASPRS, pp. 401-407.

Uddin, M.S., Steveninck, E.R, Stuip, M., Shah, M.A.R., 2013. Economic valuation of provisioning and cultural services of a protected mangrove ecosystem: A case study on Sundarbans Reserve Forest, Bangladesh. Ecosystem Services, 5, pp. 88–93. https://doi.org/10.1016/j.ecoser.2013.07.00.

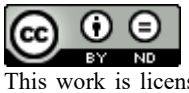

IN SITU (TREE TALKER) AND REMOTELY-SENSED MULTISPECTRAL IMAGERY (SENTINEL-2) INTEGRATION FOR CONTINUOUS FOREST MONITORING: THE FIRST STEP TOWARD WALL-TO-WALL MAPPING OF TREE FUNCTIONAL TRAITS

S. Francini[1,2,3], I. Zorzi[1*], F. Giannetti[1], F. Chianucci[4], D. Travaglini[1], G. Chirici[1], C. Cocozza[1]

[1] Dipartimento di Scienze e Tecnologie Agrarie, Alimentari, Ambientali e Forestali, Università degli Studi di Firenze
[2] Dipartimento di Bioscienze e Territorio, Università degli Studi del Molise
[3] Dipartimento per la Innovazione nei sistemi Biologici, Agroalimentari e Forestali, Università degli Studi della Tuscia
[4] CREA – Research Centre for Forestry and Wood, Arezzo, Italy

KEYWORDS: Tree talker, Sensors, Tree-functional traits, Modelling, Remote Sensing, Deep learning

ABSTRACT:

Monitoring tree functional traits is essential for understanding forest ecosystems' capability to respond to climate change. Advancements in continuous proximal sensors and IoT technologies hold great potential for monitoring forest and tree ecosystem processes at the finest spatial and temporal scale. An example is the TreeTalker (TT) technology, which features sensors for measurements of the radial growth, sap flow, multispectral light transmission, air temperature, and humidity at tree level with an hourly frequency rate. Such information can be linked with remote sensing data acquired by the Sentinel-2 (S2) mission, allowing for scaling results over more spatially extensive areas. Firstly, we compared six TT with four S2 spectral bands with similar wavelengths. No correlation was found for blue, green and red channels (R^2 ranged between 0.04 and 0.09) while higher values were found for the near-infrared channel ($R^2 = 0.9$). To obtain an accurate prediction of TTs bands, also for those TTs bands which wavelengths are not similar to that of S2 bands, we implemented a Sentinel-2 to TreeTalker model (S2TT) by using an 8-layers fully connected deep neural network. The model was tested by using 23 Sentinel-2 imagery and data acquired by 40 TreeTalkers located in two different sites in Tuscany (a beech and a silver fir forest stand) in the period between 2020-07-15 and 2020-11-15. The R^2 ranged between 0.61 (B7, blue) and 0.96 (B6, near-infrared band). The S2TT model represents the first link between remote sensing and TreeTalkers, which might allow predicting tree functional traits using Sentinel-2 imagery.

1. INTRODUCTION

Forests cover approximately 31% of the global terrestrial surface (FAO, 2020) and, in combination with soil organic matter, account for between 40% and 60% of all terrestrial carbon (Pan et al., 2011). As a result, forests have an important mitigation role in controlling the greenhouse gas balance, through carbon sequestration and respiration (Bonan, 2008). While *in situ* measurements are essential to collect forest attributes, the cost- and time-consuming nature of ground measurements inherently prevent the collection of spatially representative and temporally continuous information with field methods. For this reason, combining *in situ* measurements with remotely sensed spectral information (Marcelli et al., 2020) has been of interest since the beginning of optical satellite remote sensing. Recently, a new device named Tree Talker (TT) has been developed to constantly monitor tree level ecophysiological properties (Valentini et al., 2019). TT data acquisition and collection occurs hourly, with data being transmitted in real-time to a server using communication protocols. Although these sensors can benefit from efficient technology to collect and store large amounts of data (Roblek et al., 2016), still several studies consider just a few trees (Nourtier et al., 2014; Oberhuber et al., 2014), limiting the possibility to use TT for complementing and integrating multitemporal, high spatial resolution satellite data for extending results at larger geographical scales.

In this context, remote sensing offers an effective opportunity for TT data spatialization over larger areas (Hawryło et al., 2020). The combination of open access data (Woodcock et al., 2008) and cloud computing platforms such as Google Earth Engine (GEE) (Gorelick et al., 2017) makes the application of complex algorithms for large areas possible (Francini et al., 2021, Giannetti et al., 2020). Moreover, the Copernicus Earth observation program of the European Union developed the Sentinel-2 mission which provides open data with 10-m spatial resolution and revisiting times of 2-3 days at mid-latitudes (with two satellites) (Drusch et al. 2012).

This study aims to create the first link between remote sensing and TTs with the future perspective of tree functional traits spatialization. Firstly, we compared six TT with four S2 spectral bands with similar wavelengths using scatter plots and R^2. Secondly, we developed a deep neural network model for the prediction of TTs bands using Sentinel-2 imagery. The method was tested and validated in the period between 2020-07-15 and 2020-11-15 on 40 TTs located in two different forest sites in Tuscany, central Italy, with contrasting forest structures (deciduous broadleaved versus evergreen coniferous forests).

2. MATERIAL AND METHODS

2.1. Reference dataset construction

2.1.1. TreeTalkers

TTs were installed in July 2020 in two different sites located in Tuscany (central Italy). 20 TTs were installed in a pure silver fir (*Abies alba* Mill) stand in the Vallombrosa forest (43° 44' 14.6"N, 11° 32' 58" E), and 20 in a pure beech (*Fagus sylvatica* L.) stand in Sant'Antonio Forest (43° 42' 49" N,11° 34' 52" E). Detailed information on TTs devices, server, and data storage were given in Zorzi et al. (in review) while information related to wireless sensor network technology was given in Bayne et al., (2017). TTs send more than 30k attributes every single day: 18 variables relative to tree ecophysiological processes (e.g. radial growth, sap flow) and two multispectral sensors (AMS AS7262 and AS7263) featuring 12 bands in the visible near-infrared electromagnetic spectrum. More specifically, TTs acquire six bands (B1-B6) in the near-infrared spectrum with a wavelength ranging between 610 and 860 nm and six bands (B7-B12) in the

* Corresponding author

visible spectrum with a wavelength ranging between 450 and 650nm.

2.1.2. Sentinel-2

We selected all Sentinel-2 images acquired over the two study areas in the period between 2020-07-15 and 2020-11-15 and with a cloud cover smaller than 70%, resulting in 23 images (Figure 1). We filtered out images covered by clouds more than 70% because these images are more prone to geographical location errors, due to the challenges of performing geometrical corrections when ground control points are obscured (White et al., 2017).

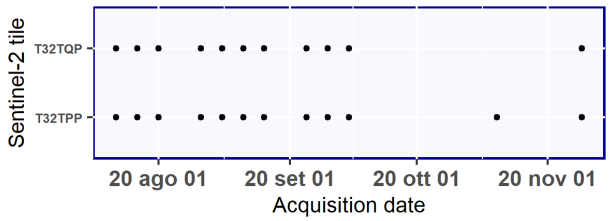

Figure 1: Sentinel-2 images processed

Sentinel-2 mission acquires one image every 3-5 days. In this study, images were acquired at 12:18 AM until the 20th of October while subsequent images were acquired at 11:18 AM. Differently, TTs acquire data every 60 minutes. To overcome these inconsistencies, we calculated the median of 5 TTs acquisitions in a 300-minute time window around each Sentinel-2 acquisition. As a result, we obtained a reference dataset of 778 TTs and Sentinel-2 spectral bands records.

2.2. TTs and Sentinel-2 bands comparison

Six of the TTs bands have wavelengths similar to that of S2 spectral bands (Table 1). For these bands, we compared TTs digital numbers and Sentinel-2 reflectance using scatter plots and calculating the Pearson correlation coefficient (R^2) calculated for (i) the whole reference dataset, (ii) the *F. sylvatica,* and (iii) the *A. alba* trees in the reference dataset.

Table 1. S2 and TT bands with similar wavelengths

	S2 wavelength range (nm)	TT wavelength (nm)
Blue	457.5-522.5 (B2)	500 (B8)
Green	542.5-577.5 (B3)	570 (B10)
Red	650-690 (B4)	650 (B12)
		680 (B2)
NIR	784.5-899.5 (B5)	810 (B5)
		860 (B6)

2.3. Neural network model

Deep neural networks consist of series of layers (groups of nodes) that facilitate learning through successive representations of the input data (Abadi et al., 2017). The data are transformed in each layer using weights, which are specific parameters that link the nodes of subsequent layers (Hawryło et al., 2020). Then each node applies an activation function to the input data. We constructed a single deep neural network taking as input all Sentinel-2 bands and outputting all TTs bands (Figure 2). First, using Sentinel-2 bands, we calculated a set of 45 normalized differential indices based on the 45 pairs of bands available combining the 10 Sentinel-2 input bands (layer 1 in Figure 2). For detailed information on indices calculation and Fully Connected Neural Networks see D'Amico et al. (in review). Each node in the neural network applies to the input data an "activation function", which facilitates learning by normalization of data. We used two consecutive and complementary activation functions (ReLU and Tanh) for which a detailed analysis is given in Li et al. (2020). To prevent overfitting and to ensure model generalizability, we introduced in the neural network three dropout layers (Figure 2) to randomly discard some (in our case 10%) of the nodes from the network during each training session. In this way, each training sub-network is different, allowing to prevent overfitting and to improve the model generalizability, i.e., the capacity of the model to perform well also when applied to new data or new areas (Srivastava et al., 2014). TensorFlow (https://www.tensorflow.org/) was used to accomplish the validation and test of the neural network .

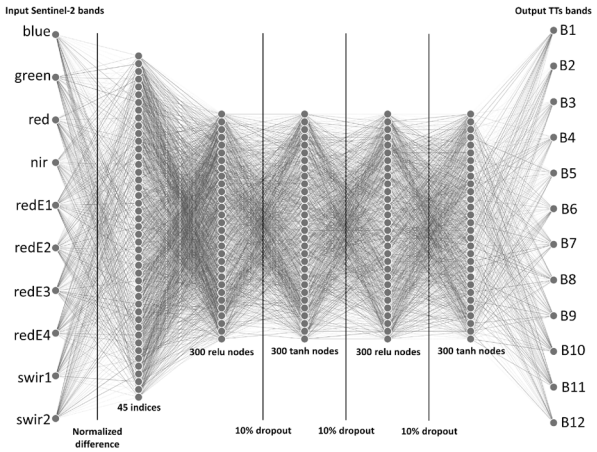

Figure 2: Deep neural network structure

2.4. Training, validation, and performance evaluation

As suggested by Laurin et al., (2020) and Hawrly et al. (2020), we divided our dataset into three sets: (1) the training (60% of data) to adjust nodes weights, (2) the validation (20% of data) to evaluate the accuracy during training and thus decide how to adjust the weights in the training, and (3) the test (20% of data) to assess the performance of the model. More specifically, the performance of the model was evaluated by comparing predicted band values against reference values using scatter plots and by calculating the R^2 for (i) the whole test set, (ii) the *F. sylvatica,* and (iii) the *A. alba* trees separately.

3. RESULTS AND DISCUSSIONS

The TTs and Sentinel-2 bands comparison revelated small correlations for the optical channels, more specifically, for blue, green, and red the R^2 ranged between 0.04 and 0.09 (Figure 3). Differently, the R^2 for the bands in the near-infrared channel was consistently higher (0.9). This can be due to the capacity of these bands in discriminating between coniferous (*A. alba*) and broadleaves (*F. sylvatica*) (Figure 3). Indeed, the R^2 calculated for the same bands (nir and B5, nir and B6), considering single species, were consistently smaller. More specifically, in *A. alba* the R^2 were 0.18 and 0.27 while in *F. sylvatica* they were 0.59, 0.58. A stronger relationship between above and below canopy multispectral data was expected, such limited correlation in the visible area suggest relevant differences between above and

below canopy reflectance and demonstrate the need for more in depth investigations.

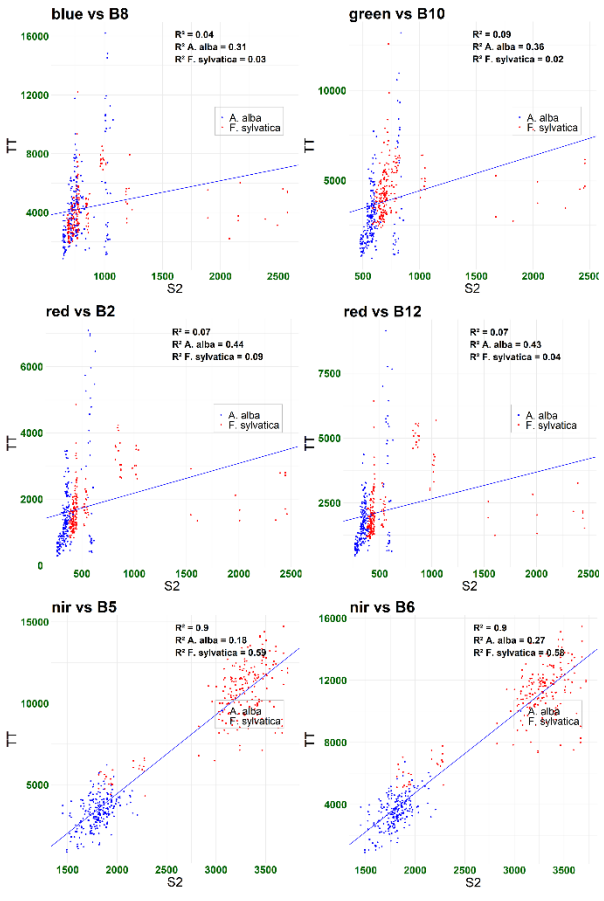

Figure 3. TTs and S2 bands scatter plots. For each of the six bands, the R^2 is shown for A. alba and F. sylvatica, and for both forest species together.

Using the neural network, the R^2 values between reference and prediction were statistically significantly greater compared with the linear correlation, ranging between 0.96 (B6, in the near infra-red channel) and 0.61 (B7, in the blue channel). The R^2 calculated for the fir stand ranged between 0.46 (B5) and 0.83 (B12), while the R^2 calculated for the beech stand ranged between 0.45 (B9) and 0.83 (B6). Scatter plots of bands 3, 4, 5, and 6 (Figure 4) showed that the reflectance values of coniferous and broadleaves were separated, suggesting that these bands should be preferred for classification/discrimination tasks. Results showed significant differences between bands in terms of R^2, for example, B5 and B6 were the bands that generally returned larger accuracy especially for discriminating between broadleaves and coniferous.

Registered differences may be considered as a guidance for future research activities, but further investigations are required. More in-depth analysis of plot characteristics (e.g., canopy cover, density, health, etc.) should be conducted to identify possible patterns with model performance. The developed neural network permitted the construction of a single model able to predict all TT bands using all Sentinel-2 bands at once. In this way, the prediction of each TT band depends on all the Sentinel-2 bands. Indeed, while the correlation between S2 and TT bands in the blue, green, and red channels was null (R^2 between 0.04 and 0.09) using the neural network we were able to predict the same bands with grater accuracies (R^2 between 0.62 and 0.81).

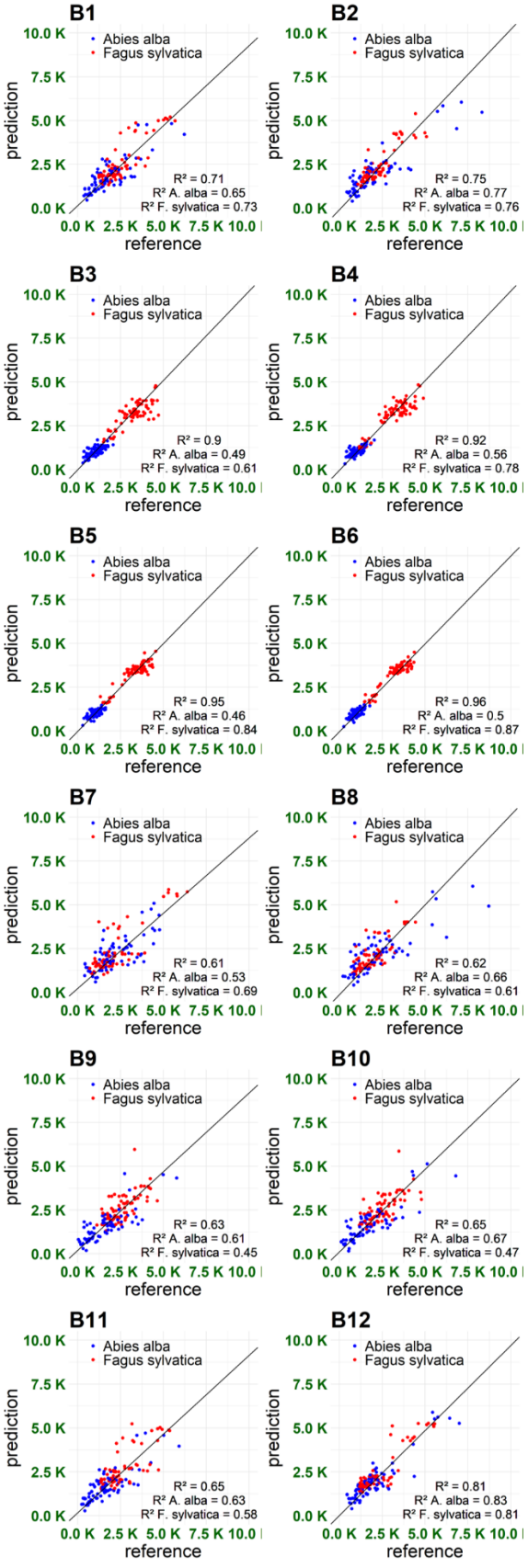

Figure 4. Model accuracy. Scatter plot of prediction and reference colored by species and R^2 showed for all the data, for A. alba and F. sylvatica.

4. CONCLUSIONS

This study presents for the first time a correlative analysis between the below and the above canopy reflectance measured by the TTs and Sentinel-2 imagery. The results of this study suggest that the below canopy reflectance measured by the TTs can be predicted accurately using Sentinel-2 imagery. Although almost no correlation between singular TTs and Sentinel-2 bands was found in the visible wavelengths (Figure 3), using a single deep neural network taking as input all Sentinel-2 bands and outputting all TTs bands (Figure 2) we obtained grater accuracies (Figure 4).

Herein we demonstrated an approach that in the future can be used for wall-to-wall spatial estimation of tree functional traits registered hourly by TTs. If future research will succeed in pursuing this objective, continuous large-scale monitoring of tree functional traits in a simple, highly automated, and cheap way, will be possible. This holds great potential for monitoring forests' health, timely and over large areas, which is crucial to understand the capacity of forests to react to climate change.

REFERENCES

Abadi, M., Isard, M., Murray, D.G., 2017. A computational model for TensorFlow an introduction, in: MAPL 2017 - Proceedings of the 1st ACM SIGPLAN International Workshop on Machine Learning and Programming Languages, Co-Located with PLDI 2017. https://doi.org/10.1145/3088525.3088527

Bayne, K., Damesin, S., & Evans, M. (2017). The internet of things–wireless sensor networks and their application to forestry. *NZ Journal of Forestry*, *61*(4), 37.

Bonan, G. B. (2008). Forests and climate change: Forcings, feedbacks, and the climate benefits of forests. *Science*, *320*(5882), 1444–1449. https://doi.org/10.1126/science.1155121

D'Amico, G., Francini, S., Giannetti, F., Vangi, E., Travaglini, D., Chianucci, F., Mattioli, W., Grotti, M., Puletti, N., Corona, P., Chirici, G. (in review). Automatic mapping of poplar plantations using Sentinel-2 imagery: a deep learning approach. Giscience & Remote Sensing.

FAO, 2020. Global Forest Resources Assessment 2020: key findings. Rome. https://doi.org/10.4060/ca8753en.

Francini, S., McRoberts, R.E., Giannetti, F., Marchetti, M., Scarascia Mugnozza, G., Chirici, G., 2021. The Three Indices Three Dimensions (3I3D) algorithm: a new method for forest disturbance mapping and area estimation based on optical remotely sensed imagery. Int. J. Remote Sens., 42:12, 4697-4715. https://doi.org/10.1080/01431161.2021.1899334.

Giannetti, F., Pegna, R., Francini, S., McRoberts, R.E., Travaglini, D., Marchetti, M., Scarascia Mugnozza, G., Chirici, G., 2020. A New Method for Automated Clearcutlear-cut Disturbance Detection in Mediterranean Coppice Forests Using Landsat Time Series. *Remote Sens.*, *12*, 3720. https://doi.org/10.3390/rs12223720.

Gorelick, N., Hancher, M., Dixon, M., Ilyushchenko, S., Thau, D., Moore, R., 2017. Google Earth Engine: Planetary-scale geospatial analysis for everyone. Remote Sens. Environ. 202, 18–27. https://doi.org/10.1016/j.rse.2017.06.031.

Hawryło, P.; Francini, S., Chirici, G.; Giannetti, F.; Parkitna, K.; Krok, G.; Mitelsztedt, K.; Lisańczuk, M.; Stereńczak, K.; Ciesielski, M.; Wężyk, P.; Socha, J. The Use of Remotely Sensed Data and Polish NFI Plots for Prediction of Growing Stock Volume Using Different Predictive Methods. *Remote Sens.* 2020, *12*, 3331. https://doi.org/10.3390/rs12203331

Laurin G.V., Francini S., Luti T., Chirici G., Pirotti F., Papale D. Accepted 6th November 2020. Satellite open data to monitor forest damage caused by extreme climate-induced events: a case study of the Vaia storm in Northern Italy. Forestry An International Journal of Forest Research

Marcelli, A., Mattioli, W., Puletti, N., Chianucci, F., Gianelle, D., Grotti, M., et al. (2020). Large-scale two-phase estimation of wood production by poplar plantations exploiting Sentinel-2 data as auxiliary information. SILVA FENNICA, 54(2).

Nourtier, M., Chanzy, A., Cailleret, M., Yingge, X., Huc, R., & Davi, H. (2014). Transpiration of silver Fir (Abies alba mill.) during and after drought in relation to soil properties in a Mediterranean mountain area. *Annals of Forest Science*, *71*(6), 683–695. https://doi.org/10.1007/s13595-012-0229-9

Oberhuber, W., Gruber, A., Kofler, W., & Swidrak, I. (2014). Radial stem growth in response to microclimate and soil moisture in a drought-prone mixed coniferous forest at an inner Alpine site. *European Journal of Forest Research*, *133*(3),467–479. https://doi.org/10.1007/s10342-013-0777-z

Pan, Y., Birdsey, R.A., Fang, J., Houghton, R., Kauppi, P.E., Kurz, W.A., Phillips, O.L., Shvidenko, A., Lewis, S.L., Canadell, J.G., 2011. A large and persistent carbon sink in the world's forests. Science 333.6045 (2011): 988-993. https://doi.org/10.1126/science.1201609.

Roblek, V., Meško, M., & Krapež, A. (2016). A Complex View of Industry 4.0. *SAGE Open*, *6*(2). https://doi.org/10.1177/2158244016653987

Srivastava, N., Hinton, G., Krizhevsky, A., Sutskever, I., Salakhutdinov, R., 2014. Dropout: A Simple Way to Prevent Neural Networks from Overfitting. J. Mach. Learn. Res. 15, 1929–1958.

Valentini, R., Marchesini, L. B., Gianelle, D., Sala, G., Yarovslavtsev, A., Vasenev, V. I., & Castaldi, S. (2019). New tree monitoring systems: From industry 4.0 to nature 4.0. *Annals of Silvicultural Research*, *43*(2), 84–88. https://doi.org/10.12899/asr-1847

White, J.C., Wulder, M.A., Hermosilla, T., Coops, N.C., Hobart, G.W., 2017. A nationwide annual characterization of 25 years of forest disturbance and recovery for Canada using Landsat time series. Remote Sens. Environ. 194, 303–321. https://doi.org/10.1016/j.rse.2017.03.035.

Woodcock, C.E., Allen, R., Anderson, M., Belward, A., Bindschadler, R., Cohen, W., Gao, F., Goward, S.N., Helder, D., Helmer, E., Nemani, R., Oreopoulos, L., Schott, J., Thenkabail, P.S., Vermote, E.F., Vogelmann, J., Wulder, M.A., Wynne, R., 2008. Free access to Landsat imagery. Science, 320, 5874, 1011. https://doi.org/10.1126/science.320.5879.1011a.

Zorzi, I., Francini,I., Chirici, G., Cocozza, C., (in review) The TreeTalkersCheck R package: an automatic daily routine to check physiological traits of trees in forest. Ecological Informatics

MONITORING THIRTY-FIVE YEARS OF ITALIAN FOREST DISTURBANCE USING LANDSAT TIME SERIES

C. Borghi[1], S. Francini[1,2,3*], M. Pollastrini[1], F. Bussotti[1], D. Travaglini[1], M. Marchetti[2], M. Munafò[4], G. Scarascia-Mugnozza[3], D. Tonti[2], M. Ottaviano[2], C. Giuliani[4], A. Cavalli[3], E. Vangi[1,2], G. D'Amico[1], F. Giannetti[1], G. Chirici[1]

1. Department of Agriculture, Food, Environment and Forestry, Università degli Studi di Firenze. Via San Bonaventura, 13, 50145 Firenze, Italy – (costanza.borghi, saverio.francini,, martina.pollastrini, filippo.bussotti, davide.travaglini, elia.vangi, giovanni.damico, francesca.giannetti, gherardo.chirici)@unifi.it

2. Dipartimento di Bioscienze e Territorio, Università degli Studi del Molise, Pesche, Isernia, Italy – (marchettimarco, daniela.tonti, ottaviano)@unimol.it

3. Dipartimento per l'Innovazione dei sistemi Biologici, Agroalimentari e Forestali, Università degli Studi della Tuscia, Via San Camillo de Lellis, Viterbo, Italy – (gscaras@unitus.it, alice.cavalli@studenti.unitus.it)

4. ISPRA - Italian National Institute for Environmental Protection and Research - (michele.munafo, chiara.giuliani)@isprambiente.it

*Corresponding author: saverio.francini@unifi.it

KEYWORDS: Remote sensing, Forest disturbance, Sustainable Forest Management, Landsat imagery, Google Earth Engine, Ecosystems, Climate change

ABSTRACT:

Forest ecosystems have a crucial role for biodiversity conservation, providing a large set of ecosystem services. Understanding and assessing forest disturbance regimes on a large spatial and temporal scale is a prerequisite setting up sustainable forest management solutions. In this context, Remote Sensing is an efficient tool frequently used in land-use change detection. The present work is aimed at spatially estimating forest disturbing events occurred in Italy in the period 1985-2019. Using Landsat time series and the 3I3D forest disturbance detection algorithm, we analyzed "extreme" forest disturbance patterns and their evolution in the last 35 years. We found a total of 472 events, with the highest incidence (96) in the period 1990 - 1994. The accuracy of the 3I3D algorithm was estimated using a photo-interpreted dataset of nine random-sampled squared cells of 225 km^2 each, distributed in the Italian region. Omission error for the 3I3D map ranged from a minimum of 37.43% to a maximum of 64.62% (mean value of 47.07%) while the commission error between 36.80% and 83.92%, with an average of 49.60%. Results suggest that occurrence of severe disturbance events do not seem to increase over time in the study period.

1. INTRODUCTION

Forest ecosystems cover approximately one-third of Earth's land surface (Hansen et al., 2013). They supply water, provide livelihoods, mitigate climate change, and are essential for sustainable food production (MEA, 2005). However, deforestation and forest degradation continue at alarming rates (Senf & Seidl, 2021). FAO defines forest degradation as "the reduction of the capacity of a forest to provide goods and services" (FAO, 2011), while the Intergovernmental Panel on Climate Change (IPCC) introduces the notion of timescale, as a loss of a state persisting for a certain period (Penman, 2003).

Natural disturbances, such as fires, insect outbreaks, and windthrows are an integral part of ecosystem dynamics in forests around the globe. They occur as relatively discrete events and form characteristic regimes of typical disturbance frequency, sizes, and severity over extended spatial and temporal scales (Seidl et al., 2017). Nevertheless, forests nowadays must also cope with the anthropogenic intensification of stressors that affect their condition, either directly or indirectly through climate change, pollution, and invasive species (Trumbore et al., 2015).

Forest disturbance regimes have changed thoroughly in many ecosystems in recent years, with climate change being the major driver of disturbance changes (Seidl et al., 2011). Indeed, severe and wide-ranging negative impacts may be expected in most European regions over the next few years (Linder et al., 2010). Such alterations have the potential to impact forests profoundly due to their lack of rapid adaptation (Seidl et al., 2017). Therefore, understanding and quantifying the forest vulnerability to disturbances is crucial to assess climate change impacts and to develop effective mitigation and adaptation strategies. In this scenario, Remote Sensing (RS) offers an effective way to monitor and mapping forest disturbance. Nowadays, the union of open access data and cloud computing platforms, such as Google Earth Engine (Gorelick et al., 2007), makes it possible to monitor large areas timely (Francini et al., 2020) and in a cost-effective manner (Gomes et al. 2020). In a recent paper, Francini et al. (2021) presented an unsupervised algorithm (3I3D) that detects forest changes by analyzing the trends of three vegetation indices used as axes for a three-dimensional space; 3I3D was then successfully used for the whole Italy, with an accuracy of 97% (Francini et al., 2021 in review).

In this work, we apply the 3I3D algorithm using Landsat Best Available Pixel (BAP) composites (White et al., 2014) to predict forest disturbances in Italy over the period 1985-2019. The aim of this study was to identify the incidence of particularly large disturbance events in the Italian forests and evaluate how this pattern varied over time. The accuracy of the forest disturbance map was then determined through the photointerpretation of nine random-sampled square cells. Then, the map's omission and commission errors were assessed through a confusion matrix.

2. MATERIALS AND METHODS

The study area coincides with the Italian forested area, defined using a fine-resolution forest/non-forest mask (D'Amico et al., 2021; Vangi et al., 2021). According to the last Italian NFI (INFC, 2007), forest vegetation and other wooded lands occupy approximately 10 mln ha, about 34% of the Italian national territory. Employing Landsat time-series imagery as input data, we applied BAP composite procedure, as described in White et al. (2014), and the 3I3D algorithm proposed by Francini et al.

* Corresponding author

(2021), to create 35 forest disturbance maps at 30 m spatial resolution, one for each year of the analysis.
Utilizing the 3I3D-derived maps, we calculated the area of forest disturbances for each province (NUTS3 are called Provinces in Italy) over the study period. Then, the data were aggregated at the regional (NUTS2) and national levels (NUTS1). Additional analyses were performed in order to identify extreme forest disturbance events. First, we estimated for each Province the "standard disturbed area" as the average of the 35 disturbed areas registered for that Province by the 3I3D map. Then, we identified for each Province Extreme Events (EEs) as forest disturbances which were 80% greater than the standard.
The performance of 3I3D used with Sentinel-2 imagery was assessed in Francini et al. (2021) and Francini et al. (in review). Here we assessed the algorithm's accuracy when applied to Landsat images using a reference dataset. Nine 15-km side square areas (225 km^2 each), were chosen around Italy using simple random sampling and analyzed through photointerpretation of high-resolution multi temporal orthophotos and satellite images. The location of the reference areas is shown in Figure 3. The same reference dataset was then used to assess the accuracy of the forest disturbance map proposed by Senf & Seidl (2021), aiming at comparing the performance of both approaches.
To evaluate maps' accuracy, we calculated (i) the number of true positives, corresponding to pixels correctly classified as disturbed forest, (ii) the number of true negatives, corresponding to pixels correctly classified as undisturbed forest, (iii) the number of false positives, corresponding to pixels incorrectly classified as disturbed, and (iv) the number of false negatives, corresponding to pixels incorrectly classified as undisturbed. Subsequently, those parameters were used to evaluate the maps' omission and commission errors through a confusion matrix (Kubat et al.1998).

3. RESULTS

Figure 1 illustrates the annual disturbed forest area in Italy during the period 1985-2019. The results show that the greatest events were detected in 1991 and 2016 with respectively 110591.30 and 100022.90 hectares of disturbed forest, respectively. In percentage, the most affected Region was Umbria with 22.43% of its total forest area disturbed during the 35-years study period, while the least was Emilia Romagna with 3.26%.

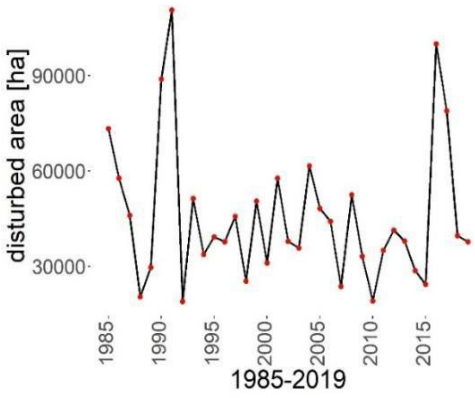

Figure 1. The trend of disturbed forest area in Italy during the period 1985-2019

The number of EEs over the 35 years was 472. As shown in Table 1, the occurrence of EEs does not increase over the time.

Table 1. Number of extreme events that occurred over the analysis period 1985-2019

	1985 - 1989	*1990 - 1994*	*1995 - 1999*	*2000 - 2004*	*2005 - 2009*	*2010 - 2014*	*2015 - 2019*	**TOT**
n°	76	96	67	66	57	44	66	**472**

The years 1985 and 1991 registered the highest number of EEs, with 28 episodes each, while the lowest number of EEs was 3 in 2000 and 2010 (figure 2).

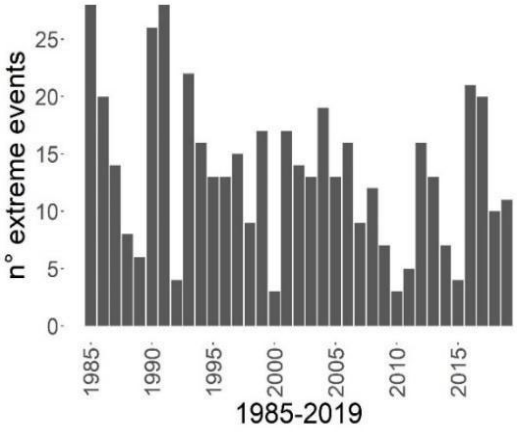

Figure 2. Trend of extreme events occurred in Italy during the period 1985-2019

46% of the EEs occurred over the period 1985-1995 (Figure 3).

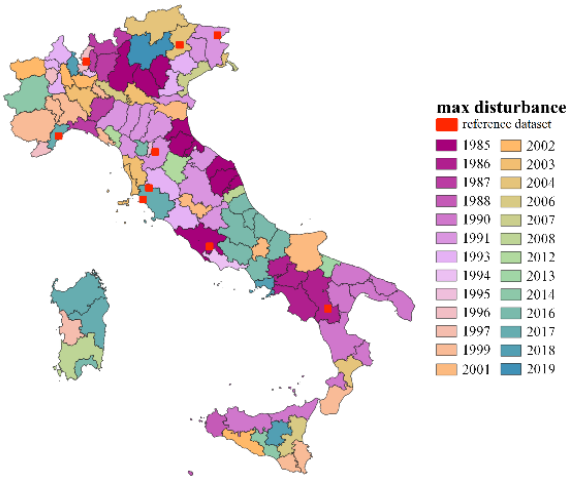

Figure 3. Years when the largest forest disturbance event occurred, per province. In red, the 9 plots of the reference dataset.

Table 2. 3I3D (1) and Senf and Seidl' (2) maps accuracies.

	Omission Errors		Commission Errors	
Min	37.43 (1)	40.72 (2)	36.80 (1)	34.46 (2)
Mean	47.07 (1)	58.20 (2)	49.60 (1)	51.14 (2)
Max	64.62 (1)	70.94 (2)	83.92 (1)	78.42 (2)

4. DISCUSSION

In the present work, we analyzed the Italian forest disturbance regime over the period 1985-2019. Before this study, available forest disturbance maps detected for each pixel just one

disturbance. More specifically, the Global forest change map shows for each pixel the last disturbance that occurred after 2000 (Hansen et al., 2013) while the Senf & Seidl (2021) map shows the disturbance with the largest magnitude. Whereas Hansen and Senf & Seidl's maps contain a single layer, here we analyzed 35 years and maps independently, avoiding the loss of information about multiple events occurring in the same place, in different periods. While their incidence was expected to be increasing over time (Senf & Seidl, 2021), especially harvesting (Ceccherini et al., 2020), our results do not confirm this trend (Figure 1). Differently, the EEs incidence (Figure 2) suggests an overall decrease over time (Table 1).

The highest numbers of EEs, registered in 1985 and 1991, could be correlated to the exceptionally cold weather in Italy in those years, which caused severe damages, even if not permanent (Bartolozzi & Fontanazza, 1999). However, the current climate change effects in the Mediterranean zone suggest an increment in the frequency of hot days, heat waves, heavy precipitation events, and fewer cold days with a lower risk of freezing events. For example, the record-breaking drought that affected Europe during the July 2016–June 2017 period (Garcia et al., 2021), caused extensive stress to Italian forests, especially in *Quercus* sp. and beech forests, with huge defoliation and leaf discoloration. These events were correctly registered using our procedure as shown in Figure 2. Severe drought causes higher vulnerability to forests (Forzieri et al., 2021), especially towards pest outbreaks (McDowell et al., 2011).

The results we obtained confirm the utility of satellite data in forest disturbance detection (Pontius et al., 2020), thanks to the high level of accuracy that can be obtained using forest disturbance detection algorithms.

To calculate the accuracy of the disturbance map based on the 3I3D algorithm (Table 2), we used a reference dataset, as proposed by Francini et al. (2021). We acknowledge that the photo-interpreted dataset is not error-free. Moreover, while disturbed polygons may be correctly classified, a partial identification of larger events could lead to a dwindling accuracy. Thus, the most reliable accuracy evaluation methods of forest disturbance maps are based on a reference dataset selected by stratification of the predicted maps (Olofsson et al., 2014). Furthermore, three out of nine validation plots were in the Alps (Figure 3). In this area, meager accuracy is expected due to (i) larger number of clouds (Hermosilla et al., 2016), (ii) extreme slopes that complicate images geometrical correction (White et al., 2016), (iii) consistent presence of snow and (iv) a prevailing continuous cover forestry with silviculture activities in small patches. For those reasons, accuracy assessment on the presented maps could lead to an error overrate. Nonetheless, the comparison between 3I3D and Senf & Seidl's forest disturbance maps accuracy shows an overall better performance of the former (Table 2). The 3I3D algorithm presented an average of 11.13% on omission and 3.54% on commission errors less than Senf & Seidl's forest disturbance map. Moreover, the 3I3D algorithm is easily tunable using Google Earth Engine, and, depending on the task, omission or commission error rates can be tuned. Evidently, as the omission errors decrease, the commission errors increase, as the commission errors decrease, omission errors increase.

5. CONCLUSIONS

Using Landsat BAP composites, Google Earth Engine, and the 3I3D algorithm, we mapped forest disturbances in Italy over the period 1985-2019 detecting 472 EEs in 107 Italian provinces. The rate of EEs was quite stable during the investigated period.

The distribution of EEs has significant implications for understanding how large forest disturbance events change their pattern over the years. The awareness of variations in disturbance regimes is also crucial to evaluate forests' stress response.

The present work contributes to existing knowledge on how climate change interferes with forest disturbance regimes and how events' magnitude and frequency change in a long time series. However, further analysis are needed to identify forest disturbance drivers and how their incidence varied over the time.

REFERENCES

Bartolozzi, F., and Fontanazza, G., 1999. Assessment of frost tolerance in olive (Olea europaea L.). Scientia Horticulturae, 81(3), 309-319. https://doi.org/10.1016/S0304-4238(99)00019-9

Ceccherini, G., Duveiller, G., Grassi, G. et al., 2020. Abrupt increase in harvested forest area over Europe after 2015. Nature 583, 72–77. https://doi.org/10.1038/s41586-020-2438-y

D'Amico, G., Vangi, E., Francini, S., Giannetti, F., Nicolaci, A., Travaglini, D., Massai, L., Giambastiani, Y., Terranova, C., Chirici, G., 2021. Are we ready for a National Forest Information System? State of the art of forest maps and airborne laser scanning data availability in Italy. iForest 14: 144-154. - https://doi.org/10.3832/ifor3648-014

Drusch, M., Del Bello, U., Carlier, S., Colin, O., Fernandez, V., Gascon, F., ... & Bargellini, P., 2012. Sentinel-2: ESA's optical high-resolution mission for GMES operational services. Remote sensing of Environment, 120, 25-36. https://doi.org/10.1016/j.rse.2011.11.026

FAO, 2011. Assessing Forest Degradation: Towards the Development of Globally Applicable Guidelines.

FAO, 2015. Global Forest Resources Assessment 2015: How have the world's forests changing? Rome, Italy.

FAO, 2020. Global Forest Resources Assessment 2020: Main report. Rome. https://doi.org/10.4060/ca9825en

Forzieri, G., Girardello, M., Ceccherini, G., Spinoni, J., Feyen, L., Hartmann, H., ... & Cescatti, A., 2021. Emergent vulnerability to climate-driven disturbances in European forests. Nature communications, 12(1), 1-12. https://doi.org/10.1038/s41467-021-21399-7

Francini, S., McRoberts, R.E., Giannetti, F., Mencucci, M., Marchetti, M., Scarascia Mugnozza, G., and Chirici, G., 2020. Near-real time forest change detection using PlanetScope imagery, European Journal of Remote Sensing, 53:1, 233-244. https://doi.org/10.1080/22797254.2020.1806734

Francini, S., McRoberts, R. E., Giannetti, F., Marchetti, M., Scarascia Mugnozza, G., and Chirici, G., 2021. The Three Indices Three Dimensions (3I3D) algorithm: a new method for forest disturbance mapping and area estimation based on optical remotely sensed imagery. International Journal of Remote Sensing, 42(12), 4697-4715. https://doi.org/10.3390/rs12223720

Francini S., McRobers E. R., D'Amico G., Coops N. C., Hermosilla T., White J. C., Wulder M. A., Marchetti M., Scarascia Mugnozza G., Chirici G., 2021 (*in review*). An open science and open data approach for statistically robust estimation of forest disturbance area. Science of Remote Sensing

Giannetti, F., R. Pegna, S. Francini, R. E. McRoberts, D. Travaglini, M. Marchetti, G. Scarascia Mugnozza, and G.

Chirici. 2020. A New Method for Automated Clear-cut Disturbance Detection in Mediterranean Coppice Forests Using Landsat Time Series. Remote Sensing 12 (22): 3720. https://doi.org/10.3390/rs12223720

Gomes, V.C., Queiroz, G.R., and Ferreira, K.R., 2020. An overview of platforms for big earth observation data management and analysis. Remote Sensing, 12(8), 1253. https://doi.org/10.3390/rs12081253

Gorelick, N., Hancher, M., Dixon, M., Ilyushchenko, S., Thau, D., Moore, R., 2017. Google Earth Engine: Planetary-scale geospatial analysis for everyone. Remote Sens. Environ. 202, 18–27. https://doi.org/10.1016/j.rse.2017.06.031

Hansen, M.C., Potapov, P.V., Moore, R., Hancher, M., Turubanova, S.A., Tyukavina, A., Thau, D., et al., 2013. High-Resolution Global Maps of 21st-Century Forest Cover Change. Science 342 (6160): 850–853. American Association for the Advancement of Science. http://doi.org/10.1126/science.1244693

Hermosilla, T., Wulder, M. A., White, J. C., Coops, N. C., Hobart, G. W., and Campbell, L. B., 2016. Mass data processing of time series Landsat imagery: pixels to data products for forest monitoring. International Journal of Digital Earth, 9(11), 1035-1054. https://doi.org/10.1080/17538947.2016.1187673

INFC, 2007. Le stime di superficie 2005-seconda parte. In Inventario Nazionale delle Foreste e dei Serbatoi Forestali di Carbonio; Tabacchi, A.G., De Natale, F., Di Cosmo, L., Floris, A., Gagliano, C., Gasparini, P., Salvadori, I., Scrinzi, G., Tosi, V., Eds.; MiPAF–Corpo Forestale dello Stato-Ispettorato Generale, CRA-ISAFA: Trento, Italy. Available online: http://www.infc.it (accessed on 1 June 2021).

Kennedy, R.E., Yang, Z., and Cohen, W.B., 2010. Detecting Trends in Forest Disturbance and Recovery Using Yearly Landsat Time Series: 1. LandTrendr - Temporal Segmentation Algorithms. Remote Sensing of Environment 114 (12): 2897–2910. https://doi.org/10.1016/j.rse.2010.07.008

Lindner, M., Maroschek, M., Netherer, S., Kremer, A., Barbati, A., Garcia-Gonzalo, J., ... and Marchetti, M., 2010. Climate change impacts, adaptive capacity, and vulnerability of European forest ecosystems. Forest ecology and management, 259(4), 698-709. https://doi.org/10.1016/j.foreco.2009.09.023

McDowell, N.G., Beerling, D.J., Breshears, D.D., Fisher, R.A., Raffa, K.F., and Stitt, M., 2011. The interdependence of mechanisms underlying climate-driven vegetation mortality. Trends in ecology & evolution, 26(10), 523-532. https://doi.org/10.1016/j.tree.2011.06.003

MEA (Millennium Ecosystem Assessment), 2005. Ecosystems and Human Well-Being: Biodiversity Synthesis. Washington, DC: World Resources Institute.

Olofsson, P., Foody, G.M., Herold, M., Stehman, S.V., Woodcock, C.E., Wulder, M.A., 2014. Good practices for estimating area and assessing accuracy of land change, Remote Sens. Environ. 42-57. https://doi.org/10.1016/j.rse.2014.02.015

Penman, J., Gytarsky, M., Hiraishi, T., Krug, T., Kruger, D., Pipatti, R., ... and Wagner, F., 2003. Good practice guidance for land use, land-use change and forestry. Good practice guidance for land use, land-use change and forestry. ISBN 4-88788-003-0

Pontius, J., Schaberg, P., & Hanavan, R., 2020. Remote Sensing for Early, Detailed, and Accurate Detection of Forest Disturbance and Decline for Protection of Biodiversity. In Remote Sensing of Plant Biodiversity (pp. 121-154). Springer, Cham. https://doi.org/10.1007/978-3-030-33157-3_6

García-Herrera, R., Garrido-Perez, J. M., Barriopedro, D., Ordóñez, C., Vicente-Serrano, S.M., Nieto, R., Gimeno, L., Sorí, R., and Yiou, P., 2019. The European 2016/17 Drought, Journal of Climate, 32(11), 3169-3187. https://doi.org/10.1175/JCLI-D-18-0331.1

Seidl, R., Schelhaas, M. and Lexer, M., 2011. Unraveling the drivers of intensifying forest disturbance regimes in Europe. Global Change Biol. 17, 2842–2852. https://doi.org/10.1111/j.1365-2486.2011.02452.x

Seidl, R., Thom, D., Kautz, M., Martin-Benito, D., Peltoniemi, M., Vacchiano, G., ... and Reyer, C. P., 2017. Forest disturbances under climate change. Nature climate change, 7(6), 395-402. https://doi.org/10.1038/nclimate3303

Senf, C., and Seidl, R., 2021. Mapping the forest disturbance regimes of Europe. Nature Sustainability, 4(1), 63-70. https://doi.org/10.1038/s41893-020-00609-y

Trumbore, S., Brando, P., and Hartmann, H., 2015. Forest health and global change. Science, 349(6250), 814-818. https://doi.org/10.1126/science.aac6759

Vangi, E., D'Amico, G., Francini, S., Giannetti, F., Lasserre, B., Marchetti, M., McRoberts, R.E., Chirici, G., 2021. The Effect of Forest Mask Quality in the Wall-to-Wall Estimation of Growing Stock Volume. Remote Sens., 13, 1038. https:// doi.org/10.3390/rs13051038

White, J. C., Wulder, M. A., Hobart, G. W., Luther, J. E., Hermosilla, T., Griffiths, P., ... & Guindon, L., 2014. Pixel-based image compositing for large-area dense time series applications and science. Canadian Journal of Remote Sensing, 40(3), 192-212. https://doi.org/10.1080/07038992.2014.945827

White, J.C., Coops, N.C., Wulder, M.A., Vastaranta, M., Hilker, T., Tompalski, P., 2016. Remote Sensing Technologies for Enhancing Forest Inventories: A Review. Can. J. Remote. Sens. 42.5, 619-641. https://doi.org/10.1080/07038992.2016.1207484.

Multitemporal LiDAR data for forest carbon monitoring in Mediterranean Forest

G. D'Amico[1]*, F. Giannetti[1], E. Vangi[1,2], C. Borghi[1], S. Francini[1,2,3], D. Travaglini[1], G. Chirici[1]

[1] Dipartimento di Scienze e Tecnologie Agrarie, Alimentari, Ambientali e Forestali, Università degli Studi di Firenze - (giovanni.damico, francesca.giannetti, elia.vangi, costanza.borghi, saverio.francini, davide.travaglini, gherardo.chirici)@unifi.it
[2] Dipartimento di Bioscienze e Territorio, Università degli Studi del Molise
[3] Dipartimento per la Innovazione nei sistemi Biologici, Agroalimentari e Forestali, Università degli Studi della Tuscia

KEY WORDS: LiDAR, growing stock volume, small-scale forest management, carbon sequestration.

ABSTRACT:

Forests are widely recognized as essential ecosystems for sequestering carbon and to mitigate the increase of atmospheric carbon dioxide, though could lose, or reduce this function under future climatic change. To maintain or improve carbon mitigation and to assess species adaptation to climate change small-scale forest monitoring is crucial, especially in Mediterranean forests where warmer and drier seasons are expected. Airborne Laser Scanner (ALS) data are efficiently used for defined carbon mapping, but few studies have used multi-temporal lidar surveys to evaluate carbon sequestration in Mediterranean forests.
This study focuses on the forested area of Monte Morello (Florence, Central Italy) which was surveyed by ALS in 2008 and 2015 with scan densities of 1.5 and 4.4 pulse/m^2, respectively. Herein, we compare the multitemporal ALS data with field forest inventory plots to estimate growing stock volume (GSV) and carbon sequestration in Mediterranean mixed broadleaved and coniferous forests. Independently of laser sampling rate we estimate, using an area-based approach, the forest GSVs and carbon sequestrations for 2008 and 2015 using random forests and a multiple linear regression model ($R^2 = 0.9$; RMSE% = 17%). Based on the multitemporal maps, we derived information related to (i) forest growth, (ii) forest species carbon sequestration, (iii) small-scale forest management. The entire study area increased sequestered carbon by 58%, mainly for coniferous mixed forests. Overall, our study describes a well-suited technique for multitemporal ALS analysis and highlighting the potential of the use of multitemporal ALS data to map forest resources for forest management activities.

1. INTRODUCTION

Forests supply a vast array of forest ecosystem services such as timber, recreation, landscape, they store carbon, and regulate the water cycle and climate (Eggleston et al., 2006, Vizzarri et al., 2015). In this context, Sustainable Forest Management (SFM) ensures the perpetuation of forest ecosystem services, but requires information on several forest variables that must be acquired to monitor the state of forest ecosystems and to plan specific forest management activities, especially in a climate change context. Nowadays, to monitor forest ecosystems, the use of spatially explicit forest variables derived integrating remote sensing data and field measures are considered essential to conduct site-specific sustainable forest management activities.
Among remote sensing technology, Light Detection And Ranging (LiDAR) data collected by Airplane or helicopter platforms (i.e., Airborne Laser Scanning, ALS), is considered the most useful technology to map forest ecosystems since from laser pulse it is possible to model and estimate the 3D structure of forests and to easily estimate biophysical forest variables (e.g. tree heights, vertical structure, growing stock volume, carbon stock) (Dubayah & Drake, 2000; Babcock et al., 2015). In fact, in the last decades, many studies demonstrated the utility of ALS to monitor forest resources (Nelson, 2013; Kangas et al., 2018). Given its proven capabilities in mapping forest variables, the use of ALS data is increasing rapidly worldwide (Zolkos et al., 2013), and many countries, such as Sweden, Finland, Denmark, invested in the wall-to-wall acquisition of ALS data to support forest inventory programs.
Increased availability of ALS data provides an opportunity to measure and study forest ecosystem dynamics over time (Dubayah et al., 2010). However, despite the potential of using multitemporal ALS data to support forest change monitoring, its implementation in small-scale sustainable forest management activities is still limited (Dassot et al., 2011).
Zhao et al. (2018), used four multitemporal ALS surveys in Scotland for monitoring forest carbon stock, while Cao et al. (2016), estimated forest biomass dynamics in subtropical forests. Some researchers underline that to use multitemporal ALS data efficiently many practical problems need to be overcome as the availability of ancillary ground data coherent with the multitemporal ALS acquisition, effects of variation in ALS sampling, and the analysis methods used to elaborate ALS data and to model forest variables (Næsset, 2009; Zhao et al., 2011). Most forest biophysical variables, such as biomass and carbon stock, can be estimated by ALS via correlative models, requiring paired forest inventory data for model calibration (Næsset et al., 2005).
This study aims to assess the utility of multitemporal ALS data for tracking forest and carbon dynamics in a Mediterranean study area. An emphasis is on evaluating and improving multitemporal ALS methods to measure forest changes over time at grid levels, including biomass change, and carbon stock. To do so we acquired two ALS data from surveys executed in 2008, and 2015, over a Mediterranean mixed broadleaf and coniferous forest. The ALS data were combined with field plots data acquired in 2014 and used to quantify forest changes at grid levels. We also estimated biomass and carbon stock over time, using ancillary data to calibrate ALS models.

2. MATERIALS

2.1 Study area

The study was carried out in Monte Morello, a forest area located near Florence's urban area in Central Italy (43°85' N, 11°23' E). Specifically, the study area corresponds to the overlapping forest area of two ALS surveys, for a total of 1465 ha. The area is characterized by a typical Mediterranean climate, with rainfall concentrated in spring and autumn and dry summer. Elevation ranges between 600 m and 700 m a.s.l. The dominant species are conifers (*Cupressus sempervirens* L., *Pinus nigra* Arn.) that originated from reforestation programmes of the last century, and oaks (*Quercus cerris* L., *Quercus ilex* L., *Quercus pubescens* L.) (Bottalico et al., 2017) (Fig. 1).

* Corresponding author

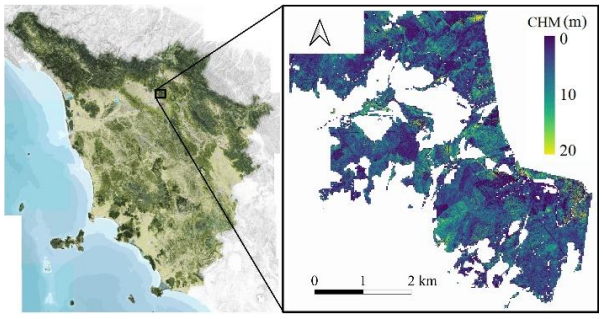

Figure 1. Study area.

2.2 Field plot data

Local forest inventories were carried out using a tessellated stratified sampling scheme (Barabesi and Franceschi, 2011) based on a 0.4 × 0.4 km grid. In each of the 41 grid units, a point was randomly selected among the forest area, constructing a sample of 41 points. A 13-m radius circular plot was established with a center at each sampling points. The plot coordinates were recorded using a GNSS receiver. Diameters at breast height (DBH, 1.30 m) were measured for all living trees with DBH ≥ 2.5 cm, for all callipered tree the height (H) was also recorded (Bottalico et al., 2017). In each field plot, the GSV was calculated by aggregating tree total GSV, estimated at tree level from species-specific allometric equations (Tabacchi et al., 2011).

2.3 Forest map

The CORINE Land Cover (CLC) project of the European Environment Agency, consists of a land cover map; it is based on a nomenclature system of 44 classes produced by photointerpretation of high-resolution satellite imagery. CLC uses a minimum mapping unit of 25 hectares. For this study, we acquired the CLC map for the reference year 2018, which for Italy provides an IV level of detail that can be assimilated to the forest types.

2.4 ALS data and processing

The first ALS survey available for the study area was carried out in winter 2008 with an ALS ALTM (Airborne Laser Terrain Mapper) Gemini sensor that operated at a flight height of 3000 m a.s.l. The sensor recorded two echoes per pulse with an average density of approximately 0.7 points/m^2. The second flight was carried out in May 2015 with a RIEGL LMS-Q680i laser scanner. The flying altitude was 1100 m above terrain level. Full-waveform ALS data were registered and discretized to a point density of 10 points/m^2. Standard pre-processing with LAStools (Isenburg, 2017) was used to remove noise in the ALS data and ALS echoes were classified as ground/non-ground. The relative heights above ground for echoes classified as non-ground were calculated and used to construct a canopy height model (CHM) with a spatial resolution of 1 m using the adaptive triangulated irregular network algorithm (Axelsson, 2000). For each plot, 54 echo-based and metrics were calculated (Hawryło et al., 2020) using the package *lidR* for R (Russell et al., 2020). The study area was tessellated into 23×23m pixels whose size mimicked the area of the field plots measured in the field. As for the field plots, 54 ALS metrics were calculated for each pixel.

3. METHODS

We combined ALS metrics and field data to derive forest variables for both ALS surveys, examining the temporal change. We used area-based ALS metrics at grid levels (23×23m coherent with field survey) as independent variables and field data as dependent variables to evaluate the accuracy of multiple modelling strategies and to estimate biomass and carbon dynamics.

3.1 GSV dynamics estimation

Carbon sequestration and its change were estimated from the GSV values predicted through regression models by relating field-based volume with ALS metrics.
We tried two model techniques (i) multiple linear regression model (MLR), and (ii) the random forests (RF) (Breiman et al., 2001). MLR techniques entail the use of model:

$$y_i = \beta_0 + \beta_1 x_{1i} + \ldots + \beta_p x_{pi} + \varepsilon_i \quad (1)$$

where i indexes sample units, y_i denotes the single response variable, p≥1 denotes the number of predictor variables, j =1, …, p indexes the predictor variables, βj is the respective regression coefficient, and ε_i denotes a random residual term assumed to be distributed N (0, σ_i^2). The model was optimized by comparing all possible combinations of all numbers of predictors with coefficients estimated using ordinary least squares.
RF is a decision tree algorithm and nowadays is among the most popular ensemble methods for classifying and predicting forest variables (Breiman, 2001). Its effectiveness is supported both empirically and theoretically, especially due to its reliance on not just one decision tree but an ensemble of trees as a strategy to improve model robustness. Specifically, RF uses a randomly chosen subset of predictors at each splitting node. RF was optimized by selecting the combination of predictor variables and parameter values (ntree and mtry) that minimized the root mean square error (RMSE) calculated using the leave-one-out (LOO) cross validation technique (McRoberts et al., 2015). The model fitting and optimization phase was performed using the *randomForest* package within R.
The most accurate models derived by MLS and RF were used to predict the GSV for all 23×23m grid cells of the study area to produce a 23×23m resolution GSV map for 2015. The same models were also used to predict the GSV using as predictor the 2008 ALS metrics. Negative GSV predictions were set to 0 in both years (Chirici et al., 2020). For each method, we calculated the coefficient of determination (R^2) between the measured and predicted values, the root mean square error (RMSE), the relative RMSE (RMSE%) and the mean absolute error (MAE).

$$RMSE = \sqrt{\sum_{i=1}^{n}(\hat{y}_i - y_i)^2 / n} \quad (2)$$

$$MAE = \sum_{i=1}^{n} |(\hat{y}_i - y_i)| / n \quad (3)$$

where $\hat{y}_i$ and y_i are respectively the predicted and ground reference values of GSV for the ith sample plot and n is the number of plots. The RMSE% were calculated as the percentage of the average ground reference value of GSV.

3.2 Carbon sequestration

For every CLC forest typology, starting from GSV estimation, the amount of aboveground forest biomass (t ha^{-1}) was estimated, for every forest typology, through the species-specific relationships presented in Federici et al. (2008). Finally, we calculated carbon sequestration, defined as the rate of change in forest carbon stock. Forest carbon stock was simply converted from aboveground biomass, derived by ALS metrics, using a generic scaling factor of 0.5 (Zhao et al., 2018); therefore, carbon

sequestration was obtained as the change in total tree biomass in each pixel per year, scaled by 0.5. Positive values of carbon sequestration indicated sinks associated with carbon accumulation from natural growth, while negative were carbon sources due to various disturbances.

4. RESULTS

Both imputation methods produced comparable results with only limited differences. Independently of the parameter used for evaluating the results, RF achieved the greatest accuracy. R^2 ranged between 0.89 and 0.91; RMSE between 38.3 m^3 ha^{-1} and 38.7 m^3 ha^{-1}; and RMSE% between 17.0% and 17.1% (Fig 2).

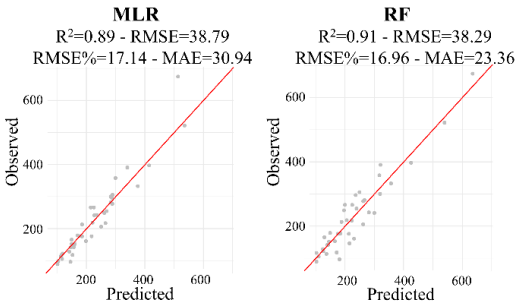

Figure 2. Scatterplots of GSV observations versus predictions for both the imputation approaches. R^2, RMSE, RMSE%, and MAE are based on LOO-CV during the optimization phase.

Of the 54 available predictors considered during the optimization phase, only 10 variables were selected by both the models. In terms of the usefulness of the predictors, the percentile values of point height variables were the most frequently selected, zq20, zq45 and zq75 for the MLS model and, zq70, zq75, zq85, qz90, zq95 for RF. In both the models the standard deviation of point heights (zsd) and the 75 percentile values of point heights were also selected. The other variables that were selected at least once were the maximum value of point heights (zmax) and the cumulative percentage of returns from the second height layers, considering the height measures divided into 10 equal intervals (zcum2). RF optimization involved 300 regression trees.
Considering these limited differences in models results the easier MLR model was selected for the following estimation phase. The MLR model was used to predict GSV for each one of the 27,701 23×23m resolution forest grid cells in the study area. GSV predictions ranged between 0 and 598m^3 ha^{-1} with a standard deviation of 98.0 m^3 ha^{-1} for 2015, while in 2008, GSV predictions ranged between 0 and 588m^3 ha^{-1} with a standard deviation of 90.7 m^3 ha^{-1}.

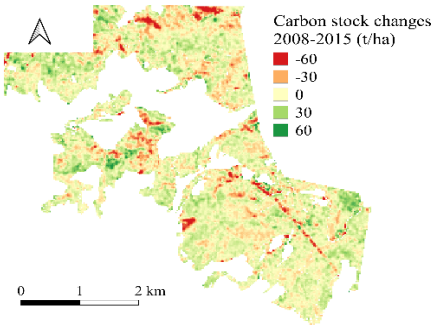

Figure 3. Dynamics in carbon storage over the study period.

The estimated aboveground forest biomass in the grid cells had values that ranged between 0 and 550 t ha^{-1} with a standard deviation of 73 t ha^{-1} for 2008 and between 0 and 574 t ha^{-1} with a standard deviation of 68 t ha^{-1} for 2015. Next, forest carbon stock maps were derived for both years. The carbon stored between the two surveys was in total 15195 t, while the carbon sources due to various disturbances were 11539 t, for net sink of 3656 t (Fig. 3).

5. DISCUSSION

In our work we used data from two ALS surveys, to estimate the stored forest carbon and its dynamics in a study area in central Italy. We observed an increase in total carbon storage of 58%, mainly for coniferous mixed forests with 2133 t sequestered (3.54 t ha^{-1}; 0.44 t ha^{-1} y^{-1}). On the other hand, most of the losses were mainly in broadleaves mixed forests with 590 t lost (1.62 t ha^{-1}; 0.20 t ha^{-1} y^{-1}).
The results we achieved demonstrate the usefulness of multitemporal ALS data to monitor forest GSV and carbon stock changes, which is crucial to support sustainable forest management, conservation in the Mediterranean area. Although RF was found to be the most accurate method, only small differences in prediction accuracies were found with the multiple linear regression (Chirici et al., 2020).
Despite the potential usefulness of ALS data to support sustainable forest management is well documented by a vast number of studies, a wall-to-wall ALS coverage in Italy is not available yet (59% of Italian forests) and only a very limited portion of forests are covered by multitemporal data (33% of Italian forests) (D'Amico et al., 2021). This limit the application of the methodology we presented in this contribution over large areas. Moreover, for our study, the lack of field data collected close in time to the first ALS survey, can be considered a limiting factor in verifying the effectiveness of the 2008 GSV estimation (Næsset et al., 2005). However, we demonstrated that also in Mediterranean forests, where more changes are expected due to climate change effects (Ogaya & Peñuelas, 2021), the use of multitemporal ALS data can be considered as the best way to spatially estimate forest dynamics.

6. CONCLUSION

Two main conclusions can be drawn from this work. Firstly, ALS data are confirmed as a reliable and efficient source of information for modeling carbon stock, even in complex Mediterranean forest areas. Secondly, the capability of ALS data to accurately predict forest carbon storage allows the use of simple parametric models, indeed both the tested modeling approaches predicted GSV with comparable results.
Overall, for ecological and environmental monitoring, the use of ALS data is expected to be further increased. The role of LiDAR technology (from aerial or terrestrial surveys) will be even more essential in supporting research and management activities, such as those related to carbon science forest degradation, biodiversity conservation, and land use. Under this point of view, Italy is still waiting for a complete ALS wall-to-wall coverage, that will have to be updated regularly to facilitate the prediction of forest variables and their trends in space and time with greater accuracy (Chirici et al., 2020).

7. REFERENCES

Axelsson, P., 2000. DEM generation from laser scanner data using adaptive TIN models. Int. Arch. Photogramm. Remote. Sens. 33, 111–118.

Babcock, C., Finley, A.O., Bradford, J. B., Kolka, R., Birdsey, R., Ryan, M.G., 2015. LiDAR based prediction of forest biomass using hierarchical models with spatially varying coefficients.

Remote Sensing of Environment, 169, 113-127. https://doi.org/10.1016/j.rse.2015.07.028

Barabesi, L., Franceschi, S., 2011. Sampling properties of spatial total estimators under tessellation stratified designs. Environmetrics 22, 271–278. https://doi.org/10.1002/env.1046

Bottalico, F., Chirici, G., Giannini, R., Mele, S., Mura, M., Puxeddu, M., McRoberts, R.E., Valbuena, R., Travaglini, D., 2017. Modeling Mediterranean forest structure using airborne laser scanning data. Int. J. Appl. Earth Obs. Geoinf. 57, 145–153. https://doi.org/10.1016/j.jag.2016.12.013

Breiman, L. Random Forests. Machine Learning 45, 5–32 (2001). https://doi.org/10.1023/A:1010933404324

Cao, L., Coops, N.C., Innes, J.L., Sheppard, S.R., Fu, L., Ruan, H., She, G., 2016. Estimation of forest biomass dynamics in subtropical forests using multi-temporal airborne LiDAR data. Remote Sens. Environ. 178, 158–171. https://doi.org/10.1016/j.rse.2016.03.012

Chirici, G., Giannetti, F., McRoberts, R.E., Travaglini, D., Pecchi, M., Maselli, F., Chiesi, M., Corona, P., 2020. Wall-to-wall spatial prediction of growing stock volume based on Italian National Forest Inventory plots and remotely sensed data. Int. J. Appl. Earth Obs. Geoinf., 84, 101959. https://doi.org/10.1016/j.jag.2019.101959

D'Amico, G., Vangi, E., Francini, S., Giannetti, F., Nicolaci, A., Travaglini, D., Massai, L., Giambastiani, Y., Terranova, C., Chirici, G., 2021. Are we ready for a National Forest Information System? State of the art of forest maps and airborne laser scanning data availability in Italy. iForest 14: 144-154. https://doi.org/10.3832/ifor3648-014

Dassot, M., Constant, T., Fournier, M., 2011. The use of terrestrial LiDAR technology in forest science: application fields, benefits and challenges. Ann. For. Sci. 68, 959–974. https://doi.org/10.1007/s13595-011-0102-2

Dubayah, R.O., Drake, J.B., 2000. Lidar remote sensing for forestry. Journal of forestry 98.6 (2000): 44-46. https://doi.org/10.1093/jof/98.6.44

Eggleston, S., Buendia, L., Miwa, K., Ngara, T., Tanabe, K., 2006. IPCC guidelines for national greenhouse gas inventories. Institute for Global Environmental Strategies Hayama, Japan.

Federici, S., Vitullo, M., Tulipano, S., De Lauretis, R., Seufert, G., 2008. An approach to estimate carbon stocks change in forest carbon pools under the UNFCCC: the Italian case. iForest 1: 86-95. https://doi.org/10.3832/ifor0457-0010086

Hawryło, P., Francini, S., Chirici, G., Giannetti, F., Parkitna, K., Krok, G., Mitelsztedt, K., Lisanczuk, M., Sterenczak, K., Ciesielski, M., Wezyk, P., Socha, J., 2020. The Use of Remotely Sensed Data and Polish NFI Plots for Prediction of Growing Stock Volume Using Different Predictive Methods. Remote Sens., 12(20), 3331. https://doi.org/10.3390/rs12203331

Isenburg, M., 2017. LAStools - efficient LiDAR processing software, from http://rapidlasso.com/LAStools.

Kangas, A., Astrup, R., Breidenbach, J., Fridman, J., Gobakken, T., Korhonen, K.T., Maltamo, M., Nilsson, M., Nord-Larsen, T., Næsset E., Olsson H., 2018. Remote sensing and forest inventories in Nordic countries – roadmap for the future, Scandinavian Journal of Forest Research, 33:4, 397-412. https://doi.org/10.1080/02827581.2017.1416666

McRoberts, R.E.; Næsset, E.; Gobakken, T., 2015. Optimizing the k-Nearest Neighbors technique for estimating forest above-ground biomass using airborne laser scanning data. Remote Sens. Environ., 163, 13–22. https://doi.org/10.1016/j.rse.2015.02.026

Næsset, E., 2009. Effects of different sensors, flying altitudes, and pulse repetition frequencies on forest canopy metrics and biophysical stand properties derived from small-footprint airborne laser data. Remote Sens. Environ. 113, 148–159. https://doi.org/10.1016/j.rse.2008.09.001

Næsset, E., Bollandsås, O.M., Gobakken, T., 2005. Comparing regression methods in estimation of biophysical properties of forest stands from two different inventories using laser scanner data. Remote Sens. Environ. 94, 541–553. https://doi.org/10.1016/j.rse.2004.11.010

Nelson, R., 2013. How did we get here? An early history of forestry lidar1. Can. J. Remote. Sens. 39, S6–S17. https://doi.org/10.5589/m13-011

Ogaya, R., Peñuelas, J., 2021. Climate Change Effects in a Mediterranean Forest Following 21 Consecutive Years of Experimental Drought. Forests, 12, 306. https://doi.org/10.3390/f12030306

Roussel, J.R., Caspersen, J., Béland, M., Thomas, S., Achim, A., 2017. Removing bias from LiDAR-based estimates of canopy height: accounting for the effects of pulse density and footprint size. Remote Sens. Environ. 198, 1–16. https://doi.org/10.1016/j.rse.2017.05.032

Tabacchi, G., Di Cosmo, L., Gasparini, P., Morelli, S., 2011. Stima del volume e della fitomassa delle principali specie forestali italiane. Equazioni di previsione, tavole del volume e tavole della fitomassa arborea epigea. Consiglio per la Ricerca e la sperimentazione in Agricoltura. Trento. 412 pp. (*In Italian*).

Vizzarri, M., Tognetti, R., Marchetti, M., 2015. Forest Ecosystem Services: Issues and Challenges for Biodiversity, Conservation, and Management in Italy. Forests, 6, 1810-1838. https://doi.org/10.3390/f6061810

Zhao, K., Popescu, S., Meng, X., Pang, Y., Agca, M., 2011. Characterizing forest canopy structure with lidar composite metrics and machine learning. Remote Sens. Environ. 115, 1978–1996. https://doi.org/10.1016/j.rse.2011.04.001

Zhao, K., Suarez, J.C., Garcia, M., Hu, T., Wang, C., Londo, A., 2018. Utility of multitemporal lidar for forest and carbon monitoring: Tree growth, biomass dynamics, and carbon flux. Remote Sens. Environ. 204 883–897. https://doi.org/10.1016/j.rse.2017.09.007

Zolkos, S., Goetz, S., Dubayah, R., 2013. A meta-analysis of terrestrial aboveground biomass estimation using lidar remote sensing. Remote Sens. Environ. 128, 289–298. https://doi.org/10.1016/j.rse.2012.10.017

New Remote Sensing tools in precision farming

CAN MEADOWS MOWING BE DETECTED BY REMOTE SENSING? A POSSIBLE ANSWER BASED ON SENTINEL-2 IMAGE TIME SERIES IN THE CAP FRAMEWORK

F. Sarvia*, S. De Petris, E. Borgogno-Mondino

Department of Agricultual, Forest and Food Sciences, University of Turin, L.go Braccini 2, Grugliasco 10095, Italy - (filippo.sarvia, samuele.depetris, enrico.borgogno)@unito.it

KEY WORDS: common agricultural policy, service prototype development, mowing detection

ABSTRACT:

Grassland management is essential for ecosystems and sustainable agriculture. EU support farmers through its Common Agricultural Policy requiring a proper management of meadows/pastures. The institutional agencies in charge of delivering contributions ask for more efficient control tools, making verifications faster and convenient. In this work, a prototype service is proposed, based on Sentinel-2, data to support paying agencies during their controls with the specific goal of detecting, mapping and quantifying the number of grass cuts along its growing season. This work was solicited by the Piemonte Regional Agency for Payments in Agriculture (ARPEA); the procedure was tested in the province of Vercelli (Piemonte - NW Italy) and relies on Copernicus Sentinel-2 data. The procedure was tested for the 2019 growing season, aiming at detecting and counting mowings of meadows. Temporal dynamics of reference mowed and not-mowed fields (represented by the local NDVI temporal profile) were compared. A significant decrease of the NDVI value was observed, possibly associated to mowing operations. The analysis was based on the adoption of the Fast Fourier Transform applied to the local NDVI profile. This made possible to detect managed grass fields and give an estimated count of numbers and timing of mowings. A map was generated showing the spatial distribution of managed grass fields featured by the correspondent number of mowings. A validation was performed with reference to available ground data from ARPEA. Results demonstrate that Sentinel-2 data can effectively support controls made by paying agencies in the framework of the EU to optimize allocation of available subsidies.

1. INTRODUCTION

Grassland management is essential for a proper assessment of ecosystems and for the establishment of sustainable agriculture. Farmers operate as managers of the countryside, shaping landscape and providing public benefits (Primdahl and Kristensen, 2011). The European Union (EU) finances farmers through the common agricultural policy (CAP) contributions, requiring that proper management actions are applied to grasslands and pastures, mainly for environmental purposes (Pe'er et al., 2020; Roederer-Rynning, 2010). "Greening payments" specifically support farmers that adopt, or maintain, agricultural practices that favour the achievement of environmental and climate-related goals that are not reflected in market prices (Matthews, 2013).

In order to receive CAP "greening" contribution farmers must have to perform 3 main activities (Birkhofer et al., 2018): a) crop diversification (different crops makes soil and ecosystems more resilient); b) maintaining of permanent grassland; c) preservation of the 5% of arable land to host areas for biodiversity (Ecological Focus Area – EFA). Maintaining permanent grassland consists of disposing a piece of terrain, not included in the ordinary crop rotation, for 5 or more years hosting grass or other forage crops (wild or cultivated). Additionally, these areas have to be managed and maintained active through agronomic operations, included mowing.

It is worth to remind that farmers who intend to access CAP subsidies must apply to the competent Paying Agency (PA); in the Piemonte region ARPEA (Piemonte Agency for Payments in Agriculture) is the reference institution. Recently, farmers' applications must give accurate and updated information on the size of the area the grants are required for and about farm organizational features. Moreover, as required by Art. 17 of Reg. (EU) N. 809/2014, applications must be based on geospatial data.

In this framework, data provided by the Copernicus program through the European Space Agency (ESA) (Drusch et al., 2012) and including free high-resolution satellite data for land cover/use monitoring (Guliyeva, 2020; Malenovskỳ et al., 2012), can be an important resource (https://scihub.copernicus.eu/). Vegetation indices (VI) from Sentinel-2 (S2) data are well known, in literature, to provide many information about surfaces in both time and space domains (Borgogno-Mondino et al., 2019; De Petris et al., 2021, 2020; Halabuk et al., 2015; Sarvia et al., 2021b, 2021a, 2019; Weiss et al., 2020). They can certainly play a key role in the context of controls, permitting PA faster, global and cost-effective verifications, included those related to grassland management during the year (Sarvia et al., 2021b).

In this work, authors propose a prototype service based on S2 data aimed at supporting PA control procedures for detecting, mapping and quantifying the number of mowings operated in meadows along their growing season. The service was tested in the Vercelli province (Piemonte region - NW Italy) with reference to a S2 Level 2A image time series made of 30 images and covering the 2019 growing season. The analysis was conducted at the plot scale and was based on the preliminary generation of a the correspondent NDVI image time series. The local NDVI temporal profile was analysed by the Fast Fourier Transform (FFT) making possible to get an estimate of the number of mowings (NM) operated locally.

2. MATERIALS AND METHODS

2.1 Study area

According to ARPEA's recommendation, an area of interest (AOI) was selected within the Vercelli province (Piemonte -

* Corresponding author

NW Italy, Fig. 1). AOI is characterized by an extensive agriculture with a prevalence of submerged crops (rice); a significant number of meadows are however present in the area.

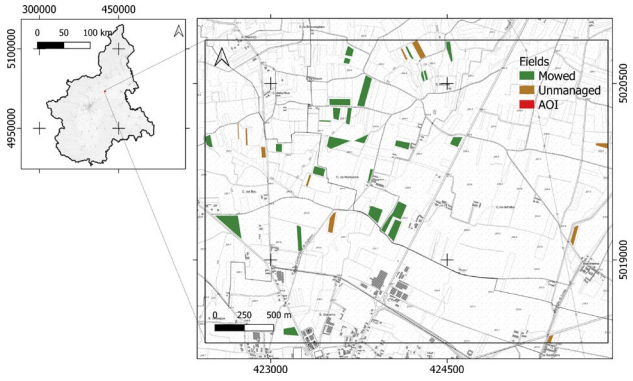

Figure 1. Study area. Mowed (green) and unmanaged (brown) fields considered for the mowing count analysis. Reference system: WGS84/UTM zone 32N, EPSG: 32632.

2.2 Satellite Data

According to the local mowing calendar (Sarvia et al., 2021b), a total of 30 S2 images were collected covering the period 24th April 2019 - 21st September 2019, from the Copernicus Open Access Hub geoportal (scihub.copernicus.eu). Level 2A product is delivered calibrated in "at-the-bottom of the atmosphere" (BOA) reflectance, permitting immediate usability for land applications. S2 images were supplied as 100 km x 100 km tiles orthoprojected in the WGS84 UTM reference frame (Delwart, 2015). It is worth to remind that S2 Level 2A product is supplied with auxiliary data (namely, Scene Class Layer, SCL) providing information about pixel quality and meaning.

2.3 Reference Data

ARPEA performed several interviews to local farmers in order to collect information about main agronomics operations (the number of mowing). A total of 34 fields, covering about 19.4 ha, were provided to validate mowing identification derived from satellite data (Figure 1). Specifically, 25 plots were labelled as mowed (ranging from 2 to 4 mowings per year) while 9 as unmanaged (Table 1).

Number of fields	Number of Mowings	Size (ha)
9	0	2.9
1	2	0.5
10	3	5.1
14	4	10.9

Table 1. Reference data used for validation.

2.4 NDVI Time Series Generation

S2 band 8 (NIR and band 4 (red) were used to compute the correspondent wide range NDVI. During NDVI computation all "bad" observations occurring at the single pixel position were masked out using the provided SCL layer. Remaining observations were further filtered by a Savitzky-Golay filter (kernel size: 3 observations before and 3 after, smoothing function: 1st order linear). The resulting local NDVI profile was then regularized by linear interpolation at a 5 days temporal step. Regularization is mandatory if a FFT-based approach have to be applied. A time series of 30 images (different form the native ones) was consequently obtained and used for successive analyses.

Finally, the resulting NDVI profile was averaged at plot level. Plot/field borders used for NDVI averaging (by GIS zonal statistics) were provided as polygon vector layer by ARPEA. All these operations were performed by a IDL (Interactive Data Language) self-developed routine.

2.5 Mowing Counting

The analyses focused only on meadows in the AOI as mapped by Sarvia (2021) from a previous classification step. What the procedure has to do, is the identification of the type of management. In order to preliminary mask out fields that most probably were not managed the following condition was tested for the local NDVI profile: NDVI standard deviation (time domain) < 0.08. This value is a tentative threshold deduced by interactive exploration of sample NDVI profiles, that made evident how managed (i.e. cut) fields showed an important NDVI variation along the season given by the repeated mowings. Consequently, meadows showing a low NDVI temporal variation were assumed as the most promising candidates to be labelled as unmanaged grass fields and subsequently coded with 0 mowing. With regard to fields with standard deviation > 0.08, a specification of moving frequency came from the successive operations relaying on FFT analysis. This was adopted assuming that mowing of meadows happens periodically along their growing season. With reference to the frequency spectrum generated by FFT, the strongest frequency different from the fundamental one (i.e. the one having the larger amplitude) was used as predictor of the periodic cuts of grass. Specifically, the number of mowings (NM) was set equal to the value of the strongest frequency. This was mapped to generate the correspondent mowing map (MM) to allow PAs to proceed with greening payments controls on meadow management. MM accuracy was finally tested with reference to control fields provided by ARPEA.

3. RESULTS AND DISCUSSIONS

3.1 Mowing Counting

An example of NDVI temporal profile from a meadow and its correspondent FFT spectrum is shown in Figure 2.

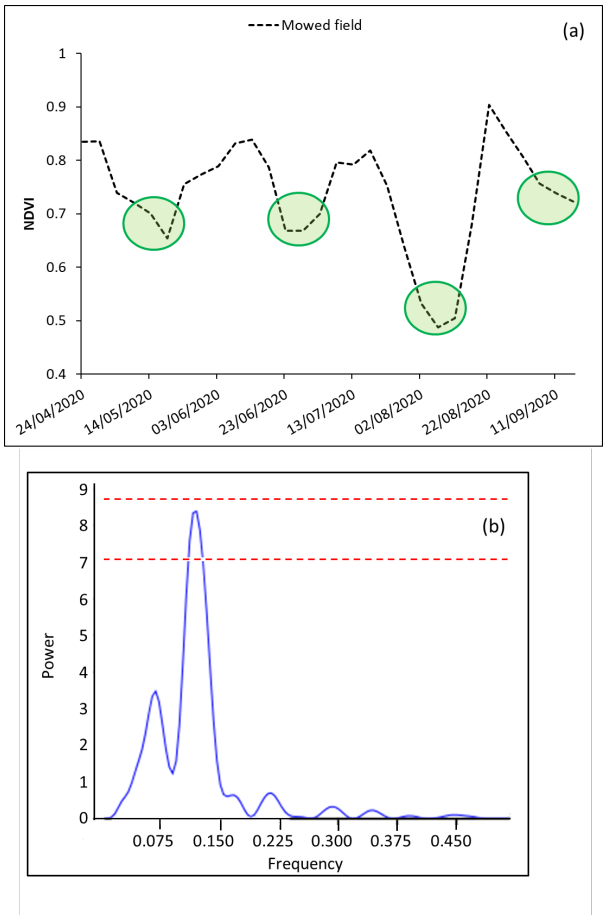

Figure 2. (a) Examples of Normalized Difference Vegetation Index (NDVI) temporal profiles of a mowed field; green circles represent mowings. (b) correspondent frequency spectrum. Frequency is scaled between 0 and 1 with respect to the number of observations (30). Consequently, the resulting number of mowings is 0.1207 (strongest frequency) x 30 ≈ 4.

MM and the corresponding confusion matrix are reported in Figure 3 and Table 2, respectively.

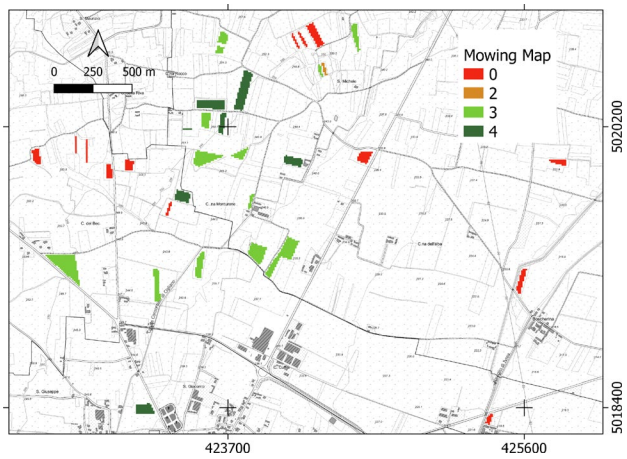

Figure 3. Count of mowings as detected by FFT operated on the local NDVI temporal profile. Reference system: WGS84/UTM zone 32N, EPSG: 32632.

MM Overall Accuracy (OA) was 62%. Nevertheless, it was found that the User's Accuracy (UA) was high for classes having 0 (unmanaged) and 3 mowings (> 70%). Conversely, it was very low for fields with 2 and 4 mowings. Differently, the Producer's Accuracy (PA) was very high for fields with 4 mowings (> 85%), medium-high for fields with 0 and 3 mowings (> 0.55%) and very low for fields with 2 mowings.
In spite of this residual criticality, it is worth to remind that CAP payments are not interested in detecting the right number of mowings; they have just to detect if a filed is managed or not. Consequently, further refinements of the procedure should be majorly addressed to solve misclassification problem related to class at 0 mowings. This appears to be slightly overestimated by the proposed procedure, making it cautionary at this point.

Mowing count		Classification				Total
		0	2	3	4	
Reference	0	8	0	1	0	9
	2	0	0	1	0	1
	3	2	0	7	1	10
	4	3	1	4	6	14
Total		13	1	13	7	34

Table 2. Confusion matrix of mowing map count.

4. CONCLUSIONS

In this work, a prototype service was proposed to support paying agencies during the control phases for detecting, mapping and quantifying the number of mowings made on meadows during the year. This work was solicited by ARPEA; the procedure was tested within the Vercelli province (Piemonte - NW Italy). For this purpose, 30 Copernicus Seninel-2 level 2A images, covering the period 24th April 2019 - 21st September 2019, were processed according to the local mowing calendar. Consequently, the NDVI profile was computed and monitored for the entire period since a drastic drop in the NDVI profile can be assumed as a mowing. Considering this practice as a periodically activity, the standard deviation was assessed to detect the unmanaged grass fields while the frequency of the NDVI profile was analysed by FFT and the number of mowing was calculated generating the correspondent MM. Finally, MM was validated with local reference data. Results show that mowing count is consistent with CAP controls requirements, making possible to quite satisfyingly detect managed (mowings count > 0) and not managed (mowings count = 0) grass fields. The procedure appears to overestimate the number of not-managed fields and this is the issue to take majorly care about in future developments. Nevertheless, the procedure appears to be easily manageable and customizable, making possible to control, map and count the number of mowings in a fast and cost-effective way. A crucial issue is certainly related to the pre-processing step concerning native data filtering and regularization.

ACKNOWLEDGEMENTS

We would like to thank Dr. Elena Xausa and Dr. Gianluca Cantamessa, technicians by ARPEA, for having provided guidelines and fundamental operational information useful to reach the results presented in this work.

REFERENCES

Birkhofer, K., Fevrier, V., Heinrich, A.E., Rink, K., Smith, H.G., 2018. The contribution of CAP greening measures to conservation biological control at two spatial scales. Agric. Ecosyst. Environ. 255, 84–94.

Borgogno-Mondino, E., Sarvia, F., Gomarasca, M.A., 2019. Supporting insurance strategies in agriculture by remote sensing: a possible approach at regional level, in: International Conference on Computational Science and Its Applications. Springer, pp. 186–199.

De Petris, S., Sarvia, F., Borgogno-Mondino, E., 2020. A New Index for Assessing Tree Vigour Decline Based on Sentinel-2 Mul-titemporal Data. Appl Tree Fail. Risk Manag Remote Sens Lett.

De Petris, S., Sarvia, F., Gullino, M., Tarantino, E., Borgogno-Mondino, E., 2021. Sentinel-1 Polarimetry to Map Apple Orchard Damage after a Storm. Remote Sens. 13, 1030. https://doi.org/10.3390/rs13051030

Delwart, S., 2015. SENTINEL-2 User Handbook. European Space Agency. Available from: https://earth. esa. int/documents

Drusch, M., Del Bello, U., Carlier, S., Colin, O., Fernandez, V., Gascon, F., Hoersch, B., Isola, C., Laberinti, P., Martimort, P., 2012. Sentinel-2: ESA's optical high-resolution mission for GMES operational services. Remote Sens. Environ. 120, 25–36.

Guliyeva, S.H., 2020. Land Cover/Land Use Monitoring for Agriculture Features Classification. Int. Arch. Photogramm. Remote Sens. Spat. Inf. Sci. 43, 61–65.

Halabuk, A., Mojses, M., Halabuk, M., David, S., 2015. Towards detection of cutting in hay meadows by using of NDVI and EVI time series. Remote Sens. 7, 6107–6132.

Malenovskỳ, Z., Rott, H., Cihlar, J., Schaepman, M.E., García-Santos, G., Fernandes, R., Berger, M., 2012. Sentinels for science: Potential of Sentinel-1,-2, and-3 missions for scientific observations of ocean, cryosphere, and land. Remote Sens. Environ. 120, 91–101.

Matthews, A., 2013. Greening agricultural payments in the EU's Common Agricultural Policy. Bio-Based Appl. Econ. 2, 1–27.

Pe'er, G., Bonn, A., Bruelheide, H., Dieker, P., Eisenhauer, N., Feindt, P.H., Hagedorn, G., Hansjürgens, B., Herzon, I., Lomba, Â., 2020. Action needed for the EU Common Agricultural Policy to address sustainability challenges. People Nat. 2, 305–316.

Primdahl, J., Kristensen, L.S., 2011. The farmer as a landscape manager: Management roles and change patterns in a Danish region. Geogr. Tidsskr.-Dan. J. Geogr. 111, 107–116.

Roederer-Rynning, C., 2010. The Common Agricultural Policy, in: Policy-Making in the European Union. Oxford University Press, pp. 181–205.

Sarvia, F., De Petris, S., Borgogno-Mondino, E., 2021a. Exploring Climate Change Effects on Vegetation Phenology by MOD13Q1 Data: The Piemonte Region Case Study in the Period 2001–2019. Agronomy 11, 555. https://doi.org/10.3390/agronomy11030555

Sarvia, F., De Petris, S., Borgogno-Mondino, E., 2019. Remotely sensed data to support insurance strategies in agriculture, in: Remote Sensing for Agriculture, Ecosystems, and Hydrology XXI. International Society for Optics and Photonics, p. 111491H.

Sarvia, F., Xausa, E., Petris, S.D., Cantamessa, G., Borgogno-Mondino, E., 2021b. A Possible Role of Copernicus Sentinel-2 Data to Support Common Agricultural Policy Controls in Agriculture. Agronomy 11, 110.

Sentinel, E.S.A., 2014. 3-Missions-Sentinel Online. ESA Paris Fr.

Weiss, M., Jacob, F., Duveiller, G., 2020. Remote sensing for agricultural applications: A meta-review. Remote Sens. Environ. 236, 111402.

ESTIMATION OF BIOPHISICAL PARAMETERS IN RICE CROPPING SYSTEM FROM SENTINEL-2 DATA AND HYBRID APPROACH: PERSPECTIVE FOR PRECISION AGRICULTURE APPLICATION

Marta Rossi [1]*, Gabriele Candiani [2], Marco Gianinetto [3,2], Francesco Nutini [2], Mirco Boschetti [2]

[1] Università degli Studi Milano – Bicocca, DISAT, Piazza della Scienza 1, 20126 Milano, Italy
[2] IREA, National Research Council, Via Bassini 15, 20133 Milano, Italy (candiani.g, nutini.f, boschetti.m)@irea.cnr.it
[3] Department of Architecture, Built Environment and Construction Engineering (DABC), Politecnico di Milano, Via Ponzio 31, 20133 Milano, Italy – marco.gianinetto@polimi.it

KEY WORDS:
Rice crop monitoring, Hybrid modelling, Precision Agriculture, Sentinel-2, Multispectral Remote Sensing, Canopy Nitrogen Content, Leaf Area Index.

ABSTRACT:

The availability of information able to assess crop nutritional status in space and time is a crucial issue to support sustainable agriculture in smart farming framework. Remote sensing techniques have become popular methods to support precision farming activities by producing spatial variability maps of crop conditions. In this framework, an experimental activity has been conducted to estimate Leaf Area index (LAI) and test potentiality of Canopy Nitrogen Content (CNC) retrieval, due to the importance of these parameters for assessing crop nutritional status. This study focuses on rice and retrievals have been conducted using a hybrid approach based on Radiative Transfer Model (RTM) simulations and Machine Learning Regression Algorithms (MLRA). A Look Up Table of rice spectra, with a cardinality of 2000 samples, was generated ranging crop parameters as input to the PROSPECT-PRO RTM. Simulations were resampled to 8 bands Sentinel 2-like configuration and were then used to train Gaussian Process Regression (GPR) and Neural Network (NN) MLR algorithms, also testing a sample selection procedure based on Active Learning (AL). Cross-validation results showed good performance for LAI retrieval using both the standard hybrid model (GPR: R2 ~ 0.78 , NN: R2 ~ 0.72) and AL approach (GPR: R2 ~ 0.71, NN: R2 ~ 0.67). Preliminary tests conducted to estimate CNC revealed promising results for plant nutritional status assessment. The within-field spatial variation of estimated CNC from Sentinel-2 (S2) data in a precision farming experiment resulted coherent with the observed heterogeneity in the field and to corresponding prescription maps used to manage the fertilisation.

1. INTRODUCTION

If in the last century production and consumption of food happened parallel to each other, nowadays the global megatrends (climate change, population growth, technological change, etc) gradually cause the supply-demand balance to shift. Considering this scenario, farmers are forced to increase the yields, while at the same time protecting their most important production factor, the environment, natural resources like soil from degradation, water and air from pollution and climate from emissions of greenhouse gases (FAO 2016). Remote sensing can contribute for a continuous monitoring of plant development and relative Nitrogen (N%) concentration during all growth stages to improve farm management: in this context, precision farming reveals to be a current promising solution, since holding the potential to provide farmers the capacity to assess, understand and manage the within-field variability, as a prerequisite to define sustainable agro-practices able to reduce farming costs and environmental impact (Nutini et al., 2018).
Rice is considered the world's most important staple crop, being globally cultivated and representing a strategic crop for food security in many countries. Italy contributes with almost 50% (Eurostat 2019, https://agridata.ec.europa.eu/extensions/DashboardRice/RiceProduction.html) to the European rice production. The study area of Lomellina (Pavia province, Italy) produces almost 5 million quintals of rice per year. Nitrogen (N), which is applied through fertilisation in agro-practices, is fundamental for maximising crop production and minimizing environmental impact. Therefore, a sustainable fertilisation is a pre-requisite for modern agriculture, and it can be achieved assessing crop status in space and time.
From rice spectral signature it is possible to assess vegetation biophysical and biochemical variables. This study focuses on the estimation of Leaf Area Index (LAI), which is defined as the green leaf area per unit of ground surface area, representing a proxy of total crop biomass and Canopy Nitrogen Content (CNC), measured in grams of N in crop per m^2 of ground area, representing the quantity of N uptake by the plant leaves (i.e. the canopy). Indeed, according to recent model developments, it is possible to simulate directly, thanks to PROSPECT-PRO model (Féret et al., 2021), the effect of Leaf Nitrogen Content (LNC) [$g\ cm^{-2}$] on leaf spectra. Once coupled with a canopy model (i.e., SAIL4) it is possible to assess effect at plant level. Through inversion of such leaf-canopy radiative transfer model (PROSAIL-PRO) it is possible to estimate CNC, as recently demonstrated for wheat and corn (Berger et al., 2020).
In this framework, this study aims at testing a hybrid retrieval approach, useful for rice monitoring as a support to precision farming activities. The first step consisted in assessing the potentiality of the PROSAIL-PRO RTM for rice spectra simulation taking into account the influence of the background. After, a hybrid retrieval approach is developed by i) generating a rice specific Look Up Table (LUT), setting different background

* Corresponding author

and vegetation parameters, and ii) training different ML algorithms. Finally, contribution of an Active Learning (AL) was tested as an optimisation process for LUT sampling selection. Results are then validated using independent datasets, in view of assessing the model exportability in real operational conditions. Finally, the obtained maps of rice parameters of interest, which have been generated from Sentinel-2 (S2) data for the year 2018 on SATURNO project study area (Nutini et al., 2021), are analysed in terms of temporal and spatial information provided for rice crop monitoring and discussed as a contribution in precision farming application.

2. MATERIAL AND METHODS

2.1 Study area and datasets exploited

The field measurements of the experimental datasets employed in this study used to test the PROSAIL-PRO RTM were collected by CNR-IREA and analysed in Stroppiana et al., 2009 and consist of two agronomic experiments carried out in 2004 and 2006 in Opera (south of Milano - Italy, Lat 45°23', Long 9°11'). Specifically, they included full resolution FieldSpec® spectral data and crop (rice) parameters from ground measurements. A 2018 dataset from SATURNO project of CNR-IREA was also used to validate the hybrid model when applied to real S2 imagery to generate biophysical parameters' maps. The ground measurements of the parameters of interest were acquired for the 2018 dataset in real farm condition, in Lomellina study area, which is one of the biggest rice districts in Italy and Europe (Nutini et al., 2021). The S2 dataset for 2018 crop season from SATURNO project included 9 clear sky images over the Lomellina study area (01/06/18, 16/06/18, 21/06/18, 26/06/18, 01/07/18, 06/07/18, 26/07/18, 31/07/18, 05/08/18).

2.2 Hybrid method: RTM + MLRA

Hybrid methods for biophysical variables retrieval rely on the generation of simulated spectra using physically based RTMs for the training of ML Regression Algorithms (MLRAs), under the assumption of a more general applicability as compared to the training carried out using measured data, since RTMs allow to simulate a wide and crop-specific range of leaf and canopy parameters.

2.2.1 Simulated rice spectra and LUT generation: First, the PROSAIL-PRO model was tested to assess the reliability in rice spectral simulation performance, by providing the input parameters required (i.e., leaf and canopy level parameters, sun-view geometry and the background soil reflectance), using the data from the experimental datasets available (i.e., 2004 and 2006 datasets). Due to the variability of spectral backgrounds characterizing rice cropping systems (i.e., dry/wet soil and flooded condition)., the effect of different conditions has been tested. Error metric (Mean Absolute Error - MAE) between measured and simulated spectra were computed for the different conditions in the experiment (phenological stage, fertilisation level and background presence). Results showed that when the appropriate background types were provided to the model, a reliable simulation could be obtained, with an overall MAE less than 5% on the full spectral range, for both the tested datasets (Figure 1). On the contrary, when only one type of soil was provided, a higher MAE was obtained, ranging between 8%-12%, meaning a less reliable simulation of the real crop conditions.
After this test, the PROSAIL-PRO MATLAB script provided by CNR-IREA was run to simulate in a short time a large LUT training database (2000 samples), containing realistic ranges of variation of biophysical variables considering both measured values from 2006 dataset and reference data from literature (Campos-Taberner et al., 2016) and their corresponding simulated spectra, exploiting different backgrounds due to their ascertained importance in reproducing realistic spectra. For the LUT, a cardinality of 2000 random samples was chosen, since representing a reasonable numerosity compared to the state-of-the-art literature (Verrelst et al., 2020).

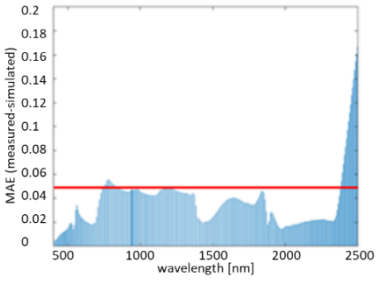

Figure 1. Results from spectral comparison in terms of MAE for 2004 dataset (panel a) and 2006 dataset (panel b). After 2300 nm spectra were atmospherically contaminated. Error estimated are therefore not considered. The red line represents the 5% MAE threshold.

2.2.2 ML algorithms: The MLRA model training was performed for Gaussian Process Regression (GPR) and Neural Network (NN) algorithms using ARTMO software (https://artmotoolbox.com/). GPR is considered one of the most promising kernel-based ML method for vegetation properties retrieval, having the advantage of providing uncertainty estimates on the predictions (Verrelst et al., 2020), while NN is potentially more accurate than other estimation techniques since it optimises directly over the variables of interest (Delloye et al., 2018). The Single Output model was performed, with 5% of Gaussian Noise added to both the parameters and spectra, as proposed for hybrid retrieval procedures to generalize the model and prevent overfitting on the RTM outputs (Verrelst et al., 2020). A cross-validation was performed with random partitioning of observations in 10 subsets (k-fold strategy). A data reduction (i.e., subset of LUT) procedure based on AL was also tested using ARTMO's AL module. AL is a subfield of ML seeking to optimize models to improve performance through intelligent sampling of training datasets (Verrelst et al., 2020). It is an iterative process which selected the best subsets of spectra from the original 2000 samples' LUT. 5 different diversity and uncertainty criteria where tested. Euclidean distance-based diversity (EBD), angle-based diversity (ABD) cluster-based diversity (CBD), variance-based pool of regressors (PAL), and residual regression AL (RSAL).
The reduced LUTs obtained as output, containing the optimal performing samples for the analysed LAI and CNC parameters (305 and 153 samples, respectively), were given as input to MLRA Toolbox to train the GPR and NN algorithms.

2.2.3 Sentinel 2 - Spectral configuration: Since this study focused on satellite S2 images, simulated spectra were resampled to a S2-like 8 bands spectral configuration (i.e., bands from 3 to 8, 11 and 12), this choice is conformed to European Space Agency (ESA) SENTINEL2 Toolbox, which excludes also band B2 (490 nm) according to ATBD (Algorithm Theoretical Based Document (Weiss and Baret, 2016) and findings from recent publication (Upreti et al., 2019).

3. RESULTS

3.1 Hybrid validation results

LAI estimation in cross-validation resulted well-correlated with independent data for both GPR and NN algorithms and both standard hybrid (R2 ~ 0.78 with GPR, R2 ~ 0.72 with NN) and AL optimization approach (R2 ~ 0.71 with GPR, R2 ~ 0.67 with NN) (Figure 2, panels a, b). CNC estimates were quite well correlated for low measured (independent) values (< 4 [$g\ m^{-2}$]) . Slightly better accuracy was obtained when using GPR algorithm (R2 ~ 0.37) with respect to NN (R2 ~ 0.33). An improvement is evidenced when using the AL method (passing from R2 ~ 0.37 to R2 ~ 0.45 with GPR and from R2 ~ 0.33 to R2 ~ 0.47 with NN) (Figure 2, panels c, d). AL results show a less evident saturation effect.

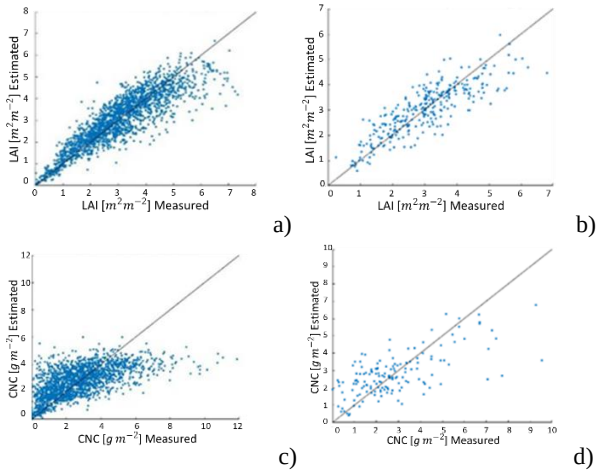

Figure 2. LAI [m^2m^{-2}] (panels a, b) and CNC [$g\ m^{-2}$] (panels c, d) estimated values against measured (independent) in cross-validation phase, using the hybrid retrieval approach with GPR algorithm, considering the 2000 samples LUT (left panels) and the reduced LUTs from AL optimization (right panels)

The robustness and exportability of the model was assessed performing a validation using real farm condition datasets (2018 – SATURNO project). Results showed that LAI estimates were well correlated with measured values (data not showed), whereas CNC estimates showed the same saturation behaviour after 3-4 [$g\ m^{-2}$], obtained in cross-validation phase, when compared to ground plant nitrogen uptake values (data not showed), although not representing a problem for model application to support fertilisation application at tillering and stem elongation phase, since for this purpose low values of CNC are expected in field. In general, the best accuracy results were obtained using the hybrid method with AL optimization and GPR algorithm, for both the parameters. The best method was consequently applied to the 9 selected level 2A S2 images that covered the Lomellina study area in the period from June to August of 2018 (from emergence to heading stage). Five of these images matched with ground measurements (Nutini et al., 2021).

From the generated LAI map, it was analysed the reliability of crop growth time series according to phenological development at both district (entire Lomellina) and farm level (single field) (Figure 3). The temporal maps from June to August resulted in agreement with the expected physical process of rice growth, with LAI estimates increasing in time from 0 to 6 [m^2m^{-2}].

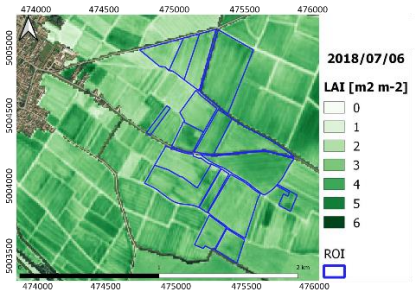

Figure 3. Example of retrieved LAI maps for the 6th of July. The blue polygons represent the Region Of Interest (ROI).

CNC map's reliability was further assessed by performing a within-field analysis. These maps were compared to the prescription maps generated in the SATURNO project for Variable Rate Technology (VRT) application (Figure 4).

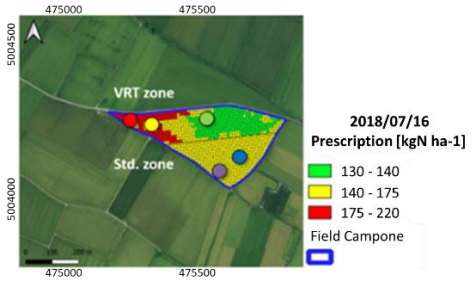

Figure 4. Prescription map from SATURNO project and selected samples, coloured circles, from 6th of July CNC map.

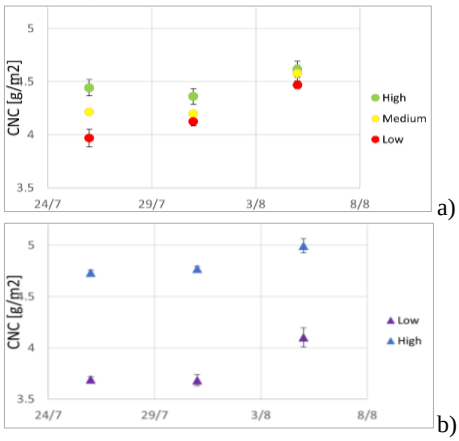

Figure 5. Temporal series (end of July- beginning of August 2018) of CNC estimates after 17th of July fertilisation, extracted in correspondence of the sample areas (coloured circles, Figure 4) for VRT (panel a) and Std. (panel b) zones

Figure 5 shows the prescription map used to fertilise the field with VRT on the 17th of July: upper part was managed with three

target doses (140, 175 and 220 [$kg\ ha^{-1}$]) of "Urea" according to crop condition (below, average and above) as detected with a smart scouting approach while the lower part of the field was managed with a standard homogeneous fertilisation dose (175 [$kg\ ha^{-1}$]) (Nutini et al., 2021). Sample areas were selected in the map, corresponding to i) high, medium and low and ii) high and low CNC estimates in the upper and lower part of the field, respectively. These 5 sample areas were selected on the 6th of July image, where the different ranges were well visible.
The CNC time series corresponding to the selected sample areas were extracted using the "Profile Tool" QGIS plugin, in order to investigate the effect of variable rate fertilisation against the standard dose application (Figure 5). The analysis showed the positive consequence of the VRT fertilisation applied in the upper part, on the 17th of July, according to the prescription, resulting in a final homogeneous N plant content, although plants were having different growing conditions at the beginning. On the contrary, in the homogeneously managed half of the field, lower part, differences in rice crop development were kept after the fertilisation, reflecting a non-optimized N management.

4. DISCUSSION

LAI generated maps resulted reliable EO-derived products to describe the crop development in the study area, at both district and farm level. Those maps also provided the information needed to assess differences occurring in different farms or fields due to multiple factors such as rice variety, sowing date, water management and soil quality hence nutritional status. The analysis of LAI temporal profile can be useful to monitor different crop growing behaviours as a consequence of different management conditions. The within-field nutritional spatial variation highlighted by the CNC generated maps resulted coherent with the observed heterogeneity in the field in agreement with VRT fertilisation management. Comparison of CNC estimates in area from different fertilisation techniques (i.e., the VR and the standard), highlighted how the lower dose of fertiliser used in the VRT zone with high CNC values, saved up to 20% on N application while maintain proper crop growth. From these findings, it can be stated that such digital geo-products represent a promising decision-supporting spatial information contribution to support crop monitoring and fertilisation management purposes, in the precision farming framework.

5. CONCLUSIONS

From the experiments, it resulted that the rice simulated spectra using the PROSAIL-PRO model agreed well with measured data when a representative database of background reflectance is provided (overall MAE lower than 5%). The hybrid retrieval approach, provided accurate estimates, showing improvement in the performance when an AL method is used. In general, the GPR algorithm provided slightly more accurate results than the NN. LAI estimates were always robust, whereas CNC estimates showed a saturation behaviour for measured values greater than 4 [$g\ m^{-2}$], although not representing a problem for a model application to support fertilisation agro-practices. The source of variability in the estimation for high values need to be further investigated, since CNC estimation from RTM is a quite new approach in remote sensing. The application of the model to satellite images was able to provide crop monitoring information at district and farm level. Within-field detected variability is the foreseen information requested by user community for a quantitate support of sustainable fertilisation. In conclusion the proposed method demonstrated the feasibility of a direct estimation of biophysical variables from S2 products as a contribution for precision farming applications.

ACKNOWLEDGEMENTS

The research activities have been framed in the CNR-DIPARTIMENTO DI INGEGNERIA, ICT E TECNOLOGIE PER L'ENERGIA E I TRASPORTI project "DIT.AD022.180 Transizione industriale e resilienza delle Società post-Covid19 (FOE 2020)", sub task activity "Agro-Sensing".

REFERENCES

Berger, K., Verrelst, J., Féret, J.-B., Hank, T., Wocher, M., Mauser, W., Camps-Valls, G., 2020. Retrieval of aboveground crop nitrogen content with a hybrid machine learning method. Int. J. Appl. Earth Obs. Geoinf. 92, 102174. https://doi.org/10.1016/j.jag.2020.102174

Campos-Taberner, M., García-Haro, F.J., Camps-Valls, G., Grau-Muedra, G., Nutini, F., Crema, A., Boschetti, M., 2016. Multitemporal and multiresolution leaf area index retrieval for operational local rice crop monitoring. Remote Sens. Environ. 187, 102–118. https://doi.org/10.1016/j.rse.2016.10.009

Delloye, C., Weiss, M., Defourny, P., 2018. Retrieval of the canopy chlorophyll content from Sentinel-2 spectral bands to estimate nitrogen uptake in intensive winter wheat cropping systems. Remote Sens. Environ. 216, 245–261. https://doi.org/10.1016/j.rse.2018.06.037

Nutini, F., Confalonieri, R., Crema, A., Movedi, E., Paleari, L., Stavrakoudis, D., Boschetti, M., 2018. An operational workflow to assess rice nutritional status based on satellite imagery and smartphone apps. Comput. Electron. Agric. 154, 80–92. https://doi.org/10.1016/j.compag.2018.08.008

Nutini, F., Confalonieri, R., Paleari, L., Pepe, M., Criscuolo, L., Porta, F., Ranghetti, L., Busetto, L., Boschetti, M., 2021. Supporting operational site-specific fertilization in rice cropping systems with infield smartphone measurements and Sentinel-2 observations. Precis. Agric. https://doi.org/10.1007/s11119-021-09784-0

Stroppiana, D., Boschetti, M., Brivio, P.A., Bocchi, S., 2009. Plant nitrogen concentration in paddy rice from field canopy hyperspectral radiometry. F. Crop. Res. 111, 119–129. https://doi.org/10.1016/j.fcr.2008.11.004

Upreti, D., Huang, W., Kong, W., Pascucci, S., Pignatti, S., Zhou, X., Ye, H., Casa, R., 2019. A comparison of hybrid machine learning algorithms for the retrieval of wheat biophysical variables from sentinel-2. Remote Sens. 11. https://doi.org/10.3390/rs11050481

Verrelst, J., Berger, K., Rivera-Caicedo, J.P., 2020. Intelligent Sampling for Vegetation Nitrogen Mapping Based on Hybrid Machine Learning Algorithms. IEEE Geosci. Remote Sens. Lett. 1–5. https://doi.org/10.1109/lgrs.2020.3014676

Weiss, M., Baret, F., 2016. S2ToolBox Level 2 products: LAI, FAPAR, FCOVER - Version 1.1. Sentin. ToolBox Level2 Prod. 53.

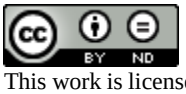

RETRIEVAL OF MAIZE BIOPHYSICAL VARIABLES FROM MULTISPECTRAL AND HYPERSPECTRAL EO DATA USING A HYBRID APPROACH

M. Ranghetti [1]*, M. Boschetti [1], M. Gianinetto [2,1], G. Tagliabue [3], C. Panigada[3], G. Candiani[1]

[1] IREA, National Research Council, Via Bassini 15, 20133 Milano, Italy – (ranghetti.m, boschetti.m, candiani.g)@irea.cnr.it
[2] Department of Architecture, Built Environment and Construction Engineering (DABC), Politecnico di Milano, Via Ponzio 31, 20133 Milano, Italy – marco.gianinetto@polimi.it

[3] Remote Sensing of Environmental Dynamics Lab., Dip. Scienze dell'Ambiente e del Territorio, Università Milano-Bicocca, 20126 Milano, Italy – (giulia.tagliabue, cinzia.panigada)@unimib.it

KEY WORDS: Precision Farming, Radiative Transfer Modelling, Machine learning, BV Estimation, Hybrid Approach

ABSTRACT:

Assessing crops health and status is becoming relevant to support farmers' decisions and actions for a sustainable agriculture. The use of remote sensing techniques in agriculture has become widely popular during the past years. Earth Observing (EO) data can greatly contribute to constantly monitor crops phenology and to estimate important vegetation biophysical parameters.
This work presents a hybrid approach, which exploits the PROSAIL-PRO model and Machine Learning (ML) algorithms, to estimate maize biophysical variables, such as Canopy Chlorophyll Content (CCC) and Leaf Area Index (LAI). The test site is represented by two maize fields located near Grosseto (Tuscany, IT), where two field campaigns were carried out in July 2018. During the same period, the airborne sensor Hyplant-DUAL acquired two images of the test site. These images were used to simulate PRISMA and Sentinel-2 data in order to investigate the difference of the retrieval performance between hyperspectral and multispectral EO data. Results show similar performance between Sentinel-2 and PRISMA. The ML algorithms, providing the best performance (GPR and NN) within the hybrid framework, were then applied to actual Sentinel-2 images. The retrieval results for LAI and CCC were compared to estimations assessed through the ESA S2Toolbox. The comparison showed that the proposed method provides better results than those achieved through S2Toolbox, for both LAI (R^2 = 0.85 and MAE = 0.39; S2Toolbox: R^2 = 0.35 and MAE = 0.87) and CCC (R^2 = 0.73 and MAE = 0.20; S2Toolbox: R^2 = 0.29 and MAE = 0.68).

1. INTRODUCTION

Agricultural practices can lead to different environmental threats, such as water consumption, biodiversity loss, pollutants' leaching and emissions. The assessment of crops health and status can support farmers' decisions and actions for a sustainable agriculture. This is the context where precision farming becomes relevant.
Precision farming is a management strategy used to "apply the right treatment in the right place at the right time" (Gebbers & Adamchuk, 2010). It is an important component of smart farming, which aims at an information-driven optimization of all aspects of a farming system (Bach et al., 2016).
Precision farming thus holds the potential for increasing yields on limited land while saving resources and preventing environmental pollution (Plant et al., 2000).
In this context, assessing vegetation status and health through Earth Observation (EO) data become relevant for the determination of some important biophysical vegetation variables (BVs).
Different methods can be found in literature for BVs retrieval such as parametric and nonparametric, linear and nonlinear regression methods, as well as physically-based methods using radiative transfer models (RTMs) and, more recently, hybrid approaches.
During the last decades, simple empirical parametric models were employed for the retrieval of biophysical parameters by using narrowband vegetation indices. Since few regions of the electromagnetic spectrum are exploited by using vegetation indices, a limitation in the retrieval of specific vegetation parameters may arise.
To overcome this situation, nonparametric methods could be employed. In general, nonparametric methods seek to best fit the training data, whilst maintaining some ability to generalize the unseen data. Nonlinear nonparametric methods are also known as machine learning regression algorithms (MLRAs).
Physically-based methods represent an alternative to the regression methods. They use RTMs for simulating the reflectance of vegetation measured by an EO sensor.
Hybrid methods are increasingly used in literature (Berger, Verrelst, Féret, Hank, et al., 2020; Berger, Verrelst, Féret, Wang, et al., 2020; Verrelst et al., 2020). In this approach, RTM are used in combination with MLRAs. Thus, hybrid methods have the transferability guaranteed by the use of a physically-based method and the computationally efficiency and flexibility provided by the regression method.
The goal of this work is the evaluation of a hybrid approach for the estimation of BVs, such as Canopy Chlorophyll Content (CCC) and Leaf Area Index (LAI) of maize crops, from hyperspectral and multispectral sensors.
In particular, this study tested the most recent version of PROSAIL (PROSAIL-PRO, Féret et al., 2020) and several MLRAs. The PROSAIL-PRO model was used to generate a database with hundreds of simulated vegetation reflectance spectra (Look Up Table - LUT). This database was then used to train different combinations of ML algorithms and feature selection configurations to estimate crop BVs. The best performing combinations were then applied to actual Sentinel-2

* Corresponding author

data. The best results obtained from the hybrid approach were then compared to LAI and CCC estimated from S2Toolbox.

2. MATERIAL AND METHODS

The following sections describe the study area, field measurements, EO dataset and the steps involved in the hybrid approach for the BV retrieval.

2.1 Study area and fields measurements

The study area is located in Tuscany (42°49′47.02″ N 11°04′10.27″ E; elev. 2 m a.m.s.l.), central Italy, North of Grosseto and 20 km away from the coastline.
Within the study area, two maize crops, from two different farms, Le Rogaie (around 76 ha) and Ceccarelli (around 33 ha), were selected as test sites. These two fields feature different irrigation systems and different sowing dates.
During June and July 2018, two field campaigns were carried out on the two fields, in order to collect a comprehensive dataset of biochemical and biophysical parameters. In particular LAI was measured with a LAI-2200 (LI-COR Biosciences, USA) and Leaf Chlorophyll Content (LCC) was measured with SPAD (Konica Minolta, Japan) and DUALEX (Force-A, France). CCC was calculated as LAI * LCC. The field activities included CAL/VAL radiometric measurements performed with spectroradiometer SPECTRAL EVOLUTION SR-3500 (https://spectralevolution.com/products/hardware/compact-lab-spectroradiometers/sr-3500/) and vegetation measurements and sampling. 33 Elemental Sampling Units (ESU) of almost 20x20 m were identified for the field campaign. Each ESU includes up to 4 plots of 10x10 m, for a total of 87 plots.

2.2 Airborne and spaceborne EO dataset

The study area was acquired by the HyPlant-DUAL hyperspectral airborne sensor on 7th and 30th July 2018. HyPlant-DUAL dataset was spectrally resampled at PRISMA (PRISMA-like) and Sentinel-2 (S2-like) wavelengths. PRISMA-like spectra were compared to radiometric field measurements in order to remove noisy bands presenting a mean absolute error greater than 5%: the final spectral configuration includes 155 bands. In the case of both S2 datasets (actual and simulated form HyPlant-DUAL), B1, B2, B9, B10 were removed to be consistent with ESA S2Toolbox (Weiss & Baret, 2016), while B8a was removed by Sen2R (Ranghetti et al., 2020). Therefore, the final spectral configuration for S2-like dataset includes 8 bands: B3, B4, B5, B6, B7, B8, B11, B12.
In addition, actual Sentinel-2 images were also available on the area of interest. The Sentinel-2 images acquired on 8th July and 2nd August 2018 (the S2 images closest to the field campaign) were then downloaded with Sen2R (Ranghetti et al., 2020).
Table 1 resumes the EO dataset used in this study.

Dataset	Acquisition date
PRISMA-like	07/07/2018
S2-like	07/07/2018
Sentinel-2	08/07/2018
PRISMA-like	30/07/2018
S2-like	30/07/2018
Sentinel-2	02/08/2018

Table 1. Airborne and spaceborne EO datasets.

2.3 Hybrid approach

2.3.1 PROSAIL-PRO: The RTM tested in the hybrid approach proposed in this work is PROSAIL-PRO. It combines two RTMs: the leaf PROSPECT-PRO model and the canopy 4SAIL model. Starting from structural and biophysical parameters as inputs, PROSPECT-PRO simulates reflectance at the leaf level from 400 nm to 2500 nm. The outputs of the PROSPECT-PRO are used by the 4SAIL, together with other variables, such as plant structural parameters, viewing angles and soil background to simulate the vegetation reflectance at canopy level.

2.3.2 Development of the training LUT: The PROSAIL-PRO was used to simulate canopy reflectances based on the combination of different input, characterizing the crop, the soil and the sun-sensor geometry.
Assumptions on the distribution of the above input variables needs to be done. Each PROSAIL-PRO input was modelled according to Normal or Uniform distributions. For each variable, the ranges of these distributions (mean and standard deviation for Normal distribution; min and max values for Uniform distribution) were set according to both field measurements and literature (Weiss & Baret, 2016), in the case measurements were not available.
Those inputs were then randomly sampled according to their distribution and used to simulate, through the PROSAIL-PRO, canopy reflectances of maize crops in the range 400–2500 nm with a spectral resolution of 1 nm. These reflectances were then resampled at the selected PRISMA (155 bands) and Sentinel-2 (8 bands) wavelengths. The final training database includes both input variables and PRISMA-like or S2-like reflectance spectra.
A Gaussian white noise of 5% was also added to inputs and canopy reflectances, in order to get more realistic data.

2.3.3 MLRA training phase: The training phase was performed using different ML regression algorithms for the retrieval of LAI and CCC. The algorithms used in this study include Partial Least Square Regression (PLSR), Gaussian Process Regression (GPR), Support Vector Regression (SVR), Artificial Neural Networks (ANN) and Random Forests (RF).

2.3.4 Validation phase and maps generation: The trained models were then applied to the datasets reported in Table 1.
The 87 field measurements of BVs carried out in the two maize fields in Grosseto were used to validate the hybrid models, comparing measured and estimated BVs values.
Moreover, for Sentinel-2 images, the best retrieval results for LAI and CCC, from the above-mentioned algorithms, were compared to the estimates from ESA S2Toolbox (Weiss & Baret, 2016). Due to the different spatial resolution between HyPlant-DUAL and actual Sentinel-2 images, the validation statistics were computed by averaging the BV values belonging to the same ESU.
Finally, the best performing algorithms were applied to the datasets (PRISMA-like, S2-like and actual S2) to generate maps of LAI and CCC over the investigated maize crops.
The training, validation and generation of maps were performed using ARTMO (Verrelst et al., 2011).

3. RESULTS AND DISCUSSION

This section shows the results of the influence of LUT size, as well as the results of LAI and CCC estimations from the proposed hybrid approach and the S2Toolbox.

3.1 Impact of LUT size on retrieval performance

The impact of the database size on the retrieval performance was investigated for all the BVs. Several LUTs ranging from 1000 to 9000 samples, with a 1000 samples step, were generated in the S2-like configuration. These LUTs were then used to train retrieval models for LAI and CCC and were validated against field measurements.
Figure 1 shows, as example, the impact of the training database size on the accuracy and training time of the selected models for CCC. The increase in the size of the training dataset leads to a minor improvement in the model statistics. On the other hand, the training time rises significantly, in particular for GPR. A similar pattern was verified also for LAI. Therefore, a LUT of 2000 samples was considered a good trade-off between accuracy and time.

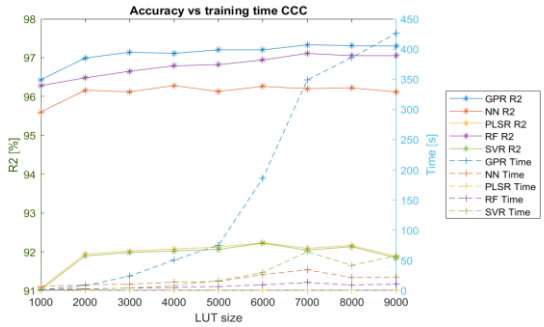

Figure 1. Impact of the training database size on the models' accuracy (R^2) and training time for CCC.

3.2 Hyperspectral vs multispectral BVs retrieval

The comparison of the best results for CCC and LAI estimated from PRISMA-like and S2-like dataset are resumed in Figure 2.

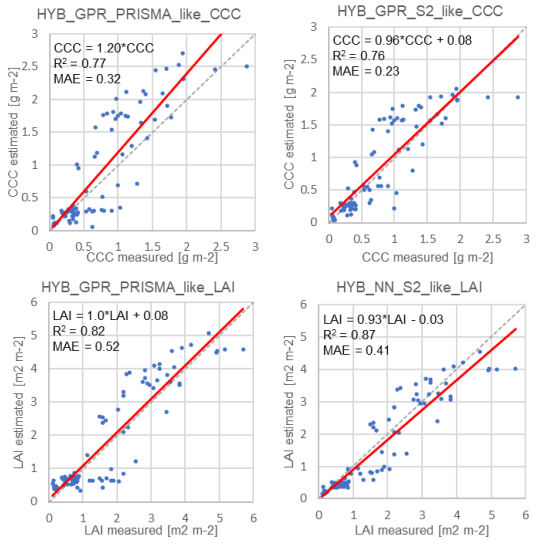

Figure 2. Comparison of CCC (top) and LAI (bottom) estimation from PRISMA-like (left) and S2-like (right) dataset using the hybrid approach (GPR and NN).

In general, retrieval results for CCC and LAI show very good performances for both PRISMA-like and S2-like dataset. For both BVs, S2-like achieved slightly better performance than PRISMA-like, in terms of MAE (CCC: 0.23 for S2 and 0.32 for PRISMA; LAI: 0.41 for S2 and 0.52 for PRISMA). Even if PRISMA provided a better correlation coefficient (R^2 = 0.77) than S2 (R^2 = 0.76) for CCC, there is an overestimation of this BV of 20%. Moreover, it is worth noting that PRISMA-like gives better estimates than S2-like at high values, highlighting a saturation effect for S2-like.
Among the tested ML algorithms GPR provided the best results for CCC and LAI retrieved from PRISMA-like. Whereas NN performed better for LAI estimated from S2-like.

3.3 Hybrid vs S2Toolbox BVs retrieval

The best performing algorithms, for the retrieval of CCC and LAI from S2-like, were applied to the actual Sentinel-2 images, acquired on 8th July and 2nd August 2018. S2Toolbox was applied to the same dataset to assess both BVs.

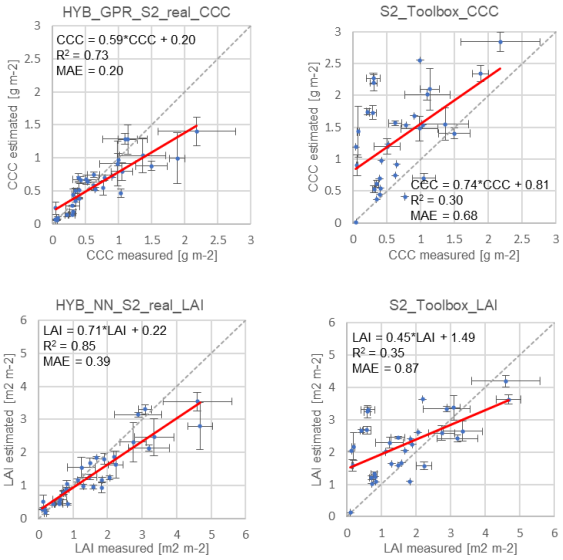

Figure 3. Comparison of CCC (top) and LAI (bottom) estimations from Sentinel-2 data using hybrid approach (left) and S2Toolbox (right).

Retrieval results, using the hybrid approach and S2Toolbox, are resumed in Figure 3. Considering the hybrid approach, from the scatterplots in Figure 2 and Figure 3, it is clear how the retrieval performed on real data leads to a general underestimation of the BVs: specifically, the angular coefficient of the regression line is generally lower than the slope for S2-like retrieval. This worsens the saturation effect observed in S2-like data. However, despite this issue, the hybrid approach provides good results for both CCC (R^2 = 0.73, MAE = 0.20) and LAI (R^2 = 0.85, MAE = 0.39).
Regarding ESA S2Toolbox, the estimations show much lower accuracy for both CCC (R^2 = 0.30, MAE = 0.68) and LAI (R^2 = 0.35, MAE = 0.87). These poor results could be explained considering that the NN algorithm in the S2Toolbox was trained with a comprehensive LUT which should be representative of the main vegetation types around the globe. While this global training data may be suitable for modelling the average vegetation status, they might not represent the status of specific areas. Thus, fine-tuned ad-hoc models, such as those proposed in this work, can lead to significantly better estimates.

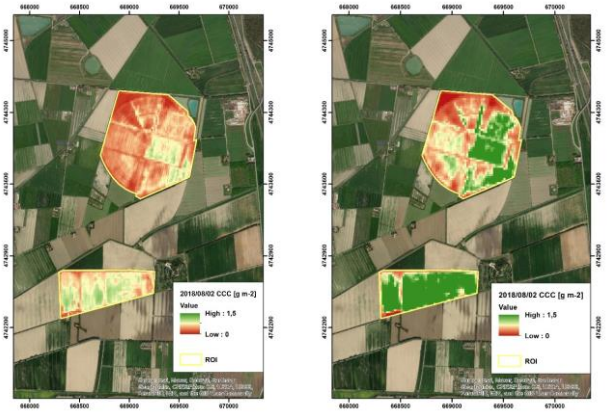

Figure 4. Comparison of CCC maps estimated from Sentinel-2 image acquired on 2nd August 2018 using the hybrid approach (left) and S2Toolbox (right).

Figure 4 shows the comparison of CCC maps estimated from Sentinel-2 image acquired on 2nd August 2018 using the hybrid approach (left) and S2Toolbox (right). As it was expected from the scatterplot, the map estimated from S2Toolbox presents many more saturated pixels especially for high CCC values.

4. CONCLUSIONS

This work proposed a hybrid method, which combines the radiative transfer model PROSAIL-PRO and several ML regression algorithms (PLSR, GPR, SVR, ANN and RF), for the estimation of CCC and LAI. The exploited EO dataset, acquired from both airborne and spaceborne sensors, includes both hyperspectral (PRISMA-like) and multispectral data (simulated and actual Sentinel-2 data).

The analysis on the impact of LUT size on retrieval performance showed that increments in LUT size have a minor impact on retrieval accuracy. On the other hand, an increase in the training time was observed, especially for GPR. For this reason, a LUT of 2000 samples was considered a good trade-off between accuracy and time.

The comparison between hyperspectral and multispectral data (simulated from the airborne imager HyPlant-DUAL) for the retrieval of CCC and LAI showed very good performances for PRISMA-like and S2-like dataset. For both BVs, S2-like achieved slightly better performance than PRISMA-like, even though S2-like estimates showed a saturation effect visible at high CCC and LAI values.

The best performing algorithms for S2-like were applied to actual Sentinel-2 data and compared to the results obtained using ESA S2Toolbox. The validation of these two approaches showed that the proposed hybrid method provides better estimates than S2Toolbox for both CCC and LAI, highlighting the need for specific algorithms tuned for specific areas.

ACKNOWLEDGEMENTS

The project activities have been framed in the CNR-DIPARTIMENTO DI INGEGNERIA, ICT E TECNOLOGIE PER L'ENERGIA E I TRASPORTI project “DIT.AD022.180 Transizione industriale e resilienza delle Società post-Covid19 (FOE 2020)”, sub project activity “Agro-Sensing”.

The research leading to these results was conducted within “ESA RFP/3-15502/18/NL/IA: CHIME RCS, Mission Requirement Consolidation Study” and its related CCN (Ref. HYS-CN-ISP-PM-0001), funded by the European Space Agency.

REFERENCES

Bach, H., Mauser, W., & Klepper, G. (2016). Earth observation for food security and sustainable agriculture. *European Space Agency, (Special Publication) ESA SP*.

Berger, K., Verrelst, J., Féret, J. B., Hank, T., Wocher, M., Mauser, W., & Camps-Valls, G. (2020). Retrieval of aboveground crop nitrogen content with a hybrid machine learning method. In *arXiv*. https://doi.org/10.1016/j.jag.2020.102174

Berger, K., Verrelst, J., Féret, J. B., Wang, Z., Wocher, M., Strathmann, M., Danner, M., Mauser, W., & Hank, T. (2020). Crop nitrogen monitoring: Recent progress and principal developments in the context of imaging spectroscopy missions. In *Remote Sensing of Environment*. https://doi.org/10.1016/j.rse.2020.111758

Féret, J. B., Berger, K., de Boissieu, F., & Malenovský, Z. (2020). Prospect-pro for estimating content of nitrogen-containing leaf proteins and other carbon-based constituents. In *arXiv*. https://doi.org/10.1016/j.rse.2020.112173

Gebbers, R., & Adamchuk, V. I. (2010). Precision agriculture and food security. In *Science* (Vol. 327, Issue 5967). https://doi.org/10.1126/science.1183899

Plant, R. E., Pettygrove, G. S., & Reinert, W. R. (2000). Precision agriculture can increase profits and limit environmental impacts. *California Agriculture*. https://doi.org/10.3733/ca.v054n04p66

Ranghetti, L., Boschetti, M., Nutini, F., & Busetto, L. (2020). “sen2r”: An R toolbox for automatically downloading and preprocessing Sentinel-2 satellite data. *Computers and Geosciences*, *139*. https://doi.org/10.1016/j.cageo.2020.104473

Verrelst, J., Berger, K., & Rivera-Caicedo, J. P. (2020). Intelligent Sampling for Vegetation Nitrogen Mapping Based on Hybrid Machine Learning Algorithms. *IEEE Geoscience and Remote Sensing Letters*. https://doi.org/10.1109/lgrs.2020.3014676

Verrelst, J., Rivera, J. P., Alonso, L., & Moreno, J. (2011). ARTMO: an Automated Radiative Transfer Models Operator toolbox for automated retrieval of biophysical parameters through model inversion. *Proceedings of EARSeL 7th SIG-Imaging Spectroscopy Workshop, Edinburgh, UK*.

Weiss, M., & Baret, F. (2016). S2ToolBox Level 2 products: LAI, FAPAR, FCOVER - Version 1.1. *Sentinel2 ToolBox Level2 Products*.

A REPRODUCIBLE WORKFLOW TO DERIVE CROP PHENOLOGY AND AGRO-PRACTICE INFORMATION FROM SENTINEL-2 TIME SERIES: A CASE STUDY FOR SARDINIA CROPPING SYSTEMS

Luigi Ranghetti [1,2*], Francesco Nutini [1], Donato Cillis [2], Mirco Boschetti [1]

[1] Institute for Remote Sensing of Environment, Consiglio Nazionale delle Ricerche, Via Bassini 15, 20133 Milano, Italy
[2] IBF Servizi S.p.A., Via Cavicchini 2, 44037 Jolanda di Savoia (FE), Italy

KEY WORDS: Sentinel-2, Time Series Analysis, Crop Phenology, Data processing, Software engineering.

ABSTRACT:

Sentinel-2 data are widely used to estimate phenological parameters for agronomic applications, although processing methods are often difficult to reproduce and the efficiency of estimations is often not verified. In this contribution we describe a workflow used in the framework of E-crops project (https://bit.ly/cnr-ecrops) for the analysis of *Bonifiche Ferraresi* farm in Arborea (Sardinia): creation of the data archive (2018-2020), extraction and smoothing of $MSAVI_2$ time series, identification and interpolation of relevant crop cycles and computation of phenological metrics. Algorithms were developed as R functions and publicly released in the R package "sen2rts" (https://sen2rts.ranghetti.info), so to facilitate reproducibility and methodology generalisation. Estimates were validated using farm information: good agreement was found between detected seasons and cultivated crops and among SOS estimates and sowing dates. These findings are encouraging to further develop "sen2rts" in order to manage a wider range of crop types and to extract additional information (e.g. crop categories).

1 INTRODUCTION

Remote sensing represents a valuable added-value source of information to integrate farmer declaration as a basis for operational crop monitoring systems, whose functioning appear to be even more crucial in several domains (e.g. in the context of the post-2020 European Common Agricultural Policy – CAP, which is evaluating the introduction of an automated monitoring system from remote data in the framework of the Integrated Administration and Control System; Rousi et al., 2021).
Among available datasets, Sentinel-2 data (S2) are being increasingly used for agriculture monitoring thanks to the fine spatial and temporal resolutions, particularly suitable to retrieve crop phenology and agro-practices at parcel level (Segarra et al., 2020).
Many use cases are known in literature concerning the detection and analysis of crop seasonality from S2 data, although information on crop phenology is mainly retrieved as intermediate step for applications like crop detection and mapping, while the attention dedicated to test the efficiency of S2 imagery for the estimation phenological metrics is scarce (Misra et al., 2020). Moreover, the reproducibility of the methods used in these works is often difficult or not possible, since they are only theoretically described. Another obstacle frequently encountered by researchers is that operations needed to build and analyse S2 time series are generally time consuming, both in terms of computation time and because scientists need to prepare and implement their processing steps at low level.
In order to simplify these operations, the R package "sen2rts" was built to provide functions and methods for the processing and analysis of S2 time series. Exploiting this package, users can easily retrieve data and build time series following the workflow described in the package documentation. The implemented workflow was applied to the *Bonifiche Ferraresi* farm of Arborea (Sardinia – Italy) in order to detect crop cycles and to estimate sowing dates; this contribute shows a proof of concept for this application, presenting some preliminary results about the usefulness and reliability of these estimations.

2 MATERIALS AND METHODS

2.1 Study area

The study was performed in Sardinia (Arborea, 39° 47' ± 2' N, 8° 36.5' ± 0.9' E, 945 hectares; see Figure 1), on the fields of the farm *Bonifiche Ferraresi*. This estate, left aside until 2017, was then cultivated exploiting intensive organic and innovative farming techniques with a wide range of crops, among which the most represented are cereals (durum wheat, barley and triticale), maize, herbages (Italian rye-grass, alfalfa and clover) and legumes.
Information about field boundaries, cultivation plans (years 2018-2020) and sowing dates was provided by the farm. In this study we considered the information related to the above-mentioned crops (with the exception of legumes and alfalfa), covering a total of 116 and 84 records about crop types and sowing dates, respectively.

2.2 Remotely sensed data

S2 data were used to produce maps of the $MSAVI_2$ spectral index (Qi et al., 1994) over the study area from 2017-10-01 to 2020-12-31. Original level-2A (bottom-of-atmosphere reflectances) archives were downloaded from ESA Open Hub when available, or from Google Cloud Storage otherwise. In case level-2A images were not available, they were generated from the corresponding level-1C (top-of-atmosphere reflectances) archives using Sen2Cor for atmospheric and topographic correction. Images were then cropped over the estate's boundaries, and the $MSAVI_2$ index was computed:

* Corresponding author

$$\mathrm{MSAVI}_2 = 2b_8 + 1 - \sqrt{\frac{(2b_8+1)^2 - 8(b_8 - b_4)}{2}} \quad (1)$$

where b_8 = NIR band (842 nm), 10 m resolution;
b_4 = red band (665 nm), 10 m resolution.

Scene CLassification maps (SCL) and quality indicators for CLouD probabilities (CLD; TAS Team, 2021) were also generated from S2 images, to provide ancillary quality information (e.g. cloud-covered surfaces, presence of shadows) to be used in the extracting and smoothing processes.
The output archive is composed of 496 images (one per sensing date), acquired by both Sentinel-2A and 2B sensors over the orbits 22 and 65, with a temporal resolution of 4 images every 10 days.
All the described operations were performed using the R package "sen2r" (Ranghetti et al., 2020).

2.3 Time series processing workflow

MSAVI_2 time series were extracted from the S2 archive on farm's fields and processed in order to smooth them and recognise the cropping seasons of interest. In detail:

1. raw time series were extracted from MSAVI_2 images considering, for each available date, the weighted average of pixels included in each single field according to polygon boundaries of vector crop map (pixel weight is assigned from quality flag derived from SCL and CLD information);
2. smoothed time series were obtained applying a three-iteration Savitzky-Golay filter, filtering and weighting values in consideration of their quality flags;
3. daily time series were generated interpolating missing days with a spline function;
4. crop cycles were identified cutting time series in correspondence of relevant local minima, and keeping a maximum number of two cycles for each year (cycles with a maximum value between February and May and between June and mid-October were labelled as "winter" and "summer" crops, respectively);
5. each crop cycle was interpolated with a double logistic function (Gu et al., 2003; method inherited from R package "phenopix" – Filippa et al., 2016).

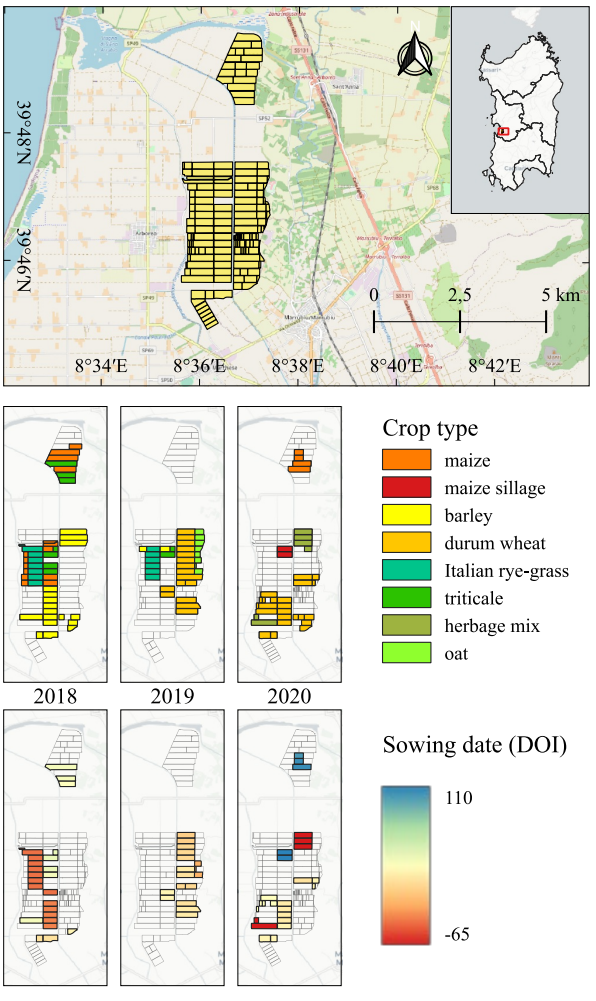

Figure 1: Position of the study area, together with crop type and sowing dates.

2.4 Analysis

Phenological metrics about timing of start and end of cropping cycles (SOS and EOS, respectively) were extracted from the interpolated crop cycles and compared with crop information obtained from the farm. SOS were identified as the dates when the ascending logistic curve reaches the 10% of the maximum slope (first derivative), while EOS as the dates when the descending logistic curve reaches the maximum slope. Considering that SOS does not correspond to the estimated sowing date, the SOS' measure was computed as follows:

$$\mathrm{SOS}' = \mathrm{SOS} - \frac{1}{n}\sum_{i=1}^{n} \Delta d_i \quad (2)$$

where $\Delta d_i = \mathrm{SOW}_i - \mathrm{SOS}_i$
SOW_i = i-th sowing date,
SOS_i = i-th Start Of Season date

SOS' was validated against SOW with a Leave-One-Out Cross Validation (validation metrics indicated in Section 3.2 refer to SOS' values computed with this method).
Association between detected crop cycles and field information was made associating the categories of "cereals" and "herbages" with cycles labelled as "winter", and "maize" with cycles labelled as "summer". SOS' estimations were compared with the corresponding sowing dates provided by the farm.

2.5 Methods and code reproducibility

The processing steps described in Section 2.3 and the methods to derive phenological metrics cited in Section 2.4 represent a workflow which can be generalised and exploited for several cases of time series analysis. For this reason, particular attention was paid to build the corresponding methods as functions, exported in the form of a R package and released with a GNU-GPL3 free license (Ranghetti, 2021a). The package "sen2rts" is currently in beta version; documentation is available at https://sen2rts.ranghetti.info/.
All the performed analysis can be easily reproduced using the R code supplied as supplementary material (Ranghetti, 2021b).

3 PRELIMINARY RESULTS

3.1 Identification of crop seasonality

A cycle with the proper seasonality (winter or summer) was detected from S2 time series in correspondence of almost all the considered crops (113 over 116). Observing the time series of the 3 remaining crops (an example is shown in Figure 2, 2nd panel),

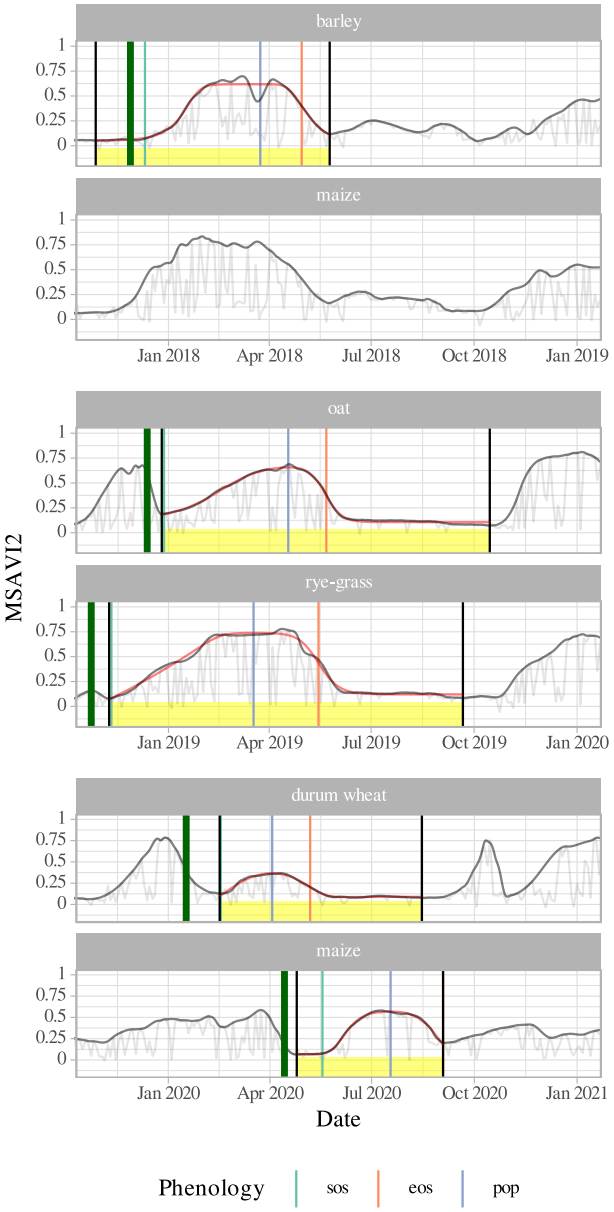

Figure 2: $MSAVI_2$ time series over six example fields. Light-grey lines join raw values (point 1 of the list in section 2.3); dark grey curves represent daily smoothed values (point 3); vertical black segments and yellow boxes delimit the crop cycles (point 4) corresponding to field information; coloured thin vertical lines represent estimated phenological metrics (see legend); green thick vertical lines indicate sowing dates.

it appears realistic to suppose an error in the crop register (remote data highlight the presence of winter cycles, which are not compatible with maize crops).

Figure 2 shows the comparison between raw and smoothed time series, highlighting the ability of the implemented smoothing method to fit the upper envelope of raw data. The method for cutting cycles resulted suitable to correctly isolate relevant portions of time series; cycles separated by periods of bare soil (e.g. 3rd, 4th and 5th panels) were cut in correspondence of the local minima, with the consequence that the period of bare soil could be assigned equally to the preceding or the subsequent

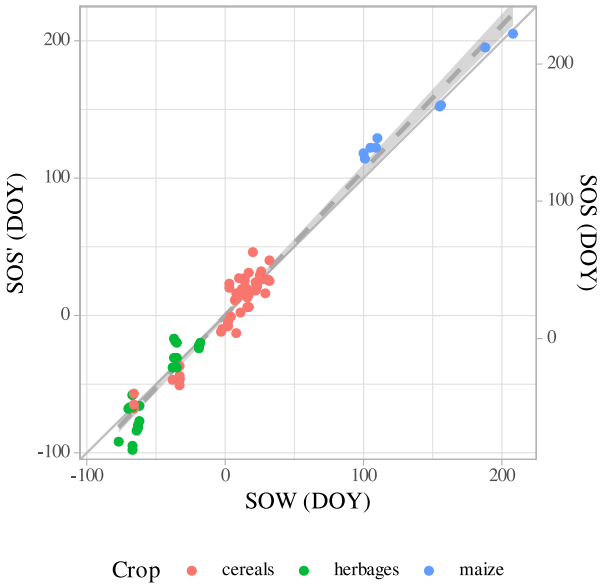

Figure 3: Comparison between known sowing dates (SOW) and estimated dates (SOS and SOS' – see text).

cycle. Nevertheless, this did not affect the methods for cycle interpolation and identification of phenological phases, while the use of a threshold methods over first resulted robust to the presence or absence of a starting plateau (while thresholding $MSAVI_2$ values in presence of a starting plateau led to early estimates in some cases).

3.2 Comparison between SOS estimations and sowing dates

A good agreement between SOS and sowing dates was found: difference (Δd) is 16.85 ± 11.33 days (R^2 = 0.97, DF = 82). Computing SOS' with formula (2) allowed estimating sowing dates with a Mean Average Error lower than 10 days (MAE = 8.84, RMSE = 11.40). However, the usability of SOS' as a proxy of the sowing dates is subject to the climatic peculiarity of the considered study area and it is expected to be crop dependent. Further attention should be devoted to different contexts, in which dormancy could interpose among sowing events and growing seasons (Manfron et al., 2017).

A relevant result of this case study is that, as highlighted by Figure 3, the agreement between estimated and known dates was also recorded within crops (cereals: R^2 = 0.89, DF = 47; herbages: R^2 = 0.80, DF = 24; maize: R^2 = 0.97, DF = 7).

4 CONCLUSIONS

In this study we presented a workflow to process Sentinel-2 time series in order to detect seasonal crop cycles and extract phenological metrics. Algorithms were developed in the form of an open source R package ("sen2rts"), so to provide an easy-to-use tool for S2 time series analysis and to facilitate code reproducibility. The workflow was applied to the use case of the farm *Bonifiche Ferraresi* in Sardinia, demonstrating its usability to detect crop cycles and estimate phenological metrics. The comparison between estimated dates of Start of Season (SOS) and the known sowing dates showed a good agreement (R^2 = 0.97), confirming that the analysis of $MSAVI_2$ temporal profiles can be used to derive sowing dates in contexts similar to the considered use case.

This analysis used sowing dates as reference information, for two reason: since the possibility to estimate them by remote represents a valuable target, and because of the relative facility to retrieve this information. Next steps will involve the direct comparison between estimated and observed phenological phases, as well as the use of a broader datasets in different geographic areas (including additional farms, or considering the use of sowing dates from CAP declarations) for which sowing dates are available.

ACKNOWLEDGEMENTS

This work was performed as part of the project "E-Crops – *Tecnologie per l'Agricoltura Digitale Sostenibile*" (ARS01_01136, https://bit.ly/cnr-ecrops), funded by European Union and by the Italian "*Programma PON Ricerca e Innovazione 2014-2020* – Area Agrifood" in the framework of the topics of smart specialisation planned by the Italian *Programma Nazionale per la Ricerca* (PNR – National Research Program).
We thank the society *Bonifiche Ferraresi S.p.A.* for the availability to share field information used in this work.

REFERENCES

Filippa, G., Cremonese, E., Migliavacca, M., Galvagno, M., Forkel, M., Wingate, L., Tomelleri, E., Morra di Cella, U., Richardson, A. D., 2016. Phenopix: a R package for image-based vegetation phenology. *Agricultural and Forest Meteorology*, 220, pp. 141-150. doi: 10.1016/j.agrformet.2016.01.006.

Gu, L., Post, W.M., Baldocchi, D., Black, T.A., Suyker, A.E., Verma, S.B., Vesala, T., Wofsy, S.C., 2009. Characterizing the Seasonal Dynamics of Plant Community Photosynthesis Across a Range of Vegetation Types. In: *Phenology of Ecosystem Processes*, pp. 35-58, Ed: Noormets A., Springer, New York).

Manfron, G., Delmotte, S., Busetto, L., Hossard, L., Ranghetti, L., Brivio, P. A., Boschetti, M., 2017. Estimating inter-annual variability in winter wheat sowing dates from satellite time series in Camargue, France. *International journal of applied earth observation and geoinformation*, 57, pp. 190-201. doi: 10.1016/j.jag.2017.01.001.

Misra, G., Cawkwell, F., Wingler, A., 2020. Status of Phenological Research Using Sentinel-2 Data: A Review. *Remote Sensing*, 12 (17), 2760. doi: 10.3390/rs12172760.

Qi, J., Chehbouni, A., Huete, A. R., Kerr, Y. H., & Sorooshian, S., 1994. A modified soil adjusted vegetation index. *Remote sensing of environment*, 48(2), pp. 119-126. doi: 10.1016/0034-4257(94)90134-1.

Ranghetti, L., Boschetti, M., Nutini, F., Busetto, L., 2020. sen2r: An R toolbox for automatically downloading and preprocessing Sentinel-2 satellite data. *Computers & Geosciences* 139, 104473. doi: 10.1016/j.cageo.2020.104473.

Ranghetti, L., 2021a. sen2rts: Build and Analyse Sentinel-2 Time Series. R package version 0.4.0. doi: 10.5281/zenodo.4682829.

Ranghetti, L., 2021b. Time series analysis on Arborea: preliminary results. doi: 10.5281/zenodo.4945650.

Rousi, M., Sitokonstantinou, V., Meditskos, G., Papoutsis, I., Gialampoukidis, I., Koukos, A., Karathanassi, V., Drivas, T., Vrochidis, S., Kontoes, C., Kompatsiaris, I., 2021. Semantically Enriched Crop Type Classification and Linked Earth Observation Data to Support the Common Agricultural Policy Monitoring. *IEEE Journal of Selected Topics in Applied Earth Observations and Remote Sensing*, 14, pp. 529-552. doi: 10.1109/JSTARS.2020.3038152.

Segarra, J., Buchaillot, M.L., Araus, J.L., Kefauver, S.C., 2020. Remote Sensing for Precision Agriculture: Sentinel-2 Improved Features and Applications. *Agronomy*, 10, 641. doi: 10.3390/agronomy10050641.

TAS Team, 2021. Sentinel-2 Products Specification Document, v. 14.6. Available online (accessed June 21, 2021) https://sentinel.esa.int/documents/247904/685211/Sentinel-2-Products-Specification-Document.

Urban Health from Space: actual and past scenarios

How Much Greenness Can Mitigate Urban Warming? A Tentative Answer Based on Thermal Data from Landsat Missions

T. Orusa [1]*, S. De Petris[2], F. Sarvia[2], E. Borgogno-Mondino[2]

[1] Department of Agricultural, Forest and Food Sciences (DISAFA) - IN.VA Spa, Località L'Île-Blonde, 5, Brissogne (AO)
tommaso.orusa@unito.it ; torusa@invallee.it
[2] Department of Agricultural, Forest and Food Sciences (DISAFA) - GEO4Agri DISAFA Lab, Università degli studi di Torino Largo Paolo Braccini 2, Grugliasco (TO) 10095, Italy; enrico.borgogno@unito.it; filippo.sarvia@unito.it; samuele.depetris@unito.it;

KEY WORDS: Landsat TIRS, Corine Land Cover 2018, Google Earth Engine (GEE), R Studio, Vegetation, Turin, Climate Change, Pettitt's test.

ABSTRACT:

Urban areas temperature conditions appears to be relevant in defining wellbeing of people, suggesting that some analyses have to be made concerning possible effects of climate change. In this study, monthly Landsat 4, 5, 7, 8 Land Surface Temperature (LST) monthly composites covering the period 1984-2020 were processed by Google Earth Engine (GEE) to test the existence of increasing trends in the study area. This concerned the whole municipality of Torino (Piemonte, NW Italy) and focused on the role that built and green areas can play in a metropolitan context of about 800,000 inhabitants in the global warming framework. The basic idea was to demonstrate how free available data from long-lasting satellite missions (like the Landsat one) could support planning policies by supplying quantitative estimates of both temperature trends and consequent relationship with land cover classes that constitute the urban patchwork. City management will represent a great challenge for future policy makers and topologic relationship between green and built areas will be an important issue to deal with. With these premises, green and built areas were mapped by the CORINE land cover level 3 map. A time series of LST images from the Landsat missions was generated by GEE and analyzed at pixel level to test local trend. Preventively pixels possibly switched from one class to another were recognized and masked out. Only class-invariant pixels were retained and used to test temperature trends. For these pixels, LST trend was modelled by a 1st order polynomial and the significance of the related gain evaluated. Significant gain values were averaged at class level (built and green classes). Built areas showed a steeper increasing trend than vegetated ones. Assuming that vegetation can partially compensate temperature increasing, a paradigmatic case study was proposed to translate such information in planning concerns. It relied on the assumption that the municipality of Torino could be considered like a closed system made of two classes completely filling the area included within its administrative borders. If, along time and for planning reasons, an area moves from one class to the other, one has to admit that one class gains the same area that the other losses. Within these constraints, a model was developed to test how long a switching strategy where built zones turn to green ones can maintain the present average temperature condition over the area. It was found that, in spite of whatever planning efforts, the mitigation effect by green areas will stop within few years.

1. INTRODUCTION

Urban areas have bloomed through decades worldwide with consequent variation in land surface temperature (LST) regimes (Wang et al., 2018). One of the most critical features of urban sprawl is the amount, type and pattern of built/asphalted areas that are required to house people and supporting their activities (Sarvia et al., 2021; De Petris et al., 2021). Presently, built areas appear to expand unreasonably faster than local populations in the most of parts of the world (d'Amour et al., 2017). In the meantime, average temperatures are wherever increasing due to the ongoing climate change (Orusa and Borgogno Mondino, 2021), making especially urban environments more critical. One of the biggest challenges today is trying to manage this joint effect by providing new tools for a sustainable planning of our cities (Borgogno-Mondino et al., 2015; Orusa and Borgogno-Mondino, 2019; Orusa et al., 2020).

In this context, satellite data from long-operational missions (i.e. NASA Landsat) can represent a useful tool for exploring spatial and time pattern of LST within urban contexts, making possible to provide some information to address future urban planning policies. In addition, cloud-based geospatial analysis platforms, like Google Earth Engine (GEE, Gorelick et al., 2017), can be easily accessed to achieve such analysis in a very effective and synthetic way. In particular, LST maps derived from satellite thermal (TIR) imagery are crucial to explore time trends of local temperatures (heat fluxes) and trying to relate them to land cover classes (like built and vegetated areas). Satellite-base LST analyses are increasingly proposed as successful tool for assessing urban micro-climate and in support of management of human settlements, with special concerns about the role of greenness in the mitigation of temperature increasing (De Petris et al., 2021; Marconcini et al., 2017)

Urban planners, inhabitants and public institutions are looking for low-cost methods to boost urban heat mitigation as a response to the joint effect of the ongoing global warming and urban sprawl. Under this premises, green areas (GA) including urban forestry, green roofs and other possible nature based solutions represent an opportunity to mitigate such threats (Coutts et al., 2013). Green areas have different thermal advantages showing an insulation effect for the underlying soil (Coutts et al., 2013). Greenness-based solutions are commonly referred to as a key approach to reduce heat-related phenomena in urban areas. Unreasonably, in the past decades, urban areas have been interested by the replacement of natural covers with impervious urban materials, inducing several variations in the biophysical patterns and, therefore, changes in local heat fluxes (Marconcini et al., 2017). It is worth to remind that an abundance of studies focuses on the mitigation benefits of green areas against temperature increasing and many works play around the heat islands topic; nevertheless a general lack can be found in scientific literature about the relationship between LST trends and land cover classes in urban areas. In particular, there are no studies, according to our knowledge, concerning the proposition of possible quantitative scenarios of urban planning, nor about the definition of the time ranges that any favourable planning choice (e.g. new GAs in place of built areas, BA) is expected to generate a significant mitigation effect within. It is authors' will

* Corresponding author

trying to fill this gap, providing a simplified pilot methodology able to give immediate answers to this question.

1.1 Study Area

The present study concerned the whole urban area of the municipality of Torino (Piemonte, NW Italy) (Fig. 1).

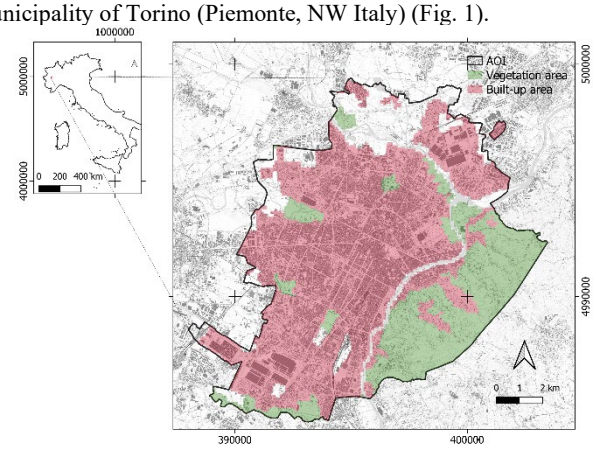

Fig. 1 *Study area: municipality of Torino (Piemonte, NW Italy). Reference system is WGS84 UTM32N*

2. MATERIALS AND METHODS

Available Data

The United States Geological Survey (USGS) provides TOA brightness temperature images (hereinafter called T_b) as obtained from the thermal sensors of Landsat satellites. USGS T_b images collection 1 (from Landsat 4-5-7-8 missions, sensors TM, ETM+, TIRS) can be accessed through GEE. USGS also provides the correspondent at-the-surface reflectance calibrated bands that can be, similarly, accessed through GEE. Additionally, the quality assessment band (BQA) is available too making possible to to retrieve cloud coverage and shadowing information. All the bands are supplied with a Ground Sampling Distance (GSD) of 30 m. Coarser thermal bands have been oversampled using a bilinear approach (Chander et al., 2009). Data were aggregated by averaging of "good" observations (from BQA) at month level and a monthly time series generated covering the period 1984-2020. It resulted in 444 images.

In order to map built and vegetated classes in the study area (hereinafter called AOI) the Corine Land Cover 2018 (CLC18) level 3 was used. CLC18 was obtained for free from the Copernicus Land Monitoring Service (https://land.copernicus.eu/pan-european/corine-land-cover).

Table 1. *Corine Land Cover classes used to map built and vegetated areas in AOI.*

Code Meaning	CLC Code	Code aggregation	Area (ha)
Artificial surfaces - Continuous urban fabric	111	1	1632.8
Artificial surfaces - Discontinuous urban fabric	112	1	5773.9
Artificial surfaces - Industrial or commercial units	121	1	929.8
Artificial surfaces - Green urban areas	141	2	484.1
Agricultural areas - Land principally occupied by agriculture, with significant areas of natural vegetation	243	2	1314.6
Forest and semi natural areas - Broad-leaved forest	311	2	1130.6

CLC2018 level 3 is the most detailed level according to the hierarchical classification system adopted by the CORINE Land Cover project (Büttner, 2014). As representatives of green (code 1) and built (code 2) areas in AOI different CLC2018 Level 3 native classes were considered and aggregated (see table 1). A total of 8336.5 and 2929.3 ha resulted for BA and GA, respectively.

Data Processing

Landsat data were processed in GEE (Gorelick et al., 2017) by adopting the approach proposed by Ermida et al. (2020). Surface emissivity maps, needed for LST computation from Tb images, were obtained according to the Fractional Vegetation Cover (FVC) approach of eq. 1 (Rubio et al., 1997).

$$\varepsilon = FVC_{\varepsilon v} + (1 - FVC)_{\varepsilon s} \quad (1)$$

where $FVC_{\varepsilon v}$ and $FVC_{\varepsilon s}$ are the FVC values computed for a completely vegetated and a pure bare soil pixel, respectively. FVC can be computed with reference to eq.2 (Carlson and Ripley, 1997).

$$FVC = \left[\frac{\mathrm{NDVI} - \mathrm{NDVI_s}}{\mathrm{NDVI_v} - \mathrm{NDVI_s}}\right]^2 \quad (2)$$

where $NDVI_s$ and $NDVI_v$ are the NDVI values corresponding to completely bare soil and vegetated pixels, respectively. According to previous studies (Jiménez-Muñoz et al., 2009), $NDVI_s$ and $NDVI_v$ were set to 0.2 and 0.86, respectively.

Once emissivity maps were obtained for all the acquisitions, correspondent LST images were finally computed by the Statistical Mono-Window (SMW) algorithm from the Climate Monitoring Satellite Application Facility (CM-SAF). This technique uses an empirical relationship between T_b and LST (Ermida, 2018), based on a linearization of the radiative transfer equation showing an explicit dependence from emissivity (eq. 3).

$$LST = A_i\left(\frac{T_b}{\varepsilon}\right) + \frac{B_i}{\varepsilon} + C_i \quad (3)$$

where T_b is the TOA brightness temperature, and ε is the surface emissivity. A_i, B_i, and C_i are coefficients modelling the Total Column Water Vapor (TCWV) effect on LST. These coefficients are made available by NCEP/NCAR re-analysis 1 project and can be accessed and used through GEE depending on the considered Landsat collection.

LST Trends vs Land Cover Classes

Once LST image time series was generated, correspondent trends were analysed at pixel level in the period 01/01/1984 – 31/12/2020. In order to select only pixels that possibly did not change their meaning (class) along the entire period, the Pettitt's test (James et al., 1987) was locally applied. It is aimed at testing if any significant breakpoint could be found along the time series, somehow detecting the moment when the pixel passed from one class to another. These pixels represent areas where land cover/land use changed thus affecting local emissivity. If this possibility was not taken into account results could drive to wrong deductions concerning the average behaviour of the area. For changed pixels, the date of transition was mapped. For unchanged pixels the local trend was approximated by a 1st order polynomial and the significance of gain tested according to its p-value. All pixels showing a p-value < 0.02 were not considered in the following analyses.

Pixel reduction shifted class areas down to 8221.5 ha and 2914.4 ha for BA and GA classes, respectively, demonstrating that the most of pixels suffered from significant LST trend (increasing) in the considered period.

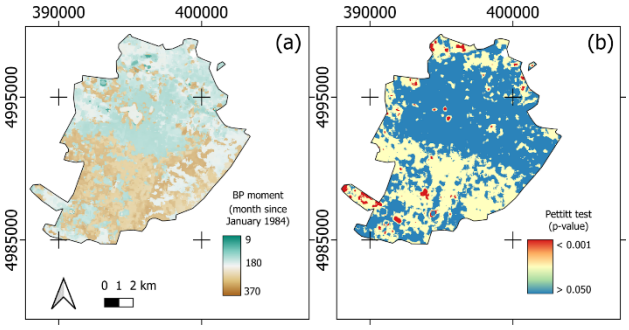

Fig.2 (left) Map of breakpoint occurrences (number of month from January 1984). (right) Map showing the p-value of the gain estimate for the local 1st order polynomial trend.

Frequency distributions of LST trend gain values for BA and GA classes were also summarized in a boxplot (figure 3).
In order to test the significance of difference between LST trends of GA and BA classes, the statistical distributions of the correspondent gain values were compared by the Mann-Whitney (MW) non parametric test (one-tailed, Nachar and others, 2008). The MW null hypothesis was that trend gain values of GA pixels had an identical distribution as built ones (alfa level was set equal to 0.05). The MW test proved that a significant difference exists between the two classes (U value = 1498885763, @p < 0.001).
The mean value of LST gains were found equal to 0.0095 °C/month and 0.0080 °C/month for BA and GA, respectively. All statistical analyses were performed using the Past software v. 4.04 (Hammer et al., 2001); conversely, spatial analysis was operated by SAGA GIS 7.0 (Conrad et al., 2015).

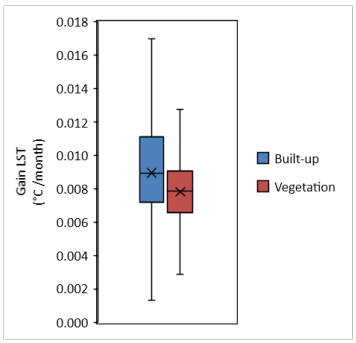

Fig.3. Boxplot showing the statistical distribution of gain values for the built and vegetated classes, respectively.

Results showed that GA present a weaker increasing LST trend than BA, probably due to the different emissivity values and their related seasonal behaviour. In particular, it can be hypothesized that evapotranspiration plays a key role against the general increasing of temperature, thus mitigating the climate induced effects in urban contexts, as widely proved in several studies (Dimoudi and Nikolopoulou, 2003; Qiu et al., 2013).

From Analysis to Planning

Once trends were modelled by a 1st order polynomial, an average model was defined for both BA ad GA. Class-dependent models were obtained by averaging, at class level, local LST trend gain values, as previously computed and mapped. Equations 4 and 5 reports the average models describing the trends of BA and GA respectively (t = number of months counted from January 1984, temperatures in K degrees).

$$T_{BA}(t) = 0.0095 \cdot t + 292.37 \quad (4)$$
$$T_{GA}(t) = 0.0080 \cdot t + 287.62 \quad (5)$$

It can be easily noticed from offset values that averagely, GA showed an average temperature about 4.75 degrees lower than BA in 1984. Today, GA and BA temperature difference is 5.39 degrees in spite that both the classes have increased their temperature.
With these premises, that highlight how vegetation can partially compensate temperature increasing, a paradigmatic case study was done to translate such information in planning concerns. The basic idea was to consider the municipality of Torino like a closed system made of two classes completely filling the area included within its administrative borders. The only reasonable action to contrast LST increasing trend, appears to be the substitution of BA (possibly located in abandoned industrial sites) with GA. If, along time and for planning reasons, an area moves from BA to GA (or vice versa), one has to admit that one class gains the same area that the other losses. Within these constraints, a model can be easily developed to test how long a switching strategy where built zones turn to green ones can maintain the present average temperature condition over the area.
The model (eq. 6) maintains constant the temperature at the reference period (T_m^0 in eq. 4) and estimate the area (ΔB) that has to turn to GA from BA to guarantee no increasing of the municipality average temperature.

$$\Delta B = \frac{T_m^0 - B_0 T_B^1 - G_0 T_G^1}{T_G^1 - T_B^1} \quad (6)$$

where B_0 and G_0 are the BA and GA areas, respectively, at the reference time that defines the AOI average temperature to be maintained constant in spite of the trends; T_B^1 and T_G^1 the expected temperature of BA and GA, respectively, as estimated by the class-related model of correspondent LST trends.
A simulation that assumes as reference time the present year (2021), assuming that B_0 = 8336.5 ha (about 74 %) and G_0= 2929.3 ha (about 26 %), was run generating the scenario of figure 4. The average ROI temperature was set to 295.06 K and was obtained as the area-averaged sum of temperature estimates for BA and GA from the models of eq. 4 and 5.

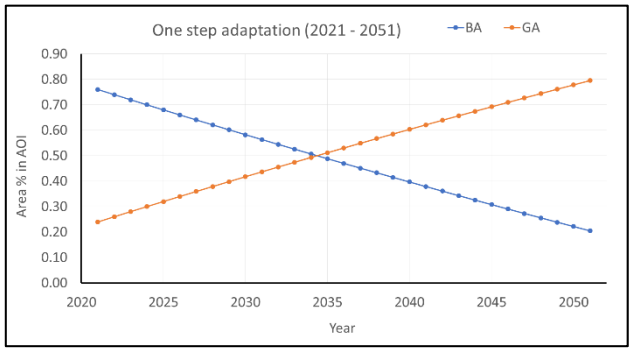

Fig. 4. Graph showing the percentage amount of area that has to migrate from BA to GA to compensate the ROI average temperature increasing

It can be noticed that, about the 2% of the present BA has to be yearly converted to GA to compensate the average temperature increasing over the whole AOI. Since the actual possibilities of switching BA to GA are limited from the needs of people and company, administrators should immediately get an estimate of potential areas that can be somehow converted, in order to forecast when no action will be anymore possible. Authors can imagine that no more than 10-15 % of present built areas will can be converted to GA. This means that, if nothing will globally

change, the year 2026 could represent the moment when other interventions will have to be programmed to face this problem.

3. CONCLUSIONS

Urban areas temperature conditions appear to be relevant in defining wellbeing of people, suggesting that some analyses have to be made concerning possible effects of climate change. Urban planners, inhabitants and public institutions are looking for low-cost methods to boost urban heat mitigation as a response to the joint effect of the ongoing global warming and urban sprawl. under this premises, green areas (GA) including urban forestry, green roofs and other possible nature based solutions represent an opportunity to mitigate such threats. This work, based on free dataset and tools, demonstrated, in the Torino municipality study area that: a) averagely, temperature is increasing; b) BA show a steeper increasing trend than GA; c) a planning/development strategy based on the switch between BA and GA could somehow mitigate the average temperature increasing; d) the mitigation effect based on greenness improvement can be effective for a limited time, that depends on the potential areas that actually can be programmed to move from BA to GA. In spite of a well known story telling, greenness strategy has no chance to solely face the temperature increasing problem related to the global warming. Other more effective actions have to be proposed by planners.

REFERENCES

Borgogno-Mondino, E., Fabietti, G., Ajmone-Marsan, F., 2015. Soil quality and landscape metrics as driving factors in a multi-criteria GIS procedure for peri-urban land use planning. Urban For. Urban Green. 14, 743–750.

Büttner, G., 2014. CORINE land cover and land cover change products, in: Land Use and Land Cover Mapping in Europe. Springer, pp. 55–74.

Carlson, T.N., Ripley, D.A., 1997. On the relation between NDVI, fractional vegetation cover, and leaf area index. Remote Sens. Environ. 62, 241–252.

Chander, G., Markham, B.L., Helder, D.L., 2009. Summary of current radiometric calibration coefficients for Landsat MSS, TM, ETM+, and EO-1 ALI sensors. Remote Sens. Environ. 113, 893–903.

Conrad, O., Bechtel, B., Bock, M., Dietrich, H., Fischer, E., Gerlitz, L., Wehberg, J., Wichmann, V., Böhner, J., 2015. System for automated geoscientific analyses (SAGA) v. 2.1. 4. Geosci. Model Dev. 8, 1991–2007.

Coutts, A.M., Daly, E., Beringer, J., Tapper, N.J., 2013. Assessing practical measures to reduce urban heat: Green and cool roofs. Build. Environ. 70, 266–276.

d'Amour, C.B., Reitsma, F., Baiocchi, G., Barthel, S., Güneralp, B., Erb, K.-H., Haberl, H., Creutzig, F., Seto, K.C., 2017. Future urban land expansion and implications for global croplands. Proc. Natl. Acad. Sci. 114, 8939–8944.

De Petris, S., Squillacioti, G., Bono, R., Borgogno-Mondino, E., 2021. Geomatics and epidemiology: Associating oxidative stress and greenness in urban areas. Environ. Res. 197, 110999.

Dimoudi, A., Nikolopoulou, M., 2003. Vegetation in the urban environment: microclimatic analysis and benefits. Energy Build. 35, 69–76.

Ermida, S., 2018. Harmonization of Remote Sensing Land Surface Products: correction of clear-sky bias and characterization of directional effects.

Ermida, S.L., Soares, P., Mantas, V., Göttsche, F.-M., Trigo, I.F., 2020. Google earth engine open-source code for land surface temperature estimation from the landsat series. Remote Sens. 12, 1471.

Gorelick, N., Hancher, M., Dixon, M., Ilyushchenko, S., Thau, D., Moore, R., 2017. Google Earth Engine: Planetary-scale geospatial analysis for everyone. Remote Sens. Environ. 202, 18–27.

Hammer, Ø., Harper, D.A., Ryan, P.D., others, 2001. PAST: Paleontological statistics software package for education and data analysis. Palaeontol. Electron. 4, 9.

James, B., James, K.L., Siegmund, D., 1987. Tests for a change-point. Biometrika 74, 71–83.

Jiménez-Muñoz, J.C., Sobrino, J.A., Plaza, A., Guanter, L., Moreno, J., Martínez, P., 2009. Comparison between fractional vegetation cover retrievals from vegetation indices and spectral mixture analysis: Case study of PROBA/CHRIS data over an agricultural area. Sensors 9, 768–793.

Ma, S., Pitman, A., Hart, M., Evans, J.P., Haghdadi, N., MacGill, I., 2017. The impact of an urban canopy and anthropogenic heat fluxes on Sydney's climate. Int. J. Climatol. 37, 255–270.

Marconcini, M., Heldens, W., Del Frate, F., Latini, D., Mitraka, Z., Lindberg, F., 2017. EO-based products in support of urban heat fluxes estimation, in: 2017 Joint Urban Remote Sensing Event (JURSE). IEEE, pp. 1–4.

Nachar, N., others, 2008. The Mann-Whitney U: A test for assessing whether two independent samples come from the same distribution. Tutor. Quant. Methods Psychol. 4, 13–20.

Orusa, T., Borgogno Mondino, E., 2021. Exploring Short-Term Climate Change Effects on Rangelands and Broad-Leaved Forests by Free Satellite Data in Aosta Valley (Northwest Italy). Climate 9, 47.

Orusa, T., Mondino, E.B., 2019. Landsat 8 thermal data to support urban management and planning in the climate change era: a case study in Torino area, NW Italy, in: Remote Sensing Technologies and Applications in Urban Environments IV. International Society for Optics and Photonics, p. 111570O https://doi.org/10.1117/12.2533110.

Orusa, T., Orusa, R., Viani, A., Carella, E., Borgogno Mondino, E., 2020. Geomatics and EO Data to Support Wildlife Diseases Assessment at Landscape Level: A Pilot Experience to Map Infectious Keratoconjunctivitis in Chamois and Phenological Trends in Aosta Valley (NW Italy). Remote Sens. 12, 3542.

Qiu, G., LI, H., Zhang, Q., Wan, C., Liang, X., Li, X., 2013. Effects of evapotranspiration on mitigation of urban temperature by vegetation and urban agriculture. J. Integr. Agric. 12, 1307–1315.

Rubio, E., Caselles, V., Badenas, C., 1997. Emissivity measurements of several soils and vegetation types in the 8–14, μm Wave band: Analysis of two field methods. Remote Sens. Environ. 59, 490–521.

Sarvia, F., De Petris, S., Borgogno-Mondino, E., 2021. Exploring Climate Change Effects on Vegetation Phenology by MOD13Q1 Data: The Piemonte Region Case Study in the Period 2001–2019. Agronomy 11, 555.

Wang, S., Ma, Q., Ding, H., Liang, H., 2018. Detection of urban expansion and land surface temperature change using multi-temporal landsat images. Resour. Conserv. Recycl. 128, 526–534.

A REMOTE SENSING INDEX FOR ASSESSING PERI-URBAN ECOSYSTEM SERVICES: A CASE FROM TUSCANY (ITALY)

E. Barbierato*, I. Bernetti, I. Capecchi

DAGRI, Agriculture, Food and Forestry Systems School, 50144 Piazzale delle Cascine Florence, Italy - (elena.barbierato, iacopo.bernetti, irene.capecchi)@unifi.it

KEY WORDS: Remote sensing, Peri-urban areas, Urban ecosystem services, Pressure-State-Response framework, Dempster-Shafer rules,

ABSTRACT:

This work proposes a Resilience Index of Ecosystem Services (RIES) that is based on remote sensing to assess the ecological quality of highly anthropized territories. The study area is characterized as an urbanized area of Florence and Prato in central Tuscany (Italy). The proposed method was derived from the Pressure-State-Response (PSR) framework, which focuses on the notion of causality and involves the selection and measurements of three categories indicators: environmental state, anthropogenic pressure and climatic response.
The first of which consists of the Ecosystem Services Provision Index (ESPI), which is derived from the Cascade theory and is evaluated using two statistics of the seasonal dynamics of the normalized difference vegetation index (NDVI), that are calculated from Sentinel 2 images: the annual mean (mean NDVI) and the intra-annual Coefficient of Variation of the NDVI (CV NDVI). The calculation is as follows: ESPI = average NDVI * (1-NDVI CV).
The second category is characterized by the Normalized Difference Built-up Index (NDBI) and is derived from the Sentinel 2 images.
The third is composed of the climate resilience index, which is calculated by combining the Land Surface Temperatures (LST) with the Tasseled Cap - wetness index both from Landsat 8 images.
These three macro indices are aggregated through a Dempster–Shafer rule of combination with weights derived using a Principal Components Analysis (PCA). The aggregation of these macro indices allows us to obtain the RIES index.

1. INTRODUCTION

1.1 Literature references and aim

Periurbanization is a phenomenon that has occurred in many European cities causing multiple side effects, both from an architectural point of view such as urban sprawl and from an environmental point of view with damage to agriculture (Galli et al., 2010). This phenomenon has generated peri-urban areas that are hybrid areas concentrated on the fringes of the peripheries of city and occur with different spatial configurations. Nevertheless, they are very important and vital for urban populations (Fleury et al., 1997). In the literature, the importance of maintaining ecosystem services to cope with global environmental change has led to the development of many systems for classifying and assessing ecosystem functions and services (Millennium Ecosystem Assessment, 2005). This has also been made possible by the development of remote sensing technologies and geographic information systems that have provided ecologists with valuable tools to rapidly identify, monitor, and assess spatiotemporal changes in the environment (Kerr and Ostrovsky, 2003; Huang et al., 2012) and their ecological status (Dale and Beyeler, 2001; Lin et al., 2016).
However, despite the increasing effectiveness of remote sensing technologies for use in large-scale environmental monitoring, the reliability of studies based on satellite data is undermined by the uncertainty generated by human disturbances. For this reason, this study, understanding resilience as the capacity to respond positively to the adversities caused by artificialisation (Luthar et al. 2000), aimed to assess residual ecological quality in highly anthropized territories through the remote sensing-based Resilience Index of Ecosystem Services (RIES), using a probabilistic approach that considers uncertainty.

2. MATERIALS

2.1 Study area and data collection

The study area is a peri-urban urbanized plain of the Florence and Prato cities, located in the central part of the Tuscany region (Italy), defined by WGS 84 coordinates as min 10.98878, 43.71782 and max 11.35538, 43.92694. We chose this study area because it is the most artificialized area in the region and consists of 55% artificial, 35% agricultural, 8% forest and 2% water covers. The input data were remote sensing data from two different sensors:

- 12 Sentinel2 images, level 2A, R022_T32TPP, from December 10, 2019 to November 19, 2020.
- 4 Landsat8 OLI-TIRS images, path 132 and row 030, from June 17 to September 5, 2020.

3. THEORY AND METHOD

The proposed method was derived from the *Pressure-State-Response* (PSR) framework, which focuses on the notion of causality (Hughey et al., 2004), and involves the selection and measurements of three categories indicators: environmental state, anthropogenic pressure and climatic response (Hu and Xu, 2018). These indicators were then weighted with PCA and aggregated with the Dempster-Shafer rules according to two lines of evidence: resilience of ecosystem services (H1) and vulnerability of ecosystem services (H2).

3.1 Environmental state

The first index we propose is the Ecosystem Services Provision Index (ESPI) which was derived from the Cascade theory (Potschin et al., 2016) and is evaluated using two statistics of the

* Corresponding author

seasonal dynamics of the Normalized Difference Vegetation Index (NDVI), which are calculated from the Sentinel 2 images:

i. the annual mean of the NDVI ($\overline{NDVI}$);
ii. intra-annual Coefficient of Variation of the NDVI ($CV\ NDVI$).

The equation is the following:

$$ESPI = \overline{NDVI} * (1 - CV\ NDVI) \quad (1)$$

where $\overline{NDVI}$ = mean Normalized Difference Vegetation Index, calculated using: $\rho_{NIR} - \rho_{RED}/\rho_{NIR} + \rho_{RED}$
$CV\ NDVI$ = Coefficient of Variation of the NDVI

Paruelo et al. (2016) demonstrated that the ESPI is strongly related to ES such as soil carbon sequestration, evapotranspiration, groundwater recharge, and biodiversity.

3.2 Anthropogenic pressure

The anthropization index is also derived from Sentinel 2 images using the NDBI, or Normalized Difference Built-up Index (Xu et al., 2018).
Similar to the ESPI, we used the annual mean of this index ($\overline{NDBI}$) and its Coefficient of Variation ($CV\ NDBI$). The equation is the following:

$$NDBI = \overline{NDBI} * (1 - CV\ NDBI) \quad (2)$$

where $\overline{NDBI}$ = mean Normalized Difference Built-up Index, calculated through $(\rho_{SWI1} - \rho_{NIR}/\rho_{SWI1} + \rho_{NIR})$
$CV\ NDVI$ = Coefficient of Variation of the NDVI

3.3 Climatic response

The climate index was derived from Landsat 8 images via the Land Surface Temperature (LST), as follows:

$$LST = BT/(1 + (\lambda\, BT/\rho) * \ln(\varepsilon_\lambda)) \quad (3)$$

where BT = brightness temperature
λ = wavelength of emitted radiance
ε_λ = emissivity

In addition, the Tasseled Cap wetness index (WET) (Kauth and Thomas, 1976) was determined using the following equation (WET):

$$WET = (\rho_{BLUE} * 0.1511) + (\rho_{GREEN} * 0.1973) + (\rho_{RED} * 0.3283) + (\rho_{NIR} * 0.3407) + \rho_{SWIR1} * (-0.7117)) + (\rho_{SWIR2} * (-0.4559)) \quad (4)$$

where ρ_i = Landsat8 waves

3.4 Aggregation procedure: Dempster-Shafer rules

The assessment and monitoring of ecosystem services in peri-urban areas are hampered by multiple uncertainties and lack of knowledge. Because they experience changes over time and are not stationary, they cannot be described using only objective probabilities. The scheme that has most often been applied in the literature to characterize uncertainty is the Dempster-Shaffer theory (DST) (Dempster, 1969; Shafer, 1976). This method is derived from Bayesian subjective probability theory and combines different lines of evidence that come from various sources of knowledge and information to obtain degrees of belief for different hypotheses. In our study, we defined two lines of evidence: first, H1: resilience of ecosystem services supported by the ESPI and WET results, H2: non-resilience, i.e., vulnerability of ecosystem services supported by the NDBI and LST results.
The treatment of uncertainty in the DST focuses on the concept of "plausibility" and does not need require complete information in the event space. Therefore, this theory allows the use of two different values to express belief in a specific proposition, or belief in its negation. The DS probability (p) is the following:

$$p(H1) + p(H2) + p(H1, H2) = 1 \text{ and thus}$$
$$p(H1) + p(H2) < 1, \quad (5)$$

The remaining $p(H1, H2)$ represents the contribution to uncertainty. In the DST, there is high uncertainty when there is strong evidence of vulnerable and resilient ecosystem services in the same location. The evaluation of the hypothesis is based on the concept of Basic Probability Assignment (BPA), which represents the contribution that a certain factor I a supports a specific line of evidence. In our approach, the BPA evaluation is based on the fuzzy functions NI (Yager, 1999), built using our four indicators and a weighted normalization, as follows:

$$NI = \begin{cases} 0 & I \geq P_I^{90} \\ 1 - \frac{P_I^{10}}{P_I^{90} - P_I^{10}} \cdot I & P_I^{90} > I > P_I^{10} \\ 1 & I \leq P_I^{10} \end{cases} \quad (6)$$

where P_I^{90} = 90th percentile indicator frequency distribution
P_I^{10} = 10th percentile indicator frequency distribution
$I = \{NDVI, NDBI, LST, WET\}$

The normalization weights were derived from a Principal Components Analysis (PCA), which was adopted to identify the relative importance of each index. By employing a PCA, the weight of each factor is automatically and objectively assigned according to the contribution of each factor to the principal components, and avoids any form of subjectivity (Hu and Xu, 2018).
For the H1 line of evidence, resilient ecosystem services, ESPI and WET are aggregated using the orthogonal sum (Shafer, 1976) rule of combination:

$$BPA_x(i,j) = BPA_{i,x} \_|\_ BPA_{i,y} = BPA_{i,x} * (1 - BPA_{j,x})/1 - BPA_{i,x} * BPA_{j,x} \quad (7)$$

To map the probability of the resilient ecosystem services (m(H1)), the following used:

$$m(H1) = \_|\__r^{H1}(BPA_{r,x}) r = 1, \dots, R \quad (8)$$

where $\_|\_$ = orthogonal sum,
$r = 1, \dots, V$ = all indicators of resilience.

For the H2 line of evidence, vulnerable ecosystem services were calculated on the basis of the NDBI and LST map, using the following equation:

$$m(H2) = \_|\__v^{H2}(BPA_{v,x}) r = 1, \dots, V \quad (9)$$

where $\_|\_$ = orthogonal sum,
$v = 1, \dots, R$ = all indicators of vulnerability.

The aggregation of H1 and H2 is performed by adopting the Dempster rule. The uncertainty degree of the location is derived from the significant presence and significant absence of resilient ecosystem services in the same area:

$$Bel(H1) = m_{H1} * 1 - m_{H2}/1 - m_{H1} * m_{H2} \quad (10)$$
$$Bel(H2) = m_{H2} * 1 - m_{H1}/1 - m_{H2} * m_{H1} \quad (11)$$
$$U(H1, H2) = m_{H2} * 1 - m_{H1}/1 - m_{H2} * m_{H1} \quad (12)$$

where $Bel(H1)$ and $Bel(H2)$ are beliefs regarding resilient and vulnerable ecosystem services. Note that the belief interval represents the uncertainty degree of location as derived from the occurrence of low resilient and low vulnerable ecosystem services in the same location.

4. RESULTS

The results of the PCA are shown in Table 1, taking into account the first row that explains 64% of the variance.

	ESPI	WET	LST	NDBI	VE
PC1	0.569	0.4571	-0.5198	-0.4439	64.11%
PC2	0.6083	-0.7425	-0.2068	0.1895	18.46%
PC3	0.1163	0.4113	-0.3853	0.8179	11.70%

Table 1. PCA results. VE = variance explained

Figure 1a shows the parameters of the probability distributions calculated using the Dempster-Shaffer model described in the previous paragraph. The probability of having resilient ecosystem services revealed safe values, with an average of 0.42 and a median of 0.41. Further, the distribution was between 0 and 0.76, in which the first quartile was equal to 0.25 and the third to was equal to 0.60. Even the probability of having vulnerable ecosystem services revealed critical values, with an average of 0.24 and a median of 0.23. Here again, the probability between 0 and 0.72, in which the first quartile was equal to 0.11 and the third was equal to 0.35. Finally, the uncertainty was relatively low with a median of 0.34, in which the first and third quartiles were equal to 0.28 and 0.39, respectively.

The general risk conditions highlighted by these results were geographically differentiated. Figure 1b shows how the indicators of the resilient ecosystem services are higher in the southern and southeastern areas of the study area. Meanwhile, the vulnerable ecosystem services (Figure 1c) recorded critical values in the middle and southwest areas of the study area. Uncertainty (Figure 1d), in general, was very low, and is absent in areas of higher resilience and more present in vulnerable ecosystem service areas.

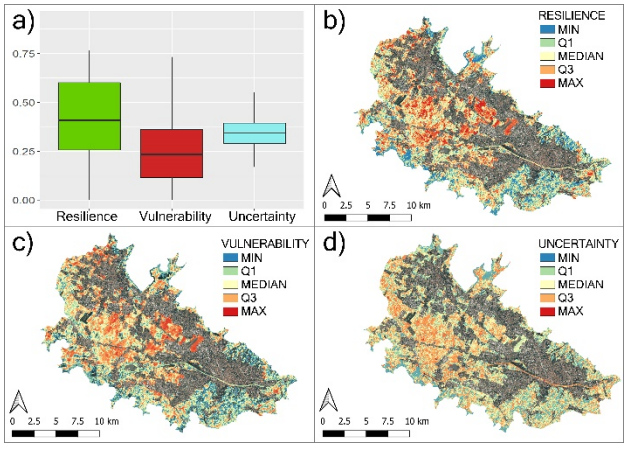

Figure 1. a) Boxplot of frequency distribution; b) Probability of resilient ecosystem services; c) Probability of vulnerable ecosystem services; d) Uncertainty

As shown in Figure 2, the probabilities of resilience, vulnerability and uncertainty were marked, respectively, as green, red and blue bands of an RGB image, in order to generate a "false color" map defined by the legend. This result represents the Resilience Index of Ecosystem Services (RIES).

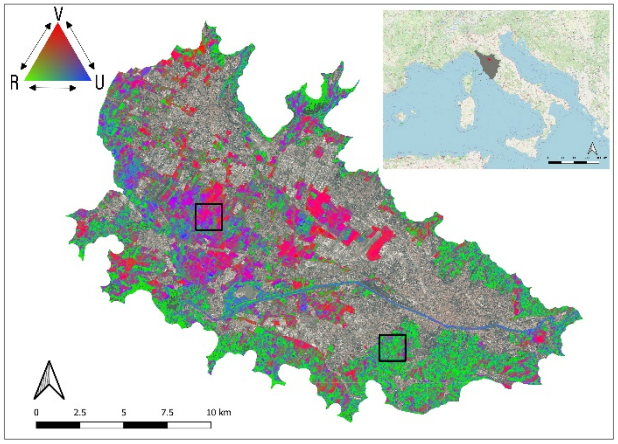

Figure 2. Resilience Index of Ecosystem Services (RIES), false color composition: green= Resilience (R); red= Vulnerability (V); blue= Uncertainty (U)

The most critical vulnerable ecosystem services situation were identified in a large part of the study area (colors from red to purple); the areas where uncertainty prevails (colors from blue to purple) were relatively rare but concentrated in the southwest area of the plain and the areas in which highly resilient ecosystem services occur were mainly located in the east.

Figure 3 shows the two specific opposing spatial landscape configurations: the first pattern (on the left column) is characterized by a bare soil, open fields without trees and sparse vegetation; and while the second (on the right column) is a landscape rich in hedges and trees.

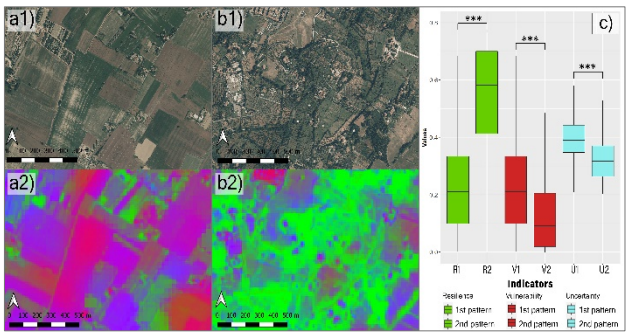

Figure 3. a1) - b1) Patterns 1 and 2, respectively, rural aerial views, a2) - b2) patterns 1 and 2 rural resilience index of ecosystem services (RIES); c) Boxplot comparison.

Figure 3c shows the boxplots for indicator categories and the Student's t-test results for pairs of indicators. All the comparisons between adjacent assessments were found to be highly significant $p > 99{,}9\%$.

Finally, the Table 2 lists the probability distribution parameters in the rural configurations considered, wherein the mean and median values of resilience (R01) increased significantly in the second configuration (R02). Conversely, vulnerability (V01) and uncertainty (U01) were greater in the first configuration than in the second configuration (V02, U02).

Boxplot values	R01	R02	V01	V02	U01	U02
Min	0.00	0.04	0.00	0.00	0.19	0.20
1st Qu	0.09	0.42	0.09	0.04	0.34	0.26
Median	0.21	0.58	0.21	0.11	0.39	0.31
Mean	0.22	0.55	0.22	0.14	0.39	0.32
3rd Qu	0.33	0.70	0.33	0.22	0.44	0.37
Max	0.74	0.76	0.74	0.54	0.60	0.60

Table 2. Boxplot values of rural patterns. R01, V01, U01= Resilience, Vulnerability, Uncertainty of first pattern; R02, V02, U02= Resilience, Vulnerability, Uncertainty of second pattern

5. DISCUSSION

The proposed method allowed us to identify the problems caused by the urbanization processes and evaluate how agricultural land use affects the quality of ecosystem services. The first rural configuration is made up of intensive crops, a greater likelihood of vulnerability. Meanwhile, the second rural configuration, is much more resilient as it is made up mainly of olive groves and tree vegetation. The study has allowed us not only to analyse the ecological conditions of the area considered but also to identify which agricultural configurations are most resilient to anthropogenic pressure. Despite the major limitation of necessarily having to use two different sensors, the RIES is a valid indicator that can act as a useful tool for urban and landscape planners to monitor and identify solutions to preserve the ecological integrity of these complex areas, consequently promoting the well-being of citizens.

6. CONCLUSIONS

This study is purely methodological and represents the first step of testing. However, future research will expand and test this method while considering three issues:

- increasing the number of analyzed indices to achieve a comprehensive assessment of ecosystem services;
- realizing a temporal analysis to understand how the phenomenon has developed over time and how much the RIES has changed;
- testing a system that allows the analysis of an entire territory and not only the peri-urban agricultural areas.

REFERENCES

Assessment, M. E. (2005). Ecosystems and human well-being (Vol. 5, p. 563). United States of America: Island press. ISBN 92 4 156309 5.

Dale, V. H., & Beyeler, S. C. (2001). Challenges in the development and use of ecological indicators. Ecological indicators, 1(1), 3-10. https://doi.org/10.1016/S1470-160X(01)00003-6.

Dempster, A. P. (1969). Upper and lower probability inferences for families of hypotheses with monotone density ratios. The Annals of Mathematical Statistics, 40(3), 953-969. https://doi.org/10.1214/aoms/1177697600.

Fleury A., Donadieu P. (1997). De l' agriculture pèri-urbaine à l'agriculture urbaine. Le Courrier de l' environnement de l'INRA 31. https://hal.archives-ouvertes.fr/hal-01204863.

Galli, M., Lardon, S., Marraccini, E., & Bonari, E. (2010). Agricultural management in peri-urban areas. In The experience of an international workshop. Gezzanho, Felice Editore. ISBN: 978-88-6019-440-4.

Hu, X., & Xu, H. (2018). A new remote sensing index for assessing the spatial heterogeneity in urban ecological quality: A case from Fuzhou City, China. Ecological Indicators, 89, 11-21. https://doi.org/10.1016/j.ecolind.2018.02.006.

Huang, J., Pontius Jr, R. G., Li, Q., & Zhang, Y. (2012). Use of intensity analysis to link patterns with processes of land change from 1986 to 2007 in a coastal watershed of southeast China. Applied Geography, 34, 371-384. https://doi.org/10.1016/j.apgeog.2012.01.001

Hughey, K. F., Cullen, R., Kerr, G. N., & Cook, A. J. (2004). Application of the pressure–state–response framework to perceptions reporting of the state of the New Zealand environment. Journal of Environmental Management, 70(1), 85-93. https://doi:10.1016/j.jenvman.2003.09.02.

Kauth, R. J., & Thomas, G. S. (1976, January). The tasselled cap--a graphic description of the spectral-temporal development of agricultural crops as seen by Landsat. In LARS symposia (p. 159). http://docs.lib.purdue.edu/lars_symp/159.

Kerr, J. T., & Ostrovsky, M. (2003). From space to species: ecological applications for remote sensing. Trends in ecology & evolution, 18(6), 299-305. https://doi.org/10.1016/S0169-5347(03)00071-5.

Lin, T., Ge, R., Huang, J., Zhao, Q., Lin, J., Huang, N., ... & Yin, K. (2016). A quantitative method to assess the ecological indicator system's effectiveness: a case study of the ecological province construction indicators of China. Ecological indicators, 62, 95-100. https://doi.org/10.1016/j.ecolind.2015.11.027.

Luthar, S.S., Cicchetti, D., Becker, B. (2000) The construct of resilience: A critical evaluation and guidelines for future work. Child Development, 71(3), 543–562. https://doi.org/10.1111/1467-8624.00164.

Paruelo, J. M., Texeira, M., Staiano, L., Mastrángelo, M., Amdan, L., & Gallego, F. (2016). An integrative index of Ecosystem Services provision based on remotely sensed data. Ecological Indicators, 71, 145-154. https://doi.org/10.1016/j.ecolind.2016.06.054.

Potschin, M., & Haines-Young, R. (2016). Conceptual frameworks and the cascade model. OpenNESS Ecosystem Services Reference Book. European Centre for Nature Conservation, Tilburg, The Netherlands.[online] URL: http://www.openness-project.eu/library/reference-book/cascade-model.

Shafer, G. (1976). A mathematical theory of evidence (Vol. 42). Princeton university press.

Xu, R., Liu, J., & Xu, J. (2018). Extraction of high-precision urban impervious surfaces from sentinel-2 multispectral imagery via modified linear spectral mixture analysis. Sensors, 18(9), 2873. https://doi.org/10.3390/s18092873.

Hu, X., & Xu, H. (2018). A new remote sensing index for assessing the spatial heterogeneity in urban ecological quality: A

case from Fuzhou City, China. Ecological Indicators, 89, 11-21. https://doi.org/10.1016/j.ecolind.2018.02.006.

Yager, R. R. (1999). A class of fuzzy measures generated from a Dempster–Shafer belief structure. International Journal of Intelligent Systems, 14(12), 1239–1247. https://doi.org/10.1002/(SICI)1098-111X(199912)14:12<1239::AID-INT5>3.0.CO;2-G

SATELLITE DATA FOR STRUCTURAL MONITORING OF HISTORICAL BUILDING: THE TEMPLE OF MINERVA MEDICA IN ROME

M.F. Sabba' [1]*, M. Lerna [2], M. Diaferio [3], D. Foti [4]

[1] Dept. Civil Engineering and Architecture, Polytechnic University of Bari, Bari, Italy – mariafrancesca.sabba@poliba.it
[2] Dept. Civil Engineering and Architectural, Polytechnic of Bari, Bari, Italy – michela.lerna@poliba.it
[3] Dept. Civil, Environmental, Land, Construction and Chemistry, Polytechnic of Bari, Bari, Italy – mariella.diaferio@poliba.it
[4] Dept. Civil Engineering and Architectural, Polytechnic of Bari, Bari, Italy – dora.foti@poliba.it

KEY WORDS: Differential Synthetic Aperture Radar Interferometry (DInSAR), Structural Monitoring, Historical Building

ABSTRACT:

The Differential Synthetic Aperture Radar Interferometry is a remote sensing technique to acquire deformation velocity and displacement time-series of large territorial areas. The aim of this work is to develop operational methodologies that allow to assess the structures conservation state by integrating information from traditional monitoring systems with the remote sensing application, in order to monitor permanently structures and infrastructure with a historical relevance and developing specific maintenance programs. It is verified that this processing technique is an adequate tool, even in real-time, to monitor any damage or potential critical issues in the case of exceptional events such as earthquakes or landslides. The case study is the Temple of Minerva Medica in Rome, a masonry building characterized by an important historical-artistic value. The data-analysis shows as the use of satellite monitoring can be a valid tool for the structural safety, allowing to identify a vulnerability map of archaeological sites and historical buildings. The data interferometric processing was carried out using a Graphic Information System (GIS) software.

1. INTRODUCTION

Archaeological monuments are frequently subjected to environmental phenomena with direct and indirect impacts, often worsening. These problems can be of particular concern above all for the management of those sites characterized by a high density of heritage, so it becomes difficult, as well as expensive, an ordinary maintenance effective to prevent structural instability events.

In this regard, it becomes necessary to define sustainable asset management strategies by the use of technologies capable of detecting conservational criticisms, on extended survey areas and providing highly detailed information. It is possible by the availability of huge spatial radar data archives, including those acquired in the last two decades from the synthetic opening radar sensors (SAR) through European Space Agency (ESA)'s ERS-1/2 and ENVISAT missions (Cigna, 2014).

Among the remote sensing techniques, the synthetic opening radar interferometry based on the processing of images acquired by spatial radar sensors has the potential to become a routine method for the preventive diagnosis of archaeological heritage, at various scales of analysis, from the whole site to the single monument. The processing approaches (Persistent Scatterer Interferometry (PSI)) allow reconstructing superficial deformations that affect the land and artificial structures in temporal and spatial evolution (Bru, 2013; Yang, 2016). The processed satellite images allow generating persistent Measuring Points (MP) for the whole monitoring period obtaining a deformation time series.

In particular, the Differential Synthetic Aperture Radar Interferometry (DInSAR) has demonstrated to be an effective tool for non-invasive deformation analysis on vast areas producing spatially dense deformation maps with a highly precision level. Furthermore, using long data sequences acquired from different sensors, the Advanced DInSAR technique called Small Baseline Subset (SBAS) approach allows to provide long-term deformation time series to ensure the monitoring of the movement of the urban area (Arangio, 2017; Bonano, 2017; De Corso, 2020; Lanari, 2007; Zeni, 2011).

In recent years the city of Rome with its vast archaeological heritage, has been chosen to test the effectiveness of interferometric techniques for the preventive diagnosis of deformation that threatens the structural stability of archaeological sites, through the study of satellite data collected with different satellite interferometry techniques.

Traditional SAR interferometry can estimate movements with an accuracy of the centimeter order; it is important to emphasize that generally does not allow to carry out punctual estimates, but only together analysis to identify macroscopic phenomena in place (extension> 0.2 km^2). To contain these phenomena, 90 advanced interferometric techniques (Advanced DInSAR - ADInSAR) have been developed that use a series of radar images related to the same area on which different radar targets are identified, used to measure displacements. This technique provides the complete description of the temporal evolution of the deformations by avoiding the sampling of the phenomenon through the study of two different acquisitions (master and slave). Thus, the multi-interferogram technique is based on the definition of permanent reflectors (Persistent Scatters-PS) on-site, capable of not altering their electromagnetic properties for any geometric and climatic conditions, thus preserving the phase information over time (Yang, 2016).

This research aims to develop techniques and operational protocols for the integration of the information acquired through satellite data with those acquired by traditional on-site non-destructive monitoring technologies(Diaferio, 2014; Diaferio, 2015; Foti, 2014), in order to allow monitoring permanently of the health-state of structures and infrastructure, as well as cultural relevance goods, programs extraordinary maintenance

* Corresponding author

and evaluate, even real-time, any damage or potential criticalities in the case of exceptional events.

2. DINSAR – SBAS TECHNIC

The DINSAR - SBAS approach, applied to data collected by ES-1 and ERS-2 radar systems, allows the study of soil deformation on two distinct spatial scales, to extend the temporal coverage of monitored phenomena. The acquisitions are carried out on:

- Low-resolution regional scale, which exploits medium interferograms (multi-look) and generates average deformation speed maps and the corresponding time series related to very large areas (about km 100×100), with a ground resolution typically about m 100×100 (Zeni, 2011).
- Local scale, with full resolution, which exploits interferograms (single-look) generated with full spatial resolution (5-10 m), to detect and analyze local deformation on individual buildings and artificial structures (Zeni, 2011).

The key steps to recover movement time series are:

1. Choice of pairs of data used for generating interferograms in order to mitigate the phenomena of operation. In this phase, constraints are introduced on the spatial and temporal baseline between the orbits for the acquisition of images will be, in order to maximize the number of pixels coherent in multi-look interferograms;
2. Recovery phase, named "phase unlock" of the original phase. This operation allows us to process the data available on a grid, useful in order to improve the performance of the algorithm in areas with relatively low coherence values;
3. Combination of interferograms with the Singular Value Decomposition (SVD) method which allows to regularize the problem and generate the minimum standard solution that guarantees a valid solution;
4. Space-temporal filtration able to estimate and remove artifacts due to atmospheric inhomogeneities between acquisition pairs. This operation is based on the observation that the phase component of the atmospheric signal is highly related in space but scarcely over time and allows correcting these errors without the need to obtain additional information from the ground (Lanari, 2007).

3. CASE OF STUDY

The monumental building of study case is commonly known as "Temple of Minerva Medica" and is located in Rome at altitude 50.7 m S.L.M., near Termini station and a urban trams passage. The archaeologists believe that it was an ancient nymphaeum of the 4th century D.C, connected to the water supply network. It is a masonry building with a decagonal plant of the diameter of 25 m, covered by a dome with a maximum height of 32 m (Figure 1(a)). On each side, except the entrance on the north-west side, semi-circular niches of variable depth of 4.28 m to 4.65 m are positioned. Above these, there are arched windows (Figure 1(b)). Ten pillars support the dome, which, starting from a polygonal shape gradually assumes a hemispherical appearance. There are ten main ribs and secondary winds that give it the "umbrella" appearance.

The ribs are made up of five parallel brick layers that become three at the top of the dome, where the concrete is replaced by pumice and mortar to lighten the weight. The ribs were elevated simultaneously with the concrete flow casting and arranged in horizontal layers and were used to create the frame for the concrete casting (Figure 1(c)).

Outside the dome consists of five large angular steps that rest on the decagonal drum with the high of 1.53 m. In the 1828, the structure suffered a slow and constant degradation with the collapse of the dome took place, then submitted to a restoration intervention in the 1940s. Since then, only partial interventions were carried out, mostly of maintenance of a buffer of localized structural problems.

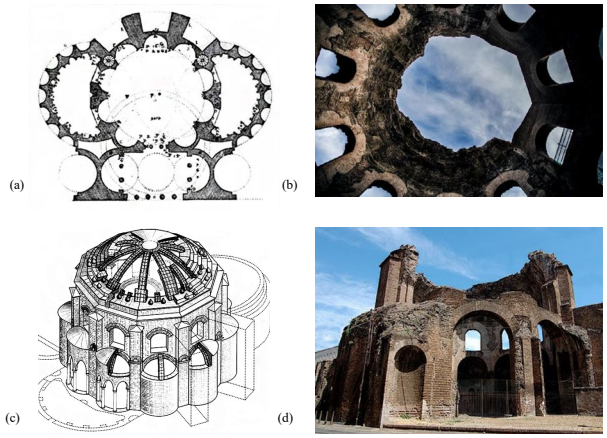

Figure 1. Minerva Temple: (a) Plan, (b) dome; (c) 3D reconstruction, (d) Side view [https://www.romanoimpero.com/2015/02/ tempio-di-minerva-medica.html].

Crack patterns are present in the pillars foundation structures, due to the modest stiffness levels of soil, the high levels of stress transmitted on the pillars, the presence of older structures. As regards the classification of the seismic danger of the site, the Italian Technical Code Standard (MIT, 2018) suggests identifying the reference period" VR expressed as the product of V_n the structural nominal life and C_U the coefficient of use. Given the extraordinary opening of the Temple for guided tours organized by the Special Superintendency Authority of Rome, a coefficient of use equal to 0.7 corresponding to Class I was chosen.

The Temple is characterized by a seismic acceleration on the ground equal to 0.10-15g, referred a 10% probability of overcoming in 50 years. To define the seismic design action, the effect of the local seismic response can be assessed by a simplified approach that is based on the classification of the subsoil according to the values of the propagation speed of the V_S shear waves, obtained by specific tests. Furthermore, the site is located at a topographic average quote of 50.7 m S.L.M. and has morphology of type T1 category (MIT, 2018).

3.1 Analysis of satellite monitoring data

The results obtained from the processing of data collected by ASI for the municipality of Rome provided by the Italian National Research Council (CNR), are archived in a database which reports, for each identified PS, a series of information relating to the time interval considered. The identified points are returned on a grid of m 0.87x1.1 and refer to a resolution cell of about m 2.7x2.8 with a sampling done on a grid of m 2.2x2.2 (Figure 2). The dataset covers the period between 2011 and 2019 with a time shift of 4 months.

Within the database provided by CNR and acquired by ASI, the ASCII files containing the satellite data acquired from the ascending and the descending orbit, relating to the Temple of Minerva Medica, have been selected. The open-source geographic information system *QGis 3.10 A Coruña* has been adopted for the analysis. Among the monitored parameters, the mean annual deformation speed expressed in cm/year was considered. It was possible to organize, study and process the points by editing the symbols of the individual points and classify them according to the range of values significant for the

analysis of both the ascending and descending satellite orbit. Figures 3-4 show the distributions of the values of the annual velocities (cm/year) relative to the two satellite orbits.

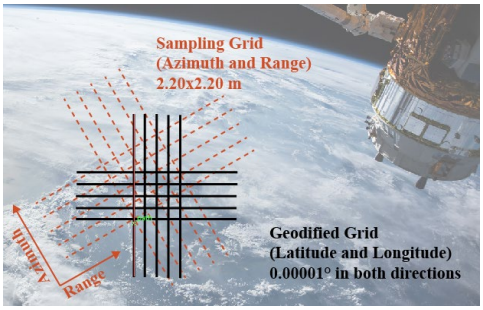

Figure 2. Representation of the geodified grid (black) and sampling grid (orange)

Figure 3. Spatial distribution of annual velocity values (cm/year) relating to the ascending orbit [*QGis3.10 A Coruña*]

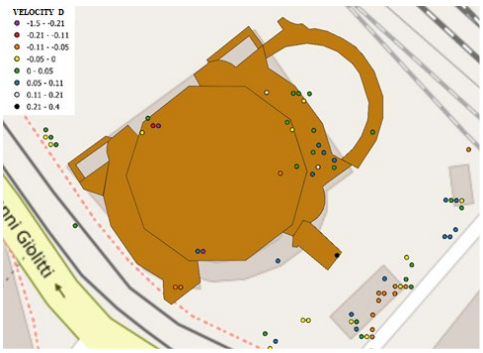

Figure 4. Spatial distribution of annual velocity values (cm/year) relating to the descending orbit [*QGis3.10 A Coruña*]

A subsequent processing of the satellite measurements relating to annual velocity values (vel) is aimed at evaluating the actual distribution of the points measured within the identified intervals (see the results in Tables 1-2).

Points 108 and 87 were monitored, respectively, for the ascending and descending orbit. In the first case, 35% of the points detected with annual velocity values in a range of 0-0.14 cm/year (20 points out of 57 total) exceed the average value of ~ 0.03 cm/year, while 61% of the points with velocity values between -0.19 and 0 cm/year (31 points out of 51 total) exceed the average value equal to ~ -0.035 cm/year.

In the second case, 44% of the points detected with annual velocity values between 0 and 0.27 cm/year (23 points out of 52 total) exceed the average value of ~ 0.05 cm/year, while 63% of the points with velocity values in the range of -0.34-0 cm/year (22 compared to the total 35) exceed the average value of ~ -0.07 cm/year.

Velocity Range	Number of points
cm/yaer	
-1.50 < vel < -0.21 (violet)	0
-1.21 < vel < -0.11 (red)	3
-1.11 < vel < -0.05 (orange)	10
-0.50 < vel < 0.00 (yellow)	38
0.00 < vel < 0.05 (green)	46
0.05 < vel < 0.11 (blue)	10
0.11 < vel < 0.21 (grey)	1
0.21 < vel < 0.40 (black)	0

Table 1. Velocity distribution relative to the ascending orbit

Velocity Range	Number of points
cm/yaer	
-1.50 < vel < -0.21 (violet)	3
-1.21 < vel < -0.11 (red)	2
-1.11 < vel < -0.05 (orange)	14
-0.50 < vel < 0.00 (yellow)	17
0.00 < vel < 0.05 (green)	27
0.05 < vel < 0.11 (blue)	20
0.11 < vel < 0.21 (grey)	3
0.21 < vel < 0.40 (black)	1

Table 2. Velocity distribution relative to the descending orbit

The second monitored parameter is the Consistency (con); it is an indicator relating to the reliability of the satellite measurement. The distribution of the points observed at the consistency value changes is shown in Figures 5-6 and in Tables 3-4.

Figure 5. Distribution of monitored points as the consistency variation relating to the ascending orbit [*QGis3.10 A Coruña*]

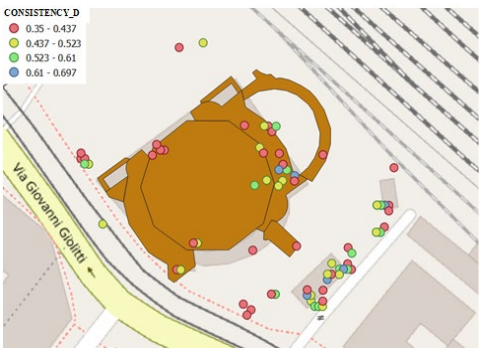

Figure 6. Distribution of monitored points as the consistency variation relating to the descending orbit [*QGis3.10 A Coruña*]

Consistency Range	Number of points
0.351 < con < 0.395 (red)	28
0.395 < con < 0.460 (yellow)	26
0.460 < con < 0.533 (green)	23
0.533 < con < 0.798 (blue)	31

Table 3. Distribution of points based on the value of consistency - ascending orbit

Consistency Range	Number of points
0.350 < con < 0.437 (red)	40
0.437 < con < 0.523 (yellow)	25
0.523 < con < 0.610 (green)	15
0.610 < con < 0.697 (blue)	8

Table 4. Distribution of points based on the value of consistency - descending orbit

With regard to the ascending orbit, the monitored points have maximum and minimum consistency values equal to 0.80 and 0.35, respectively, while for the descending one the values are 0.70 and 0.35, respectively. For the ascending orbit 44% of the points (equal to 48) exceed the average value of approximately 0.49, while for the descending one the average value of 0.47 is exceeded by 43% of the 38 observed points. The points with the highest values of both annual velocity and consistency value have been identified as the most relevant and reliable for monitoring purposes. They are the following: ascending orbit ID 17585 and descending orbit ID 152767.
The location of these points is shown in Figure 7, while their velocity and consistency are shown in Table 5. The time series of the selected points are shown in Figures 8-9.

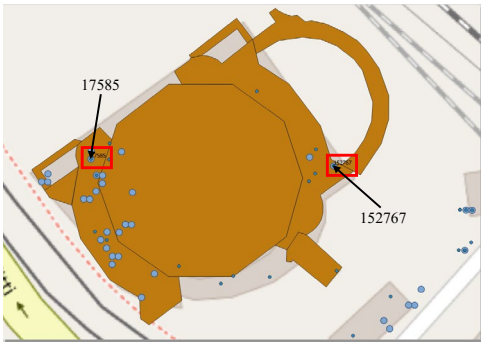

Figure 7. Points identified for structural monitoring [*QGis3.10 A Coruña*]

Orbit	Identity code (ID)	Annual Velocity	Consistency
		cm/year	
Ascending	17585	0.0816	0.553
Descending	152767	0.0618	0.638

Table 5. Characteristics of the most representative points.

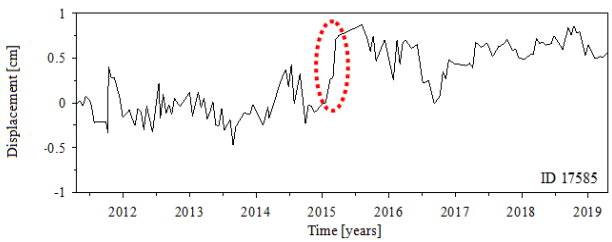

Figure 8. Distribution of annual velocity values (cm/year) relating to the ascending orbit ID 17585 [*QGis3.10 A Coruña*]

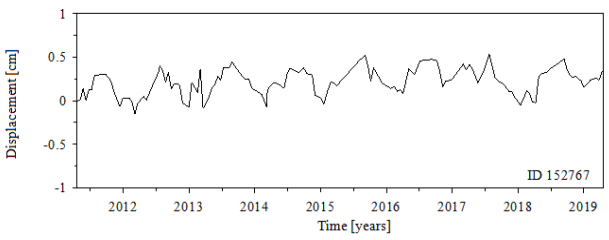

Figure 9. Distribution of annual velocity values (cm/year) relating to ID 152767 [*QGis3.10 A Coruña*]

In the first case, the point ID 17585 seems to be affected little by thermal fluctuations due to seasons change. The movement trend is quite irregular and, in particular, in the first part of 2015 it seems to have suffered a permanent deviation of almost 1 cm (Figure 8). Instead, in the second case, the time series shown at point ID 152767, appears to be regularly affected by annual temperature variations (Figure 9).

4. CONCLUSIONS

Considering the vast Italian historical and archaeological heritage that requires a careful structural monitoring plan in order to guarantee its conservation, the present research conducted has shown how satellite interferometry is a valid support tool for on-site monitoring campaigns which, in some cases, turn out to be burdensome and expensive.
The adoption of this technique makes it possible to create a temporal archive of data from whose processing it is possible to identify the areas subject to different levels of deformation for the evaluation of the health-state of the structure, and to know its history, studying the development of structural deformations in the aftermath. In this context, the use of satellite series, considering the availability of images with high spatial resolutions, should be included in the structural risk prediction and prevention phase, allowing to identify and map the areas of interest that form the basis for any risk mitigation activity. Future developments intend to evaluate the reliability of the new satellite monitoring methodologies by comparing them with the results obtained with on-site monitoring.

ACKNOWLEDGEMENTS (OPTIONAL)

This research is part of ReLuis Project, DPC-ReLUIS 2019-2020, WP6 (Monitoring and satellite data), Task 6.3 - Buildings of historical and monumental interest and archaeological areas.

REFERENCES

Arangio, S., Calò, F., Di Mauro, M., Bonano, M., Marsella, M., Manunta, M., 2014. An application of the SBAS-DInSAR technique for the assessment of structural damage in the city of Rome. In: *Structure and Infrastructure Engineering*, 10(11), pp. 1469-1483. doi.org/10.1080/15732479.2013.833949

Bonano, M., Manzo, M., Casu, F., Manunta, M., Lanari, R., 2017. DinSAR for the monitoring of cultural heritage sites. In: *Sensing the Past* (pp. 117-134). Springer, Cham.

Bru, G., Herrera, G., Tomás, R., Duro, J., De la Vega, R., Mulas, J., 2013. Control of deformation of buildings affected by subsidence using persistent scatterer interferometry. In: *Structure and infrastructure engineering*, 9(2), pp.188-200.

Cigna, F., Bateson, L. B., Jordan, C. J., Dashwood, C., 2014. Simulating SAR geometric distortions and predicting Persistent Scatterer densities for ERS-1/2 and ENVISAT C-band SAR and InSAR applications: Nationwide feasibility assessment to monitor the landmass of Great Britain with SAR imagery. In: *Remote Sensing of Environment*, 152, pp. 441-466.

De Corso, T., Mignone, L., Sebastianelli, A., Del Rosso, M. P., Yost, C., Ciampa, E., Ullo, S., 2020. Application of DInSAR technique to high coherence satellite images for strategic infrastructure monitoring. arXiv preprint arXiv:2004.09501.

Diaferio, M., Foti, D., Giannoccaro, N.I., 2014. Identification of the modal properties of a building of the Greek heritage. In: *Key Engineering Materials*, 628, pp 150-159. doi:10.4028/www.scientific.net/KEM.628.150

Diaferio, M., Foti, D., Gentile, C., Giannoccaro, N.I., Saisi, A. (2015). Dynamic testing of a historical slender building using accelerometers and radar. In: *Proc. of the 6th International Operational Modal Analysis Conference*, May 12-14, Gijón, Spain, paper ID 153, pp.129-130, ISBN: 978-84-617-3880-9.

Foti, D., 2014. Non-destructive techniques and monitoring for the evolutive damage detection of an ancient masonry structure. In: *Key Engineering Materials*, 628, pp 168-177. doi:10.4028/www.scientific.net/KEM.628.168.

Lanari, R., Casu, F., Manzo, M., Zeni, G., Berardino, P., Manunta, M., Pepe, A., 2007. An overview of the small baseline subset algorithm: A DInSAR technique for surface deformation analysis. In: *Deformation and Gravity Change: Indicators of Isostasy, Tectonics, Volcanism, and Climate Change*, pp. 637-661. doi.org/10.1007/978-3-7643-8417-3_2

MIT - Ministry of Infrastructures and Trasport, 2018: Ministry Decree of the 17Th Jan 2018. Adjournment of Technical Code Standard for Constructions (in Italian). Supplemento ordinario n. 8 alla Gazzetta Ufficiale del 20-2-2018. Rome, Italy. https://www.gazzettaufficiale.it/eli/id/2018/2/20/18A00716/sg

Yang, C. H., Kenduiywo, B. K., Soergel, U., 2016. Change Detection Based on Persistent Scatterer Interferometry-A New Method of Monitoring Building Changes. In: ISPRS *Annals of Photogrammetry, Remote Sensing & Spatial Information Sciences*, 3(7).

Zeni, G., Bonano, M., Casu, F., Manunta, M., Manzo, M., Marsella, M., Pepe, A., Lanari, R., 2011. Long term deformation analysis of historical buildings through the advanced SBAS DInSAR technique: The case study of the city of Roma (Italy). In: *Journal of Geophysics and Engineering*, 8(S1). doi:10.1088/1742-2132/8/3/S01

ESTIMATION OF MULTITEMPORAL DRY DEPOSITION OF AIR POLLUTION BY URBAN FORESTS AT CITY SCALE

V. Fanara [1], G. Chirici [1], C. Cocozza [1], G. D'Amico [1], F. Giannetti [1], S. Francini [1,2,3], F. Salbitano [1], A. Speak [1], E. Vangi [1,2], D. Travaglini [1,*]

[1] Dept. of Agriculture, Food, Environment and Forestry, University of Florence, 50145 Florence, Italy – valeria.fanara@stud.unifi.it (gherardo.chirici, claudia.cocozza, giovanni.damico, francesca.giannetti, fabio.salbitano, andrew.speak, davide.travaglini)@unifi.it
[2] Dept. of Biosciences and Territory, University of Molise, 86100 Campobasso, Italy – elia.vangi@unifi.it
[3] Dept. for Innovation in Biological, Agri-Food and Forestry Systems, University of Tuscia, 01100 Viterbo, Italy – saverio.francini@unifi.it

KEY WORDS: ecosystem services, LAI, leaf area index, canopy cover, LiDAR, canopy height model, PM_{10}, air quality

ABSTRACT:

Air pollution is a major problem for many cities worldwide. Urban forests provide a wide range of ecosystem services for human well-being, including recreation, urban temperature regulation, and air purification. The present study investigated the use of two Airborne Laser Scanning (ALS) datasets to estimate changes in dry deposition of particulate matter (PM_{10}) by urban forests in the city of Florence. The spatial distribution of urban forests was mapped by photointerpretation of aerial images and classified into seven forest types. The leaf area index (LAI) was estimated using a regression model between LAI data and forest canopy cover from ALS data. The potential of PM_{10} removal by urban forests was estimated using pollution deposition equations and pollution concentrations measured at urban monitoring stations in 2013 and 2018. Our results show that PM_{10} removal by urban forests in the city of Florence decreased from 2013 to 2018. In the study area natural and human induced forest disturbances (e.g. wind storms and coppicing) occurred in the examined period, which reduced the forest canopy cover and the potential removal of air pollution by urban forest as well. Our study confirms that canopy cover is a good predictor for LAI. However, caution on the fact that our results were partially affected by the date of acquisition of remote sensing products.

1. INTRODUCTION

Cities are open and dynamic systems, which consume, transform and release materials and energy, interacting with humans and other systemic components.
Air pollution is a major problem for many cities worldwide affecting the health of citizens. Urban forests provide a wide range of ecosystem services for human well-being, including recreation, urban temperature regulation, and air purification (Ferrini et al., 2020).
Urban forests and trees are excellent filters, as they reduce harmful ultraviolet radiation and air pollution, noise and negative sensorial perception. This filtering function aids in decreasing some direct and indirect negative impacts on human health (Nowak et al., 2014). Besides improving air quality, urban forests can also have a positive role on perceived restorativeness and self-reported well-being benefits (Carrus et al., 2015).
To estimate air pollution removal by the urban forest, modeling has been used. One of the most used models is i-Tree Eco dry deposition model (e.g., Nowak and Crane, 2006).
To reduce the sampling effort when studying the spatially-explicit dry deposition capacity of urban forests, a model was developed by Bottalico et al. (2017) using the city of Florence as a case study, which was based on an integration of different high spatial resolution datasets and GIS analysis.
The aim of the present study was to investigate the use of two Airborne Laser Scanning (ALS) datasets to estimate changes in dry deposition of particulate matter (PM_{10}) by urban forests in the city of Florence. We used the model developed by Bottalico et al. (2017), which was slightly modified to adapt the model to multitemporal analysis.

* Corresponding author

2. MATERIALS AND METHODS

2.1 Study area

The study was carried out in the Municipality of Florence (Italy), which extends on 102 km^2. The urban forests cover 10.4% of the total municipality area. Deciduous broadleaves is the prevalent forest type and the remaining forest area is represented by mixed forest types with conifers, deciduous and evergreen broadleaves (Bottalico et al., 2017).

2.2 Data

The following remote sensing products available on-line were used. Color infrared high resolution (pixel = 0.2 m) aerial orthophotos acquired in 2019, Digital Terrain Model (DTM) and Digital Surface Model (DSM) in grid format (pixel = 1 m) obtained from ALS acquired in 2007 under leaf-on conditions were downloaded from http://www.regione.toscana.it/-/geoscopio-wms. DTM and DSM (pixel = 1 m) from ALS data acquired in early spring in 2017 were available at https://opendata.comune.fi.it/. As of this writing, these are the only known ALS surveys carried out for the entire Municipality of Florence. The Canopy Height Model (CHM) was obtained for the years 2007 and 2017 by subtracting the DTM from DSM.
Monthly PM_{10} data (years 2013 and 2018) were obtained from pollutant monitoring stations (Bassi, Boboli, Gramsci, Mosse) available for Florence; averages from the stations were used (Figure 1).
The urban forest map in vector format and the leaf area index (LAI) map in grid format (pixel = 18 m) for the entire

Municipality of Florence were also available for the year 2013 (Bottalico et al., 2017). The forest map was obtained by photointerpretation of color infrared (pixel = 0.5 m) aerial orthophotos using the FAO (2010) forest definition and seven forest types. The LAI map was obtained using a linear regression model between in-field LAI data and ALS-derived metrics. More details can be found in Bottalico et al. (2017).

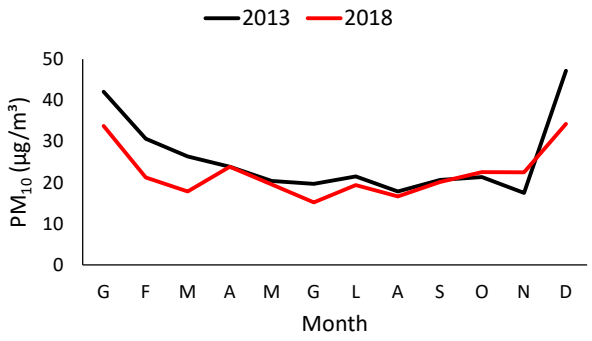

Figure 1. Seasonal trend of PM_{10} concentrations in the air.

2.3 Urban forest map

The orthophotos acquired in 2019 were used to update the urban forests map for the year 2013 by visual interpretation and manual delineation of seven forest types, as reported in Bottalico et al. (2017): conifers (FC1), deciduous broadleaves (FC2), evergreen broadleaves (FC3), mixed conifers, deciduous and evergreen broadleaves (FC4), mixed deciduous and evergreen broadleaves (FC5), mixed conifers and deciduous broadleaves (FC6), mixed conifers and evergreen broadleaves (FC7). Since a common definition for urban forest is not available worldwide, we used the standard FAO (2010) forest definition.

2.4 Leaf area index estimation

The LAI map in grid format (pixel = 18 m) for the year 2013 (Bottalico et al., 2017) was used to model the relationships between LAI and urban forest canopy cover (in %). For each cell of the grid, the canopy cover was computed as the ratio between the urban forest area within the cell and the cell area. The urban forest area in the cell was computed taking into account the 2013 urban forest map (Bottalico et al., 2017) and the height of the forest (> 5 m) from the 2007 CHM. We used 70% of the cells as training to model the relationships between LAI and canopy cover and the remaining 30% as test for model validation.

The exponential model was then used to estimate the LAI for the years 2013 and 2018, for the latter, the urban forest canopy cover was computed as described above taking into account the 2019 urban forest map (see section 2.3) and the height of the forest (> 5 m) from the 2017 CHM.

2.5 Modeling air pollution deposition at leaf level and pollution removal at city scale

The dry deposition of PM_{10} at leaf level for each forest type was obtained using the mean monthly pollutant deposition for the annual series (2013 and 2018) and the methodology used in other studies (e.g., Nowak, 1994; Hirabayashi et al., 2012; Bottalico et al., 2017):

$$Pm_{10}\ deposition = \left(\sum_{i=1}^{12} V_d \cdot C_i \cdot T_i \cdot 24 \cdot 3600\right)$$

where V_d is the dry deposition velocity (m/s) for PM_{10}, which was set to an average value of 0.0064 m/s based on the median deposition velocity from the literature (Lovett, 1994) and a 50% resuspension rate of particles back to the atmosphere (Zinke, 1967), as described by Hirabayashi et al. (2012); C_i is the mean monthly PM_{10} concentration (g/m^3) (Figure 1); and T_i is the number of days per month. As in Bottalico et al. (2017), we assumed that the growing season was 1st April to 30th September for deciduous broadleaves and throughout the year for Mediterranean conifers and evergreen broadleaves.

The pollution removal of PM_{10} at city scale for each forest type in the years 2013 and 2018 was obtained by multiplying the leaf-unit deposition by the area (m^2) covered by the forest type and by LAI; LAI values were kept constant in the growing season for deciduous species and throughout the year for evergreen species.

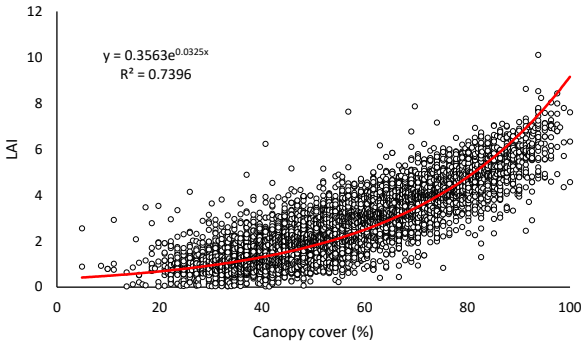

Figure 2. Relationship between LAI and forest canopy cover.

3. RESULTS

The spatial distribution and composition of the urban forests in the Municipality of Florence did not change in the examined period, except for very few new deciduous broadleaves forest patches emerging in the countryside surrounding the city center, which in 2013 did not respect the minimum percentage of canopy cover (10%), according to standard FAO forest definition. The total area of the urban forests increased by less than 1% in the time period, deciduous broadleaves is still the prevalent forest type (55% of the total forest area), while mixed forest types with conifers, deciduous and evergreen broadleaves are almost equally represented, as already reported by Bottalico et al. (2017).

The minimum canopy cover provided by tree crowns taller than 5 m as from CHM was 5% and 4% in 2013 and 2018, respectively, the maximum was 100% in both years. Table 1 reports the distribution of forest area into canopy cover classes for 2013 and 2018.

Canopy cover	2013	2018
0-20%	0.5	14.9
20-40%	17.8	26.0
40-60%	40.3	27.6
60-80%	31.0	21.8
80-100%	10.4	9.7
Total	100.0	100.0

Table 1. Distribution of the urban forest area (in %) into canopy cover classes in 2013 and 2018.

The agreement between LAI estimated by the model based on in-field LAI data and ALS-derived metrics (Bottalico et al., 2017) and LAI predicted on test sites by the exponential model

based on canopy cover from CHM (this study) was good, with $R^2 = 0.7435$, RMSE = 0.80, and relative RMSE = 31%.
LAI values estimated by exponential model ranged between 0.418 and 9.189 in 2013 and between 0.361 and 9.189 in 2018, being 9.189 the maximum value provided by the model in case of a full canopy cover (100%).
Annual PM_{10} removal accounted for 169.6 tons and 130.8 tons in 2013 and 2018, respectively. The monthly totals of PM_{10} removal per unit of urban forest area (Figure 3) were similar to the trend of PM_{10} concentration in air registered by monitoring stations (Figure 1), that is a peak in the month of December.

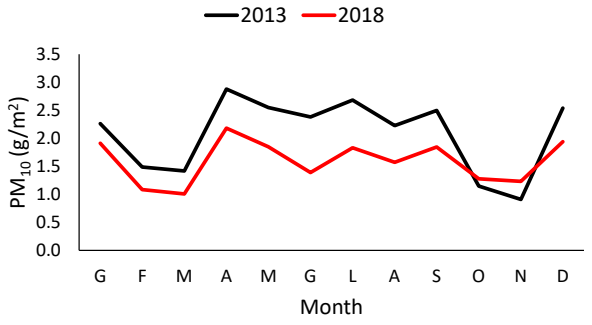

Figure 3. Monthly totals of PM_{10} removal by the urban forest in the Municipality of Florence.

Removal rates per forest area (g/m^2) and total annual removal (tons) by forest types are reported in Table 2. The rates for conifers (FC1), evergreen broadleaves (FC3), and mixed forest types (FC7) were higher than for deciduous broadleaves (FC2).

Forest type	2013		2018	
	Rate	Total	Rate	Total
FC1	39.0	16.4	46.9	19.6
FC2	13.9	49.8	5.9	20.8
FC3	52.1	10.7	41.9	8.5
FC4	26.1	26.3	22.8	24.1
FC5	29.0	7.4	30.9	7.9
FC6	19.9	8.2	13.8	5.9
FC7	55.5	50.8	46.8	44.0
Total	-	169.6	-	130.8

Table 2. PM_{10} removal in 2013 and 2018 (totals in tons and rates in g/m^2 of forest cover) by the urban forest in the Municipality of Florence (for forest types descriptions see section 2.3).

Figure 4 reports the spatial distribution of PM_{10} removal in 2013 and 2018 by the urban forests in the Municipality of Florence. The Figure shows that the urban forests in the northern part of the study area had the greatest total removal of PM_{10}.

4. DISCUSSION AND CONCLUSIONS

We investigated the use of multitemporal ALS data to estimate changes in PM_{10} removal by urban forests in the Municipality of Florence. CHM derived from ALS was used to assess the urban forest canopy cover, which was used as a predictor variable to model LAI variations in the study area with an exponential function.
The model function resulted in good linear agreement (R^2 = 0.7435) with LAI estimates obtained with a model based on ground measurements and ALS-derived metrics.
In 2013 the amount of air pollution removal at city scale (169.6 tons) was similar to that reported (171.3 tons) by Bottalico et al. (2017) for Florence. Our results show that in 2018 PM_{10} removal decreased by 23%.

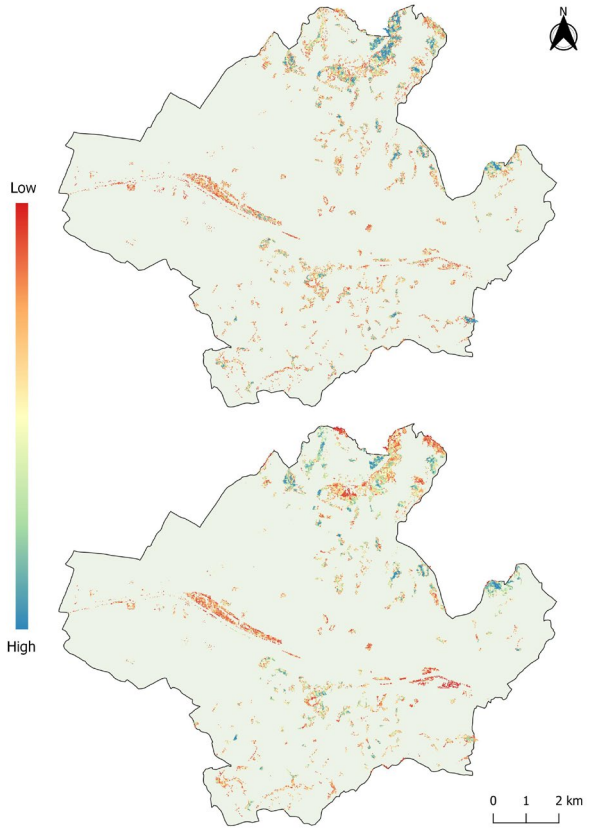

Figure 4. Spatial distribution of the annual (2013 above, 2018 below) removal of PM_{10} by the urban forest in the Municipality of Florence.

Because the urban forests distribution and composition was almost stable between 2013 and 2018, the reduction in pollution removal can be associated with changes in forest structure due to natural disturbances or human induced. In the Municipality of Florence and in other forest areas in Tuscany, extreme events due to wind storms occurred in 2015. Forest damages were reported for parks in the urban area (e.g. Anconella and Albereta) and for forest stands in the area of Mount Morello in the northern part of the study area (Chirici et al., 2016). In addition, forestry practices like coppicing in deciduous stands in the peri-urban zone have changed forest structure during the examined period, at least in the first years after the cut. These forest disturbances (wind storms and forest management practices) reduced the canopy cover in the study area (Table 1), and the potential removal of air pollution by urban forest as well. It is worth noting that our ALS-based model took into account the vegetation density and its temporal and spatial variability within the study area.
However, variations in the canopy cover detected by changes in the CHM could be affected by the date of acquisition of remote sensing data. In our study, we used ALS data acquired in 2017 in early spring with a flight operated not for vegetation either forestry applications (Corona et al., 2012). Deciduous broadleaves start the leaf expansion at the same springtime, thus we recommend caution on PM_{10} removal decrease reported in our study, as it could be partially affected by the date of acquisition of ALS data.

Other limitations of this study that need to be further investigated are: small green areas and street trees were not considered because of the use of the FAO forest definition; we estimated air pollution removal using ALS data and pollution concentration from ground stations which were not collected in the same vegetative season; we did not take into account periods of wet deposition.
Nevertheless, our study confirms that canopy cover is a good predictor for LAI estimations as reported in other studies (e.g., Zhang et al., 2019). Moreover, the results indicate that, when a reliable model between LAI and forest canopy cover is found, the model itself can be extended to assess multitemporal LAI values using canopy cover derived from ALS data collected in different years. However, it is worth noting that canopy cover might be obtained using other remote sensing products, like aerial or satellite images (Zhang et al., 2019; Huang et al., 2021) whose time series availability is greater than ALS data, as it is for the city of Florence and for most of the Italian territory (D'Amico et al., 2021).

ACKNOWLEDGEMENTS

The study was carried out within the research project "Establishing Urban FORest based solutions In Changing Cities" (EUFORICC), funded by the PRIN 2017 program of the Italian Ministry of University and Research.

REFERENCES

Bottalico, F., Travaglini, D., Chirici, G., Garfì, V., Giannetti, F., De Marco, A., Fares, S., Marchetti, M., Nocentini, S., Paoletti, E., Salbitano, F., Sanesi, G., 2017. A spatially-explicit method to assess the dry deposition of air pollution by urban forests in the city of Florence, Italy. Urban Forestry & Urban Greening, 27: 221-234. http://dx.doi.org/10.1016/j.ufug.2017.08.013.

Carrus, G., Scopelliti, M., Lafortezza, R., Colangelo, G., Ferrini, F., Salbitano, F., Agrimi, M., Portoghesi, L., Semenzato, P., Sanesi, G., 2015. Go greener, feel better? The positive effects of biodiversity on the well-being of individuals visiting urban and peri-urban green areas. Landscape and Urban Planning, 134: 221-228. https://doi.org/10.1016/j.landurbplan.2014.10.022

Chirici, G., Bottalico, F., Giannetti, F., Rossi, P., Del Perugia, B., Travaglini, D., Nocentini, S., Marchi, E., Foderi, C., Fioravanti, M., Fattorini, L., Guariglia, A., Ciancio, O., Bottai, L., Corona, P., Gozzini, B., 2016. Assessment of forest damage following the wind storm of the 5th of March 2015 in Tuscany (Italy). L'Italia Forestale e Montana, 71: 197-213. (In Italian) http://dx.doi.org/10.4129/ifm.2016.4.02

Corona, P., Cartisano, R., Salvati, R., Chirici, G., Floris, A., Di Martino, P., Marchetti, M., Scrinzi, G., Clementel, F., Travaglini, D., Torresan, C., 2012. Airborne Laser Scanning to support forest resource management under alpine, temperate and Mediterranean environments in Italy. European Journal of Remote Sensing, 45: 27-37. https://doi.org/10.5721/EuJRS20124503.

D'Amico, G., Vangi, E., Francini, S., Giannetti, F., Nicolaci, A., Travaglini, D., Massai, L., Giambastiani, Y., Terranova, C., Chirici, G., 2021. Are we ready for a National Forest Information System? State of the art of forest maps and airborne laser scanning data availability in Italy. iForest, 14: 144-154. http://dx.doi.org/10.3832/ifor3648-014

FAO, 2010. Global Forest Resources Assessment 2010. Food and Agriculture Organization of the United Nations, Rome.

Ferrini, F., Fini, A., Mori, J., Gori, A., 2020. Role of Vegetation as a Mitigating Factor in the Urban Context. Sustainability, 12: 4247. https://doi.org/10.3390/su12104247.

Hirabayashi, S., Kroll, C.N., Nowak, D.J., 2012. Development of a distributed air pollutant dry deposition modeling framework. Environmental Pollution, 171: 9-17. https://doi.org/10.1016/j.envpol.2012.07.002.

Huang, X., Wu,W., Shen, T., Xie, L., Qin, Y., Peng, S., Zhou, X., Fu, X., Li, J., Zhang, Z., Zhang, M., Liu, Y., Jiang, J., Ou, P., Huangfu, W., Zhang, Y., 2021. Estimating Forest Canopy Cover by Multiscale Remote Sensing in Northeast Jiangxi, China. Land, 10, 433. https://doi.org/10.3390/land10040433.

Lovett, G.M., 1994. Atmospheric deposition of nutrients and pollutants in North America: an ecological perspective. Ecological Applications 4, 629-650. https://doi.org/10.2307/1941997.

Nowak, D.J., 1994. Air pollution removal by Chicago's urban forest. In: McPherson, E.G., Nowak, D.J., Rowntree, R.A. (Eds.), Chicago's Urban Forest Ecosystem: Results of the Chicago Urban Forest Climate Project. USDA Forest Service, Northeastern Forest Experimental Station, Radnor, PA, pp. 63-81.

Nowak, D.J., Hirabayashi, S., Bodine, A., Greenfield, E., 2014. Tree and forest effects on air quality and human health in the United States. Environmental Pollution, 193: 119-129. http://dx.doi.org/10.1016/j.envpol.2014.05.028

Nowak, D.J., Crane, D.E., Stevens, J.C., 2006. Air pollution removal by urban trees and shrubs in the United States. Urban Forestry & Urban Greening, 4: 115–123. http://dx.doi.org/10.1016/j.ufug.2006.01.007.

Zhang, D., Liu, J., Ni, W., Sun, G., Zhang, Z., Liu, Q., Wang Q., 2019. Estimation of Forest Leaf Area Index Using Height and Canopy Cover Information Extracted From Unmanned Aerial Vehicle Stereo Imagery. IEEE Journal of Selected Topics in Applied Earth Observations and Remote Sensing, 12: 471-481. https://doi.org/10.1109/JSTARS.2019.2891519.

Zinke, P.J., 1967. Forest interception studies in the United States. In: Sopper, W.E., Lull, H.W. (Eds.), Forest Hydrology. Pergamon Press, Oxford, pp. 137-161.

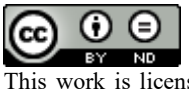

INVESTIGATING SPACEBORNE REMOTE SENSING TECHNIQUES FOR BURIED NURAGHI STRUCTURES IDENTIFICATION: THE NURAGHE NANNI ARRU' CASE STUDY

Carlino Casari [1]*, Roberto Demontis [1], Eva Lorrai [1], Laura Muscas [1], Stefania Amici [2,3], Vittorio Cannas [2]

[1]CRS4 (Center for advanced studies, research and development in Sardinia), 09010 Pula, Italy - (casari, demontis, eva, muscas)@crs4.it
[2] Spacearth Technology, 00143 Roma, Italy - (stefania.amici, vittorio.cannas)@spacearth.net
[3] Istituto Nazionale di Geofisica e Vulcanologia, via di Vigna Murata 605, 00143, Roma, Italy - stefania.amici@ingv.it

KEY WORDS: Archaeology, Nuraghe, Remote Sensing, Detecting methods

ABSTRACT:

The present work aims to define a methodology for archaeological sites investigation through the pervasive use of satellite remote sensing technologies. Spaceborne sensing techniques have been used by archeologists for prospecting landscapes to characterise site changes and detecting features of interest. Our approach is based on the so-called archeological proxy indicators where we investigate the use of satellite remote sensing for an initial identification of potential areas of interest and then other in-situ techniques for data comparison and validation to eventually define the best approach to be used for buried nuraghi archeological remains.
For this study, the nuraghe Nanni Arrù located in south Sardinia has been selected. It is one of the most important finds in recent times as it partially highlights towers, rooms and wall traces of a surrounding village. These characteristics confirm the complexity of the monument which represents an ideal use case for the definition of an innovative methodological model to be replicated in the whole region.

1 INTRODUCTION

The Nuragic civilization developed in the Italian territory of Sardinia island from the Bronze Age (18th century BC) to the 2nd century AD. The name comes from the most distinctive expression of their architecture, the tower-fortresses, 'nuraghes' (Lilliu, 2006). It is estimated that there are about 5200 Nuraghes (red dots in Figure1), more than 750 Domus de Janas (literally "house of the fairies", pre-Nuragic chamber tombs - green dots in Figure 1) have been discovered, more than 60 holy wells (light blue dots in Figure 1), more than 500 giants' graves (yellow dots in Figure 1), more than 200 villages (blue dots in Figure 1) (Demontis et al., 2015), (Demontis et al., 2020),

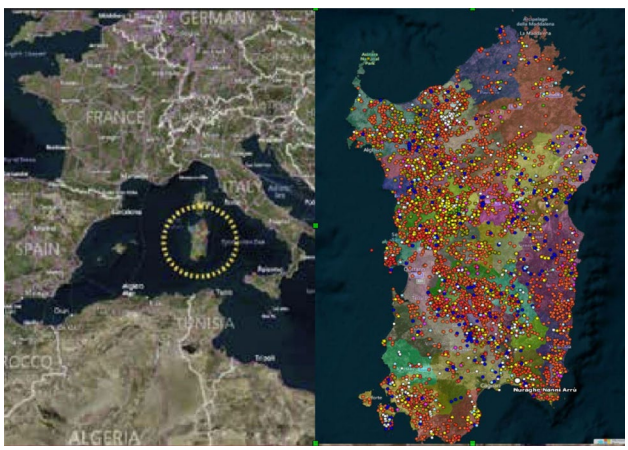

Figure 1. The map of Sardinia island showing the distribution of pre nuragic and nuragic archeological sites at http://nurnet.crs4.it/nurnetgeo

* Corresponding author

However, many other evidences are believed to be present on the island. Although there are several examples of isolated nuraghi, in Sardinia the nuraghe is often surrounded by the village or by other findings. In this context it would be helpful to identify and perimeter potential hidden archaeological structures. As a case study, the area of the nuraghe Nanni Arrù has been selected as it is supposed to be surrounded by villages.
Our approach starts with the visual interpretation of the archeological proxy indicators such as crop, soil, shadow and damp mark [Lasaponara, Masini, 2012] that can be seen from air by using optical remote sensing. To do this, we used very high spatial resolution images from regional historical aerial orthophoto (Table 1) available as WMS (Web Map Service) on http://www.sardegnageoportale.it/ and the Google Earth. In fact, Aerial photography has been used to reveal buried structures although with some limitations. (Scollar et al 1990).
Finally, because of the nuraghi can be found near cultivated areas, in pastoral areas, in rocky landscape, in hilly sites, as well as in forest areas, multispectral satellite data (i.e. Sentinel 2) and not-optical data (i.e. Thermal) will be explored to try to discover the largest number of buried structures (Trogu et al 2014). Proximal remote sensing such as a drone equipped with optical/thermal cameras providing data at very high resolution (VHR) will be used for data comparison (Parcak, 2009), (La Saponara and Masini, 2011), (Chen et al., 2017).
The expected project result will be the identification of the best approach(es) to use for the archeological remains of buried nuraghi (Fallavollita et al, 2013).

In this study we present the very preliminary results of this work.

2 METHODOLOGY

In this paragraph, we describe the techniques tested in this first phase of the project for the identified case study.

2.1 Nanni Arrù nuraghe

The Nanni Arru' Nuraghe is located at about Lat 39° 17' 32.5'' N, 9° 17' 16.00'' E and covers about 2000 $m^{2.}$ (excavated area). As one of the most important finds in recent times, the Nuragic area of Nanni Arrù was discovered in the early 1990s and some initial excavations were carried out in the period between 1994 and 1999 under the coordination of the Executive Inspector of the Archaeological Superintendency. Excavations have identified a four-lobed fortified structure (Figure 1) consisting of a central keep with four towers, three of which leaning against the keep and a larger one in opposite direction, in order to leave room for a large courtyard.

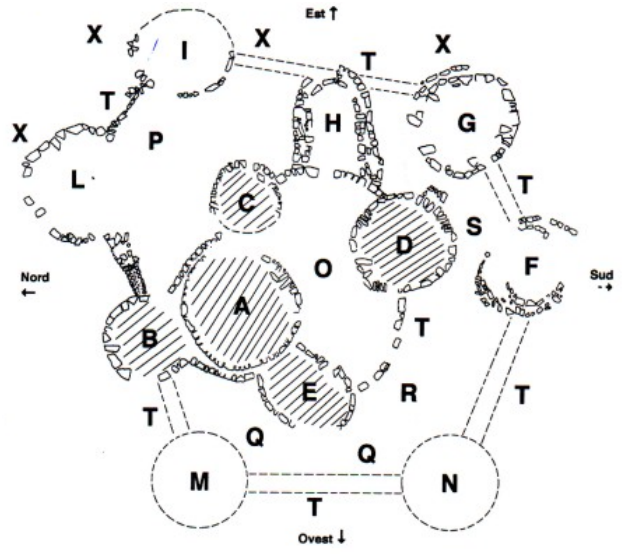

Figure 2. Archaeological survey of the Nanni Arrù site

Figure 3. RGB image taken from Google Earth (19 June 2019)

The excavations have also partially brought to light other towers, for a total of ten rooms, and traces of the surrounding village walls (Figure 3).

In fact, nuraghi with complex or multi-lobed structures generally have an adjacent or a nearby village (e.g. Barumini) and/or burial sites such as giants' tombs.
In support of this thesis, during the 1994-1999 surveys, the finds of pebbles from the Nuragic era in the area north of the nuraghe, and the possible presence of a giants' tomb about 140m north-east of the nuraghe are particularly useful.
In the area subject to excavation, there are still traces of human presence even in Roman times.
The area surrounding Nanni Arru' is characterized by numerous agriculture plots of diverse sizes and it is promising in terms of revealing buried structures.

2.2 Chosen approach for the study of the area

The techniques developed to discover buried structures use diverse typology of sensors operating in diverse regions of the electromagnetic field such as Visible, Thermal and Microwaves. The presence of near to surface archaeological structures may influence terrain and vegetation:
-it may modify the ground color tone, either in the presence of vegetated or bare soil
-it may influence the vegetation growth and the soil moistures resulting in crop marks. Negative crop marks are usually associated with the presence of walls and positive marks above buried ditches and pits (Donoghue, 2003).

2.2.1 Aerial photography

Aerial orthophoto images are available on http://www.sardegnageoportale.it. Exploring the catalogue we found 17 photos taken in the Nanni Arru' area, a selection of which is reported in Table 1, with the year of acquisition. The acquisition month is specified only for the 2019 image. We have visually inspected the orthophotos and found possible crop/soil anomalies in the same areas indicated with light blue arrows in Figure 4 and 5. The process to obtain permission to use the images in a paper is in progress.

Orthophoto RAS date	Type mark
2019 (June)	soil mark
2016	soil mark
2013	soil mark
2010	soil mark
2006	soil mark
2004	soil mark
2003	crop mark
1998/99	crop mark
1997	soil mark
1967/68	crop mark
1955	soil mark

Table1. List of the examined RAS orthophoto images and associated marks in Nanni Arru' surrounding areas.

2.2.3 Google Earth

High resolution images from Google Earth have been visually inspected for potential crop marks. Table 2 lists the imagery acquisition time and the main type of agricultural terrain (crop or soil) near the area of interest.

Google Earth date	Type mark
19 June 2019	Soil mark
17 March 2017	crop mark
9 July 2015	soil crop
14April 2013	crop (weak)
8 August 2011	crop mark
17 June 2011	ibrid
13 May 2011	crop mark
6 March 2011	soil mark
10 April 2010	crop mark
18 July 2004	soil mark

Table 2. List of the examined Google Earth images

Figure 4. Google Earth image acquired on 6 March 2011 that shows an example of possible soil marks about 140m SE from the Nanni Arrù pin point

Figure 5. Google Earth image 17 March 2017 showing crop marks at about the same distance from Nanni Arrù pinpoint

2.4 Lines extraction

The delimitation of eight macro-areas (Figure 6) has been realised using Google Earth, comparing the images available from 2019 to 2004 and selecting the areas that have more or less the same anomalies in the ground, in the different years. Previous Google Earth images could not be used due to unsuitable resolution. It can also be noticed that images up to 2004 have a different positioning than those from 2010 onwards. The choice of the areas delimitation was mainly dictated by the differences in the terrain color in most of Google Earth images, taken in different years and seasons. The resulting vector data have been imported in QGIS to overlay the orthophotos of the Sardinia Region, confirming the detected anomalies (Table1).

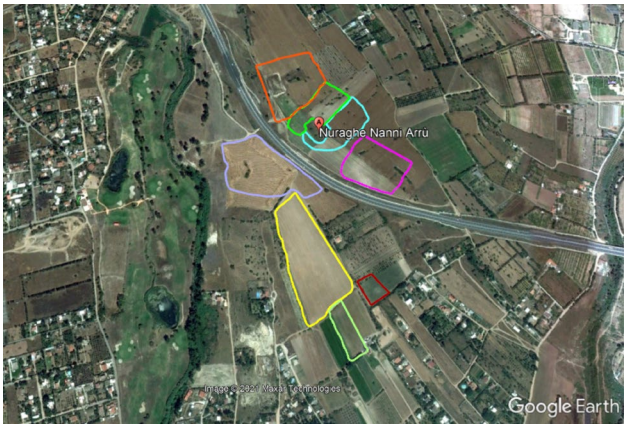

Figure 6. Possible delimitation of macro-areas containing ibrid marks (17 June 2011)

Each macro-area was therefore carefully observed, and peculiar lines or polygons with likely circular shape have been highlighted (Figure 7).

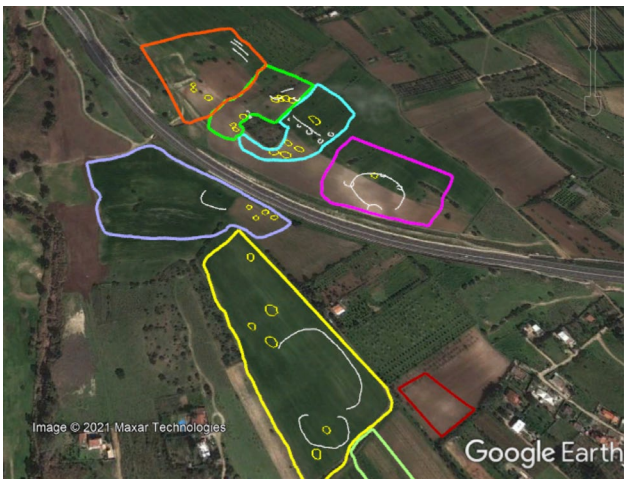

Figure 7. Small polygons (in yellow) and lines (in white) to be further investigated (6 March 2011)

Due to the fact that different years' images were examined before choosing the areas to be selected, the correspondence between crop marks and delimited polygons or lines in Figure 7 is not always evident.

It was established to first investigate the macro-areas close to the nuraghe and to temporarily omit those beyond the SS554bis road. Satellite images and in situ analysis will be done to decide which of these lines or polygons could be dismissed, and the vegetation and/or pedological indices to be taken into account.

3. CONCLUSION

In the first phase of the project we explored aerial and VHR images from Google Earth covering a period of time between 1955 to 2019 (June 19th).

Preliminary analysis based on visual inspection have highlighted three possible areas (light green, cyan, magenta in Figure 7) with several interesting features,
As the systematic identification of archaeological signs still poses a challenge due to the transient characteristics of subtle signals that are only visible under specific conditions, a multi-temporal approach will be considered to complete the analysis.
In particular, Sentinel 2 cloud free data will be exploited to capture anomalies in terms of specific indexes and time series (2017-2021).
A thermal infrared (TIR) survey over this three area is planned for summer 2021.
Meanwhile, a discussion with the archeologist who handled the Nanni Arrù excavations has been initiated.

ACKNOWLEDGEMENTS

The authors really appreciated the practical suggestions of the Archaeologist Patrizia Zuncheddu about the marks indicated by the authors and her extensive description of the Nanni Arrù area. This study is part of a scientific collaboration with the ArchaeoSardinia initiative, a project funded by the Autonomous Region of Sardinia (LR7/2007).

REFERENCES

Chen F., Lasaponara R., Masini N., An overview of satellite synthetic aperture radar remote sensing in archaeology: From site detection to monitoring, In: Journal of Cultural Heritage,Volume 23, Supplement,Pages 5-11,201 (2017)

Demontis, R., Lorrai, E. and Muscas, L., 2020. The Nurnet Geoportal an Example of Participatory Gis: A Review after Six Years. In: Open Access Journal of Archaeology and Anthropology, Volume2-Issue5 (October 2020).

Demontis, R., Lorrai, E., Muscas, L. and Spanu, V., 2015. Nurnet-A case of crowdsourcing for geographic knowledge production. In: EGU General Assembly 2015.

Donoghue D.N.M., Multispectral remote sensing for archaeology, In: Archeologia Medievale 12, 2003, 1e10.

Fallavollita, P., UAS for archaeology. New perspectives on Aerial documentation. In: ISPRS - International Archives of the Photogrammetry Remote Sensing and Spatial Information Sciences XL-1/W2(1):131-135 (2013)

Lasaponara, R. Masini, N., Remote sensing in archaeology: From visual data interpretation to digital data manipulation. In satellite Remote Sensing. A new tool for Archeology Lasaponara, R. Masini., Eds; Springer: Dordrecht, The Netherlands 2012; pp. 3-16.

Lasaponara, R. Masini, N., Satellite remote sensing in archaeology: past, present and future perspectives, Journal of Archaeological Science,Volume 38, Issue 9,2011,Pages 1995-2002,ISSN 0305-4403,
https://doi.org/10.1016/j.jas.2011.02.002.

Lilliu, G. (2006) Sardegna Nuragica, collana: Appunti di Archeologia, Edizioni Il Maestrale, Nuoro, Italy.

Parcak S.J, Satellite remote sensing for archaeology, ed. Routledge 2009.

Scollar, I.; Tabbagh, A.; Hesse, A.; Herzog, I. Archaeological Prospecting and Remote Sensing; Cambridge University Press: Cambridge, UK, 1990.

Trogu, A.; Ranieri, G.; Calcina, S.; Piroddi, L. The ancient Roman aqueduct of Karales (Cagliari, Sardinia, Italy): Applicability of geophysics methods to finding the underground remains. Archaeol. Prospect. 2014, doi:10.1002/arp.1471.

Recent advancement in Remote Sensing Technologies

OPERATIONAL SATELLITE-BASED HIGH-RESOLUTION WATER QUALITY PRODUCTS FROM FOR USE CASES AROUND THE WORLD

K. Schenk *, H. Bernert , P. Bauer

EOMAP GmbH & Co.KG, Schlosshof 4, 82229 Seefeld, Germany – (schenk, bernert, bauer)@eomap.de

KEY WORDS: Water quality, Copernicus data, seasonal trends, drinking water reservoirs, chlorophyll-a, turbidity

ABSTRACT:

Within the H2020 project PrimeWater, EOMAP is generating operational satellite-based water quality datasets for four different case studies in Europe, Australia and the USA. The applied physics-based retrieval algorithm Modular Inversion and Processing system (MIP) accounts and corrects for a variety of environmental impacts, such as atmospheric conditions, adjacent land cover, water surface and composition of water constituents as well as considering varying observation geometries and sensor properties. It delivers main water quality parameters like turbidity, chlorophyll-a concentrations, secchi disk depth, water temperature and a harmful algae bloom indicator which is sensitive to cyanobacteria. With automated routines for satellite archive access, the fully operational water quality product processing chain as well as the automated delivery mechanisms, the datasets are ingested directly into the online accessible PrimeWater platform and are further used for assimilation with modelled data. Based on Copernicus missions of Sentinel-2A/B combined with additional data from Landsat 8, spatial resolutions down to 10m pixel size allow monitoring of very small water bodies and ponds up to larger reservoirs, such as the Western Water Treatment Plant near Melbourne in Australia, Lake Harsha in USA, Lake Hume in Australia and Lake Mulargia and Flumendosa reservoir in Italy. For these use cases, all available records from 2015 onwards have been processed, with processor-internal quality control mechanisms screening automatically for e.g. cloud shadows or high influences of aerosol, resulting in pixelwise masking of unreliable data. Next to operational monitoring of water quality, the generated time series indicate clear spatial dynamics and seasonal trends.

1. INTRODUCTION

1.1 Remote Sensing for water quality retrieval

Remote sensing products show great potential to provide information on water quality status and evolution in inland and coastal water bodies. This is particularly beneficial in places where in-situ monitoring is missing or lacking due to practical or financial constraints. For the calculation of water quality parameters, the reflected light spectrum detected by multispectral satellite sensors is used: The light is absorbed and scattered as a function of the particles and dissolved materials in the waterbody (Heege et al. 2019) and can be directly related to relevant water quality parameters such as turbidity and suspended matter, phytoplankton and its main pigment chlorophyll-a, or coloured dissolved organic matter (Dörnhöfer et al., 2016). Still, the measured signal at the satellite sensor can be strongly impacted by several variable factors, such as varying atmospheric aerosols, water surface reflections, scattered light from adjacent land areas and the observation geometry. The accurate correction of all of these impacts is therefore the prerequisite for the successful satellite data analysis (Karle et al. 2019). Physics-based inversion and processing algorithms define the state-of-the-art especially for inland water quality processors, accounting for the mentioned impacts (Dörnhöfer et al, 2018, Giardino et al. 2012).

1.2 Available Sensors

Several suitable multispectral satellite sensors are currently available, including the Multispectral Instrument (MSI) on-board Sentinel-2A/B, Ocean and Land Colour Imager (OLCIS) on Sentinel-3A/B, Moderate Resolution Imaging Spectroradiometer (MODIS), Operational Land Imager (OLI) on Landsat 8 and many more. These sensors differ in the number of spectral bands, radiometric stability and sensitivity to light as well as in their spatial and temporal resolution. In this study, high-resolution data from Landsat 8 (©USGS) with 30m spatial grid size and 16 days revisit time as well as Sentinel-2 (©COPERNICUS) in 10 m spatial resolution with a revisit interval of approximately 5 days, are used in order to cover the small inland water bodies in focus of the study.

2. METHODOLOGY

2.1 EWS-MIP Processing chain EOMAP

Sentinel-2 A/B and Landsat 8 data have been processed using EOMAPs proven physics-based Modular Inversion and Processing System (MIP), which is orchestrated by the EOMAP Workflow System (EWS). While the EWS manages the workflow itself, the MIP architecture systematically handles the independent properties of sensor parameters and specific optical properties as well as the radiative transfer relationships. Radiative transfer modelling in the coupled atmosphere-water systems is based on the reference model Finite Element-Method (FEM) with 30 years of development history (Kiselev et al. 2004). The main processing steps, also displayed in Figure 1, consist of data import and conversion from raw digital numbers to physical units, land-water-cloud differentiation, adjacency correction, sunglint correction, correction for altitude effects, coupled retrieval of atmospheric (Heege et al. 2014) and in-water properties, calculation of secondary / tertiary (non-physics-based) products and processor internal and manual quality control.

* Corresponding author

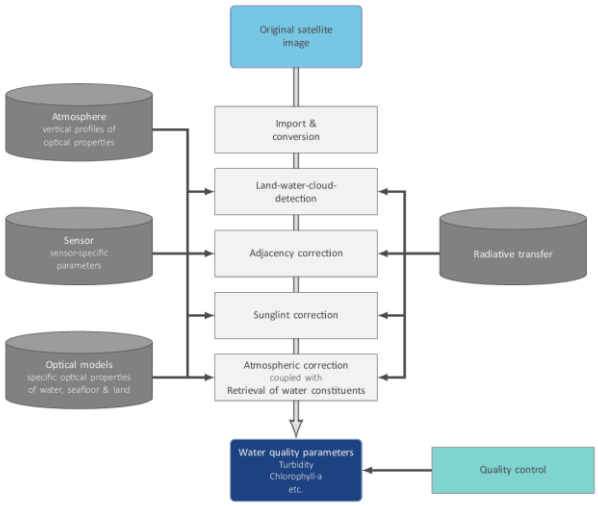

Figure 1. Processing steps of the EOMAP workflow system

2.2 Overview Pilot Use Cases

The operational processing chain has been implemented in four different pilot use cases worldwide covering very small ponds of the Western Water Treatment Plant near Melbourne in Australia, but also the larger drinking water reservoirs Lake Mulargia and Flumendosa reservoir in Italy, Lake Harsha in USA and Lake Hume in Australia (Figure 3).

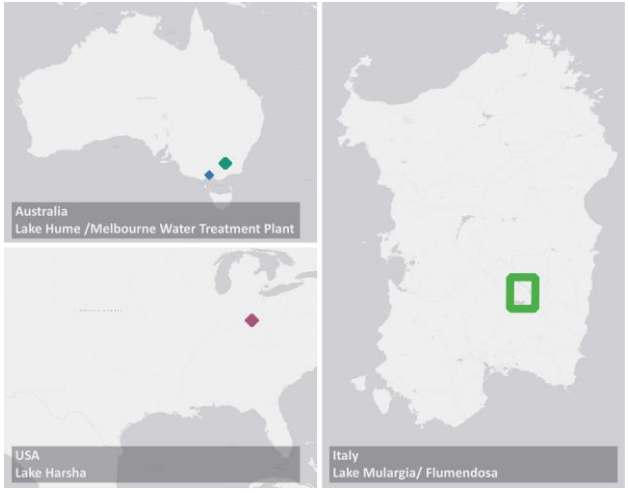

Figure 3. Pilot Use Cases in Australia (upper left), USA (lower left) and Sardinia/Italy (right); background: ESRI Gray (light)

The reservoirs are also used for recreational activities, hydropower and/or flood management with impacts to the lives of many inhabitants nearby.

2.3 Water quality parameter

For the described use cases, a set of water quality products are generated using the MIP processing chain in a fully operational way, including the most important parameters of Chlorophyll-a (CHL) in µg/l, Harmful Algae Bloom Indicator (HAB) sensitive to the appearance of Phycocyanin and Phycoerythrin, Secchi Disc Depth (SDD), Surface Water Temperature (SWT), Turbidity (TUR) and Total Suspended Matter (TSM).

2.4 Quality Control

As standard part of the operational processing, quality indicators are calculated for each detected water pixel. They consider a comprehensive range of factors impacting the product quality, including: the geometry between sun, target, and sensor, sun glint, aerosol optical depth, residuals of the measured and modelled sensor radiances and subsurface reflectances or pixels affected by cloud shadow. Thresholds define distinct values when a parameter is assumed to influence the quality. In the delivered QUC quality coding file, the different impacts can be identified, see Figure 2 example.

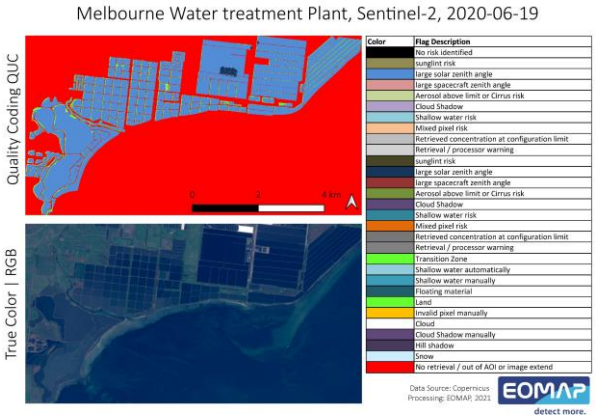

Figure 2. QUC of Sentinel-2 (2020-06-19) at Melbourne Water Treatment Plant with identified large solar zenith angle quality risk indicated in light blue

All parameters are integrated into one remaining quality parameter (QUT), allowing both an improved flagging and a quality weighting of pixels, that can later be merged into integrated 3rd level products. Additionally, this also allows for the integration into modelling routines.

2.5 Delivery and Access

Automated scripts have been put in place to download freshly archived Sentinel and Landsat data on a fixed schedule. New records are automatically ingested to the EWS and the outputs are uploaded to the PrimeWater data archive through its own Application Programming Interface (API).
For delivery, only satellite records with less than 80% cloud coverage and at least 10% of valid water pixels are used.
In addition, historical datasets for each use case, containing all available data between 2015 and 2020, have been published via the openly accessible repository Zenodo[1].

3. RESULTS

3.1 Overview of delivered records

In total, over 3,000 single satellite scenes from Sentinel-2A/B and Landsat 8 have been processed from 2015 to spring 2021. With some water bodies being covered by multiple satellite tiles and many scenes not passing the automatic quality checks, e.g. due to cloud coverage, sunglint, haze or other environmental influence factors, this number comes down to over 950 finally delivered scenes.

[1] Zenodo.org: 10.5281/zenodo.4581108, .4581196, .4582339, .4581085

3.2 Water Quality Product results

For each satellite record, the satellite-based water quality parameters have been calculated and delivered in 10m (Sentinel-2A/B) and 30m (Landsat 8) spatial resolution, giving insights to the actual water quality status and distribution patterns.
An example of the spatial distribution and the detected variability of turbidity is shown in the turbidity product derived from Sentinel-2 imagery recorded on the 2021-03-05 for Lake Harsha in Figure 4.

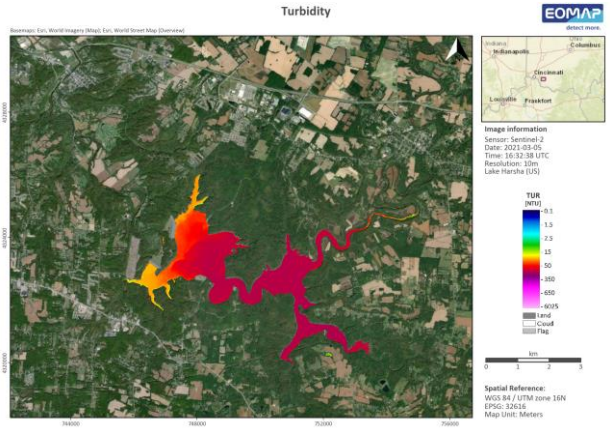

Figure 4. Turbidity (TUR) map Lake Harsha 2021-03-05, contains @Copernicus Sentinel-2 data (2021)

As the main river tributaries are located in the Northeast and Southeast, higher turbidity values can be found in the East, decreasing towards the western part of the lake.

Similar to this, also the Secchi Disk depth calculated from the Sentinel-2 record on 2021-03-03 shows the spatial distribution in the use case of Lake Hume, with highest SDD values occurring in the mid-southern part near the outlet.

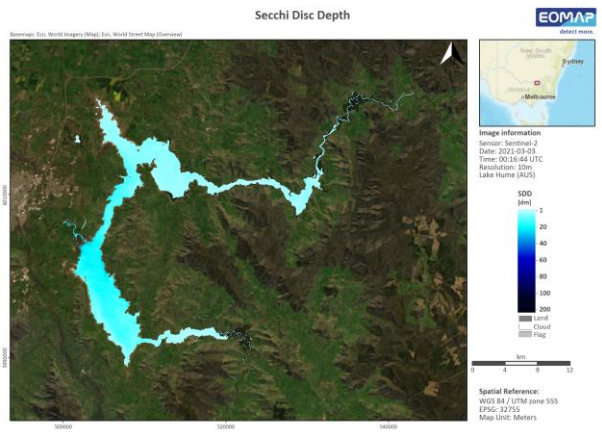

Figure 5. Secchi Disk Depth in Lake Hume 2021-02-27, contains @Copernicus Sentinel-2 data (2021)

In Figure 6, an example for Chlorophyll-a product in Lake Mulargia (South) and the adjacent Flumendosa (North) reservoir recorded on the 2021-02-27 depict the differences in the concentration levels between the two artificial reservoirs. Mulargia reservoir shows higher Chlorophyll-a values, while lower concentrations are indicated for Flumendosa reservoir.

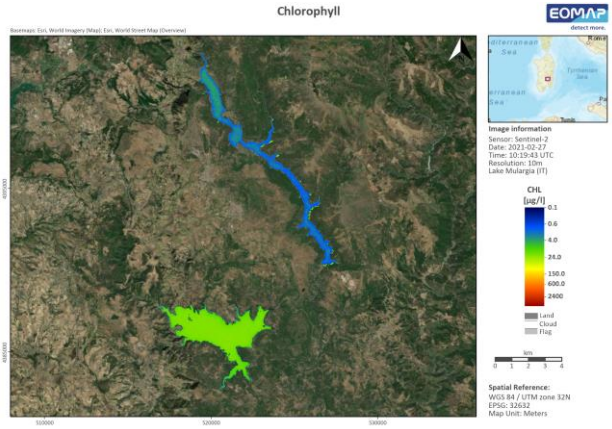

Figure 6. Chlorophyll-a map Mulargia and Flumendosa 2021-03-03, contains @Copernicus Sentinel-2 data (2021)

The knowledge of the status in the both reservoirs can be used in management by directing fresh water from the northern Flumendosa to the southern Mulargia in case of occurring algae blooms or increased turbidity to improve the water quality[2].

Much smaller in scale, the single ponds of the Melbourne Western Water Treatment Plant feature a high variability of the calculated qualitative HAB indicator for the 2021-03-06 using Sentinel-2 (see Figure 7).

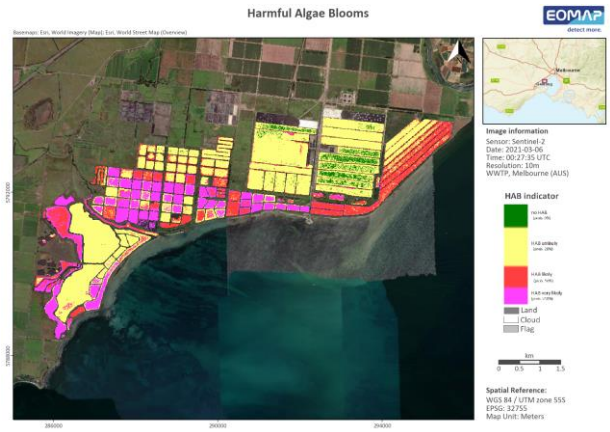

Figure 7. Harmful Algae Bloom indicator map Melbourne Water Treatment Plant 2021-03-06, contains @Copernicus Sentinel-2 data (2021)

Ponds with very high risk of Cyanobacteria bloom can be easily distinguished from the ones less affected using the satellite-based product and operational control can be facilitated enabling fast reaction times and prevention activities.

3.3 Water Quality Time series

Next to the analysis of single records, satellite-based time series can support identifying seasonal and long-term trends.

In Lake Harsha, the time series derived from Landsat 8 and Sentinel-2 show an increase at the beginning of the year in spring time with values over 40 NTU up to 120 NTU, followed by low values during summer and autumn below 20 NTU (Figure 8).

[2] https://www.primewater.eu/mulargia-dam/

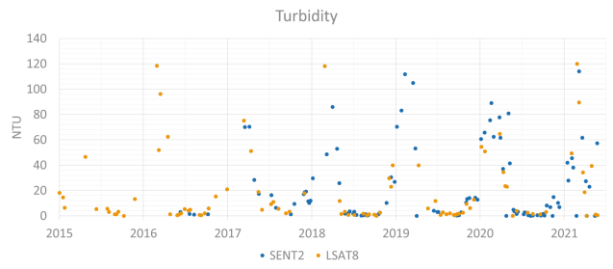

Figure 8. Lake Harsha central station (-84.118 E, 39.013 N) Turbidity time series 2015-2021

Closely related to the turbidity, Secchi Disk Depth can also strongly vary within the different seasons. As shown in the Mulargia reservoir results, extracted at a southern station, clear water conditions and high SDD of up to 9m typically occur in summer, while reduced visibility and low SDD values are present in winter times with values mainly below 1m (Figure 9).

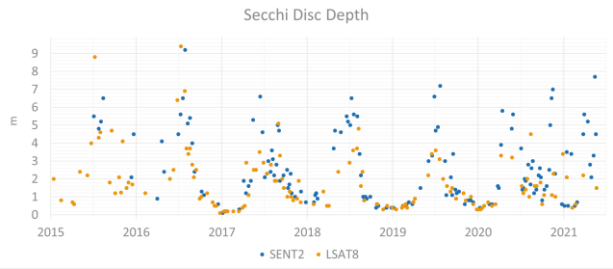

Figure 9. Lake Mulargia south station Secchi Disk Depth Time series (9.254 E, 39.606 N)

Seasonal occurrence of algae blooms and its interannual changes can be identified through the calculated chlorophyll-a concentrations from the multispectral satellite sensors. By this method, annual comparisons can also be drawn. As seen in the example of Lake Hume (Figure 10), the year 2017 – with average values around 10 µg/l – greatly differs from the two surrounding years 2016 and 2018, where values up to and higher than 40 µg/l were detected. Landsat and Sentinel-2A/B both follow the same seasonal dynamics of the blooming periods.

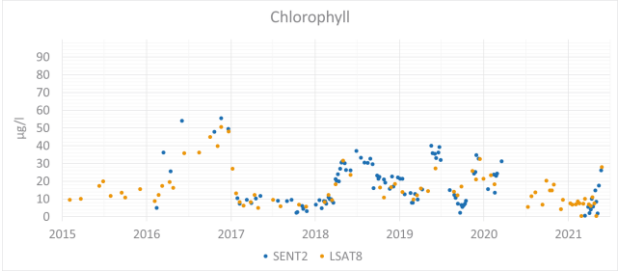

Figure 10. Lake Hume central station Chlorophyll-a Time series (147.037 E, -36.127 N)

4. CONCLUSIONS

The calculated high-resolution satellite-based time series in the four pilot use cases can help to identify spatial and seasonal trends for a set of important water quality related parameters. Together with easy access through the PrimeWater online platform, the produced data sets can support local drinking water stakeholders in their management and monitoring obligations with up-to-date information. Quality indication is a crucial asset to be included in operational delivery mechanisms, for both, user acceptance and for assimilation with modelling results used in forecasting of water quality. Ongoing developments in the retrieval algorithm, such as improved accounting for differentiation between inorganic and organic absorption in highly turbid waters, further lead to more stable and transferable results.

ACKNOWLEDGEMENTS

This study was supported by the European Union's Horizon 2020 research and innovation programme PrimeWater project (Delivering Advanced Predictive Tools form Medium to Seasonal Range for Water Dependent Industries Exploiting the Cross-Cutting Potential of EO and Hydro- Ecological Modelling) under grant agreement No 870497H2020.

REFERENCES

Bresciani M, Giardino C., Stroppiana D., Dessena M.A., Buscarinu P., Cabras L, Schenk K., Heege T., Bernert H., Bazdanis G. and Tzimas A., 2019. Monitoring water quality in two dammed reservoirs from multispectral satellite data, European Journal of Remote Sensing 52, pp. 113-122

Dörnhöfer, K. and Oppelt, N., 2016. Remote sensing for lake research and monitoring – Recent advances. Ecological Indicators 64, pp. 105–122

Dörnhöfer, K., Klinger, P., Heege, T. and Oppelt, N., 2018. Multi-sensor satellite and in situ monitoring of phytoplankton development in a eutrophic-mesotrophic lake. Science of the Total Environment 612, pp. 1200-1214

Giardino, C., Candiani, G., Bresciani, M., Lee, Z., Gagliano, S. and Pepe, M., 2012. BOMBER: A tool for estimating water quality and bottom properties from remote sensing images. Computers & Geosciences 45, pp. 313-318

Heege, T., Schenk K. and Wilhelm M.-L., 2019. Water Quality Information for Africa from Global Satellite Based Measurements: The Concept Behind the UNESCO World Water Quality Portal. in: Embedding Space in African Society. The United Nations Sustainable Development Goals 2030 Supported by Space Applications, pp. 8-92

Heege, T., Kiselev, V., Wettle, M. and Hung N.N., 2014. Operational multi-sensor monitoring of turbidity for the entire Mekong Delta. International Journal of Remote Sensing, Special Issues Remote Sensing of the Mekong, 35 (8), pp. 2910-2926

Karle, N., Wolf, T., Heege, T., Schenk, K., Klinger, P. and Schulz, K., 2019. Satellite Remote Sensing of Chlorophyll and Secchi Depth for Monitoring Lake Water Quality – A Validation Study. Processings for the SPIE remote sensing publication conference

Kiselev, V. and Bulgarelli, B., 2004. Reflection of light from a rough water surface in numerical methods for solving the radiative transfer equation. Journal of Quantitative Spectroscopy and Radiative Transfer 85, pp. 419-435

CUBESATS: PAVING THE WAY TOWARDS AN EFFECTIVE RELIABILITY – ORIENTED APPROACH

G. Fois and G. Mura *

DIEE, University of Cagliari, 09123 Piazza D'Armi Cagliari, Italy – (g.fois20@studenti, giovanna.mura)@unica.it

KEY WORDS: CubeSats, COTS, Reliability, Design for Reliability, Debris, LEO

ABSTRACT:

CubeSats enable the development of a new Space economy towards a Space that is now open and accessible to all kinds of activities, industries and even end-users. However, the failure rate of these satellites is high enough to significantly contribute to the Low-Earth Orbit congestion. This issue can be addressed with a gradual decrease of the formation rate of new debris, while removing the existing one, to prevent future collisions. To ensure a long-term sustainability in Space, a Design for Reliability approach on the new generation of CubeSats could enable a safe and effective maintenance in LEO. Reliability procedures applied from the beginning of the design process can significantly improve the mission success rates.

1. INTRODUCTION

1.1 Introduction

Earth Observation and Remote Sensing is considered the most significant and fastest-growing segment in the small satellite market. Earth observation services primarily cover the monitoring of agricultural fields, detection of climatic changes, disaster mitigation, meteorology, and several other resources. Micro and nanosatellites offer the opportunity to assess and address climate changes and their sustainability on a global scale. CubeSats are widely used in this context, enabling the development of a new Space economy, with its renovated market accessible to all kinds of activities, industries and universities. Nowadays, the percentage of failure for University-built CubeSats within the first six months of operation is estimated to be slightly below 50% (Langer, 2016). Moreover, failed CubeSats are a liability for other satellites, increasing orbital debris due to collision or system failure. As Space becomes more congested, the threat of collision of new satellites and rocket launches with "Space junk" has grown. For these reasons, debris in Space challenge the usefulness of building spacecraft in LEO.

Reliability should represent a vital characteristic of a Space system and must be properly evaluated to assure the mission objectives. Designing a reliable product today is genuinely a concurrent engineering process. A Space-qualified component has undergone rigorous, and therefore costly, testing and validation. On the other hand, Space-qualified components are expensive and limited in specific abilities.

Speaking about CubeSats, the utilization of commercial-off-the-shelf components (COTS) for Space applications is a must as they limit the cost and time associated with the mission's development.

Nevertheless, to stay attractive and affordable, traditional Space testing cannot be implemented in CubeSat projects. A *buy-and-flying* approach poses a threat to the Space environment because not all COTS are suitable for Space.

Properly analysis and design/testing methods should ensure that the dependability targets are met, maintaining the reduced costs and timing. In this paper, a preliminary built-in reliability approach based on Design for Reliability (DfR) procedures aims at reducing failures to ensure the mission profile expectation. The study starts from a small-scale project funded by Fondazione di Sardegna under the project ARGOSAT-Microsatellite cluster to observe optical transients in Astronomy. It aims to acquire global requirements, their translation into DfR-oriented requirements and the subsequent high-level design of the system elements for the microsatellite constellation. These evaluations can easily be extended to other missions.

2. CUBESATS: CRITICALITIES AND RELIABILITY

2.1 CubeSats philosophy

In the past, the satellite design philosophy was dominated by highly reliable components and conservative designs built for durability under extreme environmental conditions of Space, featuring redundancies and extensive qualification and performance testing at part, sub-system and integrated system levels. (Perdu, 2018)

The arrival of CubeSats changed the traditional philosophy favouring utilizing state-of-the-art COTS components able to offer increased low-cost performance.

A CubeSat is a small satellite whose basic unit form is a 10cm edge cube, namely 1U. They can be 1U, 2U, 3U, or 6U in size and typically weighs less than 1.33 kg per U.

NASA defines COTS as "any grade [part] that is not Space qualified and radiation hardened".

The design approach for CubeSats usually consists in building and launching fast, using COTS electronics. Due to budgetary and time constraints, the number of tests performed is reduced up to zero compared to the ones Space agencies are using for their high-reliability, expensive and large spacecraft.

The reliability of electron devices depends on their capability to withstand stresses. The most prominent environmental aspects that affect electronics in Space are noise, vibration and shocks, outgassing, electrostatic discharges, atomic oxygen, vacuum, Space radiations, temperature fluctuations.

Intrinsically weak devices may react extremely fast to the applied stress, causing early failures. The reduced or annulled testing phase induces a critically high number of early failures (above 50% from 1994 to 2017). It is sensibly contributing to

* Corresponding author

the risk of congesting the Low-Earth Orbit (LEO) and the Geosynchronous-Equatorial Orbit (GEO) with debris. Relying on natural decay is unsustainable because this process lasts from decades to centuries, depending on the orbital altitude. Otherwise, the solution proposed of moving the satellites by propulsive means to an orbit closer to earth before retirement, where earth's drag eventually brings objects back into the earth's atmosphere, appears at the moment, not resolutive.

2.2 Debris

The term orbital or Space debris includes old spacecraft and satellites no longer in use, fragments of various sizes, and multiple launchers stages. Collisions with other spacecraft can generate debris clouds that could ignite a collision avalanche known as Kessler syndrome.
Moreover, debris could represent a serious safety issue for terrestrial. A recent example is provided by the uncontrolled re-entry of a portion of the CZ-5B rocket in May 2021.
A detailed overview of the concerns related to debris has been recently proposed in (Murtaza, 2020).
The debris issue can be faced by reducing the probability of new debris, by removing the existing debris and by preventing future collisions. Actions can be related to mitigation (to limit the creation of more debris), remediation (to remove debris from orbit), and Space situational awareness (to prevent operational satellite collision). On several occasions, the International Space Station changed its trajectory to avoid Space debris, which is one solution to prevent collisions.
More sustainable solutions include using lasers to vaporize Space debris or remotely controlled vehicles to remove Space junk from orbit. A reliability-oriented approach during the design phase of the satellite can lead to a systematic reduction of the failures extending the mission success and duration. In addition, even though the removal of a satellite from its orbit presents large amount of challenges, the concept of Design for Removal is paving the way to ease the removal of future satellites.

2.3 CubeSats: Reliability concerns

From a reliability standpoint, a Cubesat is a complex system, containing many components, on which six significant subsystems can be identified: structure, communication, power, attitude determination and control, command and data handling, and the payload.
The evaluation proposed in (Langer, 2016) showed that the overall reliability of CubeSats is strongly dominated by high rates of dead-on-arrival (DOA) cases, where the satellite is ejected from the deployer but never achieved a detectable functional state. The 2-year reliability estimation ranges from 65.49% on the upper end of the confidence interval to 48.49% on the lower one after two years in orbit. The authors suggested that a significant percentage of those DOA and infant mortality early failure cases could have been avoided by more careful and adequate system-level functional testing on the ground.
The three main subsystems that cause the most CubeSat failures within the 90 days are the electrical power system, on-board computer and communication system, and, in addition, there is the "unknown" category.
It is fundamental to avoid or reduce the large number of infant mortality cases, to evolve the CubeSats into more reliable platforms.
Finally, even (Swartwout, 2013) pointed out that many early failures are due to inadequate system-level functional testing, i.e. the spacecraft was not operated (or not long enough operated) in a flight-equivalent state before launch.

2.4 Design for Reliability (DfR)

Reliability is defined as "the probability that an item can perform its intended function for a specified interval under stated conditions" (MIL-STD-721C).
The Design for Reliability (DfR) ensures that a system performs the specified function within the customer's use environment over the expected lifetime. It refers to the process of designing reliability into a product since the design phase.
The DfR includes an entire set of procedures and practices that support product design from early in the concept stage through to obsolescence, and where the reliability engineering is built into the total development cycle. It relies on reliability engineering tools and a proper understanding of when and how to use them throughout the design cycle.
In the Space context, the DfR can be beneficial to achieve the expected reliability of the system for the predicted mission duration.
By following reliability- oriented approach, it is fundamental to point out the significant criticalities, the mandatory requirements, and what aspects of mission assurance can significantly improve the mission success rates. From this evaluation, a reduced set of tests can be defined able to screen early failures and enhancing the probability of success.

2.5 CubeSats: Reliability improvements

A DfR approach at the system level can significantly reduce the satellite failure rate. In addition, the application of this technique at the component level could lead the assessments in terms of obsolescence, de-rating, redundancy where possible. Finally, component/ system-level tests can ensure a high level of confidence and the success of the mission.
Targeted screening and reduced qualification procedures on the components should be individuated based on the specific mission profile.
The inputs to identify the mission are its orbit, the duration and device shielding. It is crucial to determine the level of reliability needed, to address budget and time constraints concerning the components being selected. In this context, (Langer, 2017) proposed a reliability estimation tool able to estimate their required functional testing time on subsystem and system level at an early project stage to function the targeted reliability goal for the designed CubeSat. Anyway, it is not intended to replace the environmental tests needed for verifying Space hardware (e.g. thermal-vacuum tests, mechanical stress tests, radiation tests).
Since the design phase, in synergy, Failure Modes, Effects Analysis (FMEA) and Fault Tree Analysis (FTA) can support a reliability-oriented approach.
FMEA (MIL-STD-1629A) and FTA (MIL-STD-882) are complementary techniques.
FMEA is an inductive method that identifies all the possible failure modes of a single component in the system and their possible failure mechanisms. It lists the resulting consequences associating with a risk priority number. The FMEA can be extended to Failure Modes, Effects and Criticality Analysis (FMECA) by adding a criticality analysis.
FTA is a deductive method that takes an undesirable state in the system. Using a logic tree illustrates how specific faults, or combinations thereof, will lead to the undesired state. The individuation of the "cut set," which is a collection of events that, when combined, will result in the failure of the selected top event is a key aspect of this procedure.
FMEA can manage CubeSat reliability data and prioritize criticalities early in the design phase to prevent failures

(Menchinelli, 2018). Fault Tree Analysis (FTA) can be used not only for investigating the anomalies to help recover the mission as proposed in (Stevina, 2020) but even for a preliminary evaluation of the possible events able to cause failures (Vesely, 2002) (Bidner, 2010).
The combination of FMEA and FTA can be beneficial in detecting the undesired events that have the highest chance of happening. The analysis of the system from two different points of view enables corrective actions that include the selection of components with higher reliability, the derating for critical elements, and redundancy or additional detection methods.
The overall Cubesat reliability cannot be achieved with the same processes and procedures used for Space-grade components. The use of COTS components in Space is increasing more and more, and there is still not a clear and homogeneous policy to follow when using these components. Nevertheless, as not all COTS are suitable for Space (Crocker, 2005) (Lu, 2012) (Mura, 2009) (Mura, 2018) (Sinclair, 2013), a buy and flying approach is risky, and an appropriate selection of COTS electronics is mandatory.
An intelligent evaluation should identify COTS components that are already intrinsically robust, highly reliable, and that natively show good robustness to the radiative environment. Moreover, burn-in (MIL-STD-883F) and screening are DfR tools that prevent infant mortality failures, typically caused by manufacturing-related problems, from happening on-orbit.
After an FMEA/FTA analysis, a reduced set of critical components can be pointed out, and proper testing addressed.
It could furthermore allow selecting a reduced set of up-screening and qualification testing that guarantees the fulfilment of the mission requirements. Consequently, a significant containing of the costs and development times of the project can be reached. In addition, for less critical devices, even existing qualification results of similar products can guide the selection and reliability assessments by structural similarity.
Automotive components have significant potential for mainly being adequate and robust in a Space application.
The Automotive business model, thanks to its ppm-level quality and reliability targets, offers the opportunity to consider Automotive components eligible for Space application. It can be beneficial due to this high-production, high reliability, well-screened market.
Qualification extension and subsequent accelerated ageing test plan based on the device family (ASIC, RF, Optoelectronic, etc.) and the specific mission profile can fill the gap. An extension of the emerging “robust qualification” Automotive policy by applying additional series of reliability tests selected through a failure mechanism driven approach is proposed in (Enrici Vaion, 2017) (Enrici Vaion, 2018).
Automotive COTS can offer reliable performance in extreme conditions with a set of reduced tests able to close discrepancies.
Thermal/vacuum and radiative tests are mandatory.
In (Stevenson, 2017) (Fernandes, 2016), comprehensive specifications on thermal tests are proposed.
(Sinclair, 2013) proposes the “Careful COTS” considered between Space-grade requirements and the buy-and-fly approach. It involves proving radiation tolerance of specific commercial parts required for the mission and implementing screening and process control to improve reliability. Moreover, radiation requirements in LEO can be assured by a reduced set of proton testing that allows exploration of total dose, displacement damage, and some single-event effects, together with controlled lot buys.
Moreover, in (Hatch, 2020), several single event tests were carried out on several automotive-grade parts for use in Spaceflight. None of the components tested suffered from catastrophic failure during testing showing intrinsically good robustness to Space.
These evaluations are the starting point of a small-scale project funded by Fondazione di Sardegna under the project "ARGOSAT- Microsatellite cluster to observe optical transients in Astronomy".
It aims to acquire global requirements, their translation into DfR-oriented requirements and the subsequent high-level design of the system elements of the microsatellite constellation.
With the ambition of providing general guidance, the idea involves the expertise necessary for any subsystem and evaluating the more reliable choice resulting from a good balance between costs and time.
The definition of a set of procedures for a thermal qualification of a CubeSat is in progress. For each procedure we will provide a justification, along with details, from a known space standard.
The solution that will be proposed does not involve only the testing phase but also includes specific analyses and additions that may help the overall system reliability.
An overestimated effort may force unnecessary inflations in terms of costs and testing time, whereas an underestimated one may hide faults to compromise the mission.
The expected results will be easily extended to other missions.

CONCLUSIONS

CubeSats are changing the new Space economy and will probably play a more critical role in the Space context soon. Despite these advantages, there are concerns that CubeSats may increase the number of Space debris. About 50% of launched CubeSats did not complete their intended mission. Around 20% of all failures occurred either during launch or during the deployment phase (Villela, 2019).
Reduced development time, size and weight constraints and the use of COTS components contribute to early failures.
COTS are not designed to work in the Space environment.
Undoubtedly, Cubesats design and development cannot operate, applying the reliability standards. It is necessary to translate them in a suitable shape for the new Space domain finding a proper balance between traditional procedures and specific requests, between reliability and costs. A reliable and sustainable new Space economy is the ultimate goal, and acting responsibly to reduce junk production is the first achievement.

ACKNOWLEDGEMENTS

This work has been founded by “Fondazione di Sardegna” under project “ARGOSAT – Microsatellite cluster for the observation of optical transients in Astronomy”, CUP: F74I19001070007.

REFERENCES

Bidner, F., 2010. Fault Tree Analysis of the HERMES CubeSat University of Colorado at Boulder.

Cassanellli, G., 2006. Failure Analysis-assisted FMEA *Microel. Reliab*. vol 46, 9–11, pp. 1795-1799.

Crocker, D., 2005. Commercial Electronic Components (COTS) and Reliability In: *56th International Astronautical Congress*, 9, pp. 5842 – 5847.

Enrici Vaion, R., 2017. Qualification extension of automotive smart power and digital ICs to harsh Aerospace mission

profiles: Gaps and opportunities. *Microelect. Reliab*. 76–77, pp. 438-443.

Enrici Vaion, R., 2018. From Automotive to Space qualification: Overlaps, gaps and possible convergence. In: *IEEE International Symposium on the Physical and Failure Analysis of Integrated Circuits (IPFA).*

Fernandes, G., 2016. Thermal Tests for CubeSat in Brazil: lessons learned and the challenges for the future. In: *67th International Astronautical Congress (IAC).*

Gohardani A.S., 2018. Small satellites: Observations and considerations. In: *AIAA Aerospace Sciences Meeting.*

Hatch, J., 2020. Recent Single Event Transients, Upsets, and Latchup Test Results for TPS3307-18, TL1431, INA129, AM26LV31 & 32 Electronic Parts. In: *IEEE Radiation Effects Data Workshop.*

Lu, J., 2012. MIM capacitor-related early-stage field failures. *Microelec. Reliab*., 52, 9–10, pp. 2073-2076.

Langer, M., 2016. Reliability of CubeSats – Statistical Data, Developers' Beliefs and the Way Forward. In: *30th Annual AIAA/USU Conference on Small Satellites*, pp. 1-12.

Langer, M., 2017. A reliability estimation tool for reducing infant mortality in Cubesat missions. In: *2017 IEEE AeroSpace Conference.*

Menchinelli, A., 2018. A Reliability Engineering Approach for Managing Risks in CubeSats. *AeroSpace 2018*, 5, 121.

Mura, G., 2009. Lot reliability issues in commercial off the shelf (COTS) microelectronic devices. *Microelec. Reliab*., 49, 9–11, pp. 1196-1199.

Mura, G., 2018. Reliability concerns from the gray market", Microelectron. Reliab., 88-90.

Murtaza, A., 2020. Orbital Debris Threat for Space Sustainability and Way Forward (Review Article). *IEEE Access*, pp. 61000-18.

Perdu, P., 2018. Failure Analysis on Space Electronics: Best Practices, Challenges and Trends. In: *2018 IEEE International Symposium on the Physical and Failure Analysis of Integrated Circuits.*

Sinclair, D., 2013. Radiation effects and COTS parts in SmallSats. In: *27th Annual AIAA/USU Conference on Small Satellites.*

Stesina, F., 2020. Investigation of a CubeSat in Orbit Anomaly through Verification on Ground. *AeroSpace*, 7, 38.

Stevenson, R., 2017. Method for CubeSat Thermal-Vacuum Cycling Test Specification. In: *47th International Conference on Environmental Systems.*

Swartwout, M., 2013. The first one hundred cubesats: A statistical look. Journal of Small Satellites, 2(2), pp. 213-233.

Vesely, W., 2002. Fault tree handbook with aerospace applications. In: *NASA office of safety and mission assurance.*

Villela, T., 2019. Towards the Thousandth CubeSat: A Statistical Overview. Int. Journal of AeroSpace Engineering 3, pp.1-13.

ORTHORECTIFICATION OF PRISMA IMAGES

V. Baiocchi [1, *], F. Giannone [2], F. Monti [1]

[1] Dept. of Geomatics Department of Civil, Constructional and Environmental Engineering, Sapienza University of Rome, I-00184 Rome, Italy – valerio.baiocchi@uniroma1.it
[2] Niccolò Cusano University Via Don Carlo Gnocchi 3, 00166 Rome, Italy - francesca.giannone@unicusano.it

KEY WORDS: Orthorectification, PRISMA, RPF, RPC, Photogrammetry

ABSTRACT:

Orthorectification is one of the most important satellite imagery pre-processing applications, as it allows to use data, for example, in geographic information systems, making the most of high or medium resolution. Since May 2020, PRISMA (PRecursore IperSpettrale della Missione Applicativa) mission, a project of the Italian Space Agency, has become fully accessible to the community. PRISMA satellite integrates a hyperspectral sensor and a medium-resolution panchromatic sensor. The products are currently available with a declared geolocation accuracy of 200 m, which ASI plans to increase to half pixel in the near future by introducing geometric treatment of the images with Ground Control Points (GCPs). However, the orthorectification of PRISMA images is not a proven and validated procedure, due to the uncertainty of satellite orbital and internal orientation data provided in the metadata file and to the lack of contributions on the subject in literature. In the present work, our contribution on possible strategies for the geometric treatment of PRISMA images is shown. The results obtained by applying the Rational Polynomial Coefficients (RPC) provided with some panchromatic images show coarse rototranslations. For this reason, a procedure was developed to restore conformity between RPCs and the panchromatic image. The best results in terms of accuracy were obtained with the rational polynomials using RPF approach, achieving residuals calculated on the Check Points (CP) in the order of one pixel, better than those supposed by ASI using GCPs. Probably even better results could be obtained with more rigorous information on RPCs or orbital and orientation parameters.

1. INTRODUCTION

The Italian Space Agency (ASI) mission PRISMA is one of the latest innovations in the area of remote sensing, characterized by an innovative hyperspectral technology. The launch of the satellite took place on 22 March 2019, from the Kourou European spaceport in French Guiana, and starting from May 2020 it reached operational conditions, becoming available to the scientific, institutional, industrial, Italian and international communities. The aim of the mission is to encourage experimentation with hyperspectral data. In fact, ASI has chosen to make this data available with a user licence for the benefit of the scientific community and national and international institutional users. The application opportunities of PRISMA data are unlimited, the hyperspectral sensor (Ground Samplig Distance 30 m) is integrated with a panchromatic sensor, 5 m spatial resolution, that improves the observation capabilities based on the recognition of geometric characteristics of the scene.
The main purpose of this paper is to carry out a study of the possible strategies for the geometric treatment of PRISMA images, a topic still poorly investigated in literature probably due to the recent availability of PRISMA products. Considering the innovativeness of the mission, the studies conducted so far have focused on possible hyperspectral applications, using already georeferenced data, however it is necessary to verify the accuracy of geolocation (Busetto et al., 2020). In fact, ASI currently declares 200 m geolocation accuracy (ASI, 2017) of the hyperspectral and panchromatic products, and it plans to improve it to half pixel in the near future, by introducing a geometric treatment of the images with GCPs. However, it must be considered that satellite images are affected by distortions due to various factors. The distortions must be corrected returning a geometrically correct and accurate representation of images also from the point of view of geographical positioning. Therefore, it is necessary to perform on satellite images a pre-processing procedure known as image orientation and, based on this, the orthorectification. In the present work, an orthorectification procedure of the PRISMA panchromatic product is presented, which has made it possible to achieve results with accuracy in the order of one pixel, better than those expected by ASI with GCPs.

1.1 The PRISMA mission

PRISMA satellite has been planned to be on a sun-synchronous orbit at an altitude of about 620 kilometres and to have an orbit with 97.851° of inclination (Loizzo et al., 2016).
The hyperspectral payload is an electro-optical instrument based on a pushbroom scanning technique and consisting of a high spectral resolution imaging spectrometer in the spectral range 0.4-2.5 μm, optically integrated with a medium resolution panchromatic camera in the spectral range 0.4-0.7 μm. The payload acquires panchromatic and hyperspectral images of the Earth's surface with a swath width of 30 km and a length of up to 1800 km, in along-track direction and at a fixed off-nadir angle. It also has the agility to acquire data up to +/-14.7° off-nadir and the daily capability to acquire up to 200,000 km^2 of imagery over the area of interest (180° W÷180° E and 70° S÷70° N). The raw data are 1000 x 1000 hyperspectral images and 6000 x 6000 temporally co-registered panchromatic images, corresponding to an area of 30 km × 30 km on the ground. The products available to end users are organised in a hierarchy of levels, according to which different co-products are offered:

- Level 1: Top-of-Atmosphere spectral radiance, radiometrically-corrected and calibrated
    - Cloud cover, Sun-glint and Land Classification masks

* Corresponding author

- Level 2B: Bottom-of-Atmosphere spectral radiance, atmospherically corrected, the geolocation coefficients are available in the metadata, but not applied
- Level 2C: like 2B products, but they also provide:
    - Water vapour, aerosols and cloud characterization
- Level 2D: Bottom-of-Atmosphere spectral reflectance, atmospherically corrected, the geolocation coefficients are appended and applied. It is the geocoded version of the level 2C products.

2. PROCESSING CHAIN

2.1 Materials

The geometric treatment was tested on two PRISMA panchromatic images, level 2C products, one of the area of Rome and the other on the Ischia island (south of Italy, in the Tyrrhenian sea). This choice was justified by the different topographical characteristics. In particular, the Ischia Island is characterised by the presence of very rapid variations in altitude from the coast to the summit of the volcanic mountain called "Monte Epomeo" (789 m orthometric height), that represent an interesting case given the importance of altimetric information in orthorectification. For this first experimentation, an attempt was made to investigate as many algorithms as possible in order to obtain a broader panorama of the geometric treatment. Therefore, both the open-source software QGis, which supports the OTB and GDAL libraries, and the commercial software OrthoEngine, were used.

Digital elevation models with a spatial resolution compatible with the average resolution of panchromatic images were used in the orthorectification procedure. For Rome image, the DEM TINITALY/01 provided by INGV (Tarquini et al. 2007) was used as a 10 m grid of cell size while for Ischia image a DEM in orthometric elevations was created starting from official cartography in scale 1:2000. For the estimation and control of the geometric model, 65 ground points (50 GCP and 15 CP) were used for each image. On both sites, points from large-scale mapping and GNSS surveys were available both with higher accuracy than the pixel size.

2.2 Exporting the panchromatic product

PRISMA products are distributed in HDF format, so it is necessary to export them in more commonly used formats, such as TIFF. The panchromatic product of L2C level, not geocoded, was exported using ENVI software version 5.5.3 which is able to read the PRISMA data distribution format. During exportation phase, it is important to check that the raster is not geocoded to avoid the return of altered data that are not congruent with the Geocoding Model parameters provided. To verify the absence of geocoding, the exported image can be imported into any GIS software to check that the graphic restitution of the raster corresponds to its internal coordinate reference system (i.e. the coordinates of the top-left corner must be 0, 0).
Opening the HDF file, ENVI initially displays the VNIR raster only. The Data Manager opens three raster files, each covering the same geographic area but providing different spectral coverage and spatial resolutions:

- VNIR 30 m resolution (400-1010 nm, 66 bands)
- SWIR 30 m resolution (920-2500 nm, 173 bands)
- Panchromatic 5 m resolution

Then, the panchromatic product can be selected and exported in TIFF format. The information regarding the Geocoding model (ASI, 2020) is contained in the HDF file, but is not attached to the exported TIFF product. For this reason, they have been attached using a text file compatible with the RPC00B format. In fact, as reported in the documentation, the geocoding model adopted for L2 products is that of Rational Polynomial Coefficients: RPC00B - Rapid Positioning Capability, as defined in the National Imagery and Mapping Agency standard (NIMA, 2000).

2.3 Orthorectification

The geometric treatment of the image initially involves the choice of a suitable orthorectification model to eliminate the image distortions. Orthorectification is often the first and most important step in obtaining accurate results from the various applications of satellite imagery (Baiocchi et al. 2010, Zollini et al. 2020). Orthorectification methods can be divided into two categories: physically based models such as the rigorous model, and empirical models such as polynomial rational functions. The rigorous model is based, according to the classic photogrammetric approach, on the reconstruction of the collinearity equations that relate the image space to the object space (Kraus, 1993). These models require knowledge of the parameters which describe the sensor and the acquisition geometry, such as the position and attitude parameters of the platform, as well as the optical-geometric parameters of internal calibration of the sensor (Toutin, 2011).
This supporting data is not provided together with PRISMA products, and the recent release has not yet allowed to carry out in-depth studies on this sensor. For this reason, the few optical geometric data available in the literature (Loizzo et al., 2016) on this specific satellite have produced inconsistent results in a preliminary test, which has therefore not been further investigated.
On the other hand, rational polynomial functions (RPFs) do not consider the geometric process of image acquisition, they represent an approximation of the rigorous method. Since they do not refer to a particular type of sensor-platform pair, they can be applied generically to any satellite image. The RPFs express the row and column values as a function of latitude, longitude, and ellipsoidal height, using a series of polynomial coefficients, as follows:

$$r_n = \frac{\sum_{i=1}^{20} LINE\_NUM\_COEFF_i \cdot \rho_i(P,L,H)}{\sum_{i=1}^{20} LINE\_DEN\_COEFF_i \cdot \rho_i(P,L,H)}$$
$$c_n = \frac{\sum_{i=1}^{20} \mathrm{SAMP}\_NUM\_COEFF_i \cdot \rho_i(P,L,H)}{\sum_{i=1}^{20} SAMP\_DEN\_COEFF_i \cdot \rho_i(P,L,H)} \quad (1)$$

Where r_n, c_n = image coordinates
P, L, H = latitude, longitude, ellipsoid height

Every rational polynomial has the following form:

$$\sum_{i=1}^{20} C_i \cdot \rho_i(P,L,H) = C_1 + C_2L + C_3P + C_4H + C_5LP + C_6L + C_7PH + C_8L^2 + C_9P^2 + C_{10}H^2 + C_{11}PLH + C_{12}L^3 + C_{13}LP^2 + C_{14}LH^2 + C_{15}L^2P + C_{16}P^3 + C_{17}PH^2 + C_{18}L^2H + C_{19}P^2H + C_{20}H^3 \quad (2)$$

Rational polynomial functions are distinguished into RPFs based on ground control points (RPF approach) and RPFs calculated from coefficients provided with the satellite images themselves (RPF with RPC approach). The difference is that in the former

case the coefficients are estimated by least squares from a set of GCPs, while in the latter case they are provided with the image to be processed. PRISMA images are supplied with the Geocoding Model information, consisting of the rational polynomial coefficients (RPCs), contained in the original HDF format file. Currently, Orfeo Toolbox (OTB) has only been validated with the rational polynomial function method (Baiocchi et al., 2020), while OrthoEngine supports all three orthorectification methods. As mentioned above, the Geocoding Model information has been manually transcribed in the RPC00B format, then, before the orthorectification procedure, it is necessary to verify that all software read the Geocoding model correctly using the otbgui_ReadImageInfo application in OTB and gdalinfo from the gdal library.
The orthorectification process using the RPF method with RPCs has been subsequently performed using OrthoEngine, the open-source applications otbgui_OrthoRectification and gdalwap, obtaining with all software an image rotated approximately 90° in the clockwise direction as output. The reasons for this inconsistency are still unclear as the RPCs are claimed to conform to the NIMA standard (NIMA, 2000).

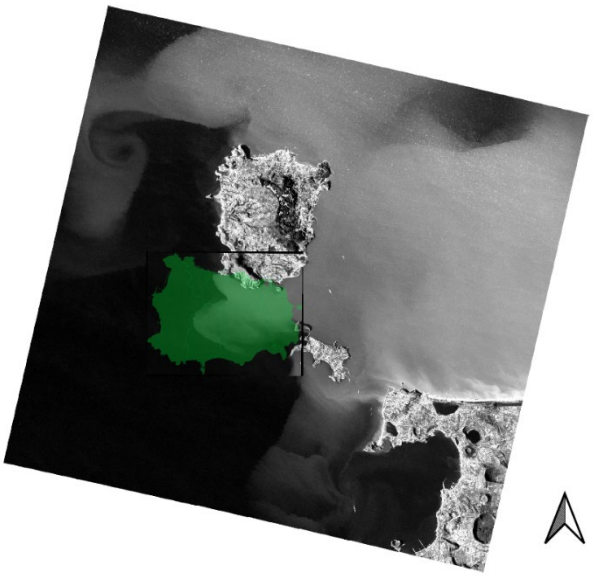

Figure 1. OrthoEngine "orthorectified" output (the raster is cropped at the DEM of the island of Ischia), superimposed on the OTB "orthorectified" output. Note that both outputs are rotated by 90° with respect to the correct position of the island of Ischia, represented in green. The island is approximately 9 km wide

Because of these problems, the method of rational polynomial functions (RPF) has been also tested, computing the coefficients by means of least squares estimation from a series of GCPs distributed homogeneously over the image. RPFs are the least correct method from a photogrammetric point of view (Toutin, 2011) and furthermore, this method has non-negligible disadvantages such as the need of a high number of GCPs, excessive sensitivity with respect to the distribution of GCPs, non-robustness against outliers and the presence of possible strong distortions in areas far from the GCPs.
In order to estimate the 78 coefficients required for the third-degree polynomials, the minimum number of points to collimate is 39 (two equations are written for each GCP). However, for the calculation to be carried out under conditions of redundancy, it is necessary to consider 20% more GCPs. For this reason, 50 points were collimated and used for the estimation of the geometric model (GCPs), and another 15 for the validation of the model (CPs). Note the importance of GCPs for processing purposes: they must be easily "recognisable" both on the image and on the ground, the accuracy of their coordinates influences the correspondence established. Therefore, the points must be homogeneously distributed on the image, otherwise the resulting model may present deformations in areas far from the GCPs.

2.4 Results

Considering the large number of GCPs required and the average resolution of the image to be processed, the GCPs were identified from vectorial cartography. For the image of Rome, vectorial cartography in scale 1:5000 provided by the Lazio Region website (Regione Lazio, 2021) was used (declared +/- 1 m horizontal accuracy, +/- 2m vertical accuracy). While for the island of Ischia the vectorial cartography in scale 1:2000 provided by the Metropolitan City of Naples was used (declared +/- 40 cm horizontal accuracy, +/- 70 cm vertical accuracy).
Points surveyed with GNSS receivers were available from previous research on higher resolution imagery, but they couldn't be used because the resolution of PRISMA products did not allow the correct identification on the image. The results of the application of the RPF method without RPC are acceptable at a first visual verification, by overlaying the orthorectified panchromatic product and vectorial cartography.

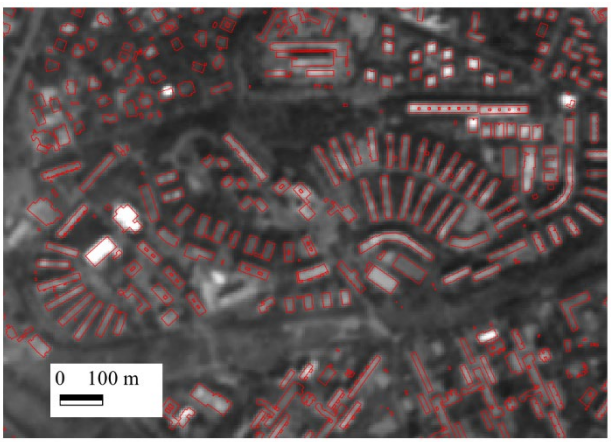

Figure 2. Portion of orthorectified panchromatic image and superimposed cartography at scale 1:5000 (Rome)

The precision of the planimetric positioning was calculated from the residuals on the GCPs, while the accuracy was calculated on the CPs.

	X RMS [m]	Y RMS [m]
GCPs	2.77	3.09
CPs	3.82	4.40

Table 1. Residuals obtained with OrthoEngine software for the image of Rome

	X RMS [m]	Y RMS [m]
GCPs	6.11	4.76
CPs	5.15	6.41

Table 2. Residuals obtained with OrthoEngine software for the image of island of Ischia

The results obtained with the RPF method confirm the local validity of the method, presenting lower precision values compared to the accuracy calculated on the CPs. The image of

Ischia presents overall higher residual values, although in the order of one pixel. The reason for this could be that the collimation of GCPs and CPs was more difficult due to the topographic characteristics of the island, which also influenced the development of the urban texture and the type of buildings. In addition to this collimation error, it must be remembered that the points were identified on vectorial cartography at large scale with the accuracy already illustrated. However, in spite of these subtle differences, the RPF approach produced residuals on the CPs in the order of the pixel, which is better than what ASI assumes using GCPs.

3. CONCLUSIONS

The present paper deals with the geometric treatment of the images acquired by PRISMA satellite platform launched and managed by the Italian Space Agency. PRISMA satellite is very recent, probably for this reason there is practically no contribution in the literature concerning the geometric treatment of the satellite itself. For this reason, it was decided to experiment different orientation strategies known in the literature with the aim to verify which ones could be the most efficient; all tests were conducted considering the major software used for the geometric treatment of satellite images. Usually, RPF with RPC and RPF approaches are used more because they do not require photogrammetric algorithms and geometric-orbit sensor information. The RPF with RPC method has given erroneous results with coarse rototranslations. The cause of this discrepancy is still under investigation as PRISMA's RPCs are claimed to comply with the NIMA (National Imagery and Mapping Agency) standard. To verify this, we recalculated the RPC parameters in NIMA standard using a large number of GCPs and in this case the image was orthorectified correctly obtaining low residuals on the CPs.

The RPF approach is usually avoided because it requires many GCPs and is not statistically robust. However, it should be noted that, given the low resolution of the image, GCPs can advantageously be acquired from vectorial cartography in scale 1:5000/1:10000, which is now available over the whole national territory. Therefore, with this specific type of image, there is no need to acquire coordinates through expensive survey campaigns with differential GPS/GNSS receivers and therefore the number of GCPs to be used is not really a critical factor.

In addition, the validation of the model estimated with the RPF approach shows that the residuals on the CPs are in the order of one pixel and therefore better than those expected by ASI with the use of GCPs. Probably with more rigorous information on RPCs or on orbital and orientation parameters even better results could be obtained, in fact previous experiments on similar satellite platforms have shown that it is possible to achieve even half a pixel of accuracy, so we believe there is certainly further room for improvement (Baiocchi et al. 2020).

Currently, our strategy is the most accurate and efficient and can give results compatible with 1:50000 at the map production stage or 1:25000 at the map update stage.

REFERENCES

ASI, 2020. PRISMA Products Specification Document Issue 2.3 Date 12/03/2020

ASI, 2017, PRISMA: prodotti. PRISMA, precursore delle missioni iperspettrali nazionali, http://prisma-i.it/images/Eventi/20170301_Workshop_ASI/Sessione%203/Colandrea.pdf

Baiocchi, V., Brigante, R., Radicioni, F., 2010. Three-dimensional multispectral classification and its application to early seismic damage assessment. Ital. J. Remote Sens., 42, 49–65.

Baiocchi, V., Giannone, F., Monti, F., Vatore, F., 2020. ACYOTB Plugin: Tool for Accurate Orthorectification in Open-Source Environments. ISPRS International Journal of Geo-Information, 9(1), 11; https://doi.org/10.3390/ijgi9010011

Busetto, L., Ranghetti, L., 2020. prismaread: A tool for facilitating access and analysis of PRISMA L1/L2 hyperspectral imagery v1.0.0, URL: https://lbusett.github.io/prismaread/, doi: https://doi.org/10.5281/zenodo.4019081

Kraus, K., 1993. Photogrammetry. Vol. 1: Fundamentals and Standard Processes, Dümmler, Bonn.

Loizzo, R., Ananasso, C., Guarini, R., Lopinto, E., Candela, L., Pisani, A.R., 2016, The PRISMA hyperspectral mission. Conference: Living Planet Symposium 2016, 9-13 May 2016, Prague, Czech Republic

National Imagery and Mapping Agency, 2000, "The Compendium of Controlled Extensions (CE) for the National Imagery Transmission Format (NITF)", VERSION 2.1, 16 November 2000

Regione Lazio, open data, last accessed 15/06/2021 http://dati.lazio.it/catalog/it/dataset/carta-tecnica-regionale-2002-2003-5k-roma

Tarquini, S., Isola, I., Favalli M., Battistini, A., 2007. TINITALY, un modello digitale di elevazione dell'Italia con una cella di 10 metri (Versione 1.0) [Data set]. Istituto Nazionale di Geofisica e Vulcanologia (INGV), https://doi.org/10.13127/TINITALY/1.0.

Toutin, T., 2011. State-of-the-art of geometric correction of remote sensing data: a data fusion perspective, International Journal of Image and Data Fusion, 2:1, 3-35, DOI: 10.1080/19479832.2010.539188

Zollini, S., Alicandro, M., Cuevas-González, M., Baiocchi, V., Dominici, D., Buscema, P.M., 2020. Shoreline extraction based on an active connection matrix (ACM) image enhancement strategy Journal of Marine Science and Engineering, 8(1), 9

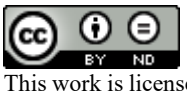

15 YEARS OF SNOW COVER RETRIEVAL AND MONITORING OVER SARDINIA BY MSG DATA

Paolo Boi *

Agenzia Regionale per la Protezione dell'Ambiente della Sardegna, pboi@arpa.sardegna.it

KEY WORDS: Snow cover, retrieval, monitoring, MSG data, visible, infrared, Sardinia.

ABSTRACT:

An automated procedure that monitors the snow cover over Italy on a monthly and annual base is presented. It is based upon daily snow cover maps. The snow retrieval has been performed using the reflectance at 0.6 µm and 1.6 µm channels and the brightness temperature at 12.0 µm channel of Meteosat Second Generation (MSG). Snow reflectance is high at 0.6 micron, but it is very low at 1.6 micron, on the contrary soil snow-free reflectances at 0.6 micron and 1.6 micron are not so different. Snow brightness temperature at 12.0 micron is lower than ice clouds tops.
The pixels are divided into cloudy, snowy, snow free. A cloudy pixel is obtained when it has been cloudy all day long, making snow retrieval impossible. The first phase of the procedure produces temporary daily snow cover maps. In a second phase the daily maps are analysed for cloud cover correction based on simple statistical hypotheses. In this way some cloudy pixels (about 10% of total) are re-processed and labelled as snow covered or snow free. Finally, daily maps are further analysed in order to obtain a monthly or annual map representing the number of snow cover days for each pixel. The procedure performance has been tested by comparison with six months GTS ground observations. Contingency tables and statistical indices have been analysed. The monitoring has produced snow cover maps since the winter 2006-2007.

1. INTRODUCTION

Snow cover is an important surface characteristic both at a local and global scale. It has a very high albedo and then influences the planetary radiation budget. It is an important water source, especially in arid and semiarid regions, so it influences the hydrological cycle at a local scale. Snow cover analysis is an important surface feature for initialising numerical weather prediction (NWP). Monitoring snow cover has therefore important applications in climate, numerical weather forecasting and hydrology. In this paper a method is presented for monitoring snow cover on a monthly and annual base, by using the visible, near-infrared and infrared channels of MSG (Meteosat Second Generation). MSG data have a good combination of spatial (3 km) and temporal resolution (15 minutes), while the polar satellites have a better spatial resolution, but worse temporal resolution (Basist et al., 1996, Hall et al., 2002, Hall et al. 1995). The principal problem for solar channel methods is the cloud cover (Romanov et al., 2000, Allen et al., 1990). Up to now this problem has been approached by using microwave data in case of cloudy pixels. This is not satisfactory because spatial resolution of microwave data is very low (about 20 to 30 km) and in mountainous or hilly regions it is not adequate. This work attempts to partially overcome the cloudiness problem by a new statistical method. A second aspect is the discrimination between snow and ice clouds, as both have high reflectance at visible channels and low reflectance at near infrared. In the literature this problem has been generally tackled by using the infrared channels and surface temperature from the meteorological model (Romanov et al., 2000). In this work the meteorological model temperature has been downscaled at the same satellite spatial resolution through a suitable spatial interpolation.

2. METHODS

2.1 The temporary daily maps

The following MSG channels have been used: VISIBLE 0.6 µm, NIR 1.6 µm AND IR 12.0 µm (Boi, 2010). At 0.6 µm the snow has higher reflectance than snow-free land, sea surface and semitransparent clouds. The NIR 1.6 µm reflectance strongly depends by the water phase: it presents low reflectance for ice clouds, snow, ice and higher reflectance for snow-free land and water clouds. This is due to high values of imaginary refraction index for ice phase at this channel. The Snow Index SI (Romanov et al., 2000), defined as the ratio between VIS 0.6 µm and NIR 1.6 µm reflectances, has values less than 1 for snow-free land and higher than 1 for snow and ice tops clouds, then it is useful to discriminate snow-free and snow surfaces. The IR 12.0 µm brightness temperature (Romanov et al., 2000) is necessary to discriminate between ice top clouds and snow by using the 2m temperature of the ECMWF atmospheric model as threshold. The first phase of the procedure produces a snow cover daily map by using the images in the previous three channels available every 15 minutes. The pixels affected by clouds in all the images are classified as cloudy pixels in the daily map, the pixels that result snowy by one image and snow-free by another one are uncertain or partly snowy, the other pixels are classified as snowy or snow-free

2.2 The algorithm

Denoting the VIS 0.6 µm reflectance by R06, the NIR 1.6 µm reflectance by R16, their ratio (Snow Index) by SI, the 12.0 µm brightness temperature by TB and the atmospheric model 2m temperature by T2M_MODEL, the algorithm is as follows (Boi, 2010):
IF SI>S1 AND R06>R1 AND T2M_MODEL-DT<TB<T2 THEN THE PIXEL IS SNOWY

* Corresponding author

IF R06 > R2 OR TB < T2M_MODEL-DT THEN THE PIXEL IS CLOUDY
ELSE THE PIXEL IS SNOW FREE

The thresholds R1 and R2 for the 0.6 µm channel are determined after the analysis of reflectance histogram both in cloud free and cloud conditions in a preliminary independent phase. The T2 threshold is 283 °K. DT is 10°K and it takes in account the model uncertainty. The algorithm has been tested for different values of SI thresholds S1 (1, 1.1, 1.2, 1.3) and the results compared to ground stations data in order to find the best threshold value. The errors on surface temperature due to uncertain ground emissivity are negligible (less than 1°C) compared to the model resolution errors (a few °C depending on the orography).

2.3 Daily maps correction for cloud cover.

In order to reduce the cloudy pixels a second phase is performed on the daily maps. It analyses three or four consecutive daily maps and follows this criterion (Boi, 2010):

SCS=SSS, SCCS=SSSS, LCL=LLL, LCS=LSS.
Where S is the snowy pixel, L the land snow free pixel, and C the cloudy pixel. SCS indicate a pixel which is snowy on the first and the third day, cloudy on the second one. In this case is very likely that it is snowy also on the second day. LCL is for a pixel that is snow-free on the first and the third day, cloudy on the second one. In this case it is very probable that it is snow-free also on the second day. LCS represents a pixel that is snow-free on the first day, and snowy on the third one. In this case the clouds of the second day have probably produced the snow fall, then the pixel is snowy also on the second day.
The verification, by comparison with stations data, will show that these hypothesis are correct. By this procedure the cloudy pixels identified as snowy or snow-free are about 10% of total.

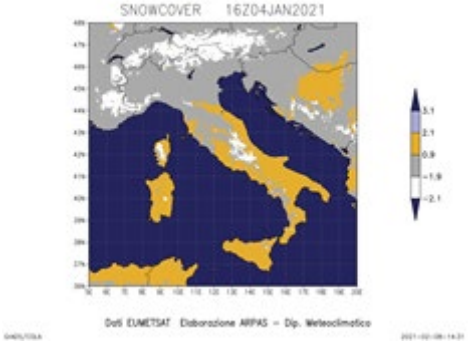

Figure 1: Snow cover daily map after cloud cover correction. The snowy pixels are white, the cloudy pixels are grey, the free-snow pixels are yellow, the sea and lakes pixels are blue.

3. VERIFICATION

The procedure has been verified by using 139 GTS (Global Telecomunication System) ground stations of Italy, between January and June 2005. The daily ground measurements (snow or no snow) has been compared with the collocated pixel information in the snow cover map by making contingency tables (snow, no snow) on monthly base. Cloudy pixels where not included in the contingency tables.
The following indices has been calculated (Wilks, 1995):

POD (PROBABILITY OF DETECTION). It is the ratio between the corrected retrieved snowy cases and the observed snowy cases. In the perfect procedure POD=1
FAR (FALSE ALARM RATE). It is the ratio between the false retrieved snowy events and the total number of retrieved snowy events. In the perfect procedure FAR=0
BIAS. It is the ratio between the number of retrieved snowy events and the observed ones. In the perfect procedure BIAS=1
FRACTION OF MISSING. It is the ratio between the missing events and the total ones. In the perfect procedure MISSING=0
FRACTION OF FALSE. It is the ratio between the false snowy events and the total ones. In the perfect procedure FALSE=0
HR (HIT RATE, OR THE FRACTION OF CORRECT). It is the ratio between the correct events (snowy and snow free) and the total ones. In the perfect procedure HR=1
TS (THREAT SCORE). Also called Critical Success Index. It is the ratio between correctly detected snowy events and the sum of estimated snowy and observed snowy. In the perfect procedure TS=1

The verification has been made both on the temporary daily maps and on the maps corrected for the cloud cover, in order to evaluate the efficiency of the cloud cover procedure correction. The missing events errors are higher than false events errors as we can see in the Figure 2 - Right, consequently the BIAS in Figure 2 - Left is low than 1. In April and May POD, FAR, BIAS and TS show worse performances than in January, February and March, but the number of snowy cases is very low and could not be statistically significant.

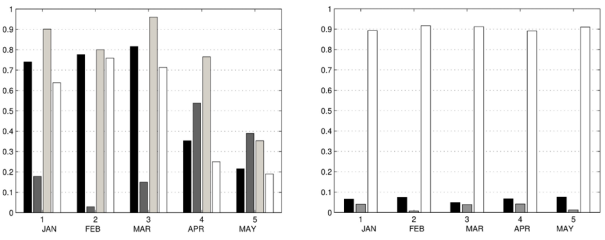

Figure 2. Statistical indices. Left : POD, black, FAR, grey, BIAS, grey light, and TS, white bar. Right: Fraction of missing, black bar, Fraction of false, grey bar, Hit Rate, white bar.

4. SNOW COVER MONITORING

Some applications of this procedure in climate monitoring are monthly or annual reports of snow cover. The Figure 3 shows the number of snow cover days for January 2021. In this kind of map the uncertainty due to the cloud cover has been reduced but not completely eliminated. In this example the fraction is calculated as the ratio between the snowy days and the sum of snowy and snow-free days. Then we assumed that this fraction is valid also for the cloudy days. This assumption is not obvious. Comparison with ground station data has proved the validity of this hypothesis. For this purpose the monthly snow cover frequency under all sky conditions and clear sky conditions only, based on ground data has been calculated. The mean difference between the conditional and the marginal frequency is of the order of 0.1% and the rms is about 1%. The Figure 4 presents the number of snow cover days on Gennargentu top between winter 2007-2008 and winter 2020-2021

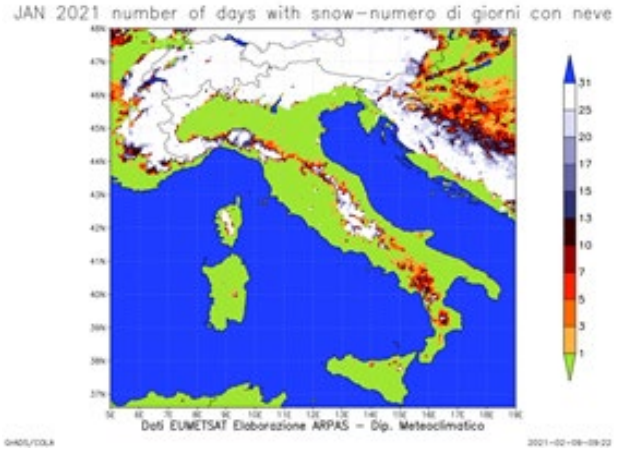

Figure 3. Monthly number of snow cover days for January 2021

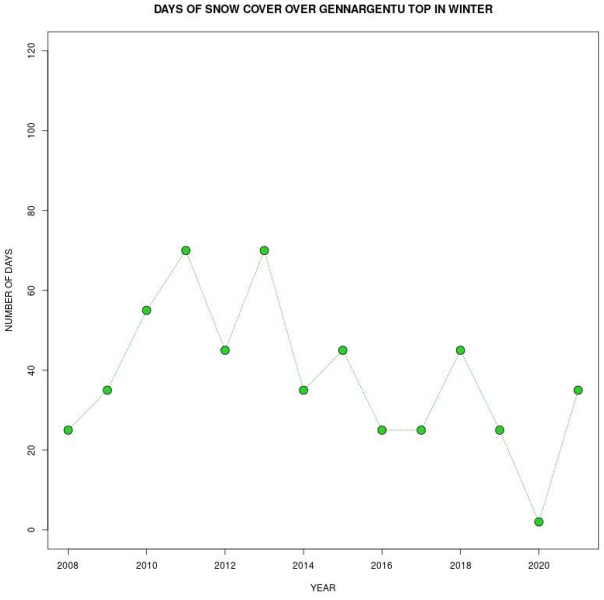

Figure 4. Days of snow cover on Gennargentu top

5. CONCLUSION

A procedure for monitoring snow cover over Italy and the alpine regions for climatologic purposes, by using visible, near infrared and infrared MSG data, has been presented. The procedure attempts to partially overcome the problem of cloud cover, when the satellite cannot see below the clouds, by using simple statistical hypotheses. In this way it is possible to recover about 10% of the total data. The verification shows that the statistical hypotheses are correct and the cloud cover correction does not introduce any significant errors. The procedure has been used to produce monthly and yearly frequency maps of snow cover. A comparison between ground observed and satellite estimated frequencies has been made. As the cloud cover has not been completely removed, its effect on estimated snow cover monthly frequency has been analysed. For this purpose the monthly snow cover frequency under all sky conditions and clear sky conditions based on ground data only has been calculated. The mean difference between the conditional and the marginal frequency is of the order of 0.1% and the rms is about 1%

REFERENCES

Allen, R.C., Durkee, P.A. and Wash, C.H., (1990) Snow/cloud discrimination with multispectral satellite measurements, J. Appl. Meteorol., **29**, pp 994-1004.

Basist, A., Garrett, D., Ferraro, R., Grody, N. and Mitchell, K., (1996), A comparison between snow cover products derived from visible and microwave satellite observations, J. Appl. Meteorol., **35**, pp 163-177.

Boi, P. - Snow cover retrieval over Italy and alpine regions using MSG data for climatologic purposes. *Meteorological Applications. 2010.Vol 17: 313-320.* DOI: 10.1002/met.172.

Hall, D.K., Riggs, G., Salomonson, V., Di Girolamo, N.E. and Bayr, K.J., (2002) MODIS snow cover products, Remote Sens. Environ., **83**, pp 181-194.

Hall, D. K., Riggs, G. A., Salomonson, V., (1995). Development of methods for mapping global snow cover using moderate resolution imaging spectroradiometer data. Remote Sensing of Environment, **54**, pp 127-140.

Kaufman, Y.J., Kleidman, R.G., Hall, D.K., Martins, J.V., Barton, J.S., (2002), Remote sensing of subpixel snow cover using 0.66 and 2.1 μm channels, Geophys. Res. Lett., **29**, art. no. 1781.

Klein, A.G., Hall, D.K., and Riggs, G., (1998), Improving snow cover mapping in forests through the use of a canopy reflectance model. Hydrolog. Process., **12**, pp 1723-1744.

Romanov, P., Gutman, G.,and Csiszar, I., (2000) Automated monitoring of snow cover over North America with multispectral satellite data, J. Appl. Meteorol., **39**, pp 1866-1880.

Romanov, P., and Gutman, G., (1997), Estimation of land surface emissivity using synergy of AVHRR- and ground-based measurements. IRS '96: Current Problems in Atmospheric Radiation,
A. Deepak Publishing, pp 1037-1041.

Wilks, D. (1995) Statistical Methods in the Atmospheric Sciences. Academic Press.

AIRBORNE OPTICAL DATA HARVESTING AND GEO-PROCESSING FOR WATER QUALITY RETRIEVAL OF LAKE MULARGIA

M. Bresciani [1]*, C. Giardino [1], S. Mangano [1], M. Pinardi [1], K. Schenk [2], T. Heege [2], M. A. Dessena [3], P. Buscarinu [3]

[1] Institute for Electromagnetic Sensing of the Environment, National Research Council of Italy (CNR-IREA), 20133 Milan, Italy - (bresciani.m, giardino.c, mangano.m, pinardi.m)@irea.cnr.it
[2] Earth Observation and MAPping GmbH & Co.KG, Seefeld, Germany – (schenk, heege)@eomap.de
[3] Ente acque della Sardegna, ENAS, Cagliari, Italy – (mantonietta.dessena, paola.buscarinu)@enas.sardegna.it

KEY WORDS: hyperspectral, bio-optical modelling, chlorophyll-a, calibration-validation, imaging spectrometers

ABSTRACT:

Satellite remote sensing provides valuable data for understanding spatial and temporal variability of water quality parameters. In particular, PRISMA and DESIS are showing increasing capabilities in water quality mapping even if further studies might be needed to fully exploit these relatively new data. In this context, high-resolution airborne hyperspectral sensors might support preliminary tests to evaluate satellite-based systems, while represent enhanced mapping tools. In the context of the H2020 PrimeWater project, this study presents the use of HySpex hyperspectral airborne data of the freshwater reservoir Mulargia (Italy) to: i) calibrate and validate algorithms to retrieve optically active parameters; ii) assess the feasibility of retrieve water quality parameters; iii) export of this knowledge on PRISMA and DESIS data. The Hyspex images were acquired on 24 September 2020 in coincidence with *in situ* data, both radiometric and water quality. HySpex data were geocoded with PARGE and atmospherically corrected with ATCOR code and the results showed a good consistency between water reflectance with *in situ* data. The retrieval of the optical properties from imagery was achieved with a spectral inversion of bio-optical modelling (namely BOMBER), parametrized with absorption and backscattering data of the site. The estimates matched well field data ($r^2 > 0.8$) and depicted the mesotrophic conditions of the reservoir with higher Total Suspended Matter in shallow coastal waters.

1. INTRODUCTION

Earth Observation (EO) techniques with optical sensors have been used for many decades to support timely and frequent acquisition of synoptic information on inland water ecosystems (*e.g.*, Palmer et al., 2015 and reference herein). In recent years, EO has become an operational tool to support traditional measurements providing, at a relatively low cost and for some bio-geophysical parameters, information on aquatic ecosystem to support a variety of applications (*e.g.*, Tyler et al., 2016).

Earth Observation systems measuring water quality are optical radiometers which include: ocean color radiometer (*e.g.*, Sentinel-3 OLCI or MODIS, with pixels of about 300–1000 m), multispectral sensors (*e.g.*, Landsat or Sentinel-2 MSI, with pixels of 10–30 m), geostationary platforms (*e.g.*, GOCI, with a 500 m pixel size) and imaging spectrometers (*e.g.*, Hyperion or PRISMA, with a pixel size of 30 m).

High spatial and spectral resolution data are essential attributes to provide accurate retrieval of water quality parameters in both optically deep and shallow waters (Dekker et al., 2005) and offer valuable data to satellite observations. In this context, high-resolution airborne hyperspectral sensors (*e.g.*, AISA, APEX, MIVIS, AVIRIS, CASI, HYMAP) represent enhanced mapping tools (*e.g.*, Dekker et al., 2011; Bresciani et al., 2012; Giardino et al., 2019). Airborne systems have been hence widely used over three decades for measuring water quality conditions in inland waters (*e.g.*, Giardino et al., 2015 and reference herein). The combination of high-spatial and high-spectral data allowed also performing preliminary tests to design satellite-based systems (*e.g.*, Koponen et al., 2002).

In the context of the H2020 PrimeWater project, this study presents the use of HySpex hyperspectral airborne data of the freshwater reservoir Mulargia (Italy) to: i) calibrate and validate algorithms to retrieve optically active parameters; ii) assess the feasibility of retrieve water quality parameters; iii) export of this knowledge on PRISMA and DESIS data.

2. MATERIALS AND METHOS

2.1 Study area

The Lake Mulargia (area of 12 km^2, and volume of 347 hm^3; Figure 1) is a dammed reservoir build on the Flumendosa river located in south Sardinia (Italy), and a catchment area of 178 km^2. The Mulargia reservoir supply drinking water to the town of Cagliari and its hinterland and for other 20 villages around in the region. The total annual abstraction for drinking water purposes is estimated to be 100 hm^3.

Figure 1. Study area. Mulargia dam (bottom) and Lake Mulargia from satellite (top).

The Mulargia waters are in meso-eutrophic state as a consequence of phosphorus loads mostly due to agriculture and livestock farming activities, with low transparency and high

* Corresponding author

conductivity representing the most important issues. A recent work (Bresciani et al., 2019) showed minimum turbidity during summer season with transparent waters, while spring and autumn seasons are generally characterized by greater turbidity and highest values of chlorophyll-a, with the presence of cyanobacteria (*Planktothrix rubescens*).

2.2 *In situ* data

The collection of *in situ* data was performed on 22, 23 and 24 September 2020 for a total of 19 stations. Figure 2 shows the location of the different sites sampled in the 3-days field campaign.

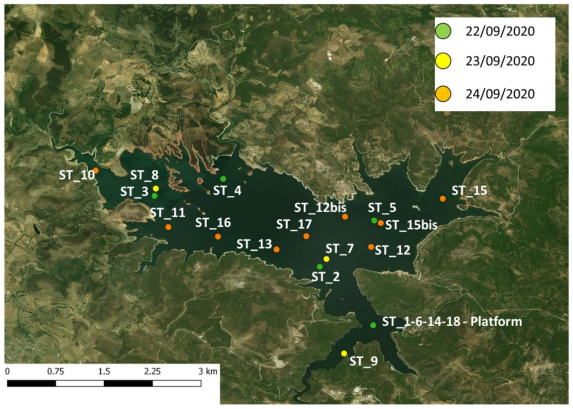

Figure 2. Location of *in situ* stations sampled in Lake Mulargia between 22nd and 24th September 2020.

The *in situ* data included: water quality parameters, spectroradiometer measurements, Inherent Optical Properties (IOP) measurements.

Water samples were collected based on the water conditions, basically to integrate the top-most water layer according to the Secchi disk depth, each water sample was filtered using Whatman GF/F glass fiber filters. Concentration of total suspend matter (TSM) were determined gravimetrically according to Strömbeck and Pierson, (2001); concentration of chlorophyll-a (Chl-a) is determined spectrophotometrically according to Lorenzen (1967) and extracted using acetone at 90%; absorption by Colored Dissolved Organic Matter (CDOM) was also measured with the spectrophotometer relative to pure water and the absorption coefficient at 440 nm.

Radiometric measurements were collected with different spectroradiometers: WISP-3, Spectral Evolution SE-3500, JB-Hyperspectral ROX. The WISP-3 and SE-3500 were used on a boat to sample all the stations and the Remote Sensing Reflectances (Rrs) was extracted based on SeaWiFS protocol (Fargion and Mueller, 2000), while ROX was deployed on the ENAS platform (cf. Figure 2) in order to have continuous measurement every 5 minutes from a fixed position.

IOP measurements includes: i) vertical profiles of total backscattering coefficient (bbtot) collected with a HOBILabs HydroScat-6; ii) water samples were collected in order to determine the absorption coefficients due to particle (ap), phytoplankton (aph), non-algal-particle (anap) and CDOM (aCDOM).

Moreover, a CTD probe was used to measure water turbidity, pH, conductivity, oxygen saturation and surface temperature and water samples collected in the first meter of the water column were added of Lugol's solution for the following phytoplankton identification and counts (biomass) (Utermöhl, 1958).

2.3 Airborne data

The airborne hyperspectral acquisition in Lake Mulargia was carried out at an altitude of 3000 meters (pixel size of 2 meters), on 24 September 2020 with HySpex VNIR 1800 sensor onboard of a Cessna 402 I-GBFE aircraft of CGR Italy. The survey consisted of two flights: the first was performed between 9:30 and10:32 UTC and the second one between 15:30 and 16:18 UTC time.

HySpex data pre-processing for geocoding and for removing the atmospheric effects was performed with PARGE and ATCOR-4 software's respectively. PARGE performs an ortho-rectification of line scanner imagery using a digital elevation model on the basis of high precision flight parameters such as GPS position and attitude angles. ATCOR-4 is a code used for the atmospheric correction of small and wide Field of View (FOV) airborne sensors (Richter, 2009). ATCOR-4 uses look-up tables generated by MODTRAN (Berk et al., 2006), relating sensor radiances and albedo for various atmospheric and geometric conditions. ATCOR-4 tool, parametrised according to airborne data (*e.g.*, viewing conditions, spectral setting) and atmospheric parameters (*e.g.*, Aerosol Optical Depth) was in fact then run to convert the at-the-sensor radiances into ground reflectance. The retrieval of the optical properties of water column from atmospherically corrected imagery was achieved with BOMBER (Giardino et al., 2012), with a specific parametrisation based on *in situ* data collected during fieldworks.

For the match-up analysis, the HySpex reflectance's data and the water quality parameters retrieved were derived from imagery data and maps by computing the average value and standard deviation of HySpex data corresponding to a square box of 5 x 5 pixels defined over the *in situ* measurements stations. Common descriptive statistical metrics, such as root mean square error (RMSE), mean absolute error (MAE), the square of the coefficient of correlation (R2) and scatterplots were used for the comparison.

3. RESULTS

The water quality parameters data showed (Figure 3) an average values of Chl-a of 1.8 mg/m^3, an average concentration of TSM of 3 g/m^3 with higher values close to the tributary and to coastal zones.

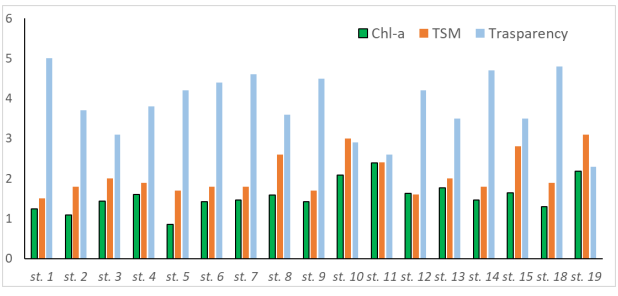

Figure 3. Chlorophyll-a concentration (mg/m^3), Total Suspended Matter concentrations (g/m3) and Transparency (m^{-1}) values in all the stations of the Lake Mulargia sampled between 22nd and 24th September 2020.

The HySpex Remote sensing reflectance obtained from ATCOR-4 and corresponding *in situ* data were then compared to evaluate the quality of the atmospheric correction. Figure 4 shows a comparison between the Rrs spectra extracted from HySpex and from *in situ* spectroradiometric measurements. The correlation coefficients were 0.66 in the blue (band at 450 nm),

0.79 in the green (band at 550 nm) and 0.76 in the red (band at 652 nm).

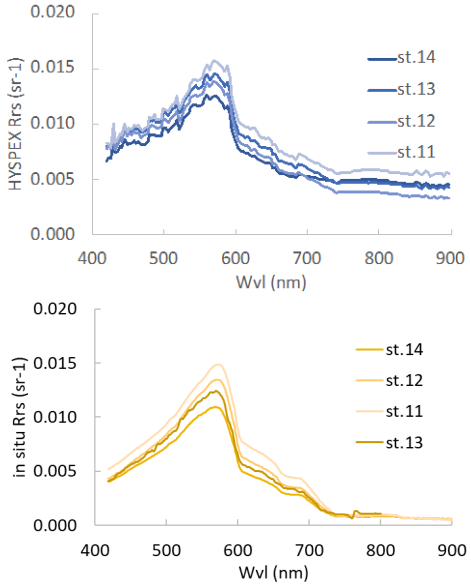

Figure 4. Example of Rrs spectra derived from ATCOR-4 (top) and *in situ* measurements (down) for the four stations sampled contemporary to the time of the HySpex morning overflight.

Figure 5 presents the pseudo true color HySpex image corresponding to three runs (namely 04, 05 and 07) of the morning flights and the water quality maps on Chl-a, TSM and CDOM concentrations retrieved applying BOMBER to the imagery data.

The results showed a higher concentration of TSM and CDOM in the Run 07 that covered a part of the Lake characterized by shallow water and that is influenced by the tributary water's. For the same reasons the northern part of the TSM maps of Run 04 and Run 05 have higher values.

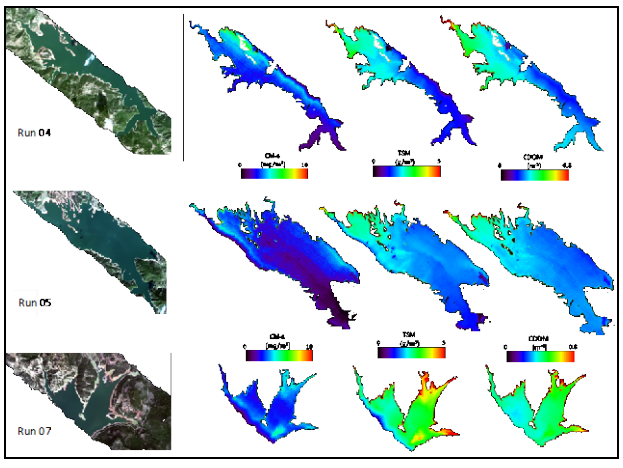

Figure 5. The pseudo true color HySpex images from different runs (04, 05 and 07) that covered Lake Mulargia and the three products (Chl-a, TSM and CDOM) obtained with BOMBER.

The first mapping of Chl-a and TSM concentrations were then compared with *in situ* data, gathered on the same day of the HySpex data acquisition as well as in nearby days. Overall, by also considering the limited range of variation of water quality products, an acceptable agreement between HySpex derived products and *in situ* data was observed (Figure 6).

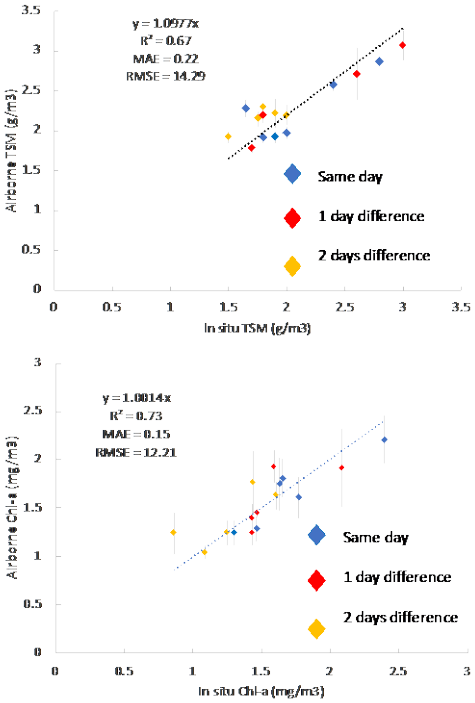

Figure 6. Scatterplots of Hyspex-derived products and *in situ* concentrations of TSM (top) and Chl-a (bottom).

In order to evaluate the variability of the response of EO resolutions to retrieve water quality information of Lake Mulargia useful reservoir managers, Hyspex data was spectrally and spatially resampled based on different optical satellite characteristics (PRISMA and DESIS). The preliminary results indicated the potentiality of both satellite hyperspectral sensors to improve water quality mapping.

4. CONCLUSIONS

The general scope of the airborne hyperspectral and *in situ* campaign was to provide a dataset for running the scientific experiments defined in the EO Science Virtual Laboratory of the PRIMEWATER project. In particular, the dataset presented in this work will support the Exploitation of multiplatform optical data for assessing water quality in Lake Mulargia reservoir in which we aim to explore concurrent measurements from *in situ*, airborne and satellite sensors.

The results clearly showed the potentiality of hyperspectral data to retrieve water quality parameters of Lake Mulargia. The preliminary results obtained showed an acceptable result for the atmospheric correction of HySpex data and a good result for the water quality parameters retrieval. In the future the integration of this dataset with different optical satellite data such as PRISMA, DESIS, Sentinel-2 and Sentinel-3 will help to understand the spatial, spectral and temporal resolution necessary to provide useful information to characterize the status of the Lake Mulargia water and could provide important information for water management.

ACKNOWLEDGEMENTS

This study was co-funded by EU Horizon 2020 project PrimeWater (grant nr. 870497). The Hyspex data was collected by Compagnia Generale Riprese aeree (CGR spa). We would like to thank Francesco Bo (CGR spa) for the support during

airborne acquisition and all the groups of ENAS for the field campaign activities.

REFERENCES

Berk, A., Anderson, G.P., Acharya, P.K., Bernstein, L.S., Muratov, L., Lee, J., Shettle, E.P. 2006. *MODTRAN5: 2006 update*. In Algorithms and Technologies for Multispectral, Hyperspectral, and Ultraspectral Imagery XII (Vol. 6233, p. 62331F). International Society for Optics and Photonics.

Bresciani, M., Bolpagni, R., Oggioni, A., Giardino, C., 2012. Retrospective assessment of macrophytic communities in southern Lake Garda (Italy) from in situ and MIVIS (Multispectral Infrared and Visible Imaging Spectrometer) data. *Journal of Limnology*, 71(1), pp.180-190.

Bresciani, M., Giardino, C., Stroppiana, D., Dessena, M. A., Buscarinu, P., Cabras, L., Schenk, K., Heege T., Bernet H., Bazdanis G., Tzimas, A., 2019. Monitoring water quality in two dammed reservoirs from multispectral satellite data. *European Journal of Remote Sensing*, 52(4), pp.113-122.

Dekker, A.G., Brando, V.E., Anstee, J.M., 2005. Retrospective seagrass change detection in a shallow coastal tidal Australian lake. *Remote Sensing of Environment*, 97, pp.415-433.

Fargion, G.S., Mueller, J.L., 2000. *Ocean Optics Protocols for Satellite OceanColor Sensor Validation*. Revision 2. NASATechinalMemo. 2000-209966. (NASA Goddard Space Flight Center: Greenbelt, MD, USA).

Giardino, C., Brando, V.E., Gege, P., Pinnel, N., Hochberg, E., Knaeps, E., Reusen, I., Doerffer, R., Bresciani, M., Braga, F., Foerster, S., 2019. Imaging spectrometry of inland and coastal waters: state of the art, achievements and perspectives. *Surveys in Geophysics*, 40(3), pp.401-429.

Giardino, C., Bresciani, M., Matta, E., Brando, V.E., 2015. *Imaging Spectrometry of Inland Water Quality in Italy Using MIVIS: An Overview*. In: T. Younos, T.E. Parece (eds.), Advances in Watershed Science and Assessment, The Handbook of Environmental Chemistry 33, pp. 61-83.

Giardino, C., Candiani G, Bresciani M, et al. (2012). BOMBER: A tool for estimatine water quality and bottom properties from remote sensing images. *Computers & Geosciences*, 45, pp.313-318.

Koponen, S., Pulliainen, J., Kallio, K., Hallikainen, M., 2002. Lake water quality classification with airborne hyperspectral spectrometer and simulated MERIS data. *Remote Sensing of Environment,* 79(1), pp.51-59.

Lorenzen, C.J., 1967. Determination of chlorophyll and pheo-pigments: spectrophotometric equations. *Limnology and Oceanography*, 12, pp.343-346.

Palmer, S.C., Kutser, T., Hunter, P.D., 2015. Remote sensing of inland waters: Challenges, progress and future directions. *Remote Sensing of Environment*, 157, pp. 1-8.

Richter, R., 2009. *Atmospheric/topographic correction for satellite imagery*. DLR report DLR-IB 565-01/09, Wessling, Germany.

Strömbeck, N., Pierson, E., 2001. The effects of variability in the inherent optical properties on estimations of chlorophyll a by remote sensing in Swedish freshwater. *The Science of the Total Environment*, 268, pp.123-137.

Tyler, A.N., Hunter, P.D., Spyrakos, E., Groom, S., Constantinescu, A.M., Kitchen, J., 2016. Developments in earth observation for the assessment and monitoring of inland, transitional, coastal and shelf- sea waters. *The Science of the Total Environment*, 572, pp. 1307-1321.

Utermöhl, H., 1958. Zur Vervollkommung der quantitative Phytoplankton Methodik. *Mitteilungen Internationale Vereinigung für Theoretische und Angewandte Limnologie*, 9, pp.1-38.

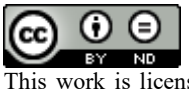

UAV PHOTOGRAMMETRY-BASED MAPPING OF SICILIAN POCKET BEACHES: FIRST APPROACH

A. Muzirafuti [1, *], M. Cascio [1], S. Lanza [1,2]

[1] Dept. of Mathematics Informatics Physics and Earth Sciences, University of Messina
muzansel@gmail.com, maria.cascio86@gmail.com, stefania.lanza@unime.it
[2] GeoloGIS s.r.l. Spin Off of the University of Messina
Via F. Stagno d'Alcontres, 31-98166 Messina, Italy

KEY WORDS: Pocket beach, Remote Sensing, Coastal erosion, drone, RTK GPS, Computer-assisted, 3D model, Geomorphology

ABSTRACT:

The Pocket Beaches (PBs) are widespread throughout the Mediterranean coast and the characteristics of their landscape make them very attractive for tourists. Along the Sicilian coast there are several Pocket Beaches. However, they have no univocal behaviour. Numerous detailed studies on Pocket Beaches have been carried out in recent years; they suggested that geometric physical parameters provide useful information for characterization of embayed coasts. These parameters allow for the analysis of coastal segments exposure to the incident waves and are usually extracted from old dataset or from hazardous fieldworks. In this study, we propose a UAV- photogrammetry-based mapping approach to study the PBs located on the coast of Sicily. With the aid of new technologies, we used drones equipped with very high-resolution camera to acquired orthophotos and 3-D representation of Sicilian PBs. The data obtained by Unmanned Aerial Vehicles were supported by Ground control Points acquired using RTK GPS which helped refine their geo-referencing precision. Computer-assisted approach was adopted to retrieve geometric parameters and eventually coastal geomorphological elements of the PBs.

1. INTRODUCTION

Pocket Beaches (PBs), are small beaches, included between two headlands (natural or artificial promontories). These headlands play an important role in the beach natural functioning, they constitute either the morphological definition of the beach system, or the structure dominating the local wave conditions..
The PBs are widespread throughout the Mediterranean coast (Bowman, 2009) and the characteristics of their exceptional natural landscape make them very attractive for tourists. Along the Sicilian coast (main island of Sicily and related archipelagos), there are several Pocket Beaches. These ones are quite varied and present a strong differentiation linked to their geodiversity. Numerous detailed studies on Pocket Beaches have been carried out in recent years (Pranzini, 2013; Klein, 2002; Bowman, 2009); they suggested that geometric physical parameters provide useful information for characterization of embayed coasts (Bowman, 2014).
These parameters allow to monitor coastal segments exposure to 1) the incident waves, 2) the response of the beaches to the big storms, 3) coastal and beach erosion and 4) nearshore morphological changes. However, these parameters are usually extracted from old dataset or from hazardous fieldworks (Bowman, 2009). Unmanned Aerial Vehicles (UAV) are photogrammetric platforms that operate autonomously, semi-autonomously or through a remote control and allow the acquisition of very high spatial resolution imageries. In addition, their ability of operating in hard-to-reach areas made UAV- photogrammetry, the cost-effective environmental survey technique. In this way, we propose a UAV- photogrammetry-based mapping approach to study the PBs located on the coast of Sicily.
We used drones equipped with very high-resolution camera to acquire orthophotos and 3-D representation of Sicilian PBs. The data obtained by UAVs has been supported by Ground Control Points (GCPs) acquired using RTK GPS which helped to refine their geo-referencing precision. Computer-assisted approach was adopted to retrieve information on geometric parameters and eventually coastal geomorphological elements of the PBs.
This study is the first geomorphological approach, conducted in the framework of the BESS project - Pocket Beach Management and Remote Surveillance System Project (BESS) (Figure 1), following other propaedeutic scientific contributions focused about: 1) the use of multispectral satellite image to explore shallow water bathymetry (Randazzo et al., 2020 and Muzirafuti et al., 2020), 2) the interaction between Posidonia o. and PBs evolution (Tomasello et al., 2020) and 3) the implementation of WebGIS Implementation for Dynamic Mapping Visualization (Randazzo et al., 2021).

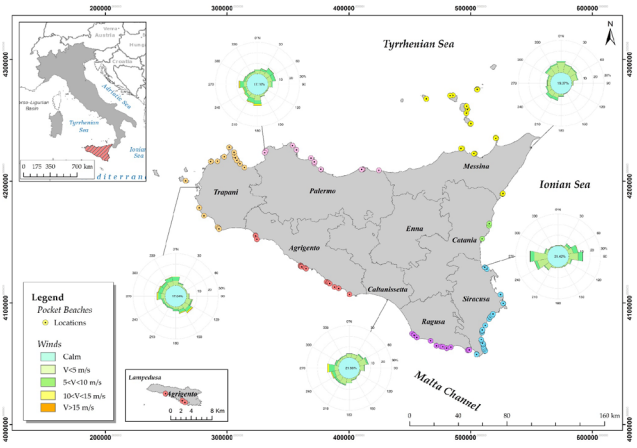

Figure 1. Map showing the locations of 117 pocket beaches (PBs) belonging the 8 coastal provinces of Agrigento, Caltanissetta, Catania, Messina, Palermo, Ragusa, Siracusa and

* Corresponding author

Trapani. in the BESS project 132 were studied, including the 15 placed between Malta and Gozo.

In the BESS project all Sicilian and Maltese PBs have been studied. The paper aims at presenting a methodological approach actually applied on Sicilian PBs, but which could be adopted for a regular monitoring of the whole Sicilian coastal area (Randazzo & Lanza, 2020).

2. MATERIAL AND METHODS

2.1 Data acquisition

Two major campaigns were carried out during the acquisition of the data analysed by BESS project. The first survey has been conducted in the spring/summer season of 2019. Due to the restrictions related to the Covid-19, the second survey has been carried out in the autumn/winter season of 2019/2020 and in the autumn winter season of 2020/2021. The surveys involved all the Sicilian and Maltese Pocket Beaches, except for the PBs located in areas close to airports where high spatial resolution satellite images (WorldView-2/3) (Ye, 2017) were used.

The surveys were carried out using different UAVs such as DJI Mavic 2 Pro, Matrices 210 RTK and the Matrice 600 Pro equipped with optical sensors (Figure 2a). To acquire images, the surveys were carried out from an acquisition altitude of about 65 m with camera at Nadir angle view. Image frames were taken, with an overlap between successive frames equal to 75% on the horizontal and 75% on the vertical. To improve the positioning accuracy of images, for each survey, GCPs were acquired and used for georeferencing purpose.

GCPs coordinates were acquired using the Topcon Hyper HR Base Rover satellite acquisition system. This system is composed of a BASE and ROVER differential GPS in RTK (Real Time Kinematic) mode (Figure 2b). The reference system used for the acquisition of the GCPS was the WGS84 UTM 33 N (EPSG 32633). During GCPs acquisition, localization accuracy per GCP was set to 0.02 m. In addition, measures were taken, to reduce the mean errors in the three coordinate directions, by recording the value provided by high number satellites.

Figure 2. Example of AUV used for acquisition of the data Matrix 600 (a) and the Topcon Hyper HR Base-Rover satellite acquisition system used for GCPs data acquisition (B).

In average, 39 hours 29 minutes and 11 seconds were used during the second photogrammetry survey for 109 PBs located on 7 provinces of Sicily. With the longest flight lasting 2h 6 min 53 sec while the shortest flight lasted 5 min 3 sec.

2.2 Dataset creation

Images acquired during the surveys were processed using the Pix4D Mapper software. This software allows to integrate aerial images and CGPs to generate very high spatial resolution georeferenced orthophotos, Digital Surface Model (DSM) and Digital Elevation Model (DEM). The process involves five steps including a) importing the images; b) identification of clearly recognizable points in the various frames; c) correlation between homologous points during the matching phase; d) bundle-adjustment processing; and after inserting the GCPs, e) the generation of very high-resolution spatial (up to 1.5 cm) georeferenced orthophotos and DSM (Figure 3).

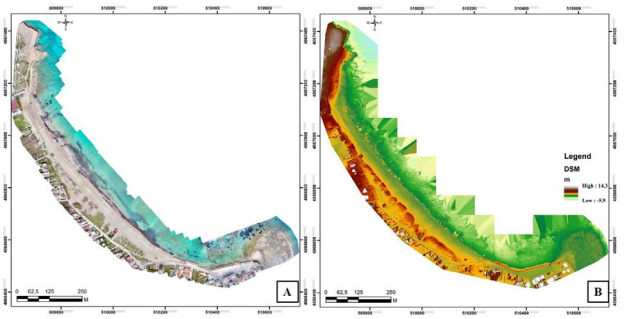

Figure 3. Example of orthophoto and Digital Surface Model (DSM) obtained from the survey conducted on the PB of Noto-Fondo Morte (Siracusa) within the project with the label SIC76SR09.

In total, 1258 GCPs were acquired for accessible 90 PBs located on the coast of seven provinces of Sicily. For Messina province 258 GCPs were used acquired, the highest number of GCPs was acquired on the coast of Siracusa (318 GCPs) while the small number was acquired on 2 PBs of Catania (22 GCPs). For the provinces of Agrigento, Palermo, Ragusa and Trapani, 48, 122, 268 and 222 GCPs were acquired respectively.

Integration of GCPs in images processing plays an important role for dataset georeferencing evaluation. They allow to evaluate the absolute position uncertainty, which is in our case up to 4 cm of precision, and eventually georeferencing precision accuracy of the dataset where the average range of mean RMS error is estimated at 0.01 to 0.1 m.

2.3 Data processing

While UAV- photogrammetry technique was used to acquire very high-resolution spatial (up to 1.5 cm) georeferenced orthophotos and DEM, computer-assisted approach was adopted for their analysis. It is important to note that very high-resolution spatial orthophotos and DEM consume a lot of processing power. In this way, we use high performing hardware and sophisticated software to retrieve information on geometric parameters and eventually coastal geomorphological elements of the PBs. We used 3 desktop computers with Intel(R) Xeon(R) CPU E5-1620 v4, 3.50 GHz processor and 32,0 GB of Random-Access Memory (RAM) and ArcGIS 10.2 software to process the data. The following geometric parameters (Bowman, 2014) were extracted from the dataset:

Ro is the rope between the two headlands, defining the PB [m];
S1 is the length of the embedding [m]
S2 is the length of the beach itself [m];
S3 is the linear distance of the segment stretched between the limits of the beach [m];
S2p represents the maximum beach width;
Sp beach surface [m^2];
a represents the indentation, so the perpendicular distance [m] between the midpoint of **Ro** and **S1**;
am represents the distance between the midpoint of Ro and the widest sector of the beach.

To guarantee the precision of retrieve information, manual digitization approach has been adopted and used. Retrieved

information were represented on maps (Figure 4). These are parameters which are mainly involved in the computation of indentation index, embaymentization index and the bay filling index (Bowman, 2014). They are crucial for classification and characterisation of PBs, but we also considered 1) the closure depth in terms of position: if external, internal or on the rope, 2) the geological characteristics of the headlands and 3) the dominating wind.

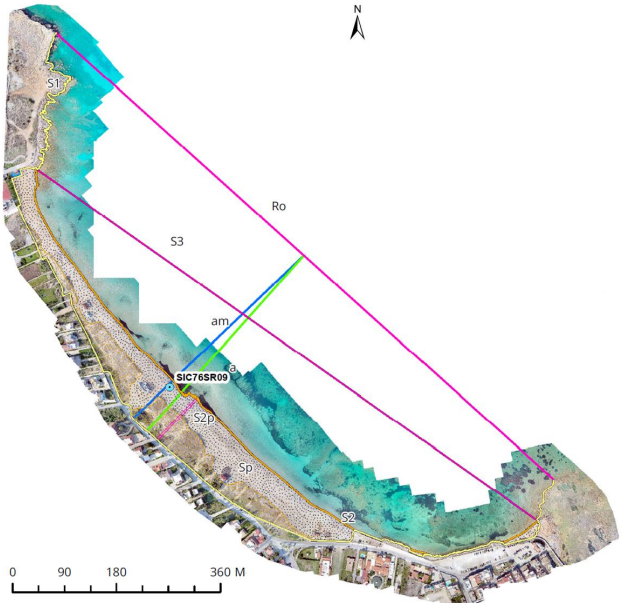

Figure 4. Plainview of the geometric parameters obtained from orthophoto of the survey conducted on a PB (in this case Noto-Fondo Morte Siracusa individuated).

3. RESULTS AND DISCCUSIONS

For the 117 PBs located on the coast of Sicily, we present the statistical summary including the range of geometric parameters and their corresponding number of PBs. While 2 campaigns were conducted during the BESS project, here the results of analysis of the second survey are presented. The results show that:

- **Ro** has an average high values varying between 2188 and 504 m representing 21 PBs; the average mean values vary between 497 and 200 m representing 50 PBs, the average low values vary between 196 and 27 m, representing 33 PBs; while the highest and lowest values are 4349 and 19 m for the PB of Modica-Maganuco and the PB of Santa Flavia Porto di Spagna respectively.
- **(S1)** has an average high values varying between 3287 and 977 m representing 26 PBs, the average mean values vary between 970 and 366 m representing 57 PBs, the average low values vary between 360 and 113 m representing 30 PBs; while the highest and lowest values are 5548 and 99 m for the PB of Modica-Maganuco and the PB of Custunaci Agliareddi respectively.
- **(S2)** has an average high values varying between 1598 and 307 m representing 35 PBs, the average mean values vary between 297 and 121 m representing 43 PBs, the average low values vary between 119 and 35 m representing 35 PBs; while the highest and lowest values are 1,919 and 11 m for the PB of Scicli-Sampieri Fornace Penna and the PB of Mazara-Torretta Granitola (North) respectively. **(S2p)** is not significative at this point.
- **(S3)** has an average high values varying between 1379 and 402 m representing 24 PBs, the average mean values vary between 309 and 109 m representing 59 PBs, the average low values vary between 107 and 20 m representing 30 PBs; while the highest and lowest values are 1770 and 11 m for the PB of Scicli-Sampieri Fornace Penna and the PB of Mazara-Torretta Granitola (North) respectively.
- **(Sp)** has an average high values vary between 70,002 and 10,179 m^2 representing 31 PBs, the average mean values vary between 9,809 and 1,006 m^2 representing 62 PBs, the average low values vary between 840 and 58 m^2 representing 20 PBs; while the highest and lowest values are 78061 and 33 m^2 for the PB of Scicli-Sampieri Fornace Penna and the PB of Mazara-Torretta Granitola (North) respectively.
- **(a)** has an average high value varying between 720 and 304 m representing 16 PBs, the average mean values vary between 286 and 86 m representing 67 PBs, the average low values vary between 82 and 21 m representing 31 PBs; while the highest and lowest values are 788 and 16 m for the PB of Siracusa-Fontane Bianche (North) and the PB of Panarea Preistorico respectively. **(am)** follows the same pattern.

These values, taken together, do not give us the possibility of arriving at a clear explanation. For this reason, we have selected the most identifying ones, from the geomorphological point of view, like the rope and the arrow and we have observed them, according to their different geological context.

In fact, it is important to underline that Sicily represents an extraordinary index of differentiation from the geological point of view (GEODIVERSITY) which is reflected into the coastal features (Lanza & Randazzo, 2011; 2013). In this paper we try to relate the shape of the PBs in function of the prevalent lithologies outcropping around them. Trying to simplify, we identified: 1) igneous rocks belonging the Etna Volcano (Catania) and the Aeolian Islands, 2) metamorphic rocks present in the western province of Messina, 3) flysch and clayey series outcropping in the eastern province of Messina, east of Palermo and in an area between Trapani and Agrigento, 4) hard limestones into both the Iblean Plateau (Siracusa and Ragusa) and the Mountains of Trapani (including part of the territory of Palermo), 5) soft limestones (prevalently marles) of the provinces of Agrigento, and finally 6) the sedimentary deposits of the Caltanissetta coastline.

To further have another two control keys we introduce the wind dominance in five different sectors around the island coastline and finally we consider the position of the closure depth of each single Pocket Beach.

The relationship between headland spacing **(Ro)** and bay indentation **(a)** has been evaluated for the PBs located in different geological settings (Figure 5).

For each group of PBs the location of the Closure depth (Cd) has been determined: 1) inshore from both headlands, 2) offshore from one headland and 3) offshore from both headlands.

Its locations allow to classify the PBs in three categories:

- Closed: for the Cd located inshore from both headlands
- Semi-closed: for the Cd located offshore from one headland
- Open: for the Cd located offshore from both headlands.

The results reveal that, many PBs located in hard limestones settings are open with headland spacing varies between 50 and 550 m. For those located in soft limestones, this number increases with a mix of open and semi-closed PBs. Many mixed closed and semi-closed PBs is in igneous rocks. Sedimentary deposits, metamorphic rocks, flysch and clayey series each hold a small number of semi-closed and closed PBs (Figure 5).

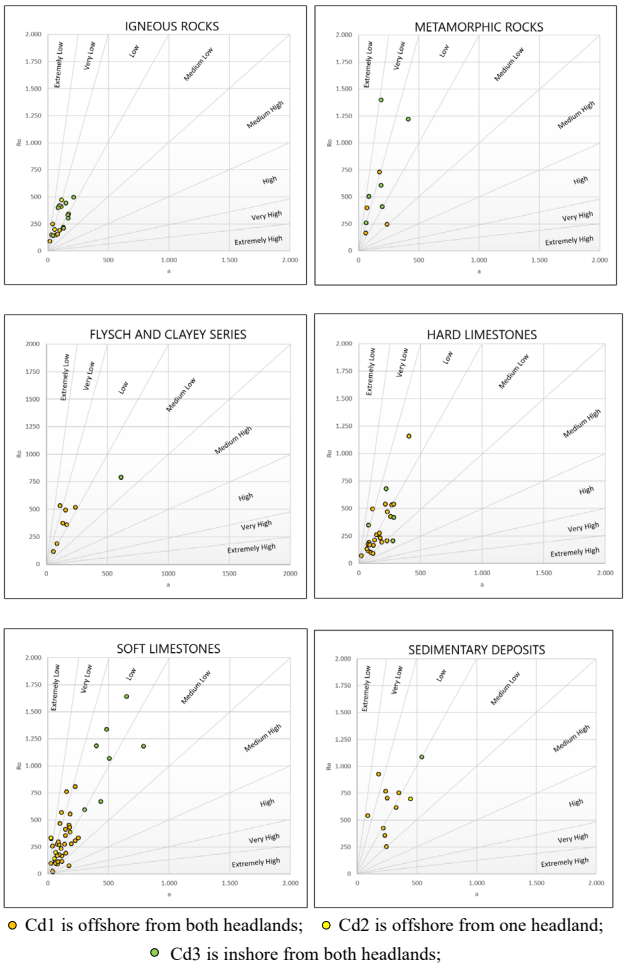

Figure 5. Evaluation of embayment of the PBs located in different geological settings based on headland spacing **(Ro)** and bay indentation **(a).**

The results indicate that the proposed methodology provide updated and precise information on the shape and the size of the PBs.

4. CONCLUSIONS

In this study, UAV- photogrammetry-based mapping technique is used to acquire very high-spatial resolution imageries of the PBs locate d on the coast of Sicily. The UAV- photogrammetry-based mapping allows for the creation of very detailed and updated high resolution imageries adapted for small changes evolution analysis. The acquired imageries are analysed using computer-assisted approach which allows for extraction of very precise extraction of geomorphological parameters information.
The proposed methodology can be used for regular monitoring of standard beach areas.
For the future study, information obtained, in this study, will be involved in the computation of indentation index, embaymentization index and the bay filling index needed for the classification and characterisation of PBs of Sicily.

REFERENCES

Bowman, D., Rosas, V., Pranzini, E., 2014. Pocket beaches of Elba Island (Italy)—Planview geometry, depth of closure and sediment dispersal. *Estuarine Coastal Shelf Sci*ence vol. 138, pp. 37–46.

Bowman, D., Guillen, J., Lopez, L., Pellegrino, V., 2009. Planview Geometry and morphological characteristics of pocket beaches on the Catalan coast (Spain*). Geomorphology*, vol. 108, pp. 191–199.

Eugenio, F., Martin, J., Marcello, J., Bermejo, J.A. 2013. Worldview-2 high resolution remote sensing image processing for the monitoring of coastal areas. 21st European Signal Processing Conference, 9–13 Sept., Marrakech, Morocco, 1–5.

Klein, A.H.F., Filho, L.B., Schumacher, D.H., 2002. Short-term beach rotation processes in distinct headland bay beach systems. *Journal of Coastal Research*, Vol. 18, pp. 442-458.

Lanza, S., Randazzo G., 2011. Improvements to a Coastal Management Plan in Sicily (Italy): new approaches to borrow sediment management. Journal of Coastal Research, SI 64 1357 – 1361.

Lanza, S., Randazzo G., 2013. Tourist-beach protection in north-eastern Sicily (Italy). Journal of Coastal Conservation, 17,1, 49-57.

Muzirafuti, A., Barreca G., Crupi A., Faina G., Paltrinieri D., Lanza S., Randazzo G., 2020. The Contribution of Multispectral Satellite Image to Shallow Water Bathymetry Mapping on the Coast of Misano Adriatico, Italy. Journal Marine Science and Engineering, 8, 126, pp 1- 21.

Pranzini, E., Rosas, V., Jackson, N.L., Nordstrom, K.F., 2013. Beach Changes due to sediment delivered by streams to pocket beaches during a major flood", *Geomorphology*, vol. 199, pp. 36–47.

Randazzo, G., Lanza, S., 2020. Regional Plan against Coastal Erosion: A Conceptual Model for Sicily. *Land*, Vol. 9, pp. 307.

Randazzo, G., Barreca, G., Cascio, M., Crupi, A., Fontana, M., Gregorio, F., Lanza, S., Muzirafuti, A., 2020. Analysis of Very High Spatial Resolution Images for Automatic Shoreline Extraction and Satellite-Derived Bathymetry Mapping. *Geosciences*, Vol. 10, pp. 172.

Randazzo, G., Cascio, M., Fontana, M., Gregorio, F., Lanza, S., Muzirafuti, A., 2021. Mapping of Sicilian Pocket Beaches Land Use/Land Cover with Sentinel-2 Imagery: A Case study of Messina Province. *Land*, Vol. 10, pp. 678.

Randazzo, G., Italiano F., Micallef A., Tomasello Ag., Zammit A., D'Amico S., Saliba O., Cascio M., Cavallaro F., Crupi A., Fontana M., Gregorio F., Lanza S., Muzirafuti A., 2021. WebGIS Implementation for Dynamic Mapping and Visualization of Coastal Geospatial Data: A Case study of BESS Project. International Journal of Geo-Information.

Tomasello, A., Cassetti F.P., Savona A., Pampalone V., Pirrotta M., Calvo S., Signa G., Andolina C., Mazzola A., Vizzini S., Muzirafuti A., Lanza S., Randazzo G., 2020. The use of very high-resolution images for studying Posidonia oceanica reefs. Vie et milieu - Life and environment, 70 (3-4): 25-35.

Ye, B., Tian, S., Ge, J., Sun, Y., 2017. Assessment of WorldView-3 Data for Lithological Mapping. *Remote Sensing*, vol. 9, pp.1132.

EXPLOITATION OF IMAGING SPECTROSCOPY DATA FROM PRISMA AND DESIS FOR WATER QUALITY MAPPING

C. Giardino*, M. Bresciani, A. Fabbretto, S. Mangano

Institute for Electromagnetic Sensing of the Environment, National Research Council of Italy (CNR-IREA), 20133 Milan, Italy - (giardino.c, bresciani.m, fabbretto.a, mangano.m)@irea.cnr.it

KEY WORDS: satellite products, validation, aquatic ecosystems, hyperspectral

ABSTRACT:

This study presents a first exploitation of imagery data acquired by the current hyperspectral satellite sensors PRISMA and DESIS for water quality applications. In particular, a general description of the two missions, respectively developed by the Italian and German space agencies, is initially provided for presenting the main features of the sensors. The standard Level 1 (L1) and Level 2 (L2) products acquired by both sensors are then presented for their support for water quality retrieval. A preliminary analysis on the estimation of signal-to-noise ratio (SNR) from L1 products over open waters is indicating SNR, apart at short wavelengths where imagery data showed a lower value, is comparable with Sentinel-2 MSI values. A variety of L2 products for inland and coastal waters are then presented in terms of remote sensing reflectance (Rrs, in sr^{-1} units) in view of aquatic ecosystem mapping. The analysis, which is also supported by *in situ* reference data, overall indicates that even if some applications might be developed with the standard L2 PRISMA and DESIS products, an ad-hoc processing might be necessary to include the specific requirements of atmospheric correction of water targets, especially in clear marine waters. Satellite imaging spectroscopy products are also comparable to synergic multispectral missions (e.g. Sentinel-2 MSI, Sentinel-3 OLCI); this finding is promising to meet spectral, temporal and spatial requirements typical for aquatic ecosystems applications.

1. INTRODUCTION

Satellite imaging spectroscopy is one of the fastest growing research areas in remote sensing owing to its diagnostic power by means of discrete spectral bands that are contiguously sampled over the spectral range with which a target is observed data. The sensor technique has been first used in airborne imaging spectroscopy since the early 1980s and later in spaceborne hyperspectral missions from the end of the 1990s onwards (Rast and Painter, 2019). Such technical progress obviously allowed several environmental applications to be developed. For the specific case of aquatic ecosystems several examples on spaceborne hyperspectral applications have been developed with Hyperion (e.g. Kutser, 2004), HICO (e.g. Garcia et al., 2014), CHRIS (e.g. Casal et al., 2011) and more recently with DESIS and PRISMA (Giardino et al., 2020). Although not specially designed to capture the generally low radiances of waters, imagery data gathered from these sensors potentially allow the optical properties of water column and bottom to be finely characterised. To the aim it is relevant to both characterise the top-of-atmosphere signal (typically delivered as Level 1 product) and the reflectance at the ground, which is the result of the correction for the light scattered or absorbed by the atmosphere plus second order radiometric effects (e.g. adjacency). The qualification of ground reflectance, usually delivered as Level 2, is also a key step for the retrieval and monitoring of geophysical, geo-biophysical, and geo-biochemical parameters.

The aim of this study is to extend the qualification of Level 1 PRISMA products from Giardino et al. (2020) to quantify the signal to noise ratio (SNR) of Level 1 products. Then, first examples on qualification of Level 2 products from PRISMA and DESIS are presented by comparing satellite data to *in situ* measurements acquired in both inland and coastal waters. Moreover, Recognising the role of Copernicus (e.g. Sentinel-2 MSI and Sentinel-3 OLCI) for inland and coastal waters applications, concurrent multispectral observations were added to the comparison.

2. MATERIALS AND METHOS

2.1 PRISMA and DESIS

PRISMA, a mission fully funded by Italian Space Agency (ASI), is an Earth Observation (EO) system with innovative, electro-optical instrumentation that combine a hyperspectral sensor with a medium- resolution panchromatic camera. The PRISMA orbit is characterized by a repeat cycle of approximately 29 days. Although the revisit time in nadir-looking configuration is of 29 days, the system is capable of acquiring images distant 1000km in a single pass (with a total rotation left to right side looking and vice versa) so that the temporal resolution can be significantly improved. The PRISMA Payload is composed by an Imaging Spectrometer (or Hyperspectral Imager), able to take images at 30 m resolution in a continuum of spectral bands ranging from 400 to 2500 nm, and a 5 m resolution Panchromatic Camera. The PRISMA system provides the capability to acquire, downlink and archive images for about 200,000 km^2 daily over the primary area of interest defined as: longitude in the range 180°W - 180°E; latitude: in the range 70°S - 70°N (Candela et al., 2016). The main specifications of PRISMA are shown in Table 1.

DESIS is a hyperspectral instrument integrated in the Multi-User-System for Earth Sensing (MUSES) platform installed on the International Space Station (ISS). The mission is operated by Teledyne Brown Engineering (TBE), Alabama, USA, and the German Aerospace Center (DLR), Germany. DESIS is realized as a pushbroom imaging spectrometer spectrally sensitive over the VNIR range from 400 to 1000 nm with a spectral sampling distance of 2.55 nm (Alonso et al., 2019). The launch of DESIS to ISS was on June, 29th 2018. The commissioning and validation phases were finished in March

* Corresponding author

2019. DESIS is now working operationally and will continue at least until the end of 2023. The main specifications of DESIS (https://www.dlr.de/eoc/desktopdefault.aspx/tabid-13614) instruments) are shown in Table 1.

Table 1. Main specifications of PRISMA and DESIS.

Item	PRISMA	DESIS
Launch	22 March 2019	29 June 2018
Coverage	70° N to 70° S	55° N to 52° S
Target lifetime	5 years	2018-2023
Orbit	SSO 615 km 10:30 LTDN	MUSES platform on ISS
Number of bands	VNIR: 66 (440-1010 nm), SWIR: 174 (920-2505 nm), PAN: 1 (400-700)	235 (no binning), 118 (binning 2), 79 (binning 3), 60 (binning 4)
Spectral coverage	440 nm to 2505 nm	402 nm to 1000 nm
Ground sampling distance	Hyperspectral: 30 m, PAN: 5 m	30 m
Signal-to-Noise ratio	>160:1 VNIR, >100:1 SWIR, >240:1 PAN	195 (w/o binning), 386 (4 binning) (based on laboratory calibration) (albedo 0.3 @ 550 nm)
Radiometric resolution	12 bits	13 bits + 1 bit gain
Swath	30 km	30 km

For the purposes of this study a series of PRISMA and DESIS products have been downloaded from the two space agencies' portals according to the following processing levels:

- PRISMA Level 1 (L1): TOA (Top-of-Atmosphere) radiometrically and geometrically calibrated HYP and PAN radiance images.
- PRISMA Level 2 (L2D): Geolocated and geocoded atmospherically corrected HYP and PAN images.
- DESIS Level 1 (L1C): Georeferenced and Resampled Product.
- DESIS Level 2 (L2A): Atmospheric Compensated Product.

The products have been tasked and searched based on the availability of corresponding match-ups of in *in situ* data and synergic multispectral observations (e.g. Sentinel-2); the latter not described in Section 2 for sake of brevity.
The L1 and L1C products were analysed to compute the SNR values of PRISMA and DESIS respectively as in Wettle et al. (2004). The L2D and L2A were plotted with corresponding measurements gathered from *in situ* data and for corresponding spectra obtained from Sentinel-2 and Sentinel-3. To evaluate the comparison the common statics were used (i.e. Root Mean Square Errore (RMSE), Spectral Angle (SA), and square of the coefficient of correlation (R2)).

2.2 In situ data

Figure 1 shows the geographic distribution of locations providing *in situ* data to be compared with PRISMA and DESIS. The sites are distributed globally and cover a wide range of turbidity and trophic conditions of inland and coastal waters.
For each site, *in situ* measurements of water reflectance were gathered from AERONET-OC during the overpass of PRISMA. AERONET-OC is instrumental in satellite ocean colour validation activities through standardized measurements performed at different sites with a single measuring system and protocol, calibrated with an identical reference source and method, and processed with the same code (Zibordi et al., 2004). In recent years, AERONET-OC has also supported the radiometric characterization of Landsat-8, Sentinel-2 and PRISMA for aquatic applications (Ilori et al., 2019; Giardino et al., 2020).

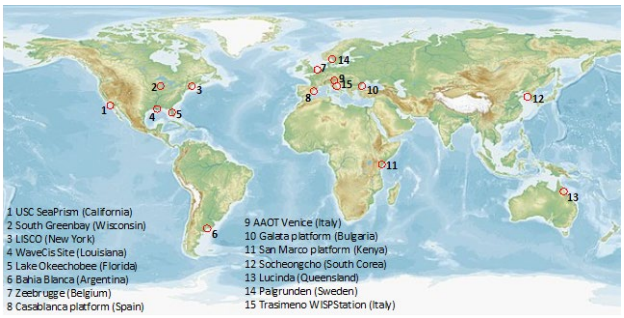

Figure 1. Location of *in situ* stations providing reference data to qualify L2 products; all stations are part of AERONET-OC save for site 15 (WISPStation).

Within the sites distributed all over the globe, a check was carried out to select those which had synchronous measures with PRISMA acquisitions; for DESIS the work is so far limited to station 15; a total of 22 match-ups were totally found. The AERONET-OC data collected closer to the sensing time of satellite overpasses were transformed in above water remote sensing reflectance as described in Vanhellemont (2019); in case of WISPStation *in situ* data already provided values in Rrs units (Peters et al., 2018). An area corresponding to 3 by 3 pixels was used to extract Rrs in correspondence of the *in situ* stations.

3. RESULTS

Figure 2 shows the SNR computation representative of water surfaces for both PRISMA and DESIS. Overall values from the two missions are similar and comparable to the SNRs computed from Pahlevan et al. (2017) for Sentinel-2 over waters.

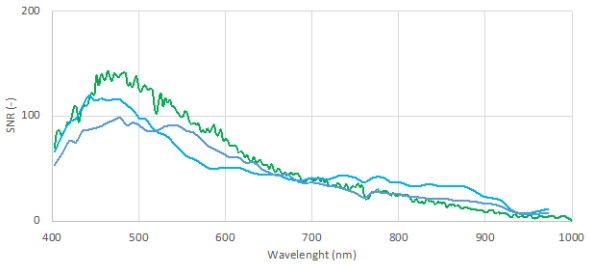

Figure 2. SNR values corresponding to TOA radiances from PRISMA (blue) and DESIS (green), for Sun zenith angles varying from 25° to 36°.

Figures 3, 4 and 5 shows examples of the comparison of Level 2 products and ancillary measurements used as reference. In particular:

- Figure 3 shows the comparison of PRISMA L2D and a subset of AERONET-OC data; overall there is a good match-ups apart the cases in which the spectral signature is preserved but there is a difference of about 0.01 sr^{-1} in terms of magnitude (e.g. South-Greenbay, SanMarco platform). In some cases (e.g. Lucinda, AAOT Venise) neither the spectral shape and the magnitude are comparable.
- Figure 4 shows a comparison of DESIS L2A products with corresponding WISPStation data from which it can be argued the good corresponde both in terms of shape and magnitude.
- Figure 5 shows an exmaples of DESIS L2A when compared to data gathered from other multispectral

missions such as Sentinel-2 and Sentinel-3, whose value is essential in water quality remote sensing (e.g. Pahlevan et al., 2020).

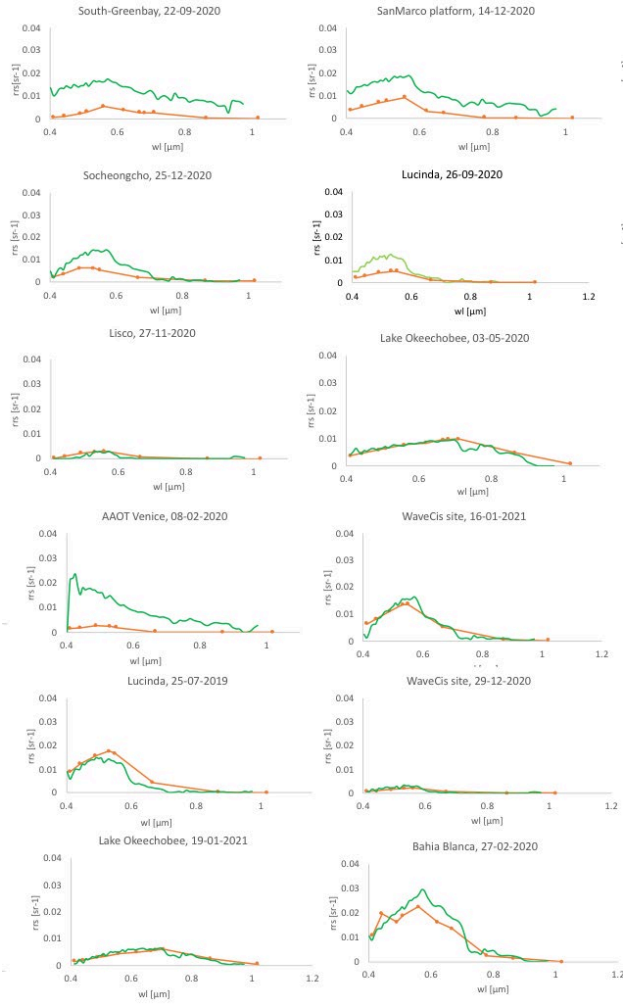

Figure 3. L2D spectra measured by PRISMA (green lines) and corresponding *in situ* data (orange) for a subset of AERONET-OC sites (cf. Fig. 1).

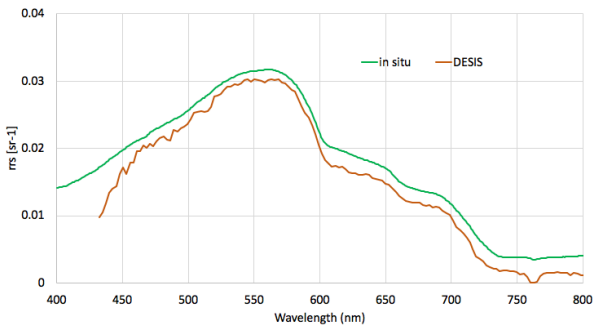

Figure 4. L2A spectra measured by DESIS (green lines) and corresponding *in situ* data (orange) from the WISPStation in Lake Trasimeno (cf. Fig. 1).

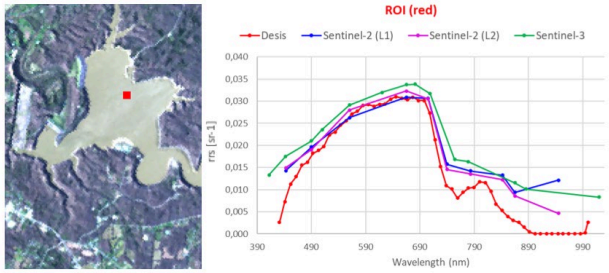

Figure 5. Comparison of DESIS L2A products with Sentinel-2 MSI and Sentinel-3 OLCI for Lake Harsha, USA (not reported in Fig. 1 because there are no *in situ* data as reference).

The overall match-ups between PRIMSA and *in situ* data is given in Table 4, while for DESIS the work is in progress to obtain a higher number of match-ups for computing the statistics.

Table 4. Statistical analysis of comparison between PRISMA vs *in situ*, Sentinel-2 MSI and Sentinel-3 OLCI.

	PRISMA vs in situ			
	R^2	RMSE	SA	N
L1	0.98	0.9-4.7 ($mWm^{-2}sr^{-1}nm^{-1}$)	0.8-3.4	9
L2D	0.81	0.0012-0.0093 (sr-1)	11-26	21

	PRISMA vs Sentinel-2		PRISMA vs Sentinel-3	
	R^2	RMSE	R^2	RMSE
L1	0.97	0.1-6.5 ($mWm^{-2}sr^{-1}nm^{-1}$)	0.98	0.8-5.4 ($mWm^{-2}sr^{-1}nm^{-1}$)
L2D	0.79	0.0013-0.0117 (sr-1)	0.80	0.0012-0.0110 (sr-1)

4. CONCLUSIONS

This study reports a first qualification of PRISMA and DESIS products water applications. In particular recent findings from Giardino et al. (2020) on PRISMA L1 products have been extended to compute the SNRs of both sensors. Since the average values of SNRs of PRISMA and DESIS are comparable to Sentinel-2 MSI water-related applications seems feasible with both missions. For Level 2 data, even if major efforts have been so far dedicated to PRISMA, the products in terms of Rrs seems of both PRISMA and DESIS resulted comparable to both *in situ* and satellite data from synergic missions.

ACKNOWLEDGEMENTS

This works would have not been possible without the support of PIs of AERONET-OC and of Water Insight for WISPStation. We are grateful to Andrea Pellegrini for his valuable support in PRISMA data processing. ASI and DLR are acknowledged for providing PRISMA and DESIS imagery respectively. This study was co-funded by EU Horizon 2020 projects PrimeWater (grant nr. 870497) and EOMORES (grant nr. 730066) and by the Italian Space Agency (ASI) with PRISCAV (grant nr. 2019-5-HH.0) project.

REFERENCES

Alonso, K., Bachmann, M., Burch, K., Carmona, E., Cerra, D., de los Reyes, R., Dietrich, D., Heiden, U., Holderlin, A., Ickes, J., et al., 2019. Data products, quality and validation of the DLR Earth Sensing Imaging Spectrometer (DESIS). *Sensors*, 19, pp. 4471

Candela, L., Formaro, R., Guarini, R., Loizzo, R., Longo, F., Varacalli, G., 2016. *The PRISMA Mission*. In Proceedings of the 2016 IEEE International Geoscience and Remote Sensing Symposium (IGARSS), Beijing, China, 10–15 July 2016, pp. 253–256

Casal, G., Kutser, T., Dominguez-Gomez, J.A., Sanchez-Carnero, N., Freire, J., 2011. Mapping benthic macroalgal communities in the coastal zone using CHRIS-PROBA mode 2 images. *Estuar. Coast. Shelf Sci.*, 94, pp. 281–290

Garcia, R.A., Fearns, P.R.C.S., McKinna, L.I.W., 2014. Detecting trend and seasonal changes in bathymetry derived from HICO imagery: A case study of Shark Bay, Western Australia. *Remote Sensing of Environment*, 147C, pp. 186–205

Giardino, C., Bresciani, M., Braga, F., Fabbretto, A., Ghirardi, N., Pepe, M., ... & Brando, V.E., 2020. First Evaluation of PRISMA Level 1 Data for Water Applications. *Sensors*, 20(16), pp. 4553

Ilori, C., Pahlevan, N., Knudby, A., 2019. Analyzing Performances of Different Atmospheric Correction Techniques for Landsat 8: Application for Coastal Remote Sensing. *Remote Sens*ing, 11, pp. 469

Kutser, T., 2004. Quantitative detection of chlorophyll in cyanobacterial blooms by satellite remote sensing. *Limnol. Oceanogr.*, 49, pp. 2179–2189d

Pahlevan, N., Smith, B., Schalles, J., Binding, C., Cao, Z., Ma, R., ... & Stumpf, R., 2020. Seamless retrievals of chlorophyll-a from Sentinel-2 (MSI) and Sentinel-3 (OLCI) in inland and coastal waters: A machine-learning approach. *Remote Sensing of Environment*, 240, pp. 111604

Peters, S., Laanen, M., Groetsch, P., Ghezehegn, S., Poser, K., Hommersom, A., De Reus, E., Spaias, L., 2018. *WISPStation: A new autonomous above water radiometer system.* In Proceedings of the Ocean Optics XXIV Conference, Dubrovnik, Croatia, 7–12 October 2018

Rast, M., Painter, T.H., 2019. Earth observation imaging spectroscopy for terrestrial systems: an overview of its history, techniques, and applications of its missions. *Surv. Geophys*., 40, pp. 303–331

Vanhellemont, K., 2019. Adaptation of the dark spectrum fitting atmospheric correction for aquatic applications of the Landsat and Sentinel-2 archives. *Remote Sens. Environ*., 225, pp. 175–192

Wettle, M., Brando, V.E., & Dekker, A.G., 2004. A methodology for retrieval of environmental noise equivalent spectra applied to four Hyperion scenes of the same tropical coral reef. *Remote Sensing of Environment*, 93(1-2), pp. 188-197

Zibordi, G., Melin, F., Hooker, S.B., D'Alimonte, D., Holben, B., 2004. An autonomous above-water system for the validation of ocean color radiance data. *IEEE Trans. Geosc. Rem. Sens.*, 42, pp. 401–415

SAR SMALL SATELLITE CONSTELLATIONS: ADDED VALUE VS. EXISTING EARTH OBSERVATION SPACE SYSTEM

V. Mastroddi, L. Soli *, C. Ciancarelli, A. Nassisi, A. Intelisano

Thales Alenia Space, Via Saccomuro 24, 00131 Rome, Italy – (vanessa.mastroddi, luca.soli, carlo.ciancarelli, annamaria.nassisi, arturo.intelisano)@thalesaleniaspace.com

KEY WORDS: Small satellite, Earth Observation, SAR sensor, high revisit, constellations, critical infrastructure, emergency management

ABSTRACT:

Small satellites offer important advantages in creating new opportunities for implementing spatially-distributed space-based systems in Constellations. In this paper we focus on new emerging earth observation application and concepts, that can be used or are being used to create data collection systems via small satellites. The “complementarity” of small satellite constellations in term of revisit/coverage/resolution/band/responsiveness versus existing asset like Copernicus and Italian assets such as COSMO Sky-Med has been also investigated with the purpose to provide an improvement on emergency management, infrastructure monitoring and other domains, with a wider use of "space technology" and to offer solution closer to user needs also in term of further temporal resolution improvement. In particular, the focus of the Small SAT Constellation is on the need to improve revisit time, change detection and responsiveness, having heterogeneous on board sources (e.g. radar, optical) and supplying more quickly the information needed for the decision making process. A space mission embarking SAR instrument is capable of “all-weather” observations, sensing the Area day and night and imaging through clouds. These aspects identify small satellite as the perfect asset for a quick response after the occurring of a natural disaster/damage being able to grant the necessary information over the area of interest in any condition.

1. INTRODUCTION

Nowadays the request for an improvement of "services for emergency management" (crisis management) in different domains, with a wider use of "space technology", increases continuously. It is in fact universally recognized that, the prevention phase or the management of post-emergency phase of a crisis event cannot ignore the possibility of observing from space to know its precise location.

Small satellites constellation can provide an immediate impact in terms of added-value services to increase the national capacity to rapidly acquire information in response to a sudden crisis occurrence on various geographical scales (earthquakes, floods, morphological stability, devastation by multiple factors, fire, etc..).

This paper focuses in particular on the need to improve revisit time observation capability thanks to a distributed constellation of satellites to enable prompt reaction or quicker intervention than the current space system based on larger spacecraft. This can complement the Italian national high performance asset COSMO Sky-Med, for an effective answer to the National user needs.

The paper analyses the critical infrastructure use case highlighting the major user needs and the relevant results of the mission concepts.

2. OVERVIEW OF EXISTING ASSETS

Both SAR and Optical missions are envisaged to respond to the various needs using the complementarity of the different sensors, and investigating the possibility of data fusion.

The SAR mission is capable of “all-weather” observations, sensing the Area day and night and imaging through clouds. For these aspects it is identified an adequate asset for a quick response after the occurring of a natural disaster/damage, granting continuous information over the Area.

On the other hand the Optical mission has the advantage of sensing the environment with a process that is more similar to what our eyes see.

Several earth observation constellations, either institutional or commercial, optical and SAR, are already in orbit or planned in the next years.

Small SAR satellites devoted to commercial constellations have been recently launched also by new space actors, among these we mention as example: Capella space (US), Iceye (FIN) and Synspective (Japan). These new actors, proceeded with an incremental prototypal and business driven approach with the ambition to populate in the upcoming years constellations up to tens of small satellites to provide high revisit data. At present:

Iceye (FIN) (https://www.iceye.com) since 2018 has launched 14 small X band SAR satellites, at present twelve satellites seems still operative in orbit and capable to provide images within 5 days with a declared (http://https://www.iceye.com) revisit capability up to 36 hours. Iceye is planning to increase the constellation up to 18 satellites in the next years.

* Corresponding author

Capella space (US) (https://www.capellaspace.com/) has already operative in orbit 2 small X band SAR satellites, capable to provide images as commercial services. Cappella space is planning to increase the constellation up to 36 satellites in the next few years.

Synspective (JP) (https://synspective.com/) has already operative in orbit one small X band SAR satellite prototype named "Strix-α" and it is going to launch a second prototypenamed "StriX-β" scheduled on late 2021. It plans to increase its constellation up to 6 satellite within 2023.

Small Optical satellite for commercial constellation are more developed with respect to the SAR small satellite constellation; among these we can mention Planet labs a US new space company founded in 2010. At present Planet labs operates more than 200 satellites (of which 180 satellite are 3U cube sat of about 5,8kg) capable to provide high and medium resolution images by tasking commercial services with revisit up to few hours (limited by the light and weather conditions). Moreover, in US the Black-sky optical commercial small satellites constellation, plans to have 16 satellites in orbit in short term. The small satellites of Black-sky constellation are manufactured by Leostella US company which isa joint venture between Spaceflight Industries and Thales Alenia Space.

Other Large space companies are already able to provide optical and SAR very high resolution imaging thanks to larger satellite in constellations (e.g. the Maxar company US optical constellation, the European Airbus Intelligence constellation Optical and SAR, and as Thales Alenia Space as Space Alliance through e-GEOS by the Italian COSMO Sky-Med SAR constellation).

3. HIGH REVISIT CAPABILITY NEEDS AND END USER EXPECTATION

Critical infrastructure includes the vast network of highways, connecting bridges and tunnels, railways, utilities and critical buildings. Transportation, commerce, clean water and electricity all rely on these vital systems (https://www.dhs.gov/science-and-technology/critical-infrastructure).

Resilience in the context of **critical infrastructure** was first defined in 2009 as "the ability to absorb, adapt to, and/or rapidly recover from a potentially disruptive event" (National Infrastructure Advisory Council. Critical Infrastructure, 2009).

The European Programme for Critical Infrastructure Protection (EPCIP) is a framework including various measures cooperating to improve the protection of critical infrastructure in the EU. These measures include the establishment of the European Reference Network for Critical Infrastructure Protection (ERNCIP), coordinated by the JRC (*Joint Research Centre)*. Improving resilience of critical infrastructures has become a priority for the authorities around the globe (https://ec.europa.eu/jrc/en/research-topic/critical-infrastructure-protection).

The space systems has already demonstrated the effective contribution to increase the resilience of the critical infrastructures and can improve with the Small SAT Constellation by providing, with the proper timing, the necessary information in order to prevent or to manage potentially disruptive events.

Space-borne SAR technology offer the advantage to not be dependent from weather and light conditions and can assure information at any time the SAR satellites pass over the critical infrastructures.

Therefore, high revisit (up to few hours) SAR satellite constellations can support critical infrastructure for:

- Early warning detection
- Emergencies management
- Disaster Assessment
- Recovery.

It is to be mentioned that SAR satellites constellation can support also "routine monitoring" to detect and confirm dangerous anomalies on the critical infrastructure and on the related corridor area (i.e. third parts interferences, landslides, floods, heavy wet snow, etc…) by using change detection SAR interferometric methods with resolutions up to 1-3 meters. Space borne SAR technologies allow also displacement measures with accuracy up to few millimetres of the infrastructures (i.e. power towers, pipelines, bridges, railways etc..) or of the corridor terrain by proper temporal series analyses. All these capabilities can be very useful in particular for managing infrastructure located in very remote areas (like high mountains), with difficult of access for operators and not covered by GMS or other communication systems.

Extreme climate events are currently more frequent due to the climate changes (i.e. storms, tornadoes, floods, heavy or wet snow events) and represent a potentially disruptive event for critical infrastructures. Thanks to the meteorological alert systems it is possible to forecast in advance (12-48 hours) the critical events and the relevant geographical areas. In that case, an high revisit with Small SAT SAR constellation may schedule the observation 12-48 hours in advance to monitor all the specific critical infrastructural areas involved in the dangerous meteorological events. This capability makes the infrastructure operators aware of the status of integrity-warnings by the remote sensing information, that are useful to define the mitigation and recovery operations. The very low data latency (up to less than one hour) is a key aspect for this purpose.

In other cases for which the critical events cannot be forecast in advance (e.g. earthquakes, not forecastable landslides etc., because at present is not possible to represent them by physic function to determine the evolution), an high revisit SAR constellation allow to have a very fast responsiveness, thanks to acquisition of the area of interest in less than few hours after the event, to provide the disaster assessment and to support the emergency management operations.

Based on the above considerations a Small SAT SAR satellite high revisit constellation which support the critical infrastructures, shall be very flexible in term of:

- high system responsiveness: as capability to schedule observation in less than 2 hours from the request on the Area of Interest
- very low data latency: a data age less than 1 hour from the observation of the area of interest
- high revisit: 3 hours or better to monitor the area of interest
- capacity to monitor many critical areas of interest along a territory in case of several emergencies
- resolution: up to 1 meter in order to support the disaster assessment

- interferometric capacity. in order to support the change detection and displacement monitoring.

4. BENEFIT OF COMPLEMENTARITY W.R.T. THE CURRENT NATIONAL ASSETS

The selection of satellite orbit is strongly related to spacecraft mission and operations requirements.

Repeating ground track orbits are resonant with the Earth's rotation. They have the advantage that the satellite passes over the same location after a regular interval of time. The main advantage of a repeating ground track is the continuous sampling of the planet's surface on a repeating and regular basis. This feature is very useful for the assessment of changes on the area of interest with systematic observations.

Sun-synchronous (SSO) orbits keep the line of nodes of the satellite's orbit fixed relative to the Sun and they are able to provide global coverage at all latitudes with the only limitation to observe the same area always at the same local time, which could be valuable for some specific applications.

Orbit inclination (i) is used to orient the orbital plane and it is a measurement of the orbital plane's tilt relative to the equatorial plane. Specific inclinations can be chosen with the aim to obtain an increased view capability over an Area of Interest.

Moreover, orbits with a lower inclination angle (not polar or SSO orbits), can observe the same area with different local times and aspect angles (usually much larger than the SSO).

Therefore, depending on the purpose of a specific mission the more appropriate orbit and constellation are going to be defined.

The Italian radar satellite constellation COSMO Sky-Med, offers already a significant contribution to emergency management providing timely and accurate radar images as for example from flood mapping to earthquake damage assessment during a considerably high number of real emergency events see (Grandoni et al., 2014)

The COSMO Sky-Med four satellite constellation, which recently increased his capabilities with the new satellites of the Cosmo Second Generation (CSG), provides a full interferometric coverage @ 3m resolution in X band of the Italian territory every about two weeks by the so called "Map Italy" program. The constellation guarantees the passage over the Italian territory of the satellites twice in a day: at 6:00 UTC and at 18:00 UTC, and it is also able to provide very high sub-metric resolution radar imaging. The CSK system responsiveness in the emergency mode is 18 hours (https://earth.esa.int/web/eoportal/satellite-missions/c-missions/cosmo-skymed). Of course the access to the CSK constellation is regulated by institutional rules (https://earth.esa.int/web/eoportal/satellite-missions/c-missions/cosmo-skymed), and also E-Geos offer an emergency service (http://share.egeos-services.it/disaster-management.html).

Moreover it's to be mentioned also the Copernicus emergency management service, which leverage the Copernicus space asset capabilities (https://emergency.copernicus.eu/). **Copernicus EMS On Demand Mapping** provides on-demand detailed information for selected emergency situations that arise from natural or man-made disasters anywhere in the world. Users of this service can be entities and organisations at regional, national, European and international level and the data are available free of charge on routinely basis but not on demand services are foreseen.

A dedicated high revisit SAR satellite constellation can allow Italian entities, like the critical infrastructure operators, to easily access from the space the monitoring of infrastructures to increase their resilience.

The SAR Payload proposed for a mission of satellites' constellation dedicated to critical infrastructure is an X-band Synthetic Aperture Radar (SAR) based on an innovative antenna concept, to be easily embark-able on small spacecraft.

To respond to the user expectation for the critical infrastructure needs a small SAR satellite constellation with a deployment of 6 satellites to put in place for:

- obtaining systematic coverage
- improving the revisit time performance increasing the number of accesses w.r.t. the current national assets
- having the possibility of several constellation configurations for interferometry.

After a first analysis among all possible solutions for constellation configurations of six satellites, an equal distribution of two satellites over three orbital planes shows the highest improvement in terms of maximum and average revisit time. The SAR satellite is able to access on right and left side w.r.t. the flight direction with a range of access in term of incidence angle of 20°-60°. As it is possible to see in Figure 1 this configuration allows an average revisit time below 3.6 hours over the accessible area (which for the choose orbit is around ±60°) and it is important to highlight that it allows an average revisit time below 2.5 hours (see Figure 2) over the Europe and Mediterranean areas (that represent the Areas of Interest) in line with the user needs (section 3).

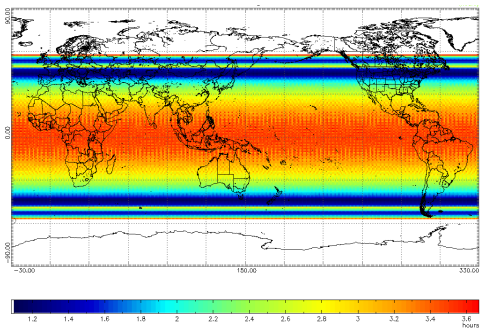

Figure 1. Average Revisit Time over the accessible area

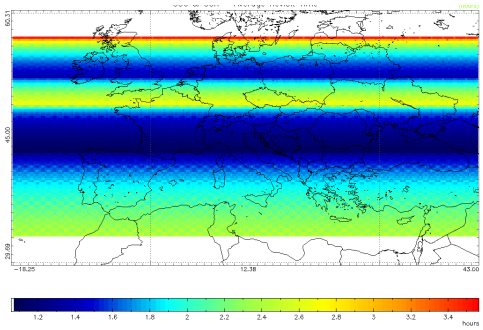

Figure 2. Average Revisit Time on European & Mediterranean areas

For the emergency management service the responsiveness of the whole system is a very important key aspect. For this performance is not only important the displacement of the space

segment but a crucial aspect is also the capability to task each satellite and the possibility to download the science data as soon as possible after the acquisition. Figure 3 shows the average system response time performance for the mentioned constellation. As it is possible to see over the European area the performance is below 12 hours. This value has been achieved considering the possibility to task the satellite 2 times during the day and using a network of downlink opportunities with about 27 minutes of contact time per orbit.

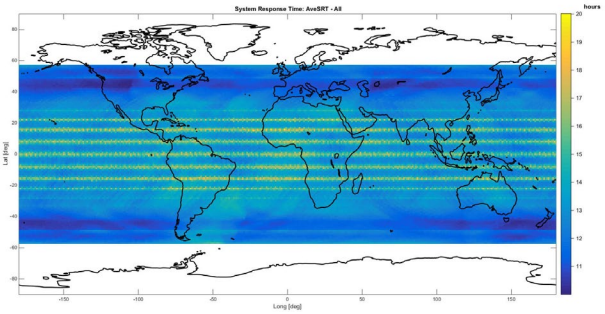

Figure 3. Average System Response Time Performance

The proposed Small SAR constellation + COSMO Sky-Med and Cosmo Second Generation can be used jointly to improve accessible area and revisit performance on a global scale. As shown in the following colorimetric maps the merge of the two constellations allow to achieve an average revisit time on Area Of Interest of ~ 1.5 hour by benefiting of both national assets and to better exploit the national investment.

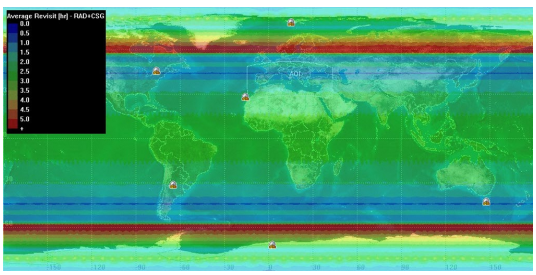

Figure 4. Small SAR constellation + COSMO Sky-Med Average revisit time on global scale

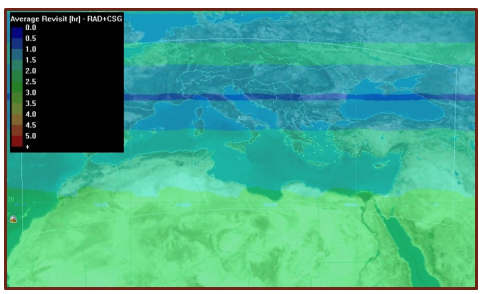

Figure 5. Small SAR constellation + COSMO Sky-Med Average revisit time zoom on Mediterranean area (Area of interest).

5. CONCLUSION

After an accurate analysis of main user needs for critical infrastructure applications, a preliminary mission analysis to complement COSMO Sky-Med mission through a small SAR satellite constellation has been proposed. The COSMO Sky-Med system is able to provide a worldwide accessibility thanks to the use of a SSO orbit, while the small SAR satellite constellation allows an improvement of the revisit time performance over the area of interest, taking benefit of the inclined orbit design to maximize the access on the European zone.

Thales Alenia Space, as System engineer of COSMO Sky-Med, has an a unique position to define the small SAR Satellite constellation which is able to provide different observation angle together with the capability to acquire with a different local time; with respect to the sensing of COSMO Sky-Med it enhances the field of potential application and the information content.

REFERENCES

Grandoni D., Battagliere M.L., Daraio M.G., Sacco P., Coletta A., Di Federico A., Mastracci F. - Space-Based Technology For Emergency Management: The COSMO-SkyMed Constellation Contribution. Procedia Technology 16 (2014) 858 – 866.

https://www.capellaspace.com/

https://www.dhs.gov/science-and-technology/critical-infrastructure

https://earth.esa.int/web/eoportal/satellite-missions/c-missions/cosmo-skymed

https://ec.europa.eu/jrc/en/research-topic/critical-infrastructure-protection

https://emergency.copernicus.eu/

https://www.iceye.com

http://share.egeos-services.it/disaster-management.html

https://synspective.com/

National Infrastructure Advisory Council. Critical Infrastructure Resilience Final Report and Recommendations, U.S. Department of Homeland Security, Washington, DC, 2009

SPACE ECONOMY AND EO SMALLSAT

A. Nassisi [1]*, P. Santoriello [2], A. Iovane [2], J. Canettieri [2], I. Patatti [3]

[1] Thales Alenia Space , Via Saccomuro 24, 00131 Rome, Italy (Annamaria.nassisi@thalesaleniaspace.com)

[2] Thales Alenia Space Internship (pietrosantoriello@gmail.com, alba.iovane@gmail.com, julian.canettieri@hotmail.it)

[3] ASI, Via del Politecnico, 00133 Roma, Italy (isabella.patatti@est.asi.it)

KEY WORDS: Space activities, creativity, diversity, Earth observation, Small Satellites

ABSTRACT:

During the last decades, the space arena is changing with new actors shaping new business modelling, and with the new space economy phenomenon calling for new commercial and economic competencies. The space sector is experiencing unprecedented transformation and developments in different countries around the world, since major technological advances put the industry under the spotlight on the global innovation stage. Global competition is increasing with new entrants bringing ambitions and increasing commercial space business, as public and private investors look for new sources of economic growth, especially in the form of diversity and creativity. Space is also contaminated from other sectors and diversity is driving teamwork, business models, and technology approaches. In particular, the EO Small Satellite constellations drive market demands towards Earth Observation information closer to the user needs, instead of traditional images and services. An analysis of the phenomena will be performed in order to highlight the dynamics, trends and future perspectives expected, driven by different forms of innovation and transformative change. Furthermore, it will be addressed how these new phenomena could play a role of a multiplier to create public and private goods and contribute to space economy growth for Europe.

1. INTRODUCTION

1.1 Overview

Space activities are expanding worldwide, with a record number of nations and commercial companies investing in the space programs. Every day, more and more down-to-earth applications are derived from satellites data and space activities, which are contributing to the creation of new economic activities that, more often than not, are overlooked in the initial investments in space infrastructures.

The rise of new space technologies and innovations are attracting attention and larger amounts of total capital, coming both from private and public players. In this context, the space economy is projected to grow and markets to expand, as space activities are becoming more interconnected with terrestrial systems and consumer products. Digitalization is gradually impacting the entire space sector, from newcomers to incumbents, by creating new opportunities and vertical integration of end-to-end systems.

The exploration of space and the use of digital systems have changed the world, society and economy in just one generation by connecting people and things, even though the timing and drivers of these two revolutions have been dissimilar, the resulting organizing synergies allowed the two to reap mutual benefits from each other.

It is important to note that the inclusion of new players in the space market is in an intrinsic relationship with the need to acquire new skills and new technologies: the competition regime involves the constant adoption of new models to survive in an extremely dynamic environment.

* Corresponding author

The constant updating of paradigms and lines of action in the industrial field also involves an increasingly diversified level of innovative skills, both from the technological point of view and from the managerial and communicative point of view.

1.2 Earth Observation and New Space Economy

The momentum of Earth Observation (EO) New Space Economy has been opening doors between public, private actors and investors, space and planet Earth, well-established companies and New Space entrepreneurs, space and non-space industries. Furthermore, as the space sector is transforming, policy makers play an important role in the fostering of innovation and entrepreneurship and ensuring a sustainable and equitable growth. By joining forces, transforming spectators into actors and by extending the economic sphere of Earth into space by removing the finite character of planet Earth, the industry is contributing through diversity to a sustainable future.

Digital revolution is catching up and doing things smarter, better, faster and cheaper. The digital era is based on an exponential growth of information and analysis: more data, coming from increasingly diverse sources are processed more hastily by increasingly efficient algorithms.

The convergence between the economy of data and information, with the age of Artificial Intelligence (AI), data analytics, and machine learning (ML), allows the relevance of the space to become more and more apparent. Since the space sector is the only solution that can provide dependable and inexpensive global coverage, it becomes clear the need to team up with diverse realities to deliver the best outcome possible.

The space sector is recognizing the need to foster more competition and innovation in order to lower the barrier of entry.

2. EO SMALL SATELLITE CONSTELLATION

1.1 EO Market Trend

Historically, the Earth Observation (EO) sector has been financed by governments to provide images for institutions and defence needs. Nowadays, the emergence of big data businesses that added value to images from space, coupled with the rising number of private satellite manufacturers, resulted in the creation of a private sector value chain, intertwined with the public one. As a consequence, EO is currently experiencing a huge change in its core business models, as the ever-improving capabilities and the miniaturization of technologies allowed the convergence of the commercial, military and civilian domains.

This is in stark contrast with the approach of the past, and it is important to understand the role of new and diverse actors in the space sector, which is not just technical and industry-specific, but also socio-economical.

Constellation capabilities are driven from data collection, in as near real time as possible and at low cost, high temporal resolution and reduced latency, components miniaturization, advanced technology solutions for performant & competitive miniaturized payloads and large use of COTS. EO Small Satellites constellations intend to develop application on both "traditional" market and new solutions.

Initially driven by the USA, the small satellite market is becoming global with other established space countries. The small satellite technology adoption has been slow in China, India and Russia due to the availability of domestic launch vehicles, and less pressure has been put on satellite cost and mass reduction efforts. The first small satellite operators emerged in the early 2010. Since then, the value chain has constantly been evolving, with flux of new entrants at all level of the value chain, especially in downstream value-added applications where the greatest activity and revenue generation is happening. The abundance of available data to analyse, coupled with the low capex requirements associated with the software industry, means that this segment of value chain is exploding (Euroconsult, 2020).

In the period 2019-2028, the EO Small Satellite Manufacturing Market (Optical and Radar) target the 1-500kg mass category and the cumulative value is estimated about $9,0 Billion.

The segmentation into mass category are: 1-10 kg (namely CubeSat), 10-50 kg, 50-100kg, 100-500kg with the following percentage:

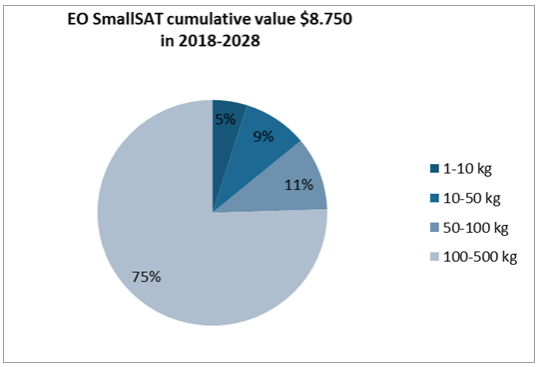

Figure 1. EO Small satellite manufacturing market Value by Mass category (NSR, 2019)

The major part of revenue coming from 100-500kg class and by regions

The Small Satellite Constellation has addressed new ability by creating new use cases. Standardization, miniaturization, COTS HW and electronics integration have played a significant role in enabling at smaller sizes and a fraction of the CAPEX. The small satellite industry tends to favor vertical integration due to of its needs for mass production enabling economies of scale, faster innovation cycles and better supply chain control (Euroconsult, 2020).

The adoption of manufacturing technologies, such as additive manufacturing, to help minimize the costs, mass and number of parts. New solutions for both on board (e.g. on-board processing to reduce the amount of unused data in case of optical instrument) and ground (e.g. cloud-based solutions) have been identified. All these solutions have influenced the price of data/services through a lower-cost approach and potentially disrupting the market, although this market still to be demonstrated.

The operators span from university and research to commercial and government. They have different interest and while the university and research (UPO, University and Public Organisation) invest mainly in research (1-50kg mass category) to test new technologies and materials, the Government and Military are focused 100-500kg due to the higher performance requested. The Commercial is not stable and span in all the categories:

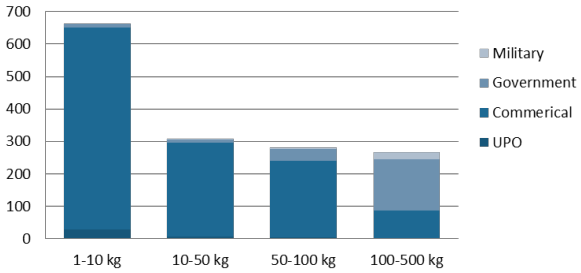

Figure 2. EO Small Satellite to launch by Operator type (NSR, 2019)

Numerous companies have developed satellite solutions, largely based on constellation projects, to deliver better services and reach out to new users. These solutions are supported by new ventures and entrepreneurs investing in the so-called “new space or “adaptive space” environment. Established and emerging government agencies are now endorsing small satellite for operational mission either in single or constellation (Eurosconsult, 2020).

New service areas are emerging based on deriving analytics from vast quantities of multi-sourced data. Operators are sharing agreements with other services provides for which they data can be applied to the services company analytics solutions (Euroconsult, 2020).

The Earth Observation Small Satellite constellations Optical satellites have been present for years, while radar is a more recent phenomenon within the small satellite class.

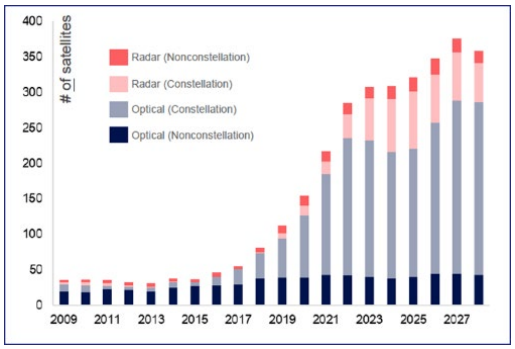

Fig 3. Commercial EO satellite in operation (Euroconsult, 2020)

The growth will be mainly driven by constellation replenishment cycle and new government and military interest from developing regions. EO Small Satellite solutions have a market less-stable because the simpler platforms can compromise accuracy. Radar satellite number estimated in the last decade 2019-2028 foresee an high growth respect to the previous decade. Radar Constellation is estimated to have a boost in growth in the next decade with respect to the optical due to the entering on the market of the new actors for SAR (Synthetic Aperture Radar). There is an increasing awareness on the SAR imagery value, respect to the past, and it is growing the interest on this type of instrument and stimulating the commercial low cost SAR systems. These SAR SmallSAT Constellation cover the whole value chain including new technologies like Cloud Computing and Analytics. Miniaturization of the SAR payload and new constellation will drive for persistence monitoring.

Euroconsult has identified more than 50 companies that have announced intentions to develop such constellations and the most mature initiative are represented by: Planet, BlackSky, CO3D for Optical and Iceye, Capella and Synspective for the Radar (Euroconsult, 2020). The radar recent phenomenon are channelling new approaches by addressing the commercial market based with creativity and diversity in promoting new technologies as shown in their communication on social media (Iceye and Capella YouTube channels). The maturity and status of the initiative already started, and in development, is increasing and it is foreseen to grow within the 2024.

However, it is important to consider how not all these constellations have the same level of maturity and many remain at a very early concept stage (Euroconsult, 2020) and constellations like I-QPS, PredaSAR, UmbraLabs have a low maturity level, with less satellites deployed than announced or only prototypes.

2.2. New Scenario

Future demand for government satellites begins with social needs, as expressed through political priorities for space and related expenditures for civilian as well as military space systems. The “social demand” for space translates differently in established space countries and in emerging space countries. For the countries now committing to space technology development, national prestige and socio-economic development will remain the two main priorities. Small Satellites are easier to finance for emerging countries than traditional satellites, which are larger and more capable (Euroconsult, 2020).

The constellations of Small EO (Earth Observation) Satellites have given rise to important developments in information, data and their distribution, emphasizing trends and playing a key role in changing the face of the satellite sector with access to space made more affordable than ever before.

The new actors are now able to launch their own space programmes, enabled by scientific advances that were previously unimaginable: new companies, like start-ups that initially act as a research laboratory and try to attract funds with their smart approach and more related to real needs, emerging countries for which access to the Small Satellite market is more feasible due to lower costs and lastly scientific institutions that essentially develop CubeSat as study projects in which students can be involved. In the last five years, numerous companies have developed satellite solutions, largely based on constellation projects, to deliver better services and reach out to new users. These solutions are supported by new ventures and entrepreneurs investing in the so-called “new space” or “adaptive space” environment.

The new actors usually bring new approaches prioritizing cost over performance and reliability. The scope is to beam their applications and contents directly to the customer. They also accept higher risk levels to bring costs down, while traditionally, the space industry has been driven by a high quality, high cost, low risk approach.

Private initiatives are emerging rapidly, with some undertaking satellite manufacturing internally because of recurring needs and the creation of partnerships emphasizes this change of landscape. The market is aided by advances in satellite systems miniaturization, permitted by new technologies in space and space-related sectors, particularly in computational technology and data analytics.

Earth Observation constellation targets are based on high revisit acquisition (up to daily), lower data cost and Artificial Intelligence analytics, to build change-detection solutions (Euroconsult, 2020). Advances on the IT (Information Technology) side are allowing for post-processing improvements in image accuracy. Greater emphasis is now on the ground segment, as the lower-cost space segment solutions allow the deployment of applications/services to their customers with great efficiency.

Positioning in such a dynamic and constantly evolving area, was driven by two fundamental factors that have influenced the sustained and rapid changes in new technologies and new models of approach to space: creativity and diversity. They represent two key elements for technological, commercial and economic growth and are the basis of the regime that outlines the space economy today (Nassisi et alter, IAC 2020).

New players, new technologies and new skills require the industry to move at a rapid pace, as it needs to have immediate links and to be able to meet technological and commercial challenges. In this environment, being competitive, means knowing and analysing competitors, exploiting both these two factors.

Global competition in the space arena is constantly growing and public and private investors are looking for economic growth, which translates into the search for talent and creativity. This factor is not only the reason for an economic investment, but it is the element that most conditions the demand in the market and that the most revolutionizes the basic characteristics. Venture capitalists are investing more heavily in the space sector due to the fact that, although it has a high level of risk uncertainty, it also has the potential of positive returns (OECD, 2019).

2.3. New Paradigm

The new paradigms and new approaches have influenced the upstream sector as to guarantee access to the market to new actors. The aim of these new actors is to build a low-cost constellation to provide low-cost and high revisit data for building change detection analytics. The establishment of an effective link and coordination that balances the needs of the downstream sector with the possibilities offered by new technologies in the manufacturing sector is essential.

Diversity is identified in characteristics such as age, gender, sexual orientation, origins, physical abilities but also to the level of education, geography, religion and income. Specifically, the promotion and pursuit of innovation in the field of space necessarily passes by the consideration of skills and experiences completely horizontal, no longer only and exclusively vertical (Nassisi et alter, IAC 2020).

Creativity and diversity are reshaping the way the space industry is presented to the public: the direction in which all companies (both established and start-ups) are pushing is to bring space technologies closer to ordinary people.

The use of social networks in raising brand awareness and giving life to a real narrative regarding the space industry is a key to success in the market: a successful communication combines history, feelings, commitment to a common goal for the good world, heroism and a sense of togetherness.

3. EO SMALL SATELLITE MARKET DYNAMIC

The small satellite market is very lively and experiences significant changes, with new business plans, consolidations among different segment of the value chain, as well as merge and acquisition (M&A) (Euroconsult 2020). The EO market for Small Satellites fits perfectly into these dynamics: continuous technological developments and innovations define the Earth Observation for both optical and radar applications. In the next decade, space market survey reports (NSR 2019) have predicted an increase in satellites for Earth Observation mainly driven from Constellation.

3.1. New system technologies and contamination

Earth Observation's new and low-cost constellation aim is to provide change detection and high temporal resolution. This has been made possible by the advancement of miniaturization permitted by new technologies and advances in contamination with the Information Technologies (IT) sectors with Artificial Intelligence (AI), machine learning (ML), big data and others. The adoption of manufacturing technologies, such as additive manufacturing, to help minimize the costs, mass and number of parts. Improving the performance of a payload may impact the design of the spacecraft and the cost. For example for radar constellation, to face competition and respond to customer demand, Capella decided to increase its antenna aperture to reach 25cm resolution, increasing the mass from 40kg to 100kg, while for optical constellation Planet lowered the altitude of Skysats by 100km, increasing resolution from 72cm to 50cm but decreasing lifetime or increasing the number of bands for Dove (from 4 band to 8band) to increase value to market such as agriculture (Euroconsult, Nov 2020).

New solutions for both on board (e.g. on-board processing to reduce the amount of unused data in case of optical instrument) and ground (e.g. cloud-based solutions) have been identified. For example in some case on board processing capabilities are implemented to reduce the amount of unused data. These capabilities are mainly implemented for optical payload and the AI (artificial intelligence) algorithm on board will allow to discharge the data affected from cloud coverage. Other approach foresee the use of miniaturisation technologies not always applicable for all payload type.

All these solutions have influenced the price of data/services through a lower-cost approach and potentially disrupting the market, although this market still to be demonstrated.

The manufacturing sector is also affected in this area by very fast innovation cycles, as a result of the rhythms imposed by the market and which require up-to-date and innovative skills and efficiency. In this area, given the elements of the market, start-ups proliferate and they are expected to proliferate in the future, which with their intrinsic characteristics increase the number of new entrants in the market (Euroconsult, 2020).

The technical advancement are expanding the mission capability of the small satellite, making them more resilient, effective and a lower cost asset.

Large satellite still remain competitive in very high performance and life time (by reducing replacements cycle time). The small satellite life time span from 3 to 5 time shorter than for traditional satellites, so the launch rate is higher to maintain nominal operations and also the replenishment cycle is part of the strategy to incrementally improve the system performance.

3.2. New Business Model

From hardware building and integration to satellite operations, ground stations and analytics, the small satellite ecosystem is maturing and evolving. While some companies are establishing niches and specialising, others move into the “Small satellites as Services” (SaaS) business model. The increased accessibility is beneficial to new entrants to the space sectors as the SaaS business model remove complexity and barriers to entry. Additionally, this granularity offers transparency over the value chain which improve the confidence of industry outsiders and customer to step out of the satellite value chain. While SaaS may not meet the needs of all customers at all time and it addresses the most common market needs (Euroconsult, 2020)

The key success factor for this type of solution is to capture government clients as "anchor tenancy" and other commercial partnerships with the aim to develop vertical markets incentivized by their revisit capability and advanced analytics and the selection of more profitable applications as well. It seems necessary for the years to come to *“strengthen the ecosystem of public support mechanisms by introducing more flexibility and more commercial orientation*”(de Concini, 2019).

The Big Data segment (e.g. financial services and market intelligence) in the Earth Observation industry is the fastest growing sub-segment, wherein satellite operators and analytics providers push to derive deeper actionable insights for their end customers.

The private sector and the Small Satellites Earth Observation market in Europe, although not as developed as the one in the USA, is already flourishing: what an innovative and dynamic market, such as the Small Satellites operating in Earth Observation, can offer, through horizontal skills is the ability to meet social and commercial needs and demand for different developments and applications in society.

4. CONCLUSIONS

The new models and new dynamics that are realized with these assumptions in the market of Earth Observation have a formidable impact not only in the economic increase but also in an implementation and a transformation of the services coming from the data that can benefit and be a help to society.

Indirect value and benefits in space applications can arise from those characteristics and values of diversity and creativity that determine the ability of the market and the Earth Observation environment to be a vehicle for well-being and to be an improvement for life in societies, primarily European.

In conclusion, an effective link between upstream and downstream is needed in order to unleash all the indirect effects and potential from the new models of the space market.

REFERENCES

NSR “Small Satellites Markets” 6th edition, November 2019.

A. Nassisi, I.Patatti, “Role of women in the New Space Economy Environment as Game Changers and Innovators”, NSE Forum 2019

Euroconsult “Prospects for the Small Satellites Market. A Global Supply and Demand Analysis of Government and Commercial Satellites up to 500kg”, 6th edition, July 2020.

Euroconsult “Earth Observation Satellite Systems Market”, 13th edition, November 2020

de Concini A., Toth J., “The Future of the European Space Sector. How to Leverage Europe’s Technological Leadership and Boost Investments for Space Ventures”, European Investment Bank, 2019.

Nassisi A., Patatti I., “Entrepreneurship and a Diversity Approach to Space Economy”, 71st International Astronautical Congress (IAC) – The CyberSpace Edition, 12-14 October 2020.

OECD “The Space Economy in Figures. How Space Contributes to the Global Economy”, 2019.

PWC “Main trends and Challenges in the Space Sector” 2nd edition, December 2020

Il Sole 24 Ore “Lo Spazio Centrale per la Terra più Sostenibile. Noi Portabandiera dell’Ecosistema Italiano” March 2021.

Webinar European Parliament “Il Nuovo Programma Spaziale Europeo: Autonomia strategica e opportunità per l’industria e la competitività”, ww.FASI.biz, 2021.

Iceye youtube page:
https://www.youtube.com/channel/UC1QbqV9V2z-Z7A1SY4oOkLA
Capella Space youtube page:
https://www.youtube.com/channel/UC96FAnsH2F3lTEDSXOgYlPA

EXPLORING POTENTIALITIES OF THE NEW "REMOTE SENSING PIEMONTE" OPEN SERVICE FOR AGRO-FORESTRY APPLICATIONS

E. Borgogno-Mondino *, F. Sarvia , S. De Petris

Department of Agricultual, Forest and Food Sciences, University of Turin, L.go Braccini 2, Grugliasco 10095, Italy - (samuele.depetris, filippo.sarvia, enrico.borgogno)@unito.it

KEY WORDS: Piemonte Region Geoportal, Sentinel 2, Services, Progetto Telerilerilevamento Piemonte, spectral indices, temporal profiles

ABSTRACT:

The Copernicus program has made publicly available data from several constellations of Earth Observation satellites. Among them, data from the Sentinel 2 (S2) constellation, available since autumn 2015, represent a useful information asset for medium-scale surveys (1:50000-1:25000 map scale). S2 technical features (geometric, spectral and temporal resolutions) make it a valuable support for several environmental applications involving land analysis/monitoring. In this framework, the Agriculture and Forestry Offices of the Piemonte Region (NW-Italy) administration, have supported a specific project named "Remote Sensing Piemonte" that was implemented by the CSI-Piemonte company with the scientific supervision of the Agro-Forestry Geomatics Research Group (GEO4Agri) of the University of Torino. The project was aimed at supporting technological transfer of Copernicus Sentinel 2 data and, in particular, at making not-skilled users closer to this type of technology. The final output was a freely accessible and usable web based service providing ready-to-use composite products with a regional coverage; namely: true and false colour RGB composites and monthly composite maps of spectral indices (NDVI, NDWI, EVI, NBR). These outputs can be accessed, navigated and queried by standard geo-services (WMS) or by a dedicated webGIS application, included the extraction of spectral indices temporal profiles. In this work, some case studies concerning possible exploitations of this type of service are exemplified with special concerns about operative issues that agro-forestry users (i.e. regional technicians, environmental agency, farmers, agricultural consortia, agricultural insurances companies and agronomist/foresters) can be interested in.

1. INTRODUCTION

The EU Copernicus Program has, in fact, made publicly available data from several constellations of Earth Observation satellites. Out of them, data from Sentinel 2 constellation (S2), available since autumn 2015, represent a useful information asset for medium-scale surveys (typically ranging between 1:50000-1:25000 map scales). S2 technical features (geometric, spectral and temporal resolutions) make it a valuable support for several environmental applications involving land analysis/monitoring. In particular, its temporal resolution (5 days) allows a continuous monitoring of large area. This feature is particularly useful while working with vegetation, whose dynamics determine changes in its spectral properties along the year. Human management can also induce significant changes both in time and space domains. S2 mapping capability is therefore an effective tool to detect spectral anomalies that can support local institutions in their monitoring analysis and corroborating deductions for administrative procedures purposes. Unfortunately, technological transfer appears to be still limited, but the development of services based on these data is moving to be an actual scenario (De Petris et al., 2019, 2020, 2021; Sarvia et al., 2019, 2020a). In this context, the complexity of remotely sensed data pre-processing is one of the main reasons for its slow uptake by geomatics non-skilled users like institutional technicians, agronomists, foresters and farmers. From this point of view, pre-processed products coupled with a web-based platform should allow an immediate access to images making users able to directly focus on the required information. Within this framework, in 2019, the Piemonte Region (NW Italy) administration launched a project for the preparation and supplying, through its cartographic Geoportal, of semi-finished products obtained from the S2 data. The explicit project goal, consistent with the expectations about the technological transfer of these data by the Copernicus Program of the European Union, was to attract users making S2 images more familiar and immediately usable through a web-based service. The latter was intended for different users, mostly coming from regional offices dealing with territorial issues. It was imagined that various tasks, requiring continuous cartographic updating and needs for monitoring, could benefit from the use of such service (e.g. monitoring or control of agricultural crops, soil consumption, forest cuts, forest fires and flood events, etc.). Accordingly, the "Remote Sensing Piemonte" project was launched, whose data and services have been made freely available to users from October 2020 in a dedicated section of the Piemonte Geoportal: www.geoportale.piemonte.it/cms/progetti/telerilevamento-piemonte. The initiative was promoted, and largely supported, by both the Department for Agriculture and the Department for Environment, Energy and Territory of the Piemonte Region administration. CSI Piemonte company was in charge of supplying technical support for the implementation of the system, while the Agro-Forestry Geomatics Research Group (GEO4Agri) from the Department of Agricultural, Forestry and Food Sciences of the University of Torino, scientifically supervised the whole project.

The proposed system relies on S2 multispectral data that, depending on the band (ranging between 400-2500 nm), are acquired with a geometric resolution varying between 10 and 60 m; temporal resolution (nominal acquisition frequency) is 5 days. The developed system makes use of automatic data download services from the Copernicus EU archive (Open Hub) and implements automatic image processing procedures aimed at generating semi-finished products, such as monthly composite maps of spectral indices and true and false color RGB composites

* Corresponding author

with a regional coverage. Outputs can be managed by standard geo-services (WMS) or by a dedicated webGIS application. Geographic interoperability of WMS made also possible the development of a specific application for the interactive query of temporal profiles from spectral indices monthly time series, permitting their presentation as graphs.
In this work, some case studies concerning possible exploitations of this type of service are exemplified with special concerns about operative issues that agro-forestry users (i.e. regional technicians, environmental agency, farmers, agricultural consortia, agricultural insurances companies and agronomist/foresters) can be interested in.

2. MATERIALS AND METHODS

The service makes use of data from the Copernicus Open Hub (https://scihub.copernicus.eu/userguide/5APIsAndBatchScripting) that are obtained through dedicated API (Application Programming Interface) continuously feeding the service. The system relies on the S2MSI2A product (Level 2A) that is supplied already ortho-projected into the WGS-84 UTM 32N coordinate system and radiometrically calibrated in at-the-ground reflectance. The whole regional coverage requires a total of 12 tiles (downloading unit covering an area of 100 x 100 km) to be processed for each acquisition date. Images are continuously downloaded, stored and processed by the system to generate ready-to-use semi-finished products. Two products types are currently generated by the system and made accessible through both WMS and webGIS application: (a) a monthly time series of composite spectral index maps (table 1); (b) trimestral true and false colour composites.

Table 1. Spectral Indices that are currently generated and exposed by the system as monthly composite maps with regional coverage (b = band).

Index	Formula	Reference
NDVI	NDVI= (b8-b4)/(b8+b4)	(Rouse et al., 1974)
EVI	EVI=2.5· (b8-b4)/(b8+6·b4-7.5·b2+1)	(Karnieli et al., 2010)
NBR	NBR= (b8-b12)/(b8+b12)	(Chen et al., 2011)
NDWI	NDWI= (b3-b11)/(b3+b11)	(Zhang et al., 2012)

Spectral index composites were designed to ensure, once a month, cloud free conditions for all the pixels of the scene. This is obtained by exploring all acquisitions operated in the considered month. For each pixel, a different date can be selected as the one to be used within the composite. The proper date is chosen, at pixel level, looking for the one contemporarily showing a “good” code in the SC (Scene Classification) layer (supplied with the L2A product) and presenting the monthly highest NDVI value. SC codes are reported in table 2. The “good” ones correspond to the 2,3,4,5,6,7,11 values. The NDVI maximum value found in the processed month for every pixel of the scene becomes the driver for all the following computations concerning other indices at that position.
Proposed indices were selected according to the expected application fields that were remarked by the potential users caming, first of all, from the regional administration. One of their priorities was an index able to describe vegetation cover/status and, consequently, to assess biomass phenology and conditions.

Table 2. SC layer codes.

Class code	Description	Class code	Description
0	No Data	6	Water
1	Saturated or defective	7	Unclassified
2	Dark areas	8	Cloud medium probability
3	Cloud shadows	9	Cloud high probability
4	Vegetation	10	Thin Cirrus
5	Not-vegetated	11	Snow

For this task, the Normalized Difference Vegetation Index (NDVI, Rouse et al., 1974) was selected as representative of a wider family of vegetation indices (VI). NDVI is known to be suitable to characterize canopy and vegetation vigour in the agricultural and forestry context (Sripada et al., 2005) and many studies show its high correlation with Leaf Area Index (LAI) (Wang et al., 2005; Zhang et al., 2012). Additionally, EVI was also considered to take care about extreme situations where vegetation canopy was highly dense or, conversely, where it alternated to a background with a pattern smaller than pixel geometric resolution (mixed pixels). EVI, in fact, appears to be less sensitive to saturation problems over dense canopies (Hufkens et al., 2012) and to reduce the influence of background and atmosphere (Xiao et al., 2003).
Regarding the identification and monitoring of forest burnt areas, the main VI, according to literature, appears to be the Normalized Burn Ratio (NBR) (Chen et al., 2011; Escuin et al., 2008). NBR is ordinary computed combining the near infrared and mid-infrared regions (Filipponi, 2018; Quintano et al., 2018). The analysis of burned areas should typically follow two approaches, the first one take in consideration the first good (cloudless) image after the fire event (M. J. L. García and Caselles, 1991) , while the second one follows a multi temporal approach (Heredia et al., 2003), resulting in the difference between two images pre and post fire.
Concerning NDWI, also known as NDSI (Normalized Difference Snow Index (Hall et al., 2002), it was selected to support snow/ice–related and water quality-related applications, that are mandatory for a region that is significantly covered by mountains (Alps) and lakes.
As far as RGB colour composites are concerned, they were generated by mosaicking the 12 "best looking" (minimum cloud cover) images, acquired in the considered trimester, correspondent to the S2 tiles covering the area. Currently, the available RGB composites are the following: a) R = band4 (red), G = b3 (green), B = band2 (blue) intended for true color; b) R = b8 (NIR), G = b4 (red), B = b3 (green) intended for vegetation analysis; c) R = b8 (NIR), G = b11 (SWIR1), B = b4 (red) intended for agronomic and pedological applications. Both products can be accessed by a dedicated web-based interface that allows the visual inspection of images and the extraction/visualization of spectral index temporal profiles. These can concern both polygon, or point, geometrical features that the user can interactively draw or import (Geojson format) onto the scene. With special concern about the possibility of easily extract and download these profile for application purposes, the system offers the possibility of downloading as text files.
In this framework, the present work present some operational and immediately achievable applications that the system outputs can users to efficiently face: a) forest fire detection; b) detection and characterization of summer, winter and permanent agricultural crops; c) detection of crop damages from hailstorm; d) forest harvesting detection and characterization.

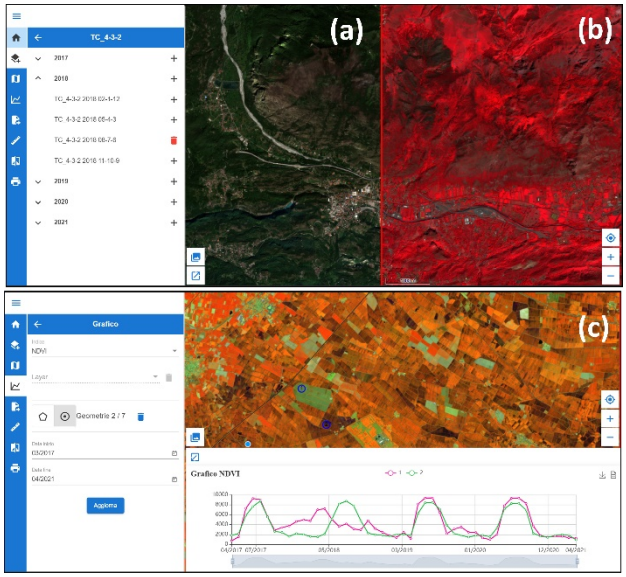

Figure 1. (a) True colour image (R:b4, G:b3, B:b2); (b) False colour image (R:b8, G:b4, B:b3); (c) NDVI temporal profile from two points corresponding to crop fields.

Examples will be faced with reference to different study areas that were preliminary mapped through vector polygon layers. These were therefore imported into the system in GeoJson format georeferenced into the geographic WGS84 reference frame.

Using system capabilities, the correspondent averaged VI temporal profiles were extracted and downloaded as .csv text files. The observation time range and the selected spectral index are reported, for the 4 examples, in Table 2.

Application	Index	Period
Forest fire detection	NBR	04/2017-12/2018
Phenological analysis of agricultural crops	NDVI	11/2019-12/2020
Detection of hailstorm event	NDVI	01/2019-12/2019
Detection and characterization of forest harvesting	NDVI	01/2019 -12/2020

Table 2. Applications reported in this work demonstrating effectiveness of the data supplied through the Remote Sensing Piemonte Service.

For each profile and according to the correspondent application, an interpretation was given trying to make explicit the operational meaning of this type of information. The goal is not providing a scientifically sounding case study, but making unskilled users closer to this technology, offering some interpretation keys that can activate their interest longing for the maximisation of the use of such valuable public service.

Reference Data

Forest fires detection was exemplified with reference to the fire occurred in the Susa Valley (Piemonte Region, NW Italy) in October 2017. From the regional forest fires database (http://www.sistemapiemonte.it/montagna/incendi/cartografiaIncendi.shtml) a vector map was downloaded containing two areas: one run by fire and one unburned, sizing 23 ha and 8.5 ha respectively (Fig. 2a).

The example concerning detection and characterization of crops, was achieved using a vector map provided by the Piemonte Agency for Payments in Agriculture (ARPEA), locating one reference field for each investigated crop category. A single field was used as representative of the correspondent category. Wheat, corn and meadow reference fields, sizing 1.7 ha, 1.4 ha and 0.5 ha respectively, were used as paradigms for the winter, summer and permanent crop categories (Fig. 2b).

Regarding hail effects monitoring the Reale Mutua insurance company provide a vector map representing few reference fields affected by a hail event occurred in Vercelli province (Piemonte - NW Italy) on 6th July 2019 (Sarvia et al., 2020b). In particular a corn field damaged (in the municipality of Vercelli) and one undamaged (in the municipality of Borgo Vercelli) were considered in this context, sizing about 8.5 ha and 4.5 respectively (fig. 2c).

Finally, for how to concern reference data about the detection and characterization of forest harvesting were provided by the High Susa Valley Forest Consortium. In particular, two forest areas were analyzed, one cut in winter 2019 and the other not, sizing 1.9 ha and 1.7 respectively (Fig. 2d).

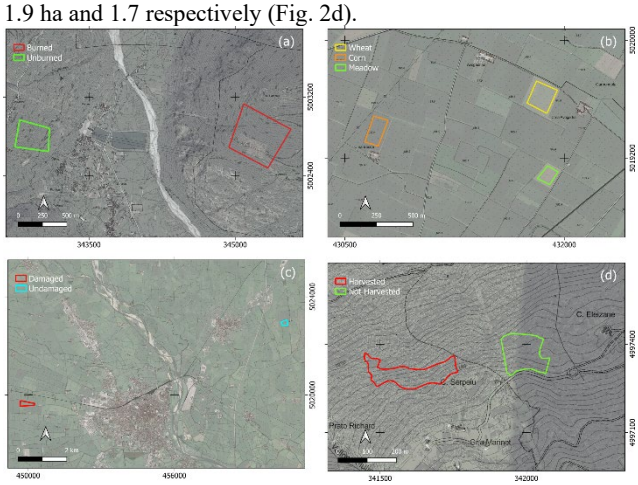

Figure 2. Sample areas. (a) Burnt/Unburnt areas; (b) Crop fields; (c)Hail damaged/undamaged fields; (d) harvested/not-harvested areas.

3. RESULTS AND DISCUSSIONS

As far as forest fires-related application is concerned NBR temporal profiles of burned and unburned areas as obtained from the regional service were graphically compared (Figure 3a). It can be, immediately, noted that in October 2017 NBR value of burned areas rapidly decreased; in these areas, in the following phenological season (2018) the NBR profile remained flat, while unburned areas continued their ordinary trend.

As far as crop detection is concerned, it can be noted that the NDVI temporal profile of summer, winter and permanent crops can represent a robust discriminant whereas one intends to operate a crop classification (figure 3b). Assuming that the yearly phenological season starts when NDVI > 0.4 it can be observed that corn shows a summer development (April-September) that is consistent with the local agronomical calendar (Sarvia et al., 2021). Differently, wheat shows a development occurring in winter-spring time (January-June). Meadow, being a permanent crop, defines a NDVI temporal profile having small variations and always remaining over 0.5 along the year.

It can be noted that these monthly-aggregated temporal profiles can only provide an overall description of the main phenological trend. This makes possible to map crop types in a classification context; conversely, it is not suitable for monitoring purposes aimed at a precision farming approach for crop management.

With respect to crops damage assessment by hail, NDVI temporal profiles of a damaged and not-damaged corn fields were compared (Figure 3c) and an interpretation given about the hail storm occurred in the area in July 2019. A significant impact was

observed conditioning damage crop development. In figure 3c it can be noted that after the event, the NDVI profile of the undamaged field regularly continues its development up to reaching values higher than 0.8 according to maize development calendar (May - September). Differently, the damaged field, after the event showed lower NDVI values slightly higher than 0.5, confirming that its growing was somehow interrupted and making probable, there, a yield loss at the end of the season.
Finally, focusing on forest harvesting, two consecutive phenological seasons were analysed by comparing the behaviour of an harvested and a not-harvested area (figure 3d). Since tree cuts ordinarily are done in winter, no sudden and immediate significant change can be observed in the correspondent NDVI profile. Conversely, comparing NDVI profiles from harvested and not-harvested areas in the vegetative period following the cut it can be noted that two phenological "bells" are present, where the one related to the harvested area remain lower than the one from undamaged fields. This typical trend, supports the hypothesis that forest disturbance occurred during winter. In spite of these simple considerations, the tool appears to be an immediate and user-friendly support for regional forest technicians. Especially when looking for illegal forest harvesting, the service makes possible to focus ground controls onto a limited number of candidate areas possibly located with these type of data.

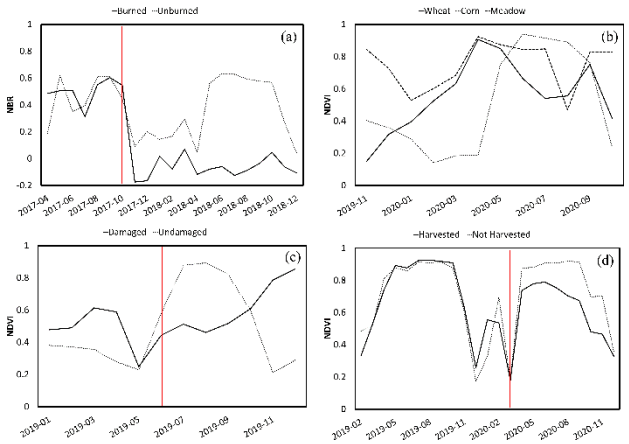

Figure 3. Spectral indices time series for the sample polygons. (a) NBR profiles for burnt/not-burnt areas (red line = fire occurrence); (b) NDVI profiles for damaged/undamaged maize fields during their 2019 growing season (red line = hailstorm occurrence); (d) NDVI profiles for harvested/not-harvested forest areas.

4. CONCLUSIONS

In this work, the public web-based service named "Remote Sensing Piemonte", made available through its institutional geoportal by the Piemonte Region administration, was preliminary tested to show its potentialities for operational purposes mainly related to regional technicians needs. In particular, with reference to 4 tasks, the possibilities offered by the multi-temporal spectral index profile extractor tool were discussed. Results are promising and the expectation is that the tool could enter ordinary workflow that regional administration have to supply to citizens.

ACKNOWLEDGEMENTS

We would like to thank Dr. Evelyn Joan Momo for providing data and valuable tips about local forest information.

REFERENCES

Chen, X., Vogelmann, J.E., Rollins, M., Ohlen, D., Key, C.H., Yang, L., Huang, C., Shi, H., 2011. Detecting post-fire burn severity and vegetation recovery using multitemporal remote sensing spectral indices and field-collected composite burn index data in a ponderosa pine forest. Int. J. Remote Sens. 32, 7905–7927.

De Petris, S., Berretti, R., Guiot, E., Giannetti, F., Motta, R., Borgogno-Mondino, E., 2020. Detection And Characterization of Forest Harvesting In Piedmont Through Sentinel-2 Imagery: A Methodological Proposal. Ann. Silvic. Res. 45, 92–98.

De Petris, S., Boccardo, P., Borgogno-Mondino, E., 2019. Detection and characterization of oil palm plantations through MODIS EVI time series. Int. J. Remote Sens. 1–15.

De Petris, S., Sarvia, F., Gullino, M., Tarantino, E., Borgogno-Mondino, E., 2021. Sentinel-1 Polarimetry to Map Apple Orchard Damage after a Storm. Remote Sens. 13, 1030.

Escuin, S., Navarro, R., Fernández, P., 2008. Fire severity assessment by using NBR (Normalized Burn Ratio) and NDVI (Normalized Difference Vegetation Index) derived from LANDSAT TM/ETM images. Int. J. Remote Sens. 29, 1053–1073.

Filipponi, F., 2018. BAIS2: Burned Area Index for Sentinel-2. Proceedings 2, 364.

García, M.J.L., Caselles, V., 1991. Mapping burns and natural reforestation using thematic Mapper data. Geocarto Int. 6, 31–37.

Hall, D.K., Riggs, G.A., Salomonson, V.V., DiGirolamo, N.E., Bayr, K.J., 2002. MODIS snow-cover products. Remote Sens. Environ., The Moderate Resolution Imaging Spectroradiometer (MODIS): a new generation of Land Surface Monitoring 83, 181–194.

Heredia, Á., Martínez, S., Quintero, E., Piñeros, W., Chuvieco, E., 2003. Comparación de distintas técnicas de análisis digital para la cartografía de áreas quemadas con imágenes LANDSAT ETM+. GeoFocus Rev. Int. Cienc. Tecnol. Inf. Geográfica 216–234.

Hufkens, K., Friedl, M., Sonnentag, O., Braswell, B.H., Milliman, T., Richardson, A.D., 2012. Linking near-surface and satellite remote sensing measurements of deciduous broadleaf forest phenology. Remote Sens. Environ., Remote Sensing of Urban Environments 117, 307–321.

Karnieli, A., Agam, N., Pinker, R.T., Anderson, M., Imhoff, M.L., Gutman, G.G., Panov, N., Goldberg, A., 2010. Use of NDVI and Land Surface Temperature for Drought Assessment: Merits and Limitations. J. Clim. 23, 618–633.

Quintano, C., Fernández-Manso, A., Fernández-Manso, O., 2018. Combination of Landsat and Sentinel-2 MSI data for initial assessing of burn severity. Int. J. Appl. Earth Obs. Geoinformation 64, 221–225.

Rouse, J.W., Haas, R.H., Schell, J.A., Deering, D.W., Harlan, J.C., 1974. Monitoring the vernal advancement and retrogradation (green wave effect) of natural vegetation. NASAGSFC Type III Final Rep. Greenbelt Md 371.

Sarvia, F., De Petris, S., Borgogno-Mondino E., 2020a. Multi-scale remote sensing to support insurance policies in agriculture: from mid-term to instantaneous deductions. GIScience Remote Sens. 57, 770–784.

Sarvia, F., De Petris, S., Borgogno-Mondino, E., 2020b. A Methodological Proposal to Support Estimation of Damages from Hailstorms Based on Copernicus Sentinel 2 Data Times Series, in: International Conference on Computational Science and Its Applications. Springer, pp. 737–751.

Sarvia, F., De Petris, S., Borgogno-Mondino, E., 2019. Remotely sensed data to support insurance strategies in agriculture, in: Remote Sensing for Agriculture, Ecosystems, and Hydrology XXI. International Society for Optics and Photonics, p. 111491H.

Sarvia, F., Xausa, E., Petris, S.D., Cantamessa, G., Borgogno-Mondino, E., 2021. A Possible Role of Copernicus Sentinel-2 Data to Support Common Agricultural Policy Controls in Agriculture. Agronomy 11, 110.

Sripada, R.P., Heiniger, R.W., White, J.G., Weisz, R., 2005. Aerial Color Infrared Photography for Determining Late-Season Nitrogen Requirements in Corn. Agron. J. 97, 1443–1451.

Wang, Q., Adiku, S., Tenhunen, J., Granier, A., 2005. On the relationship of NDVI with leaf area index in a deciduous forest site. Remote Sens. Environ. 94, 244–255.

Xiao, X., Braswell, B., Zhang, Q., Boles, S., Frolking, S., Moore, B., 2003. Sensitivity of vegetation indices to atmospheric aerosols: continental-scale observations in Northern Asia. Remote Sens. Environ. 84, 385–392.

Zhang, B., Wu, D., Zhang, L., Jiao, Q., Li, Q., 2012. Application of hyperspectral remote sensing for environment monitoring in mining areas. Environ. Earth Sci. 65, 649–658.

Planet Care from Space

Edited by Dessena M.A., Melis M.T and Rossi P. "***Planet Care from Space***" is the second volume of "***Trends in Earth observation***", a series published by the Italian Society of Remote Sensing (AIT).
This volume, organized in 7 thematic chapters, includes 45 contributions.

Edited by Dessena M.A, Melis M.T. and Rossi P.

Maria Antonietta Dessena works at the Regional Water Agency where (Enas) and she deals with the management and monitoring of water resources also by advanced technologies. She promote international cooperation projects for the use and enhancement of water resources at national and international level within the framework of APQ, ENI CBCMED, Horizon2020, etc. She was researcher at CORISA until 1993. This last two years she is responsible of PRIMEWATER projects within the Horizon2020 program on the theme of water quality assessment and short-term forecasts with the help of remote sensing and the MEDISS ENI CBCMED project. He has taught on remote sensing in numerous courses including FAO and UNESCO and from 2000 to 2003 as Professor in charge of the course of Remote Sensing at the University of Sassari. She is a member of AIT Association since 1986 and she is a member of the Board on AIT and on the ASITA Scientific Council. She is the author of more than 90 publications and co-author of book.

Maria Teresa Melis, graduated in Geology on 1985, PhD in Remote Sensing application to arid and semiarid geomorphological mapping. She is professor in Geomatics, and responsible for the TeleGIS Remote Sensing Laboratory, at the University of Cagliari, Italy. She was vice- President of the Italian Association of Remote Sensing and actually she is co-chair of the III Commission "Remote sensing" in ISPRS (International Society for Photogrammetry and Remote Sensing), Thematic Information Extraction. Member of the Scientific Council of ASITA (Federation of Italian Scientific Associations in Environmental and Land Information). Her research focuses on remote sensing applied to geological, land cover, and geomorphological analysis in remote areas (cold and hot arid lands), publishing +100 papers and contribution in books.

Patrizia Rossi is a permanent technologist since 2012 at the Department of Agriculture, Food, Environment and Forestry (DAGRI) at University of Florence
She graduated at the University of Florence where she obtained a Bachelor's Degree in Forest Science.
To date she deals with the technical management of the Geomatics Laboratory (geoLab) and she is involved in various projects on the use of Remote Sensing and GIS data. She is the Editorial Office Administrator of the European Journal of Remore Sensing, the internazional journal published by Taylor&Francis on behalf of AIT

ISSN 2612-7148

ISBN 978-88-944687-0-0